

**Physics of transition metal chalcogenides based on  
deeper investigation of their phase-diagram and crystal  
growth mechanism**

by

**Monika  
10PP17A26045**

A thesis submitted to the  
Academy of Scientific & Innovative Research  
for the award of the degree of  
DOCTOR OF PHILOSOPHY  
in  
SCIENCE

Under the supervision of  
**Dr. Pankaj Poddar**



**CSIR-National Chemical Laboratory, Pune**

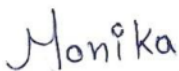


Academy of Scientific and Innovative Research  
AcSIR Headquarters, CSIR-HRDC campus  
Sector 19, Kamla Nehru Nagar,  
Ghaziabad, U.P. – 201 002, India

**May, 2022**

## Certificate

This is to certify that the work incorporated in this Ph.D. thesis entitled, “Physics of transition metal chalcogenides based on deeper investigation of their phase-diagram and crystal growth mechanism”, submitted by Monika to the Academy of Scientific and Innovative Research (AcSIR), in partial fulfillment of the requirements for the award of the Degree of Doctor of Philosophy in Science, embodies original research work carried-out by the student. We further certify that this work has not been submitted to any other University or Institution in part or full for the award of any degree or diploma. Research material(s) obtained from other source(s) and used in this research work has/have been duly acknowledged in the thesis. Image(s), illustration(s), figure(s), table(s) etc., used in the thesis from other source(s), have also been duly cited and acknowledged.



**(Signature of Student)**

Monika

04.05.2022



**(Signature of Supervisor)**

Dr. Pankaj Poddar

04.05.2022

## **STATEMENTS OF ACADEMIC INTEGRITY**

I, Monika, a Ph.D. student of the Academy of Scientific and Innovative Research (AcSIR) with Registration No. 10PP17A26045 hereby undertake that the thesis entitled “Physics of transition metal chalcogenides based on deeper investigation of their phase-diagram and crystal growth mechanism” has been prepared by me and that the document reports original work carried out by me and is free of any plagiarism in compliance with the UGC Regulations on “*Promotion of Academic Integrity and Prevention of Plagiarism in Higher Educational Institutions (2018)*” and the CSIR Guidelines for “*Ethics in Research and in Governance (2020)*”.

Monika

**Signature of the Student**

Date: 04.05.2022

Place: Pune

---

It is hereby certified that the work done by the student, under my/our supervision, is plagiarism-free in accordance with the UGC Regulations on “*Promotion of Academic Integrity and Prevention of Plagiarism in Higher Educational Institutions (2018)*” and the CSIR Guidelines for “*Ethics in Research and in Governance (2020)*”.

Pankaj

**Signature of the Supervisor**

Name: Dr. Pankaj Poddar

Date: 04.05.2022

Place: Pune

*Dedicated to*  
*my world,*  
*my parents Santosh &*  
*Kailash Ghalawat*  
*&*  
*The almighty God*

## ACKNOWLEDGEMENTS

*I thank God for making my life so wonderful, giving me this chance, and giving me the capacity to succeed.*

*There are so many people whose support, encouragement, and inspiration are very much necessary to fulfil my cherished dream. For me, this thesis is such an important destiny, and I am indeed indebted to many people for their wishes and blessings in completing this journey. I take this opportunity to acknowledge and extend my sincere gratitude to all these people who have been involved, directly or indirectly, in making the research work described in this thesis possible.*

*First and foremost, I would like to express my sincere gratitude to my mentor Dr. Pankaj Poddar for introducing me to this exciting interdisciplinary science field and for his dedicated help, advice, inspiration, encouragement, and continuous support throughout my Ph.D. His enthusiasm, integral view on research, and mission to provide only high-quality work and not less have made a deep impression on me. During the last more than 4 years from his interactions, I have learnt extensively from him, including how to raise new possibilities, regard an old question from a new perspective, approach a problem by systematic thinking, data-driven decision making, and exploiting serendipity. I owe him lots of gratitude for having me shown this way of research. He constantly emphasizes on inculcating the habit of critical thinking and teaches us about dos and don'ts in science and life. Apart from this, I admire his way of teaching, where he starts from a basic level and move towards an advanced level to make any topic crystal clear and simpler. His knowledge in every subject has impressed me a lot. I feel fortunate and privileged to be associated with him and part of his research group.*

*I would also like to thank my doctoral advisory committee members, Dr. B L V Prasad, Dr. T. G. Ajithkumar, Dr. Shubhangi B. Umbarkar, and Dr. D. S. Reddy for their time, constructive suggestions, guidance, and support. I owe a great deal of appreciation and gratitude to my external expert Dr. P.K. Khanna, DIAT Pune, for evaluating my work in my up-gradation meetings. I warmly thank him for his precious time, advice, and discussion on my work.*

*I extend my sincere thanks to the present Director of CSIR-NCL Dr. Ashish Lele, and Dr. Ashwini Kumar Nangia (former Director), for giving me an opportunity to work in this prestigious institute and making the facilities available to carry out the research. I am also grateful to the Head of Physical and Materials Chemistry Division, Dr. T. Ajithkumar, Dr. P. A. Joy (former HoD), and Dr. B. L. V. Prasad (former HoD) for their kind help during the course of my Ph.D. Many thanks to the staff members of our division, who have helped me with the routine official work. I wish to thank all the administrative and*

*non-teaching staff of CSIR-NCL for their kind support and assistance over the years on various occasions.*

*I am also grateful to many people in the Center for Materials Characterization division, NCL, who have assisted me during my tenure. My sincere thanks to Mr. S. S. Deo, Mr. R. S. Gholap, Venkatesh, Sheetal, Chetan and Harsha for their timely help in XPS, TEM, and SEM measurements. I would also like to thank Dr. Suresh Gokhale and Dr. Rupali Waichal ma'am, for providing access to the Raman instrument.*

*My special thanks to Dr. Rajesh Gonnade for his teaching on the XRD subject in the course work; the knowledge he shared was outstanding and helped me throughout my research work. Many thanks for explaining the space groups. I want to express my deepest gratitude to Dr. Guruswamy Kumaraswamy, IIT Bombay for his teaching on SAXS in the course work. He also provided WAXS, which helped to start my research in the initial days of Ph.D.*

*I am also grateful to my collaborators for introducing me to the interdisciplinary science— Dr. Chinnakonda S. Gopinath (NCL) for introducing me to the catalysis field, Dr. Virendra Kumar Meena (NIV) and Dr. Atanu Basu (NIV) for giving me the opportunity to explore the biophysics field.*

*I am grateful to the University Grants Commission (UGC), India, for providing me with the necessary funding and fellowship to pursue research at NCL.*

*I also take an opportunity to thank my seniors from the lab, Dr. Puneet Khandelwal, Dr. Mousumi Sen, Dr. Preeti Padhye. However, they had moved away from NCL when I joined the lab, but the surprise meetings with them have inspired me to do well in science. I will always remember the experiences they've shared, and I hope to stay in touch with them.*

*I also thank postdoc seniors from our lab Dr. Geeta Sharma, Dr. Chiti Tank, Dr. Manorama lakhe, Dr. Subodh Gautam (special thanks bhaiya for giving me the best advice for PhD), and Dr. Bhavana Joshi (special thanks di for being so kind), for the interesting discussions. I would also like to thank my current labmates Shubhra di (special thanks di for your kind support in my journey), Dinesh and Manisha (special thanks lab ka chota bcha for making my last 1 year beautiful) for creating a learning and cordial environment in the lab.*

*It would be incomplete without thanking my lovely senior Dr. Monika Malik ☺ with whom I have learned so much in research. She has familiarized me with all the chemistry concepts. Thank you di, for your support. Supriya, my dearest friend, has always been there to support and encourage me when the PhD challenges appeared impossible. I can't forget all the masti and dance we did together in the last five years. I will always remember late night discussions and chitchats with Monika di and Supriya ☺.*

*I thank you both for your company, love, and care. I want to thank Saurabh for making good memories together in the last 1 year.*

*I extend many thanks to my NCL seniors, juniors and friends— Amrita (thank you for making my PhD days so enjoyable my tuffaan ☺), Himanshu (thanks for annoying me), Ravi Ranjan, Indranil, Vinita, Shreelata, Lakshmi, Rohit, Inderjeet (I hate you), to my lovely girls: Priya (thank you my Rajasthani bhabhi), Priyanka, Pooja, Kalyani, Manali (thank you my true love), Anuradha. Thanks to chota bcha Kritika, Tubai (thanks mote for annoying me in last 3 years), Debu (thanks for always coming in my last-minute plans), Rajni, Hari, Kranti, Soumya, Smita, Ravi, Surya, Neha, Chandan, Vishal. Special thanks to seniors: Betsy di, Abha di, Ragini di, Bhawana di, Reshma di, Monika Mathur di, Shailja di, Vipin bhaiya, Shebeeb bhaiya, Pavan bhaiya, Kartika di, Aakash bhaiya, Mohan bhaiya, Ambarish bhaiya (special thanks for supporting me), Ram bhaiya, Arun bhaiya (special thanks for magnetic measurements without them it was not possible), Abhijit bhaiya (special thanks for encouraging me), Govind bhaiya, Ashish bhaiya, Ruchi di, Reddy Anna, Anupam bhaiya, for being a valuable part of my life at NCL. How can I forget our MasterChef Sujeet and Chotu bhaiya, thanks for giving me the best meals during the last 5 years.*

*I would like to express my heartfelt gratefulness to my mummy, Mrs. Santosh and papa, Mr. Kailash, who provided endless love and unmatched support throughout my life. You both have been a constant source of inspiration in every walk of my life. Thank you for believing and keeping patience with me. I would also like to express my affection to my brothers (KP Bhaiya, Rahul Bhaiya, Sandeep, Anku), sisters (Nishu, Anshu, Gotiya), Bhabhi's (Munesh, Kaamini, Nishu), and my little girl Ditvi for their constant moral support. Wholehearted thanks to two special persons in my life, Golu and Henu, with whom I spent the most wonderful time. I can't express my bonding with both of you in words here. Thank you for understanding and being with me in my tough times. Thank you, Golu, for supporting me at every turn; it would not have been possible without you. Grateful to you for being there for me.*

*It gives me immense pleasure to thank everyone who helped me on this journey.*

## *Table of Contents*

### **Chapter 1: Introduction**

1.1 Introduction.....	3
1.1.1 Formation of hard-condensed matter and crystallinity .....	3
1.1.2 Importance of nano dimensions in polycrystalline solids.....	4
1.1.3 Growth process of solids from solution route.....	5
1.1.4 Crystal habit: termination of the growth process.....	15
1.1.5 Example: Growth process to crystal habit.....	21
1.2 Transition metal chalcogenides.....	24
1.3 What distinguishes chalcogenides from oxides?.....	26
1.4 Transition metal selenide.....	27
1.5 Fe-Se system.....	29
1.5.1 Journey of the Fe-Se system .....	29
1.5.2 The binary Fe-Se system.....	30
1.6 Magnetic structure of Fe-Se system.....	32
1.6.1 Magnetic structure of $\text{Fe}_3\text{Se}_4$ .....	32
1.6.2 Magnetic structure of $\text{Fe}_7\text{Se}_8$ .....	33
1.7 Importance of nano dimensions in magnetic properties.....	34
1.8 Synthesis routes.....	36
1.9 Magnetic study of Fe-Se nanoparticles.....	38
1.9.1 Why do the magnetic characteristics of $\text{Fe}_3\text{Se}_4$ differ from others? .....	38
1.10 Various factors that can influence the magnetic properties in Fe-Se system.....	41
1.11 Objective of the thesis.....	43
1.12 Outline of the thesis.....	44
1.13 References.....	46
<b>Chapter 2: Prediction of Crystal Growth Habit of Fe-Se Crystal System using Various Models</b>	
2.1 Introduction.....	56



2.2 Methodology.....	61
2.3 Results and discussion.....	61
2.3.1 Crystal habit of Fe-Se system using BFDH approach.....	61
2.3.2 Crystal morphology of Fe-Se system using HP approach.....	64
2.3.3 Evaluating surface free energy of various planes of Fe-Se system using BBA approach.....	71
2.4 Conclusion.....	74
2.5 References.....	75
<b>Chapter 3: Study of Phase-Evolution Mechanism of Fe-Se System at Nanoscale: Optimization of Synthesis Conditions for the Isolation of Pure Phases and their Controlled Growth</b>	
3.1 Introduction.....	81
3.2 Thermal decomposition-based synthesis of Fe-Se system at nanoscale.....	83
3.2.1 Synthesis of Fe-Se system to examine the phase transformation.....	84
3.2.2 Synthesis for single-phase formation.....	84
3.2.3 Synthesis to examine the role of OLA.....	85
3.3 Characterization techniques.....	85
3.4 Results and discussion.....	86
3.4.1 The study of the effect of reaction temperature, Fe-Se stoichiometry, and organic solvents on the phase formation.....	86
3.4.2 Optimization of synthesis conditions for single phase formation.....	92
3.4.3 Role of OLA .....	94
3.4.4 Formation mechanism .....	96
3.4.5 Material characterization— X-ray diffraction.....	98
3.4.6 Material characterization— electron microscopy imaging and diffraction study.....	100
3.4.7 Predicted crystal habit versus experimental morphology of Fe-Se system.....	103
3.4.8 Thermal study.....	108
3.4.9 X-ray photoemission spectroscopy analysis.....	109
3.5 Conclusions.....	111
3.6 References.....	112

## **Chapter 4: Remarkable Effect of Fe and Se Composition on Magnetic Properties—Comparative Study of the Fe-Se System at the Nanoscale**

4.1 Introduction.....	118
4.2 Characterization techniques.....	119
4.3 Results and discussion.....	119
4.3.1 Magnetic properties of the FeSe <sub>2</sub> NPs.....	120
4.3.2 Magnetic properties of the Fe <sub>3</sub> Se <sub>4</sub> and Fe <sub>7</sub> Se <sub>8</sub> NPs.....	123
4.3.3 Magnetic property of the FeSe NPs.....	128
4.3.4 Magnetic properties of the Fe-Se system.....	130
4.4 Conclusions.....	132
4.5 References.....	133

## **Chapter 5: Study of Growth Kinetics of Fe<sub>3</sub>Se<sub>4</sub> Nanocrystallites and the Influence of Size and Shape Tunability on their Magnetic Properties**

5.1 Introduction.....	140
5.2 Thermal decomposition-based synthesis of Fe <sub>3</sub> Se <sub>4</sub> NPs.....	144
5.2.1 For the synthesis of Fe <sub>3</sub> Se <sub>4</sub> nanorods (FS <sub>NR-T °C</sub> ) samples.....	144
5.2.2 For the synthesis of Fe <sub>3</sub> Se <sub>4</sub> nanoplatelets (FS <sub>PL-330 °C</sub> ).....	145
5.2.3 For the synthesis of Fe <sub>3</sub> Se <sub>4</sub> quasi-spheres (FS <sub>QS-330 °C</sub> ).....	146
5.3 Characterization techniques.....	146
5.4 Results and discussion.....	147
5.4.1 Growth process.....	147
5.4.2 Structural and morphological investigations of Fe <sub>3</sub> Se <sub>4</sub> NPs using XRD and TEM.....	151
5.4.3 Effect of Fe <sub>3</sub> Se <sub>4</sub> crystallite size on the M-H curves at 300 K.....	161
5.4.4 Effect of Fe <sub>3</sub> Se <sub>4</sub> crystallite size on the M-H curves at 10 K.....	166
5.4.5 Effect of Fe <sub>3</sub> Se <sub>4</sub> shape on the M-H curves at 300 K.....	166
5.4.6 Effect of Fe <sub>3</sub> Se <sub>4</sub> shape on the M-H curves at 10 K.....	168
5.4.7 Magnetic property: blocking temperature.....	168
5.5 Conclusions.....	172
5.6 References.....	172

**Chapter 6: Influence of M in Monoclinic M<sub>3</sub>Se<sub>4</sub> (M= Fe, Co, and Ni) Compounds on the Structure, Morphology, and Magnetic Properties at Nanoscale**

6.1 Introduction.....	179
6.2 Thermal decomposition-based synthesis of M <sub>3</sub> Se <sub>4</sub> compounds at the Nanoscale.....	181
6.3 Characterization techniques.....	182
6.4 Results and discussion.....	183
6.4.1 Structural and morphological investigations of M <sub>3</sub> Se <sub>4</sub> NPs using XRD and TEM .....	183
6.4.2 Crystal habit of M <sub>3</sub> Se <sub>4</sub> NPs using BFDH and HP model.....	186
6.4.3 Correlation between theoretically predicted crystal habit and experimental morphological of M <sub>3</sub> Se <sub>4</sub> NPs.....	192
6.4.4 XPS analysis of M <sub>3</sub> Se <sub>4</sub> NPs.....	195
6.4.5 Remarkable effect of M in monoclinic M <sub>3</sub> Se <sub>4</sub> compounds on magnetic properties at nano-dimensions.....	197
6.5 Conclusion.....	203
6.6 References.....	203

**Chapter 7: Summary and Future Scope**

7.1 Summary of the thesis.....	209
7.2 Directions for future work.....	211

**Abstract****List of publications**

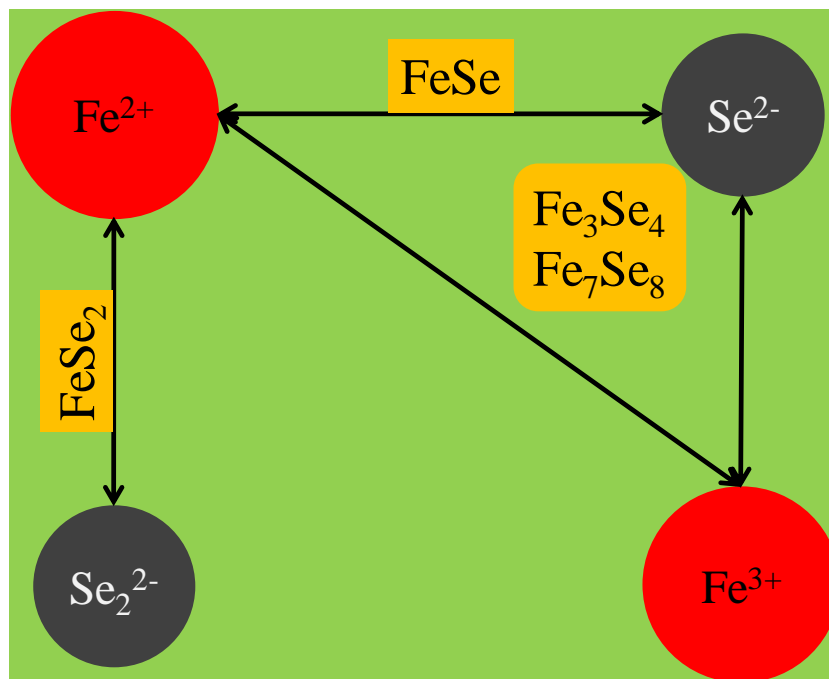
## List of abbreviations

1	Nanocrystalline	NC
2	Gibbs energy barrier	$\Delta G$
3	Quantum dots	QD
4	Classical nucleation theory	CNT
5	Nanoparticles	NPs
6	Non-Classical nucleation theory	NCNT
7	Wide-angle X-ray scattering	WAXS
8	Transmission electron microscopy	TEM
9	Pre-Nucleation Clusters	PNCs
10	Burton-Cabrera-Frank	BCF
11	Crystallization via particle attachment	CPA
12	X-ray diffraction	XRD
13	Space group	SG
14	Periodic Bond Chain	PBC
15	Hartman and Perdok	HP
16	Flat	F
17	Stepped	S
18	Kinked	K
19	Attachment energies	AE
20	Bravais, Friedel, Donnay, and Harker	BFDH
21	Inter-planar spacing	$d_{hkl}$
22	Rate of growth	$R_{hkl}$
23	Relative growth rates	RGR
24	Effective mass approximation	EMA
25	Morphological importance	MI
26	Transition metal chalcogenides	TMCs
27	Metal chalcogenides (MC)	MC
28	Transition metal dichalcogenides	TMDs
29	Transition metal sulfides	TMSs
30	Transition metal selenides	TMSes
31	Density of states	DOS
32	Hydrogen evolution reaction	HER
33	Oxygen evolution reaction	OER
34	Vanadium dichalcogenides	$VX_2$
35	Iron-selenium	Fe-Se
36	Room temperature	RT
37	Curie temperature	$T_C$
38	Nanometres	nm
39	Magnetic nanoparticles	MNPs
40	Saturation magnetization	$M_S$
41	Coercivity	$H_C$
42	Remnant magnetization	$M_R$
43	Average blocking temperature	$T_B$

44	Anisotropy constant	$K_u$
45	Broken bond approximation	BBA
46	Surface energy	SE
47	Oleylamine	OLA
48	1-octadecene	1-ODE
49	Thermo-gravimetical analysis	TGA
50	X-ray photoemission spectroscopy	XPS
51	Round-bottom	RB
52	Octadecylamine	OCD
53	n-Octadecane	n-ODE
54	Field-emission-scanning-electron-microscopy	FESEM
55	Binding energies	BE
56	Physical Property Measurement System	PPMS
57	Vibrating sample magnetometer	VSM
58	Magnetization versus temperature	M-T
59	Zero-field-cooled	ZFC
60	Field-cooled	FC
61	Magnetization versus field	M-H
62	Crystal field splitting	CFS
63	Rare-earth	RE
64	Maximal energy product	$(BH)_{max}$
65	Effective magnetic anisotropy constant	$K_{eff}$
66	Full width at half maxima	FWHM
67	Superconducting quantum interference device	SQUID
68	Relative intensities	RI
69	Anisotropy field	$H_a$
70	Magnetic susceptibility	$\chi$

# Chapter 1

## Introduction



## Highlights

*The chapter starts with a discussion on the crucial role of nucleation and growth in formation of crystalline materials in solids.*

*Nucleation and growth theories are discussed, and the growth termination conditions are also highlighted.*

*The importance of these concepts is briefly explained by the ZnO example.*

*Further, the importance of transition metal chalcogenides in various areas of science is discussed followed by discussion on the selenide's uniqueness.*

*The Fe-Se system shares the most unique properties due to the complex crystal structures. The magnetic properties hugely change with change in the stoichiometry of Fe and Se.*

*Iron-selenium binary phases are mentioned in detail. Synthesis methods used so far to fabricate the Fe-Se system at the nanoscale by chemical methods have also been discussed.*

*The interesting magnetic properties of  $Fe_3Se_4$  are highlighted and a literature review is explored including the crystal structure, chemical synthesis routes, and the magnetic properties of the Fe-Se system.*

**Keywords:** Materials Physics, Theory of Nucleation and Growth, Transition Metal Chalcogenides, Magnetism in Nanoscale Materials.

## 1.1 Introduction

### 1.1.1 Formation of hard-condensed matter and crystallinity

Solid-state materials are classified based on the periodic arrangement of atoms or ions with respect to one another. Many of the naturally occurring and man-made solids are crystalline. A crystalline material consists of a repeating or periodic arrangement of atoms over large atomic distances. This implies that long-range ordering is present where atoms reorganize themselves in a repetitive three-dimensional pattern upon solidification, and each atom is bonded to its nearest-neighbor atoms<sup>1-2</sup>.

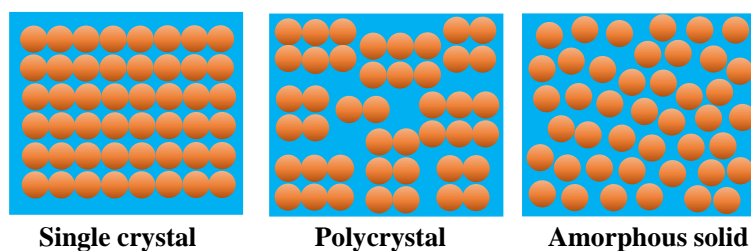


**Figure 1.** The solids are categorized according to their crystalline order. The periodicity of the atomic structure in each type of solid material is illustrated in the figure. The brown circle represents the atom.

According to crystallinity, the solids are classified into three categories—

- a) Single-crystalline solids (infinite periodicity): These materials have a crystal structure that repeats periodically over the entire volume. Each atom is associated with all other equivalent atoms by translational symmetry<sup>1-2</sup>.
- b) Polycrystalline solids (local periodicity): They are composed of many individual crystallites or grains. The long-range ordering is present within each grain in the atomic structure, the same as a single crystal. There is no periodicity over the entire volume of the material due to the absence of a relationship between neighboring grains<sup>1-2</sup>.
- c) Amorphous solids (no long-range order): They do not have long-range order and thus no translational symmetry. However, the structure is not truly irregular. The short-range ordering is present in the structure, giving rise to approximately-defined distances between atoms<sup>1-2</sup>.

The fundamental difference between these three categories is the arrangement of atoms according to their translational symmetry over the length scale. The difference in structure



between these three classes of solids decides many of the physical properties, including mechanical, optical, magnetic, and electronic behavior.

The majority of the time, the natural crystals interrupt their long-range ordering. There are very few naturally occurring solids that are made up of a single crystal, such as salt, quartz, diamond, Iceland spar, and topaz<sup>3</sup>. Solids are usually polycrystalline in nature and are constructed by several numbers of smaller crystallites. These smaller crystallites are microscopic and oriented differently with highly defective boundaries. An amorphous layer of solid holds these crystals together. For example, materials such as common metals, ice, rocks, and ceramics are polycrystalline in nature, where the order and orientation are very random<sup>4</sup>. The polycrystalline solid growth process or processing conditions determine the final structure and properties.

### **1.1.2 Importance of nano dimensions in polycrystalline solids**

The study of nanostructured materials has recently become a highly interdisciplinary research field. Research on these materials began during the mid-1980s after Gleiter et al.<sup>5</sup> introduced the concept of nanostructured materials for the first time. Since then, many new directions in research and technologies have opened up as a result of the ability to alter the physical and chemical properties of solids by altering their dimensions at the nanoscale. The studies are focused heavily on systematic variation in the electronic structure of materials with size at nanometer scales.<sup>6</sup>

Nanocrystalline (NC) materials are polycrystalline materials whose crystallites (grain sizes) are up to nearly 100 nm in size, at least in one of their dimensions. These materials bridge the gap between amorphous materials having short-range order and conventional coarse-grained materials. The extremely small dimensions of these materials ensure that a significant component of the atoms is located at the grain boundaries, which provides special characteristics.<sup>6</sup> It is very often true that NC materials have distinct properties from traditional polycrystalline materials. NC materials exhibit enhanced diffusivity, increased strength/hardness, improved ductility/toughness, higher electrical resistivity, reduced density, superior soft magnetic properties, reduced elastic modulus, lower thermal conductivity, higher thermal expansion coefficient, and increased specific heat in comparison to conventional materials. In this field, sustained efforts have yielded interesting results in applications such as

fluorescent sensors in biological applications, magnetic materials, UV protection films, photocurrent generation in various devices, catalytic reactions, optical switches, nanotweezers, and other devices.<sup>7-13</sup>

However, the synthesis of nanocrystals of the required crystal structure and morphology is crucial for realizing these applications. The formation process of materials highly influences crystal structure and morphology. In order to meet this requirement, it is essential to understand the formation process of solids at the nanometric scale. Since it is easy to implement and offers a high degree of versatility, the solution route synthesis of nanocrystals has become the preferred method for obtaining these nanocrystals.<sup>14</sup>

### **1.1.3 Growth process of solids from solution route**

Precipitation, co-precipitation, and other processes that lead to solids from liquid solutions are essential to nature and industry. More than 70% of all solid materials manufactured in the chemical industry are produced by precipitating solutions. Two sequential events are generally involved in these processes, namely nucleation, and growth. Numerous real-life processes involve nucleation and growth. A few of them are addressed below.<sup>15-16</sup>

Ice formation has 2 stages— nucleation and continuous ice growth<sup>17</sup>. The nucleolus of ice is established as the drop of water touches the sub-zero surface after a time delay. This process is regulated by the thermodynamics of the ice water-surface system, which is defined by the Gibbs energy barrier ( $\Delta G$ ). The  $\Delta G$  depends on the surface factor, which is the function of surface geometry (nano or micro) and higher free energy<sup>17</sup>. Through these parameters, ice nucleation can be tuned. Followed by ice nucleation, the growth process starts which is controlled by heat transfer. Two extreme conditions can explain ice growth. First one is when the ice formation occurs without air flow and the rate of ice growth is determined by substrates heat transfer. The second case is when ice growth occurs in an airy climate where the ice growth rate is primarily governed by variable heat transfer<sup>17</sup>. All the ideas about ice formation on the surface apply to a single, isolated drop. However, in practice, too many droplets in a given area can disrupt the nucleation and growth process, causing an ice bridge phenomenon, which causes the vapor source to sink because of a vapor pressure difference between the ice droplet and nearby liquid droplets<sup>17</sup>.



**Figure 2.** The nucleation of CO<sub>2</sub> on a finger.

Similarly, there are numerous other examples showing nucleation and growth of crystals: sugar crystals growing on a string, crystallization of a snowflake over a dust particle, and putting your finger in a glass of soda will cause CO<sub>2</sub> bubbles to nucleate around it as shown in Figure 2<sup>18</sup>.

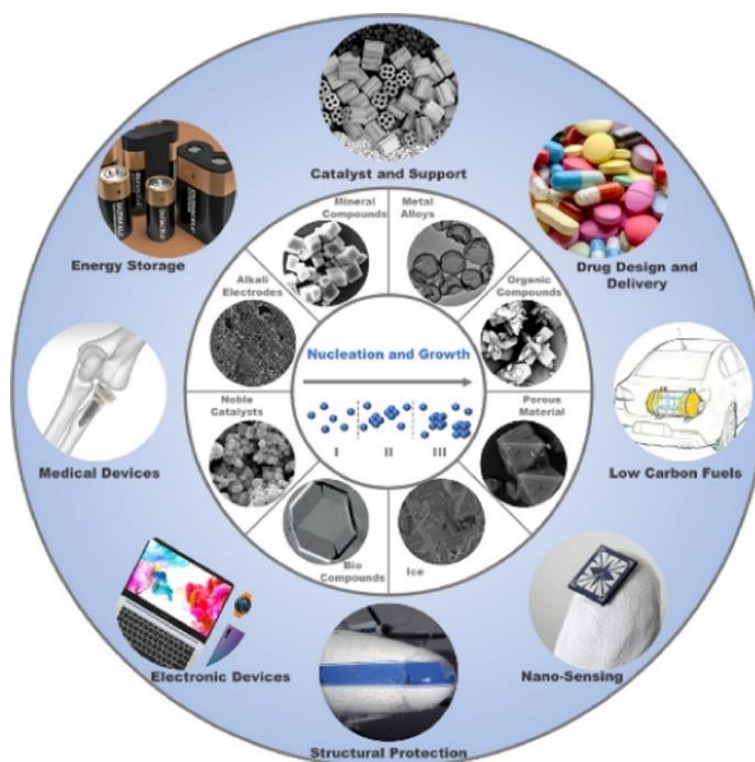


**Figure 3.** Using nucleation and growth to drive the development of advanced materials and their applications.

As shown in Figure 3, nucleation and growth play an essential role in developing advanced materials and applications. In the chemical industry, the selectivity and activity of catalysts (e.g., Pt, RuO<sub>2</sub>, TiO<sub>2</sub>) strongly depend on the morphology, crystallinity, and surface. In the pharmaceutical industry, the tablets (e.g., digoxin) bioavailability is affected by the

hygroscopicity, crystallinity, and shape. In the health industry, the nanodimensions biosensors (such as plasmonic gold nanoparticles, fluorescent quantum dots (QD)) properties are crucial to morphology, crystallinity, dopants, surface charges, morphology, and capping density ligands<sup>19</sup>.

For the synthesis of these materials, several successful attempts have been made using a solution-phase methods, like hydro- and solvo- thermal, a polyol-assisted, an electrochemical, and a seed-mediated process. However, to gain better control over the synthesis that leads to a material with prime properties for particular applications, it is necessary to recognize the atomic or molecular level processes that result in the various macroscopic states and the methodologies that determine pathway selection, especially for complex systems.<sup>19</sup>

The initial phase in the development of these materials is nucleation, in which monomers (such as atoms, ions, or molecules) form a new thermodynamic structure at the atomic or molecular level; the second step is growth, in which monomers are integrated into the surface of the nuclei as they grow larger. As a result, these nucleation and growth processes are critical for accurately controlling the final solid material's structural traits and qualities. The nucleation and growth theories will be discussed below, followed by applying them in the material. Nucleation and growth both have two theories— classical and non-classical.<sup>19</sup>

#### **a) Classical nucleation theory (CNT)**

Volmer, Weber, Becker, Doring, and Frenkel have done the pioneering work on this theory in the 1920s and 1930s. Initially, CNTs were proposed to explain the condensation of vapors into liquids and later carried out to other liquid-solid equilibrium systems, for example, saturated liquids crystallization. This theory is most often used to explain the formation of novel thermodynamic phases or new structures in terms of a continuum. Depending on whether or not there is a foreign body, nucleation is classified into two categories— homogeneous and heterogeneous (Figure 4).<sup>19</sup>

Homogenous nucleation is the process of primary nucleation in a chemically homogeneous medium. However, it might happen if a foreign substance acts as the active center of the first monomer unit (e.g., atoms, ions, or molecules) and this process is termed as the heterogeneous nucleation. When the dissolved cluster of the same species is present in the system, it is called secondary nucleation. Liquid solutions are, to some extent, homogenous media, which assures

that internal nucleation is homogeneous in theory. However, heterogeneous nucleation in a solution is caused by the existence of multiple heterogeneities at the molecular level (such as solvent, different kinds of monomers, contaminants, and the container wall).<sup>19</sup>

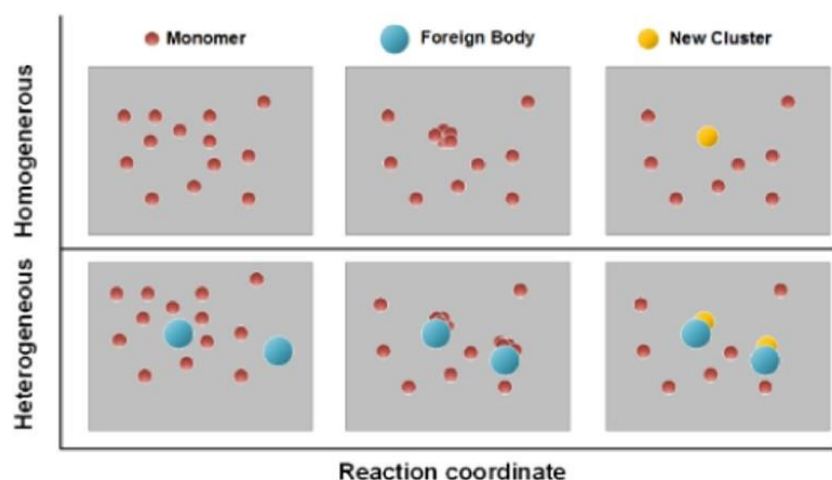


**Figure 4.** Homogeneous and heterogeneous nucleation processes.

This is more difficult than typical metal and alloy solidification. According to CNT, the interface tension, temperature, and supersaturation are prime governing parameters for both types of nucleations. The LaMer and Dinegar extended the CNT for colloidal particles and nanoparticles (NPs). According to the LaMer model, NP creation involves immediate nucleation (also known as burst nucleation) and diffusion-controlled growth. The agglomeration criteria are not taken into account in this model. It is essential to note that to date, the LaMer model is the single theory for narrowly dispersed colloidal particles/NPs via self-assembly.<sup>19</sup>

The shortcomings of CNT are:

1. For some binary spherical clusters (such as ethanol-water), the composition of the cluster surface may differ significantly from the bulk.
2. The assumption of immobilized nucleation is not always valid in practice. CNT cannot account for nucleation rate when the nucleation driving force fluctuates frequently, and the cluster size distribution cannot relax quickly enough to achieve a stationary state.
3. CNT does not work for small clusters having 20–50 molecules.
4. Originally developed for vapor-liquid systems, CNT cannot provide information on the path from solution to crystallization.<sup>19</sup>

## b) Non-Classical nucleation theory (NCNT)

The hypothesis was presented to explain complicated behaviour and events that do not fit in CNT, such as the empirically observed intermediate phases in solution crystallization. NCNT is not replaced but complements the CNT. However, comprehensive NCNTs applied in all systems have not yet been developed. This is an important and complex research field, but only limited literature are dedicated to improving NCNT.<sup>19</sup>

In CNT, the nucleation solids are subjected to a single-step process where the cluster reaches a critical size and becomes thermodynamically stable. This continues to grow spontaneously (Figure 5a), while in NCNT, additional steps are present to describe the intermediate states.

The NCNT can be represented by 2 basic processes: a two-step nucleation mechanism and the concept of a pre-nucleation cluster, regardless of whether the generated intermediates are thermodynamically metastable or stable (Figures 5b and c). The pre-nucleation clusters in the pre-nucleation clusters hypothesis were previously considered to be thermodynamically stable but did not have an interface boundary, whereas the dense liquid-like phase in the two-step nucleation process was previously supposed to be thermodynamically metastable.<sup>19</sup>

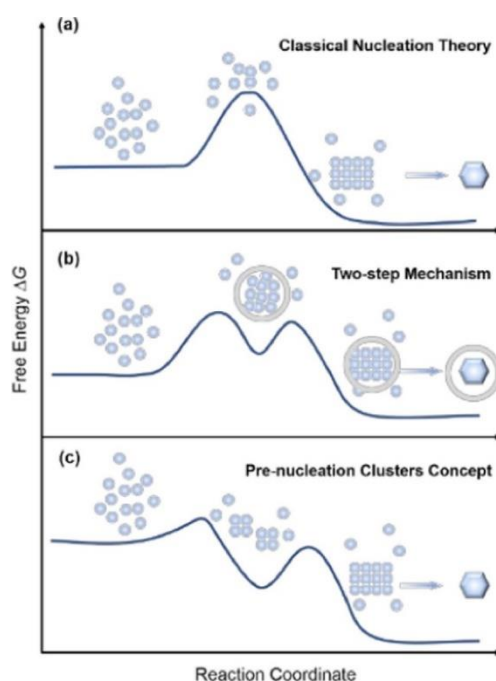


**Figure 5.** Mechanisms for crystal nucleation: (a) Classical nucleation theory, (b) Two-step nucleation mechanism, and (c) Pre-nucleation clusters concept.

## Two-Step nucleation

Derived from the numerical simulations of protein crystal nucleation, Wolde and Frenkel postulated the two-step nucleation mechanism. The creation of a liquid-like phase with a lower nucleation barrier  $\Delta G$  compared to a conventional nucleation process is thought to be the initial step toward producing a critical cluster. Wolde and Frenkel offer an approach for controlling protein nucleation without influencing growth rate by manipulating the system's composition (e.g., adding non-ionic polymer). As a result, the interaction spectrum changes, resulting in a metastable liquid-liquid critical point. Guided by this, particle morphology and size control techniques are available by modifying local ligand and solvent environments.<sup>19</sup> Later in the lysozyme protein crystallization process, additional experimental proof for liquid-liquid phase separation is provided by Vekilov and Galkin. They use static light scattering to examine the shift in phase boundary and drastically alter the nucleation rate by adding glycerol and polyethylene glycol to the mixture, as recommended by Wolde and Frenkel. The two-step nucleation method has been expanded and applied to the cooling crystallisation of small compounds by Davey and co-workers. It was discovered that two phases, a solute-rich dark phase and a solute-lean light phase, formed. Nucleation happened in both phases, according to the gas chromatography compositional study, but the majority of domains are created in the dark phase.<sup>19</sup>

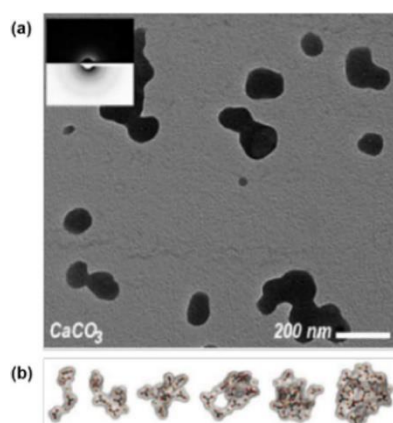


**Figure 6.** (a) Transmission electron microscopy (TEM) image of liquid-like precursors formed by  $\text{CaCO}_3$  and (b) Molecular dynamics simulations for the evolution of dense liquid clusters

The presence of liquid-like precursors for the nucleation of inorganic crystals, primarily  $\text{CaCO}_3$ , has been proven experimentally and computationally. In-situ wide-angle X-ray

scattering (WAXS) was used to track the production of crystalline carbonate phases from liquid-like precursors, and liquid-like precursors were described using transmission electron microscopy (TEM), as shown in Figure 6a.

Wallace and co-workers expect the creation of a dense liquid phase by liquid-liquid separation, in which  $\text{CaCO}_3$  nucleation occurs, based on the experimental findings. The cluster dynamics reported via MD simulation match those observed by TEM (Figure 6b).

In summary, there are two key notations in the two-step nucleation mechanism:

1. There are two energy obstacles to jump: the nucleation of dense liquid-like clusters and the formation of crystals largely within the dense liquid phase via structural transition.
2. Here between dense liquid and bulk liquid phases, there is a phase boundary.<sup>19</sup>

### **Pre-Nucleation clusters (PNCs) concept**

Although analogous processes have previously been reported for biomineralization and the production of organic NPs, Colfen and co-workers were the first to propose the PNCs idea. The "non-classical" PNCs method for building various inorganic and organic crystals appears to be supported by experimental and theoretical data. In summary, the PNCs approach has five essential concepts that distinguish it from Wolde and Frenkel's two-step nucleation mechanism<sup>19</sup>:

1. Because PNCs are thermodynamically stable clusters with "solute" properties, there is no phase boundary between them and the bulk solution.
2. PNCs are mostly made up of solid-forming monomers (atoms, molecules, and ions), but they can also contain other chemical species.
3. Phase separation is aided by PNCs, which are molecular precursors.
4. PNCs are very dynamic entities that alter their configuration on time scales comparable to molecular rearrangements in solution.
5. PNCs may have structural motifs that are similar to or related to one of the crystalline polymorphs.<sup>19</sup>

### **c) Classical and non-classical crystal growth**

The features of resultant products formed in the system are determined by particle growth and nucleation. Furthermore, crystal growth conditions and rate considerably influence product



purity and crystal structure. The layer-by-layer addition of monomers on an existing crystal surface may also be ascribed to crystal size expansion in the classical crystal growth framework, and the thermodynamic driving force, such as supersaturation  $S$ , dictates the growth mechanism.<sup>19</sup> This traditional approach, on the other hand, merely catches a portion of the picture. Nanoscience and biomineralization, for example, have supplied multiple pieces of data that challenge the traditional hypothesis. Crystal size enlargement can also be attributed to particle assembly via both oriented and non-oriented attachment or aggregation in the non-classical crystal growth framework (Figure 7).<sup>19</sup>

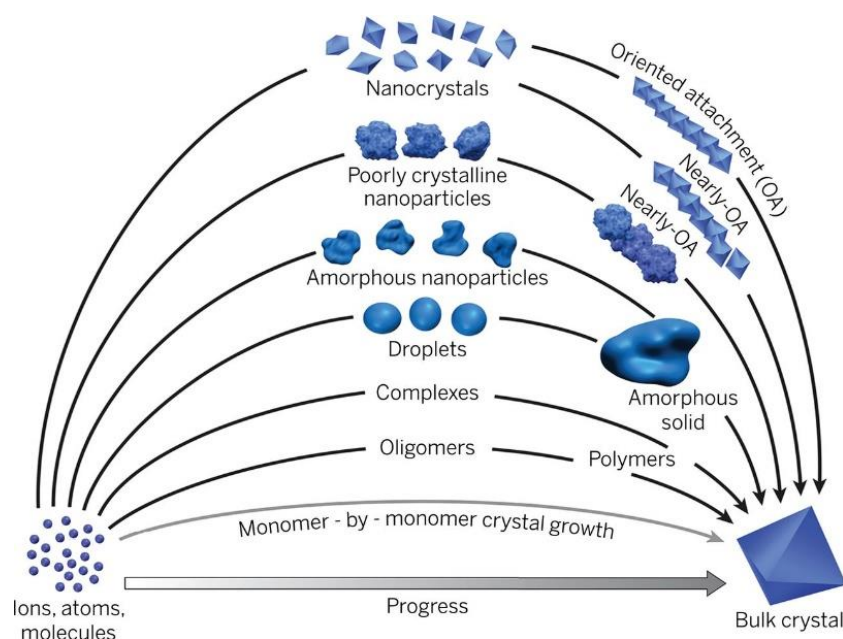


**Figure 7.** In classical models of crystal growth, crystals are produced by monomer-by-monomer addition of ions, atoms, or molecules (grey curve). In contrast, non-classical crystal growth occurs by adding higher-order species ranging from multi-ion complexes to fully formed nanocrystals.

The thermodynamic factors of the process, such as temperature, pressure, and supersaturation, as well as other variables in the system, such as additives, impact the two processes differently.<sup>19</sup>

### Classical crystal growth by monomers

The mechanism of classical crystal growth is divided into two parts. A diffusional step is followed by a surface reaction step, which is also referred to as the particle integration step.

The fundamental, thermodynamic driving force for particle growth can be represented as the difference in chemical potential between the standing and the equilibrium states. Two-dimensional growth theories, the Burton-Cabrera-Frank (BCF) Model and the diffusion layer model, which is theoretically simpler than the other two, have all been presented to describe crystal growth.<sup>19</sup> Before the particle integration stage, the solute must diffuse across the boundary layer, according to the diffusion layer model. It is easier to calculate the particle growth rate if the dimension of concern is first clarified. Particle growth rate (i.e., linear growth rate with a unit of length per unit time) is a function of supersaturation in general.<sup>19</sup> The higher the supersaturation, the faster the growth rate:

$$G = k_g (S - 1)^g \text{-----(1)}$$

where  $k_g$  denotes the crystal growth rate constant (function of solubility and temperature),  $S$  denotes supersaturation, and  $g$  denotes the growth order. The parabolic growth law is obtained when  $g$  is equal to 2 at low supersaturation. The control step for growth in the formation of polyhedral crystals with smooth sides is particle integration into a surface. The value of  $g$  grows exponentially when supersaturation is raised. The surface becomes rough and unstable as the supersaturation level further rises, and the value of  $g$  comes to 1. Because of the large number of nucleation sites accessible in the solution, particle integration onto the surface is no longer a control step, and particle growth is now governed by diffusion.<sup>19</sup> In crystal development, the two transporting processes, i.e., heat and mass transfer, are linked in terms of the difference in chemical potential associated to changes in temperature and activity. The degree of condensation of the environmental phase determines the degree of contribution from the relevant transport process. Furthermore, supersaturation drives nucleation or crystal formation, which is influenced by temperature and activity. Controlling the supersaturation level and heat and mass transfer processes over time, for instance, could aid in the regulation of nucleation and growth, revealing how the properties and characteristics of the final products could be tuned.<sup>19</sup>

### **Growth by particle attachment and aggregation**

As previously stated, creating a critical nucleus at low supersaturation is an uncommon occurrence. Integration is truly in charge of the growing process. Thus, a basic growth by monomers that interact through Brownian motion may be observed, and it closely fits the

classical growth hypothesis. More complicated interactions between monomers and particles are found when supersaturation rises. The addition of monomers to the solution, as well as collisions and coalescence with other particles, are all factors in particle growth. A review by De Yoreo and colleagues revealed broad notions concerning crystallization via particle attachment (CPA). Consider the interaction between free-energy landscapes and reaction dynamics, as depicted in Figure 8, to understand key characteristics of classical growth theory and CPA.<sup>19</sup>

Figure 8a depicts classical growth, which is characterized by a monomer-by-monomer development route. The attachment of various precursor particles, such as oligomers, droplets, amorphous particles, or fully grown nanocrystals, is discussed in Figure 8b-e, which depicts particle-based routes. Non-classical growth ideas currently available focus on defining how clusters arise in mono- and polycrystalline systems. The related rate equations and models for CPA, on the other hand, are currently lacking. As a result, there is currently a dearth of molecular and quantitative knowledge of particle-attachment processes.<sup>19</sup>

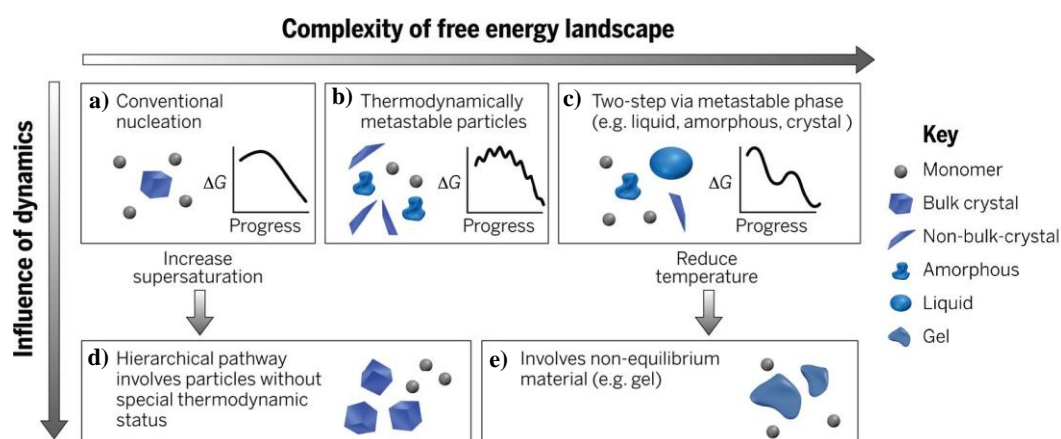


**Figure 8.** Crystallization by a wide variety of pathways. The possible pathways by which monomers form a stable bulk crystal, and the physical mechanisms that give rise to them, can have thermodynamic (a to c) and kinetic (d and e) origins. a) Classical monomer-by-monomer addition, b) aggregation of metastable particles, such as liquid, amorphous, or poorly crystalline particles, or oriented (and nearly oriented) attachment of metastable nanocrystals, c) crystallization via the formation of a metastable bulk phase, such as a liquid or solid polymorph, d) kinetically dominated aggregation of clusters or oligomers and e) aggregation of unstable particles whose internal structures are not those of equilibrium phases.

Surprisingly, the kinetics of solidification from a solution, which is the most common chemical approach for producing a wide range of systems with nanometer-scale dimensions has received far less attention. A collection of thermodynamic (e.g., reduction potential and surface capping) and kinetic (e.g., concentration, mass transit, temperature, and the presence of foreign species) characteristics are closely and intricately linked.<sup>19</sup> When any one of the thermodynamic or kinetic factors is modified, the type and amount of nuclei or seeds created in the early stages of synthesis can be substantially changed, resulting in variations in the forms adopted by the end products. As a result, it is critical to comprehend the nucleus and growing process in order to comprehend the outcome and alter it according to our needs.<sup>19</sup>

The crystal will grow anisotropically in different directions, and at some point, it will stop growing in each direction. The crystal exhibits a habit of growing in a way that consumes minimum energy, and each plane terminates differently. It is an interesting field of science to study crystal habits.

#### **1.1.4 Crystal habit: termination of the growth process**

Dana has supplied an excellent definition of a crystal from the viewpoint of morphological crystallography: "A crystal is the uniform polyhedral structure, limited by smooth surfaces, that a chemical compound assumes under the influence of its interatomic forces during transitioning from a liquid or gas to a solid under appropriate conditions." Recalling that the chemist considers the condition of a solute in solution somewhat analogous to the gaseous state, we see that this definition is complete. A natural consequence of this definition is the inference that a crystal is the normal form of all solid elements and chemical compounds.<sup>20-21</sup>

A definition by Antonoff supplements Dana's: " A crystal is an anisotropic, homogenous body with the natural shape of a polyhedron." This second definition implies the internal variation of structure with direction, which results in the observed variations of crystal properties with direction.<sup>20-21</sup>

The smooth plane surfaces bounding a crystal are called faces or planes. On a well-developed crystal, the faces arrange to impart a certain characteristic symmetry of form to the crystal as a whole. However, it is rare that a crystal under conditions so favorable as to yield the ideally perfect polyhedral form. The normal deviations from the ideal form are of two types; Equivalent faces on an individual crystal may vary in size, or some may even be completely

missing. It is common, too, for the faces not to be smooth and polished but instead roughened by minute elevations, depressions, striations, and the like. The crystallographer, nevertheless, in his drawings, usually depicts the crystal as an ideal polyhedron. Crystals of a given chemical compound may show a rather great diversity of form. By change in the number of faces and their relative sizes, the so-called habit may vary almost indefinitely. This is common among mineral species from different localities and is frequently observed in laboratory specimens.<sup>20-21</sup>

In practice, the internal structure is constant throughout the habit. However, variations are observed in the morphologies, and several samples have identical compositions but different external forms. The variations in crystal habit exhibited by a given species have been demonstrated to result from variations in the conditions under which the substance crystallized. There is considerable experimental evidence that small amounts of foreign material present in the crystallizing solution can affect the habit of the crystals formed.<sup>20-21</sup> Gaubert reported on the effect of methylene blue on the form of lead nitrate crystals. Usually, they appear as octahedra from pure water, but when the solution is saturated with this dye, the crystals have a cubic habit. Buckley and France et al. studied the effects of organic and inorganic foreign substances on the crystal habit of many salts, particularly alums and chlorates. Thus, sodium chlorate crystallizes as cubes from pure water, but from a solution containing a trace of sodium dithionate, its habit is completely changed to tetrahedral.<sup>20-21</sup>

### **a) History of crystallography**

Geometric shapes of crystals received considerable attention in the 17<sup>th</sup> century. J. Kepler's<sup>22</sup> discovery and examination of the intricately diverse dendritic formations of snowflakes was the first, followed by Nicolous Steno's<sup>23</sup> work on interfacial angles of rock crystals. The former was published in 1611 in the book "New Year's Gift," while the latter was published in 1669 in a treatise. Although it displayed hundreds of various dendritic patterns, Kepler deemed a crystal made of tight packing of equisized spheres.

The notion of crystal structure arose from this. We sometimes forget Steno's important contribution to the study of crystal formation since he discovered "the law of the stability of the interfacial angles." Steno explained in the treatise that

(1) Rather than microorganisms in the soil, rock crystals were produced by inorganic activity through the precipitation of small particles generated in a high-temperature aqueous solution and

(2) Growth rate anisotropy, i.e., variable growth rates in different crystals, was the reason that rock crystals took varied polyhedral shapes. The most fundamental notion in today's crystal growth research is "growth rate anisotropy." Two significant notions about crystal structure and development were surprisingly formed from observations in the 17<sup>th</sup> century: one is based on dendritic snow crystals, while the other is based on polyhedral rock crystals with flat sides.

Although Kepler regarded equal-sized spheres as crystal building units, it was a French mineralogist, R. J. Häuy<sup>24</sup>, who advocated polyhedrons, instead of spheres or ellipsoids as the starting building unit of a crystal in the 18<sup>th</sup> century, which are equivalent to today's unit cell of a crystal. As potential sorts of unit cells that may fill the space without opening, A. Bravais produced 14 lattice types called as Bravais' translation lattice. Seven crystal systems, 32 point groups, and 230 space groups were systematised as a result, and crystal geometry was created and nearly finished in the 19<sup>th</sup> century. However, crystals consisting of the unit cell wasn't proved until 1912. M. von Laue<sup>25</sup> and his students used a copper sulphate crystal to experiment with X-ray diffraction (XRD) this year. They proved that the crystal is made up of regularly ordered atoms that are explained by unit cell translation. The fast spread of crystal structures analysis by X-ray was akin to a fire ignited on a dry grass field. The physical characteristics of crystals became intelligible with chemical bonding and crystal structures, and the crystal chemistry was build based on the findings of crystal structure investigations. The morphology or morphogenesis of crystals represents the ultimate crystal growth outcomes, will be given special emphasis in this section.

Kepler was particularly interested in the dendritic formations of snow crystals. The numerous types of polyhedral crystals that a specific crystal species showed drew Steno's attention. For the first time, Bravais<sup>26</sup> law explained the relationship between morphologies and unit cell geometry, allowing scientists to better comprehend the origins of distinct polyhedral shapes shown by different crystal species. On actual crystal, crystal faces aligned to the net planes with greater reticular densities (broader interplanar spacing) form bigger than those with smaller reticular densities, according to Bravais' empirical rule. Simple cubic, octahedral, and rhombic dodecahedral shapes are taken by primitive (P), face-centered (F), and

body-centered (I) varieties of cubic system unit cells, respectively. J. D. H. Donnay and D. Harker<sup>27</sup> used this formula to expand the Bravais' law, which was depend on the geometry of 14 lattice types to 230 space groups (SG). In estimating reticular densities, the influence of symmetry elements with translation operation (screw axis and glide plane) is considered. The biggest disparities between actual and predicted forms on the Bravais' rule were reduced by recalculating the reticular densities with 230 SG. The Bravais' law states that polyhedral pyrite  $\text{FeS}_2$  crystals should be circumscribed by  $\{100\}$ ,  $\{111\}$  and  $\{110\}$ , however in actuality,  $\{210\}$  forms instead of  $\{110\}$ <sup>28</sup>. On quartz crystals, the Bravais law predicts that  $(0001)$  face will form. On natural rock crystals, the  $(0001)$  face has only been seen on rare samples. The observed differences can understand with the Donnay-Harker's expansion.

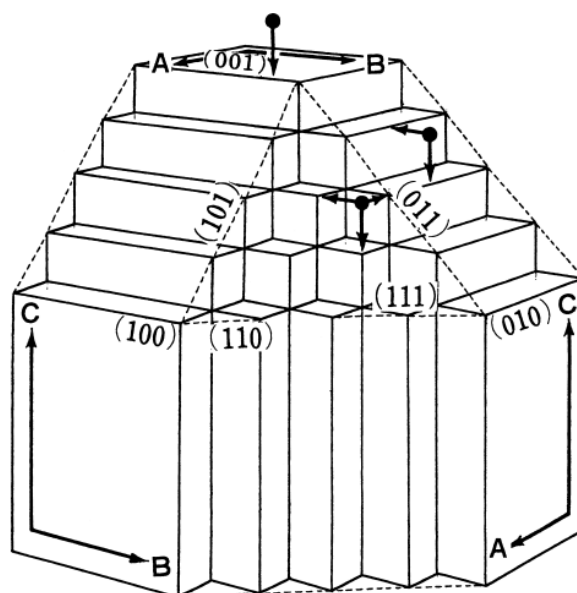


**Figure 9.** PBCs and F, S, and K faces are defined in the Hartman-Perdok model. Thick lines with arrows, A, B, and C are PBC vectors in a simple cubic crystal (Kossel crystal). F faces:  $(100)$ ,  $(010)$ ,  $(001)$ , S faces:  $(110)$ ,  $(011)$ ,  $(101)$ , K face:  $(111)$ .

The Periodic bond chain (PBC) study by Hartman and Perdok (HP) is based on a similar concept<sup>29-31</sup>. Although Bravais and Donnay-Harker focused on the relevance of planes in their theories, HP focused on zones. They attempted to identify strong PBCs in a crystal structure and divided crystal faces into three categories, flat (F), stepped (S), and kinked (K), according to the PBCs present on each face. The F faces appear largest having more than two PBCs, while

a S faces have only one PBC and K faces have none (Figure 9). On genuine crystals, S and K faces are become little or not emerge as flat faces.

Although HP analysis looks to be qualitative and random at first, later the approach was refined by computing the attachment energies (AE) of bonds. PBC research has been performed on a broad range of crystal species, with the findings providing a criterion for growth form analysis. The study was expanded to include the linked net model given by P. Bennema and applied to greater sophisticated crystals, such as regulated structures and quasicrystals, allowing it to be used to more intricate structures like garnet.<sup>28</sup>

The notion of AE is linked with the Jackson's factor by this extension. A book titled "Morphology of Crystals" summarises recent advancements. The methods described above, which were pioneered by Bravais, Donnay-Harker, and finally established by Hartman-Perdok, are intended at clarifying a crystal's ideal shape, considering that the shape is completely defined by the internal structure and the impact of external growth conditions is completely ignored.<sup>20-21, 28</sup> This type of form is referred to as a "structural form" or a "abstract form" and it has no reference to thermodynamic characteristics like temperature, pressure, or driving force. However, it's worth noting that the approach has since been improved to anticipate growth forms by factoring in the influence of external factors at interfaces.<sup>20-21, 28</sup>

The thermodynamic analysis of the equilibrium form, which was addressed by J. W. Gibbs<sup>32</sup>, P. Curie<sup>33</sup>, and G. Wulff<sup>34</sup>, is another way to comprehending the polyhedral shape. They believed that a crystal is defined by a set of crystal faces and the sum of whose surface area and surface free energies become minimum. The equilibrium form may be constructed by inscribing an in-polygon circumscribed by planes of the internal tangent at the cusps of a raspberry form created by plotting the surface energy of faces, according to Wulff's plot idea. The surface free energies are related to the typical growth rates of faces. The equilibrium form for a specific crystal under a given thermodynamic situation is unique. Neither structural variables nor the equilibrium states control the true form of real polyhedral crystals. Interest in crystal equilibrium forms dates back to Steno's time, and findings from the 18<sup>th</sup> century showed that impurity components had a significant impact on the NaCl crystal's growth morphology grown in an aqueous solution. It was also discovered that in aqueous solution, adding a little quantity of urea changes the shape of NaCl crystals from cubes to octahedrons. Impurity effects



have been the topic of much research since then, and Buckley presented the previous research and his findings on the issue.<sup>20-21</sup>

### **b) Models to calculate the crystal habit**

The relative growth rates in distinct crystallographic orientations may be used to determine the exterior form of a crystal; the slower the development in one crystallographic direction, the bigger the plane develops perpendicular to it. BFDH (Bravais, Friedel, Donnay, and Harker) model is a geometrical technique that implies the fastest developing faces have the lowest spacing between surrounding layers of materials. The inter-plane distance ( $d_{hkl}$ ) is inversely proportional to the rate of growth ( $R_{hkl}$ ) in the perpendicular direction for a given crystalline plane (hkl). We and other researchers have successfully used this approach for predicting the crystal habit of numerous crystals such as ZnO<sup>35</sup>, FeOOH<sup>36</sup>, Nd: LaVO<sub>4</sub><sup>37</sup>, BaSO<sub>4</sub><sup>29-31</sup>, GdVO<sub>4</sub><sup>38</sup>, GeO<sub>2</sub><sup>39</sup>, CaCO<sub>3</sub><sup>40</sup>, triglycine sulphate<sup>41</sup>, benzophenone<sup>42</sup>, Pb<sub>17</sub>O<sub>8</sub>Cl<sub>18</sub><sup>43</sup> etc. The BFDH model, on the other hand, failed to anticipate the actual exterior form of the developed crystal in several cases. The influence of internal crystal structure, pseudosymmetry, and the orientation of weak and strong bonds in the crystal system were not properly explored in the BFDH technique, result in these failed predictions of the observed morphology. Crystal geometry has an unavoidable role in determining the ultimate crystal habit, according to Jolanta Prywer's research<sup>44-45</sup>. The crystal planes with interfacial angles ( $\alpha + \gamma$ ) near to  $\pi$  were found to be the most apparent in the final crystal morphology. Furthermore, based on its essential growth velocity relationship with nearby faces, a crystal face turns into a corner or an edge.<sup>44-45</sup>

The HP hypothesis is another widely recognised method for forecasting crystal habit. According to this, a crystal's morphology may be represented as a convex polyhedron with multiple high and low energy faces. The F, S, and K faces are the three types of faces available.<sup>29-31</sup> The flat faces will have the most morphological value in a developing crystal's morphology set and, as a result, will be the most noticeable in crystal habit. Even though this method has effectively forecast the crystal shape of numerous materials, looking at the number of PBC vectors exist in distinct crystallographic planes is a tedious task.

Nowadays, it is widely understood that a crystal's habit is dictated by the relative growth rates (RGR) of the numerous crystals faces that surround it. As a result, it is dependent on a

number of elements that may be classed as internal and external. Internal features such as dislocations, crystal structure, and twin boundaries are related with the crystal itself. External influences include pressure, temperature, non-crystalline material, supersaturation, and the flow or convection pattern, which are all imposed on the crystal by the crystallisation circumstances. There is no such thing as a crystal habit, strictly speaking. Nonetheless, the qualities of the ideal crystal structure may be used to describe a theoretical habit in a specific way. If such habits can be established, the impact of external circumstances may be properly comprehended and even quantified.

The theoretical morphology can be obtained mainly through these two approaches, the BFDH and the HP theory. The details will be discussed in chapter 2.

### **1.1.5 Example: Growth process to crystal habit**

Many efforts have been in understanding the formation processes, including nucleation and growth of metal, metal oxides, and many more. Researchers have paid attention to predicting the crystal habits of these metal oxides to understand the experimental results. ZnO is a well-known compound and one of the crucial examples examined in the last decades. D. D. Sarma group has done excellent research and found out ZnO's formation processes.

#### **a) ZnO: Growth process**

One of the oldest and most widely studied systems is the ZnO. Until recently, unfortunately, the research of ZnO nanocrystal's growth kinetics in solutions was riddled with contradicting assertions. It has long been known that zinc acetate and a base (NaOH) may be used to make ZnO. The inclusion of a little or even negligible quantity of H<sub>2</sub>O in the fabrication of ZnO nanocrystals has been seen to greatly impact the size of the nanocrystals, which has been a fascinating element of the sample preparation.<sup>46</sup> The growth kinetics of ZnO are examined without base and solely in the presence of precisely specified quantities of water in view of comprehend the exceptional sensitivity of ZnO nanocrystalline sizes to the existence of any detectable quantity of H<sub>2</sub>O. Hu et al.<sup>47</sup> published among the first papers on the growth kinetics of ZnO utilising H<sub>2</sub>O as a reactant. They investigated the growth kinetics by monitoring time-resolved UV absorption spectra and used the effective mass approximation (EMA) to analyse the change in the band edge. EMA, on the other hand, has long been proved to overestimate

nanocrystal size and so is not a particularly accurate technique for determining nanocrystal size.

In given reactants concentration at certain temperature, a typical collection of optical absorption spectra exhibits an apparent rise in absorption intensity with increasing time. This means that the concentration of ZnO will rise over time. More importantly, with increasing time, a systematic absorption edge shift to lower energies shows a gradual increase of bigger particles. The average diameter of the nanocrystals,  $d$ , was calculated from the bandgap's dependence on particle size, using realistic tight-binding modelling of first principle electronic structure calculations for ZnO, which has been shown to provide an accurate variation in bandgap energy with size, unlike the previously proposed EMA.<sup>46</sup> The observed sizes by the absorption spectra analysis have been validated by intermittently monitoring the TEM, because the size knowledge from the absorption edge shift is generated indirectly through the influence of an electronic structure on the nanocrystals sizes.

Zinc acetate is dissociated in this process, resulting in  $Zn^{2+}$  ions. The dissociation of water in the solution produces hydroxyl ions ( $OH^-$ ). Only the surface Zn atoms are ended with a  $OH^-$  ions rather than the oxygen ion in ZnO nanocrystals, which are tetrahedrally coupled Zn and O atoms. The dehydration of these terminating  $OH^-$  ions utilising freely accessible  $OH^-$  ions in the solution results in the development of a nanocrystal. The capture of  $Zn^{2+}$  ions brought to the nanocrystal's surface is then followed by diffusion. The nanocrystal's development is further accelerated by the  $Zn^{2+}$  ion grabbing an  $OH^-$  ion, and so on.<sup>46</sup> Therefore, the reaction is



and regulated by the diffusion of  $Zn^{2+}$  ions as well as the rate of reactions occurred at the surface. As a result, both factors must be included into account while modelling the growth processes. When they evaluated the increase in the dissociation constant of  $H_2O$  by nearly 2 orders of magnitude with rising a temperature, producing a significant quantity of  $OH^-$  ions at higher temperatures, this view was qualitatively corroborated by experimental results. At higher temperatures, this dramatically speeds up the process. At higher temperatures, the growth process is projected by a diffusion-controlled mechanism.<sup>46</sup>

## **b) ZnO: Crystal habit**

Another group<sup>35</sup> predicted the ZnO crystal habits using BFDH and HP models. Based on BFDH law, the morphological importance (MI) and RGR of several ZnO crystal planes were calculated. The (001) & (00-1) planes are predicted to be the highest MI. As a result, a ZnO crystal can be shaped as a hexagonal plate having (001) and (00-1) planes being most prominent and the morphological design predicted by the BFDH rule is shown in Figure 10.<sup>35</sup>

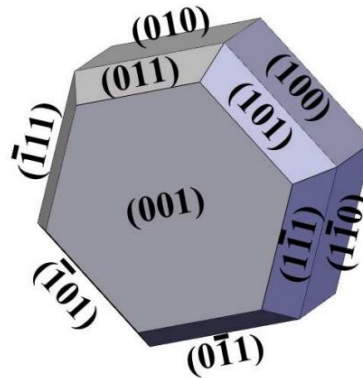


**Figure 10.** The indexed morphological drawing predicted by BFDH law; A hexagonal plate.

Using the BFDH law, the predicted crystal morphology fits the experimentally determined form of ZnO nanocrystals by multiple studies.

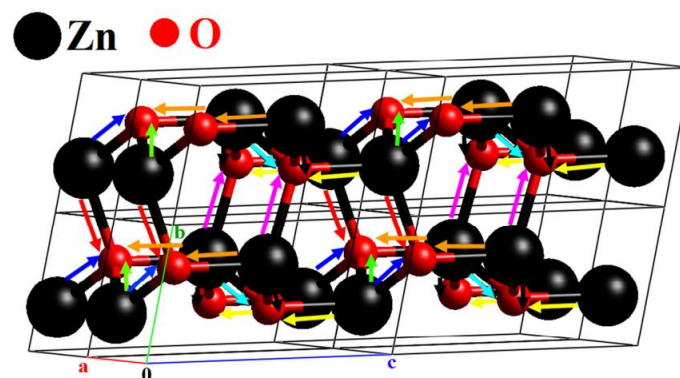


**Figure 11.** Packing diagram of ZnO crystal along with PBC vectors. The three crystallographic axes are denoted by a, b, and c.

Figure 11 shows the ZnO crystal packing diagram and multiple PBCs are presented with the distinct color arrows. Orange and yellow PBCs entirely lie in the (100), (010), (1-10), (0-10), (-100) and (-110) planes. As a result, these planes fall into the F face category, making them the most visible planes of crystal habit. (011), (101), (1-11), (0-11), (-101), (-111), (01-1), (10-1), (1-1-1), (0-1-1), (-10-1), (-11-1) planes belong to the S face category. The planes (001) and (00-1) fall into the category of least significant and, as a result, least visible planes (K faces).<sup>35</sup>

According to HP model, the 6 symmetric (010), (100), (1-10), (0-10), (-100), and (-110) planes that form a hexagonal prism have the highest MI. Thus, the shape of a hexagonal ZnO crystal structure may be represented as a hexagonal prism with hexagonal-truncated pyramids at both ends, as seen in Figure 12. It's worth noting that the theoretical crystal habits predicted by HP model matches the shape described in the literature for the formation of ZnO nanocrystals. It is also being researched for a variety of other materials.<sup>35</sup>

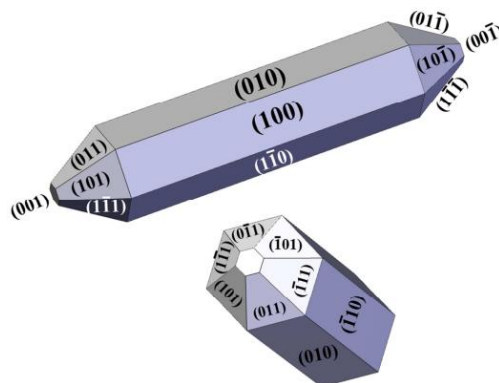


**Figure 12.** Indexed graphical morphology predicted by HP theory; A pencil or a hexagonal prism with hexagonal-truncated pyramids at both the ends.

However, the formation process and crystal habits have not been explored for complex systems like transition metal chalcogenides (TMCs) due to their complex structures. TMCs are one of the essential classes of materials in the periodic table for nanotechnology. It is essential to study the fabrication steps and crystal habits to achieve control over material and properties. In this thesis, we have made efforts to understand one of the crucial systems from TMCs, which can be extended to other systems.

## 1.2 Transition metal chalcogenides

Energy is currently one of the most pressing issues and is a chief concern among scientists. In order to meet the needs of energy-demanding areas— efficient, cost-effective, and environmentally friendly storage devices and energy conversion are essential. Materials used in these devices have a definite impact on their performance. Materials such as metal chalcogenides (MC), particularly those containing metal atoms (Fe, Co, and Ni) and chalcogen atoms, are gaining interest as potential targets for uses in devices including light-emitting-diodes, supercapacitors, solar cells, fuel-cells, Li-ion batteries, memory-devices, sensors,

magnetic materials, thermoelectric devices etc. Consequently, these compounds have been studied extensively in recent decades.<sup>48-49</sup>

Metal sulphides (such as chalcocite ( $\text{Cu}_2\text{S}$ ) and pyrite ( $\text{FeS}_2$ ))<sup>50-52</sup> are active photovoltaic materials, and because they naturally appear as minerals in the earth's crust, they are cheap and plentiful. Pyrite (also called fool's gold) has a suitable band gap of  $\sim 0.95$  eV and strong light absorption, providing high quantum efficiencies ( $\sim 90\%$ ) in devices. A roll-to-roll application of NPs, paint or ink on flexible substrates can be used to fabricate these materials, which are affordable and can be applied to huge surfaces. Several MC semiconductors, such as CdS, CdSe, PbS, and ZnS, are gaining popularity due to their easy conversion into QD at room temperature for use in narrower wavelength LEDs for display applications.<sup>53-55</sup> Materials including cobalt sulphide ( $\text{Co}_9\text{S}_8$ ) and nickel sulphide ( $\text{Ni}_3\text{S}_2$ ) have increased interest as cathode materials due to their metallic conductivity<sup>56</sup>. A remarkable oxygen reduction reaction (ORR) is carried out by cobalt selenides, tellurides, and their hybrids, which function as a catalyst for fuel cells<sup>57-58</sup>.

The ultrathin 2-D layered transition metal dichalcogenides (TMDs) hold great potential for fundamental and technological research<sup>49, 59-61</sup>. These TMDs have two equivalent valleys in the k-space and are primarily separated, allowing them to be used in valley-coupled spintronics applications<sup>62-64</sup>. Interlayer spaces in TMDs facilitate the growth of various external species, making them excellent energy storage compounds to be utilized in super capacitors, Li-ion batteries, and other energy storage devices<sup>59, 65-66</sup>. Several recent studies have demonstrated that bismuth selenide ( $\text{Bi}_2\text{Se}_3$ ) can be used as a parent matrix material for topological devices with quantum topological carrier transport<sup>67-69</sup>.

Biomedical applications have also demonstrated the potential of MCs. Bismuth selenide NPs have been utilised to monitor tumours and therapeutic actions in real time<sup>70</sup>. Drugs containing  $\text{Bi}_2\text{Se}_3$  NPs were capable of both thermo-chemotherapy and real-time imaging at the same time. A theranostic platform using iron sulphide and cobalt selenide NPs has been used for imaging and photothermal therapy<sup>71-72</sup>. Iron sulphide NPs can be employed for magnetic resonance imaging because of their super-paramagnetic nature and high near-infrared absorption.

In the wake of the discovery that high-temperature superconductivity was possible in the FeSe phase, researchers developed a great deal of interest in the iron-selenium phases<sup>73-74</sup>.

There is a great diversity in iron-selenium composites, such as superconducting, semiconductor, metallic properties, and permanent magnet-like characteristics<sup>75–77</sup>. Despite being part of the high-temperature iron-based superconductor family,  $\text{BaFe}_2\text{Se}_3$  was also found to have high ferroelectric polarization<sup>78</sup>. Others in the iron-selenium family ( $\text{CdCr}_2\text{Se}_4$ ) also exhibited multiferroic behavior<sup>79–80</sup>.  $\text{Fe}_3\text{Se}_4$  has recently shown spontaneous and reversible polarization for the first time. In  $\text{Fe}_3\text{Se}_4$  nanorods, our group<sup>81</sup> has observed the coexistence of ferroelectric and magnetic ordering (magnetoelectric coupling) at ambient temperature. As observed by our group, the ferroelectric and magnetic transition temperatures coincide and show a coupling manifested by an irregularity in the Raman shifts and dielectric constants at Tc. Despite not fully understanding how the ferroelectric ordering develops, the simultaneous presence of ferroelectric and magnetic ordering at ambient temperature in  $\text{Fe}_3\text{Se}_4$  will open new research avenues for future devices.

Figure 13 summarizes a few of the many areas of application of TMCs.

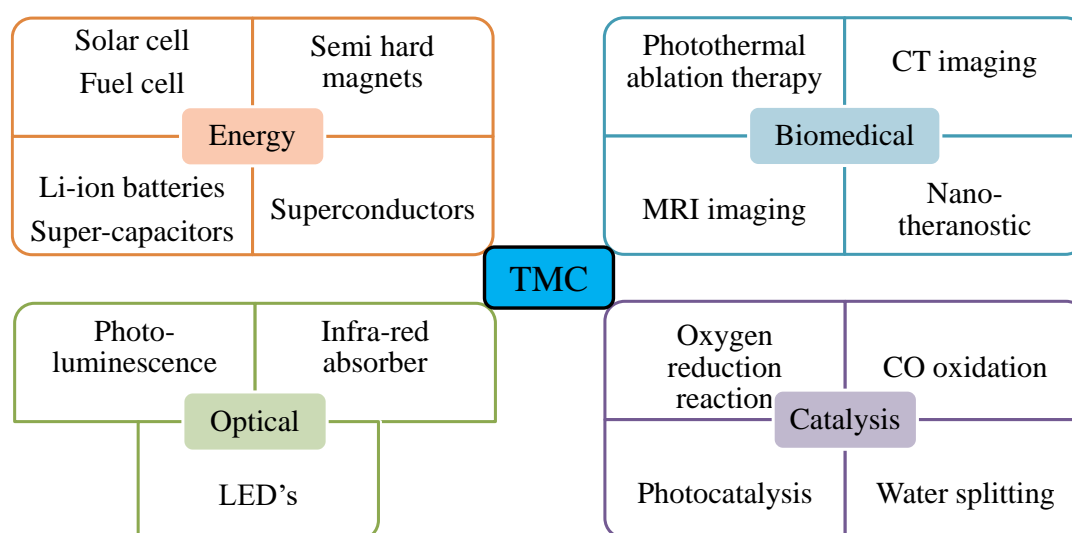


**Figure 13.** An illustration of the diverse applications of transition metal chalcogenides (TMCs).

### 1.3 What distinguishes chalcogenides from oxides?

Generally, the chalcogenides term is used to describe to the sulphides (S), selenides (Se), and tellurides (Te). They differ significantly from their oxide counterparts. Simple qualitative reasons reported by Jellinek<sup>75</sup> in his 1988 review paper explain the differences between chalcogenides and oxides. The majority of these variations are due to changes in oxygen and

chalcogen (S, Se, Te) atoms. These chalcogen atoms are heavier, larger, and less electronegative than oxygen atoms. This results in higher covalent nature of metal-chalcogen bonds compared to metal–oxygen interactions. At ambient temperature, oxygen has an oxidation state of -2; however, the oxidation states of chalcogen atoms can be less negative (for e.g., -1) due to their size and electronegativity. In contrast to oxygen, chalcogen atoms also have accessible *d* orbitals which is commonly employed to form metal-chalcogen bonds.

Chalcogenides have a narrower energy gap between the top of the valence band and the bottom of the conduction band than oxides. The valence band of oxygen is lower in energy than that of chalcogens because oxygen is more electronegative, although the conduction bands are mainly unaffected. In chalcogenides, the lowered bandgap results in a wide range of optical and electrical characteristics.

## 1.4 Transition metal selenide

TMCs cover a range of properties, from semiconductors to insulators to true metals to semimetals. These solids are utilized in various applications, including catalysis, electronics, charge-density waves, photovoltaics, and batteries<sup>48–49</sup>. So far, the studies are mainly focused on the transition metal sulfides (TMSs), while transition metal selenides (TMSes) are not fully understood due to their complexity in fabrication. However, transition metal tellurides are also not explored as they are much more complex in controlling the fabrication. In this thesis we will be exploring the TMSes.

In 1817, Jöns Jakob Berzelius discovered the selenium<sup>82</sup>. Its use in electronic equipment has historically driven the development of selenium as a semiconductor and photoconductive element, rubber compounding, glass manufacturing, and many more<sup>83</sup>. TMSes are transition metal compounds having Se atoms doped into the crystal lattices. Because selenium is in the same group as sulphur, TMSes have features that are comparable to TMSs. However, TMSes can relatively show better properties in various areas.

TMSes, for example, have piqued researchers' interest as electrode materials in electrochemical energy storage systems. The volume energy density and rate capability of TMSes as electrode materials may be higher than those of TMSs due to the relative higher density and electrical conductivity of Se or the Se atoms can draw electrons from metal atoms, acting as a base to trap positively charged protons during the electrochemical hydrogen



evolution reaction (HER). The creation of interstitial metal selenides, in contrast to metals, broadens the metal d band and induces a larger density of states (DOS) around the Fermi level, thereby increasing HER activity.<sup>84</sup>

The metal atom is always at the middle of two selenide layers in transition metal diselenides, forming a sandwich structure. The atoms in these three layers are covalently bonded, but the sole connection between the individual sheets is the weak Van der Waals force. Other atoms can easily and reversibly intercalate in the inter-chain gaps, generating intercalation compounds or intercalates, and therefore store energy in the layered conductors. Furthermore, the cation sites ( $\text{Ni}^{2+}$ ,  $\text{Co}^{2+}$ , and  $\text{Fe}^{2+}$ ) of transition metal-based catalysts have been proposed to be the electrocatalytic active centres based on chemical composition. In TMSes, the selenium anion, as well as the metal cation, plays an important role in the active catalytic sites. Both metal cations Co and Ni, as well as the anion Se, are active sites for the HER, acting as hydride-acceptor and proton acceptor centres, according to the model used to explain  $\text{CoSe}_2$  and  $\text{NiSe}_2$  for water splitting. Under the applied positive potential, metal ions are oxidised to create metal oxyhydroxide layers, which are the true catalytic sites in the oxygen evolution process (OER).<sup>84</sup>

The vanadium dichalcogenides ( $\text{VX}_2$ ) ( $X = \text{S}, \text{Se}, \text{Te}$ ) have demonstrated intrinsic magnetism.  $\text{VX}_2$  are highly desirable as magnetic 2D materials for spintronic applications because of their peculiar, odd electron configurations ( $3d^1$ ) with the potential for ferromagnetic coupling between V atoms. Based on DFT calculations, these dichalcogenides were semiconducting in the ground state. All their integrated magnetic moments were examined to be  $1\mu\text{B}$ . Additionally, the high Curie temperatures varying from 292 to 553 K as the X is changing were estimated— 292 K, 472 K, and 553 K for the  $\text{VS}_2$ ,  $\text{VSe}_2$ , and  $\text{VTe}_2$  monolayers, respectively.<sup>85</sup> As X increases, so will the magnetic transition temperature, providing a benefit in the case of Se. The magnetic transition temperature lies in the center and can be easily tuned according to application requirements. With these advantages, it's no surprise that a material's chemical composition, electrical structure, and shape have a considerable impact on its chemical and physical qualities. TMSes with a combination of transition metal cations, selenium anions, and richer morphological/structural features display excellent properties.

## 1.5 Fe-Se system

TMSes represent an important class of materials with rich phase-diagram and diverse industrial applications. The electronic (optical, magnetic, and electrical) and thermal properties are extremely sensitive to the crystalline phase, stoichiometry, shape, and size. Therefore, it is essential to reach good control over the chemistry of phase formation. Among the TMSes,  $\text{Fe}_x\text{Se}_y$  compounds (with  $x/y$  varying from 1:2 to 1:1) are of great importance because of their interesting and unique magnetic, electrical, thermal, and optical properties, which are firmly related to the Fe–Se elemental ratio as well as their crystalline structure.

### 1.5.1 Journey of the Fe-Se system

The iron-selenium (Fe-Se) system was investigated for the first time in 1933 by Hagg and Kindstrom<sup>86</sup>. They have discussed the 3 phases of the Fe-Se system – FeSe,  $\text{Fe}_3\text{Se}_4$ , and  $\text{Fe}_7\text{Se}_8$ . After 5 years, in 1938, Tengner<sup>87</sup> synthesized the 4<sup>th</sup> phase  $\text{FeSe}_2$  when synthesizing the diselenides and ditellurides. Consequently, from 1933 to 1938, all the phases were discovered. There was no study for the next 18 years. In 1956, Hirone<sup>88</sup> studied the magnetic properties of powdered  $\text{FeSe}_x$  ( $x = 1.00 \sim 1.35$ ). In the same year, Okazaki and Hirakawa<sup>89</sup> made the single crystal of  $\text{Fe}_3\text{Se}_4$  and  $\text{Fe}_7\text{Se}_8$ , studying the magnetic behavior in 1957 (by Hirakawa<sup>90</sup>). In 1964, Andresen and Leciejewicz<sup>91</sup> did the neutron diffraction of  $\text{Fe}_7\text{Se}_8$ , and after four years, in 1968 Andresen<sup>92</sup> did the same for  $\text{Fe}_3\text{Se}_4$ . In 1972, Svendsen<sup>93</sup> studied the decomposition pressure of the Fe-Se system. Finally, in 1979, Schuster<sup>75</sup> gave the phase diagram of the Fe-Se system. The iron-selenium phase diagram is shown in Figure 14 by collecting all of the relevant data in the literature. The NiAs-type structure is the only solid state at extremely high temperatures. At 458 °C, the tetragonal phase undergoes a process that produces NiAs-structure and iron. At 704 °C,  $\text{Fe}_3\text{Se}_4$  undergoes a l-transition into the hexagonal form. At 585 °C,  $\text{FeSe}_2$  melts in an incongruent manner, forming a NiAs-structured and selenium-rich liquid.<sup>75</sup>

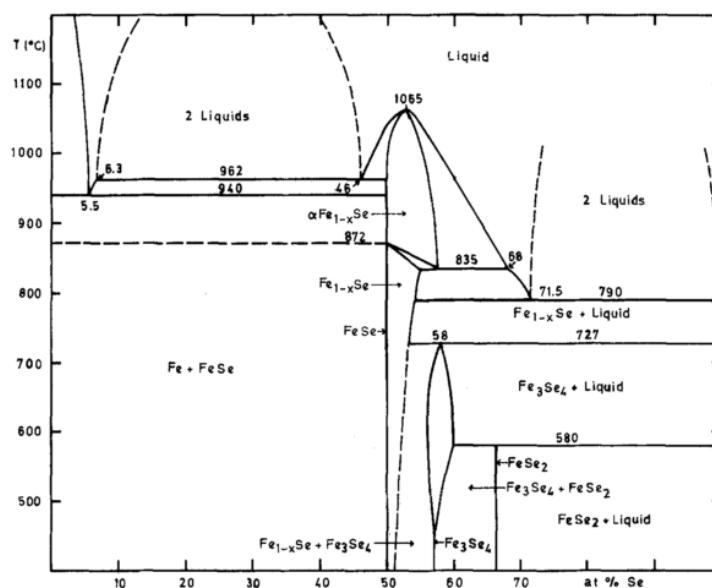


**Figure 14.** Iron--Selenium phase diagram.

### 1.5.2 The binary Fe-Se system

Thermo-analytical and XRD techniques were used to examine the iron–selenium system. In 1970, a phase diagram (temperature–concentration) was produced using all of the measurement findings, ranging from 623 to 1323 K and 20 to 66 atomic percent selenium. In Fe–Se systems, three key phases with distinct structures have been found.<sup>75, 93</sup> These three stages are addressed, as well as their structures and stability ranges.

#### a) FeSe<sub>2</sub>

This phase contains the most Se and a narrow homogeneity range (66.6 at% Se). Iron diselenide (Fe<sup>2+</sup>Se<sub>2</sub><sup>2-</sup>) at room temperature possesses an orthorhombic marcasite structure. Figure 15a shows a standard FeSe<sub>2</sub> unit cell with one formula unit having lattice parameters of  $a = 3.57 \text{ \AA}$ ,  $b = 4.79 \text{ \AA}$ , and  $c = 5.72 \text{ \AA}$  and a Pmnn SG. Every Fe atom is octahedral with 6 Se atoms (FeSe<sub>6</sub> octahedra), while each Se atom is tetrahedral with 3 Fe atoms and 1 Se atom, producing a dimer pair (Se<sub>2</sub>Fe<sub>3</sub> tetrahedra).<sup>94</sup>

#### b) Fe<sub>1-x</sub>Se

The phases with a wide homogeneity range of 51 to 59 at % Se are described by the generic formula Fe<sub>1-x</sub>Se. The hexagonal NiAs structure is observed in Fe<sub>7</sub>Se<sub>8</sub> (53.3 %) and the NiAs structure undergoes a monoclinic deformation for Fe<sub>3</sub>Se<sub>4</sub>. These phases are defined by Fe ion

vacancies in the structure. In both stoichiometric compounds  $\text{Fe}_3\text{Se}_4$  and  $\text{Fe}_7\text{Se}_8$ , the ordering of iron vacancies causes ferrimagnetism. In  $\text{Fe}_3\text{Se}_4$  and  $\text{Fe}_7\text{Se}_8$ , which have monoclinic and hexagonal NiAs-type crystal structures, respectively, these iron vacancies are restricted to every alternate metal atom layer as shown in Figure 15b, c.

However, the unit cell lattice parameters of  $\text{Fe}_3\text{Se}_4$  are  $a = 6.167 \text{ \AA}$ ,  $b = 3.537 \text{ \AA}$ , and  $c = 11.17 \text{ \AA}$  with a  $I2/m$  space group and  $\text{Fe}_7\text{Se}_8$  are  $a = 7.21 \text{ \AA}$  and  $c = 17.67 \text{ \AA}$  with a  $P_{3121}$  space group. In  $\text{Fe}_{1-x}\text{Se}$ , the Fe cations are octahedrally coordinated with 6 Se anions ( $\text{FeSe}_6$  octahedra), and the coordination polyhedron of Se is the trigonal prism created by 6 Fe ( $\text{SeFe}_6$  prisms). The ionic picture of one formula unit of  $\text{Fe}_3\text{Se}_4$  and  $\text{Fe}_7\text{Se}_8$  can be written as  $\text{Fe}^{2+}\text{Fe}_2^{3+}\text{Se}_4^{2-}$  and  $\text{Fe}_5^{2+}\text{Fe}_2^{3+}\text{Se}_8^{2-}$ , respectively.<sup>91–92, 95–96</sup>

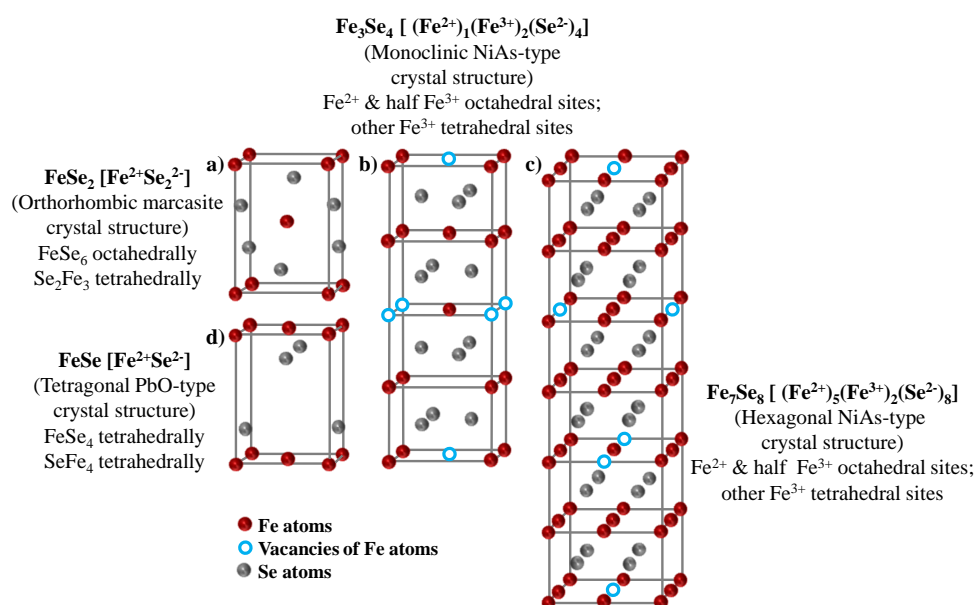


**Figure 15.** Schematic shows essential phases from the binary Fe-Se phase diagram with a different crystalline structure.

### c) FeSe

With a PbO structure and an estimated composition of  $\text{Fe}_{1.04}\text{Se}$ , this phase contains 49.02 at % Se. During this phase, there are extra iron atoms in the interstitial spaces. Layers of edge sharing  $\text{FeSe}_4$ -tetrahedra make up the crystal structure of FeSe. It is essential to note that the highest temperature phase  $\beta$ -FeSe has a tetragonal PbO-type crystal structure. The unit cell lattice parameters of FeSe ( $\text{Fe}^{2+}\text{Se}^{2-}$ ) are  $a = 3.765 \text{ \AA}$  and  $c = 5.518 \text{ \AA}$  with the  $P4/nmm$  space group.

Figure 15d shows the unit cell of FeSe: each Fe atom is tetrahedral-coordinated with four Se atoms (FeSe<sub>4</sub> tetrahedral), and each Se atom is tetrahedral-coordinated with four Fe atoms (SeFe<sub>4</sub> tetrahedral). This material has the simplest crystal structure among iron-based superconductors.<sup>73</sup>

## 1.6 Magnetic structure of Fe-Se system

Among the abovementioned four phases of the Fe–Se system, two phases (Fe<sub>3</sub>Se<sub>4</sub> and Fe<sub>7</sub>Se<sub>8</sub>) are well known for their magnetic properties, whereas the other two (FeSe<sub>2</sub> and FeSe) are known for their optical and electronic properties. FeSe<sub>2</sub> shows a broad absorption at ~1100 nm and has semiconducting properties with a bandgap ~1 eV<sup>73, 97–98</sup>. FeSe<sub>2</sub> is useful for solar energy applications due to its optical characteristics. After discovering superconductivity with a transition temperature of 8 K<sup>73</sup>, the FeSe phase drew the interest of researchers all around the world. The magnetic ordering of bulk FeSe<sub>2</sub> and FeSe generated by solid-state processes is either non-existent or very low. Bulk Fe<sub>3</sub>Se<sub>4</sub> and Fe<sub>7</sub>Se<sub>8</sub> exhibit ferrimagnetic behaviour at room temperature (RT) with the Curie temperature (T<sub>C</sub>) ~320 and 453 K, respectively<sup>91, 92</sup>.

### 1.6.1 Magnetic structure of Fe<sub>3</sub>Se<sub>4</sub>

The unit cell of Fe<sub>3</sub>Se<sub>4</sub> is extremely identical to the Cr<sub>3</sub>X<sub>4</sub> (X= S, Se, and Te), although there is no expansion of the unit cell owing to magnetic ordering as in Cr<sub>3</sub>X<sub>4</sub> compounds, according to neutron diffraction observations on bulk polycrystalline samples<sup>92</sup>. At 81 K and 371 K, two diffraction patterns were obtained. Because the only additional peaks detected were owing to  $\lambda/2$  peaks and inferred that magnetic ordering did not cause the unit cell to increase. The magnetic moments are aligned ferromagnetically within each *c*-plane and antiferromagnetically aligned in neighboring planes. The direction of moment is in the *c*-plane, and it's most likely along the diagonal face. Later research revealed that the moments are oriented along the *b*-axis<sup>92</sup>. The structural changes associated with the transition from Fe<sub>7</sub>Se<sub>8</sub> to Fe<sub>3</sub>Se<sub>4</sub> are quite minor, as seen below.

- There is a little monoclinic distortion, and the quantity of vacancies and how they are distributed in the vacancy layers varies.
- Contraction of the lattice along the *c*-axis. In this direction, the Fe-Fe distance decreases from 2.94 to 2.79 Å.

One formula unit of  $\text{Fe}_3\text{Se}_4$  can be written as  $\text{Fe}^{2+}\text{Fe}_2^{3+}\text{LSe}_4^{2+}$ , where L represents a vacancy. The alignment of magnetic moments in  $\text{Fe}_3\text{Se}_4$  unit cell is shown in Figure 16.

The moment values calculated by neutron diffraction measurements are nearly identical to the determined value of  $3.25 \mu_B$  for  $\text{Fe}^{2+}$  and  $1.94 \mu_B$  for  $\text{Fe}^{3+}$ .<sup>99</sup>

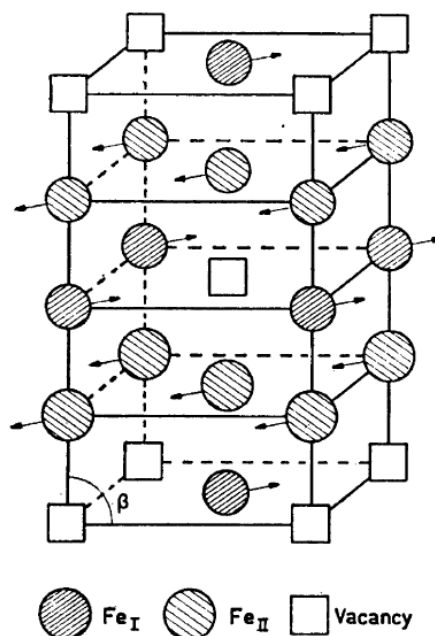


**Figure 16.** The unit cell of  $\text{Fe}_3\text{Se}_4$  shows the orientation of magnetic moments.

### 1.6.2 Magnetic structure of $\text{Fe}_7\text{Se}_8$

Iron ions in the same c-layer have magnetic moments that are parallel to one another, whereas moments in adjacent c-planes are antiparallel.  $\text{Fe}_7\text{Se}_8$  is ferrimagnetic due to a net spontaneous moment below the ordering temperature caused by a lack of iron ions in alternating layers. Hirakawa used a torque magnetometer to test the magnetic characteristics of a sample of the 4c structure. He discovered that the ferrimagnetic Curie point is  $\sim 443$  K, and that the simple magnetization direction is in the c-plane at ambient temperature. When the temperature was reduced to 220 K, the easy direction progressively rotated off of the c-plane, forming a 20-degree angle with the c-axis at 4.2 K.<sup>100</sup>

In powder samples of the 3c structure, Andresen and Leciejewicz observed a similar result. At 4.2 K, their neutron diffraction investigation revealed an  $18^\circ$  between the spin direction and the c-axis. It did, however, show that the rotation from the c-plane occurred within

a small temperature range of 120 K to 130 K. Neutron diffraction data from a later examination of single-crystal samples agree with Hirakawa's findings for the 4c structure, but imply that around 130 K, crystals with the 3c structure undergo a sudden rotation of 90°. The spontaneous moment is parallel to the c-axis below this temperature and lies in the c-plane above it.<sup>100</sup> Hirakawa evaluated the saturation magnetization of a 4c sample and found it to be 70 G/cm<sup>3</sup> which leads Hirakawa to predict the ionic model  $[Fe_4^{2+}] [Fe_2^{3+}Fe^{2+} L] Se_8^{2-}$  for the magnetic structure based on a net moment of 2 $\mu_B$ /molecule which give a saturation magnetization of 69 G/cm<sup>3</sup>, where L represents an ion vacancy and the brackets indicate successive c-planes<sup>100</sup>.

### 1.7 Importance of nano dimensions in magnetic properties

NPs are materials that have at least one dimension between 1 and 100 nanometres (nm) and typically have several hundred to 10<sup>5</sup> atoms. Magnetic nanoparticles (MNPs) are NPs that respond to a magnetic field applied to them. Nanotechnology permits chemists, engineers, physicists, and material scientists to create systems with nanoscale dimensions where the traditional rules of science do not apply. As the particle's size shrinks, the particle's surface area to volume ratio grows.<sup>101</sup> When it comes to NPs, this ratio increases dramatically, leading a high proportion of the atoms to live on the surface rather than in the particle's core. For example, about 0.15 percent of the atoms in a particle with a diameter of 1  $\mu\text{m}$  are on the surface, but over 20% of the atoms in a particle having a radius of 3 nm are on the surface. As the size of the NPs reduces, the surface-to-volume ratio rises (and as a result, the percentage of surface atoms in comparison to bulk atoms). The new physical, chemical, and mechanical characteristics of the NPs are because of their enormous surface-to-volume ratio when matched to those of the analogous bulk material.<sup>101</sup>

Some of the most important characteristics of MNPs are discussed in this thesis. This thesis does not purport to address all elements of NPs. The magnetic moment and magnetic anisotropy of NPs can vary than those of a bulk material, as is well known. Several additional magnetic characteristics, including the Neel or Curie temperatures, coercivity, and others, were discovered to differ from those of the bulk material.<sup>101</sup>

We require certain geometric and magnetic data regarding MNPs in order to study their characteristics in an acceptable manner. The geometric data includes information on the NPs' composition, size, shape, and crystal structure. Temperature dependent saturation

magnetization ( $M_S$ ), magnetization, coercivity ( $H_C$ ), remnant magnetization ( $M_R$ ), and blocking temperature ( $T_B$ ) are all examples of magnetic data. The magnetic characteristics of NPs are dominated by two key aspects that give them unique specific capabilities:

- (a) Finite-size effects (electron quantum confinement and single-domain or multi-domain structures)
- (b) Surface effects are caused by symmetry breaking at the particle's surface, dangling bonds, oxidation, surface strain, surfactants, or even differing physical and chemical structures of the interior (core) and surface (shell) components of the NP.<sup>101</sup>

Because of the tiny size of NPs, surface atoms make up a considerable portion of the total atom count. Surface contribution to magnetization becomes considerable when the fraction of surface to bulk atoms is high. A single domain particle with uniaxial anisotropy normally makes up an MNP. The magnetic moment's direction in a zero field along the easy axis is either up or down. Surface atoms, on the other hand, are exposed to different surroundings than those in the particle's core. Lattice disorder, atomic vacancies, dangling bonds, and alterations in atomic coordination, are type of defects present on the surface. Surface magnetization is caused by uncompensated disordered spins at the NP's surface as a result of these surface imperfections. The uncompensated surface spins, which are based on the particle size and degree of surface disorder, contribute to the surface magnetism. Ferromagnetism might be a ubiquitous characteristic of NPs and their oxides due to surface effects. For example, magnetic hysteresis loops were discovered in nonmagnetic materials such as aluminium oxide and cerium oxide NPs at ambient temperature. Metal nitrides (niobium nitride) have ferromagnetism effects in their NPs. Ferromagnetism was discovered in the NPs of several superconductors in their normal state. It is important to note that surface influences can cause NP magnetization to drop or increase. It has been found that the magnetization of certain oxide NPs diminishes. On the other hand, it has been observed that the magnetization of certain metallic NPs (cobalt) has increased. The decline in magnetism of oxide NPs has been associated with the presence of a magnetic dead layer on the NPs surface, the appearance of a spin-glass-like behaviour of the surface spins or the presence of canted spins. Numerous experiments have found that surface effects enhance effective magnetic anisotropy. The overall magnetization of the NP is thought to be made up of two parts: one caused by the surface spins



and the other by the particle's core. As a result, studying the magnetic behaviour of the Fe-Se combination at the nanoscale, as opposed to bulk, will be both intriguing and necessary.<sup>101</sup>

## 1.8 Synthesis routes

Several synthetic pathways have been designed and optimized for better phase control of miscellaneous inorganic NPs. Chemical approaches provide numerous significant benefits over solid-state procedures in terms of cost, control of objective products, large-scale manufacturing, and so on.<sup>102–103</sup> The solid-state pathways require heat-beat-treat iterations (involving high-temperature furnaces with the specific environment), high purity elements as precursors apart from being worse on the energy-economy scale. Moreover, there are chances of phase impurity due to poor atomic diffusion through the solid phase, leading to non-stoichiometric phases and broad phase boundaries where two or more phases could coexist. In contrast, the chemical methods are far more effective, efficient, economical, and provide better phase purity than solid routes. Besides this, these methods often require relatively much lower temperatures for the phase formation, plus easier control over the size, shape, and structure.

Several reports have dealt with fabricating the Fe-Se compounds by chemical synthesis routes in the last decade. In 2009, Lin et al.<sup>104</sup> obtained Fe<sub>3</sub>Se<sub>4</sub> and Fe<sub>7</sub>Se<sub>8</sub> NPs for the first time via the thermal decomposition method at 350 °C. Fe<sub>3</sub>Se<sub>4</sub> nanostructures were also synthesized at 300 °C via a one-pot high-temperature organic-solution-phase route<sup>105–106</sup>. In 2012, flower-like FeSe<sub>2</sub> NPs were synthesized via a solvothermal approach in the temperature range 180 °C - 300 °C<sup>107–108</sup>, and in 2014, FeSe<sub>x</sub> (x=1, 2) was synthesized at 330 °C by using the hot-injection method<sup>109</sup>. FeSe<sub>2</sub> NPs were also synthesized with the hydrothermal route at 140 °C for 13 h<sup>110</sup>. Recently, Li and their group synthesized FeSe NPs by the solvothermal reaction in an autoclave at 160 °C for 12 h, later at 220 °C for 24 h<sup>111</sup>. All methods mentioned above involved either complex synthesis conditions (high temperature or long reaction time) or expensive chemicals for synthesizing the Fe-Se system. Thus, adopting an easy and affordable reaction route (such as low-temperature, short time, and low-cost) with well-defined tunability and high crystallinity of the Fe-Se system.

**Table 1.** List of critical chemical routes to synthesis Fe-Se system.

Year	Phase	Method	Precursor	Solvent	Temp.
2009	Fe <sub>3</sub> Se <sub>4</sub> Fe <sub>7</sub> Se <sub>8</sub>	Thermal decomposition	FeCl <sub>2</sub> .4H <sub>2</sub> O + Se powder	OLA	330 °C
2011	Fe <sub>3</sub> Se <sub>4</sub>	Thermal decomposition	Fe(acac) <sub>3</sub> + Se powder	OLA	300 °C
2012	FeSe	Solvothermal decomposition	[Fe(μ <sub>3</sub> -O)(μ <sub>2</sub> -O <sub>2</sub> CCH <sub>2</sub> Cl) <sub>6</sub> (H <sub>2</sub> O) <sub>3</sub> ]NO <sub>3</sub> .H <sub>2</sub> O + Sodium selenite	-	-
2012	FeSe <sub>2</sub>	Solvothermal reduction process	Fe(OH) <sub>3</sub> + Se powder	OLA	200 °C
2012	FeSe <sub>2</sub>	Solvothermal reduction reaction	Fe(NO) <sub>3</sub> + Se powder	OLA	180 – 330 °C
2014	Fe <sub>6-7</sub> Se <sub>8</sub>	Thermal decomposition	FeCl <sub>2</sub> .4H <sub>2</sub> O + Se powder	OLA	340 °C
2014	FeSe <sub>2</sub>	Hydrothermal method	FeSO <sub>4</sub> .7H <sub>2</sub> O + SeCl <sub>4</sub>	PEG400 0, PVA, SDS, PEG600	140 °C (13 h)
2014	FeSe <sub>x</sub> (x=1, 2)	Hot-injection method	Fe(acac) <sub>2</sub> + Se powder	OA + ODE	330 °C
2016	FeSe	Hydrothermal method	FeSO <sub>4</sub> .7H <sub>2</sub> O + Se powder + NaOH + PVP + CTAB + SDS +	EG	220 °C (24 h)

## 1.9 Magnetic study of Fe-Se nanoparticles

As discussed above, among the four phases of the Fe–Se system, two phases ( $\text{Fe}_3\text{Se}_4$  and  $\text{Fe}_7\text{Se}_8$ ) are renowned for their magnetic properties, whereas the other two ( $\text{FeSe}_2$  and  $\text{FeSe}$ ) are illustrious for their optical and electronic properties.

Although bulk  $\text{FeSe}_2$  and  $\text{FeSe}$  do not exhibit any magnetic ordering or exhibit very low magnetic ordering, all previously reported solution produced samples reveal magnetic ordering in the last two phases ( $\text{FeSe}_2$  and  $\text{FeSe}$ ) also at the nanoscale due to the several defects which we will be discussing in detail in chapter 4.

Bulk and nanostructured  $\text{Fe}_3\text{Se}_4$  and  $\text{Fe}_7\text{Se}_8$  exhibit ferrimagnetic behavior at RT with the  $T_C \sim 320$  and  $453$  K, respectively. Lin et al.<sup>104</sup> described the synthesis of  $\text{Fe}_3\text{Se}_4$  and  $\text{Fe}_7\text{Se}_8$  NPs. The synthesised  $T_C$  of the synthetic  $\text{Fe}_7\text{Se}_8$  and  $\text{Fe}_3\text{Se}_4$  compounds are  $453$  K and  $340$  K, respectively, according to magnetic measurements. At  $300$  K, the obtained magnetization for  $\text{Fe}_7\text{Se}_8$  and  $\text{Fe}_3\text{Se}_4$  are  $9.6$  and  $6.9$  emu/g; the coercivity is  $687$  Oe and  $3344$  Oe, respectively. Further, it was observed that the  $\text{Fe}_3\text{Se}_4$  possesses hard magnetic properties having a large coercivity of up to  $40$  kOe at  $10$  K and  $4$  kOe at  $300$  K. In view of the large coercivity,  $\text{Fe}_3\text{Se}_4$ -based materials are believed to be a nontoxic and low-cost alternative to the rare-earth element or noble-metal-based hard-magnets. This increased coercivity is associated with large uniaxial magneto-crystalline anisotropy of  $\text{Fe}_3\text{Se}_4$ .

The globe was seeking for rare-earth-free replacement for permanent magnets applications due to the ever-growing expense of rare earth elements, environmental damage and health concerns. The semi-hard magnetic characteristics of the monoclinic iron selenide phase ( $\text{Fe}_3\text{Se}_4$  NPs) drew researchers' attention after enormous coercivity was discovered in the  $\text{Fe}_3\text{Se}_4$  NPs.

### 1.9.1 Why do the magnetic characteristics of $\text{Fe}_3\text{Se}_4$ differ from others?

For the past seven decades,  $\text{Fe}_3\text{Se}_4$  has been investigated for its magnetic characteristics. It has been known from the 1950s that the phase with a NiAs-type structure exhibits ferrimagnetic characteristics. Okazaki and Hirakawa<sup>89</sup> studied the structure of these phases in 1956 and concluded that the ferrimagnetism is due to ordered iron vacancies in the structure. Due to the existence of Fe-vacancies, the XRD patterns of single crystals  $\text{Fe}_3\text{Se}_4$  and  $\text{Fe}_7\text{Se}_8$  revealed strong spots belongs to the NiAs-type structure and few extremely weak spots designated to

the superstructures because of Fe vacancies. The vacancies are spread out as widely as feasible. The superstructure's lattice parameters are twice as big as the fundamental structure along the a and b axes, three times along the c-axis for Fe<sub>7</sub>Se<sub>8</sub> and two times for Fe<sub>3</sub>Se<sub>4</sub>. The magnetic unit cell was discovered as same as the structural unit cell in a subsequent neutron diffraction experiment on Fe<sub>3</sub>Se<sub>4</sub> in 1968<sup>28</sup>. Moments are ferromagnetically aligned in the c-plane (collinear along the b-axis), while they are antiferromagnetically aligned in the neighbouring planes.

The monoclinic phase of iron selenide (Fe<sub>3</sub>Se<sub>4</sub>) revealed several extremely intriguing new features when reduced to nanoscale. The appeal of Fe<sub>3</sub>Se<sub>4</sub> originates from the fact that it has semi-hard magnetic characteristics at ambient temperature with absence of noble metal or rare-earth atoms in nanoscale. The easy axis is along the c-plane, as shown by single crystals of Fe<sub>3</sub>Se<sub>4</sub>. Even with an external magnetic field of 11000 Oe, the sample does not saturate. Fe<sub>3</sub>Se<sub>4</sub> is a ferrimagnet with a T<sub>C</sub> of ~320 K, comparable to its sulphur counterpart Fe<sub>3</sub>S<sub>4</sub>. Unlike Fe<sub>7</sub>Se<sub>8</sub>, Fe<sub>3</sub>Se<sub>4</sub> does not display the rotation of its easy-axis with temperature. Despite the fact that this compound has been familiar to be ferrimagnetic for over half a century, the latest push began with the finding of semi-hard magnetic characteristics in Fe<sub>3</sub>Se<sub>4</sub> at room temperature. The huge coercivity (4 kOe at ambient temperature) that Fe<sub>3</sub>Se<sub>4</sub> exhibits when reduced to nanoscale is a remarkable feature.<sup>105</sup> It has a significant uniaxial anisotropy constant of around 10<sup>-7</sup> erg/cm<sup>3</sup>. The advent of huge coercivity (40 KOe) at 10 K is the compound's most appealing property (Figure 17). The saturation magnetization also rises from 5 emu/g to 15 emu/g when the coercivity increases approximately 10-fold from room temperature<sup>105</sup>. At low temperatures, the hysteresis loop is virtually squarish. Anisotropy constants of this magnitude are extremely uncommon in compounds containing no noble metal ions or rare earth metal ions.

In 2011, Gen et al.<sup>112</sup> investigated the coercivity and anisotropy of Fe<sub>3</sub>Se<sub>4</sub> nanostructures. Experiments and first-principles simulations are used to investigate the cause of this massive coercivity at low temperatures. The huge anisotropy constant (1.1 × 10<sup>7</sup> erg/cm<sup>3</sup>) resulting from ordered cation vacancy at 10 K is the reason for the significant coercivity value. The anisotropy constant (K<sub>u</sub>) may be calculated by extrapolating the hysteresis curves in hard and easy directions while the powder sample is aligned in an external magnetic field.<sup>112</sup>

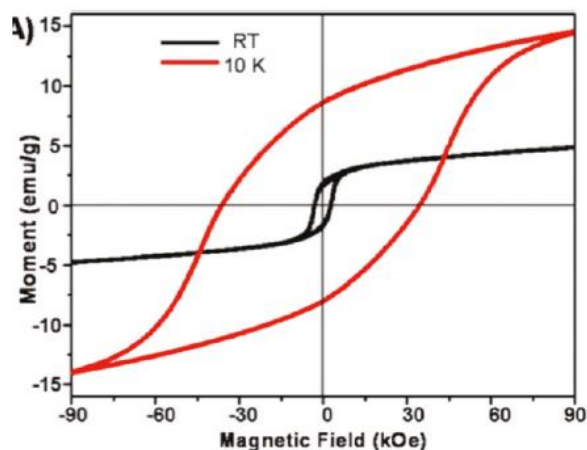


**Figure 17.** Hysteresis loops of  $\text{Fe}_3\text{Se}_4$  nanocacti were measured by the vibrating sample magnetometer option of a PPMS with a field of 90 kOe at 10 K (red curves) and room temperature (black curves). The 10 K hysteresis loops were measured after zero-field cooling.

At high field values fitting the magnetization according to the equation below is the law of approach to saturation to estimate the anisotropy constant from the material's hysteresis loop<sup>112</sup>.

$$M = M_S + A \left( \coth \frac{\mu H}{K_B T} - \frac{K_B T}{\mu H} \right) \text{-----}(2)$$

where  $M_S$  denotes saturation magnetization and  $M$  denotes an ultrafine particle's total moment. At 10 K, the observed magnetic hysteresis loop of  $\text{Fe}_3\text{Se}_4$  NPs accords to the theoretical curve for a noninteracting randomly oriented uniaxial single-domain particle system by Stoner and Wohlfarth. The  $K_u$  is proportional to the cube of the saturation magnetization  $M_S$  in each of the aforementioned studies, indicating the presence of uniaxial magneto-crystalline anisotropy in this compound.

The below-mentioned expression can estimate the critical size for the single domain size of  $\text{Fe}_3\text{Se}_4$ <sup>112</sup>

$$r_c \approx 9 \frac{(AK_u)^{1/2}}{\pi M_S^2} \text{-----}(3)$$

The exchange stiffness constant is  $A$ .  $\text{Fe}_3\text{Se}_4$  has a single domain size of roughly 2000 nm, according to calculations. As a result, NPs smaller than this can be classified as single domain

particles. The uncoordinated rotation of spins in this molecule is the magnetization reversal process.

### **1.10 Various factors that can influence the magnetic properties in Fe-Se system**

The magnetism of NPs is a hot topic in many domains, including condensed matter physics, material science, medicine, biology, and planetary science, to name a few. Nanoscale magnetic materials are being studied for high-density magnetic storage, ferrofluids, high-frequency electronics, magnetic refrigerants, high-performance permanent magnets, and other applications<sup>101</sup>. Superparamagnetism, quantum tunnelling of magnetization, and increased magnetic coercivity are only a few of the unusual properties of small magnetic particles. Specific magnetic NPs (such as CoPt, FePt) are of considerable attention for future high-density recording mediums because of their improved magnetic characteristics. Magnetic NPs are also employed in biotechnology and medicine.<sup>101</sup>

The inherent magnetic characteristics of bulk defect-free materials (e.g.,  $H_C$ ,  $M_S$ , and  $T_C$ ) are solely determined by crystallographic and chemical structure. The size and form of bulk samples analyzed aren't critical; such as the  $H_C$ ,  $T_C$  and  $M_S$  values of tiny as well as large cobalt compounds are identical. MNPs exhibit a large range of unexpected magnetic characteristics when compared to their bulk counterparts.<sup>101</sup>

Therefore, studying the Fe-Se system's magnetic behavior at the nanoscale is essential. In the Fe-Se system, 4 essential factors decide the magnetic properties of resultant materials—stoichiometry, morphology, Fe element, and Se element. As we are working on transition metal selenides, the tunability of the Se element is omitted. Additionally, the Se element influence is not easy to control by chemical route as the tellurium starts reacting at a very high temperature (melting point  $\sim 449.5$  °C). However, the other remaining 3 factors can be explored by chemical processes.

The impact of doping on the magnetic characteristics of iron selenide has been investigated by scientists. For example, the scientists observed that substituting few of the Fe atoms with other metal atoms resulted in significant changes in the material's characteristics. The efforts are largely focused on increasing the material's magnetic properties. The replacement of Co and Ni atoms in place of Fe dilutes the ferrimagnetic nature of  $Fe_3Se_4$ , and

the replaced atoms do not display localised moments in single crystals.  $\text{Co}_x\text{Fe}_{3-x}\text{Se}_4$  (where  $x = 0$  to 1) Co-doped  $\text{Fe}_3\text{Se}_4$  nanostructures revealed that the doped structures are also monoclinic<sup>113</sup>. With rising Co concentration, the  $M_s$ ,  $H_c$ , and  $T_C$  decrease. For  $x = 0.2$ , the NPs' coercivity at 10 K is lowered to 37 kOe, and for  $x = 1$ , it drops to 9 kOe. For  $x = 1$ , the  $T_C$  is reduced to less than 200 K, leading the paramagnetic nature at room temperature. Another study shows, the  $T_C$  improves when specific Fe atoms are substituted with Cr ones. The  $T_C$  for  $\text{FeCr}_2\text{Se}_4$  samples was reported to be 429 K<sup>114</sup>. According to reports, Cr-substitution improves anisotropy constant and coercivity. The  $M_s$ , on the other hand, falls monotonically as the Cr concentration rises. This is due to Cr cations having lower localised magnetic forces than Fe cations. Further, a magnetic measurement was used to explore the impact of Cu doping on the  $\text{Fe}_3\text{Se}_4$  ferrimagnetism. The solvothermal technique were applied to create a  $(\text{Fe}_{1-x}\text{Cu}_x)_3\text{Se}_4$  series with  $x = 0$  to 0.15. Cu doping generates a significant enhancement in the material's coercivity, despite the fact that only a little quantity of Cu penetrates the  $\text{Fe}_3\text{Se}_4$  structure<sup>115</sup>.

The figure of merit for assessing the quality of a permanent magnet is the maximum energy product. It is the largest rectangular area under the B-H curve in the hysteresis loop's second quadrant. It's a measurement of the material's magnetic energy. The energy product for current permanent magnetic materials for rare-earth-based magnets ranges from a few MGOe to up to 50 MGOe.

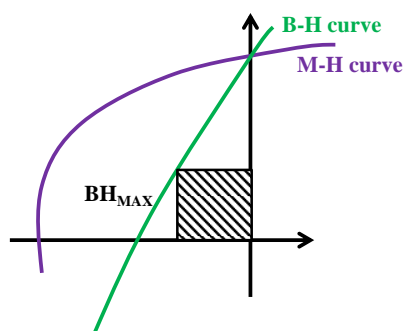


**Figure 18.** Calculation of maximum energy product is done on the second quadrant of the B-H hysteresis loop. The area of the shaded region gives the maximum energy product value for the material.

The energy product is improved by the modification of  $\text{Fe}_3\text{Se}_4$ . Our group investigates the influence of manganese ion doping on magnetic characteristics in depth. Various manganese concentrations [ $\text{Fe}_{3-x}\text{Mn}_x\text{Se}_4$  ( $x = 0.01$  to 0.2)] were synthesised, and the best

doping concentration for which the energy product was highest without affecting the  $T_C$  was discovered. The magnetization of the host matrix enhances dramatically from 4.84 to 7.54 emu/g at optimal ( $x = 0.03$ ) manganese ion doping. The value of the associated energy product was enhanced by almost 130 %. At 10 K, the energy product nearly increases by 2 order of magnitude ( $\sim 0.12$  MG Oe), making it useful in a variety of low-temperature applications.

Our team also discovered that  $\text{Fe}_3\text{Se}_4$  is a type-II multiferroic with magnetoelectric coupling at ambient temperature<sup>81</sup>.  $\text{Fe}_3\text{Se}_4$  nanorods, a hard magnet with substantial magneto-crystalline anisotropy, showed the coexistence of linked ferrimagnetic and ferroelectric ordering far beyond room temperature.  $\text{Fe}_3\text{Se}_4$  nanorods showed spontaneous, reversible ferroelectric polarisation for the first time below the magnetic  $T_C$ . In the Raman shift and dielectric constant at  $T_C$  an anomaly has been observed. The origin of ferroelectric ordering is unknown; nonetheless, the presence of ferroelectric and magnetic ordering in  $\text{Fe}_3\text{Se}_4$  at RT, as well as hard magnetic characteristics, may open up new study avenues for devices.

Researchers have made huge efforts to improve the magnetic properties by doping. However, the control over pure compounds of the Fe-Se system is not reported so far. Starting from the stoichiometry of the Fe-Se system, as the crystal structure changes, the arrangement of atoms changes, resulting in changing the magnetic behavior of any compound. Their crystal habit will be different, adding uniqueness to the magnetic behavior. Furthermore, as previously mentioned, the magnetic properties of NPs are greatly impacted by the surface effects and finite-size at the nanoscale. Their importance grows as particle size decreases. The quantum confinement of the electrons causes finite-size effects. Surface effects can be caused by differences in magnetic and chemical structures of the inner ("core") and outer layer ("shell") components of an NP, or by symmetry breakdown of the crystal structure occurs at the particle's border. It's critical to figure out how the morphology and crystal structure of the Fe-Se system affect their magnetic characteristics. Moreover, the final factor is transition metal, the important role of transition metal in deciding the resulting magnetism of compound is essential to study.

### **1.11 Objective of the thesis**

The formation process and growth termination, named crystal habits, are very important to understand and govern the material's properties more prominently. The globe was seeking for rare-earth-free substitute for permanent magnets applications because of the ever-rising



expense of rare earth elements, environmental damage, and health concerns.  $\text{Fe}_3\text{Se}_4$  NPs drew researchers' interest because of their semi-hard magnetic characteristics, which were discovered after giant coercivity was discovered in the monoclinic iron selenide phase. The research was largely focused on investigating the magnetic characteristics of doping, as mentioned in the preceding section. However, there were no efforts to achieve more control over magnet-like characteristics in the fundamental compound. A deep understanding of the formation process of the material can only help in controlling the pure compound. To fine-tune the material property, significant work is necessary.

In order to put this material to use in practical applications, it is imperative to achieve reasonable control of this material, including crystal structure/stoichiometry, size, shape, and transition metal-dependent magnetic properties. We have noticed the critical role of formation processes in deciding the final compound's crystalline properties. The structure/size/shape/transition metal-dependent properties in  $\text{Fe}_3\text{Se}_4$  are underrated, and reports are very rare. This thesis dedicates attempts in understanding and developing the tuneable  $\text{Fe}_3\text{Se}_4$  compounds and their influence on the magnetic properties; what role they play in basic comprehension and technical applications.

## **1.12 Outline of the thesis**

### **Chapter 1**

In the first chapter, we have discussed that in solids, the formation processes are essential for better understanding and controlling the material's properties. The nucleation and growth theories were discussed, followed by crystal habits. The TMCs are also addressed, as well as their applicability in many sectors. The importance of transition metal selenide as a basic and technologically relevant chemical is discussed in this chapter. The scope of the thesis is discussed after a quick overview of the Fe-Se system's literature.

### **Chapter 2**

In the second chapter, the theoretical crystal habit of all the phases of the Fe-Se system is predicted. We have examined the crystal growth morphology of all phases of the Fe-Se system using BFDH (pure crystallographic approach) and HP (periodic bond chain vector approach)

models. We have also explored the equilibrium morphology of the Fe-Se system using the broken bond approximation of surface energy minimization named as Wulff theory.

### Chapter 3

The third chapter deals with the Fe-Se system's complete phase transformation sequence using a wet-chemical method, starting from plotting the Fe-Se system phase diagram using the wet-chemical method to optimizing the appropriate conditions required to synthesize individual phases. The growth mechanism of the Fe-Se system in these conditions is also reported. The influence of different functional groups of OLA and 1-ODE: double bond and amine group in the formation of different phases of the Fe-Se system is also investigated. Finally, the reason behind the particular real-life experimental morphologies from theoretical crystal habits is discussed.

### Chapter 4

In the fourth chapter, the correlation between the phases and the magnetic properties of the Fe-Se system has been presented for the  $\text{Fe}_x\text{Se}_y$  compounds—where  $x/y$  ranges from 1:2 to 1:1. The magnetic properties vary enormously with change in Fe:Se ratio due to the change in  $\text{Fe}^{2+}/\text{Fe}^{3+}$  ratio, crystal field environment around Fe-ions, magnetocrystalline anisotropy, Fe-vacancies, and so forth. Among the four Fe-Se phases studied, two of them— $\text{Fe}_3\text{Se}_4$  and  $\text{Fe}_7\text{Se}_8$ , are ferrimagnetic below  $\sim 300$  K and show semi-hard magnetic properties. The other two phases— $\text{FeSe}_2$  and  $\beta\text{-FeSe}$  exhibit weaker magnetism. It is observed that  $\text{Fe}_3\text{Se}_4$  has the most unique and interesting magnetic properties.

### Chapter 5

According to the theories, now we know the morphologically-important planes. After examining the sequence of morphologically-important low-index planes, we correlated them with the real-life morphologies of  $\text{Fe}_3\text{Se}_4$  samples (achieved through the synthesis) and determined the growth directions in different solvent conditions. We also studied the directional growth kinetics with an increase in the thermal activation energy. We proposed the growth mechanism based on two well-known pathways—diffusion and reaction processes in the provided reaction environment. The entire roadmap is laid-out—starting from the formation of the unit cell to the diffusion and attachment of monomers and the fate of various facet

growth. Finally, we have shown how the distinct growth in various facets leads to controlling the magnetic properties. Its influence of it is studied with various parameters such as  $H_C$ ,  $M_S$ ,  $K$ , and  $BH_{max}$  at 300 K and 10 K.

## Chapter 6

In chapter 6, a conscious effort has been made in fabricating the monoclinic  $M_3Se_4$  compounds (where M can be Fe, Co, or Ni) by a thermal decomposition method. The ability to manipulate solution chemistry has been established by intensively investigating the individual role of various reaction pathways, leading to the monoclinic  $M_3Se_4$  NPs with distinct morphologies in the same reaction environment. The deep mechanistic insight helped identify the underlying reason behind the varied morphology with the help of the theoretical aspect. Furthermore, the influence of transition metal (M) on the magnetic properties is investigated for monoclinic  $M_3Se_4$  NPs. The  $Fe_3Se_4$  is observed to be well-known ferrimagnetic with a  $T_C$  of nearly 322 K. However, the other two compounds,  $Co_3Se_4$  and  $Ni_3Se_4$ , are examined to be paramagnetic overall measurement temperature range (5 K to 300 K).

## Chapter 7

Chapter 7 discusses the thesis's conclusion as well as the scope of future investigation.

## 1. 13 References

- (1) <https://www.nde-ed.org/Physics/Materials/Structure/solidstate.xhtml>.
- (2) <https://www.doitpoms.ac.uk/tlplib/atomic-scale-structure/intro.php#:~:text=Single%20crystals%20have%20infinite%20periodicity,periodically%20across%20its%20whole%20volume>.
- (3) <https://encyclopedia2.thefreedictionary.com/Single+Crystal>.
- (4) <https://physicsopenlab.org/2018/05/01/texture-in-polycrystalline-materials/#:~:text=Most%20inorganic%20solids%20are%20polycrystalline,materials%20are%20made%20of%20crystallites>.
- (5) Gleiter, H. Deformation of polycrystals: Mechanisms and microstructures, (eds) N Hansen, A Horsewell, T L.,øffers and H Lilholt (Roskilde, Denmark: Rise National Laboratory). 1981, 15-21.
- (6) Suryanarayana, C. Structure and properties of nanocrystalline materials. Bull. Mater. Sci. 1994, 17, 307-346.
- (7) E. A. Meulenkaamp, J. Phys. Chem. B, 102, 5566 (1998).
- (8) M. Bruchez Jr., M. Moronne, P. Gin, S. Weiss, A. P. Alivisatos, Science, 281, 2013 (1998).

- (9) J. Nanda, K. S. Nagaraj, B. A. Kuruvilla, G. L. Murthy, D. D. Sarma, *Appl. Phys. Lett.*, 72, 1335–1337 (1998).
- (10) C. T. Tsai, D. S. Chuu, G. L. Chen, S. L. Yang, *J. Appl. Phys.*, 79, 9105–9109 (1996).
- (11) A. T. Bell, *Science*, 299, 1688 (2003).
- (12) P. Boggild, T. M. Hansen, C. Tanasa, F. Grey, *Nanotechnology*, 12, 331 (2001).
- (13) H. Lin, S. Tzeng, P. Hsiau, W. Tsai, *Nanostruct. Mater.*, 10, 465–477 (1998).
- (14) Xia, Y.; Xia, X.; Peng, H. C. Shape-Controlled Synthesis of Colloidal Metal Nanocrystals: Thermodynamic versus Kinetic Products. *J. Am. Chem. Soc.* **2015**, 137, 7947–7966.
- (15) X. Peng, J. Wickham, A. P. Alivisatos, *J. Am. Chem. Soc.*, 120, 5343 (1998).
- (16) W. W. Yu, X. Peng, *Angew. Chem. Int. Ed.*, 41, 2368 (2002).
- (17) Hakimian, A.; Nazifi, S.; Ghasemi, H. *Physics of Ice Nucleation and Growth on a Surface*. Chapter 3, 2020, ISBN: 9781119640523.
- (18) Helmenstine, Anne Marie, Ph.D. "Nucleation Definition (Chemistry and Physics)." ThoughtCo, Feb. 16, 2021, [thoughtco.com/definition-of-nucleation-605425](https://www.thoughtco.com/definition-of-nucleation-605425).
- (19) Wu, K. J.; Tse, E. C. M.; Shang, C.; Guo, Z. *Nucleation and growth in solution synthesis of nanostructures – From fundamentals to advanced applications*. *Progress in Materials Science*, 2022, 123, 100821.
- (20) Barbara, S. *Modeling Solution Growth of Inorganic Crystals*. Thesis, University of California, 2014.
- (21) Vilau, R. B. *Growth, Morphology and Solid State Miscibility of Alkali Nitrates*. Thesis, Universitat de Barcelona, 2013.
- (22) Kepler, J. (1611) *Strena seu de nive sexangula*, Francofurti ad Moenum, Godfrey Tampach, Frankfurt; English translation "A new year's gift or on the six-cornered snowflakes", by Hardie, C., Oxford Univ. Press, Oxford.
- (23) Steno, N. (1669) *De solido intra solidum naturaliter contento dissertationis prodromus*, Florence; English translation by J. G. Winter, *The Prodrum of Nicolous Steno's dissertation concerning a solid body enclosed by process of nature within a solid*, Hafner, New York (1968).
- (24) Haüy, R. J. (1784) *Essai d'une théorie sur la structure des cristaux*, Paris.
- (25) von Laue, M. Eine quantitative prüfung der theorie für die interferenz-erscheinungen bei Röntgenstrahlen. *Sitzungsberichte der Kgl. Bayer. Akad. Der Wiss.* 1912, 363–373.
- (26) Bravais, A. (1849) *Etudes crystallographiques*, Part 1: Du Cristal considéré comme un simple assemblage de points, Paris, pp. 101–194; (1850) *Les systèmes formés par des pointes distribuées régulièrement sur un plan ou dans l'espace*, J. Ecole. Polytech., XIX, 1–128; (1851) *Etudes crystallographiques*, Ibid., XX, 101–276.

- (27) Donnay, J. D. H. and Harker, D. (1937) A new law of crystal morphology extending the law of Bravais, *Amer. Mineral.*, 22, 446–467.
- (28) Sunagawa, I. *Growth and Morphology of Crystals*. Forma, 1999, 14, 147–166.
- (29) P. Hartman and W. G. Perdok. On the relations between structure and morphology of crystals. I. *Acta Crystallogr.*, 8:49–52, 1955.
- (30) P. Hartman and W. G. Perdok. On the relations between structure and morphology of crystals. II. *Acta Crystallogr.*, 8:521–524, 1955.
- (31) P. Hartman and P. Bennema. The attachment energy as a habit controlling factor : I. Theoretical considerations. *J. Cryst. Growth*, 49:145–156, 1980.
- (32) Gibbs, J. W. (1906) On the equilibrium of heterogeneous substances, in *The Scientific Papers of J. W. Gibbs*, 1, Longmans, Green & Co., London.
- (33) Curie, P. (1885) On the formation of crystals and on the capillary constants of their different faces, *J. Chem. Edcn.*, 47, 1970, 636–637 (translation from *Bull. Soc. Franc., Min. Cryst.*, 8, 145–150).
- (34) Wulff, G. (1901) Zur Frage der Geschwindigkeit des Wachstums und die Auflösung der Kristallflächen, *Z. Krist*, 34, 449–530.
- (35) S. Goel, N. Sinha, H. Yadav, B. Kumar, On the prediction of external shape of ZnO nanocrystals. *Physica E: Low-dimensional Systems and Nanostructures*, 2018.
- (36) Song Li, Gaowu W. Qin\*, Yudong Zhang, Wenli Pei, Liang Zuo and Claude Esling. Anisotropic Growth of Iron Oxyhydroxide Nanorods and their Photocatalytic Activity. *Advanced engineering materials*, 2010, 12, 10.
- (37) Cong, H.; Zhang, H.; Sun, S.; Yu, Y.; Yu, W.; Yu, H.; Zhang, J.; Wang, J.; Boughton, R. Morphological Study of Czochralski-Grown Lanthanide Orthovanadate Single Crystals and Implications on the Mechanism of Bulk Spiral Formation. *J. Appl. Cryst.* (2010). **43**, 308-319. (47) Eftimie, E.; Avram, N.; Jelsch, C.; Nicolov, M. Morphology of the GdVO<sub>4</sub> crystal: first-principles studies. *Acta Cryst.* 2020, B76.
- (38) Eftimie, E.; Avram, N.; Jelsch, C.; Nicolov, M. Morphology of the GdVO<sub>4</sub> crystal: first-principles studies. *Acta Cryst.* 2020, B76
- (39) H. P. Wu, J. F. Liu, M. Y. Ge, L. Niu, Y. W. Zeng, Y. W. Wang, G. L. Lv, L. N. Wang, G. Q. Zhang, and J. Z. Jiang. Preparation of Monodisperse GeO<sub>2</sub> Nanocubes in a Reverse Micelle System. *Chem. Mater.* 2006, 18, 1817-1820.
- (40) W. M. M. Heijnen. The morphology of gel grown calcite. *N. Jb. Miner. Mh.*, 8:357–371, 1985.
- (41) Goel, S.; Sinha, N.; Hussain, A.; Joseph, A.; Yadav, H.; Kumar, B. Sunset yellow dyed triglycine sulfate single crystals: enhanced thermal, mechanical, optical and di-/piezo-/ferro-/pyro-electric properties. *Journal of Materials Science: Materials in Electronics*, 2018.
- (42) K J Robertst, R Dochertyt, P Bennemas and L A M J Jetten. The importance of considering growth-induced conformational change in predicting the morphology of benzophenone. *J. Phys. D. AM, Phys.* 1993, 26, 87-821.

- (43) Zhang, H.; Zhang, M.; Pan, S.; Dong, X.; Yang, Z.; Hou, X.; Wang, Z.; Chang, K.; Poeppelmeier, K.  $\text{Pb}_{17}\text{O}_8\text{Cl}_{18}$ : A Promising IR Nonlinear Optical Material with Large Laser Damage Threshold Synthesized in an Open System. *J. Am. Chem. Soc.* 2015, 137, 26, 8360–8363
- (44) J. Prywer, Three-dimensional model of faces disappearance in crystal habit, *J. Cryst. Growth.* 155 (1995) 254–259.
- (45) J. Prywer, Crystal Faces Existence and Morphological Stability from a Crystallographic Perspective, *Cryst. Growth Des.* 3 (2003) 593-598.
- (46) Viswanatha, R.; Sarma, D. D. Growth of Nanocrystals in Solution. Chapter 4, *Nanomaterials Chemistry.* 2007 WILEY-VCH, ISBN: 978-3-527-31664-9
- (47) Z. Hu, D. J. Escamilla Ramirez, B. E. Heredia Cervera, G. Oskam, P. C. Searson, *J. Phys. Chem. B*, 109, 11209 (2005).
- (48) Gao, M.-R.; Xu, Y.-F.; Jiang, J.; Yu, S.-H. Nanostructured Metal Chalcogenides: Synthesis, Modification, and Applications in Energy Conversion and Storage Devices. *Chem. Soc. Rev.* 2013, 42 (7), 2986.
- (49) Gao, M.-R.; Jiang, J.; Yu, S.-H. Solution-Based Synthesis and Design of Late Transition Metal Chalcogenide Materials for Oxygen Reduction Reaction (ORR). *Small* 2012, 8 (1), 13–27.
- (50) Puthussery, J.; Seefeld, S.; Berry, N.; Gibbs, M.; Law, M. Colloidal Iron Pyrite ( $\text{FeS}_2$ ) Nanocrystal Inks for Thin-Film Photovoltaics. *J. Am. Chem. Soc.* 2011, 133 (4), 716–719.
- (51) Lai, C.-H.; Huang, K.-W.; Cheng, J.-H.; Lee, C.-Y.; Hwang, B.-J.; Chen, L.-J. Direct Growth of High-Rate Capability and High Capacity Copper Sulfide Nanowire Array Cathodes for Lithium-Ion Batteries. *J. Mater. Chem.* 2010, 20 (32), 6638.
- (52) Zhu, L.; Richardson, B.; Tanumihardja, J.; Yu, Q. Controlling Morphology and Phase of Pyrite  $\text{FeS}_2$  Hierarchical Particles via the Combination of Structure Direction and Chelating Agents. *Crystengcomm* 2012, 14 (12), 4188–4195
- (53) Arachchige, I. U.; Brock, S. L. Sol-Gel Methods for the Assembly of Metal Chalcogenide Quantum Dots. *Acc. Chem. Res.* 2007, 40 (9), 801–809.
- (54) Shirasaki, Y.; Supran, G. J.; Bawendi, M. G.; Bulović, V. Emergence of Colloidal Quantum-Dot Light-Emitting Technologies. *Nat. Photonics* 2013, 7 (12), 933–933.
- (55) Kershaw, S. V.; Susha, A. S.; Rogach, A. L. Narrow Bandgap Colloidal Metal Chalcogenide Quantum Dots: Synthetic Methods, Heterostructures, Assemblies, Electronic and Infrared Optical Properties. *Chem. Soc. Rev.* 2013, 42 (7), 3033–3087.
- (56) Lai, C.-H.; Huang, K.-W.; Cheng, J.-H.; Lee, C.-Y.; Lee, W.-F.; Huang, C.-T.; Hwang, B.-J.; Chen, L.-J. Oriented Growth of Large-Scale Nickel Sulfide Nanowire Arrays via a General Solution Route for Lithium-Ion Battery Cathode Applications. *J. Mater. Chem.* 2009, 19 (39), 7277.
- (57) Gao, M.-R.; Gao, Q.; Jiang, J.; Cui, C.-H.; Yao, W.-T.; Yu, S.-H. A Methanol-Tolerant Pt/CoSe<sub>2</sub> Nanobelt Cathode Catalyst for Direct Methanol Fuel Cells. *Angew. Chemie Int. Ed.* 2011, 50 (21), 4905–4908.

- (58) Gao, M.-R.; Liu, S.; Jiang, J.; Cui, C.-H.; Yao, W.-T.; Yu, S.-H. In Situ Controllable Synthesis of Magnetite nanocrystals/CoSe<sub>2</sub> Hybrid Nanobelts and Their Enhanced Catalytic Performance. *J. Mater. Chem.* 2010, 20 (42), 9355.
- (59) Chhowalla, M.; Shin, H. S.; Eda, G.; Li, L.-J.; Loh, K. P.; Zhang, H. The Chemistry of Two-Dimensional Layered Transition Metal Dichalcogenide Nanosheets. *Nat. Chem.* 2013, 5 (4), 263–275.
- (60) Heine, T. Transition Metal Chalcogenides: Ultrathin Inorganic Materials with Tunable Electronic Properties. *Acc. Chem. Res.* 2015, 48 (1), 65–72.
- (61) Vogel, E. M.; Robinson, J. a. Two-Dimensional Layered Transition-Metal Dichalcogenides for Versatile Properties and Applications. *MRS Bull.* 2015, 40 (7), 558–563.
- (62) Yuan, H.; Liu, Z.; Xu, G.; Zhou, B.; Wu, S.; Dumcenco, D.; Yan, K.; Zhang, Y.; Mo, S.-K.; Dudin, P.; et al. Evolution of the Valley Position in Bulk Transition Metal Chalcogenides and Their Monolayer Limit. *Nano Lett.* 2016, 16 (8), 4738–4745.
- (63) Yeh, P.; Jin, W.; Zaki, N.; Zhang, D.; Liou, J. T.; Sadowski, J. T.; Al-Mahboob, A.; Dadap, J. I.; Herman, I. P.; Sutter, P.; et al. Layer-Dependent Electronic Structure of an Atomically Heavy Two-Dimensional Dichalcogenide. *Phys. Rev. B* 2015, 91 (4), 41407.
- (64) Ross, J. S.; Wu, S.; Yu, H.; Ghimire, N. J.; Jones, A. M.; Aivazian, G.; Yan, J.; Mandrus, D. G.; Xiao, D.; Yao, W.; et al. Electrical Control of Neutral and Charged Excitons in a Monolayer Semiconductor. *Nat. Commun.* 2013, 4, 1474.
- (65) Feng, J.; Sun, X.; Wu, C.; Peng, L.; Lin, C.; Hu, S.; Yang, J. Metallic Few-Layered VS<sub>2</sub> Ultrathin Nanosheets : High Two-Dimensional Conductivity for In-Plane Supercapacitors. 2011, 17832–17838.
- (66) Chang, K.; Chen, W. In Situ Synthesis of MoS<sub>2</sub>/graphene Nanosheet Composites with Extraordinarily High Electrochemical Performance for Lithium Ion Batteries. *Chem. Commun. (Camb).* 2011, 47 (14), 4252–4254.
- (67) Xia, Y.; Qian, D.; Hsieh, D.; Wray, L.; Pal, A.; Lin, H.; Bansil, A.; Grauer, D.; Hor, Y. S.; Cava, R. J.; et al. Observation of a Large-Gap Topological-Insulator Class with a Single Dirac Cone on the Surface. *Nat. Phys.* 2009, 5 (6), 18.
- (68) Zhang, J.; Peng, Z.; Soni, A.; Zhao, Y.; Xiong, Y.; Peng, B.; Wang, J.; Dresselhaus, M. S.; Xiong, Q. Raman Spectroscopy of Few-Quintuple Layer Topological Insulator Bi<sub>2</sub>Se<sub>3</sub> Nanoplatelets. *Nano Lett.* 2011, 11 (6), 2407–2414.
- (69) Cha, J. J.; Williams, J. R.; Kong, D.; Meister, S.; Peng, H.; Bestwick, A. J.; Gallagher, P.; Goldhaber-Gordon, D.; Cui, Y. Magnetic Doping and Kondo Effect in Bi<sub>2</sub>Se<sub>3</sub> Nanoribbons. *Nano Lett.* 2010, 10 (3), 1076–1081.
- (70) Li, Z.; Hu, Y.; Howard, K. A.; Jiang, T.; Fan, X.; Miao, Z.; Sun, Y.; Besenbacher, F.; Yu, M. Multifunctional Bismuth Selenide Nanocomposites for Antitumor Thermo-Chemotherapy and Imaging. *ACS Nano* 2016, 10 (1), 984–997.
- (71) Yang, K.; Yang, G.; Chen, L.; Cheng, L.; Wang, L.; Ge, C.; Liu, Z. FeS Nanoplates as a Multifunctional Nano-Theranostic for Magnetic Resonance Imaging Guided Photothermal Therapy. *Biomaterials* 2015, 38, 1–9.

- (72) Song, X.-R.; Wang, X.; Yu, S.-X.; Cao, J.; Li, S.-H.; Li, J.; Liu, G.; Yang, H.-H.; Chen, X. Co<sub>9</sub>Se<sub>8</sub> Nanoplates as a New Theranostic Platform for Photoacoustic/Magnetic Resonance Dual-Modal-Imaging-Guided Chemo-Photothermal Combination Therapy. *Adv. Mater.* 2015, 27 (21), 3285–3291
- (73) Hsu, F.-C.; Luo, J.-Y.; Yeh, K.-W.; Chen, T.-K.; Huang, T.-W.; Wu, P. M.; Lee, Y.-C.; Huang, Y.-L.; Chu, Y.-Y.; Yan, D.-C.; et al. Superconductivity in the PbOType Structure -FeSe. *Proc. Natl. Acad. Sci.* 2008, 105 (38), 14262–142
- (74) Mizuguchi, Y.; Tomioka, F.; Tsuda, S.; Yamaguchi, T.; Takano, Y. Superconductivity at 27 K in Tetragonal FeSe under High Pressure. *Appl. Phys. Lett.* 2008, 93 (15), 152505.
- (75) Schuster, W.; Mikler, H.; Komarek, K. L. Transition Metal-Chalcogen Systems, VII.: The Iron-Selenium Phase Diagram. *Monatshefte für Chemie* 1979, 110 (5), 1153–1170.
- (76) Xu, J.; Jang, K.; Lee, J.; Kim, H. J.; Jeong, J.; Park, J. G.; Son, S. U. Phase-Selective Growth of Assembled FeSe<sub>2</sub> Nanorods from Organometallic Polymers and Their Surface Magnetism. *Cryst. Growth Des.* 2011, 11 (7), 2707–2710.
- (77) Zhang, H.; Long, G.; Li, D.; Sabirianov, R.; Zeng, H. Fe<sub>3</sub>Se<sub>4</sub> Nanostructures with Giant Coercivity Synthesized by Solution Chemistry. *Chem. Mater.* 2011, 23 (16), 3769–3774.
- (78) Dong, S.; Liu, J.-M. M.; Dagotto, E. BaFe<sub>2</sub>Se<sub>3</sub>: A High TC Magnetic Multiferroic with Large Ferrielectric Polarization. *Phys. Rev. Lett.* 2014, 113 (18), 187204.
- (79) Hemberger, J.; Lunkenheimer, P.; Fichtl, R.; Weber, S.; Tsurkan, V.; Loidl, A. Multiferroic Behavior in. *Phys. B Condens. Matter* 2006, 378–380, 363–366.
- (80) Hemberger, J.; Lunkenheimer, P.; Fichtl, R.; Krug von Nidda, H. -a.; Tsurkan, V.; Loidl, A. Relaxor Ferroelectricity and Colossal Magnetocapacitive Coupling in Ferromagnetic CdCr<sub>2</sub>S<sub>4</sub>. *Nature* 2005, 434 (7031), 364–367.
- (81) Bishwas, M. S.; Poddar, P. Discovery of Room Temperature Multiferroicity and Magneto-electric Coupling in Fe<sub>3</sub>Se<sub>4</sub> Nanorods. *arXiv preprint* **20 Dec 2016**, arXiv:1612.06512.
- (82) Boyd, R. Selenium stories. *Nature Chem* **3**, 570 (2011).
- (83) Lu, T.; Dong, S.; Zhang, C.; Zhang, L.; Cui, G. Fabrication of transition metal selenides and their applications in energy storage. *Coordination Chemistry Reviews*, 2017, 332, 75–99.
- (84) Zeng, C.; Dai, L.; Jin, Y.; Liu, J.; Zhang, Q.; Wang, H. Design strategies toward transition metal selenide-based catalysts for electrochemical water splitting. *Sustainable Energy Fuels*, 2021, 5, 1347.
- (85) Fuh, HR., Chang, CR., Wang, YK. *et al.* Newtype single-layer magnetic semiconductor in transition-metal dichalcogenides VX<sub>2</sub> (X = S, Se and Te). *Sci Rep* 2016, 6, 32625.
- (86) Hagg, G. and Kindstrom, A. L. *Z. physik. Chem.* B22, 1933, 453.
- (87) Tengner, S; Ueber Diselenide und Ditelluride von Eisen, Kobalt und Nickel *Zeitschrift fuer Anorganische und Allgemeine Chemie*, 1938, 239, 126-132.
- (88) T. Hirone and S. Chiba, *J. Phys. Soc. Japan* II, 1956, 666.

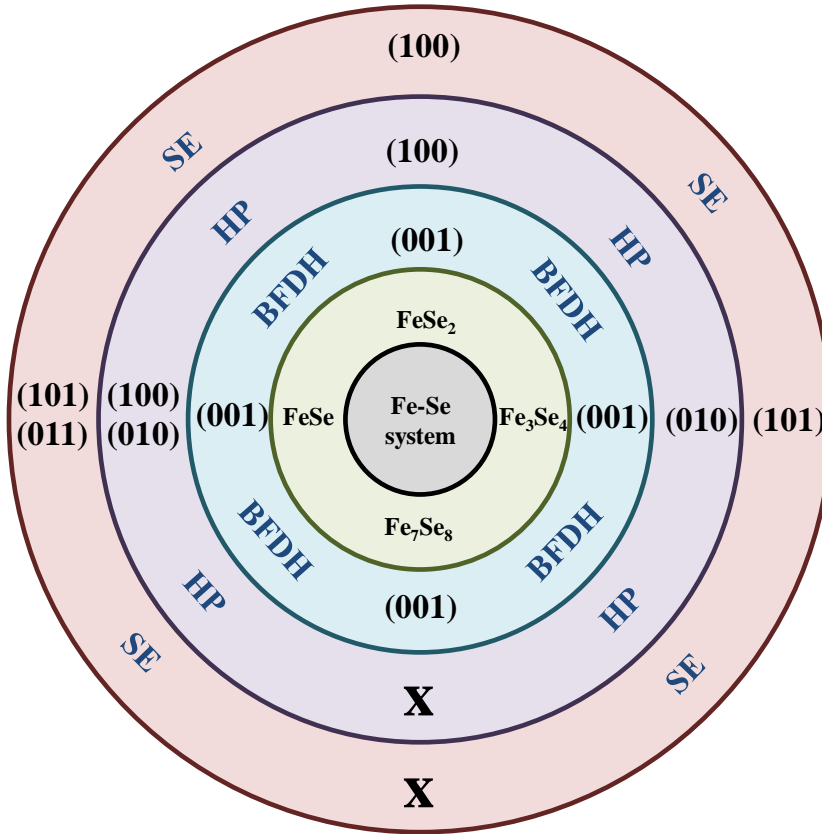


- (89) Okazaki, A.; Hirakawa, K. Structural Study of Iron Selenides FeSe X . I Ordered Arrangement of Defects of Fe Atoms. *J. Phys. Soc. Japan* 1956, 11 (9), 930–936.
- (90) Hirakawa, K. The Magnetic Properties of Iron Selenide Single Crystals. *J. Phys. Soc. Japan* 1957, 12 (8), 929–938.
- (91) Andresen, A. F.; Leciejewicz, J. A neutron diffraction study of Fe<sub>7</sub>Se<sub>8</sub>. *Le Journal de physique*, 1964, 25, 574.
- (92) Andresen, A. F.; Vestersjø, E.; Haaland, A.; Gronowitz, S.; Christiansen, H.; Rosén, U. A Neutron Diffraction Investigation of Fe<sub>3</sub>Se<sub>4</sub>. *Acta Chem. Scand.* 1968, 22, 827–835.
- (93) Svendsen, S. R.; Åkesson, G.; Krogh-Moe, J.; Songstad, J.; Pilotti, Å. Decomposition Pressures and Standard Enthalpy of Formation for the Iron Selenides FeSe, Fe<sub>7</sub>Se<sub>8</sub>, Fe<sub>3</sub>Se<sub>4</sub> and FeSe<sub>2</sub>. *Acta Chem. Scand.* 1972, 26, 3757–3774.
- (94) Lavina, B.; Downs, R.; Sinogeikin, S. The Structure of Ferroselite, FeSe<sub>2</sub>, at Pressures up to 46 GPa and Temperatures down to 50 K: A Single-Crystal Micro-Diffraction Analysis. *Crystals* 2018, 8, 289.
- (95) Okazaki, A. The Superstructures of Iron Selenide Fe<sub>7</sub>Se<sub>8</sub>. *J. Phys. Soc. Jpn.* 1961, 16, 1162–1170.
- (96) Lyubutin, I. S.; Lin, C.-R.; Funtov, K. O.; Dmitrieva, T. V.; Starchikov, S. S.; Siao, Y.-J.; Chen, M.-L. Structural, Magnetic, and Electronic Properties of Iron Selenide Fe<sub>6-7</sub>Se<sub>8</sub> Nanoparticles Obtained by Thermal Decomposition in High-Temperature Organic Solvents. *J. Chem. Phys.* 2014, 141, 044704.
- (97) Greenfield, J. T.; Kamali, S.; Lee, K.; Kovnir, K. A Solution for Solution-Produced β-FeSe: Elucidating and Overcoming Factors that Prevent Superconductivity. *Chem. Mater.* 2015, 27, 588–596.
- (98) Ganga, B. G.; Ganeshraj, C.; Krishna, A. G.; Santhosh, P. N. Electronic and Optical Properties of FeSe<sub>2</sub> Polymorphs: Solar Cell Absorber. 2013, arXiv:1303.1381. arXiv preprint.
- (99) BABOT, D.; BÉRODIAS, G.; LAMBERT-ANDRON, B. STRUCTURES MAGNÉTIQUES DE MF<sub>2</sub> Se 4 AVEC M = Ti, V, Cr, Fe, Co, Ni. *Le J. Phys. Colloq.* 1971, 32 (C1), C1-985-C1-986.
- (100) Boumford, C. An investigation of the magnetic and crystallographic structures of some iron chalcogenides. Thesis, The university of Manitoba, 1976.
- (101) Koksharov, Y. A. Magnetism of Nanoparticles: Effects of Size, Shape, and Interactions. Chapter 6, *Magnetic Nanoparticles*, WILEY-VCH Verlag GmbH & Co. KGaA, Weinheim, 2009, ISBN: 978-3-527-40790-3.
- (102) Yu, H.-D.; Regulacio, M. D.; Ye, E.; Han, M.-Y. Chemical Routes to Top-down Nanofabrication. *Chem. Soc. Rev.* 2013, 42, 6006–6018.
- (103) Clarke, G.; Rogov, A.; McCarthy, S.; Bonacina, L.; Gun'ko, Y.; Galez, C.; Le Dantec, R.; Volkov, Y.; Mugnier, Y.; Prina-Mello, A. Preparation from a Revisited Wet Chemical Route of Phase-Pure, Monocrystalline and SHG-Efficient BiFeO<sub>3</sub> Nanoparticles for Harmonic Bio-Imaging. *Sci. Rep.* 2018, 8, 10473.
- (104) Lin, C.-R.; Siao, Y.-J.; Lu, S.-Z.; Gau, C. Magnetic Properties of Iron Selenide Nanocrystals Synthesized by the Thermal Decomposition. *IEEE Trans. Magn.* 2009, 45, 4275–4278

- (105) Zhang, H.; Long, G.; Li, D.; Sabirianov, R.; Zeng, H. Fe<sub>3</sub>Se<sub>4</sub> Nanostructures with Giant Coercivity Synthesized by Solution Chemistry. *Chem. Mater.* 2011, 23, 3769–3774.
- (106) Sen Bishwas, M.; Das, R.; Poddar, P. Large Increase in the Energy Product of Fe<sub>3</sub>Se<sub>4</sub> by Fe-Site Doping. *J. Phys. Chem. C* 2014, 118, 4016–4022.
- (107) Yuan, B.; Luan, W.; Tu, S.-t. One-Step Synthesis of Cubic FeS<sub>2</sub> and Flower-like FeSe<sub>2</sub> Particles by a Solvothermal Reduction Process. *Dalton Trans.* 2012, 41, 772–776.
- (108) Yuan, B.; Hou, X.; Han, Y.; Luan, W.; Tu, S.-t. Facile Synthesis of Flake-like FeSe<sub>2</sub> Particles in Open-Air Conditions. *New J. Chem.* 2012, 36, 2101–2105.
- (109) Mao, X.; Kim, J.-G.; Han, J.; Jung, H. S.; Lee, S. G.; Kotov, N. A.; Lee, J. Phase-Pure FeSex (x = 1, 2) Nanoparticles with One- and Two-Photon Luminescence. *J. Am. Chem. Soc.* 2014, 136, 7189–7192.
- (110) Sobhani, A.; Salavati-Niasari, M. Synthesis and Characterization of FeSe<sub>2</sub> Nanoparticles and FeSe<sub>2</sub>/FeO(OH) Nanocomposites by Hydrothermal Method. *J. Alloys Compd.* 2015, 625, 26–33.
- (111) Li, D.; Pan, D.; Liu, W.; Li, X.; Chen, M.; Li, S.; Li, Y.; Tan, J.; Sun, D.; Wang, Z.; Han, Z.; Zhang, Z. Controllable Phase Transition for Layered β-FeSe Superconductor Synthesized by Solution Chemistry. *Chem. Mater.* 2017, 29, 842–848.
- (112) Long, G.; Zhang, H.; Li, D.; Sabirianov, R.; Zhang, Z.; Zeng, H. Magnetic Anisotropy and Coercivity of Fe<sub>3</sub>Se<sub>4</sub> Nanostructures. *Appl. Phys. Lett.* 2011, 99 (20), 202103.
- (113) Sathya, A.; Guardia, p.; Brescia, R.; Silvestri, N.; Pugliese, G.; Nitti, S.; Manna, L.; Pellegrino, T. Co<sub>x</sub>Fe<sub>3-x</sub>O<sub>4</sub> Nanocubes for Theranostic Applications: Effect of Cobalt Content and Particle Size. *Chem. Mater.* 2016, 28, 6, 1769–1780.
- (114) Yadav, C. S.; Pandey, S. K.; Paulose, P. L. Evolution of magnetic ordering in FeCr<sub>2</sub>Se<sub>4-x</sub>Tex; x = 0 - 4.0. <https://arxiv.org/abs/1904.06661>.
- (115) Saucedo, L. A.; Clark, J. K.; Raaj Vellore Winfred, J. S.; Strouse, G. F.; Shatruk, M. Increasing Magnetic Hardness of Fe<sub>3</sub>Se<sub>4</sub> via Cu Doping. *J. Phys. Chem. C* 2021, 125, 25784–25793.

## Chapter 2

### Prediction of Crystal Growth Habit of Fe-Se Crystal System using Various Models



## Highlights

Below, we have listed some of the important 'take-away' points from this chapter which we would like to highlight:

- 1) *Here, we have predicted the crystal growth habits of various phases of Fe-Se system.*
- 2) *We have examined the crystal growth morphology of all four prominent phases of Fe-Se system using BFDH (pure crystallographic approach) and HP (periodic bond chain vector approach) models.*
- 3) *We have also explored the equilibrium morphology of Fe-Se phases using broken-bond approximation of surface energy minimization named as Wulff theory.*

**Keywords:** Fe-Se system, crystal-growth habit, BFDH model, HP model, surface energy.

The results of this chapter will be published as —

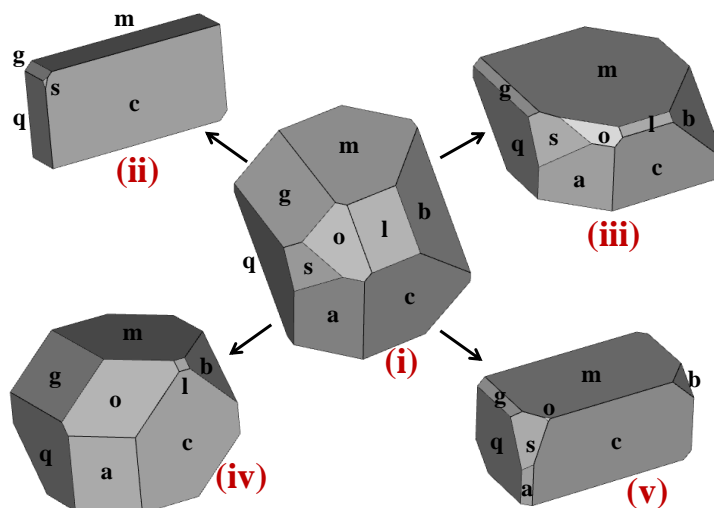
- ✓ Prediction of Crystal Growth Habit of Fe-Se Crystal System using Various Models

**Monika Ghalawat**, Pankaj Poddar\* (To be communicated)

## 2.1 Introduction

The fundamental understanding and control over the crystal morphology are essential for any industrial applications as the physical, chemical, and biological properties of crystals depend on facets exposed to the outer world and underlying anisotropy, if there is any<sup>1-3</sup>. An industrial process may prefer a particular crystal shape while another may find it completely unsuitable. For example, a nanowires-shaped ZnO crystal significantly impacts dye-sensitized solar cell photon absorption efficiency, while a needle-shaped active pharmaceutical product presents a problem in downstream processing and should be avoided<sup>4</sup>. In the chemical industries, for the preparation of solids like catalysts, pharmaceutical products, chemical intermediates, etc., crystallization from the solution process is used<sup>5</sup>. This process strongly influences the resultant materials' chemical and physical properties. Additionally, any crystalline material's size and shape distributions strongly influence its properties—end-use efficacy such as bioavailability for pharmaceuticals or reactivity for catalytic, flowability, wettability, and adhesion. Due to these prime impacts of resultant crystal morphology, the study of general methodologies for the prediction → measurement → tuning of crystal size and shape is essential. Despite significant advancements in understanding these topics for over one hundred years, these concepts are still poorly understood for transition metal chalcogenides (TMC) due to complexities in the crystal structure and phase diagram. In this chapter, an intensive investigation of the crystal habit of the Fe-Se system is presented.

In real-life experiments, various parameters such as reaction temperature, solvents, growth modifiers, and many more can influence the crystallization process that tunes the crystalline product's physicochemical properties. However, in these cases, the experimental design space is immense, and therefore trial and error routes are inefficient for the fabrication of crystalline materials with desired functionality. It is appropriate to use theoretical efforts to better understand the crystal growth formation process and meet the challenge of crystal shape engineering. In conclusion, precise crystal morphology prediction is crucial to saving time and avoiding troubleshooting crystallization processes. Based on the distinct cleavage of crystal surfaces, the predicted crystal morphology discusses the chemical entities of materials. This helps in enhancing the efficiency as well as the applicability of that particular material<sup>6</sup>. The relation between the atoms' arrangement in the crystal lattice and the resultant crystal morphology opens the path for shape-dependent properties for numerous applications (Scheme 1).



**Scheme 1.** Consider the "(i)" center crystal morphology as a predicted morphology of any material using theoretical models. If the growth conditions are tuned in such a manner to allow the favorable growth of a particular facet over other facets, then one can think of the formation of a host of various morphologies of the same material. For example, in (ii) morphology, the growth rate of the m-plane is relatively faster as compared to (i), which makes the c plane more visible, while the morphology shown in (iii) results when the m-plane is growing relatively at a slower rate result in making this plane more visible. This results in different morphologies of the same material followed by distinct properties.

All end properties strongly depend on crystal morphology, from powder density to packing to distinct properties of compound. Due to the anisotropic response of distinct crystal faces towards the physical and chemical activities. The crystal morphology strongly affects the efficiency and its applicability in different devices. The morphology defines the relative growth rate (RGR) of various crystallographic directions. The formation of a growing crystal's specific morphology results from RGR along with distinct crystallographic directions. The crystal faces differ in their growth rates, thereby affecting their appearance. It is finally predicted with a finite number of low-energy faces<sup>6</sup>.

From the earliest documented history, it was probably J. Kepler<sup>7</sup> who, in 1611, for the first time gave attention to geometric forms of crystals and informally established the roots of the concept of crystal structure by observing the varied dendritic forms of snowflakes. In his book "New Year's Gift", he discussed that a crystal was composed of closely packed equisized spheres, even though it had thousands of different dendritic forms. Kepler's contribution was followed by Nicolous Steno<sup>8</sup>, who in 1669 discussed the interfacial angles of rock crystals in

his treatise. He considered the anisotropy in growth rate —growth rates varies with crystallographic directions, which is the most basic concept of today's crystal growth science. In the 18<sup>th</sup> Century, R.J. Hauy<sup>9</sup> (1784) the polyhedrons similar to today's crystal unit cell. In the 19<sup>th</sup> Century, A. Bravais<sup>10</sup> gave the geometry of crystals. Finally, the first-ever model was proposed to study the theoretical crystal morphology by A. Bravais<sup>10</sup> (1866), G. Friedel<sup>11</sup> (1907), and J.D.H. Donnay and D. Harker<sup>12</sup> (1937). The Bravais Friedel Donnay Harker (BFDH) model is purely an over-simplified geometrical approach to examining the morphology of crystals. The model assumes that a particular plane's growth rate is inversely proportional to the interplanar spacing ( $d_{hkl}$ ), neglecting all other contributions. Thus, the plane with smaller d-spacing will grow faster in a crystal and vice-versa. This model has successfully predicted the crystal morphology of several crystal systems. While for various systems, the predicted crystal morphology was observed to be entirely different from the experiment morphology in some directions. The reason for this difference is that the BFDH law is a purely geometrical approach. The crystal structure, bond energy, and pseudo-symmetry impacts are taken into account. Additionally, it does not consider the strong and weak bond directions essential in developing any system's complete morphology.

Afterward, in 1955, P. Hartman and W.G. Perdok<sup>13-15</sup> gave one new model in three back-to-back articles. Strong and weak bonds between atoms or molecules determine the crystal structure. Hartman-Perdok (HP) provided a crystal morphology prediction model based on these bond strengths. They explained that the strong bond directions form uninterrupted periodic bond chain (PBC) vectors in the crystal structure. These vectors will guide to understanding the crystal morphology development of that system. The growing faces of the crystals are split into 3 categories according to the location of these PBC vectors. — flat (F) faces: parallel to 2 PBC vectors, stepped (S) faces: parallel to only 1 PBC vector, and kinked (K) faces: not parallel to any PBC vector. The growth of facets is proportionate to the displacement velocity and inversely to the corresponding plane's morphological importance (MI). The F face's displacement velocity is the least among all the faces, while K faces have the highest. The displacement velocity of S faces lies in between the other two categories. Thus, the sequence of faces for appearance in final morphology is  $F > S > K$ .

Apart from these two growth theories, another approach to studying a crystal's morphology is the thermodynamic investigation of equilibrium form. According to J. W. Gibbs, P. Curie, and G. Wulff— any crystal is encased with a set of planes and a minimum sum

of products of surface area and surface free energies<sup>16</sup>. When a single-crystal seed is permitted to develop in a vacuum precisely under thermodynamic control, it should evolve towards its equilibrium shape according to the calculated surface free energy (Wulff construction). Surface free energies of the distinct crystallographic facets are used to evaluate equilibrium shapes. Face growth rates are proportionate to the surface free energies. An equilibrium form is unique to each crystal at a given thermodynamic condition. It is possible to obtain a simple way to evaluate the surface free energy of crystals surrounded by a vacuum by considering only the interactions between the nearest neighbors via the broken bond approximation (BBA)<sup>16</sup>.

Usually, three successful approaches—BFDH, HP, and surface energy (SE) minimization model have been used to predict the crystal morphology. These models have efficiently predicted numerous organic and inorganic crystal morphology such as ZnO<sup>17</sup>, FeOOH<sup>18</sup>, Nd: LaVO<sub>4</sub><sup>19</sup>, BaSO<sub>4</sub><sup>13-15</sup>, GdVO<sub>4</sub><sup>20</sup>, GeO<sub>2</sub><sup>21</sup>, CaCO<sub>3</sub><sup>22</sup>, triglycine sulphate<sup>23</sup>, benzophenone<sup>24</sup>, Pb<sub>17</sub>O<sub>8</sub>Cl<sub>18</sub><sup>25</sup> etc.

The methods described above are designed to interpret a crystal's ideal predicted shape, which is dictated by its internal structure, while fully ignoring the impact of external growth conditions. These crystal structures are referred to as "structural form" or "abstract form," and they have no reference to real-world reaction parameters like pressure, temperature, or driving force<sup>6</sup>. However, by theoretical calculations, one can also predict the growth forms by taking the effect of external factors. Although, the above approaches are well known and very successfully used in predicting various crystal systems' morphology. However, less attention has been given to predicting TMCs crystal habit.

TMCs are regarded as promising materials with rich phase diagrams<sup>26</sup>. It is well known that the electronic (optical, magnetic, and electrical) and thermal properties of solids are extremely sensitive to the crystalline phase, stoichiometry, shape, and size.<sup>27-31</sup>. Therefore, one of the critical challenges is obtaining control over the chemistry of phase formation of TMCs. Recently, among TMCs, much attention has been given to transition metal selenides (TMSes) because they potentially have interesting and unique chemical and physical properties<sup>32-34</sup>. As discussed in chapter 1, the Fe<sub>x</sub>Se<sub>y</sub> crystal system (with x: y varying from 1:2 to 1:1) is of great importance due to its exciting and unique thermal, optical, electrical, and magnetic properties that are directly dependent on the Fe-Se elemental ratio, crystalline structure, size, and shape<sup>35-39</sup>. Fe-Se crystal system family has four stable phases: FeSe<sub>2</sub>, Fe<sub>3</sub>Se<sub>4</sub>, Fe<sub>7</sub>Se<sub>8</sub>, and FeSe<sup>36,40</sup>.



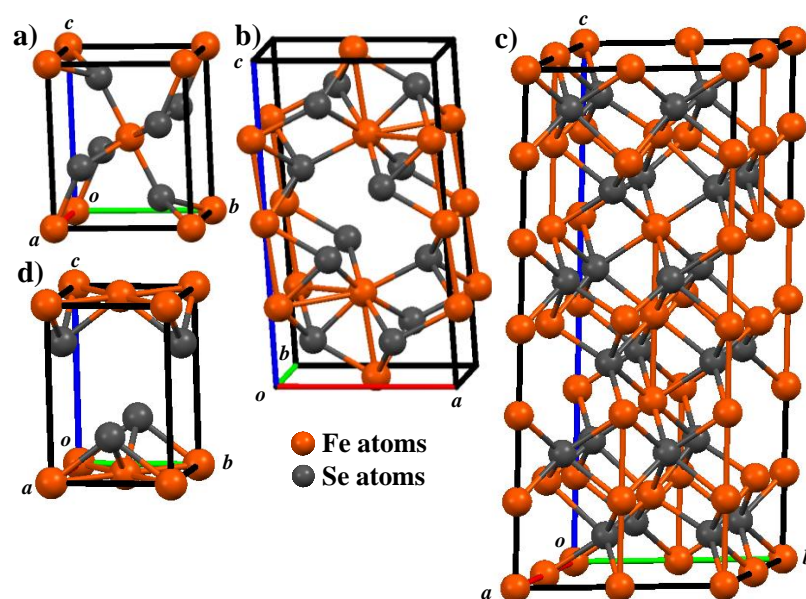


**Figure 1.** Schematic of the unit cell of a)  $\text{FeSe}_2$  having orthorhombic marcasite crystal structure, b)  $\text{Fe}_3\text{Se}_4$  having monoclinic NiAs-type crystal structure, c)  $\text{Fe}_7\text{Se}_8$  having hexagonal NiAs-type crystal structure, and d)  $\text{FeSe}$  having tetragonal PbO-type crystal structure.

The iron diselenide ( $\text{Fe}^{2+}\text{Se}_2^{2-}$ ) has an orthorhombic marcasite structure having the lattice parameters of  $a=3.58 \text{ \AA}$ ,  $b=4.79 \text{ \AA}$ , and  $c=5.72 \text{ \AA}$  with  $\text{Pmnn}$  space group (Figure 1a). Each Fe atom has an octahedral coordination with 6 Se atoms ( $\text{FeSe}_6$  octahedra), while each Se atom has a tetrahedral coordination with 3 Fe atoms and 1 Se atom, producing a dimer pair ( $\text{Se}_2\text{Fe}_3$  tetrahedra)<sup>41</sup>.  $\text{Fe}_3\text{Se}_4$  ( $\text{Fe}^{2+}\text{Fe}_2^{3+}\text{Se}_4^{2-}$ ) and  $\text{Fe}_7\text{Se}_8$  ( $\text{Fe}_5^{2+}\text{Fe}_2^{3+}\text{Se}_8^{2-}$ ) have monoclinic (Figure 1b) and hexagonal (Figure 1c) NiAs-type crystal structure, respectively with the lattice parameters of  $a=6.17 \text{ \AA}$ ,  $b=3.54 \text{ \AA}$ , and  $c=11.17 \text{ \AA}$  having  $\text{I2/m}$  space group for  $\text{Fe}_3\text{Se}_4$  and  $a=7.21 \text{ \AA}$  and  $c=17.67 \text{ \AA}$  with  $\text{P3}_121$  space group for  $\text{Fe}_7\text{Se}_8$ <sup>42-44</sup>. In the NiAs-type crystal structure of  $\text{Fe}_{1-x}\text{Se}$ , 6 Se anions ( $\text{FeSe}_6$  octahedra) octahedrally coordinate the Fe-cations, and the coordination polyhedron of Se is the trigonal prism produced by 6 Fe ( $\text{SeFe}_6$  prisms)<sup>45</sup>. The  $\text{FeSe}$  ( $\text{Fe}^{2+}\text{Se}^{2-}$ ) has a tetragonal PbO-type crystal structure with the lattice parameters of  $a=3.765 \text{ \AA}$  and  $c=5.518 \text{ \AA}$ , having the  $\text{P4/nmm}$  space group (Figure 1d). In  $\text{FeSe}$ , every Fe atom is tetrahedral-coordinated with four Se atoms ( $\text{FeSe}_4$  tetrahedral), and each Se atom is tetrahedral-coordinated with four Fe atoms ( $\text{SeFe}_4$  tetrahedral)<sup>46</sup>.

Among these four phases, two ( $\text{FeSe}_2$  and  $\text{FeSe}$ ) are recognized for their optical and electronic properties, while the other phases ( $\text{Fe}_3\text{Se}_4$  and  $\text{Fe}_7\text{Se}_8$ ) are studied for their magnetic properties<sup>47-52</sup>. The  $\text{FeSe}_2$  has an indirect bandgap of  $\sim 1.0 \text{ eV}$  with p-type semiconductor,

resulting in a potential compound for photovoltaic devices<sup>53-54</sup>. Iron chalcogenides are favorable for biological applications among all semiconducting materials due to the least possible toxicity. Further, FeSe exhibits a direct bandgap of  $\sim 1.23$  eV<sup>53-54</sup>. Besides, FeSe undergoes a superconducting transition at  $\sim 8$  K<sup>46</sup>. At the nanoscale, FeSe<sub>2</sub> and FeSe also reveal magnetic ordering. In the other two phases (Fe<sub>3</sub>Se<sub>4</sub> and Fe<sub>7</sub>Se<sub>8</sub>), both at bulk and nano-dimensions, they exhibit ferrimagnetic behavior with the Curie temperature ( $T_C$ ) of nearly 320 K and 453 K, respectively<sup>54</sup>. Fe<sub>3</sub>Se<sub>4</sub> acquires hard magnetic properties with a large coercivity of nearly 40 kOe at 10 K and 4 kOe at 300 K<sup>50</sup> and is believed to be an alternative to the noble-metal or rare-earth element hard-magnets<sup>55-56</sup>. The presence of multiple phases with tremendously different crystal structures reveals the system's complexity.

The diversity of bonding and crystal structure in the Fe-Se system give rise to drastically varying physical and chemical properties. The crystal habit also has a crucial impact in deciding these properties and controlling the material's functionality. Therefore, the prediction of crystal morphology of the Fe-Se system is of great interest and importance in view of fundamental understanding and applications. In this contribution, the Fe-Se system's crystal habit has been predicted successfully by its internal structure using all three models—BFDH, HP, and SE models.

## 2.2 Methodology

Mercury 4.0.0 software was used to draw the internal crystal structures and packing diagrams of various stable phases of the Fe-Se family of compounds (FeSe<sub>2</sub>, Fe<sub>3</sub>Se<sub>4</sub>, Fe<sub>7</sub>Se<sub>8</sub>, and FeSe) using the reported crystallographic information with COD numbers 1011007<sup>57</sup>, 1527086<sup>58</sup>, 1528313<sup>59</sup>, and 1010298<sup>60</sup>, respectively. The indexed morphologies predicted using BFDH and HP laws were drawn using the *WinXMorph*<sup>61</sup> program.

## 2.3 Results and discussion

### 2.3.1 Crystal habit of Fe-Se system using BFDH approach

BFDH<sup>10-12</sup> model is the theoretical approach using crystal lattice geometry to predict crystal morphology. This model will simulate the crystal growth morphology for a particular crystal using  $d_{hkl}$  and space-group (SG) symmetry operations. The faces with the highest  $d_{hkl}$  and highest density will grow slowest and are the most energetically stable faces. After describing

the unit cell dimensions and space group in a crystal structure, it is pretty simple to determine the MI of several planes appearing in the resultant shape.

By following formulae, relative growth rates (RGR) and morphological importance (MI) have been calculated:

$$MI = d_{hkl} / \text{highest } d_{hkl} \quad RGR = \text{highest } d_{hkl} / d_{hkl}$$

This describes that the MI and RGR are inversely proportional to each other. The plane with the highest RGR will produce the least MI plane in the crystal and vice versa.

**Table 1.** Morphological importance of several faces of Fe-Se crystals (FeSe<sub>2</sub>, Fe<sub>3</sub>Se<sub>4</sub>, Fe<sub>7</sub>Se<sub>8</sub>, and FeSe) based on the BFDH model. The  $d_{hkl}$  represents the interplanar spacing in Å. RGR and MI are calculated relative growth rates and morphological importance, respectively.

Phase	Faces (hkl)	$d_{hkl}$ (Å)	RGR	MI
FeSe <sub>2</sub>	(00 $\bar{1}$ ), (001)	5.715	1	1
	(0 $\bar{1}$ 1), (01 $\bar{1}$ ), (011), (0 $\bar{1}\bar{1}$ )	3.6715	1.56	0.64
	( $\bar{1}$ 0 $\bar{1}$ ), (101), ( $\bar{1}$ 01), (10 $\bar{1}$ )	3.0308	1.89	0.53
	(110), ( $\bar{1}$ 10), ( $\bar{1}\bar{1}$ 0), (1 $\bar{1}$ 0)	2.8652	1.99	0.50
Fe <sub>3</sub> Se <sub>4</sub>	(001), (00 $\bar{1}$ )	11.2757	1	1
	( $\bar{1}$ 01), (10 $\bar{1}$ )	5.51003	2.04	0.49
	(101), ( $\bar{1}$ 0 $\bar{1}$ )	5.36515	2.10	0.48
	(011), (0 $\bar{1}$ 1), (0 $\bar{1}\bar{1}$ ), (01 $\bar{1}$ )	3.37832	3.34	0.29
	(110), ( $\bar{1}$ 10), ( $\bar{1}\bar{1}$ 0), (1 $\bar{1}$ 0)	3.07544	3.66	0.27
Fe <sub>7</sub> Se <sub>8</sub>	(001), (00 $\bar{1}$ -1)	17.46	1	1
	(100), ( $\bar{1}$ 00), (010), (0 $\bar{1}$ 0), ( $\bar{1}$ 10), (1 $\bar{1}$ 0)	6.2094	2.81	0.36
	( $\bar{1}$ 01), (10 $\bar{1}$ ), ( $\bar{1}$ 0 $\bar{1}$ ), (101), (011), (0 $\bar{1}$ 1), (0 $\bar{1}\bar{1}$ ), (01 $\bar{1}$ ), ( $\bar{1}$ 1 $\bar{1}$ ), ( $\bar{1}$ 11), (1 $\bar{1}\bar{1}$ ), (1 $\bar{1}$ 1)	5.8504	2.98	0.33
FeSe	(001), (00 $\bar{1}$ )	5.518	1	1
	(0 $\bar{1}$ 1), (01 $\bar{1}$ ), (011), (0 $\bar{1}\bar{1}$ ), ( $\bar{1}$ 0 $\bar{1}$ ), (101), ( $\bar{1}$ 01), (10 $\bar{1}$ )	3.110	1.77	0.56
	(110), ( $\bar{1}$ 10), ( $\bar{1}\bar{1}$ 0), (1 $\bar{1}$ 0)	2.662	2.07	0.48

According to the BFDH model, Table 1 explains the RGR and MI of low-index planes of all the Fe-Se crystal system phases.

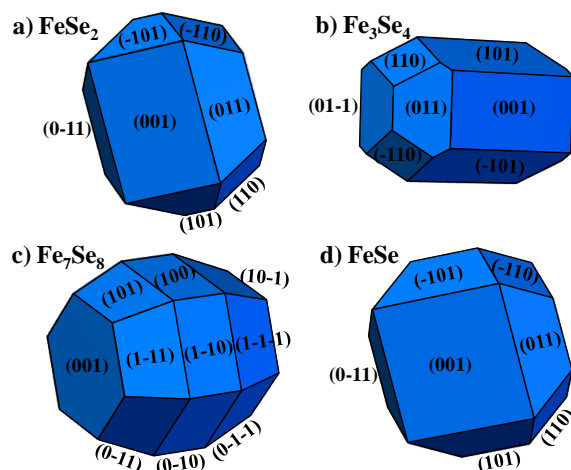


**Figure 2.** The theoretical morphology of Fe-Se crystals is predicted using BFDH model. a)  $\text{FeSe}_2$ , b)  $\text{Fe}_3\text{Se}_4$ , c)  $\text{Fe}_7\text{Se}_8$ , and d)  $\text{FeSe}$  show the indexed morphological drawing with corresponding hkl planes (black color).

#### a) $\text{FeSe}_2$

In particular, the BFDH model predicts that the (001) and (00-1) faces are of the highest MI for  $\text{FeSe}_2$  crystal. The obtained crystal growth habit is plate-like with (001) and (00-1) faces to be immensely visible, as shown in the morphological design predicted using BFDH theory in Figure 2a.

#### b) $\text{Fe}_3\text{Se}_4$

For  $\text{Fe}_3\text{Se}_4$  crystal, as shown in Table 1, (001) and (00-1) faces are of highest MI, followed by (-101), (10-1), (101), and (-10-1) planes. This results in a rod-like shape of  $\text{Fe}_3\text{Se}_4$  crystal having planes mentioned above to be on longitudinal sides, making (001) and (00-1) faces strongly visible, followed by (-101), (10-1), (101), and (-10-1) planes. While the other planes ((011), (0-11), (01-1), (0-1-1), (110), (-110), (1-10), (-1-10)) are on the edges of the rod as shown in Figure 2b.

#### c) $\text{Fe}_7\text{Se}_8$

For  $\text{Fe}_7\text{Se}_8$  crystal, the (001) and (00-1) faces are of the highest MI, as tabulated in Table 1. The predicted crystal growth habit of  $\text{Fe}_7\text{Se}_8$  is a hexagonal plate, as shown in Figure 2c, having (001) and (00-1) faces visible mainly, followed by other planes.

#### d) $\text{FeSe}$

In the last crystal of the Fe-Se system,  $\text{FeSe}$ , (001), and (00-1) faces are of the highest MI, as shown in Table 1, and the resultant crystal growth habit is the same as  $\text{FeSe}_2$  as shown in Figure 2d.

However, one of the most crucial aspects of determining the crystal's habit is the bond energies and orientations present in the crystal system. As a result, a thorough evaluation of multiple interaction energies existing between crystallizing entities in all Fe-Se system phases is critical. HP analyzed the crystal growth morphology in relation to the interaction energies between crystallizing units in 1955.

### 2.3.2 Crystal morphology of Fe-Se system using HP approach

HP<sup>13-15</sup> created a theory using the bond energies for predicting the growth morphology of any crystal. The interior crystal structure's periodic chains of strong bonds are crucial in determining the crystal's ultimate form. All the crystal faces are divided into three parts depending on the periodic chains of strong bonds named PBC vectors— the F (flat), S (stepped), and K (kinked) faces. The MI of faces for appearance in the final crystal habit is  $F > S > K$ . Further, to determine the crystal habit using this model, the list of symmetry operators of all Fe-Se system phases is necessary to verify that there should be an inversion symmetry operator within the unit cells. As if the inversion operator is not present, an intrinsic dipole moment is present within the unit cell, and this model works only for crystals with non-polar unit cells. The list of symmetry operators of all the phases of the Fe-Se system is tabulated in Figure 3.

FeSe <sub>2</sub>		Fe <sub>3</sub> Se <sub>4</sub>		FeSe	
Symm. Op.	Description	Symm. Op.	Description	Symm. Op.	Description
-x,-y,-z	Inversion centre	-x,-y,-z	Inversion centre	-x,-y,z	Rotation axis (2-fold)
-x,y,z	Mirror plane	-x,y,-z	Rotation axis (2-fold)	-x,y,z	Mirror plane
1/2+x,1/2+y,1/2-z	Glide plane	1/2+x,1/2+y,1/2+z	Centring vector	-y,-x,-z	Rotation axis (2-fold)
1/2+x,1/2-y,1/2+z	Glide plane	1/2+x,1/2-y,1/2+z	Glide plane	-y,x,-z	Rotoinversion axis (4-fold)
1/2-x,1/2+y,1/2-z	Screw axis (2-fold)	1/2-x,1/2+y,1/2-z	Screw axis (2-fold)	1/2+x,1/2+y,-z	Glide plane
1/2-x,1/2-y,1/2+z	Screw axis (2-fold)	1/2-x,1/2-y,1/2-z	Inversion centre	1/2+x,1/2-y,-z	Screw axis (2-fold)
x,-y,-z	Rotation axis (2-fold)	x,-y,z	Mirror plane	1/2+y,1/2+x,z	Glide plane
x,y,z	Identity	x,y,z	Identity	1/2+y,1/2-x,z	Rotation axis (4-fold)
				1/2-x,1/2+y,-z	Screw axis (2-fold)
				1/2-x,1/2-y,-z	Inversion centre
				1/2-y,1/2+x,z	Rotation axis (4-fold)
				1/2-y,1/2-x,z	Mirror plane
				x,-y,z	Mirror plane
				x,y,z	Identity
				y,-x,-z	Rotoinversion axis (4-fold)
				y,x,-z	Rotation axis (2-fold)

Fe <sub>7</sub> Se <sub>8</sub>	
Symm. Op.	Description
-x+y,-x,2/3+z	Screw axis (3-fold)
-y,x-y,1/3+z	Screw axis (3-fold)
x,y,z	Identity

**Figure 3.** The list of symmetry operators of all the phases of the Fe-Se system. a) FeSe<sub>2</sub>, b) Fe<sub>3</sub>Se<sub>4</sub>, c) Fe<sub>7</sub>Se<sub>8</sub>, and d) FeSe.

The data reveals that the inversion operator is present in FeSe<sub>2</sub>, Fe<sub>3</sub>Se<sub>4</sub>, and FeSe phases while absent in Fe<sub>7</sub>Se<sub>8</sub>. This implies that Fe<sub>7</sub>Se<sub>8</sub> has an intrinsic dipole moment within the unit cell, and therefore the crystal habit of these phases could not be predicted by using the HP model.

According to the HP model, Table 2 to 4 explains the RGR and MI of distinct faces of corresponding Fe-Se system phases. The RGR has been used according to the face category. For F type faces, the MI and RGR is taken as reference value. For S the RGR is higher than F and MI is lower than F. For K, MI values are minimal.

#### a) FeSe<sub>2</sub>

Figure 4 depicts a FeSe<sub>2</sub> crystal packing diagram with PBC vectors displayed as various coloured arrows.

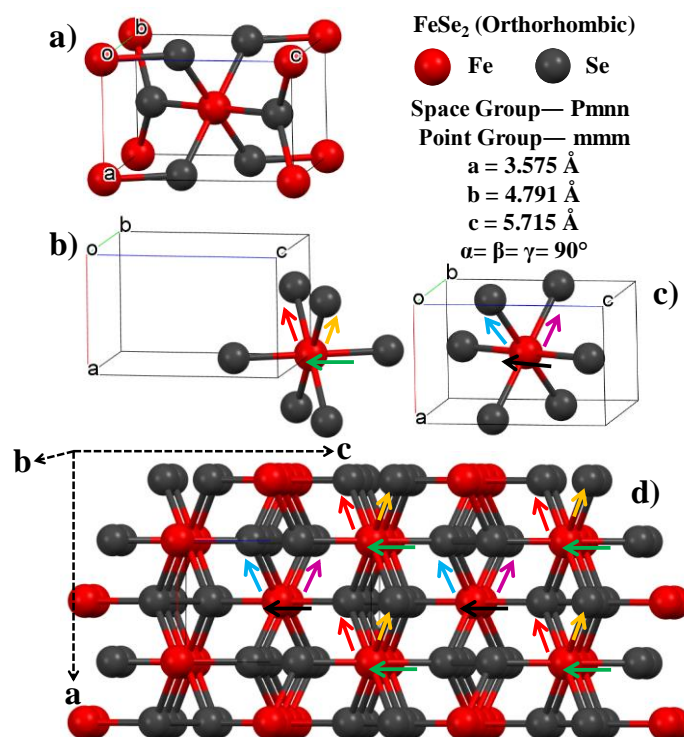


**Figure 4.** a) Unit cell of FeSe<sub>2</sub>. b) and c) Bonding of corner and center Fe atom with the PBC vectors having stoichiometry FeSe<sub>2</sub>, respectively. d) Packing diagram of FeSe<sub>2</sub> crystal along with PBC vectors. The three crystallographic axes are denoted by a, b, and c. A total of six types of PBC vectors are present— 3 attached with each center Fe atom and corner Fe atoms.

Green and black PBCs entirely lie on the (100) and (-100) planes of the FeSe<sub>2</sub> structure. Accordingly, these planes are in the F category of faces and are most prominent in the resulting crystal shape. A large component of green and black PBC vectors lie on the (010) and (0-10) planes. Thus, these faces correspond to the S faces. Similarly, other planes [(001), (00-1), (011), (0-1-1), (01-1), (0-11), (110), (-1-10), (-110), (1-10), (111), (-1-1-1), (-111), (1-1-1), (11-1), (-1-1-1), (-11-1), (1-11)] also comes under the S categories according to different PBC vectors.

(101), (-101), (10-1), and (-10-1) faces are not parallel to any PBC. Thus, they belong to the K category having the least visibility in the final morphology.

**Table 2.** Morphological importance of several faces of FeSe<sub>2</sub> crystal based on HP model. All the faces are categorized according to their alignment with PBC vectors.

S. No.	Faces (hkl)	PBC vectors lying parallel to (hkl) planes	Face category	MI
1	(100), ( $\bar{1}00$ )	Green and black	F	Largest
2	(001), (00 $\bar{1}$ )	Large component of red, orange, blue and pink	S	Large
3	(010), (0 $\bar{1}0$ )	Large component of Green and black	S	Large
4	(011), (0 $\bar{1}\bar{1}$ )	Large component of black, red and orange	S	Large
5	(01 $\bar{1}$ ), (0 $\bar{1}1$ )	Large component of green, blue and pink	S	Large
6	(110), ( $\bar{1}\bar{1}0$ )	Large component of black, green, pink and red	S	Large
7	( $\bar{1}10$ ), (1 $\bar{1}0$ )	Large component of blue, orange, green and black	S	Large
8	(111), ( $\bar{1}\bar{1}\bar{1}$ )	Large component black, pink and red	S	Large
9	( $\bar{1}11$ ), (1 $\bar{1}\bar{1}$ )	Large component black, blue and orange	S	Large
10	(11 $\bar{1}$ ), ( $\bar{1}\bar{1}1$ )	Large component of green and red	S	Large
11	( $\bar{1}\bar{1}\bar{1}$ ), (1 $\bar{1}1$ )	Large component of orange, green and blue	S	Large
12	(101), ( $\bar{1}01$ ), (10 $\bar{1}$ ), ( $\bar{1}0\bar{1}$ )	No PBC vector lie along this planes	K	Smallest

All the planes of different categories for FeSe<sub>2</sub> crystal based on the HP model are tabulated in Table 2. The HP model predicts that the (100) and (-100) faces are the highest MI for FeSe<sub>2</sub> crystal. Therefore, the crystal habit of FeSe<sub>2</sub> crystal is very small cylindrical-like with upper planes as (100) and (-100) to be immensely visible, as shown in the morphological design determine using HP model in Figure 5.

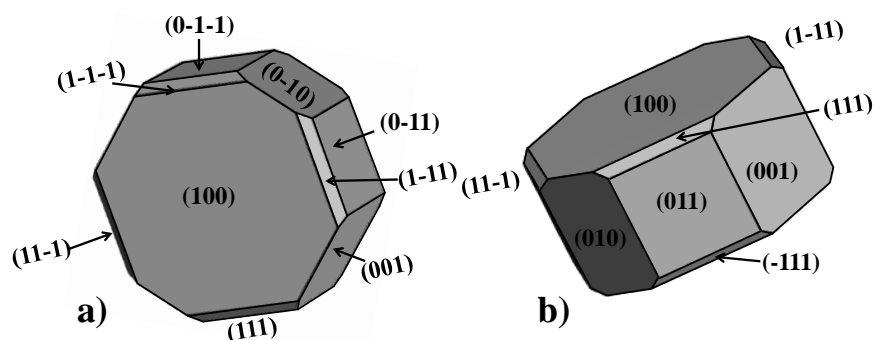


**Figure 5.** Theoretical morphology of  $\text{FeSe}_2$  crystal predicted using HP model. The figure shows the indexed morphological drawing with corresponding hkl planes (black color)— a) the upper view of the morphology with the highest MI of (100) plane and b) the side view of the morphology.

### b) $\text{Fe}_3\text{Se}_4$

Figure 6 displays the packing diagram of  $\text{Fe}_3\text{Se}_4$  having a blue cloud shape PBC vector. PBC vector entirely lies on the (010) and (0-10) planes of the  $\text{Fe}_3\text{Se}_4$  structure. Accordingly, these planes are in the F category of faces and are most visible in the final crystal shape.

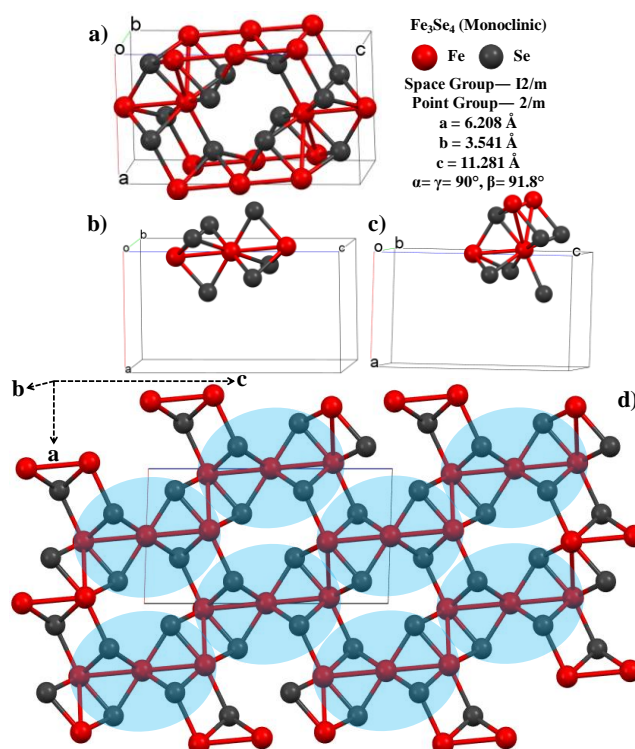


**Figure 6.** a) Unit cell of  $\text{Fe}_3\text{Se}_4$ . b) and c) Bonding of two different Fe atoms present in the  $\text{Fe}_3\text{Se}_4$  crystal. d) Packing diagram of  $\text{Fe}_3\text{Se}_4$  crystal along with 1 PBC vector represented by blue cloud having stoichiometry  $\text{Fe}_3\text{Se}_4$ . The three crystallographic axes are denoted by a, b, and c.



Large component of PBC vectors lie on the (001), (00-1), (101), (-101), (10-1), (-10-1), (110), (-110), (1-10), (-1-10), (011), (0-11), (01-1), (0-1-1), (111), (-1-1-1), (-111), (1-11), (11-1), (1-1-1), (-11-1), and (-1-11) planes. Thus, these faces correspond to the S faces. The (100) and (-100) planes belong to the K category and have the least visibility in the final morphology as no PBC lies along these faces. All the planes of different categories for  $\text{Fe}_3\text{Se}_4$  crystal based on the HP model are tabulated in Table 3.

**Table 3.** Morphological importance of several faces of  $\text{Fe}_3\text{Se}_4$  crystal based on HP model. All the faces are categorized according to their alignment with PBC vectors.

S. No.	Faces (hkl)	PBC vectors lying parallel to (hkl) planes	Face category	MI
1	(010), (0 $\bar{1}$ 0)	Blue	F	Largest
2	(001), (00 $\bar{1}$ ), (101), ( $\bar{1}$ 0 $\bar{1}$ ), (10 $\bar{1}$ ), ( $\bar{1}$ 01), (110), ( $\bar{1}$ 10), (1 $\bar{1}$ 0), ( $\bar{1}$ 1 $\bar{0}$ ), (011), (0 $\bar{1}$ 1), (01 $\bar{1}$ ), (0 $\bar{1}$ 1 $\bar{1}$ ), (111), ( $\bar{1}$ 1 $\bar{1}$ ), ( $\bar{1}$ 11), (1 $\bar{1}$ 1), (11 $\bar{1}$ ), (1 $\bar{1}$ 1), ( $\bar{1}$ 1 $\bar{1}$ ), ( $\bar{1}$ 11)	Large component of blue	S	Large
3	(100), ( $\bar{1}$ 00)	No PBC vector lies along this planes	K	Smallest

The HP model predicts that the (010) and (0-10) faces are the highest MI for  $\text{Fe}_3\text{Se}_4$  crystal. Therefore, the crystal habit of  $\text{Fe}_3\text{Se}_4$  crystal is very small, hexagonal-cylindrical-like with upper planes as (010) and (0-10) to be immensely visible, as shown in morphological design determined using HP model in Figure 7.

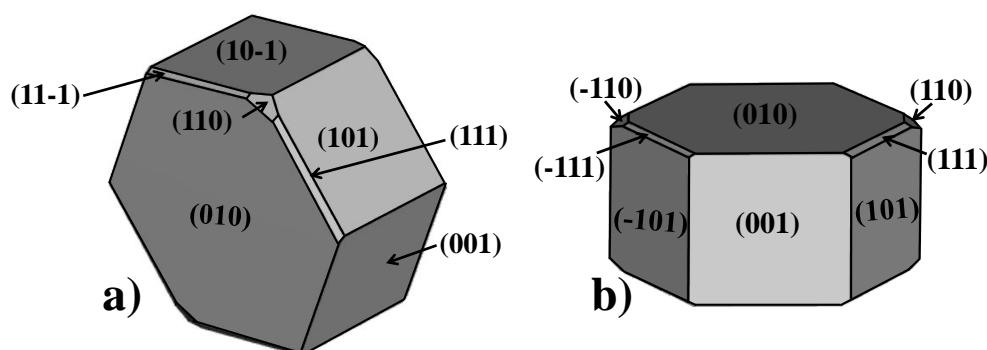


**Figure 7.** Theoretical morphology of  $\text{Fe}_3\text{Se}_4$  crystal predicted using HP model. The figure shows the indexed morphological drawing with corresponding hkl planes (black color). a) The upper view of the morphology with the highest MI of the (010) plane and b) the side view of the morphology.

## c) FeSe

Figure 8 displays the packing diagram of FeSe having 4 PBC vectors illustrated by distinct color arrows— green, black, orange, and blue.

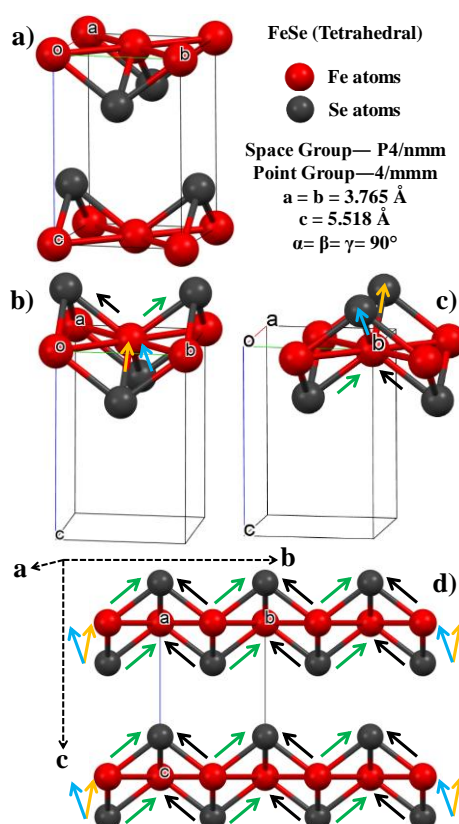


**Figure 8.** a) Unit cell of FeSe. b) and c) Bonding of center and corner Fe atom with the PBC vectors having stoichiometry FeSe, respectively. d) Packing diagram of FeSe crystal along with PBC vectors. A total of four types of PBC vectors are present— black, green, blue, and orange. The three crystallographic axes are denoted by a, b, and c.

Green and black PBC vectors lie entirely on the (100) and (-100) planes of the structure. The other 2 PBC vectors (orange and blue) entirely lie on the (010) and (0-10) planes. Accordingly, these planes are in the F faces and are most prominent in the resultant crystal shape. A significant component of different PBC vectors lies on the distinct planes, as shown in Table 4.

Thus, these faces correspond to the S faces. (001), (00-1), (110), (-110), (1-10), and (-1-10) faces belong to the K category having the least visibility in the final morphology with no PBC vectors lie along these planes. All the planes of different categories for FeSe crystal based on the HP model are tabulated in Table 4. HP model predicts that the (100), (-100), (010), and (0-10) faces are of the highest MI for FeSe crystal. Therefore, the crystal habit of the FeSe

crystal is rod-like with longitudinal planes as (100), (-100), (010), and (0-10) to be immensely visible, as shown in the morphological drawing predicted using HP theory in Figure 9.

**Table 4.** Morphological importance of several faces of FeSe crystal based on HP model. All the faces are categorized according to their alignment with PBC vectors.

S. No.	Faces (hkl)	PBC vectors lying parallel to (hkl) planes	Face category	MI
1	(100), ( $\bar{1}00$ )	Green and black	F	Largest
2	(010), ( $0\bar{1}0$ )	Orange and blue		
3	(101), ( $\bar{1}0\bar{1}$ )	Large component of green, black and orange	S	Large
4	( $\bar{1}01$ ), ( $10\bar{1}$ )	Large component of green, black and blue		
5	(011), ( $0\bar{1}\bar{1}$ )	Large component of green, blue and orange		
6	( $0\bar{1}1$ ), ( $01\bar{1}$ )	Large component of orange, black and blue		
7	(111), ( $\bar{1}\bar{1}\bar{1}$ )	Large component of green and orange		
8	( $1\bar{1}\bar{1}$ ), ( $\bar{1}11$ )	Large component of green and blue		
9	( $11\bar{1}$ ), ( $\bar{1}\bar{1}1$ )	Large component of black and blue		
10	( $1\bar{1}1$ ), ( $\bar{1}1\bar{1}$ )	Large component of black and orange		
11	(001), ( $00\bar{1}$ ), (110), ( $\bar{1}10$ ), ( $1\bar{1}0$ ), ( $\bar{1}\bar{1}0$ )	No PBC vector lies along this planes	K	Large

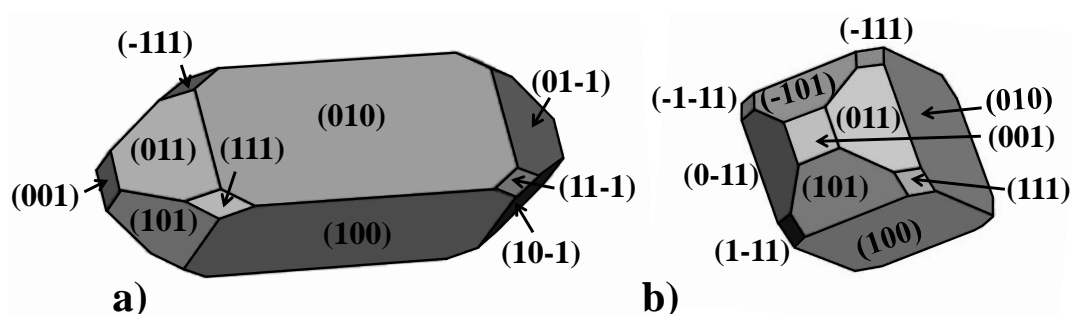


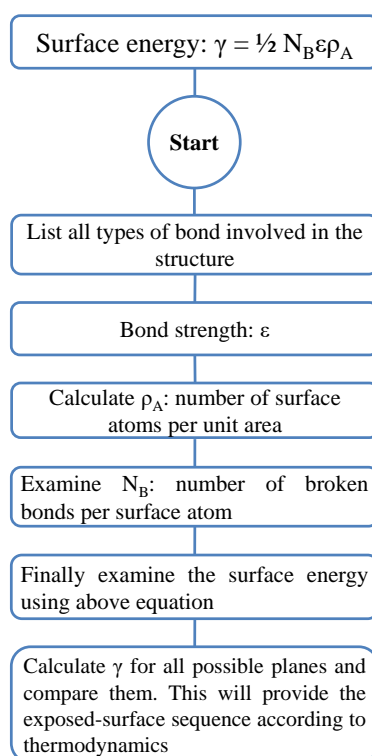
**Figure 9.** Theoretical morphology of FeSe crystal predicted using HP model. The figure shows the indexed morphological drawing with corresponding hkl planes (black color). a) the side view of the morphology with the highest MI of (010) and (100) plans, and b) the upper view of the morphology.

### 2.3.3 Evaluating surface free energy of various planes of Fe-Se system using BBA approach

The specific surface free energy is defined as the rise in free energy per unit area when a crystal produces a fresh surface. The energy required to break the bonds between atoms to form new surfaces may be utilized to evaluate the surface-free energy. The surface free energy of a crystallographic plane can be studied using the BBA, which considers only interactions between the closest neighbours<sup>16</sup>:

$$\gamma = \frac{1}{2} N_B \epsilon \rho_A \text{ ----- (1)}$$

The component 1/2 is present in the following equation because each bond contains two atoms. where  $N_B$  is the no. of broken bonds per surface atom (or per surface unit cell),  $\epsilon$  is the bond energy, and  $\rho_A$  is the no. of surface atoms per unit area (A). The crystal structure may be used to compute  $N_B$  and  $\rho_A$  for various low-index planes. To evaluate the surface energy of the distinct plane, please follow the flow chart mentioned in Scheme 2.



**Scheme 2.** The flow chart evaluates the surface energy of any plane in a particular material.

The  $\epsilon$  parameter is taken from the prior reports— Fe-Fe (~1.68 eV), Se-Se (~3.43 eV), and Fe-Se (~2.74 eV). Therefore, the Fe-Se system's surface free energies of low-index planes were determined using equation 1.

Particularly, the surface free energy of low-index planes in FeSe<sub>2</sub> lattice increases as—

$$\gamma (100) < \gamma (010) \sim \gamma (111) \sim \gamma (101) < \gamma (001) < \gamma (011) < \gamma (110)$$

Thus, the MI planes are in this sequence for FeSe<sub>2</sub>

$$(100) > (010) \sim (111) \sim (101) > (001) > (011) > (110)$$

The sequence for Fe<sub>3</sub>Se<sub>4</sub> is well explained and examined—

$$\gamma (101) < \gamma (001) < \gamma (010) < \gamma (100) \sim \gamma (011) < \gamma (110) \sim \gamma (111)$$

and the MI planes sequence is

$$(101) > (001) > (010) > (100) \sim (011) > (110) \sim (111)$$

In case of FeSe, the surface energy for low-index planes follows the following order—

$$\gamma (101) = \gamma (011) < \gamma (100) = \gamma (010) < \gamma (110) < \gamma (001) \sim \gamma (111)$$

and the MI planes sequence is

$$(101) = (011) > (100) = (010) > (110) > (001) \sim (111)$$

In the case of Fe<sub>7</sub>Se<sub>8</sub>, due to the involvement of many atoms and bonds in each facet, the BBA route is not applicable to calculate surface energy because the approximation here will increase hugely.

In a vacuum, the facets will grow to minimize the total surface energy; therefore, the high-energy planes will add atoms at a higher rate than the lower energy planes. Consequently, the faces exposed on the surface will be in the sequence discussed above for each phase. The total surface energy of a crystal is equal to the sum of the surface energies of all the crystal faces  $\gamma_i A_i$  for the  $i^{\text{th}}$  crystal face of a crystal. The total surface energy is minimum and does not fluctuate with time in equilibrium circumstances.

$$\frac{d}{dt} (\sum_i \gamma_i A_i) = \sum_i \gamma_i \frac{dA_i}{dt} = 0 \text{ ----- (2)}$$

As per the Wulff theory, the thermodynamic growth will follow the overall surface energy minimization principle, and a hybrid shape exposing a mixture of different planes in the correct proportion will become the victory of thermodynamics.

The BBA provides a straightforward method for evaluating the surface free energy of nanocrystals surrounded by a vacuum. However, excluding a few factors like the interactions with 2<sup>nd</sup> and 3<sup>rd</sup> nearest neighbors, surface reconstruction, and the actual chemical environment

of the surfaces could result in remarkable errors in determining the surface free energies of distinct faces, mainly with larger indices. The computational modeling provides a more precise route for calculating surface free energies with fewer errors than the above method. Thus, both approaches may reach a similar conclusion but with differing error bars. Besides, the real-life reactions of materials are much more complicated than the simplified thermodynamical model due to the kinetic control over the reaction.

The MI planes have been examined for the Fe-Se system using three well-known theories in the above sections. All the findings that correspond to the distinct model are summarized in Table 5.

**Table 5.** Comparing the MI of several faces of Fe-Se crystals based on various models—BFDH, HP, and SE.

Models Phases	BFDH	HP	SE
FeSe <sub>2</sub>	(001) > (011) > (101) > (110)	(100) > (001) ~ (010) ~ (011) ~ (110) ~ (111) > (101)	(100) > (010) ~ (111) ~ (101) > (001) > (011) > (110)
Fe <sub>3</sub> Se <sub>4</sub>	(001) > (101) > (011) > (110)	(010) > (001) ~ (101) ~ (110) ~ (011) ~ (111) > (100)	(101) > (001) > (010) > (100) ~ (011) > (110) ~ (111)
FeSe	(001) > (011) ~ (101) > (110)	(100) ~ (010) > (101) ~ (011) ~ (111) > (001) ~ (110)	(101) = (011) > (100) = (010) > (110) > (001) ~ (111)

The observation shows that a MI facet varies according to the model in each crystal. As BFDH is a pure crystallographic theory, the obtained results are pure geometrically important planes in respective phases. In all three-phase, the highest and lowest MI planes are the same. Further, the concept of bond energy is included in the theories (HP and SE model). Although, both the models consider the concept of bond energies. However, the results are distinct

because one model predicts the growth morphology (HP approach), which considers the direction of strong bonds, while the other is equilibrium morphology (SE approach), which considers the bond energy of each bond involved in the particular plane. There are similarities also in some cases, as in FeSe<sub>2</sub>, the highest MI is the same in both models HP and SE [(100) plane]. However, there are more dissimilarities as the initial approach is distinct.

The real-life reactions of materials are much more complicated than the simplified theoretical models due to the involvement of external factors in the reaction. Here, two morphologies have been predicted— growth and equilibrium morphology. Furthermore, the correlation between the predicted and real-life experimental morphologies is necessary. It will be interesting to examine which morphologies are closed with the experimental results among the above theories and why? These theoretical findings will help us in understanding the experimental observations. These approaches can be extended to other TMCs to understand better the morphologies followed by controlling them and tuning the properties.

## 2.4 Conclusion

This chapter aims to predict the crystal habit of the Fe-Se system, starting from FeSe<sub>2</sub> to Fe<sub>3</sub>Se<sub>4</sub> to Fe<sub>7</sub>Se<sub>8</sub> and finally, FeSe crystals from their internal crystal structures. They all have different crystal structures: FeSe<sub>2</sub> (orthorhombic), Fe<sub>3</sub>Se<sub>4</sub> (monoclinic), Fe<sub>7</sub>Se<sub>8</sub> (hexagonal), and FeSe (tetragonal), which makes this system complex. These three well-known methodologies, namely: (1) BFDH model, (2) HP model, and (3) SE minimization using BBA, were utilized to determine the crystal habit of Fe-Se system crystals. It is appropriate to conclude all the above-acquired results as follows:

1. From the BFDH model, after utilizing the space-group symmetry operation and interplanar spacing  $d_{hkl}$ , the external crystal morphology of all the phases of Fe-Se system crystals has been successfully predicted. FeSe<sub>2</sub> and FeSe has plate-like crystal morphology with (001) & (00 $\bar{1}$ ) planes being the largest visible. Fe<sub>3</sub>Se<sub>4</sub> has rod-like external morphology with (001), (00 $\bar{1}$ ), ( $\bar{1}01$ ), (10 $\bar{1}$ ), ( $\bar{1}0\bar{1}$ ) & (101) planes being strongly visible. Fe<sub>7</sub>Se<sub>8</sub> has a hexagonal shape with (001) and (00 $\bar{1}$ ) faces of the highest MI, followed by other planes on the longitudinal side.
2. In the HP model, after utilizing the PBC vectors, i.e., strong bonds, the crystal morphology of all the phases of Fe-Se system crystals has been successfully predicted. According to the inversion operator, for Fe<sub>7</sub>Se<sub>8</sub>, this model could not predict the crystal habit. In FeSe<sub>2</sub>, a very small cylindrical shape with upper planes as (100) and ( $\bar{1}00$ ) to be immensely visible has been

predicted as a crystal habit using the HP model. The crystal habit of  $\text{Fe}_3\text{Se}_4$  crystal is very small hexagonal-cylindrical like with upper planes as (010) and  $(0\bar{1}0)$  to be immensely visible has predicted. The FeSe crystal is predicted as rod-like with longitudinal planes as (100),  $(\bar{1}00)$ , (010), and  $(0\bar{1}0)$  to be immensely visible.

3. In last model, MI planes are predicted using surface free energy minimization theory with BBA. Particularly, the MI low-index planes in  $\text{FeSe}_2$  lattice are in this sequence  $(100) > (010) \sim (111) \sim (101) > (001) > (011) > (110)$ . For  $\text{Fe}_3\text{Se}_4$ — $(101) > (001) > (010) > (100) \sim (011) > (110) \sim (111)$ . For FeSe, it follows the following order— $(101) = (011) > (100) = (010) > (110) > (001) \sim (111)$ .

Among the abovementioned method, the two models —BFDH and HP approaches provide the growth morphologies, while the SE model gives us the equilibrium morphology.

## 2.5 Reference

- (1) Hadjittofis, E.; Isbell, M. A.; Karde, V.; Varghese, S.; Ghoroi, C.; Heng, J. Y. Y. Influences of Crystal Anisotropy in Pharmaceutical Process Development. *Pharm Res.* 2018, 5, 35.
- (2) Corpinot, M. K.; Bučar, D. K. A Practical Guide to the Design of Molecular Crystals. *Cryst. Growth Des.* 2019, 19, 2, 1426–1453.
- (3) Colwell, K. A.; Jackson, M. N.; Torres-Gavosto, R. M.; Jawahery, S.; Vlasisavljevich, B.; Falkowski, J. M.; Smit, B.; Weston, S. C.; Long, J. R. Buffered Coordination Modulation as a Means of Controlling Crystal Morphology and Molecular Diffusion in an Anisotropic Metal–Organic Framework. *J. Am. Chem. Soc.* 2021, 143, 13, 5044–5052.
- (4) McCune, M.; Zhang, W.; Deng, Y. High Efficiency Dye-Sensitized Solar Cells Based on Three-Dimensional Multilayered ZnO Nanowire Arrays with "Caterpillar-like" Structure. *Nano Lett.* 2012, 12, 7, 3656–3662.
- (5) Kramer, H. J. M.; Rosmalen, G. M. Crystallization. *Encyclopedia of Separation Science.* 2000, 64-84
- (6) Barbara, S. Modeling Solution Growth of Inorganic Crystals. Thesis, University of California, 2014.
- (7) Kepler, J. (1611) *Strena seu de nive sexangula*, Francofurti ad Moenum, Godfrey Tampach, Frankfurt; English translation "A new year's gift or on the six-cornered snowflakes", by Hardie, C., Oxford Univ. Press, Oxford.
- (8) Steno, N. (1669) *De solido intra solidum naturaliter contento dissertationis prodromus*, Florence; English translation by J. G. Winter, *The Prodromus of Nicolous Steno's dissertation concerning a solid body enclosed by process of nature within a solid*, Hafner, New York (1968).
- (9) Haüy, R. J. (1784) *Essai d'une théorie sur la structure des cristaux*, Paris.
- (10) A. Bravais. *Etudes Crystallographiques*. Paris: Gauthier-Villars, 1866.
- (11) M. G. Friedel. *Etudes sur la loi de Bravais*. Bull. Soc. Franc. Miner., 9:326, 1907.



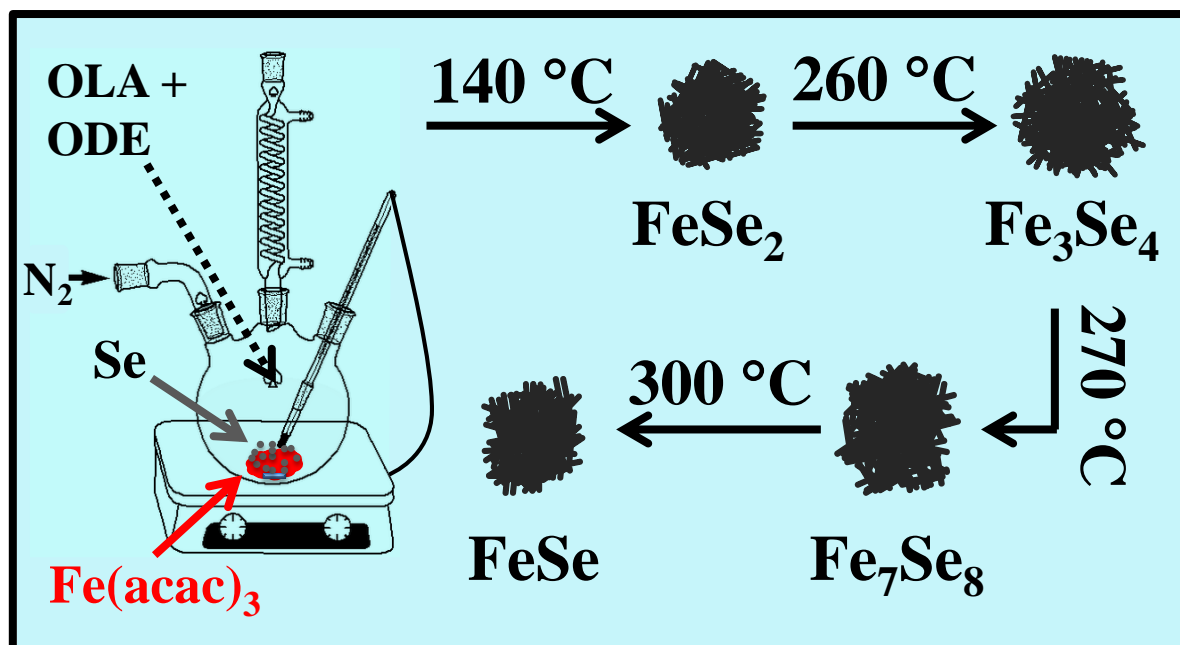
- (12) J. D. H. Donnay and D. Harker. A new law of crystal morphology extending the law of bravais. *Amer. Min.*, 22:446, 1937.
- (13) P. Hartman and W. G. Perdok. On the relations between structure and morphology of crystals. I. *Acta Crystallogr.*, 8:49–52, 1955.
- (14) P. Hartman and W. G. Perdok. On the relations between structure and morphology of crystals. II. *Acta Crystallogr.*, 8:521–524, 1955.
- (15) P. Hartman and P. Bennema. The attachment energy as a habit controlling factor : I. Theoretical considerations. *J. Cryst. Growth*, 49:145–156, 1980.
- (16) Xia, Y.; Xia, X.; Peng, H. C. Shape-Controlled Synthesis of Colloidal Metal Nanocrystals: Thermodynamic versus Kinetic Products. *J. Am. Chem. Soc.* 2015, 137, 7947–7966.
- (17) S. Goel, N. Sinha, H. Yadav, B. Kumar, On the prediction of external shape of ZnO nanocrystals. *Physica E: Low-dimensional Systems and Nanostructures*, 2018.
- (18) Song Li, Gaowu W. Qin\*, Yudong Zhang, Wenli Pei, Liang Zuo and Claude Esling. Anisotropic Growth of Iron Oxyhydroxide Nanorods and their Photocatalytic Activity. *Advanced engineering materials*, 2010, 12, 10.
- (19) Cong, H.; Zhang, H.; Sun, S.; Yu, Y.; Yu, W.; Yu, H.; Zhang, J.; Wang, J.; Boughton, R. Morphological Study of Czochralski-Grown Lanthanide Orthovanadate Single Crystals and Implications on the Mechanism of Bulk Spiral Formation. *J. Appl. Cryst.* (2010). **43**, 308-319.(47) Eftimie, E.; Avram, N.; Jelsch, C.; Nicolov, M. Morphology of the GdVO<sub>4</sub> crystal: first-principles studies. *Acta Cryst.* 2020, B76.
- (20) Eftimie, E.; Avram, N.; Jelsch, C.; Nicolov, M. Morphology of the GdVO<sub>4</sub> crystal: first-principles studies. *Acta Cryst.* 2020, B76
- (21) H. P. Wu, J. F. Liu, M. Y. Ge, L. Niu, Y. W. Zeng, Y. W. Wang, G. L. Lv, L. N. Wang, G. Q. Zhang, and J. Z. Jiang. Preparation of Monodisperse GeO<sub>2</sub> Nanocubes in a Reverse Micelle System. *Chem. Mater.* 2006, 18, 1817-1820.
- (22) W. M. M. Heijnen. The morphology of gel grown calcite. *N. Jb. Miner. Mh.*, 8:357– 371, 1985.
- (23) Goel, S.; Sinha, N.; Hussain, A.; Joseph, A.; Yadav, H.; Kumar, B. Sunset yellow dyed triglycine sulfate single crystals: enhanced thermal, mechanical, optical and di-/piezo-/ferro-/pyro-electric properties. *Journal of Materials Science: Materials in Electronics*, 2018.
- (24) K J Robertst, R Dochertyt, P Bennemas and L A M J Jetten. The importance of considering growth-induced conformational change in predicting the morphology of benzophenone. *J. Phys. D. AM, Phys.* 1993, 26, 87-821.
- (25) Zhang, H.; Zhang, M.; Pan, S.; Dong, X.; Yang, Z.; Hou, X.; Wang, Z.; Chang, K.; Poepelmeier, K. Pb<sub>17</sub>O<sub>8</sub>Cl<sub>18</sub>: A Promising IR Nonlinear Optical Material with Large Laser Damage Threshold Synthesized in an Open System. *J. Am. Chem. Soc.* 2015, 137, 26, 8360–8363
- (26) Jellinek, F. Transition Metal Chalcogenides. Relationship between Chemical Composition, Crystal Structure and Physical Properties. *React. Solids* 1988, 5, 323–339.
- (27) Lan, M.; Xiang, G.; Nie, Y.; Yang, D.; Zhang, X. The Static and Dynamic Magnetic Properties of Monolayer Iron Dioxide and Iron Dichalcogenides. *RSC Adv.* 2016, 6, 31758–31761.

- (28) Lin, C.-R.; Lu, S.-Z.; Lyubutin, I. S.; Korzhetskiy, Y. V.; Wang, S.-C.; Suzdalev, I. P. Synthesis and Magnetic Properties of Iron Sulfide Nanosheets with a NiAs-like Structure. *J. Appl. Phys.* 2010, 107, 09A335.
- (29) Liu, A.; Chen, X.; Zhang, Z.; Jiang, Y.; Shi, C. Selective Synthesis and Magnetic Properties of FeSe<sub>2</sub> and FeTe<sub>2</sub> Nanocrystallites Obtained through a Hydrothermal Co-Reduction Route. *Solid State Commun.* 2006, 138, 538–541.
- (30) Kamimura, T.; Sato, M.; Takahashi, H.; Mori, N.; Yoshida, H.; Kaneko, T. Pressure-Induced Phase Transition in Fe-Se and Fe-S Systems with a NiAs-Type Structure. *J. Magn. Magn. Mater.* 1992, 104–107, 255–256.
- (31) Lupu, D.; Bucur, R. V. Possible Anionic Clusters and Mixed Valence Effects in Transition Metal Chalcogenides and Oxides. *J. Phys. Chem. Solids* 1978, 39, 285–290.
- (32) Lu, T.; Dong, S.; Zhang, C.; Zhang, L.; Cui, G. Fabrication of transition metal selenides and their applications in energy storage. *Coordination Chemistry Reviews* 2017, 332, 75–99.
- (33) Xia, B.; Gao, D.; Xue, D. Ferromagnetism of two-dimensional transition metal chalcogenides: both theoretical and experimental investigations. *Nanoscale*, 2021, 13, 12772.
- (34) Zeng, C.; Dai, L.; Jin, Y.; Liu, J.; Zhang, Q.; Wang, H. Design strategies toward transition metal selenide-based catalysts for electrochemical water splitting. *Sustainable Energy Fuels*, 2021, 5, 1347.
- (35) Jain, B. K.; Singh, A. K.; Chandra, K. An Investigation of Binary System Fe-Se. *J. Phys. F: Met. Phys.* 1978, 8, 2625–2630.
- (36) Okazaki, A.; Hirakawa, K. Structural Study of Iron Selenides FeSe<sub>x</sub>. I Ordered Arrangement of Defects of Fe Atoms. *J. Phys. Soc. Jpn.* 1956, 11, 930–936.
- (37) Reddy, V. K.; Chetty, C. S. Mössbauer Studies in Fe-Se System. *Phys. Status Solidi* 1975, 32, 585–592.
- (38) Hirone, T.; Maeda, S.; Tsuya, N. On the Ferrimagnetism of Iron Selenides. *J. Phys. Soc. Jpn.* 1954, 9, 496–499.
- (39) Hirone, T.; Chiba, S. The Magnetic Properties of FeSe<sub>x</sub> with the NiAs Structure. *J. Phys. Soc. Jpn.* 1956, 11, 666–670.
- (40) Schuster, W.; Mikler, H.; Komarek, K. L. Transition Metal-Chalcogen Systems, VII.: The Iron-Selenium Phase Diagram. *Monatsh. Chem.* 1979, 110, 1153–1170.
- (41) Lavina, B.; Downs, R.; Sinogeikin, S. The Structure of Ferroselite, FeSe<sub>2</sub>, at Pressures up to 46 GPa and Temperatures down to 50 K: A Single-Crystal Micro-Diffraction Analysis. *Crystals* 2018, 8, 289.
- (42) Andresen, A. F. A Neutron Diffraction Investigation of Fe<sub>3</sub>Se<sub>4</sub>. *Acta Chem. Scand.* 1968, 22, 827–835.
- (43) Andresen, A. F.; Leciejewicz, J. A Neutron Diffraction Study of Fe<sub>7</sub>Se<sub>8</sub>. *J. Phys.* 1964, 25, 574–578.
- (44) Okazaki, A. The Superstructures of Iron Selenide Fe<sub>7</sub>Se<sub>8</sub>. *J. Phys. Soc. Jpn.* 1961, 16, 1162–1170.
- (45) Lyubutin, I. S.; Lin, C.-R.; Funtov, K. O.; Dmitrieva, T. V.; Starchikov, S. S.; Siao, Y.-J.; Chen, M.-L. Structural, Magnetic, and Electronic Properties of Iron Selenide Fe<sub>6-7</sub>Se<sub>8</sub> Nanoparticles Obtained by Thermal Decomposition in High-Temperature Organic Solvents. *J. Chem. Phys.* 2014, 141, 044704.

- (46) Hsu, F.-C.; Luo, J.-Y.; Yeh, K.-W.; Chen, T.-K.; Huang, T.-W.; Wu, P. M.; Lee, Y.-C.; Huang, Y.-L.; Chu, Y.-Y.; Yan, D.-C.; Wu, M.- K. Superconductivity in the PbO-Type Structure  $\alpha$ -FeSe. *Proc. Natl. Acad. Sci. U.S.A.* 2008, 105, 14262–14264.
- (47) Yuan, B.; Luan, W.; Tu, S.-t. One-Step Synthesis of Cubic FeS<sub>2</sub> and Flower-like FeSe<sub>2</sub> Particles by a Solvothermal Reduction Process. *Dalton Trans.* 2012, 41, 772–776.
- (48) Yuan, B.; Hou, X.; Han, Y.; Luan, W.; Tu, S.-t. Facile Synthesis of Flake-like FeSe<sub>2</sub> Particles in Open-Air Conditions. *New J. Chem.* 2012, 36, 2101–2105.
- (49) Gao, M.-R.; Lin, Z.-Y.; Jiang, J.; Yao, H.-B.; Lu, Y.-M.; Gao, Q.; Yao, W.-T.; Yu, S.-H. Selective Synthesis of Fe<sub>7</sub>Se<sub>8</sub> Polyhedra with Exposed High-Index Facets and Fe<sub>7</sub>Se<sub>8</sub> Nanorods by a Solvothermal Process in a Binary Solution and Their Collective Intrinsic Properties. *Chem.Eur. J.* 2011, 17, 5068–5075.
- (50) Zhang, H.; Long, G.; Li, D.; Sabirianov, R.; Zeng, H. Fe<sub>3</sub>Se<sub>4</sub> Nanostructures with Giant Coercivity Synthesized by Solution Chemistry. *Chem. Mater.* 2011, 23, 3769–3774.
- (51) Sen Bishwas, M.; Das, R.; Poddar, P. Large Increase in the Energy Product of Fe<sub>3</sub>Se<sub>4</sub> by Fe-Site Doping. *J. Phys. Chem. C* 2014, 118, 4016–4022.
- (52) Long, G.; Zhang, H.; Li, D.; Sabirianov, R.; Zhang, Z.; Zeng, H. Magnetic Anisotropy and Coercivity of Fe<sub>3</sub>Se<sub>4</sub> Nanostructures. *Appl. Phys. Lett.* 2011, 99, 202103.
- (53) Mao, X.; Kim, J.-G.; Han, J.; Jung, H. S.; Lee, S. G.; Kotov, N. A.; Lee, J. Phase-Pure FeSe<sub>x</sub> (x = 1, 2) Nanoparticles with One- and Two-Photon Luminescence. *J. Am. Chem. Soc.* 2014, 136, 7189–7192.
- (54) Ghalawat, M.; Poddar, P. Study of the Phase-Evolution Mechanism of an Fe–Se System at the Nanoscale: Optimization of Synthesis Conditions for the Isolation of Pure Phases and Their Controlled Growth. *Langmuir* 2020, 36, 2012–2022.
- (55) Ghalawat, M.; Poddar, P. Study of Growth Kinetics of Fe<sub>3</sub>Se<sub>4</sub> Nanocrystallites and the Influence of Size and Shape Tunability on their Magnetic Properties. *J. Phys. Chem. C* 2021, 125, 7932–7943.
- (56) Ghalawat, M.; Poddar, P. Remarkable Effect of Fe and Se Composition on Magnetic Properties-Comparative Study of the Fe–Se System at the Nanoscale. *J. Phys. Chem. C* 2022, 126, 4655–4663.
- (57) Tengner, S, *Z.Anorg.Allg.Chem.* (1938), **239**, 126
- (58) Andresen, A.F., van Laar, R., *Acta Chemica Scandinavica (1-27,1973-42,1988)* (1970), **24**, 2435
- (59) Andresen, A.F., Leciejewicz, J., *Journal de Physique (Paris)* (1964), **25**, 574
- (60) Haegg, G, Kindstroem, A L, *Zeitschrift fuer Physikalische Chemie, Abteilung B: Chemie der Elementarprozesse, Aufbau der Materie.* (1933), 22, 453
- (61) Kaminsky, W. From CIF to virtual morphology using the WinXMorph program. *J. Appl. Cryst.* (2007). 40, 382–385.

### Chapter 3

#### Study of Phase-Evolution Mechanism of Fe-Se System at Nanoscale: Optimization of Synthesis Conditions for the Isolation of Pure Phases and their Controlled Growth



## Highlights

Below, we have listed some of the important 'take-away' points from this chapter:

- 1) *We explored a complete phase transformation sequence of Fe-Se system using a wet-chemical method results in plotting the phase diagram.*
- 2) *We investigated the influence of different functional groups of OLA and 1-ODE (double bond and amine group) on the formation of different phases of Fe-Se system.*
- 3) *We studied the growth mechanism of Fe-Se system in these conditions.*
- 4) *We have also optimized the appropriate conditions required to synthesize individual phase of Fe-Se system.*
- 5) *We have also examined the reason behind the particular real-life experimental morphologies from theoretical crystal habits.*

**Keywords:** phase-evolution, nucleation and growth, formation mechanism, iron selenides.

The results of this chapter are published as—

- ✓ Study of the Phase-Evolution Mechanism of an Fe-Se system at the Nanoscale: Optimization of Synthesis Conditions for the Isolation of Pure Phases and their Controlled Growth

**Monika Ghalawat**, Pankaj Poddar\* Langmuir 2020, 36, 8, 2012–2022

### 3.1 Introduction

Nucleation and growth phenomena decide the development of both natural and human-made condensed matters. As we proceed towards the nanoscale dimensions, materials can showcase their bulk counterparts' different physical and chemical properties. For this reason, understanding the nucleation and growth processes is vital for the cogent design of functional nanoparticles (NPs) with precise composition, crystalline phase, size, and shape for medicine applications, catalysis, nanoelectronics, etc<sup>1-10</sup>. With advancements in the characterization techniques, it is possible to microscopically and spectroscopically observe the nucleation and growth at different time scales, which were inaccessible earlier, giving us newer insights for phase control<sup>9</sup>. Several synthetic pathways have been designed and optimized for better phase control of miscellaneous inorganic NPs<sup>11</sup>. Compared to the solid-state methods, the chemical routes have illustrated several benefits in cost-effectiveness, control of objective products, large-scale production, and so-on<sup>12,13</sup>. Apart from being worse on the energy-economy scale, the solid-state pathways require heat-beat-treat iterations (involving high-temperature furnaces with the specific environment), and high purity elements as precursors. Moreover, there are chances of phase impurity due to poor atomic diffusion through the solid phase, leading to the formation of non-stoichiometric phases and broad phase boundaries where two or more phases could coexist. In contrast, the chemical methods are far more efficient, economical, and provide better phase purity than solid-state routes. Besides this, these methods often require relatively much lower temperatures for the phase formation, plus easier control over the size, shape, and structure.

Transition metal chalcogenides (TMCs) represent an important class of materials with rich phase-diagram and diverse industrial applications<sup>14</sup>. The electronic (optical, magnetic, and electrical) and thermal properties are susceptible to the crystalline phase, stoichiometry, shape, and size<sup>15-19</sup>. Therefore, it is essential to reach good control over the chemistry of phase formation. As discussed in chapter 1, among the TMCs,  $\text{Fe}_x\text{Se}_y$  compounds (with  $x:y$  varying from 1:2 to 1:1) are of great importance because of their fascinating and unusual electrical, magnetic, thermal, and optical properties that are remarkably related to the Fe-Se elemental ratio as well as their crystalline structure<sup>20-25</sup>. The family of iron selenides has four stable phases:  $\text{FeSe}_2$ ,  $\text{Fe}_3\text{Se}_4$ ,  $\text{Fe}_7\text{Se}_8$ , and  $\text{FeSe}$ <sup>21,26</sup>. Particularly, iron diselenide ( $\text{Fe}^{2+}\text{Se}_2^{2-}$ ) has an orthorhombic marcasite structure. The conventional unit cell of  $\text{FeSe}_2$  represented in Figure 1a contains one formula unit having the unit cell<sup>27</sup>. Figures 1b & 1c show that  $\text{Fe}_3\text{Se}_4$  and  $\text{Fe}_7\text{Se}_8$

have monoclinic and hexagonal NiAs-type crystal structures, respectively<sup>28–30,31</sup>. The ionic picture of one formula unit of  $\text{Fe}_3\text{Se}_4$  and  $\text{Fe}_7\text{Se}_8$  can be written as  $\text{Fe}^{2+}\text{Fe}_2^{3+}\text{Se}_4^{2-}$  and  $\text{Fe}_5^{2+}\text{Fe}_2^{3+}\text{Se}_8^{2-}$ , respectively<sup>28,29</sup>. It is essential to note that the highest temperature phase— $\beta$ -FeSe has a tetragonal PbO-type crystal structure<sup>32</sup>. Figure 1d shows the unit cell of FeSe ( $\text{Fe}^{2+}\text{Se}^{2-}$ ).

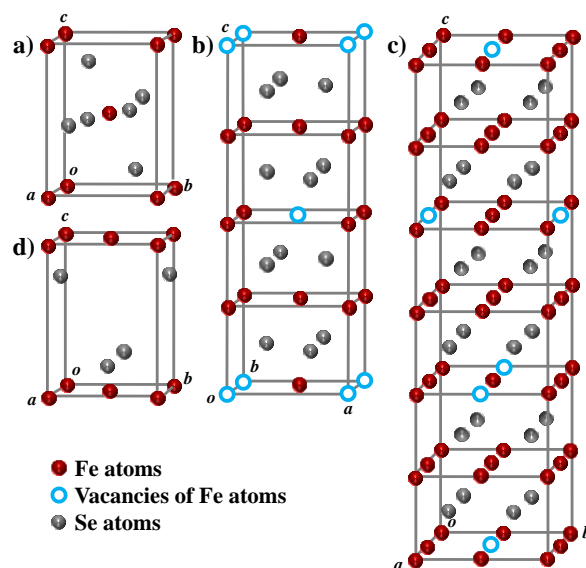


**Figure 1.** Schematic of the unit cell of a)  $\text{FeSe}_2$  having orthorhombic marcasite crystal structure, b)  $\text{Fe}_3\text{Se}_4$  having monoclinic NiAs-type crystal structure, c)  $\text{Fe}_7\text{Se}_8$  having hexagonal NiAs-type crystal structure, and d) FeSe having tetragonal PbO-type crystal structure. Open blue circles represent cations vacancies while solid red circles represent Fe cations. Solid grey circles represent Se anions.

The diversity of bonding and crystal structure in the Fe-Se system give rise to drastically varying chemical and physical properties, as discussed in Chapters 1 and 2. Among the abovementioned four phases of the Fe-Se system, two phases ( $\text{Fe}_3\text{Se}_4$  and  $\text{Fe}_7\text{Se}_8$ ) are well known for their magnetic properties<sup>31</sup>, while the other two ( $\text{FeSe}_2$  and FeSe) are known for their optical properties<sup>33–35</sup>. The existence of multiple phases with abundantly different crystal structures indicates the system's complexity, and therefore, phase-selective syntheses were quite challenging for this system.

Several reports have dealt with fabricating the Fe-Se compounds by chemical synthesis routes in the last decade. In 2009, Lin et al.<sup>36</sup> obtained  $\text{Fe}_3\text{Se}_4$  and  $\text{Fe}_7\text{Se}_8$  NPs for the first time via the thermal decomposition method at 350 °C.  $\text{Fe}_3\text{Se}_4$  nanostructures were also synthesized at 300 °C by a one-pot organic-solution-phase route<sup>37,38</sup>. In 2012, flower-like  $\text{FeSe}_2$  NPs were

synthesized via a solvothermal approach in the temperature range 180 °C - 300 °C<sup>34,35</sup>, and in 2014, FeSe<sub>x</sub> (x=1, 2) were synthesized at 330 °C by using the hot-injection method<sup>33</sup>. FeSe<sub>2</sub> NPs were also synthesized by the hydrothermal route at 140 °C for 13 h<sup>39</sup>. Recently, Li and the group synthesized FeSe NPs by the solvothermal reaction in an autoclave at 160 °C for 12 h, later at 220 °C for 24 h<sup>40</sup>. All methods mentioned above involved either complex synthesis conditions (high temperature or long reaction time) or expensive chemicals in synthesizing the Fe-Se system. Thus, adopting an easy and affordable reaction route (such as low-temperature, short time, and low-cost) with a well-defined shape and high crystallinity of the Fe-Se system is essential.

In this chapter, a simple one-pot thermal decomposition method is reported to synthesize the Fe-Se system in a single reaction by using oleylamine (OLA) as a reducing agent and 1-octadecene (1-ODE) as an accelerating agent<sup>41</sup>. Moreover, a complete phase transformation sequence was carefully drawn for the first time using a wet-chemical method. In order to understand the interaction between various functional groups of solvent and precursors, several experiments were done with amines, alkenes, and alkanes, as well as the influence of reaction parameters on the phase evolution of the Fe-Se system, was also examined. Finally, the formation mechanism of the Fe-Se system was proposed under these conditions. Additionally, the required synthesis conditions were optimized for crystallizing individual phases, and the obtained particles were investigated by transmission electron microscopy (TEM), X-ray diffraction (XRD), thermo-gravimetric analysis (TGA), and X-ray photoemission spectroscopy (XPS). The last section has intensively investigated the correlation between the theoretically predicted crystal habits (discussed in chapter 2) and experimental findings. Furthermore, the reason behind particular experimental crystal morphology formation has also been discussed.

### **3.2 Thermal decomposition-based synthesis of Fe-Se system at nanoscale**

This work presents the optimization of reaction parameters to find suitable synthesis conditions to crystallize various phases of the iron selenide family of compounds by following the one-pot thermal decomposition method. Typically, Fe(acac)<sub>3</sub> [Iron (III) acetylacetonate; 99.99%; Sigma-Aldrich] was used as an organometallic precursor and Se [Selenium powder; 99.99%; Sigma-Aldrich] as a selenium precursor for synthesizing Fe-Se system in an organic solvent. To examine the sequence in which various Fe-Se phases evolve out of solution chemistry—seven prolonged reactions were performed with three different solvent conditions by varying



the temperature from 30 °C - 340 °C. Additionally, the effect of stoichiometry has been intensively studied with one solvent environment.

### **3.2.1 Synthesis of Fe-Se system to examine the phase transformation:**

#### **Synthesis of Fe-Se System in OLA and 1-ODE**

To study the effect of stoichiometry on the phase-transformation—five prolonged reactions were performed by varying the amount of Se from 37.5 wt % to 100 wt %, the stoichiometry of Fe:Se ranging from 1:0.75 (0.35 g, 0.059 g) to 1:2 (0.35 g, 0.158 g). All the reactions were executed in the organic solvent of 10 mL of 1-ODE [1-octadecene; 90%; Sigma-Aldrich] and 15 mL of OLA [Oleylamine; 70%; Sigma-Aldrich] in a 100 mL three-neck round-bottom (RB) flask under the blanket of nitrogen with constant magnetic stirring. The temperature has been increased from 30 °C to 340 °C at a ramping rate of 2 °C min<sup>-1</sup>. For every 10 °C rise in the temperature, hold-time was ~30 min. 2 mL aliquots were taken out with a long needle-glass syringe to study the phase evolution in each step. All the samples were preserved in small glass vials and naturally cool down to room temperature (RT) for further investigation by wide angle X-ray scattering (WAXS). The phase diagram was plotted after assembling the WAXS results, which inferred the effect of stoichiometry along with temperature on phase transformation of Fe-Se system.

#### **Synthesis of Fe-Se System in OLA**

To study the effect of solvents on phase transformation—one synthesis was done by following the same procedure mentioned above, except that only the OLA (15 mL) was used as an organic solvent with the stoichiometry of 1:1.

#### **Synthesis of Fe-Se System in OLA and Pre-dissolved Se Powder in 1-ODE**

In order to examine the effect of solvents, one more reaction was done with the same procedure as mentioned earlier, except that the Se powder was pre-dissolved in 1-ODE under a nitrogen environment with constant magnetic stirring at 30 °C for 6 h.

All the samples were intensively investigated using WAXS, and the results gave us an idea about the synthesis conditions needed to form the individual phase of the Fe-Se system.

### **3.2.2 Synthesis for single-phase formation:**

#### **Synthesis of FeSe<sub>2</sub>**

In a typical reaction of FeSe<sub>2</sub>, 1 mmol of Fe(acac)<sub>3</sub> (0.353 g) and 2 mmol of Se powders (0.158 g) were added to 15 mL of OLA in a 100 mL three-neck RB flask. The mixture was stirred

under a flow of high-purity nitrogen gas at 30 °C. After that, the temperature was increased to 150 °C at a ramping rate of 2 °C min<sup>-1</sup> and hold on to 150 °C for 2 h. A thermometer was placed inside the RB-flask, and the temperature was kept stable within ±1.0 °C during the 2 h long dwell-time at 150 °C. The solution was cooled to RT by removing the heating source. After cooling, 20 mL of 2-propanol was added to the solution to give a black precipitate, which was further separated from the solution by centrifugation. The obtained sample was rewashed with a mixture of 15 mL n-hexane and 10 mL 2-propanol. In the end, the precipitate was attained by vacuum drying the resultant product at RT and was utilized for further characterization.

### **Synthesis of Fe<sub>3</sub>Se<sub>4</sub>**

A 1.5 mmol portion of Fe(acac)<sub>3</sub> (0.53 g) and 2 mmol of Se (0.158 g) were mixed in 15 mL of OLA at 30 °C. The solution mixture was hold on to 120 °C for 0.5 h. Further, the temperature was raised at a ramping rate of 2 °C min<sup>-1</sup> up to 200 °C and 5 °C min<sup>-1</sup> was used to reach a maximum temperature of 260 °C; at which the sample was maintained for 2 h.

### **Synthesis of Fe<sub>7</sub>Se<sub>8</sub>**

A 1.75 mmol of Fe(acac)<sub>3</sub> (0.618 g) and 2 mmol of Se (0.158 g) were added in 15 mL of OLA at 30 °C. The mixture was heated to the designed temperature (230 °C) at a ramping rate of 5 °C min<sup>-1</sup>, and then the ramping rate was decreased to 2 °C min<sup>-1</sup> to increase the temperature at 280 °C and kept at this temperature for 4 h.

### **Synthesis of FeSe**

This synthesis is similar to the synthesis of Fe<sub>7</sub>Se<sub>8</sub> with stoichiometry 1:1, except that the Se was pre-dissolved in 10 mL of 1-ODE at 30 °C with constant magnetic stirring for 6 h.

### **3.2.3 Synthesis to examine the role of OLA**

These syntheses are similar to the above synthesis (FeSe<sub>2</sub> and Fe<sub>3</sub>Se<sub>4</sub>). The mere exception involves the use of 1-ODE, OCD [Octadecylamine; 97%; Sigma-Aldrich], and n-ODE [n-Octadecane; 99%; Alfa Products] instead of OLA as an organic solvent individually.

## **3.3 Characterization techniques**

The progress of phase formation in the prolonged reactions was monitored using WAXS. All measurements were made using Rigaku R Axis IV equipped with a microfocus source (Cu K<sub>α</sub> radiation, λ = 0.154 nm, 1.2 kW rotating anode generator). The scanning time was set at 3 min for all the samples. The distance between the sample and the detector was kept constant at 80

mm for all samples. Powder XRD graphs were done on a PANalytical X'PERT PRO instrument ( $\lambda = 1.54 \text{ \AA}$ ) in  $2\theta$  range of  $10^\circ - 80^\circ$ . The size, morphology, SAED, and lattice images were characterized by using a FEI Tecnai T20 TEM equipped with a super twin lens (s-twin) operated at 200 keV accelerating voltage. The powders were dispersed in n-hexane and then drop-casted on a carbon-coated copper TEM grid with 200 mesh and loaded in a single tilt sample holder. The Hitachi S-4200 system recorded the field-emission-scanning-electron-microscopy (FESEM) images. The thermal stability studies were done with a heating rate of  $10 \text{ }^\circ\text{C}/\text{min}$  using the TGA SDT model Q600 of TA Instruments Inc. USA. The XPS spectra were recorded on Thermo Fisher Scientific Instruments (K Alpha+) with X-ray source ( $h\nu = 1486.6 \text{ eV}$ ) of monochromatic Al K alpha having 6 mA beam current and 12 kV voltage operated at 150 W with the help of a Physical Electronics 04-548 dual Mg/Al anode. A UHV system has a base pressure of  $\leq 5 \times 10^{-9}$  Torr. The analysis depth was nearly 10 to 15  $\text{\AA}$ . From surface normal, both the incident and take-off angles are at  $55^\circ$ . The spot size on the sample was  $400 \text{ }\mu\text{m}$ . The XPS data were resolved using XPSPEAK 4.123. Carbon was taken for reference for binding energy during the analysis. The XPS measurements were done on the exposed surface of the nanoparticles without any surface treatment.

### 3.4 Results and discussion

#### 3.4.1 The study of the effect of reaction temperature, Fe-Se stoichiometry, and organic solvents on the phase formation

Using the solid-state method, Grivel et al.<sup>42</sup> reported that with an increase in the temperature Fe-Se system shows the phase transformation in the following sequence:  $\text{FeSe}_2 \rightarrow \text{Fe}_3\text{Se}_4 \rightarrow \text{Fe}_7\text{Se}_8 \rightarrow \beta\text{-FeSe}$  at  $300 \text{ }^\circ\text{C}$ ,  $320 \text{ }^\circ\text{C}$ ,  $\sim 340 \text{ }^\circ\text{C}$ ,  $350 \text{ }^\circ\text{C} - 370 \text{ }^\circ\text{C}$ , respectively. The phase  $\beta\text{-FeSe}$  transforms into  $\delta\text{-FeSe}$  at  $480 \text{ }^\circ\text{C}$ , and its reversal to the  $\beta\text{-FeSe}$  was detected during cooling.<sup>42</sup> However, due to the inherent drawbacks of the solid-state method, the phase boundaries were not sharply defined; often, at a particular temperature, phases co-evolved at a phase boundary leading to impurity.<sup>42</sup> In contrast, the chemical methods are often energy-efficient, atom economical, provide sharper and cleaner phase boundaries yielding high purity phases, and provide control over size, shape, and structure.

The thermal decomposition approach was used to figure out the nucleation-growth processes and phase formation mechanism. A series of experiments were performed by varying reaction temperatures from  $30 \text{ }^\circ\text{C}$  to  $340 \text{ }^\circ\text{C}$ , Fe to Se precursor ratio, and organic solvents.

OLA was used as a reducing agent in these reactions and 1-ODE as an accelerating agent. Initially, to study the effect of stoichiometry, five prolonged reactions were performed by changing the precursor ratio (Fe:Se) in the presence of both OLA and 1-ODE as an organic solvent. A small number of specimens were collected from the ongoing reaction vessel after every 10 °C rises in temperature, and the WAXS technique examined these specimens (as shown in Figure 2, which reveals the diffraction pattern of reactions 1 to 5).

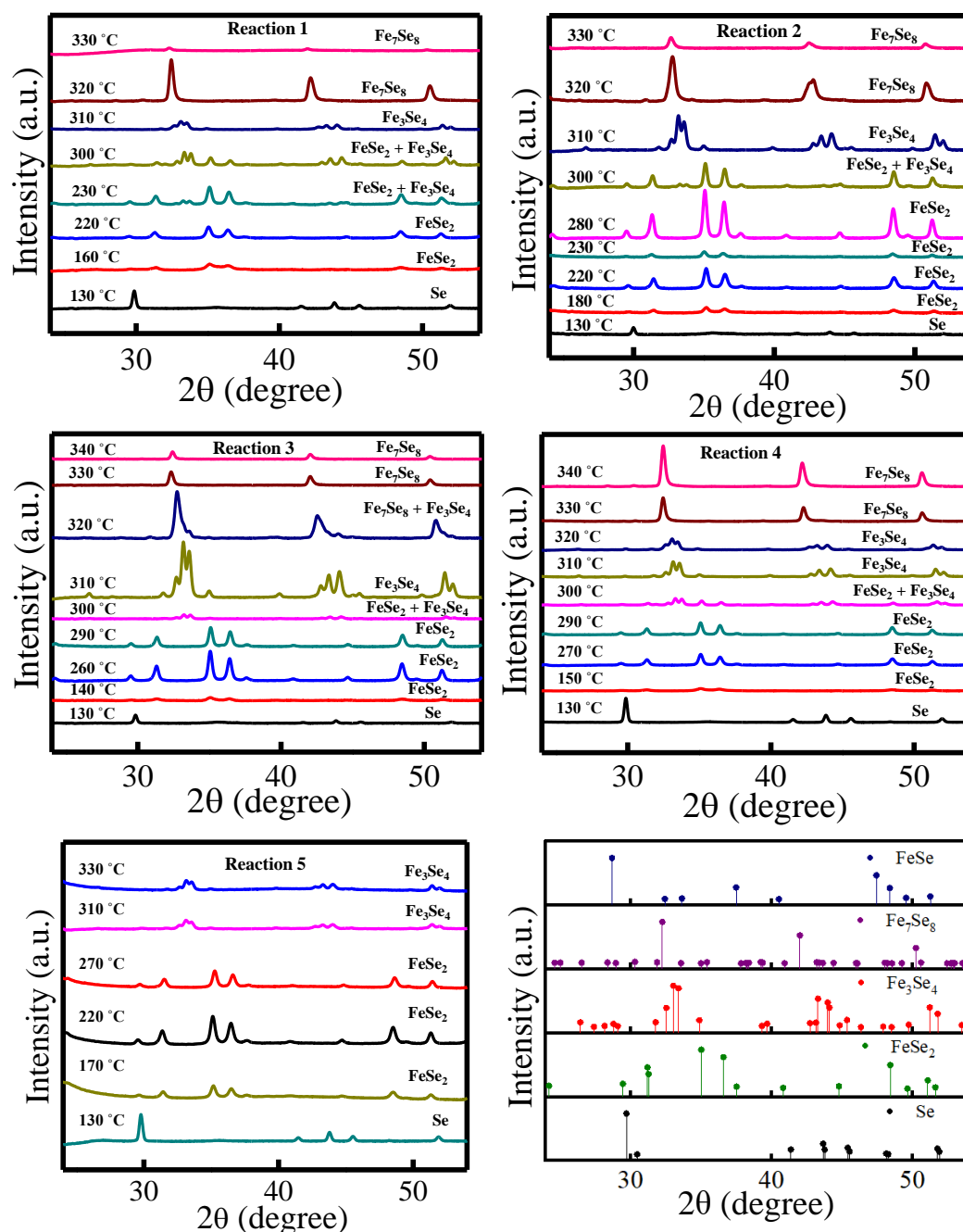


**Figure 2.** Results of diffraction patterns of reaction 1 to 5 samples collected at various temperatures. The reference “International Centre for Diffraction Data” (ICDD) number for

Se, FeSe<sub>2</sub>, Fe<sub>3</sub>Se<sub>4</sub>, Fe<sub>7</sub>Se<sub>8</sub> and FeSe are 96-901-2502, 96-901-2552, 96-152-7087, 96-901-5077, and 96-432-9646, respectively.

Afterward, the phase diagram was constructed based on the WAXS data analysis, as exhibited in Figure 3.

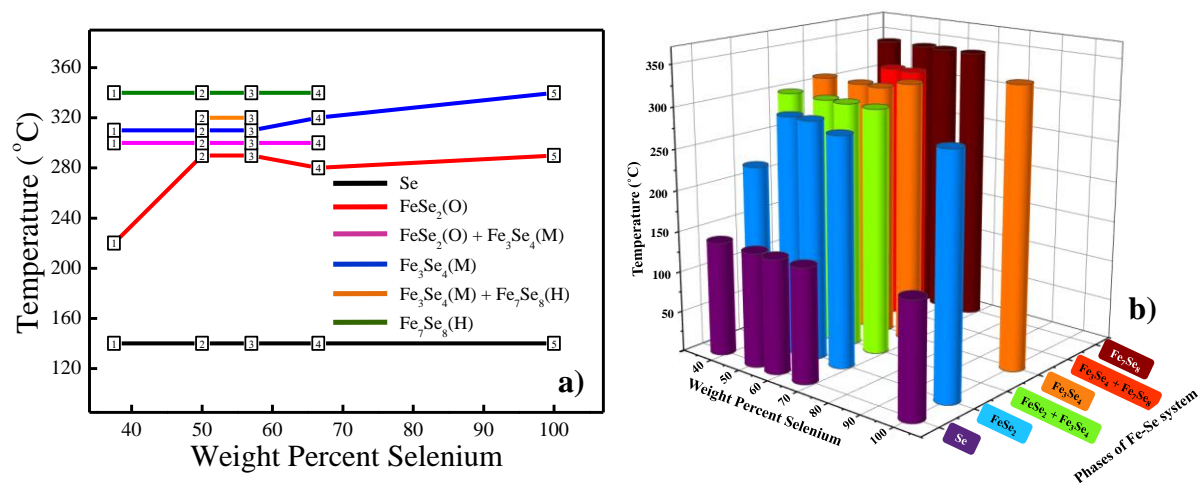


**Figure 3.** Iron - selenium phase diagram a) 2-dimensional representation and b) 3-dimensional representation (present work). Symbols 1 to 5 (in square boxes) represent the outcome of five prolonged reactions with different stoichiometry. Here the amount of Se varied from 37.5 wt % to 100 wt %, the stoichiometry of Fe:Se ranging from 1:0.75 (0.35 g, 0.059 g) to 1:2 (0.35 g, 0.158 g) in OLA and 1-ODE with temperature range 30 °C - 340 °C. The black line (at 140 °C) shows the Se band; after that, FeSe<sub>2</sub> starts forming up to the red line, further Fe<sub>3</sub>Se<sub>4</sub> starts forming, and so on. As the temperature increases, phase evolution was observed from FeSe<sub>2</sub> → Fe<sub>3</sub>Se<sub>4</sub> → Fe<sub>7</sub>Se<sub>8</sub>. The phase evolution was strongly dependent on stoichiometry, in Fe rich side, it was very swift as compared to Se rich side. O, M, and H represents the orthorhombic, monoclinic, and hexagonal structures of corresponding phases, respectively. (The different colour lines reveal the corresponding phase boundaries at that particular wt % Se.)

Initially, the diffraction peaks from Se were visible in the whole range of wt % Se (indexed to ICDD card 96-901-2502). Upon heating from 30 °C up to 140 °C, the Se peaks became significantly weaker, and nearby 150 °C peaks of FeSe<sub>2</sub> emerged without any impurity phase (Se peaks). As discussed earlier, it was reported using the solid-state method that FeSe<sub>2</sub> emerges as the first detectable Fe-Se phase.<sup>42</sup> We believe that there is one possible reason contributing to the formation of FeSe<sub>2</sub> at the beginning of the reaction. FeSe<sub>2</sub> formation kinetics is faster than the other phases of the Fe-Se system. The formation of the FeSe<sub>2</sub> structure requires

Se-Se dimers ( $\text{Se}_2^{2-}$  state), which are readily available from the elemental selenium. On the other hand, the other phases require monomeric  $\text{Se}^{2-}$  ions, which are available at relatively higher temperatures, requiring more energy to break the Se-Se bonds. On the Fe-rich side of the phase diagram, X-ray analysis of specimen at 37.5 wt % Se revealed that the single phase  $\text{FeSe}_2$  was observed up to 220 °C. Along with  $\text{FeSe}_2$ , the  $\text{Fe}_3\text{Se}_4$  phase starts appearing at 230 °C for 37.5 wt % Se. While going towards the selenium-rich side from 50 wt % to 100 wt % Se, single phase  $\text{FeSe}_2$  was detected up to 290 °C  $\pm$  10 °C. For 50 wt % - 66 wt % Se along with the  $\text{FeSe}_2$  phase,  $\text{Fe}_3\text{Se}_4$  was also observed around 300 °C. Finally, with a slight increase in temperature up to  $\sim$  310 °C,  $\text{Fe}_3\text{Se}_4$  single phase was detected in WAXS data over the whole range of wt % Se. For 37.5 wt % Se, the  $\text{Fe}_3\text{Se}_4$  phase emerges relatively earlier in the reaction—probably due to the lower Se/Fe atomic ratio. At 37.5 wt % Se, the amount of Se atoms is less, and the availability of  $\text{Fe}^{2+}$  and  $\text{Fe}^{3+}$  ions are more due to excess of iron atoms, resulting in swiftly transforming the phases towards the iron-rich phases. At 37.5 wt % Se (iron-rich), the single phase  $\text{Fe}_7\text{Se}_8$  was detected at 320 °C. When the wt % Se was adjusted in the range 50 wt % - 57 wt %, the diffraction peaks of  $\text{Fe}_7\text{Se}_8$  started emerging together with the  $\text{Fe}_3\text{Se}_4$  at around 320 °C and with a slight increase in temperature ( $\sim$ 330 °C), single phase  $\text{Fe}_7\text{Se}_8$  was observed. When the wt % Se was increased to 66.6 wt % Se, the single phase  $\text{Fe}_7\text{Se}_8$  was detected at around 330 °C. At 100 wt % Se,  $\text{Fe}_7\text{Se}_8$  was not observed up to 340 °C, which signifies that the conversion from  $\text{Fe}_3\text{Se}_4$  to  $\text{Fe}_7\text{Se}_8$  would not be possible in excess of selenium—there was no iron present to transform the present phase into the next iron-rich phase ( $\text{Fe}_7\text{Se}_8$ ). It is worth mentioning that the solution turns into the gel after 340 °C. The sequence observed by varying the stoichiometry in the presence of OLA and 1-ODE is  $\text{FeSe}_2 \rightarrow \text{Fe}_3\text{Se}_4 \rightarrow \text{Fe}_7\text{Se}_8$ , and afterward, no reaction was possible due to gel formation.

To study the effect of solvent, one reaction was done with OLA as an organic solvent (Table 1 A, Figure 4). As the temperature increases from laboratory temperature ( $\sim$ 30 °C) to 130 °C, the peak intensity of Se starts to reduce slowly and then disappears. As listed in table 1, Fe-precursor (source of  $\text{Fe}^{2+}$ ) and Se-precursor (source of  $\text{Se}_2^{2-}$ ) began to react at around 110 °C with the production of very small portion of  $\text{FeSe}_2$ . The diffraction peaks of single phase  $\text{FeSe}_2$  were observed at  $\sim$ 140 °C. From 110 °C onwards, this reaction arise to move slowly, but it speeds rapidly when the melting point of Se ( $T_{\text{Melt}} = 221$  °C) is reached. Beyond this stage, the  $\text{FeSe}_2$  diffraction peak intensities start declining, and  $\sim$ 230 °C  $\text{FeSe}_2$  peaks coexist with  $\text{Fe}_3\text{Se}_4$  peaks. Finally,  $\sim$ 250 °C single phase  $\text{Fe}_3\text{Se}_4$  was detected in WAXS data that remained

intact up to 270 °C. At a somewhat higher temperature (~280 °C) than the Fe<sub>3</sub>Se<sub>4</sub> phase, the Fe<sub>7</sub>Se<sub>8</sub> phase occurs. As the temperature increases, the Fe<sub>3</sub>Se<sub>4</sub> phase starts disappearing, and Fe<sub>7</sub>Se<sub>8</sub> becomes the primary phase. Before being turned into a gel, it reaches a temperature of 340 °C. The sequence observed by removing the accelerating agent is again the same as above FeSe<sub>2</sub> → Fe<sub>3</sub>Se<sub>4</sub> → Fe<sub>7</sub>Se<sub>8</sub>.

**Table 1.** Results of XRD patterns from the specimens collected at various reaction temperatures were carried out by changing the solvents. Here, OLA was used in reaction A and OLA + 1-ODE in reaction B with a temperature range of 30 °C - 340 °C. In reaction B, complete phase transformation was observed below 300 °C.

Reaction	Fe precursor	Se precursor	Solvent	Temperature-range (°C)	Phase	Remark
A	Fe(acac) <sub>3</sub>	Se powder	OLA	30 – 100	Se	
				110 – 130	Se + FeSe <sub>2</sub>	
				140 – 220	FeSe <sub>2</sub>	
				230 – 240	FeSe <sub>2</sub> + Fe <sub>3</sub> Se <sub>4</sub>	
				250 – 270	Fe <sub>3</sub> Se <sub>4</sub>	
				280 – 340	Fe <sub>7</sub> Se <sub>8</sub>	
B	Fe(acac) <sub>3</sub>	Se powder	OLA + 1-ODE	30 – 100	Se	Se powder was pre – dissolved in 1-ODE at 30 °C for 6 h
				110 – 230	FeSe <sub>2</sub>	
				240 – 250	FeSe <sub>2</sub> + Fe <sub>3</sub> Se <sub>4</sub>	
				260	Fe <sub>3</sub> Se <sub>4</sub> + FeSe <sub>2</sub>	
				270	Fe <sub>7</sub> Se <sub>8</sub>	
				280 – 300	FeSe	

To further study the effect of solvents, an additional step was added in the reaction mentioned in the earlier section—the Se powder was pre-dissolved in 1-ODE with constant stirring at 30 °C and used as the Se precursor, which resulted in accelerating the reaction due to easier availability of selenium (Table 1 B, Figure 4). Upon heating from 30 °C to 100 °C, only the diffraction peaks of Se were observed in WAXS. From 110 °C, the diffraction peaks of FeSe<sub>2</sub> start appearing, and the peak intensity increases when the temperature is raised to 140 °C. Single phase FeSe<sub>2</sub> was observed up to 230 °C. With the further rise in temperature, the peak intensity of the FeSe<sub>2</sub> phase decreases, and the Fe<sub>3</sub>Se<sub>4</sub> phase increases and gradually become the primary phase.

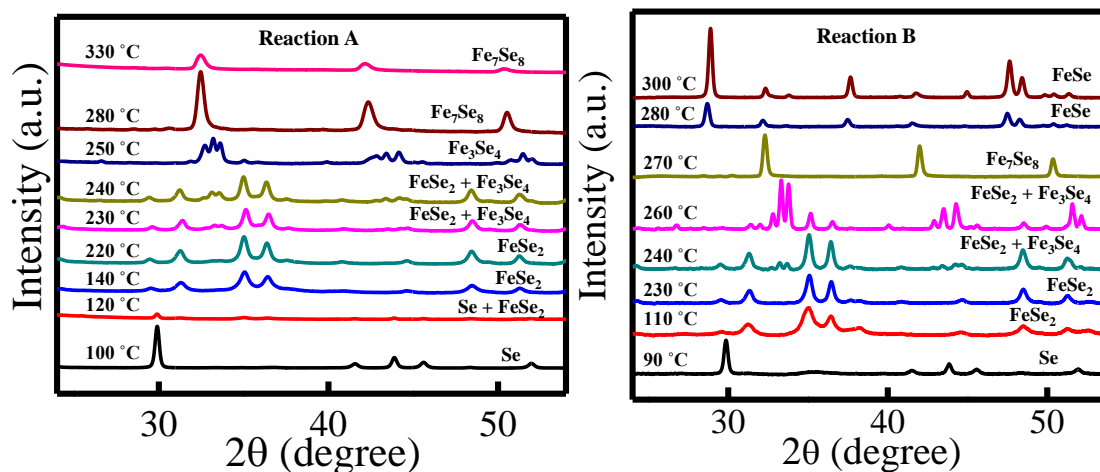


**Figure 4.** Results of diffraction patterns of reaction 1 to 5 samples collected at various temperatures. Complete phase evolution of the Fe-Se system was observed under 300 °C.

The conversion reaches a maximum of around 260 °C. Further, with a slight increase in temperature (~270 °C), the WAXS pattern showed the formation of a single phase  $\text{Fe}_7\text{Se}_8$ , and with another 10 °C rises (~280 °C),  $\text{Fe}_7\text{Se}_8$  transformed into a new phase—FeSe with an increase in the FeSe peak intensity up to 300 °C. Beyond 300 °C, no reaction was possible due to gel formation.

Thus, this study concludes the following sequence of Fe-Se phase formation (between 110 °C - 300 °C):  $\text{FeSe}_2$  (orthorhombic marcasite)  $\rightarrow$   $\text{Fe}_3\text{Se}_4$  (monoclinic NiAs)  $\rightarrow$   $\text{Fe}_7\text{Se}_8$  (hexagonal NiAs)  $\rightarrow$  FeSe (tetragonal PbO structure). It was also found that among all of the experiments mentioned above, one with pre-dissolved Se powder in 1-ODE is critical due to the formation of a complete Fe-Se family of nanoparticles below 300 °C—the highest temperature phase FeSe was obtained when Se powder was pre-dissolved in 1-ODE while it was absent in the earlier cases. We infer that pre-dissolving Se in the accelerating agent (1-ODE) accelerates the reaction rate and finally helps in the formation of FeSe, which was not formed even at a much higher temperature with other solvent conditions. Using the solid-state method, the Fe-Se phase transformation occurred between 300 °C - 370 °C. However, in this study, phase transformation temperature was reduced to 110 °C - 300 °C: all the phases formed below 300 °C. Thus, using solution chemistry, the phase transformation temperature range of the Fe-Se system was reduced to a significantly lower temperature value.



### 3.4.2 Optimization of synthesis conditions for single phase formation

By analyzing the effects of variations in reaction parameters on the phase transformation, the minimum possible temperature was optimized for the formation of each Fe-Se phase. Table 2 summarizes the outcomes of these variations. This clearly reveals that the lowest possible temperature required for the pure FeSe<sub>2</sub> phase is 150 °C, below which there were always Se impurities. For the other three subsequent phases, the minimum required temperature was above the Se melting point ( $T_{\text{melt}} = 221$  °C). Above 221 °C, the cleavage of the Se-Se dimer pair results in FeSe<sub>2</sub> instability. For synthesizing single phase Fe<sub>3</sub>Se<sub>4</sub>, the minimum possible temperature required was found to be 260 °C, below which there was always an impurity of the FeSe<sub>2</sub> phase. Prolonging the synthesis at 260 °C could form Fe<sub>7</sub>Se<sub>8</sub>. However, there were chances of getting some impurities. The pure phase of Fe<sub>7</sub>Se<sub>8</sub> was obtained only at 280 °C. It is essential to observe that the formation of both Fe<sub>3</sub>Se<sub>4</sub> and Fe<sub>7</sub>Se<sub>8</sub> phases also depends upon the reaction temperature ramped up. In order to synthesize the highest temperature phase FeSe, it required a much longer duration at that temperature where Fe<sub>7</sub>Se<sub>8</sub> was formed; still, there were a tiny amount of impurities.

As mentioned in the earlier section, an accelerating agent is required for synthesizing the FeSe phase, which accelerates the reaction. Resulting in forming the above three phases faster and at last, the FeSe phase also. However, after merely adding an accelerating agent during the synthesis of FeSe, it was observed that Fe<sub>7</sub>Se<sub>8</sub> was always present as an impurity phase along with FeSe. To overcome this phase impurity problem, pre-dissolved Se powder in 1-ODE was added with Fe(acac)<sub>3</sub> and OLA at constant stirring, resulting in a single-phase formation of FeSe. Therefore, it was possible to synthesize the single phase FeSe by keeping the reaction conditions similar to the one that was optimized for the formation of Fe<sub>7</sub>Se<sub>8</sub>, except for adding an accelerating agent. An alternative route for synthesizing FeSe was also recognized. In this method, the reaction conditions were kept similar to the synthesis of Fe<sub>7</sub>Se<sub>8</sub> up to 300 °C, but the reaction time was prolonged till 7 h. However, the drawback of this route is that a longer hold-time at 300 °C resulted in gel formation, decreasing the amount of product. Whether increase the amount of OLA and/or 1-ODE, the phases were the same as before for that particular temperature with pertinent time. Thus, this study gave us the information about minimal temperature required for synthesizing individual phases of the Fe-Se system.

**Table 2.** The data shows the optimized conditions needed to synthesize the individual phase. The reaction conditions were determined by detailed phase identification studies using XRD on various specimens collected from the reactions at varying conditions, as mentioned in the table.

Phases	Solvent	Ramping Rate	Temp. (°C)	Time (h)	Remarks
FeSe <sub>2</sub>	OLA	2 °C min <sup>-1</sup>	150	2	Single phase FeSe <sub>2</sub> NPs.
Fe <sub>3</sub> Se <sub>4</sub>	OLA	2 °C min <sup>-1</sup>	230	8	Fe <sub>3</sub> Se <sub>4</sub> + FeSe <sub>2</sub> (impurity phase).
		2 °C min <sup>-1</sup>	240	6	
		2 °C min <sup>-1</sup>	250	5	
		120 °C - 0.5 h + 2 °C min <sup>-1</sup> → 200 °C + 2 °C min <sup>-1</sup> → 250 °C	250	4	Fe <sub>3</sub> Se <sub>4</sub> + FeSe <sub>2</sub> (impurity phase).
		2 °C min <sup>-1</sup>	260	5	
		120 °C - 0.5 h + 2 °C min <sup>-1</sup> → 200 °C + 2 °C min <sup>-1</sup> → 250 °C	260	2	Single phase Fe <sub>3</sub> Se <sub>4</sub> NPs.
Fe <sub>7</sub> Se <sub>8</sub>	OLA	2 °C min <sup>-1</sup>	270	4	Fe <sub>3</sub> Se <sub>4</sub> + FeSe <sub>2</sub> (impurity phase).
		5 °C min <sup>-1</sup> → 230 °C + 2 °C min <sup>-1</sup> → 270 °C	270	4	Fe <sub>7</sub> Se <sub>8</sub> + Fe <sub>3</sub> Se <sub>4</sub> (impurity phase).
		2 °C min <sup>-1</sup>	280	4, 5	
		5 °C min <sup>-1</sup> → 230 °C + 2 °C min <sup>-1</sup> → 280 °C	280	4	Single phase Fe <sub>7</sub> Se <sub>8</sub> NPs.
FeSe	OLA	5 °C min <sup>-1</sup> → 230 °C + 2 °C min <sup>-1</sup> → 280 °C	280	4	Fe <sub>7</sub> Se <sub>8</sub> .
	OLA + 1-ODE	5 °C min <sup>-1</sup> → 230 °C + 2 °C min <sup>-1</sup> → 280 °C	280	4	FeSe + Fe <sub>7</sub> Se <sub>8</sub> (impurity phase).
	OLA + 1-ODE	5 °C min <sup>-1</sup> → 230 °C + 2 °C min <sup>-1</sup> → 280 °C	280	4	Single phase FeSe NPs. (Se powder was pre-dissolved in 1-ODE)
	OLA	5 °C min <sup>-1</sup> → 230 °C + 2 °C min <sup>-1</sup> → 280 °C	300	7	Single phase FeSe NPs.

### 3.4.3 Role of OLA

OLA is a primary alkylamine with a long-chain ( $C_{18}$ ) having an alkene function at the  $C_9$ - $C_{10}$  junction with a boiling point of nearly  $350\text{ }^\circ\text{C}$ . It has been demonstrated to function as an electron donor at elevated temperatures<sup>43</sup>. In order to examine the role of various OLA functions (amine function and double bond) in the above reactions, several experiments have been done using amines, alkenes, and alkanes<sup>44</sup>.

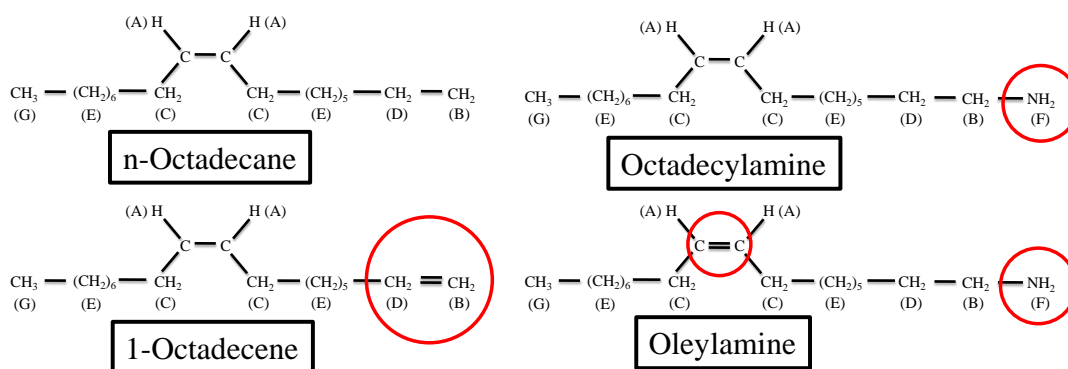


**Figure 5.** Molecular structure of all 4 organic solvents —n-Octadecane [n-ODE (alkane)], 1-Octadecene [1-ODE (alkene)], Octadecylamine [OCD (amine)], and Oleylamine [OLA (amine and alkene)].

These experiments were carried out with 1-ODE (alkene), OCD (amine), and n-ODE (alkane) as organic solvents instead of OLA (Figure 5), keeping other parameters unchanged. Table 3 shows the phase identification data from the XRD measurements of all the products at  $150\text{ }^\circ\text{C}$  and  $260\text{ }^\circ\text{C}$ . At  $150\text{ }^\circ\text{C}$ , the XRD pattern shows only Se peaks in the absence of the amine group, whether we have a double bond or not (1-ODE and n-ODE). Whereas, in the presence of an amine group (with OCD and OLA), the diffraction pattern shows the formation of single phase  $FeSe_2$ . Thus, at low temperatures, the role of the amine group is vital to reduce the Se and Fe precursor, and as the temperature increases, the role of thermal energy takes center stage in phase-formation. At  $260\text{ }^\circ\text{C}$ , with n-ODE—having neither double bond nor amine group— $FeSe_2$  phase was formed, while in the presence of double bond (1-ODE),  $Fe_3Se_4$  phase starts appearing along with  $FeSe_2$ . The synthesis carried out at  $260\text{ }^\circ\text{C}$  with OCD (having only the amine group) shows the presence of both the phases in equal amounts, i.e.,  $Fe_3Se_4$  and  $FeSe_2$ . Finally, with OLA, single phase  $Fe_3Se_4$  has been observed.

**Table 3.** Results of studies for the reaction carried out by changing the solvents (amine, alkene, and alkane groups) at various temperatures. The phase identification was made by XRD analysis.

S. No.	Solvent	Product
Below 220 °C		
1	n-Octadecane	Se
2	1-Octadecene	Se
3	Octadecylamine	FeSe <sub>2</sub>
4	Oleylamine	FeSe <sub>2</sub>
Above 220 °C		
5	n-Octadecane	FeSe <sub>2</sub>
6	1-Octadecene	FeSe <sub>2</sub> + Fe <sub>3</sub> Se <sub>4</sub> (impurity phase)
7	Octadecylamine	FeSe <sub>2</sub> + Fe <sub>3</sub> Se <sub>4</sub>
8	Oleylamine	Fe <sub>3</sub> Se <sub>4</sub>

Based on these results, it is appropriate to conclude that the amine group is a strong reducing agent while the double bond is a mild reducing agent. Although FeSe<sub>2</sub> was also formed with n-ODE (at 260 °C), where both amine group and double bond are absent which signifies that both the precursors can be reduced by thermal energy as well. The fact that as the temperature increases, the Fe(acac)<sub>3</sub> starts reducing into Fe(acac)<sub>2</sub> by thermal energy, and it reaches a maximum between 150 °C - 235 °C. This is supported well by the TGA (Figure 6), which shows that the decomposition starts from RT and becomes significant at nearly 150 °C.

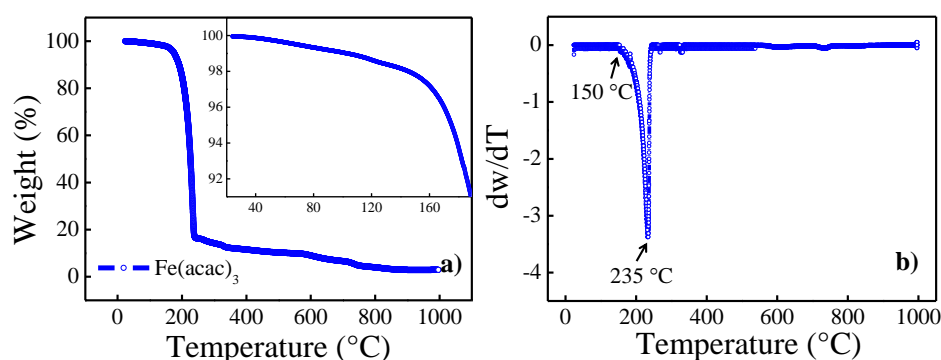


**Figure 6.** TGA (Thermogravimetry analysis) was carried out in an N<sub>2</sub> atmosphere for Fe(acac)<sub>3</sub> to determine the decomposition behavior. (a) The decomposition of acetylacetonate groups starts slowly at room temperature (30 °C), becomes significant nearby 150 °C in the form of

acetone and CO<sub>2</sub>, and goes maximum at 235 °C. (b) the first-order differentiation of weight loss with respect to temperature.

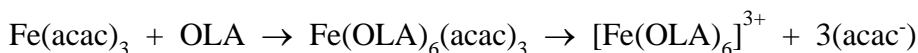
Above 221 °C, due to the increased thermal energy, the Se atoms also start reducing and result in fabricating the FeSe<sub>2</sub> at 260 °C. Altogether, the amine group, double bond, and thermal energy play an essential role in reducing the Fe and Se precursors and forming the Fe-Se compounds. As both n-ODE and 1-ODE are not appropriate solvents for reducing the Se and Fe precursors; thus, they are not favorable to the synthesis Fe-Se system. In OCD, the product yield was significantly less due to gel formation at RT (~35 °C), as the melting point of OCD is 50 °C. Thus, it is hard to remove the product from the solvent. Accordingly, OLA is the most suitable solvent for synthesizing the Fe-Se system in these conditions.

### 3.4.4 Formation mechanism

As discussed in earlier sections, temperature-dependent experiments were performed to understand the formation process of Fe-Se system comprises an initial nucleating stage followed by subsequent crystal growth process. Accordingly, based on the above analysis, the possible formation mechanism of the Fe-Se system starts from making the complexes followed by reducing the Fe and Se ions, and finally, phase formation is highlighted in scheme 1.

1.  $\text{Fe}(\text{acac})_3 \rightarrow \text{Fe}(\text{acac})_2 + \text{acetone} + \text{CO}_2$
2.  $\text{Fe}(\text{acac})_2 + \text{OLA} \rightarrow \text{Fe}(\text{OLA})_4(\text{acac})_2 \rightarrow [\text{Fe}(\text{OLA})_4]^{2+} + 2(\text{acac}^-)$
3.  $\text{Se}_n + \text{OLA} \rightarrow \text{Se-OLA complex (source of Se}_2^{2-} \text{ ions)} \rightarrow \text{Se}_2^{2-}$
4.  $\text{Fe}^{2+} + \text{Se}_2^{2-} \rightarrow \text{FeSe}_2 [\text{Fe}^{2+}\text{Se}_2^{2-}]$
5.  $\text{FeSe}_2 + 2\text{Fe}^{3+*} + 2\text{Se}^{2-} \rightarrow \text{Fe}_3\text{Se}_4 [(\text{Fe}^{3+})_2(\text{Fe}^{2+})_1(\text{Se}^{2-})_4]$  ( $T \geq 221$  °C)
6.  $\text{Fe}_3\text{Se}_4 + 4\text{Fe}^{2+} + 4\text{Se}^{2-} \rightarrow \text{Fe}_7\text{Se}_8 [(\text{Fe}^{3+})_2(\text{Fe}^{2+})_5(\text{Se}^{2-})_8]$
7.  $\text{Fe}_7\text{Se}_8 + \text{Fe}^{2+} \rightarrow 8\text{FeSe} [\text{Fe}^{2+}\text{Se}^{2-}]$

\*Unreduced Fe-precursor:



#### Scheme 1. Proposed formation mechanism of Fe-Se system.

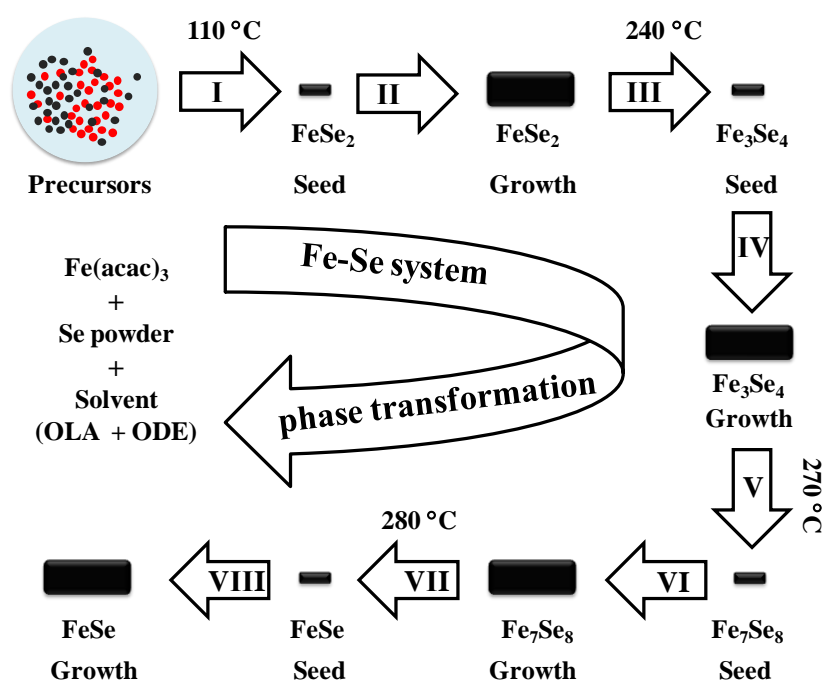
Initially, as the temperature increases, Fe(acac)<sub>3</sub> starts reducing into Fe(acac)<sub>2</sub> due to the thermal energy with the release of acetone and CO<sub>2</sub><sup>45</sup>, followed by the dissolution of Fe(acac)<sub>2</sub> into 4 OLA resulting in Fe-OLA complex as [Fe(OLA)<sub>4</sub>]<sup>2+</sup>. Here, the amine group

of OLA was attacking the acetylacetonate group of  $\text{Fe}(\text{acac})_2$ , leading to the coordination of amines with  $\text{Fe}^{2+}$ , and spontaneously replacing the  $\text{acac}^-$  ligands. Thus, the Fe-OLA complex behaves as the source of  $\text{Fe}^{2+}$  ions. Moreover, in all of the prolonged reactions, the presence of unreduced Se atoms was up to 100 °C - 140 °C, which appraises us that the Se precursor starts reacting above this temperature range. At elevated temperatures, OLA functioned as an electron donor for Se powder, reducing the Se atoms. Se starts reacting with OLA by homolytic cleavage of the Se-Se bond leading to a radical process as discussed by Bo Hou et al<sup>41</sup>. These thermally induced Se radicals attack the allylic proton of OLA, resulting in migration of the double bond, and the required hydrogen was transferred by the Se intermediate species. Thus, the Se-OLA complex acted as the source of  $\text{Se}_2^{2-}$  ions by reducing the Se atoms with the release of hydrogen from the complex. Apart from the double bond, OLA also has an amine group capable of reacting with Se atoms and furthermore reduces them<sup>41</sup>.

Afterward,  $\text{Fe}^{2+}$  gyrates around  $\text{Se}_2^{2-}$  to pursue an equilibrium state, which results in the formation of marcasite  $\text{FeSe}_2$  having an orthorhombic layer structure. It indicates that  $\text{FeSe}_2$  is directly formed by synthesizing the iron and selenium ions instead of firstly forming the iron-selenium-organic compound and then decomposes to form  $\text{FeSe}_2$ . The analysis of WAXS data (Figure 2 and Table 1) shows that a single phase  $\text{FeSe}_2$  is stable up to nearby 221 °C (melting point of Se). After this temperature, there was cleavage of the dimer pair of Se-Se atoms in  $\text{FeSe}_2$ , resulting in instability of the  $\text{FeSe}_2$  phase. Consequently, the cation and anion start transforming into the next stable state. The OLA reduces  $\text{Se}_2^{2-}$  ions of  $\text{FeSe}_2$  into  $\text{Se}^{2-}$  ions and simultaneously, the unreduced iron precursor  $\text{Fe}(\text{acac})_3$  react with 6 OLA resulting in the formation of  $[\text{Fe}(\text{OLA})_6]^{3+}$  (source of  $\text{Fe}^{3+}$ ) and transfer in the crystals which revolve around Se and Fe atom of  $\text{FeSe}_2$  to seek an equilibrium state. The arrangement of atoms results in an approach to the structure of  $\text{Fe}_3\text{Se}_4$  having NiAs type monoclinic structure, as shown in scheme 1. As the temperature increases, the amount of reduced Fe atoms ( $\text{Fe}^{2+}$ ) also increases. In order to seek an equilibrium state, they start reacting with atoms of the  $\text{Fe}_3\text{Se}_4$  unit cell. The four reduced iron ( $\text{Fe}^{2+}$ ) atoms along with four reduced selenides ( $\text{Se}^{2-}$ ) react with atoms of one unit cell of  $\text{Fe}_3\text{Se}_4$  to fabricate the new unit cell, as shown in scheme 1. Eventually, the arrangements of atoms result in a new NiAs type hexagonal  $\text{Fe}_7\text{Se}_8$  structure to endeavor an equilibrium state.

In FeSe syntheses, by pre-dissolving the Se in 1-ODE, all the initial three phases were formed swiftly. Thereafter, if the reaction was further carried out for more time at elevated temperature, all the iron atoms were reduced to  $\text{Fe}^{2+}$  state, and all the Se atoms were reduced

to  $\text{Se}^{2-}$  state. Eventually, that results in the transformation of the  $\text{Fe}_7\text{Se}_8$  phase to the  $\text{FeSe}$  tetragonal phase having all the Fe atoms in the  $\text{Fe}^{2+}$  state and Se atoms in  $\text{Se}^{2-}$  state, as shown in scheme 1. It illustrated that the phases of the Fe-Se system were mainly dependent on the reaction temperature and the ability of the Fe precursor to react with Se atoms using the organic solvents as a medium. As the temperature increases, nucleation-growth rates also increase along with OLA decomposition rate in the sample. However, the acceleration rate was increased to multiple times with 1-ODE resulting in speeding up the formation process. The solvent-precursor interaction would influence the phase of the final product. Thus, in the present formation process, the reactivity of Fe and Se governs the nucleation process while reaction temperature governs the growth process. Scheme 2 shows the schematic diagram of the growth process in the Fe-Se system.



**Scheme 2.** The proposed growth mechanism for the various phase of the Fe-Se system.

### 3.4.5 Material characterization— X-ray diffraction

As-synthesized Fe-Se phases were investigated in detail for their crystallinity and phase purity using powder-XRD, followed by the Reitveld refinement using FullProf software (Figure 7). Figure 7 illustrate the powder-XRD patterns of synthesized  $\text{FeSe}_2$ ,  $\text{Fe}_3\text{Se}_4$ ,  $\text{Fe}_7\text{Se}_8$ , and  $\beta\text{-FeSe}$  phases, which agree with their respective ICDD data card 96-901-2552, 96-152-7087, 96-901-5077, and 96-432-9646, respectively. The lack of any additional peak in all diffraction patterns implies that none of the samples have a secondary phase.

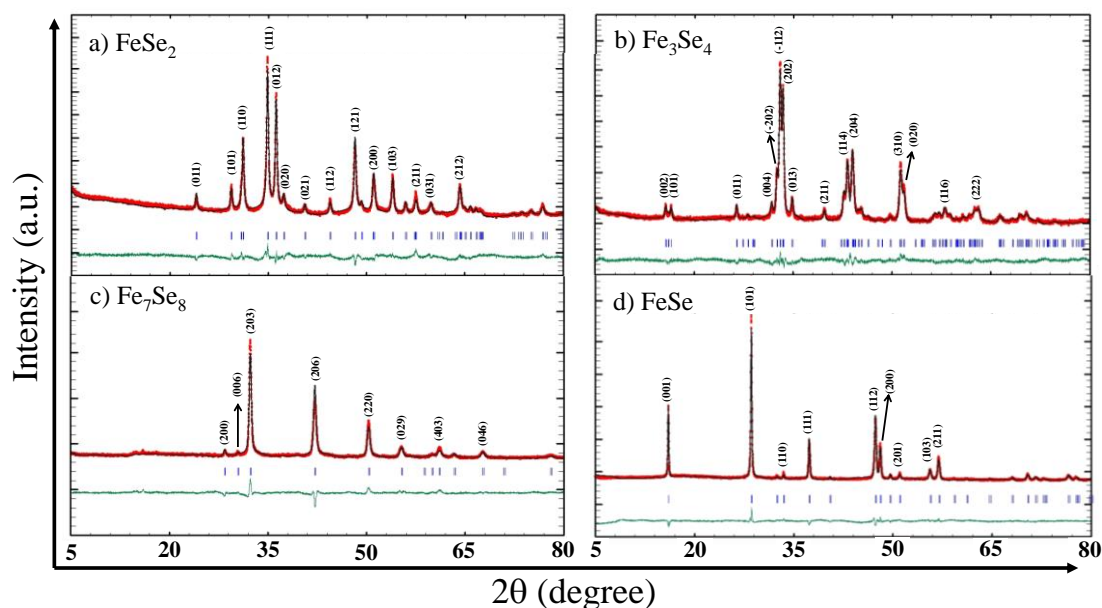


**Figure 7.** XRD pattern of a)  $\text{FeSe}_2$  b)  $\text{Fe}_3\text{Se}_4$  c)  $\text{Fe}_7\text{Se}_8$  and d)  $\text{FeSe}$  (red line), calculated XRD curve after crystal structure refinement by Rietveld method (black line),  $I_{\text{obs}} - I_{\text{cal}}$ , difference curve (green line) and Bragg position (blue vertical line) are displayed.

$\text{FeSe}_2$  have the orthorhombic crystal structure (space group (SG):  $\text{Pnmm}$ ) with calculated lattice parameters of  $a = 4.8 \text{ \AA}$ ,  $b = 5.8 \text{ \AA}$ , and  $c = 3.6 \text{ \AA}$ ,  $\alpha = \beta = \gamma = 90^\circ$ .  $\text{Fe}_3\text{Se}_4$  is in the monoclinic crystal structure (SG:  $\text{I2/m}$ ) with determined lattice parameters of  $a = 6.2 \text{ \AA}$ ,  $b = 3.5 \text{ \AA}$ , and  $c = 11.3 \text{ \AA}$ ,  $\alpha = \gamma = 90^\circ$ ,  $\beta = 91.8^\circ$ .  $\text{Fe}_7\text{Se}_8$  is in the hexagonal crystal structure (SG:  $\text{P3}_121$ ) with determined lattice parameters of  $a = 7.2 \text{ \AA}$  and  $c = 17.6 \text{ \AA}$ ,  $\alpha = \beta = 90^\circ$ ,  $\gamma = 120^\circ$ .  $\text{FeSe}$  is in the tetragonal crystal structure (SG:  $\text{P4/nmm}$ ) with calculated lattice parameters of  $a = b = 3.8 \text{ \AA}$ , and  $c = 5.5 \text{ \AA}$ ,  $\alpha = \beta = \gamma = 90^\circ$ . The refinement details are mentioned in the supporting text adjoining Table 4.

**Table 4.** Rietveld refinement data of the as-synthesized nanoparticles  $\text{FeSe}_2$ ,  $\text{Fe}_3\text{Se}_4$ ,  $\text{Fe}_7\text{Se}_8$ , and  $\text{FeSe}$ .  $\chi^2$  and  $wR_p$  (%) represented the chi-square and weighted profile R values. Unit cell parameters are denoted by  $a, b, c$ ,  $\alpha$ ,  $\beta$ , and  $\gamma$ .

	$\text{FeSe}_2$	$\text{Fe}_3\text{Se}_4$	$\text{Fe}_7\text{Se}_8$	$\text{FeSe}$
$\chi^2$	4.8	3.9	6.7	8.6
$wR_p$ (%)	10	11.9	8.6	9.8
Space group	$\text{Pnmm}$	$\text{I2/m}$	$\text{P3}_121$	$\text{P4/nmm}$
Structure	orthorhombic	Monoclinic	hexagonal	Tetragonal
$a$ ( $\text{\AA}$ )	4.8	6.2	7.2	3.8
$b$ ( $\text{\AA}$ )	5.8	3.5	7.2	3.8
$c$ ( $\text{\AA}$ )	3.6	11.3	17.6	5.5
$\alpha$	90	90	90	90
$\beta$	90	91.8	90	90
$\gamma$	90	90	120	90



### 3.4.6 Material characterization— electron microscopy imaging and diffraction study

The size, shape, and structure of all the phases (synthesized using single-phase formation conditions) were identified by FESEM and TEM. As exhibits in Figures 8 and 9, all have a quasi-spherical form with a cactus-like appearance, with many spikes growing on the surfaces facing outward.

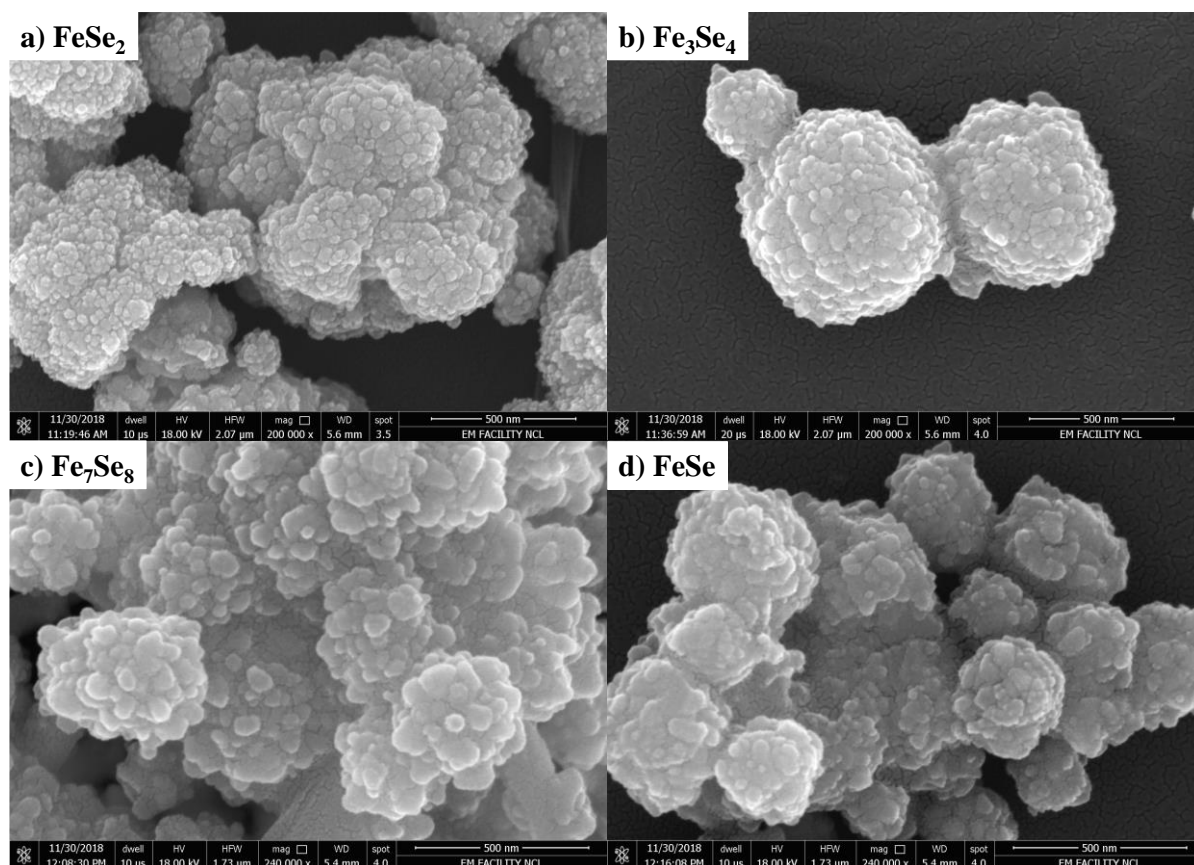


**Figure 8.** Typical FESEM images of as-synthesized a) FeSe<sub>2</sub>, b) Fe<sub>3</sub>Se<sub>4</sub>, c) Fe<sub>7</sub>Se<sub>8</sub> and d) FeSe NPs. Scale bars are 500 nm.

The TEM images (inset of Figures 9 a-d) show the precise shape of the Fe-Se nanocacti, which appear to be agglomerated as rod-shaped nanostructures. Figures 9a-d show a zoomed-in view of the single nanorod, which represents the building block of the corresponding particle shown in the inset, and Figures 9 a'-d' show lattice fringes of all the phases. The lattice fringes spacing was approximately 2.5 Å, 2.7 Å, 5.4 Å, and 5.5 Å, which corresponds to (111), (-202), (101), and (001) planes of FeSe<sub>2</sub>, Fe<sub>3</sub>Se<sub>4</sub>, Fe<sub>7</sub>Se<sub>8</sub>, and FeSe phases, respectively. The SAED pattern reveals in the inset of Figures 9 a'-d' revealed the single-crystalline nature of all the Fe-Se NPs.

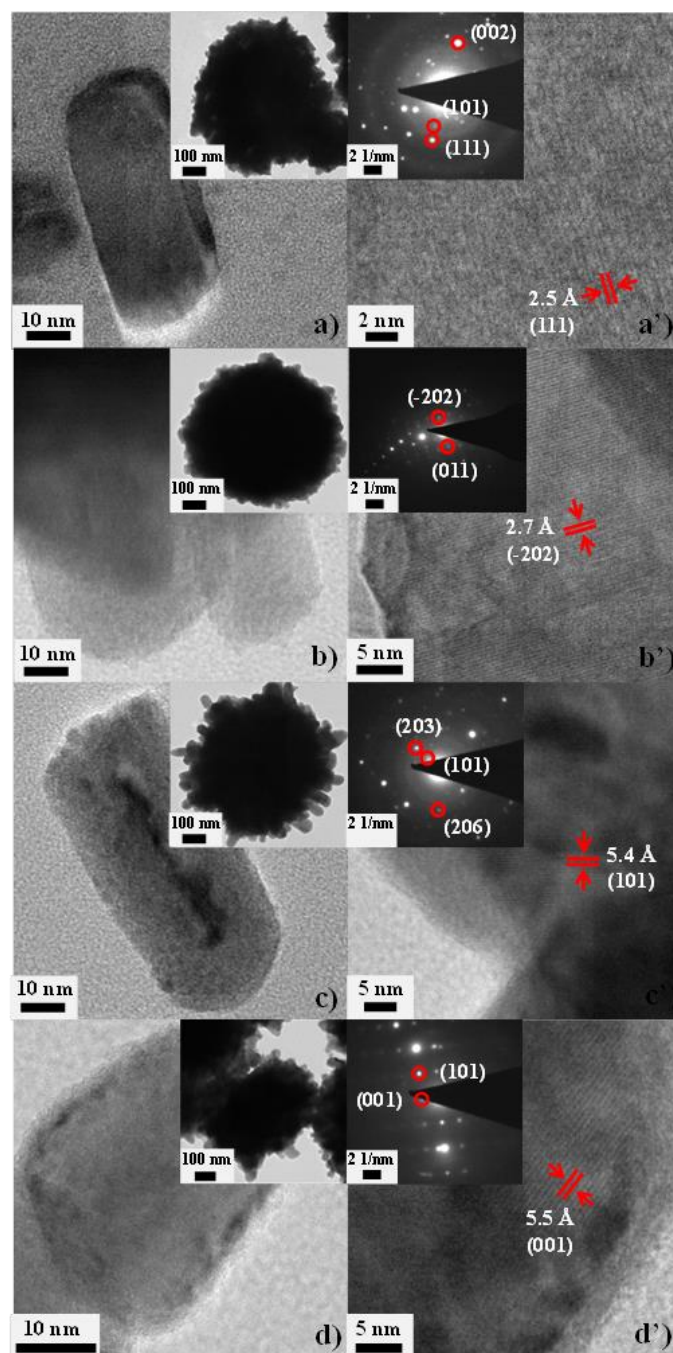


**Figure 9.** Typical TEM images of as-synthesized a)  $\text{FeSe}_2$ , b)  $\text{Fe}_3\text{Se}_4$ , c)  $\text{Fe}_7\text{Se}_8$ , and d)  $\text{FeSe}$  NPs (in the presence of OLA) show the rod-like features, and the inset shows the iron selenide nanocacti with rod-like features growing on the surface. The scale bar in the insets is 100 nm. a') to d') shows the lattice fringes space at 2.5 Å, 2.7 Å, 5.4 Å, and 5.5 Å represents the (111), (-202), (101), and (001) of Fe-Se system respectively. The inset shows the SAED pattern.

The diffraction pattern obtained for all the nanostructures were matched well with the crystal planes of the Fe-Se system and have been assigned to (002), (101), (111) planes for  $\text{FeSe}_2$ , (-

202), (011) planes for  $\text{Fe}_3\text{Se}_4$ , (203), (101), (206) planes for  $\text{Fe}_7\text{Se}_8$  and (001), (101) planes for  $\text{FeSe}$ . The d-spacings calculated from TEM were in good agreement with those given in the standard ICDD for all the phases of the Fe-Se system. Furthermore, by altering the solvents in the reaction system, the current synthetic approach not only allows for the selective synthesis of isolated phases of iron selenides by manipulating the temperature, but it may also yield novel morphologies. The TEM data revealed the strong dependence of size, shape, and stability on the solvent.

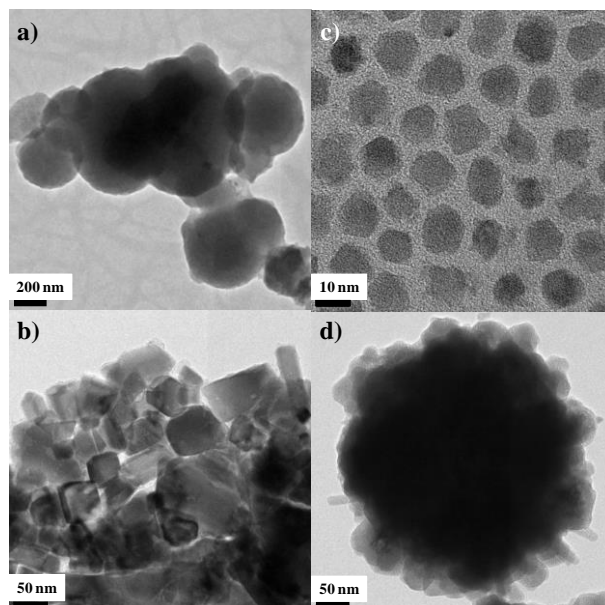


**Figure 10.** Representative TEM images of as-synthesized  $\text{FeSe}_2$  NPs in the presence of a) n-octadecane (n-ODE), b) 1-octadecene (1-ODE), c) octadecylamine (OCD) and d) oleylamine (OLA). It reveals the solvent's strong dependence on size, shape, and stability.

Figure 10 shows the formation of nanosized quasi-spheres (in the presence of n-ODE), nano-platelets (in the presence of 1-ODE), nanosized quasi-spheres (in the presence of OCD), and nanocacti having rod-like characters growing on the surface (in the presence of OLA). It is appropriate to mention that although the individual solvents give a different morphology, however, when 1-ODE was added in OLA (as per Fe-Se system synthesis conditions), there was no change in the morphology. As shown in Figure 11, OLA reveals the same morphology with or without the presence of 1-ODE, which signifies that OLA dominates over the 1-ODE in controlling the morphology.

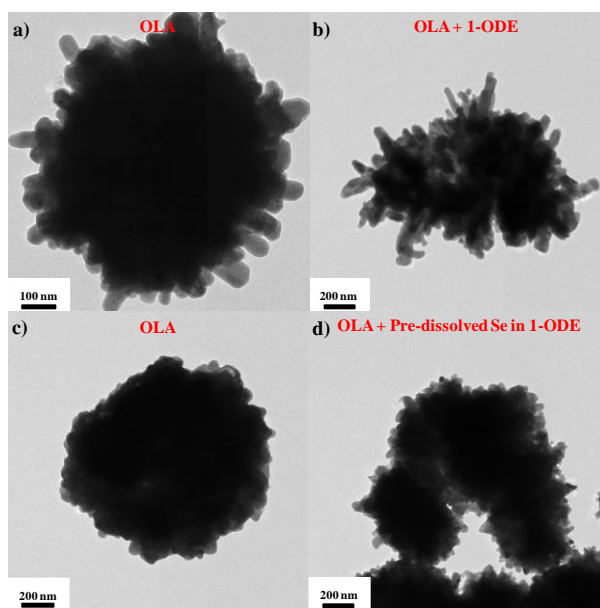


**Figure 11.** Representative TEM images of as-synthesized iron selenide NPs a)  $\text{Fe}_7\text{Se}_8$  in presence of oleylamine (OLA), b)  $\text{Fe}_7\text{Se}_8$  in presence of oleylamine (OLA) + 1-octadecene (1-ODE), c) FeSe in presence of OLA and d) FeSe in presence of OLA + pre-dissolved Se powder in 1-ODE. It reveals the dominant nature of OLA over 1-ODE, as presence of 1-ODE does not affect the morphology of NPs.

### 3.4.7 Predicted crystal habit versus experimental morphology of Fe-Se system

In the second chapter of the thesis, the morphologically important (MI) planes have been examined for the Fe-Se system using three well-known theories (BFDH, HP, and SE model). The observation shows that a MI facet varies according to the model in each crystal. As BFDH<sup>46-48</sup> is a pure crystallographic theory, the obtained results are pure geometrically important planes in respective phases. Further, the concept of bond energy is included in the theories (HP<sup>49-51</sup> and SE<sup>52</sup> model). Although, both models consider the concept of bond energies in direct or indirect ways. However, the results are distinct because one model predicts the growth morphology (HP approach) while the other is equilibrium morphology (SE approach).

The real-life reactions of materials are much more complicated than the simplified theoretical models due to the involvement of external factors in the reaction. In chapter 2, two types of morphologies have been predicted— growth and equilibrium morphology. Furthermore, the correlation between the predicted and experimental morphologies is of fundamental and application interest. In this chapter, all the phases are synthesized using the

thermal decomposition method, and under the limit of laboratory powdered XRD, all the as-synthesized specimens are single phases. The electron microscopy analysis clearly shows the rod shape of all the synthesized nanoparticles in OLA as an organic solvent.

All the theoretically-predicted morphologies of different Fe-Se crystals are compared with the experimental observations. As discussed above, in OLA, all the phases are in a rod shape.

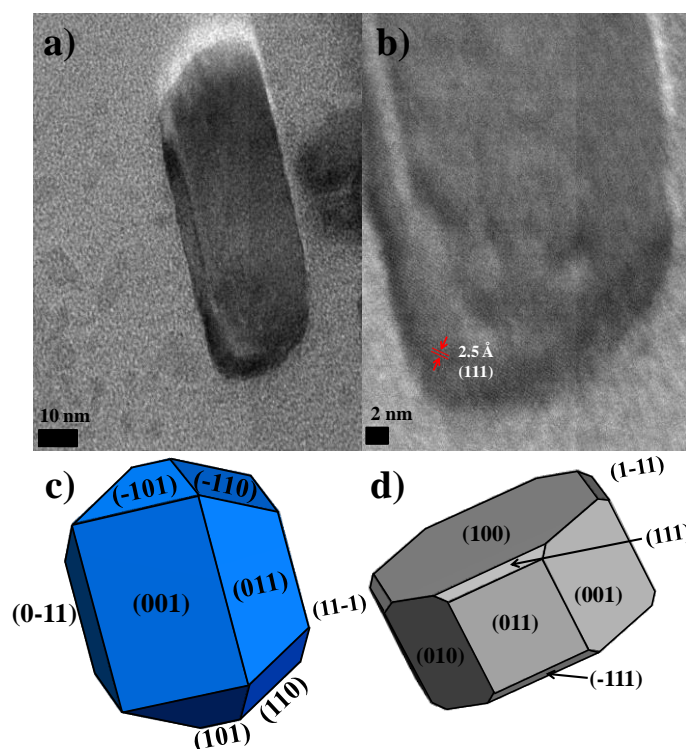


**Figure 12.** Experimental and theoretical morphology of FeSe<sub>2</sub> crystal. a) TEM images of as-synthesized FeSe<sub>2</sub> NPs (in the presence of OLA) show the rod-like features. b) The lattice fringes space at 2.5 Å represents the (111) plane of FeSe<sub>2</sub>. The predicted morphology of FeSe<sub>2</sub> using c) Bravais-Friedel-Donnay-Harker (BFDH) and d) Hartman-Perdok (HP) model shows the indexed morphological drawing with corresponding hkl planes.

For FeSe<sub>2</sub>, the edge plane is (111) having a d-spacing 2.5 Å, as shown in Figure 12b. The experimental morphology is not completely following any approach. This signifies that the kinetic control dominates the reaction due to the lowest temperature phase. However, the HP model's predicted crystal habit is closer to the experimental results than the BFDH approach, as shown in Figure 12. Additionally, the MI of planes is slightly close to SE model also [(100) > (010) ~ (111) ~ (101) > (001) > (011) > (110)]. One of the primary reasons is that the morphology observed in the experimental results is growth morphology, not an equilibrium

shape. Secondly, the bond energy has a critical influence in determining the final crystal morphology. Therefore, both the reason has been fulfilled in the case of the HP model. Thus, in the presence of OLA, the observed morphology primarily matches with the HP model for  $\text{FeSe}_2$ . Furthermore, the SE model also considers the bond energy; however, it provides the equilibrium morphology in pure thermodynamic control. Thus, the experimental morphology where kinetic control is also present will not exactly match the SE predicted MI sequence but will slightly follow the sequence. The NPs are in various shapes as the synthesis environment changes due to external changes that modify the morphology. From quasi-spherical to rods to plate-like morphology, as discussed above.

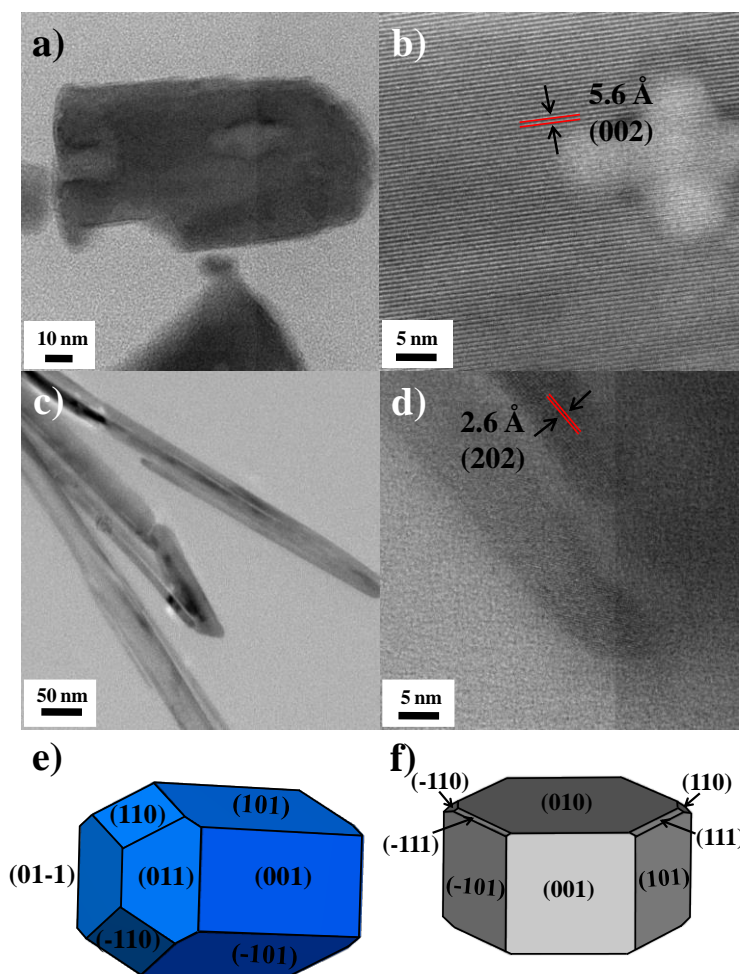


**Figure 13.** Experimental and theoretical morphology of  $\text{Fe}_3\text{Se}_4$  crystal. a) TEM images of as-synthesized  $\text{Fe}_3\text{Se}_4$  NPs (in the presence of OLA) show rod-like features. b) The lattice fringes space at  $5.6 \text{ \AA}$  represents the (002) plane of  $\text{Fe}_3\text{Se}_4$ . c) TEM images of  $\text{Fe}_3\text{Se}_4$  NPs with the rod-like features. d) The lattice fringes space at  $2.6 \text{ \AA}$  represents the (202) plane of  $\text{Fe}_3\text{Se}_4$ . The predicted morphology of  $\text{Fe}_3\text{Se}_4$  using e) Bravais-Friedel-Donnay-Harker (BFDH) and f)

Hartman-Perdok (HP) model shows the indexed morphological drawing with corresponding hkl planes.

For  $\text{Fe}_3\text{Se}_4$ , Figures 13a to 13d show that the longitudinal planes are (202) and (002) of nanorods in the presence of OLA as an organic solvent, as discussed above. It is appropriate to conclude that the (101) and (001) planes are on the longitudinal side of the  $\text{Fe}_3\text{Se}_4$  rods. The crystal habit predicted using the BFDH and HP models is well-matched with the experimental results. Additionally, the MI of planes is also close to SE model [(101) > (001) > (010) > (100) ~ (011) > (110) ~ (111)]. One of the primary reasons is that the morphology observed in the experimental results is growth morphology, not an equilibrium shape. From both the approaches (BFDH and HP model), (001) and (101) planes are on the longitudinal side. Thus, from a crystallographic point of view and bond energies, these planes will be on the longitudinal sides. Therefore, our experimental observations lead to the same results as internal approaches only lead to these results. Furthermore, as discussed above SE model also considers the bond energy minimization and gives the equilibrium morphology in pure thermodynamic control. The experimental morphology where kinetic control is also present will not exactly match with SE predicted MI sequence but moderately follow the sequence in  $\text{Fe}_3\text{Se}_4$  rods. Moreover, depending on the synthesis environment, the morphology can be tuned. For  $\text{Fe}_3\text{Se}_4$ , the shape can be tuned from nanorods to quasi-spherical to nanoplates by modifying the environment, as discussed above.

For FeSe, Figure 14 shows that the (001) plane is on the upper side of the NPs, which matches well with the BFDH model instead of the HP model, where bond energy has been considered. Additionally, the MI of planes is not matches with the SE model [(101) = (011) > (100) = (010) > (110) > (001) ~ (111)]. The prime reason for this finding is that the FeSe is synthesized at a very high temperature as this is the highest temperature phase in the Fe-Se system, which influences the morphology of this compound. As both models predict the distinct morphology, the experimental morphology will only follow one morphological path depending on the provided conditions. The FeSe fabrication has only started at very high thermal energy in our reaction conditions. At minimal energy for a particular crystal, when the reaction has begun, the crystallographic model will dominate the crystal morphology, and later the bond energy theories will also participate prominently as per the reaction environment. Since the larger the area of a crystal's face, the greater the number of intermolecular interactions in that area. Consequently, this results in the increased growth rate in that direction and subsequently

decreased MI and vice versa. Thus, here, the crystallographic approach dominates the bond energy approach.

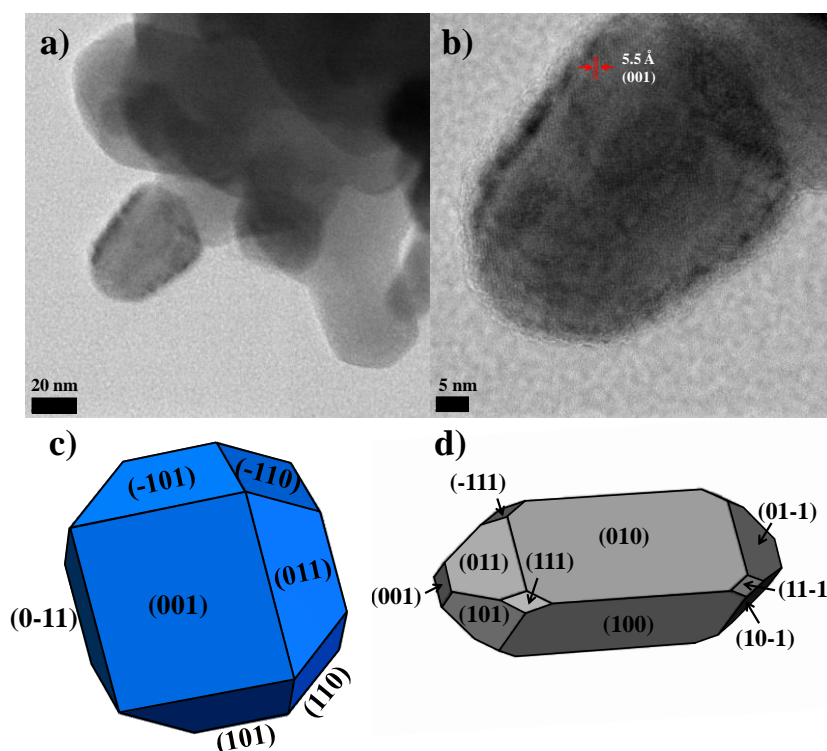


**Figure 14.** Experimental and theoretical morphology of FeSe crystal. a) TEM images of as-synthesized FeSe NPs (in the presence of OLA) show rod-like features. b) The lattice fringes space at 5.5 Å represents the (001) plane of FeSe. The predicted morphology of FeSe using c) Bravais-Friedel-Donnay-Harker (BFDH) and d) Hartman-Perdok (HP) model shows the indexed morphological drawing with corresponding hkl planes.

Among all the theories, the growth morphologies are closed with the experimental results. If both BFDH and HP models predicted the same type of crystal habit (as in the case of  $\text{Fe}_3\text{Se}_4$ ) therefore, the experimental results will be the same as both. However, if the predicted crystal habit is distinct in BFDH and HP models, therefore, depending on the reaction conditions, it can match with any of them. Primarily, the experimental morphology will follow the crystallographic approach; however, due to the influence of external experimental parameters, it can go towards the bond energy approach crystal habit. The equilibrium morphology is pure thermodynamic morphology; therefore, it will not fully match the experimental data as kinetic control is also present in our reactions. All the phases' morphologies can be tunable by giving different environments to grow different facets. Additionally, theoretical findings will help us in understanding the experimental observations.



These approaches can be extended to other TMCs to better understand the morphologies followed by controlling them, leading to tuning the properties.

### 3.4.8 Thermal study

The TGA of Fe-Se phases was carried out under a flowing nitrogen atmosphere to determine the decomposition behavior of as-synthesized NPs by heating the samples from 25 to 1000 °C at 10 °C/ min. Figure 15 shows that all the samples underwent different mass-loss behavior. The FeSe<sub>2</sub> NPs go through a four-step mass-loss while the other three phases go through only a two-step mass-loss. For each sample, the first step (<460 °C) was quite similar, which could be related to the loss of organic fragments (evaporation of capped OLA/1-ODE) accompanied by mass-loss of 3.9%, 2.3%, 2.5%, and 1.3% for FeSe<sub>2</sub>, Fe<sub>3</sub>Se<sub>4</sub>, Fe<sub>7</sub>Se<sub>8</sub>, and FeSe, respectively. In FeSe<sub>2</sub>, the second step was assigned to the decomposition of FeSe<sub>2</sub> to Fe<sub>1-x</sub>Se ~500 °C - 555 °C (mass-loss ~11.8%). The third step was assigned to the decomposition of Fe<sub>1-x</sub>Se to FeSe ~750 °C (mass-loss ~19.3%). In the final step, the decomposition of FeSe started ~875 °C (mass-loss ~29.8%) and remained up to ~1000 °C (mass-loss~ 39.5%). In the other three compounds, the second and final steps were assigned to the decomposition of corresponding compounds (Fe<sub>3</sub>Se<sub>4</sub>, Fe<sub>7</sub>Se<sub>8</sub>, and FeSe) — started at ~725 °C, 770 °C, and 875 °C (mass loss ~ 4%, 3.4%, and 4.4%), and gradually decreases up to 1000 °C (perceived mass loss: ~20%, 9%, and 18.8%) respectively.

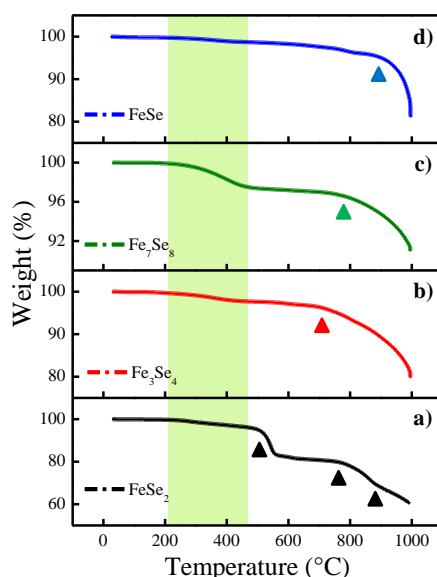


**Figure 15.** TGA plots of a) FeSe<sub>2</sub> (black curve), b) Fe<sub>3</sub>Se<sub>4</sub> (red curve), c) Fe<sub>7</sub>Se<sub>8</sub> (green curve), and d) FeSe (blue curve). The shaded region shows the loss of organic fragments, and the triangle reveals the decomposition point in corresponding compounds.

### 3.4.9 X-ray photoemission spectroscopy analysis

To further investigate the oxidation states of Fe and Se in Fe-Se phases, XPS was used, which is a highly surface-sensitive technique. The surface composition of Fe and Se was evaluated by performing multi-peak fitting analyses on XPS spectra, as shown in Figures 16, and 17. It has been observed that materials easily undergo surface oxidation as soon as they are exposed to air<sup>53</sup>.

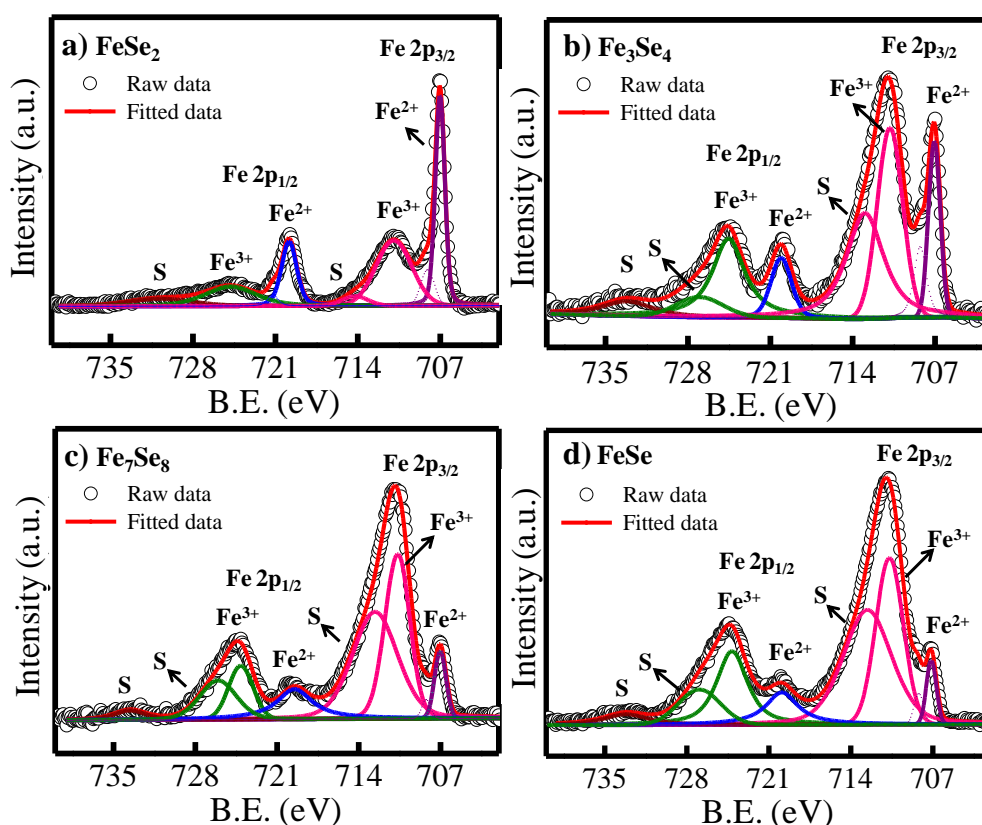


**Figure 16.** XPS spectra of as-synthesized a) FeSe<sub>2</sub>, b) Fe<sub>3</sub>Se<sub>4</sub>, c) Fe<sub>7</sub>Se<sub>8</sub>, and d) FeSe nanoparticles. The red lines show a deconvoluted curve fits.

Figure 16 shows peaks from Fe 2p core-level spectra, illustrating the occurrence of several peaks at differing binding energies (BE). The peaks situated at ~707 eV and ~720 eV are because of spin-orbit splitting in 2p level—2p<sup>3/2</sup> and 2p<sup>1/2</sup>, corresponding to an energy gap of 13 eV which indicates the presence of Fe<sup>2+</sup> state in conventional Fe-Se compounds. The other two peaks (~711 eV and 725 eV) imply the existence of a higher oxidation state (Fe<sup>3+</sup>) of the iron species in corresponding Fe-Se NPs<sup>54-55</sup>. This study is beneficial, as both Fe<sup>2+</sup> and Fe<sup>3+</sup> are required for electron neutrality in Fe<sub>3</sub>Se<sub>4</sub> and Fe<sub>7</sub>Se<sub>8</sub>. However, the presence of the Fe<sup>3+</sup> state in FeSe<sub>2</sub> and FeSe spectra indicates that the surface of these compounds may get oxidized during the sample processing and characterization. The satellite peaks were also observed at

~713 eV, 727 eV, and 734 eV in the spectra, as mentioned in Figure 16. The peaks detected at higher BE can be assigned to charge transfer satellites of  $\text{Fe}^{2+}$  and  $\text{Fe}^{3+}$  and related to XPS shakeup excitations, which are marked by a satellite peak at higher BE<sup>56-57</sup>.

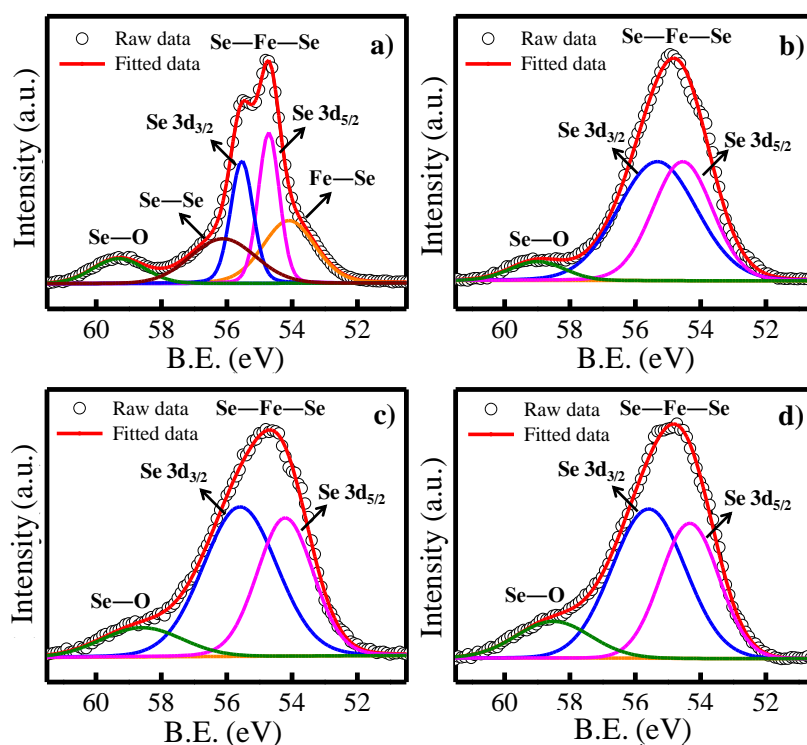
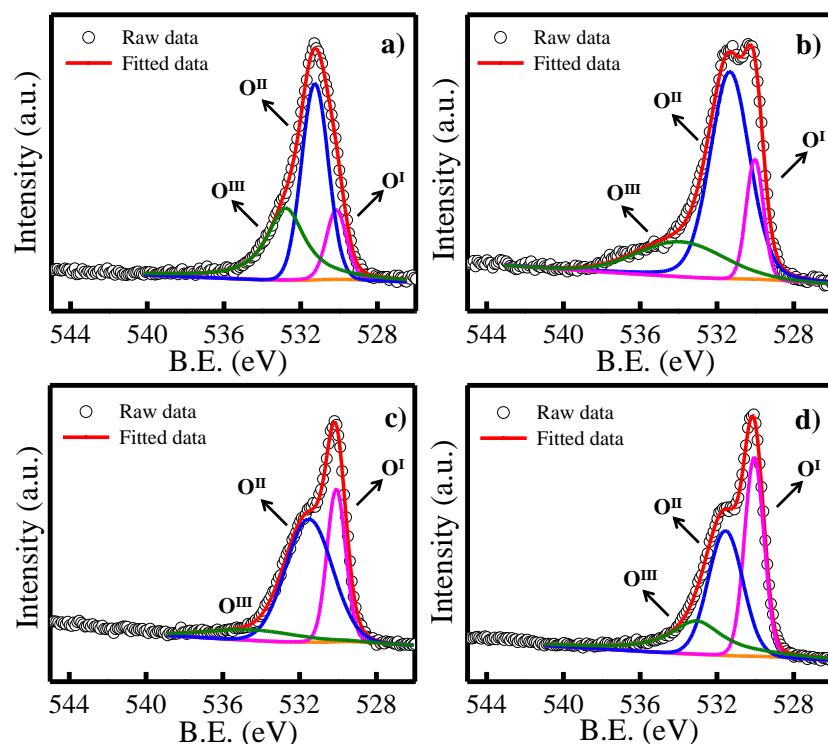


**Figure 17.** XPS spectra of as-synthesized a)  $\text{FeSe}_2$  b)  $\text{Fe}_3\text{Se}_4$  c)  $\text{Fe}_7\text{Se}_8$  and d)  $\text{FeSe}$  nanoparticles. The red lines show a deconvoluted curve fits.

The curves shown in Figure 17 correspond to Se 3d spectra, indicating the presence of Fe–Se, Se–Fe–Se, Se–Se, and Se–O peaks around ~54 eV, 54 eV–56 eV, 56 eV, and 59 eV in  $\text{FeSe}_2$  compound. In other compounds, only three peaks were observed corresponding to Se–Fe–Se and Se–O bonds nearby 54 eV–56 eV and 59 eV, which signifies the absence of the Se–Se bond in the last three phases<sup>58</sup>. Figure 18 shows the XPS spectrum of O 1s having 3 deconvoluted peaks — $\text{O}^{\text{I}}$  (~530 eV),  $\text{O}^{\text{II}}$  (~531 eV), and  $\text{O}^{\text{III}}$  (~533 eV). The  $\text{O}^{\text{I}}$  indicates that NPs' surfaces were hydroxylated to some extent<sup>59,60</sup>. The  $\text{O}^{\text{II}}$  reveals the Se species surface oxidation, persistent with the Se 3d spectra<sup>59,60</sup>. The  $\text{O}^{\text{III}}$  contribution is related to the physi-/chemisorbed  $\text{H}_2\text{O}$  on the surfaces due to the exposure of air<sup>59,60</sup>.



Phase \ Parameter	Weight Percentage					
	Fe	Se	O	C	N	Bi?
FeSe <sub>2</sub>	13.02	58.22	8.31	20.42	-	-
Fe <sub>3</sub> Se <sub>4</sub>	16.93	50.43	10.86	19.62	2.14	-
Fe <sub>7</sub> Se <sub>8</sub>	18.01	36.53	13.55	27.02	1.43	3.42
FeSe	24.05	44.11	14.17	16.29	1.36	-

**Figure 18.** XPS spectra of O 1s a) FeSe<sub>2</sub> b) Fe<sub>3</sub>Se<sub>4</sub> c) Fe<sub>7</sub>Se<sub>8</sub> and d) FeSe nanoparticles. The red lines show a deconvoluted curve fits. The table shows the weight percentage of distinct elements in all the phases of Fe-Se system.

### 3.5 Conclusions

An easy-to-control synthetic procedure was developed by heating a mixture of Fe(acac)<sub>3</sub> and Se in a coordinating organic solvent to synthesize the Fe-Se system. The process provided an appropriate nucleation and growth environment in a reaction system. We demonstrated that synthetic circumstances played a significant part in governing the phases of the Fe-Se system. OLA was used as a reducing agent to decompose the precursors, and 1-ODE was used as an accelerating agent to accelerate all the reaction steps resulting in the formation of the highest temperature phase. It was proposed that the reactivity of Fe and Se precursors primarily

governed the nucleation of Fe-Se NPs, and growth was governed primarily by the reaction temperature apart from other factors. Instead of directly forming the FeSe phase from Fe and Se precursors, intermediate products of FeSe<sub>2</sub>, Fe<sub>3</sub>Se<sub>4</sub>, and Fe<sub>7</sub>Se<sub>8</sub> phases are formed. In the following sequence in the temperature range of 110 °C - 300 °C: FeSe<sub>2</sub> → Fe<sub>3</sub>Se<sub>4</sub> → Fe<sub>7</sub>Se<sub>8</sub> → FeSe. Altogether, this thesis provides new information on the formation mechanism and phase-evolution of the Fe-Se family of compounds. It also emphasizes the essential role played by temperature and time with solvents in phase transformation. Finally, the optimized temperature required to synthesize the pure phase was reported. Additionally, the morphology of individually synthesized NPs is also correlated with the theoretical crystal habits. This method also provides control over shapes and sizes by tuning the solvents and reaction temperature-time, which tunes the properties of Fe-Se NPs. We believe that this route can also be used for synthesizing different TMCs.

### 3.6 References

- (1) Polte, J. Fundamental Growth Principles of Colloidal Metal Nanoparticles – a New Perspective. *CrystEngComm* **2015**, *17* (36), 6809–6830.
- (2) Thanh, N. T. K.; Maclean, N.; Mahiddine, S. Mechanisms of Nucleation and Growth of Nanoparticles in Solution. *Chem. Rev.* **2014**, *114* (15), 7610–7630.
- (3) Heywood, B. R.; Mann, S. Template-Directed Nucleation and Growth of Inorganic Materials. *Adv. Mater.* **1994**, *6* (1), 9–20.
- (4) Aizenberg, J.; Black, A. J.; Whitesides, G. M. Control of Crystal Nucleation by Patterned Self-Assembled Monolayers. *Nature* **1999**, *398* (6727), 495–498.
- (5) Jagannathan, R.; Parmar, A. S.; Adyanthaya, S.; Prabhune, A.; Muschol, M.; Poddar, P. In Situ Observation of Antibiotic Mediated Concurrent Growth of Two Distinct Homogeneous Populations of Gold Nanoparticles in Solution Phase. *J. Phys. Chem. C* **2009**, *113* (9), 3478–3486.
- (6) Khandelwal, P.; Singh, D. K.; Sadhu, S.; Poddar, P. Modulation of Reaction Kinetics for the Tuneable Synthesis of Gold Nanoparticles and Quantum Clusters: Application of Gold Quantum Clusters as "Turn-Off" Sensing Probe for Sn<sup>4+</sup> Ions. *Chempluschem* **2014**, *79* (1), 134–142.
- (7) Poddar, P.; Telem-Shafir, T.; Fried, T.; Markovich, G. Dipolar Interactions in Two- and Three-Dimensional Magnetic Nanoparticle Arrays. *Phys. Rev. B* **2002**, *66* (6), 060403.
- (8) Malik, M.; Padhye, P.; Poddar, P. Graphene Quantum Dots-Driven Multiform Morphologies of β-NaYF<sub>4</sub>:Gd<sup>3+</sup>/Tb<sup>3+</sup> Phosphors: The Underlying Mechanism and Their Optical Properties. *ACS Omega* **2018**, *3* (2), 1834–1849.
- (9) Sines, I. T.; Schaak, R. E. Phase-Selective Chemical Extraction of Selenium and Sulfur from Nanoscale Metal Chalcogenides: A General Strategy for Synthesis, Purification, and Phase Targeting. *J. Am. Chem. Soc.* **2011**, *133* (5), 1294–1297.

- (10) Poddar, P.; Fried, T.; Markovich, G. First-Order Metal-Insulator Transition and Spin-Polarized Tunneling in Fe<sub>3</sub>O<sub>4</sub> nanocrystals. *Phys. Rev. B* **2002**, *65* (17), 172405.
- (11) Manna, L.; Milliron, D. J.; Meisel, A.; Scher, E. C.; Alivisatos, A. P. Controlled Growth of Tetrapod-Branched Inorganic Nanocrystals. *Nat. Mater.* **2003**, *2* (6), 382–385.
- (12) Yu, H.-D.; Regulacio, M. D.; Ye, E.; Han, M.-Y. Chemical Routes to Top-down Nanofabrication. *Chem. Soc. Rev.* **2013**, *42* (14), 6006-6018.
- (13) Clarke, G.; Rogov, A.; McCarthy, S.; Bonacina, L.; Gun'ko, Y.; Galez, C.; Le Dantec, R.; Volkov, Y.; Mugnier, Y.; Prina-Mello, A. Preparation from a Revisited Wet Chemical Route of Phase-Pure, Monocrystalline and SHG-Efficient BiFeO<sub>3</sub> Nanoparticles for Harmonic Bio-Imaging. *Sci. Rep.* **2018**, *8* (1), 10473.
- (14) Jellinek, F. Transition Metal Chalcogenides. Relationship between Chemical Composition, Crystal Structure and Physical Properties. *React. Solids* **1988**, *5* (4), 323–339.
- (15) Lan, M.; Xiang, G.; Nie, Y.; Yang, D.; Zhang, X. The Static and Dynamic Magnetic Properties of Monolayer Iron Dioxide and Iron Dichalcogenides. *RSC Adv.* **2016**, *6* (38), 31758–31761.
- (16) Lin, C.; Lu, S.; Lyubutin, I. S.; Korzhetskiy, Y. V; Wang, S.; Suzdalev, I. P. Synthesis and Magnetic Properties of Iron Sulfide Nanosheets with a NiAs-like Structure. *J. Appl. Phys.* **2010**, *107* (9), 09A335.
- (17) Liu, A.; Chen, X.; Zhang, Z.; Jiang, Y.; Shi, C. Selective Synthesis and Magnetic Properties of FeSe<sub>2</sub> and FeTe<sub>2</sub> Nanocrystallites Obtained through a Hydrothermal Co-Reduction Route. *Solid State Commun.* **2006**, *138* (10-11), 538–541.
- (18) Kamimura, T.; Sato, M.; Takahashi, H.; Mori, N.; Yoshida, H.; Kaneko, T. Pressure-Induced Phase Transition in Fe-Se and Fe-S Systems with a NiAs-Type Structure. *J. Magn. Magn. Mater.* **1992**, *104-107*, 255–256.
- (19) Lupu, D.; Bucur, R. V. Possible Anionic Clusters and Mixed Valence Effects in Transition Metal Chalcogenides and Oxides. *J. Phys. Chem. Solids* **1978**, *39* (3), 285–290.
- (20) Jain, B. K.; Singh, A. K.; Chandra, K. An Investigation of Binary System Fe-Se. *J. Phys. F Met. Phys.* **1978**, *8* (12), 2625–2630.
- (21) Okazaki, A.; Hirakawa, K. Structural Study of Iron Selenides FeSe<sub>x</sub>. I Ordered Arrangement of Defects of Fe Atoms. *J. Phys. Soc. Japan* **1956**, *11* (9), 930–936.
- (22) Reddy, V. K.; Chetty, C. S. Mössbauer Studies in Fe-Se System. *Phys. stat. sol.* **1975**, *32* (5), 585–592.
- (23) Hirone, T.; Maeda, S.; Tsuya, N. On the Ferrimagnetism of Iron Selenides. *J. Phys. Soc. Japan* **1954**, *9* (4), 496–499.
- (24) Hirone, T.; Chiba, S. The Magnetic Properties of FeSe<sub>x</sub> with the NiAs Structure. *J. Phys. Soc. Japan* **1956**, *11* (6), 666–670.
- (25) Hirakawa, K. The Magnetic Properties of Iron Selenide Single Crystals. *J. Phys. Soc. Japan* **1957**, *12* (8), 929–938.
- (26) Schuster, W.; Mikler, H.; Komarek, K. L. Transition Metal-Chalcogen Systems, VII.: The Iron-Selenium Phase Diagram. *Monatshefte für Chemie* **1979**, *110* (5), 1153–1170.

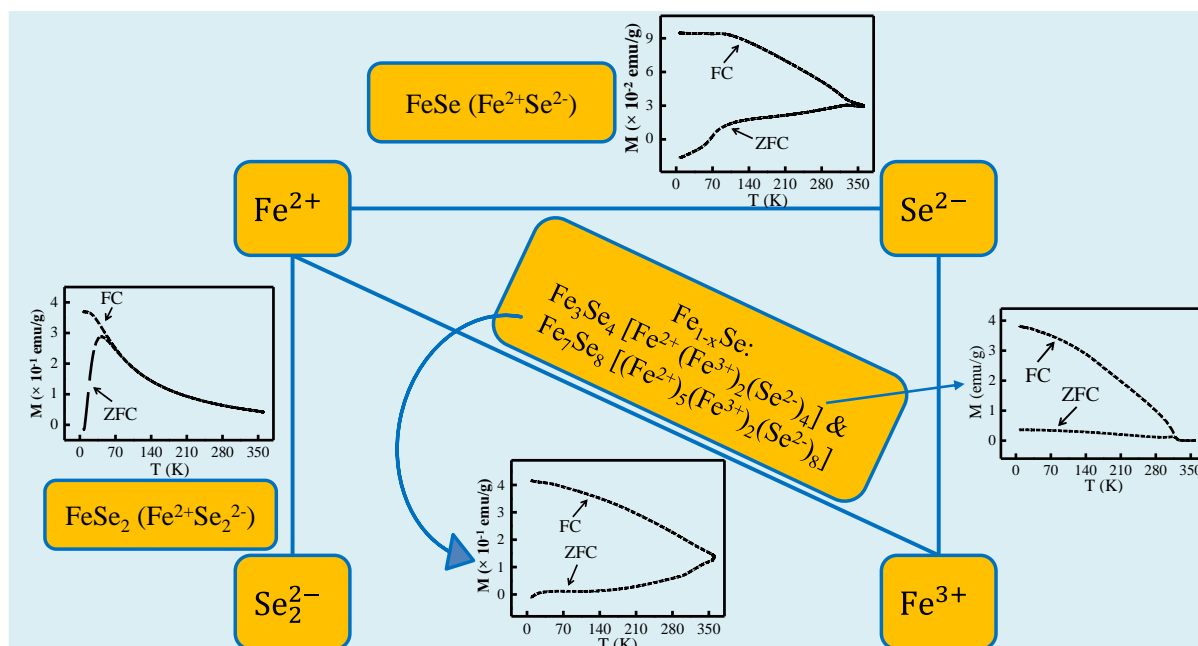
- (27) Lavina, B.; Downs, R.; Sinogeikin, S. The Structure of Ferroselite, FeSe<sub>2</sub>, at Pressures up to 46 GPa and Temperatures down to 50 K: A Single-Crystal Micro-Diffraction Analysis. *Crystals* **2018**, *8* (7), 289.
- (28) Andresen, A. F. A Neutron Diffraction Investigation of Fe<sub>3</sub>Se<sub>4</sub>. *Acta Chem. Scand.* **1968**, *22*, 827–835.
- (29) Andresen, A. F.; Leciejewicz, J. A Neutron Diffraction Study of Fe<sub>7</sub>Se<sub>8</sub>. *J. De Physique*, **1964**, *25* (5), 574–578.
- (30) Okazaki, A. The Superstructures of Iron Selenide Fe<sub>7</sub>Se<sub>8</sub>. *J. Phys. Soc. Japan* **1961**, *16* (6), 1162–1170.
- (31) Lyubutin, I. S.; Lin, C.-R.; Funtov, K. O.; Dmitrieva, T. V.; Starchikov, S. S.; Siao, Y.-J.; Chen, M.-L. Structural, Magnetic, and Electronic Properties of Iron Selenide Fe<sub>6-7</sub>Se<sub>8</sub> Nanoparticles Obtained by Thermal Decomposition in High-Temperature Organic Solvents. *J. Chem. Phys.* **2014**, *141* (4), 044704.
- (32) Hsu, F.-C.; Luo, J.-Y.; Yeh, K.-W.; Chen, T.-K.; Huang, T.-W.; Wu, P. M.; Lee, Y.-C.; Huang, Y.-L.; Chu, Y.-Y.; Yan, D.-C.; Wu, M.-K. Superconductivity in the PbO-Type Structure  $\alpha$ -FeSe. *Proc. Natl. Acad. Sci.* **2008**, *105* (38), 14262–14264.
- (33) Mao, X.; Kim, J.-G.; Han, J.; Jung, H. S.; Lee, S. G.; Kotov, N. A.; Lee, J. Phase-Pure FeSe<sub>x</sub> (x = 1, 2) Nanoparticles with One- and Two-Photon Luminescence. *J. Am. Chem. Soc.* **2014**, *136* (20), 7189–7192.
- (34) Yuan, B.; Luan, W.; Tu, S. One-Step Synthesis of Cubic FeS<sub>2</sub> and Flower-like FeSe<sub>2</sub> Particles by a Solvothermal Reduction Process. *Dalt. Trans.* **2012**, *41* (3), 772–776.
- (35) Yuan, B.; Hou, X.; Han, Y.; Luan, W.; Tu, S. Facile Synthesis of Flake-like FeSe<sub>2</sub> Particles in Open-Air Conditions. *New J. Chem.* **2012**, *36* (10), 2101–2105. (36) Lin, C. R.; Siao, Y. J.; Lu, S. Z.; Gau, C. Magnetic Properties of Iron Selenide Nanocrystals Synthesized by the Thermal Decomposition. *IEEE Trans. Magn.* **2009**, *45* (10), 4275–4278. (37) Zhang, H.; Long, G.; Li, D.; Sabirianov, R.; Zeng, H. Fe<sub>3</sub>Se<sub>4</sub> Nanostructures with Giant Coercivity Synthesized by Solution Chemistry. *Chem. Mater.* **2011**, *23* (16), 3769–3774.
- (38) Sen Bishwas, M.; Das, R.; Poddar, P. Large Increase in the Energy Product of Fe<sub>3</sub>Se<sub>4</sub> by Fe-Site Doping. *J. Phys. Chem. C* **2014**, *118* (8), 4016–4022.
- (39) Sobhani, A.; Salavati-Niasari, M. Synthesis and Characterization of FeSe<sub>2</sub> Nanoparticles and FeSe<sub>2</sub>/FeO(OH) Nanocomposites by Hydrothermal Method. *J. Alloys Compd.* **2015**, *625*, 26–33.
- (40) Li, D.; Pan, D.; Liu, W.; Li, X.; Chen, M.; Li, S.; Li, Y.; Tan, J.; Sun, D.; Wang, Z.; Han, Z.; Zhang, Z. Controllable Phase Transition for Layered  $\beta$ -FeSe Superconductor Synthesized by Solution Chemistry. *Chem. Mater.* **2017**, *29* (2), 842–848.
- (41) Hou, B.; Benito-Alifonso, D.; Webster, R.; Cherns, D.; Galan, M. C.; Fermín, D. J. Rapid Phosphine-Free Synthesis of CdSe Quantum Dots: Promoting the Generation of Se Precursors Using a Radical Initiator. *J. Mater. Chem. A* **2014**, *2* (19), 6879–6886.
- (42) Grivel, J.-C.; Wulff, A. C.; Zhao, Y.; Andersen, N. H.; Bednarcík, J.; Zimmermann, M. V. In Situ Observation of the Formation of FeSe. *Supercond. Sci. Technol.* **2011**, *24* (1), 015007.
- (43) Mourdikoudis, S.; Liz-Marzán, L. M. Oleylamine in Nanoparticle Synthesis. *Chem. Mater.* **2013**, *25* (9), 1465–1476.
- (44) Vivien, A.; Guillaumont, M.; Meziane, L.; Salzemann, C.; Aubert, C.; Halbert, S.; Gérard, H.; Petit, M.; Petit, C. The Role of Oleylamine Revisited: An Original Disproportionation Route to Monodispersed Cobalt and Nickel Nanocrystals. *Chem. Mater.* **2019**, *31* (3), 960–968.

- (45) Hoene, J. Von; Charles, R. G.; Hickam, W. M. Thermal Decomposition of Metal Acetylacetonates: Mass Spectrometer Studies. *J. Phys. Chem.* **1958**, 62 (9), 1098–1101.
- (46) A. Bravais. *Etudes Crystallographiques*. Paris: Gauthier-Villars, 1866.
- (47) M. G. Friedel. *Etudes sur la loi de Bravais*. Bull. Soc. Franc. Miner., 9:326, 1907.
- (48) J. D. H. Donnay and D. Harker. A new law of crystal morphology extending the law of bravais. *Amer. Min.*, 22:446, 1937.
- (49) P. Hartman and W. G. Perdok. On the relations between structure and morphology of crystals. I. *Acta Crystallogr.*, 8:49–52, 1955.
- (50) P. Hartman and W. G. Perdok. On the relations between structure and morphology of crystals. II. *Acta Crystallogr.*, 8:521–524, 1955.
- (51) P. Hartman and P. Bennema. The attachment energy as a habit controlling factor : I. Theoretical considerations. *J. Cryst. Growth*, 49:145–156, 1980.
- (52) Xia, Y.; Xia, X.; Peng, H. C. Shape-Controlled Synthesis of Colloidal Metal Nanocrystals: Thermodynamic versus Kinetic Products. *J. Am. Chem. Soc.* 2015, 137, 7947–7966.
- (53) Telesca, D.; Nie, Y.; Budnick, J. I.; Wells, B. O.; Sinkovic, B. Impact of Valence States on the Superconductivity of Iron Telluride and Iron Selenide Films with Incorporated Oxygen. *Phys. Rev. B* **2012**, 85 (21), 214517.
- (54) Yamashita, T.; Hayes, P. Analysis of XPS Spectra of Fe<sup>2+</sup> and Fe<sup>3+</sup> Ions in Oxide Materials. *Appl. Surf. Sci.* **2009**, 255 (18), 8194.
- (55) Yang, Z.; Zhang, J.-Y.; Liu, Z.; Li, Z.; Lv, L.; Ao, X.; Tian, Y.; Zhang, Y.; Jiang, J.; Wang, C. "Cuju"-Structured Iron Diselenide-Derived Oxide: A Highly Efficient Electrocatalyst for Water Oxidation. *ACS Appl. Mater. Interfaces* **2017**, 9 (46), 40351–40359.
- (56) Li, G.; Zhang, B.; Baluyan, T.; Rao, J.; Wu, J.; Novakova, A. A.; Rudolf, P.; Blake, G. R.; de Groot, R. A.; Palstra, T. T. M. Metal–Insulator Transition Induced by Spin Reorientation in Fe<sub>7</sub>Se<sub>8</sub> Grain Boundaries. *Inorg. Chem.* **2016**, 55 (24), 12912–12922.
- (57) Kumar, U.; Shete, A.; Harle, A. S.; Kasyutich, O.; Schwarzacher, W.; Pundle, A.; Poddar, P. Extracellular Bacterial Synthesis of Protein-Functionalized Ferromagnetic Co<sub>3</sub>O<sub>4</sub> Nanocrystals and Imaging of Self-Organization of Bacterial Cells under Stress after Exposure to Metal Ions. *Chem. Mater.* **2008**, 20 (4), 1484–1491.
- (58) Zheng, Q.; Cheng, X.; Li, H. Microwave Synthesis of High Activity FeSe<sub>2</sub>/C Catalyst toward Oxygen Reduction Reaction. *Catalysts* **2015**, 5 (3), 1079–1091.
- (59) Zhang, J.-Y.; Lv, L.; Tian, Y.; Li, Z.; Ao, X.; Lan, Y.; Jiang, J.; Wang, C. Rational Design of Cobalt-Iron Selenides for Highly Efficient Electrochemical Water Oxidation. *ACS Appl. Mater. Interfaces* **2017**, 9 (39), 33833–33840.
- (60) Xia, C.; Jiang, Q.; Zhao, C.; Hedhili, M. N.; Alshareef, H. N. Selenide-Based Electrocatalysts and Scaffolds for Water Oxidation Applications. *Adv. Mater.* **2016**, 28, 77–85.



## Chapter 4

### Remarkable Effect of Fe and Se Composition on Magnetic Properties— Comparative Study of the Fe-Se System at the Nanoscale



## Highlights

Below, we have listed some of the important 'take-away' points from this chapter which we would like to highlight:

- 1) *The correlation between the phase structure and the magnetic properties has been presented for the Fe-Se system.*
- 2) *The magnetic properties vary enormously with change in Fe:Se ratio due to the change in  $Fe^{2+}/Fe^{3+}$  ratio, crystal field environment around Fe-ions, magnetocrystalline anisotropy, Fe-vacancies, and so forth.*
- 3) *Among the four Fe-Se phases studied, two of them – $Fe_3Se_4$  and  $Fe_7Se_8$ , are ferrimagnetic below  $\sim 300$  K and show semi-hard magnetic properties. The other two phases – $FeSe_2$  and  $\beta$ - $FeSe$  exhibiting weaker magnetism are less known for their magnetic properties.*

**Keywords:** Iron selenides, phase-property relationship, magnetic properties.

The results of this chapter are published as—

- ✓ Remarkable effect of Fe and Se composition on magnetic properties— comparative study of the Fe-Se system at the nanoscale

**Monika Ghalawat**, Pankaj Poddar\* \* *J. Phys. Chem. C* 2022

## 4.1 Introduction

The selenides of iron have gotten a lot of interest in recent years due to their exciting and unusual thermal, optical, and magnetic properties.<sup>1–11</sup> The richness of physical properties also comes from the richness in the stoichiometric phases these families of compounds may exhibit. The Fe–Se system shows various stable polymorphs under ambient conditions, including FeSe<sub>2</sub> (orthorhombic marcasite), Fe<sub>3</sub>Se<sub>4</sub> (monoclinic NiAs-type), Fe<sub>7</sub>Se<sub>8</sub> (hexagonal NiAs-type), and β-FeSe (tetragonal PbO-type).<sup>12–18</sup> Depending upon the composition of Fe:Se, these compounds could be metal, semiconductors, or superconductors, and their magnetic properties also vary a lot from ferro- to ferrimagnetic.<sup>19–31</sup> It was recently observed that Fe<sub>3</sub>Se<sub>4</sub> might also show ferroelectric ordering coexisting with ferrimagnetic ordering under ambient conditions.<sup>32, 33</sup> The thermal, optical (photon harvesting), energy (supercapacitors, batteries, etc.), and catalytic properties (water splitting, etc.) of these compounds have not been explored in-depth so far. However, recently, the potential of Fe<sub>3</sub>Se<sub>4</sub> as a magnetic energy storage device was investigated, and it was found that this compound shows a colossal increase in the energy product while cooling from 300 to 10 K with the potential to replace expensive rare-earth hard magnets at lower temperatures.<sup>11, 34</sup>

The nanoscopic forms of materials can provide additional tunability of the physical and chemical properties. Although Fe-based magnetic nanostructures, such as iron, its oxides, or alloys, have all been thoroughly researched, however, the magnetic characteristics of iron chalcogenides have received relatively less attention due to the complexities associated with the synthesis of pure phases.<sup>35–48</sup>

Among the four stable phases of the Fe–Se system, two (Fe<sub>3</sub>Se<sub>4</sub> and Fe<sub>7</sub>Se<sub>8</sub>) are well known for their rich magnetic properties, whereas the other two (FeSe<sub>2</sub> and β-FeSe) are known for their interesting optical and electronic properties.<sup>19–22</sup> Bulk and nanostructured Fe<sub>3</sub>Se<sub>4</sub> and Fe<sub>7</sub>Se<sub>8</sub> exhibit ferrimagnetic nature at room temperature (RT) with the Curie temperature (T<sub>C</sub>) of ~ 320 and 453 K, respectively.<sup>23–25, 34, 49</sup> While it is known that Fe<sub>3</sub>Se<sub>4</sub> also shows ferroelectric ordering at ~ 320 K<sup>32</sup>, it will be interesting to study the existence of similar ordering in Fe<sub>7</sub>Se<sub>8</sub> in the future. Unfortunately, the magnetic ordering of FeSe<sub>2</sub> and β-FeSe is still not fully understood. There are reports related to the magnetic properties of these compounds.<sup>50–59</sup> However, the clear picture is still undefined. This chapter will address the fundamental points of magnetic nature, followed by properties.

The fabrication of iron selenide solids is quite challenging as slight stoichiometry variations often lead to significant structural, chemical, and physical changes. Unsurprisingly, the synthesis of the iron selenides at the nanoscale is significantly more challenging as they are more reactive and less stable forms due to nano-dimensions. However, the available fabrication routes are very complicated and are not flexible to achieve the desired phase. Among the various techniques for preparing iron selenide nanoparticles (NPs), thermal decomposition is a promising route for controlling the phase of the Fe-Se system, as discussed in our previous chapter.<sup>14</sup> The stoichiometry of Fe-Se can be influenced by many factors, such as the amount or type of precursors, reaction temperature, and time.

This chapter compares and contrasts the magnetic characteristics of several stable phases in the Fe-Se system ( $\text{FeSe}_2$ ,  $\text{Fe}_3\text{Se}_4$ ,  $\text{Fe}_7\text{Se}_8$ , and  $\beta\text{-FeSe}$ ). The thermal decomposition-based route is used to synthesize individual phases of the Fe-Se system, and excellent tunability of their magnetic properties is observed.

## 4.2 Characterization techniques

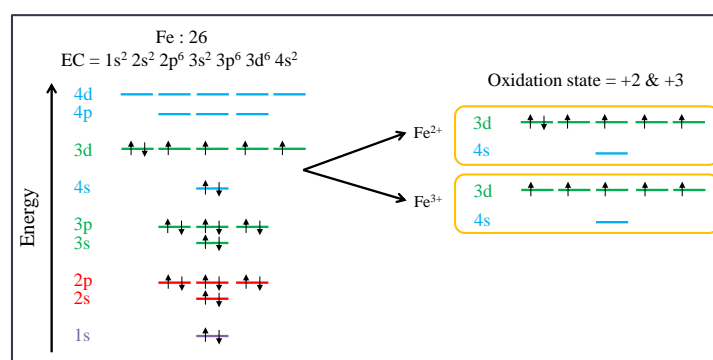
The magnetic measurements were performed using the Physical Property Measurement System (PPMS) manufactured by Quantum Design Inc., San Diego, California, equipped with a vibrating sample magnetometer (VSM) and superconducting magnet. The powder samples were precisely weighed and packed inside a plastic sample holder, which fits into a brass sample holder provided by Quantum Design Inc. with a negligible contribution to an overall magnetic signal. The magnetization versus temperature (M–T) measurements in zero-field-cooled (ZFC) and field-cooled (FC) modes was performed at a temperature sweep from 5 K to 360 K in a field of 100 Oe using the VSM attachment. The magnetization versus field (M–H) loops were collected at a rate of  $50 \text{ Oe s}^{-1}$  in a field sweep from  $\pm 60 \text{ kOe}$  at the vibrating frequency of 40 Hz.

## 4.3 Results and discussion

In Chapter 3, the iron selenide compounds, including  $\text{FeSe}_2$ ,  $\text{Fe}_3\text{Se}_4$ ,  $\text{Fe}_7\text{Se}_8$ , and  $\beta\text{-FeSe}$  were synthesized in the presence of OLA and are taken here as a specimen to investigate the phase-properties relation. The discussion in Chapter 3 shows that the as-synthesized phases are highly pure without any secondary phase under the limit of laboratory XRD. TEM was used to analyse the morphology of all the phases, which revealed a quasi-spherical form with rod-like characteristics sprouting on the surface, resembling a cactus plant. The zoomed in-view of

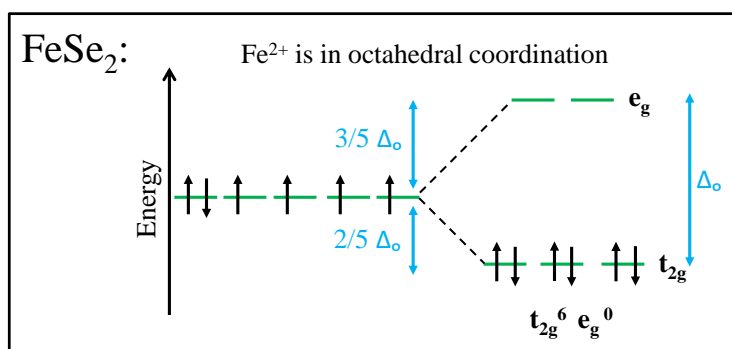
nanocacti reveals the rod shape of the Fe-Se system (agglomerated rods). Thus, nanorods are the building block in each phase of the Fe-Se system in the presence of OLA as an organic solvent.

Scheme 1 presents a schematic illustration of an electronic configuration of iron. The most likely oxidation states of iron are 2+ and 3+. The outermost shell electronic configuration of  $\text{Fe}^{2+}$  and  $\text{Fe}^{3+}$  are shown in Scheme 1. There are four unpaired electrons in  $\text{Fe}^{2+}$  and five in  $\text{Fe}^{3+}$ . Combining these two ionic states with Se anions leads to four stable structures. The interaction between the atoms is different in all these structures, leading to distinct individual properties.



**Scheme 1:** Schematic illustration of the electronic configuration of iron with two oxidation states,  $\text{Fe}^{2+}$  and  $\text{Fe}^{3+}$ .

#### 4.3.1 Magnetic properties of the $\text{FeSe}_2$ NPs



**Scheme 2.** In the  $\text{FeSe}_2$  compound, crystal field splitting of the 3d-orbitals of  $\text{Fe}^{2+}$  at the octahedral site into 3-fold  $t_{2g}$  and 2-fold  $e_g$  states.

As mentioned above, the magnetic properties of  $\text{FeSe}_2$  are not clearly discussed. There are reports for bulk<sup>49</sup> and nanoscale,<sup>52–53, 55–57</sup> stating that in bulk, there is no magnetic ordering; however, all the nanoscale synthetic  $\text{FeSe}_2$  shows a magnetic ordering due to the several defects. In this compound, each cation is octahedrally coordinated with six anions ( $\text{FeSe}_6$

octahedra), and each anion is tetrahedrally coordinated with three cations and one anion forming dimer pair ( $\text{Se}_2\text{Fe}_3$  tetrahedra).<sup>60</sup> The lack of magnetic moment at the Fe-atom was verified in a Mossbauer analysis of marcasite compounds<sup>61</sup>, suggesting that the  $\text{Fe}^{2+}$  in  $\text{FeSe}_2$  marcasite also has a low spin configuration—the completely filled  $t_{2g}$  and the completely empty  $e_g$ . Schematic 2 shows the crystal field splitting (CFS) of the d-orbitals of  $\text{Fe}^{2+}$  at the octahedral site into 3-fold  $t_{2g}$  and 2-fold  $e_g$  states having the electronic configurations of  $t_{2g}^6$  and  $e_g^0$  states of  $3d \text{Fe}^{2+}$ . Thus, iron atoms have no unpaired electron, that give rise to zero magnetic moment in  $\text{FeSe}_2$ . In conclusion, the pure  $\text{FeSe}_2$  is diamagnetic in nature. However, so many literature reports indicate magnetization.<sup>52–53, 55–57</sup> The reported synthetic  $\text{FeSe}_2$  shows a magnetic ordering due to the presence of either surface oxidation or ferrimagnetic impurities or or spin canting, and so forth.

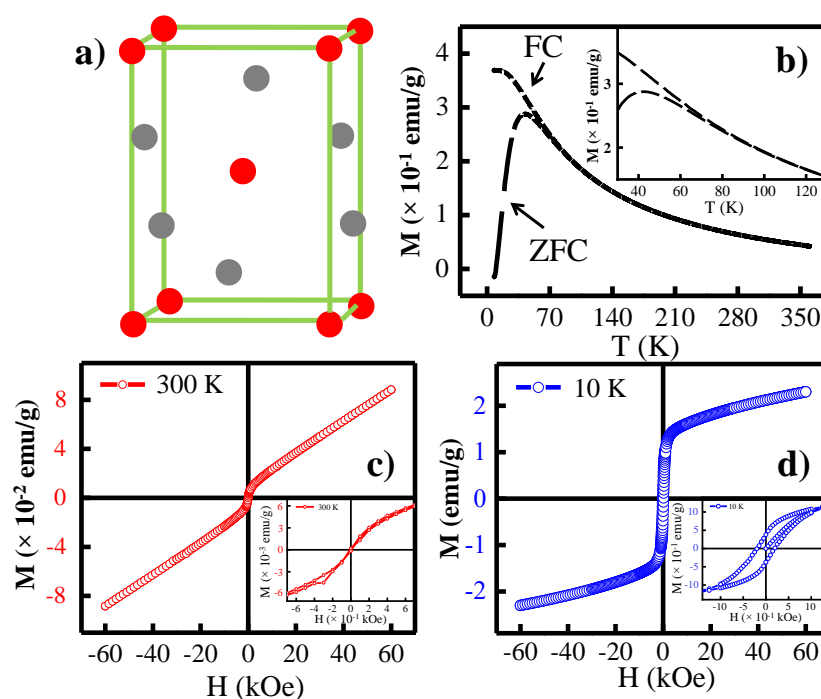


**Figure 1.** a) Schematic of the unit cell of  $\text{FeSe}_2$ , solid red circle represents the Fe cations, and the solid grey circle represents the Se anions. b) Magnetization versus temperature curves for  $\text{FeSe}_2$  (black curve) measured with an applied field of 100 Oe in FC and ZFC modes (Inset shows the zoomed-view of the curve). Hysteresis loops of  $\text{FeSe}_2$  measured by the vibrating sample magnetometer (VSM) within a field of  $\pm 60$  kOe at c) 300 K (red curves) and d) 10 K (blue curves).

Figure 1 shows the schematic of the unit cell of  $\text{FeSe}_2$  and its magnetic properties. Iron diselenide ( $\text{Fe}^{2+}\text{Se}_2^{2-}$ ) has an orthorhombic marcasite structure with the lattice parameters

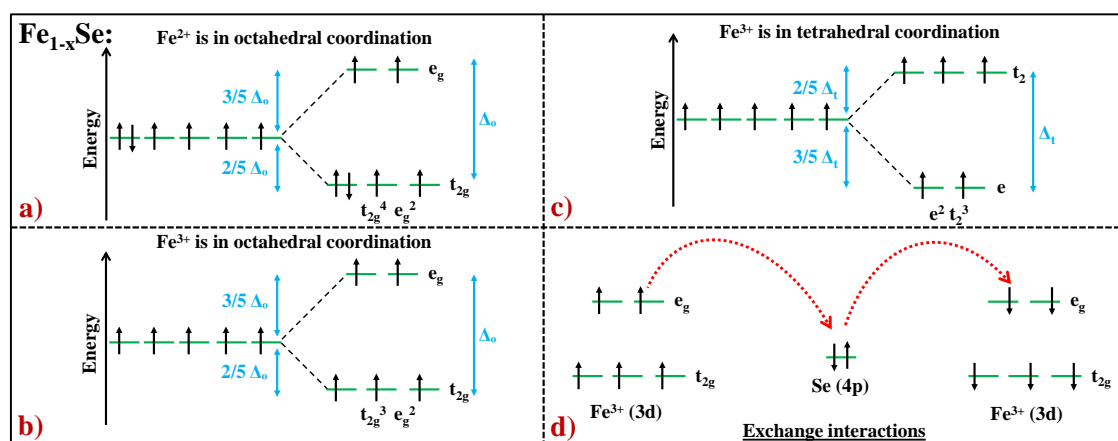
$a=3.575 \text{ \AA}$ ,  $b=4.791 \text{ \AA}$ , and  $c=5.715 \text{ \AA}$  having the Pmnn space group (SG) (Figure 1a).<sup>14,60</sup> The M-T curves in ZFC and FC modes have been observed from 7 K to 360 K at 100 Oe applied magnetic field. Figure 1b shows the M-T curves. At 45 K, the ZFC curve grew into a well-developed steplike transition; the magnetization first increased up to 45 K and then declined as the temperature dropped, indicating that the magnetic moment of the FeSe<sub>2</sub> vary as the temperature drops; this might be related to the spin-rotation with decreasing temperature. The ZFC curve identifies the average blocking temperature of ~45 K. The magnetization of ZFC and FC process shows the bifurcation below 100 K (inset, Figure 1b).

To acquire further insight into the magnetic properties of the FeSe<sub>2</sub> NPs, Figures 1c and 1d present the M-H curves for the FeSe<sub>2</sub> nanorods observed at 300 K (red plot) and 10 K (blue plot) in an applied magnetic field up to  $\pm 60$  kOe. At 300 K, the M-H loop indicates a two-step behavior. At a lower applied magnetic field, it reveals non-linear behavior. In contrast, it follows a linear M-H behavior (i.e., paramagnetic) at higher field values. However, at 10 K, it reveals a non-linear M-H curve until the highest applied magnetic field. The observed prominent non-linear hysteresis characteristics indicate the presence of magnetic ordering at both temperatures.

The inset of Figure 1c-d shows a zoomed-in view of the M-H curves at 300 K and 10 K, clearly depicting the coercivity and remanent field of FeSe<sub>2</sub>. By virtue of reduced thermal fluctuation of magnetic dipoles, the observed coercivity ( $H_C$ ) and remanence ( $M_R$ ) are 8 Oe, and  $2.0 \times 10^{-4}$  emu/g at 300 K increased to 200 Oe and 0.4 emu/g at 10 K, respectively. Although, the pure FeSe<sub>2</sub> exhibits diamagnetic properties as discussed above. However, the FeSe<sub>2</sub> generates magnetic ordering in this report due to defects.

The existence of an induced surface layer of oxides in TMCs has been identified in many materials.<sup>62-65</sup> The TMCs are very sensitive towards oxidation. The exposure to air quickly starts the formation of an oxidation layer. As discussed above in Chapter 3, XPS analysis (supported by Fe, Se, and O spectra), the surface oxidized as soon as iron selenide particles came into contact with air.<sup>14</sup> It was speculated that surface oxidation of FeSe<sub>2</sub> NPs is generating the magnetic ordering on the surface. Thus, the surface oxidized FeSe<sub>2</sub> NPs is magnetically active in contrast to their fundamental magnetic behavior. It is appropriate to conclude that the as-synthesized FeSe<sub>2</sub> NPs using organometallic chemistry are easily oxidized as soon as they come in contact with air and form a magnetic coating on the surface.

### 4.3.2 Magnetic properties of the Fe<sub>3</sub>Se<sub>4</sub> and Fe<sub>7</sub>Se<sub>8</sub> NPs



**Scheme 3.** a) and b) In the Fe<sub>1-x</sub>Se system, crystal field splitting of the 3d-orbitals of Fe cations (Fe<sup>2+</sup>/Fe<sup>3+</sup>) at the octahedral site into 3-fold  $t_{2g}$  and 2-fold  $e_g$  states. c) At the tetrahedral site (Fe<sup>3+</sup>) into 2-fold  $e$  and 3-fold  $t_2$  states. Schematic illustration of exchange interactions in the system. d) Fe<sub>1-x</sub>Se exhibits the exchange interactions: the overlap of localized electronic orbitals on Fe ion sites is mediated through their common Se ion.

In the NiAs-type crystal structures of Fe<sub>3</sub>Se<sub>4</sub> and Fe<sub>7</sub>Se<sub>8</sub>, the cations are octahedrally coordinated by six anions (FeSe<sub>6</sub> octahedra), and the coordination polyhedron of anions is a trigonal prism created by six cations (SeFe<sub>6</sub> prisms).<sup>19</sup> In Fe<sub>1-x</sub>Se compounds, there are two types of Fe ionic states Fe<sup>2+</sup> and Fe<sup>3+</sup> along with ordered Fe vacancies.<sup>66–67</sup> These arrangements give rise to the magnetic behavior of the compounds. Each layer is of the ferromagnetic order in the opposite direction from the adjacent layer, resulting in the overall ferrimagnetic nature of the compound. Scheme 3a - b shows the Fe<sub>1-x</sub>Se system CFS of the d-orbitals at the octahedral site into 3-fold  $t_{2g}$  and 2-fold  $e_g$  states having the electronic configurations of  $t_{2g}^4/t_{2g}^3$  and  $e_g^2$  states of 3d Fe cations (Fe<sup>2+</sup>/Fe<sup>3+</sup>). The Fe<sup>2+</sup> and Fe<sup>3+</sup> ions are octahedrally coordinated with 4 and 5 unpaired electrons.<sup>66</sup> Scheme 3c shows the CFS of the d-orbitals at the tetrahedral site into 2-fold  $e$  and 3-fold  $t_2$  states having the electronic configurations of  $e^2$  and  $t_2^3$  states of 3d Fe<sup>3+</sup>. The coupling is present between Fe ions. The overlap of the localised electronic orbital on Fe ion sites is facilitated by their shared Se ion, and these compounds display exchange interactions. For visualization, the exchange interactions in the Fe<sub>1-x</sub>Se system are shown in Scheme 3d with the superexchange interaction in Fe<sup>3+</sup> octahedron–octahedron example. The exchange interaction between Fe-Fe and other Fe-Se-Fe is also present in these compounds.



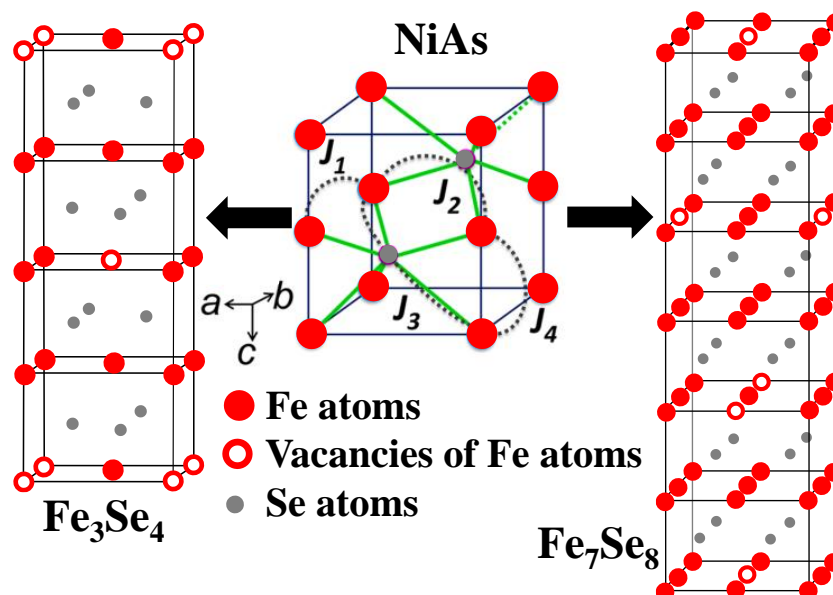
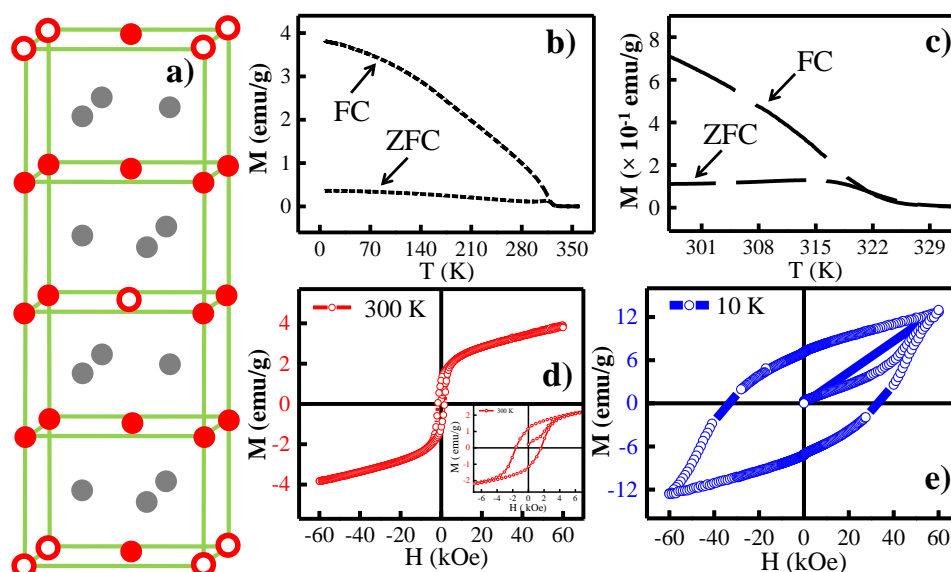


**Figure 2.** Schematic of the unit cell of NiAs type crystal structure of  $\text{Fe}_{1-x}\text{Se}$  compound. The intralayer direct Fe-Fe and  $96.3^\circ$ -superexchange Fe-Se-Fe bonds are shown by dashed lines with  $J_1$  and  $J_2$ , respectively and the interlayer  $127.6^\circ$ - and  $70^\circ$ - superexchange Fe-Se-Fe bonds are shown by dashed lines with  $J_3$  and  $J_4$ , respectively. The unit cell of the  $\text{Fe}_3\text{Se}_4$  and  $\text{Fe}_7\text{Se}_8$  crystal structure of the NiAs-type with cation vacancies.

The NiAs-type crystal structure are the fundamental crystal structure of  $\text{Fe}_{1-x}\text{Se}$  superstructures with cation vacancies. The NiAs type crystal structure has 4 interlayer and intralayer exchange contacts, as shown in Figure 2.<sup>67</sup> The  $J_1$  (Fe—Fe ferromagnetic interaction) is expected to be modest because of the huge Fe—Fe distance ( $\sim 3.6 \text{ \AA}$ ). The Fe—Se—Fe superexchange interaction, which comprises the 3 Se ions below and above the Fe layer, is denoted by the  $J_2$ . Fe—Se—Fe has a binding angle of  $96.3^\circ$  and a Fe—Se distance of  $2.6 \text{ \AA}$ . Despite having identical Fe—Se bond distances ( $2.6\text{--}2.7 \text{ \AA}$ ), the interlayer Fe—Se—Fe superexchange interactions may be separated into 2 non-equivalent bonds. For an antiferromagnetic interaction ( $J_3 < 0$ ), only Fe—Se—Fe bonds with an angle of  $\sim 127.6^\circ$  are effective. There is no effective d—p interaction for bonds with a  $70^\circ$  angle ( $J_4$ ). Intralayer interactions and certain Fe—Se—Fe superexchange interactions are thus weaker than  $127.6^\circ$  Fe—Se—Fe superexchange interactions, i.e.  $J_3 \gg J_4 > J_2 > J_1$ .

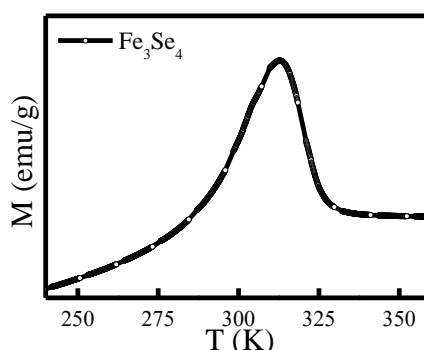
In bulk<sup>66–68</sup> as well as at nano-dimensions<sup>69</sup>, both the compounds show ferrimagnetic behaviour due to the presence of ordered iron vacancies in alternate layers (Figure 3a and 5a). The ferromagnetically aligned spins inside each plane towards the c-axis and

antiferromagnetically oriented spins in a neighbouring plane are responsible for the ferrimagnetic ordering.<sup>66–68</sup>



**Figure 3.** a) Schematic of the unit cell of  $\text{Fe}_3\text{Se}_4$ , solid red circle represents the Fe cations, open red circles represent cations vacancies, and the solid grey circle represents the Se anions. b) Magnetization versus temperature (MT) curves for  $\text{Fe}_3\text{Se}_4$  (black curve) measured with an applied field of 100 Oe in FC and ZFC modes. c) Zoomed-view of MT curve. The VSM measured hysteresis loops of  $\text{Fe}_3\text{Se}_4$  with a field of  $\pm 60$  kOe at d) 300 K (red curves) and e) 10 K (blue curves).

$\text{Fe}_3\text{Se}_4$  ( $\text{Fe}^{2+}\text{Fe}_2^{3+}\text{Se}_4^{2-}$ ) has a monoclinic NiAs-type crystal structure with the lattice parameters  $a=6.167$  Å,  $b=3.537$  Å, and  $c=11.17$  Å having the  $I2/m$  space group (Figure 3a).<sup>12,66</sup> In Figure 3b - c, the magnetization ZFC and FC of  $\text{Fe}_3\text{Se}_4$  show bifurcation below 330 K and the Curie transition temperature is nearly 322 K, below which it goes into a ferrimagnetic phase. These results are also in line with the previous findings of  $T_C \sim 320$  K in  $\text{Fe}_3\text{Se}_4$ .<sup>11,25,34</sup>



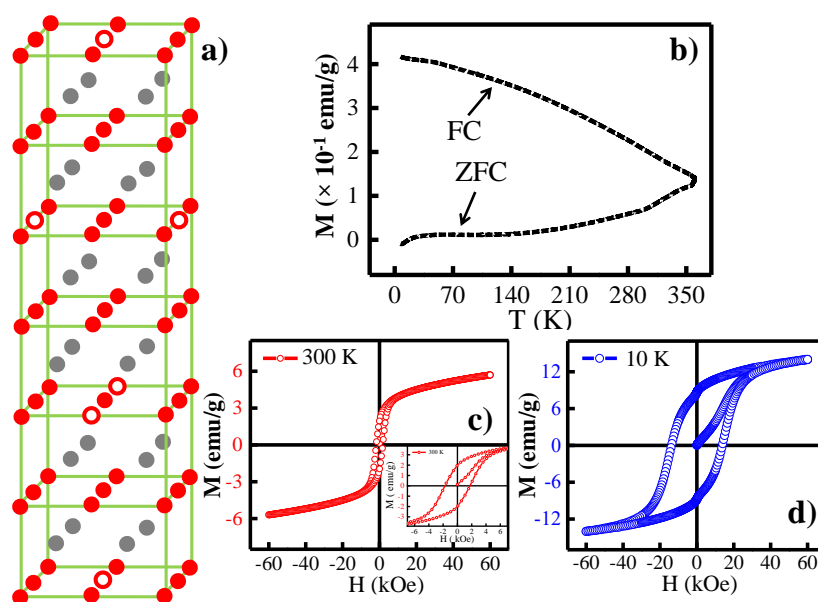
**Figure 4.** Zoomed-in view of magnetization vs. temperature (ZFC) curves of  $\text{Fe}_3\text{Se}_4$  NPs provides the superparamagnetic blocking temperature at the peak position.

Figure 4 reveals the zoomed in-view of the M-T curves in the ZFC mode, illustrating an average blocking temperature of  $\sim 313$  K with a peak in the ZFC curve. Consequently, ferrimagnetism exists in  $\text{Fe}_3\text{Se}_4$  nanorods with a transition temperature of 322 K.

Furthermore, this material reveals semi-hard magnetic properties at nanoscale.<sup>11,25,34</sup> In earlier reports, for  $\text{Fe}_3\text{Se}_4$  nanoplatelets, the observed coercivity was  $\sim 4$  kOe at 300 K, which increases to  $\sim 40$  kOe at 10 K for 90 kOe of the maximum external field.<sup>25</sup> The coercivity values for  $\text{Fe}_3\text{Se}_4$  nanorods at 300 K were reported as  $\sim 3.4$  kOe<sup>25</sup> and 2.74 kOe<sup>34</sup>. It was also reported that at 10 K temperature, the coercivity values increased almost 10-fold, that is 36 kOe<sup>25</sup> and 29.5 kOe<sup>34</sup> with 90 kOe of a maximum external field. The as-synthesized  $\text{Fe}_3\text{Se}_4$  nanorods reported in this article also exhibited semi-hard magnetic properties, and their hysteresis curves were recorded at 300 K (red curve), and 10 K (blue curve) for a field sweep up to  $\pm 60$  kOe are shown in Figure 3d - e, respectively. These hysteresis loops showed the non-linear behavior typical of the ferrimagnetic nature of  $\text{Fe}_3\text{Se}_4$  NPs as reported in the literature.<sup>11,25,34</sup> The  $H_C$  and  $M_R$  values of  $\text{Fe}_3\text{Se}_4$  were determined to be 1.6 kOe and 1.2 emu/g, respectively, which are relatively low compared to the reported data due to the reduced size of NPs.<sup>11,25,34</sup> All the phases were synthesized at minimal possible temperature with an appropriate time. Thus, the pure  $\text{Fe}_3\text{Se}_4$  phase reaction started from this stage, and growth was terminated by stopping the reaction that resulted in small NPs. A decrease in the particle size below its single domain size is known to decrease its magnetization.<sup>11</sup> Second, as the particle size decreased, the surface-to-volume ratio increased, resulting in a more significant number of surface spins per unit volume. The surface spins were uncompensated and remained disordered or canted, leading to the overall magnetization reduction with a decreased particle size.<sup>11</sup>

A massive rise in coercivity was seen at lower temperatures, and  $H_C$  increased nearly 20-fold to about 32 kOe at 10 K, and  $M_R$  increased to 7.3 emu/g, which is in perfect accordance with previous findings.<sup>11,25,34</sup> At a lower temperature, the coercivity may increase by various contributions— the reduced thermal activation energy that makes more and more spins available to orient in the field direction, the increase in the overall effective magnetic anisotropy, ferrimagnetism, and so forth.<sup>11</sup> The  $\text{Fe}_3\text{Se}_4$  NPs also induced an oxidation layer; however, their effect on overall magnetism is negligible. This compound is highly magnetized, and any small contribution will not affect the overall magnetic behavior.

$\text{Fe}_7\text{Se}_8$  ( $\text{Fe}_5^{2+}\text{Fe}_2^{3+}\text{Se}_8^{2-}$ ) has a hexagonal NiAs-type crystal structure.<sup>68,70</sup> As presented in Figure 5a, the lattice parameters  $a=7.21$  Å and  $c=17.67$  Å have the  $P3_121$  space group.<sup>68,70</sup> The divergence of magnetization ZFC and FC curves of  $\text{Fe}_7\text{Se}_8$  over the whole range of temperature up to 360 K, as shown in Figure 5b, signifies the formation of an ordered magnetic state, which may be due to the high  $T_C$  of the sample (Curie transition temperature lies above 360 K).<sup>19</sup> Thus, the  $\text{Fe}_7\text{Se}_8$  NPs are strongly coupled due to the magnetic interactions. The field dependence magnetization curve of as-synthesized  $\text{Fe}_7\text{Se}_8$  NPs exhibits a ferrimagnetic nature at both the temperature (300 and 10 K) as presented in Figures 5 c,d.



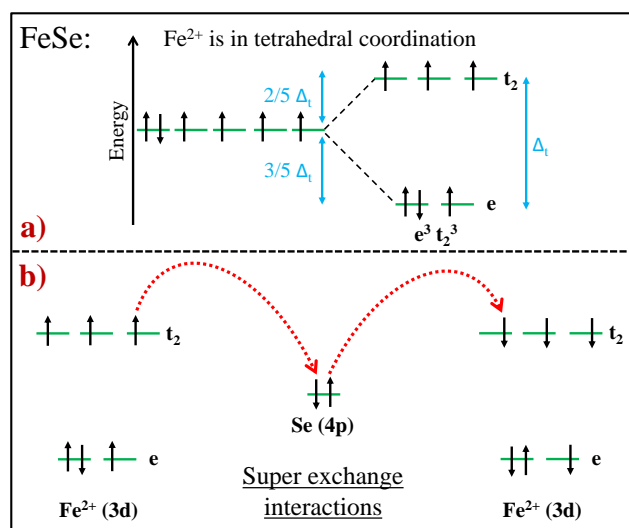
**Figure 5.** a) Schematic of the unit cell of  $\text{Fe}_7\text{Se}_8$ , solid red circle represents the Fe cations, open red circles represent cations vacancies, and the solid grey circle represents the Se anions. b) Magnetization versus temperature curves for  $\text{Fe}_7\text{Se}_8$  (black curve) measured with an applied field of 100 Oe in FC and ZFC modes. Hysteresis loops of  $\text{Fe}_7\text{Se}_8$  were measured by the VSM with a field of  $\pm 60$  kOe at c) 300 K (red curves) and d) 10 K (blue curves).

It is observed that the  $\text{Fe}_7\text{Se}_8$  NPs exhibit the hysteresis with  $M_R$  of 2 emu/g at 300 K and 8.6 emu/g at 10 K. They also exhibit a  $H_C \sim 1.8$  kOe at 300 K, which increase to  $\sim 13.8$  kOe at 10 K. At a lower temperature, the magnetic parameters may increase by various contributions as discussed above for  $\text{Fe}_3\text{Se}_4$ . Here also, oxidation layer induces at the surface; however, as in the case of  $\text{Fe}_3\text{Se}_4$  the effect on overall magnetism is negligible due to the high magnetization of the fundamental compound.

However, both the compounds ( $\text{Fe}_3\text{Se}_4$  and  $\text{Fe}_7\text{Se}_8$ ) exhibit a ferrimagnetic nature and their fundamental unit cell is also the same (NiAs-type).<sup>66–68</sup> However, the ratio of the Fe

cations and the arrangement of atoms, including cation vacancies, are different in both the compounds, which results in a distinct magnitude of ferrimagnetism. According to spin only moment,  $5\mu_B$  value is for  $\text{Fe}^{3+}$  ions having 5d-electrons and  $4\mu_B$  is for the  $\text{Fe}^{2+}$  ions having 6d-electrons.<sup>66</sup> However, the electrons are lost due to the delocalization of d-electrons and/or the covalency effect.<sup>66</sup> The observed moment values in  $\text{Fe}_7\text{Se}_8$  are from covalency effects of about 25% for both kinds of ions. The moment further reduces in  $\text{Fe}_3\text{Se}_4$  that can be ascribed to an increased covalency effect due to the lattice contraction.<sup>66</sup> Additionally, in  $\text{Fe}_3\text{Se}_4$ , the delocalization of some of the d-electrons is brought about by the short metal-to-metal distance along the c-axis. These 3-d electrons are connected with the metal-to-metal distance along c-axis, and the distance reduces from 2.94 Å to 2.79 Å upon going from  $\text{Fe}_7\text{Se}_8$  to  $\text{Fe}_3\text{Se}_4$ .<sup>66</sup> Thus, the magnetic ordering is different in both compounds because of the delocalization of the 3-d electrons and covalency effect. Besides,  $\text{Fe}_7\text{Se}_8$  requires more thermal energy to reduce the magnetic ordering than  $\text{Fe}_3\text{Se}_4$ . Therefore, as the amount of Se in NiAs-type compounds grows, the magnetic transition temperature rises progressively.

### 4.3.3 Magnetic property of the FeSe NPs



**Scheme 4.** a) In the  $\beta$ -FeSe compound, crystal field splitting of the 3d-orbitals of  $\text{Fe}^{2+}$  at the tetrahedral site into 2-fold  $e$  and 3-fold  $t_2$  states. b) Schematic illustration of exchange interactions in the system. The compound exhibits the superexchange interactions: the oxidation states of iron ions are the same. In this interaction, the overlap of localized electronic orbitals on Fe ion sites is mediated through their common Se ion.

Scheme 4a shows the  $\beta$ -FeSe system and CFS of the d-orbitals of  $\text{Fe}^{2+}$  at the tetrahedral site into 2-fold  $e$  and 3-fold  $t_2$  states having the electronic configurations of  $e^3$  and  $t_2^3$  states of

$3d\text{ Fe}^{2+}$ . Scheme 4b shows a schematic illustration of exchange interactions in the  $\beta\text{-FeSe}$ . This compound exhibits superexchange interactions.<sup>71–73</sup> The  $\beta\text{-FeSe}$  ( $\text{Fe}^{2+}\text{Se}^{2-}$ ) has a tetragonal PbO-type crystal structure with the lattice parameters  $a=3.765\text{ \AA}$  and  $c=5.518\text{ \AA}$  having the  $P4/nmm$  SG, as shown in Figure 6a.<sup>27</sup> In this compound, each cation is tetrahedrally-coordinated with four anions ( $\text{FeSe}_4$  tetrahedra), and each anion is tetrahedrally-coordinated with four cations ( $\text{SeFe}_4$  tetrahedra).<sup>14, 27</sup>

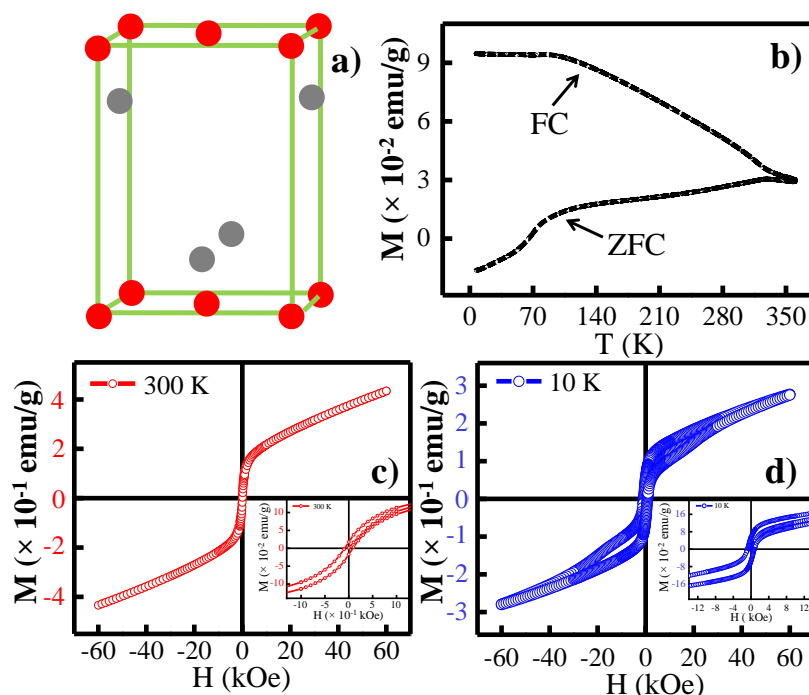


**Figure 6.** a) Schematic of the unit cell of  $\beta\text{-FeSe}$ , solid red circle represents the Fe cations, and the solid grey circle represents the Se anions. b) Magnetization versus temperature curves for  $\beta\text{-FeSe}$  (black curve) measured with an applied field of 100 Oe in FC and ZFC modes. Hysteresis loops of  $\beta\text{-FeSe}$  were measured by the VSM with a field of  $\pm 60$  kOe at c) 300 K (red curves) and d) 10 K (blue curves).

Figure 6b shows the ZFC and FC curve of  $\beta\text{-FeSe}$ . A magnetic anomaly has developed around 80 - 100 K, more prominent in the FC curve. It is known that the tetragonal phase undergoes structural transitions upon cooling. These magnetic deviations are nearly at the same temperature as observed in resistive measurements by Hsu et al.<sup>27</sup> They reported that the  $\beta\text{-FeSe}$  having a tetragonal structure with space group  $P4/nmm$  transforms into the triclinic structure with space group  $P-1$  at  $\sim 100$  K by temperature-dependent XRD.<sup>27</sup> In another study, Margadonna et al.<sup>74</sup> observed that upon cooling, the  $\beta\text{-FeSe}$  phase (tetragonal  $P4/nmm$ ) demonstrate a structural transition from tetragonal to the lower symmetry orthorhombic  $Cmma$

phase at nearly 70 K. Depending on the stoichiometry of the materials, the transition occurs over a wide temperature range (about 70–100 K).<sup>75</sup> and could be observed by temperature-dependent measurements. It is appropriate to conclude that the observed magnetic anomaly in ZFC and FC curves is due to the phase transition of the  $\beta$ -FeSe phase.

Furthermore, the field dependence magnetization was examined to acquire better understanding for the magnetic properties of  $\beta$ -FeSe at the nanoscale. In Figures 6c-d, the hysteresis loops of  $\beta$ -FeSe are non-linear and revealed the magnetic nature of NPs having a  $H_C$  and a  $M_R$  of 84 Oe and  $1.8 \times 10^{-2}$  emu/g at 300 K, respectively that increased to about 761 Oe and 0.1 emu/g at 10 K (blue curve in Figure 6d)). As in the case of FeSe<sub>2</sub>, the  $\beta$ -FeSe NPs also induced the oxidation layer, which affects the overall magnetic behavior. Therefore, the observed properties are of surfaced oxidized  $\beta$ -FeSe NPs. The non-uniform curve at 10 K may be attributed to fundamental  $\beta$ -FeSe and the surface oxidized layer.

Moreover, here it is essential to discuss the superconductivity of synthesized  $\beta$ -FeSe. It is known that  $\beta$ -FeSe shows a superconducting transition at  $\sim 8$  K.<sup>27</sup> Greenfield et al.<sup>29</sup> reported that exposure to oxygen will lead to a non-superconducting specimen of  $\beta$ -FeSe. Even in a short amount of time, specimen exposed to oxygen, air, or ambient conditions will lose their superconducting. They<sup>29</sup> demonstrated this by creating three samples: sample I (exposed to air), sample II (free from air; manufactured and treated in an inert atmosphere), and sample III (free from air/H<sub>2</sub>O; manufactured and treated in an inert atmosphere; vacuum-degassed at 100 °C and residual water removed). Sample I showed antiferromagnetic ordering; however, sample III did not demonstrate antiferromagnetic ordering and instead indicated the classic superconducting transition at 8 K. Sample II exhibited the intermediate magnetic properties. Thus, the magnetic ordering and superconductivity are competitive in  $\beta$ -FeSe. The exposure of air or water appeared to completely suppress the superconductivity and allow the magnetic ordering to persist.<sup>29</sup> In this work, the as-synthesized  $\beta$ -FeSe exhibits the magnetic ordering due to surface oxidation of NPs, while the superconductivity is completely suppressed.

#### 4.3.4 Magnetic properties of the Fe-Se system

A simple one-pot thermal decomposition route has been used to prepare the Fe-Se system with various phases, such as FeSe<sub>2</sub>, Fe<sub>3</sub>Se<sub>4</sub>, Fe<sub>7</sub>Se<sub>8</sub>, and  $\beta$ -FeSe. In contrast with bulk, FeSe<sub>2</sub> shows magnetic ordering at nanoscale due to the presence of oxide surface in NPs. The findings of magnetization studies in relation to temperature and applied field clearly show that surface oxidised FeSe<sub>2</sub> NPs have magnetic ordering at the nanoscale. As discussed in the above section

(also explained in our previous chapter<sup>14</sup>), XPS analysis confirms that materials readily undergo surface oxidation when exposed to air. Exposure to the atmosphere induces the magnetic behavior in the FeSe<sub>2</sub> compound. The oxygen atoms in the atmosphere are most likely to create a crucial localised magnetic moment on nearby Fe atoms, leading to magnetic ordering at the nanoscale. Superparamagnetism transition known as blocking temperature occurs in FeSe<sub>2</sub> and Fe<sub>3</sub>Se<sub>4</sub> NPs at around 45 and 313 K, respectively. The ferrimagnetic nature is present in the two Fe<sub>1-x</sub>Se compounds due to the number of vacancies and their ordering on every second metal layer. The shift from stoichiometry results in the formation of Fe vacancies on every second metal layer that are distributed as far apart as possible. Besides, Fe<sub>3</sub>Se<sub>4</sub> NPs show ferrimagnetic behavior with large magnetic coercivity at 300 K, which increases about 20 times at 10 K with a Curie transition temperature of ~322 K. The other NiAs based structure (Fe<sub>7</sub>Se<sub>8</sub>) also shows ferrimagnetic properties at both 10 and 300 K with a transition temperature greater than the measured temperature (360 K). The  $\beta$ -FeSe NPs reveal a deviation around 80 - 100 K due to phase transition. These NPs also show a magnetic ordering at 10 and 300 K with higher magnetization and coercivity values at 10 K. The  $\beta$ -FeSe also exhibits the magnetic ordering due to surface oxidation and completely suppresses the superconductivity nature. The surface oxidation occurs in all phases of Fe-Se system. However, in the case of Fe<sub>3</sub>Se<sub>4</sub> and Fe<sub>7</sub>Se<sub>8</sub>, the effect on magnetism is negligible due to the high magnetic nature of these compounds. While in FeSe<sub>2</sub> and  $\beta$ -FeSe, the surface oxidation affects the magnetic behavior of the fundamental compounds.

**Table 1.** The magnetic parameters—coercivity ( $H_C$ ), remanence ( $M_R$ ), and magnetization at 60 kOe ( $M_{60\text{ kOe}}$ ) for various phases of Fe-Se system are compared at 300 K and 10 K.

Parameters Phase	Size	$H_C$ (Oe)		$M_R$ (emu/g)		$M_{60\text{ kOe}}$ (emu/g)		Bulk $M_s$ (emu/g) (at 9 kOe)	Bulk $M_s$ (Gauss) (at 9 kOe)
	Width of Nanorods	300 K	10 K	300 K	10 K	300 K	10 K	78 K	78 K
FeSe <sub>2</sub>	~30 nm	8	200	$2.0 \times 10^{-4}$	0.4	0.09	2.30	-	-
Fe <sub>3</sub> Se <sub>4</sub>	~45 nm	1615	33360	1.2	7.4	3.88	13.17	0.16	15
Fe <sub>7</sub> Se <sub>8</sub>	~30 nm	1800	13800	2	8.6	5.70	14.01	0.4	35
$\beta$ -FeSe	~20 nm	84	761	$1.8 \times 10^{-2}$	0.1	0.43	0.28	0.12	7



These findings show that a simple one-pot thermal breakdown method may yield iron selenide NPs in any of the four phases, with significantly diverse physical characteristics and, more importantly, radically different magnetic properties. The magnetic parameters of the Fe-Se system at both temperatures are tabulated in Table 1. The coercivity and saturation magnetization values ( $M_{60 \text{ kOe}}$ ) for all the above phases of iron selenide NPs at 300 and 10 K are compared in Figure 7.

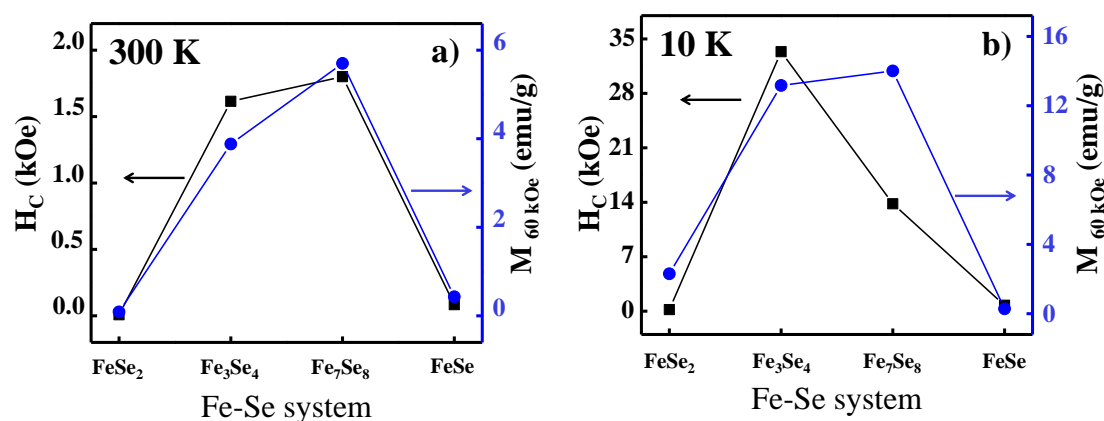


**Figure 7.** Magnetic parameters measured for the Fe-Se system at 300 K and 10 K.  $H_C$  and  $M_{60 \text{ kOe}}$  denotes coercivity and saturation magnetization at 60 kOe, respectively.

Remarkably higher magnetization and coercivity (Figure 7) are observed in both the NiAs based compounds ( $\text{Fe}_3\text{Se}_4$  and  $\text{Fe}_7\text{Se}_8$  NPs) as compared with the other two compounds ( $\text{FeSe}_2$  and  $\beta\text{-FeSe}$  NPs) because of the presence of Fe vacancies, crystal field environment around Fe-ions, two types of Fe cations, magnetic anisotropy and so forth. These values increase hugely at 10 K for the  $\text{Fe}_{1-x}\text{Se}$  compounds (Figure 7b). Thus, it is possible to customize the magnetic properties of iron selenides by controlling their phase structure. The well-regulated magnetism may lead to broad applications of magnetic carriers in storage devices, biomedicine, and catalysts.

#### 4.4 Conclusions

A simple, one-pot, thermal decomposition approach has been used to fabricate various phases of iron selenide NPs. The distinct arrangement of Fe and Se atoms results in drastically varying magnetic properties due to the change in  $\text{Fe}^{2+}/\text{Fe}^{3+}$  ratio, crystal field environment around Fe-ions, magnetocrystalline anisotropy, Fe-vacancies, and so forth. The findings reported in this study explain the excellent tuneability of magnetism in the Fe-Se system at the nanoscale. The two NiAs based phases – $\text{Fe}_3\text{Se}_4$  and  $\text{Fe}_7\text{Se}_8$ , are ferrimagnetic below  $\sim 300$  K and show semi-

hard magnetic properties. The other two phases  $\alpha$ -FeSe<sub>2</sub> and  $\beta$ -FeSe exhibit weaker magnetism and are less recognized for their magnetic properties. The surface oxidation remarkably affects the magnetic properties, especially on the phases with weak magnetization, such as FeSe<sub>2</sub> and  $\beta$ -FeSe. The surface-oxidized FeSe<sub>2</sub> and  $\beta$ -FeSe show magnetic ordering at the nanoscale. FeSe<sub>2</sub> and Fe<sub>3</sub>Se<sub>4</sub> NPs exhibit superparamagnetic transition at the blocking temperatures of ~45 and 313 K, respectively. Also, the Fe<sub>3</sub>Se<sub>4</sub> NPs show ferrimagnetism at 300 K with a large magnetic coercivity which multiplies at low temperatures. The Fe<sub>7</sub>Se<sub>8</sub> NPs show ferrimagnetism at all temperatures with a transition temperature higher than 360 K. The  $\beta$ -FeSe NPs indicate magnetic ordering at both the temperatures with a magnetic anomaly at around 80 - 100 K due to phase transition. The simple thermal decomposition route has been proven to be a brilliant method to synthesize any four phases in the Fe-Se system at the nanoscale with unique magnetic properties in each phase. This is an excellent approach to meet the specific needs of storage devices, biomedicine, and catalyst applications.

## 4.5 References

- (1) Santhoshkumar, P.; Nagaraju, G.; Shaji, N.; Sim, G. S.; Nanthagopal, M.; Sekhar, S. C.; Yu, J. S.; Lee, C. W. Hierarchical Iron Selenide Nanoarchitecture as an advanced Anode Material for high-Performance Energy Storage Devices. *Electrochim. Acta.* **2020**, *356*, 136833.
- (2) Sun, W.; Li, Y.; Liu, S.; Liu, C.; Tan, X.; Xie, K. Mechanism investigation of Iron Selenide as Polysulfide mediator for Long-Life Lithium-Sulfur Batteries. *Chem. Eng. J.* **2021**, *416*, 129166.
- (3) Zhao, F.; Shen, S.; Cheng, L.; Ma, L.; Zhou, J.; Ye, H.; Han, N.; Wu, T.; Li, Y.; Lu, J. Improved Sodium-Ion Storage Performance of Ultrasmall Iron Selenide Nanoparticles. *Nano Lett.* **2017**, *17*, 4137–4142.
- (4) Pandit, B.; Rondiya, S. R.; Shegokar, S.; Bommineedi, L. K.; Cross, R. W.; Dzade N. Y.; Sankapal, B. R. Combined Electrochemical and DFT investigations of Iron Selenide: a Mechanically Bendable Solid-State Symmetric Supercapacitor. *Sustainable Energy Fuels* **2021**, *5*, 5001-5012.
- (5) Fan, H.; Yu, H.; Zhang, Y.; Guo, J.; Wang, Z.; Wang, H.; Zhao, N.; Zheng, Y.; Du, C.; Dai, Z.; Yan, Q.; Xu, J. 1D to 3D Hierarchical Iron Selenide hollow Nanocubes assembled from FeSe<sub>2</sub>@C Core-Shell Nanorods for advanced Sodium Ion Batteries. *Energy Storage Mater.* **2018**, *10*, 48–55.
- (6) Thanikaikarasan, S.; Perumal, R.; Marjorie, S. R. Influence of Potential on Structural, Compositional, Optical and Magnetic Properties of Electrochemically grown Iron Selenide Thin Films. *J. Alloys Compd.* **2020**, *848*, 156348.
- (7) Guterding, D.; Jeschke, H. O.; Valentí, R. Basic Electronic Properties of Iron Selenide under variation of Structural Parameters. *Phys. Rev. B.* **2017**, *96*, 125107.
- (8) Rodriguez, J. P. Spin Resonances in Iron Selenide high-T<sub>c</sub> Superconductors by Proximity to a hidden Spin Density Wave. *Phys. Rev. B.* **2020**, *102*, 024521.

- (9) Lu, S.; Wu, H.; Xu, S.; Wang, Y.; Zhao, J.; Li, Y.; Abdelkader, A. M.; Li, J.; Wang, W.; Xi, K.; Guo, Y.; Ding, S.; Gao, G.; Kumar, R. V. Iron Selenide Microcapsules as Universal Conversion-Typed Anodes for Alkali Metal-Ion Batteries. *Small* **2021**, *17*, 2005745.
- (10) Ulbrich, K. F.; Campos, C. E. M. Stability of Iron Selenide Nanophases prepared by Mechanochemistry. *AIP Adv.* **2019**, *9*, 045311.
- (11) Ghalawat, M.; Poddar, P. Study of Growth Kinetics of Fe<sub>3</sub>Se<sub>4</sub> Nanocrystallites and the Influence of Size and Shape Tunability on their Magnetic Properties. *J. Phys. Chem. C* **2021**, *125*, 7932–7943.
- (12) Okazaki, A.; Hirakawa, K. Structural Study of Iron Selenides FeSe<sub>x</sub>. I Ordered Arrangement of Defects of Fe Atoms. *J. Phys. Soc. Jpn.* **1956**, *11*, 930–936.
- (13) Schuster, W.; Mikler, H.; Komarek, K. L. Transition Metal-Chalcogen Systems, VII.: The Iron-Selenium Phase Diagram. *Monatsh. Chem.* **1979**, *110*, 1153–1170.
- (14) Ghalawat, M.; Poddar, P. Study of the Phase-Evolution Mechanism of an Fe–Se System at the Nanoscale: Optimization of Synthesis Conditions for the Isolation of Pure Phases and Their Controlled Growth. *Langmuir* **2020**, *36*, 2012–2022.
- (15) Hagg, G.; Kindstrom, A. L. Röntgenuntersuchung am System Eisen-Selen. *Z. Phys. Chem.* **1933**, *22*, 453–464.
- (16) Patel, U.; Hua, J.; Yu, S. H.; Avci, S.; Xiao, Z. L.; Claus, H.; Schlueter, J.; Vlasko-Vlasov, V. V.; Welp, U.; Kwok, W. K. Growth and Superconductivity of FeSe<sub>x</sub> crystals. *Appl. Phys. Lett.* **2009**, *94*, 082508.
- (17) Okamoto, H. The Fe-Se (Iron-Selenium) System. *JPE* **1991**, *12*, 383–389.
- (18) Pomjakushina, E.; Conder, K.; Pomjakushin, V.; Bendele, M.; Khasanov, R. Synthesis, Crystal Structure, and Chemical Stability of the Superconductor FeSe<sub>1-x</sub>. *Phys. Rev. B* **2009**, *80*, 024517.
- (19) Lyubutin, I. S.; Lin, C.-R.; Funtov, K. O.; Dmitrieva, T. V.; Starchikov, S. S.; Siao, Y.-J.; Chen, M.-L. Structural, Magnetic, and Electronic Properties of Iron Selenide Fe<sub>6-7</sub>Se<sub>8</sub> Nanoparticles Obtained by Thermal Decomposition in High-Temperature Organic Solvents. *J. Chem. Phys.* **2014**, *141*, 044704.
- (20) Mao, X.; Kim, J.-G.; Han, J.; Jung, H. S.; Lee, S. G.; Kotov, N. A.; Lee, J. Phase-Pure FeSe<sub>x</sub> (x = 1, 2) Nanoparticles with One- and Two-Photon Luminescence. *J. Am. Chem. Soc.* **2014**, *136*, 7189–7192.
- (21) Yuan, B.; Luan, W.; Tu, S. T. One-Step Synthesis of Cubic FeS<sub>2</sub> and Flower-like FeSe<sub>2</sub> Particles by a Solvothermal Reduction Process. *Dalton Trans.* **2012**, *41*, 772–776.
- (22) Yuan, B.; Hou, X.; Han, Y.; Luan, W.; Tu, S. T. Facile Synthesis of Flake-like FeSe<sub>2</sub> Particles in Open-Air Conditions. *New J. Chem.* **2012**, *36*, 2101–2105.
- (23) Hirone, T.; Chiba, S. The Magnetic Properties of FeSe<sub>x</sub> with the NiAs Structure. *J. Phys. Soc. Jpn.* **1956**, *11*, 666–670.
- (24) Gao, M.-R.; Lin, Z.-Y.; Jiang, J.; Yao, H.-B.; Lu, Y.-M.; Gao, Q.; Yao, W.-T.; Yu, S.-H. Selective Synthesis of Fe<sub>7</sub>Se<sub>8</sub> Polyhedra with Exposed High-Index Facets and Fe<sub>7</sub>Se<sub>8</sub> Nanorods by a Solvothermal Process in a Binary Solution and Their Collective Intrinsic Properties. *Chemistry*. **2011**, *17*, 5068–5075.
- (25) Zhang, H.; Long, G.; Li, D.; Sabirianov, R.; Zeng, H. Fe<sub>3</sub>Se<sub>4</sub> Nanostructures with Giant Coercivity Synthesized by Solution Chemistry. *Chem. Mater.* **2011**, *23*, 3769–3774.

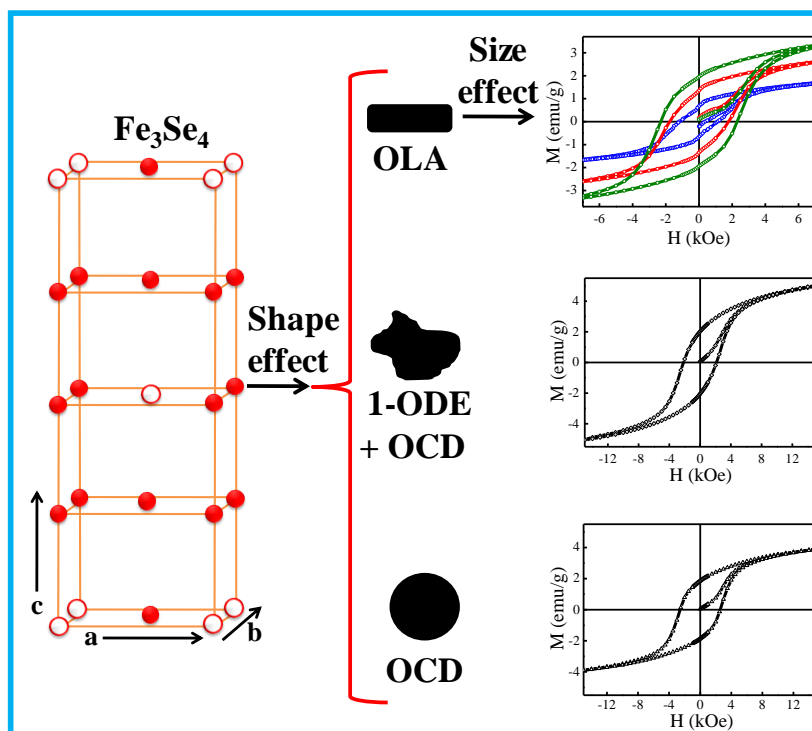
- (26) Long, G.; Zhang, H.; Li, D.; Sabirianov, R.; Zhang, Z.; Zeng, H. Magnetic Anisotropy and Coercivity of Fe<sub>3</sub>Se<sub>4</sub> Nanostructures. *Appl. Phys. Lett.* **2011**, *99*, 202103.
- (27) Hsu, F.-C.; Luo, J.-Y.; Yeh, K.-W.; Chen, T.-K.; Huang, T.-W.; Wu, P. M.; Lee, Y.-C.; Huang, Y.-L.; Chu, Y.-Y.; Yan, D.-C.; Wu, M.-K. Superconductivity in the PbO-Type Structure  $\alpha$ -FeSe. *PNAS* **2008**, *105*, 14262–14264.
- (28) Wu, X. J.; Shen, D. Z.; Zhang, Z. Z.; Zhang, J. Y.; Liu, K. W.; Li, B. H.; Lu, Y. M.; Yao, B.; Zhao, D. X.; Li, B. S.; Shan, C. X.; Fan, X. W.; Liu, H. J.; Yang, C. L. On the Nature of the Carriers in Ferromagnetic FeSe. *Appl. Phys. Lett.* **2007**, *90*, 112105.
- (29) Greenfield, J. T.; Kamali, S.; Lee, K.; Kovnir, K. A Solution for Solution-Produced  $\beta$ -FeSe: Elucidating and Overcoming Factors that Prevent Superconductivity. *Chem. Mater.* **2015**, *27*, 588–596.
- (30) Ganga, B. G.; Ganeshraj, C.; Krishna, A. G.; Santhosh, P. N. Electronic and Optical Properties of FeSe<sub>2</sub> Polymorphs: Solar Cell Absorber. *arXiv preprint 6 March 2013*, arXiv:1303.1381v1.
- (31) Thanikaikarasan, S.; Mahalingam, T.; Sundaram, K.; Kathalingam, A.; Kim, Y. D.; Kim, T. Growth and Characterization of Electrosynthesized Iron Selenide Thin Films. *Vacuum* **2009**, *83*, 1066–1072.
- (32) Bishwas, M. S.; Poddar, P. Discovery of Room Temperature Multiferroicity and Magneto-electric Coupling in Fe<sub>3</sub>Se<sub>4</sub> Nanorods. *arXiv preprint 20 Dec 2016*, arXiv:1612.06512.
- (33) Singh, D.; Gupta, S. K.; He, H.; Sonvane, Y. Prediction of new multiferroic and magnetoelectric material Fe<sub>3</sub>Se<sub>4</sub>. *arXiv preprint 27 May 2018*, arXiv:1805.10607.
- (34) Bishwas, M. S.; Das, R.; Poddar, P. Large Increase in the Energy Product of Fe<sub>3</sub>Se<sub>4</sub> by Fe-Site Doping. *J. Phys. Chem. C* **2014**, *118*, 4016–4022.
- (35) Liu, L.; Kou, H. Z.; Mo, W.; Liu, H.; Wang, Y. Surfactant-Assisted Synthesis of  $\alpha$ -Fe<sub>2</sub>O<sub>3</sub> Nanotubes and Nanorods with Shape-Dependent Magnetic Properties. *J. Phys. Chem. B* **2006**, *110*, 15218–15223.
- (36) Chatterjee, J.; Haik, Y.; Chen, C. J. Size Dependent Magnetic Properties of Iron Oxide Nanoparticles. *J. Magn. Magn. Mater.* **2003**, *257*, 113–118.
- (37) Park, T. J.; Papaefthymiou, G. C.; Viescas, A. J.; Moodenbaugh, A. R.; Wong, S. S. Size-Dependent Magnetic Properties of Single-Crystalline Multiferroic BiFeO<sub>3</sub> Nanoparticles. *Nano Lett.* **2007**, *7*, 766–772.
- (38) Ma, F.; Ma, J.; Huang, J.; Li, J. The Shape Dependence of Magnetic and Microwave Properties for Ni Nanoparticles. *J. Magn. Magn. Mater.* **2012**, *324*, 205–209.
- (39) Singh, A. K.; Srivastava, O. N.; Singh, K. Shape and Size-Dependent Magnetic Properties of Fe<sub>3</sub>O<sub>4</sub> Nanoparticles Synthesized Using Piperidine. *Nanoscale Res. Lett.* **2017**, *12*, 298.
- (40) Gabbasov, R. R.; Cherepanov, V. M.; Chuev, M. A.; Polikarpov, M. A.; Panchenko, V. Y. Size Effect of Mössbauer Parameters in Iron Oxide Nanoparticles. *Hyperfine Interact.* **2014**, *226*, 383–387.
- (41) Artus, M.; Tahar, L. B.; Herbst, F.; Smiri, L.; Villian, F.; Yaacoub, N.; Greneche, J.M.; Ammar, S.; Fievet, F. Size-Dependent Magnetic Properties of CoFe<sub>2</sub>O<sub>4</sub> Nanoparticles Prepared in Polyol. *J. Phys.: Condens. Matter.* **2011**, *23*, 506001.
- (42) Song, Q.; Zhang, Z. J. Shape Control and Associated Magnetic Properties of Spinel Cobalt Ferrite Nanocrystals. *J. Am. Chem. Soc.* **2004**, *126*, 6164–6168.
- (43) Tan, Y.; Zhuang, Z.; Peng, Q.; Li, Y. Room-Temperature Soft Magnetic Iron Oxide Nanocrystals:

- Synthesis, Characterization, and Size-Dependent Magnetic Properties. *Chem. Mater.* **2008**, *20*, 5029–5034.
- (44) Vasundhara, K.; Achary, S. N.; Deshpande, S. K.; Babu, P. D.; Meena, S. S.; Tyagi, A.K. Size Dependent Magnetic and Dielectric Properties of Nano  $\text{CoFe}_2\text{O}_4$  Prepared by a Salt Assisted Gel-Combustion Method. *J. Appl. Phys.* **2013**, *113*, 194101.
- (45) Rajendran, M.; Deka, S.; Joy, P. A.; Bhattacharya, A. K. Size-Dependent Magnetic Properties of Nanocrystalline Yttrium Iron Garnet Powders. *J. Magn. Magn. Mater.* **2006**, *301*, 212–219.
- (46) Reddy, V. A.; Pathak, N. P.; Nath, R. Particle Size Dependent Magnetic Properties and Phase Transitions in Multiferroic  $\text{BiFeO}_3$  Nano-Particles. *J. Alloys Compd.* **2012**, *543*, 206–212.
- (47) Ichiyanagi, Y.; Yamada, S. The Size-Dependent Magnetic Properties of  $\text{Co}_3\text{O}_4$  Nanoparticles. *Polyhedron.* **2005**, *24*, 2813–2816.
- (48) Chen, J. P.; Sorensen, C. M.; Klabunde, K.J.; Hadjipanayis, G.C.; Devlin, E.; Kostikas, A. Size-Dependent Magnetic Properties of  $\text{MnFe}_2\text{O}_4$  Fine Particles Synthesized by Coprecipitation. *Phys. Rev. B.* **1996**, *54*, 9288–9296.
- (49) Reddy, V. K.; Chetty, C. S. Mössbauer Studies in Fe-Se System. *Phys. status Solidi A* **1975**, *32*, 585–592.
- (50) Nouailhetas, Q.; Veneva, A. K.; Koblishka, M. R.; Naik S., P. K.; Schäfer, F.; Ogino, H.; Motz, C.; Berger, K.; Douine, B.; Slimani, Y.; Hannachi, E. Magnetic phases in Superconducting, Polycrystalline Bulk FeSe Samples. *AIP Adv.* **2021**, *11*, 015230.
- (51) Beiranvand, R.; Mehrabi, V. Structural, Electronic and Optical Properties of Bulk and Monolayer Iron Diselenide: A Density Functional Study. *Phys. Scr.* **2021**, *96*, 065803.
- (52) Lan, M.; Xiang, G.; Nie, Y.; Yang, D.; Zhang, X. The Static and Dynamic Magnetic Properties of Monolayer Iron Dioxide and Iron Dichalcogenides. *RSC Adv.* **2016**, *6*, 31758-31761.
- (53) Xu, J.; Jang, K.; Lee, J.; Kim, H. J.; Jeong, J.; Park, J. G.; Son, S. U. Phase-Selective Growth of Assembled  $\text{FeSe}_2$  Nanorods from Organometallic Polymers and Their Surface Magnetism. *Cryst. Growth Des.* **2011**, *11*, 2707–2710.
- (54) Işık, C.; Güler, N. K.; Gürsul, M.; Ekicibil, A.; Özçelik, B. The Physical and Magnetic Properties of  $\text{FeSe}_{11}$  Superconductor. *J. Phys.: Conf. Ser.* **2016**, *667*, 012002.
- (55) Shi, W.; Zhang, X.; Che, G.; Fan, W.; Liu C. Controlled Hydrothermal Synthesis and Magnetic Properties of Three-Dimensional  $\text{FeSe}_2$  Rod Clusters and Microspheres. *Chem. Eng. J.* **2013**, *215–216*, 508–516.
- (56) Sobhani, A.; Niasari, M. S. Synthesis and Characterization of  $\text{FeSe}_2$  Nanoparticles and  $\text{FeSe}_2/\text{FeO}(\text{OH})$  Nanocomposites by Hydrothermal Method. *J. Alloys Compd.* **2015**, *625*, 26–33.
- (57) Liu, A.; Chen, X.; Zhang, Z.; Jiang, Y.; Shi, C. Selective Synthesis and Magnetic Properties of  $\text{FeSe}_2$  and  $\text{FeTe}_2$  Nanocrystallites Obtained Through a Hydrothermal Co-reduction Route. *Solid State Commun.* **2006**, *138*, 538–541.
- (58) Oyetunde, T.; Omorogie, M. O.; O'Brien, P. Ferromagnetic  $\text{FeSe}_2$  from a Mixed Sulphur-Selenium Complex of Iron  $[\text{Fe}\{(\text{SePPh}_2\text{NPPh}_2\text{S})_2\text{N}\}_3]$  Through Pyrolysis. *Heliyon* **2020**, *6*, e03763.
- (59) Ulbrich, K. F.; Campos, C. E. M. Nanosized Tetragonal  $\beta$ -FeSe Phase obtained by Mechanical Alloying: Structural, Microstructural, Magnetic and Electrical Characterization. *RSC Adv.* **2018**, *8*, 8190-8198.

- (60) Lavina, B.; Downs, R. T.; Sinogeikin, S. The Structure of Ferroselite, FeSe<sub>2</sub>, at Pressures up to 46 GPa and Temperatures down to 50 K: A Single-Crystal Micro-Diffraction Analysis. *Crystals* **2018**, *8*, 289.
- (61) Garg, R.; Garg, V. K.; Nakamura, Y. Magnetic Properties of Iron Marcasite FeS<sub>2</sub>. *Hyperfine Interact.* **1991**, *67*, 447–452.
- (62) Kergommeaux, A. d.; Vincent, J. F.; Pron, A.; Bettignies, R. d.; Malaman, B.; Reiss P. Surface Oxidation of Tin Chalcogenide Nanocrystals Revealed by <sup>119</sup>Sn–Mössbauer Spectroscopy. *J. Am. Chem. Soc.* **2012**, *134*, 11659–11666.
- (63) Colombara, D.; Elanzeery, H.; Nicoara, N.; Sharma, N.; Claro, M.; Schwarz, T.; Koprek, A.; Wolter, M. H.; Melchiorre, M.; Sood, M.; Valle, N.; Bondarchuk, O.; Babbe, F.; Spindler, C.; Miredin, O. C.; Raabe, D.; Dale, P. J.; Sadewasser, S.; Siebentritt, S. Chemical Instability at Chalcogenide Surfaces Impacts Chalcopyrite Devices well Beyond the Surface. *Nat. Commun.* **2020**, *11*, 3634.
- (64) Guo, Y.; Zhou, S.; Zhao, J. Oxidation Behaviors of Two-dimensional Metal Chalcogenides. *ChemNanoMat.* **2020**, *6*, 838–849.
- (65) Albrecht, R.; Ruck, M. Chalcogenides by Reduction of their Dioxides in Ultra-Alkaline Media. *Angew. Chem. Int. Ed.* **2021**, *60*, 22570–22577.
- (66) Andresen, A. F. A Neutron Diffraction Investigation of Fe<sub>3</sub>Se<sub>4</sub>. *Acta Chem. Scand.* **1968**, *22*, 827–835.
- (67) Li, G.; Zhang, B.; Baluyan, T.; Rao, J.; Wu, J.; Novakova, A. A.; Rudolf, P.; Blake, G. R.; Groot, R. A.; Palstra, T. T. M. Metal–Insulator Transition Induced by Spin Reorientation in Fe<sub>7</sub>Se<sub>8</sub> Grain Boundaries. *Inorg. Chem.* **2016**, *55*, 12912–12922.
- (68) Andresen, A. F.; Leciejewicz, J. A Neutron Diffraction Study of Fe<sub>7</sub>Se<sub>8</sub>. *Journal De Physique* **1964**, *25*, 574–578.
- (69) Lin, C. R.; Siao, Y. J.; Lu, S. Z.; Gau, C. Magnetic Properties of Iron Selenide Nanocrystals Synthesized by the Thermal Decomposition. *IEEE Trans. Magn.* **2009**, *45*, 4275–4278.
- (70) Okazaki, A. The Superstructures of Iron Selenide Fe<sub>7</sub>Se<sub>8</sub>. *J. Phys. Soc. Jpn* **1961**, *16*, 1162–1170.
- (71) Singh, R. Unexpected Magnetism in Nanomaterials. *J. Magn. Magn. Mater.* **2013**, *346*, 58–73.
- (72) Kramers, H. A. L'interaction Entre les Atomes Magnétogènes dans un Cristal Paramagnétique,. *Physica.* **1934**, *1*, 182–192.
- (73) Anderson, P. W. Antiferromagnetism. Theory of Superexchange Interaction. *Phys. Rev.* **1950**, *79*, 350–356.
- (74) Margadonna, S.; Takabayashi, Y.; McDonald, M. T.; Kasperkiewicz, K.; Mizuguchi, Y.; Takano, Y.; Fitch, A. N.; Suard, E.; Prassides, K. Crystal Structure of the new FeSe<sub>1-x</sub> Superconductor. *Chem. Commun.* **2008**, *43*, 5607–5609.
- (75) Grechnev, G. E.; Panfilov, A. S.; Desnenko, V. A.; Fedorchenko, A. V.; Gnatchenko, S. L.; Chareev, D. A.; Volkova, O. S.; Vasiliev, A. N. Magnetic Properties of Superconducting FeSe in the Normal State. *J. Phys.: Condens. Matter* **2013**, *25*, 046004.

## Chapter 5

### Study of Growth Kinetics of $\text{Fe}_3\text{Se}_4$ Nanocrystallites and the Influence of Size and Shape Tunability on their Magnetic Properties



## Highlights

Below, we have listed some of the important 'take-away' points from this chapter which we would like to highlight:

- 1) *According to the theories, now we have the knowledge regarding the morphologically-important planes. After examining the sequence of morphologically-important low-index planes, we correlated them with the real-life morphologies of Fe<sub>3</sub>Se<sub>4</sub> samples (achieved through the synthesis) and determined the growth directions in different solvent conditions. Additionally, we also studied the directional growth-kinetics with increase in the thermal activation energy.*
- 2) *We proposed the growth mechanism based on two well-known pathways—diffusion and reaction processes in the provided reaction environment. Entire roadmap is laid-out—starting from the formation of unit cell, to the diffusion and attachment of monomers and the fate of various facet-growth.*
- 3) *Finally, we have shown as how the distinct growth in various facets leads to the control of the magnetic properties. The influence of it is studied with various parameters such as coercivity ( $H_C$ ), saturation magnetization ( $M_S$ ), magnetic anisotropy constant ( $K$ ), and the energy product  $(BH)_{max}$  at 300 K and 10 K.*

**Keywords:** Growth mechanism, Fe<sub>3</sub>Se<sub>4</sub>, size/shape effect, magnetic properties

The results of this chapter are published as —

- ✓ Study of Growth Kinetics of Fe<sub>3</sub>Se<sub>4</sub> Nanocrystallites and the Influence of Size and Shape Tunability on their Magnetic Properties

**Monika Ghalawat**, Pankaj Poddar\* *J. Phys. Chem. C* 2021, 125, 14, 7932–7943

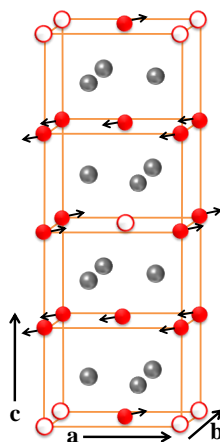


## 5.1 Introduction

The nano-dimensionality has added immense advantages in the physical and chemical property tunability through the surface to volume ratio variation<sup>1-5</sup>. The unique and novel size and shape-dependent properties displayed by nanocrystals have always posed curiosity, challenges, and opportunities<sup>6,7</sup>. Many of the wonders seen in nature can be understood by the nanoscale phenomena. Recently, considerable interest has developed in understanding the correlation between physical properties and morphology<sup>8</sup>. Besides, most electronic devices use the nanoscale components with control over the assembly of nanoscale building blocks, which is dictated by the size and shape of the nanoparticles (NPs)<sup>1</sup>. The size, shape, and crystallinity of NPs and their assembly need to be precisely controlled for magnetic materials over certain other materials as subtle changes in these parameters have a relatively larger influence on the applications such as high-density memory storage using magnetic media, magnetic read-heads, ferrofluids, or the rising importance of magnetic NPs in biomagnetic applications<sup>9-15</sup>. Although, the important role of surface and bulk arrangement of atoms in a single NP as well as the three-dimensional arrangements of NPs on the magnetic properties, has been known for more than half a century in magnetic metals and transition metal oxides<sup>16-29</sup>. However, these effects are poorly understood for their chalcogenide counterparts— M-X (M=transition elements, X=S, Se, Te) due to complexities in phase-diagram, poor control over stoichiometry, and morphology. In our previous Chapters, the complexities in the phase diagram and control over stoichiometry were studied<sup>30</sup>. In this work, an intensive investigation on the control over the morphology of Fe<sub>3</sub>Se<sub>4</sub> NPs is presented, followed by the influence of morphology on the magnetic properties.

Iron selenides are known, since the early 1950s and 1960s, to stabilize in four phases— FeSe<sub>2</sub>, Fe<sub>3</sub>Se<sub>4</sub>, Fe<sub>7</sub>Se<sub>8</sub>, and FeSe<sup>31,32</sup>. The following two out of four phases are noteworthy for their unique magnetic behavior— Fe<sub>3</sub>Se<sub>4</sub> and Fe<sub>7</sub>Se<sub>8</sub>. The phases—Fe<sub>7</sub>Se<sub>8</sub> and Fe<sub>3</sub>Se<sub>4</sub> show ferrimagnetic ordering at room temperature (RT) with the Curie temperatures (T<sub>C</sub>) ~ 453 K and ~315 K, respectively<sup>33-35</sup>. Among the two, lately, the Fe<sub>3</sub>Se<sub>4</sub> has been a center of attraction for researchers because of its high magnetic anisotropy and coercivity at ~300 K<sup>36-38</sup>. However, to date, there is little effort in systematic studies to develop controlled nucleation and growth pathways for Fe<sub>3</sub>Se<sub>4</sub> as well as size-dependent magnetic properties to develop a fundamental understanding of size/shape-property correlations<sup>36</sup>.

In 1956, Okazaki and Hirakawa<sup>32</sup> did the structural studies on a single crystal specimen of  $\text{Fe}_3\text{Se}_4$ . The unit-cell lattice parameters of  $\text{Fe}_3\text{Se}_4$  ( $\text{Fe}^{2+}\text{Fe}_2^{3+}\text{Se}_4^{2-}$ ) were calculated as  $a=6.17$  Å,  $b=3.54$  Å, and  $c=11.17$  Å with the  $I2/m$  space group (SG)<sup>32</sup>. Each  $\text{Fe}^{2+}/\text{Fe}^{3+}$  cation is octahedrally coordinated by six  $\text{Se}^{2-}$  anions ( $\text{FeSe}_6$  octahedra), and the coordination polyhedron of Se is the trigonal prism created by six  $\text{Fe}^{2+}/\text{Fe}^{3+}$  cations ( $\text{SeFe}_6$  prisms)<sup>35</sup>. In 1968, Andresen<sup>39</sup> performed neutron scattering measurements and stated that the ferrimagnetism in this compound results from ordered iron vacancies in alternate layers. The  $\text{Fe}^{2+}/\text{Fe}^{3+}$  cations and  $\text{Se}^{2-}$  anions are arranged in alternating layers along the  $c$ -axis, and the deviation from (1:1) stoichiometry leads to the formation of cation vacancies in every second Fe-layer to compensate for the iron deficiency. These vacancies are distributed as far apart as possible. Each layer has a different magnetization value, as the number of vacancies and the vacancy distribution are distinct in each layer<sup>39</sup>. The cation vacancies arise in every other Fe layer in a unit cell, as indicated in scheme 1, with a variable quantity in each alternating layer. These cation vacancies lie in the  $(-101)$  plane<sup>32,36</sup>. The spins ferromagnetically aligned inside each plane along the  $c$ -axis and antiferromagnetically aligned in a neighbouring plane with ordered iron vacancies are therefore credited with the genesis of ferrimagnetic ordering.<sup>36</sup>



**Scheme 1:** Unit cell of  $\text{Fe}_3\text{Se}_4$  showing the orientation of the magnetic moments. Solid red circles represent Fe-cations, while open red circles represent cations vacancies. Solid grey circles represent Se anions.

Many efforts have been dedicated to developing rare-earth (RE) free magnetic materials for the application of permanent magnet<sup>40-42</sup>. This has gotten a lot of attention in the scientific and industrial worlds due to the toxic and expensive RE materials. Among RE free materials,  $\text{MnBi}^{43}$  is an ambient temperature ferromagnet with a high coercivity ( $H_c$ ) ( $\sim 23$  kOe) and anisotropy constant ( $\sim 22$  Merg/cm<sup>3</sup> at 490 K). However, the high vapor pressure of Mn and a

low melting point of Bi inhibit its industrial applications. Another Fe-based compound—FePt<sup>41</sup> is also an ideal compound due to its magnetic properties, but it is unsuitable for mass applications due to the presence of Pt. In comparison, Fe<sub>3</sub>Se<sub>4</sub> is a low-cost compound with interesting magnetic properties. At nano dimensions, even without noble metal or rare-earth atoms, Fe<sub>3</sub>Se<sub>4</sub> exhibits semi-hard magnetic characteristics below its T<sub>C</sub>, which makes it a unique material<sup>36,37</sup>. Zhang et al. reported the H<sub>C</sub> of ~ 4 kOe at 300 K, increasing to ~ 40 kOe at 10 K for nanoplatelets after applying 90 kOe of maximum external field<sup>36</sup>. For nanocacti morphology, the H<sub>C</sub> around 3.4 kOe<sup>36</sup> and 2.74 kOe<sup>37</sup> were observed in two different studies, which increased nearly 10-fold (about 36 kOe<sup>36</sup> and 29.5 kOe<sup>37</sup>) at 10 K for a maximum applied external field of 90 kOe field. This is unique and interesting for low-temperature applications in particular. Large magnetic coercivity arises in Fe<sub>3</sub>Se<sub>4</sub> from its monoclinic structure with ordered iron vacancies, leading to large magnetocrystalline anisotropy: ~1.0 x 10<sup>7</sup> erg/cm<sup>3</sup> at 10 K<sup>38</sup>. This value was determined for powdered bulk samples by partially aligning them in a magnetic field along the easy axis (b-axis) of Fe<sub>3</sub>Se<sub>4</sub> and confirming the alignment using the presence of a predominant peak at (020) in the diffraction pattern and measuring the M-H loop along the hard and easy axes<sup>38</sup>. Long et al.<sup>38</sup> established that the Fe<sub>3</sub>Se<sub>4</sub> has a uniaxial type magnetocrystalline anisotropy as *K* is proportional to M<sub>S</sub><sup>3</sup>. They also estimated the critical radius<sup>38</sup> for a single-domain particle of Fe<sub>3</sub>Se<sub>4</sub>, which is about ~ 800 nm at 10 K and ~ 2000 nm at 300 K, calculated from r<sub>c</sub>

$$r_c \approx 9 \frac{(AK)^{\frac{1}{2}}}{\pi M_S^2} \text{-----(1)}$$

In which A denotes an exchange stiffness constant, M<sub>S</sub> is saturation magnetization, and *K* is the magnetic anisotropy constant. Consequently, it is appropriate to conclude that the particles below this size will lie in a single domain region.

The maximal energy product is the most important figure of merit for hard magnets defined by the notation (BH)<sub>max</sub><sup>37</sup>. Theoretically, the maximum energy product is defined as:

$$BH_{\max} = \frac{1}{4} \mu_0 M_S^2 \text{-----(2)}$$

where M<sub>S</sub> illustrates the saturation magnetization and μ<sub>0</sub> defines the magnetic permeability of free space. This equation describes a crucial role played by the M<sub>S</sub> in deciding the energy product. Therefore, for applications in hard magnetic materials, it is imperative to increase the value of M<sub>S</sub>. For Fe<sub>3</sub>Se<sub>4</sub>, the energy product ~ 4.38 kG Oe was observed at 300 K for

nanorods<sup>37</sup>, which enhanced up to 10.22 kG Oe by Mn-doping in an applied magnetic field more than 85 kOe. At 10 K, nearly a 2 order of magnitude increment  $\sim 0.12$  MG Oe<sup>37</sup> makes this compound useful for several low-temperature applications. Therefore, it is interesting as well as important to study the enhancement of the magnetic parameters of Fe<sub>3</sub>Se<sub>4</sub> by the influence of size and shape at a lower external magnetic field value than 90 kOe as cited in the earlier studies.

To examine the relationship between morphology and magnetic properties, especially the energy product, control over the morphology of NPs is essential, which is generally governed by the crystal structure, lattice defects at an early stage of crystal growth, symmetry-breaking, and reaction conditions. Among the numerous procedures, a kinetic control over the addition of chemical species from a solution phase are the simplest and most versatile by selective binding of capping molecules, ionic species, etc., to various nanocrystal facets for changing their surface free energies<sup>8,44,45</sup>. A capping agent stabilises some particular facets when it is introduced in a reaction solution. These facets will have a reduced surface free energy, resulting in nanocrystals with a shape that maximises that facet's expression. The selective affinity of the capping agents over crystalline facets they are chemisorbed differently on any crystallographic plane leading to differential addition of atoms onto planes. Solution-phase synthesis gives a potent way to manufacture diverse forms of nanocrystals, gratitude to the availability of a wide range of compounds that can function as a capping agent<sup>46</sup>. Many parameters, such as crystal structure, charge density, surface-ion-ligand interactions, electronic and surface structure of a material, or the functional group(s) of a capping agent, might influence the preferential binding of a capping agent to a certain surface. As a result, knowing the growth process is critical for morphological control.

In this work, a tunability of abundant magnetic parameters has been reported for the Fe<sub>3</sub>Se<sub>4</sub> compound by varying the size/shape of the particle at the nanoscale. This will also open various new directions for the controlled syntheses of several other TMCs. Here, the thermal decomposition method is adopted over others in order to have particles with controlled morphology. The study of systematic changes in the nucleation and growth mechanism of Fe<sub>3</sub>Se<sub>4</sub> compounds as a function of reaction parameters at the nanometric regime has been examined. This study also highlights the important points— starting by observing preferential growth according to the theoretical models and discussing the growth mechanism by diffusion process and reaction process in the provided reaction environment. A significant increase in

the  $H_C$ , magnetization ( $M_{60 \text{ kOe}}$ ), the energy product  $(BH)_{\text{max}}$ , magnetic anisotropy constant ( $K_{\text{eff}}$ ), and average blocking temperature ( $T_B$ ) of  $\text{Fe}_3\text{Se}_4$  is observed with an increase in the crystallite-size.

## 5.2 Thermal decomposition-based synthesis of $\text{Fe}_3\text{Se}_4$ NPs

In this work, a one-pot thermal decomposition method has been used to synthesize the controlled  $\text{Fe}_3\text{Se}_4$  nanocrystals. In a typical reaction,  $\text{Fe}(\text{acac})_3$  [Iron (III) acetylacetonate; 99.99%; Sigma-Aldrich] was used as an organometallic precursor and Se [Selenium powder; 99.99%; Sigma-Aldrich] as a Se precursor for synthesizing  $\text{Fe}_3\text{Se}_4$  in an organic solvent. A 0.53 g (1.5 mmol) portion of  $\text{Fe}(\text{acac})_3$  and 0.158 g (2 mmol) of Se were added to the corresponding solvent at 30 °C in a 100 mL three-neck round-bottom (RB) flask. The solution was stirred under the flow of high-purity nitrogen gas at 30 °C. After that, the temperature was raised to 120 °C and maintained for 30 min. Further, the temperature was raised at a ramping rate of 2 °C  $\text{min}^{-1}$  up to 200 °C, and 5 °C  $\text{min}^{-1}$  was used to reach the desired temperature at which the sample was maintained for a pertinent time. A thermometer was placed inside the RB-flask, and the temperature was kept stable within  $\pm 2.0$  °C. The solution was cooled to laboratory temperature by removing the heating source. After cooling, 20 mL of 2-propanol was added to the solution for washing the specimen, which was further separated from the solution by centrifugation. The obtained sample was rewashed with a mixture of 15 mL hexane and 10 mL 2-propanol. Finally, the resultant black precipitate was dried in the vacuum and utilized for further characterization.

The size effect study was done over the full range of temperature scans for synthesizing single phase  $\text{Fe}_3\text{Se}_4$  in the presence of OLA [Oleylamine; 70%; Sigma-Aldrich] (15 ml). Below 260 °C temperature, there was always  $\text{FeSe}_2$  phase impurity, as discussed in chapter 3<sup>30</sup>. While above 330 °C, no reaction was possible because the solution turned into a gel. Therefore, growth temperature was scanned in the range of 260 °C to 330 °C to study the kinetics of crystal formation.

### 5.2.1 For the synthesis of $\text{Fe}_3\text{Se}_4$ nanorods ( $\text{FS}_{\text{NR-T } ^\circ\text{C}}$ ) samples

#### Sample $\text{FS}_{\text{NR-260 } ^\circ\text{C}}$

A 0.53 g (1.5 mmol) portion of  $\text{Fe}(\text{acac})_3$  and 0.158 g (2 mmol) of Se were added to 15 mL of OLA at 30 °C in a 100 mL three-neck RB flask. The solution was stirred under the flow of high-purity nitrogen gas at 30 °C. After that, the temperature was raised to 120 °C and

maintained for 30 min. Further, the temperature was raised at a ramping rate of 2 °C min<sup>-1</sup> up to 200 °C, and 5 °C min<sup>-1</sup> was used to reach the desired temperature (260 °C) at which the sample was maintained for 120 min.

#### **Sample FS<sub>NR-300</sub> °C**

This synthesis is similar to the above synthesis, except that the final desired temperature is 300 °C and was maintained for 80 min.

#### **Sample FS<sub>NR-330</sub> °C**

This synthesis is similar to the above synthesis, except that the final desired temperature is 330 °C and was maintained for 70 min.

Though we tried several intermediate temperature conditions to optimize the synthesis; however, here, for the sake of brevity and clarity, the data on the samples formed at three particular temperatures are discussed. However, the remaining intermediate samples' experimental details (growth conditions and magnetic measurements) are also reported.

### **Intermediate samples**

#### **Sample FS<sub>NR-280</sub> °C**

This synthesis is similar to the above synthesis, except that the final desired temperature is 280 °C and was maintained for 120 min.

#### **Sample FS'<sub>NR-300</sub> °C**

This synthesis is similar to the above synthesis, except that the final desired temperature is 300 °C and was maintained for 140 min.

The reaction parameters, including solvent and temperature, were modified for shape tuning of Fe<sub>3</sub>Se<sub>4</sub>, as shown in Table 1. The study of the shape effect was done over the two solvent conditions— (1) 1-ODE [1-octadecene; 90%; Sigma-Aldrich], and OCD [octadecylamine; 97%; Sigma-Aldrich] are added together as an organic solvent, and (2) only OCD is added as a solvent, at 330 °C. In these two solvent conditions, there is always a presence of FeSe<sub>2</sub> phase below the optimized temperature (330 °C), and above it, the solution turns into the gel.

### **5.2.2 For the synthesis of Fe<sub>3</sub>Se<sub>4</sub> nanoplatelets (FS<sub>PL-330</sub> °C)**

A 0.53 g (1.5 mmol) portion of Fe(acac)<sub>3</sub> and 0.158 g (2 mmol) of Se were added to 10 mL of 1-ODE and 5 mL of OCD at 30 °C in a 100 mL three-neck RB flask. The solution was stirred

under the flow of high-purity nitrogen gas at 30 °C. After that, the temperature was raised to 120 °C and maintained for 30 min. Further, the temperature was raised at a ramping rate of 2 °C min<sup>-1</sup> up to 200 °C, and 5 °C min<sup>-1</sup> was used to reach the 330 °C, at which the sample was maintained for 120 min.

### 5.2.3 For the synthesis of Fe<sub>3</sub>Se<sub>4</sub> quasi-spheres (FSQS-330 °C)

A 0.53 g (1.5 mmol) portion of Fe(acac)<sub>3</sub> and 0.158 g (2 mmol) of Se were added to 15 mL of OCD at 30 °C in a 100 mL three-neck RB flask. The solution was stirred under the flow of high-purity nitrogen gas at 30 °C. After that, the temperature was raised to 120 °C and maintained for 30 min. Further, the temperature was raised at a ramping rate of 2 °C min<sup>-1</sup> up to 200 °C, and 5 °C min<sup>-1</sup> was used to reach the 330 °C, at which the sample was maintained for 100 min.

**Table 1.** Summary of the experimental conditions, indicating the influence of the temperature and solvent compositions on the size and shape of the products, respectively. Fe(acac)<sub>3</sub> and Se powder were used in the following reactions as Fe and Se precursors, respectively.

Samples Parameters	FSNR-260	FSNR-300	FSNR-330	FSPL-330	FSQS-330
	°C	°C	°C	°C	°C
Reaction	1	2	3	4	5
Solvent	OLA			1-ODE & OCD	OCD
<b>Step 1</b>					
Reaction temperature (± 2 °C)	120 °C				
Time (min)	30				
<b>Step 2</b>					
Reaction temperature (± 2 °C)	260 °C	300 °C	330 °C	330 °C	330 °C
Time (min)	120	80	70	120	100

## 5.3 Characterization techniques

Several analytical techniques were utilized to characterize the as-synthesized Fe<sub>3</sub>Se<sub>4</sub> NPs. Powder X-ray diffraction (XRD) patterns of the samples were recorded on a PANalytical X'PERT PRO instrument with the iron-filtered Cu-K<sub>α</sub> radiation ( $\lambda = 1.54 \text{ \AA}$ ) in 2 $\theta$  range of 10° - 80°. Following the method given by Paul Scherrer (1918), crystallite sizes were calculated considering the effect of limited particle size on XRD patterns<sup>47-49</sup>. Paul Scherrer

approximated an expression to relate peak-broadening and crystallite size. The formulae to estimate the crystallite size along the hkl plane from the measured width of their diffraction curves are given as:

$$d = \frac{K\lambda}{B \cos \theta} \text{ -----(3)}$$

Here, the width B of the diffraction curve at an intensity equal to half the maximum intensity, known as the full width at half maxima (FWHM), is usually measured in radians. The  $\lambda$  is the wavelength of the incident X-rays (for Cu  $K_{\alpha}$   $\lambda \sim 1.54 \text{ \AA}$ ),  $\theta$  is the Bragg angle corresponding to hkl plane (hkl are the Miller indices of the planes being analyzed), and K is the numerical constant typically referred to as the crystallite-shape factor, however in the absence of details of shape information,  $K = 0.94$  is a good approximation<sup>49</sup>. Instead of directly considering the B values from peak broadening, it is corrected from standard data using equation<sup>49</sup>.

$$B^2 = B_M^2 - B_S^2 \text{ -----(4)}$$

where  $B_M$  and  $B_S$  are the measured widths of the diffraction peaks of  $\text{Fe}_3\text{Se}_4$  and the standard sample. This results in subtracting the instrumental errors from the peak broadening.

The morphology was characterized using an FEI Tecnai T20 transmission electron microscopy (TEM) equipped with a super twin lens (s-twin) operated at 200 keV accelerating voltage. The powders obtained were dispersed in n-hexane and then drop-casted on a carbon-coated copper TEM grid with 200 mesh and loaded in a single-tilt sample holder. The magnetic measurements were carried out using a superconducting quantum interference device-based vibrating sample magnetometer (SQUID-VSM) manufactured by Quantum Design, Inc., San Diego, USA. The powder samples were precisely weighed and packed inside a plastic sample holder, which fits into a brass specimen holder provided by Quantum Design Inc. with a negligible contribution to the overall magnetic signal. The magnetic field dependent magnetization (M–H) loops are collected at a rate of  $50 \text{ Oe s}^{-1}$  in a field sweep from  $\pm 60 \text{ kOe}$  at the vibrating frequency of 40 Hz. The magnetization versus temperature (M–T) measurements was performed at a temperature sweep from 7 to 330 K in a field of 100 Oe following standard field-cooled (FC) and zero-field cooled (ZFC) sequences.

## 5.4 Results and discussion

### 5.4.1 Growth process

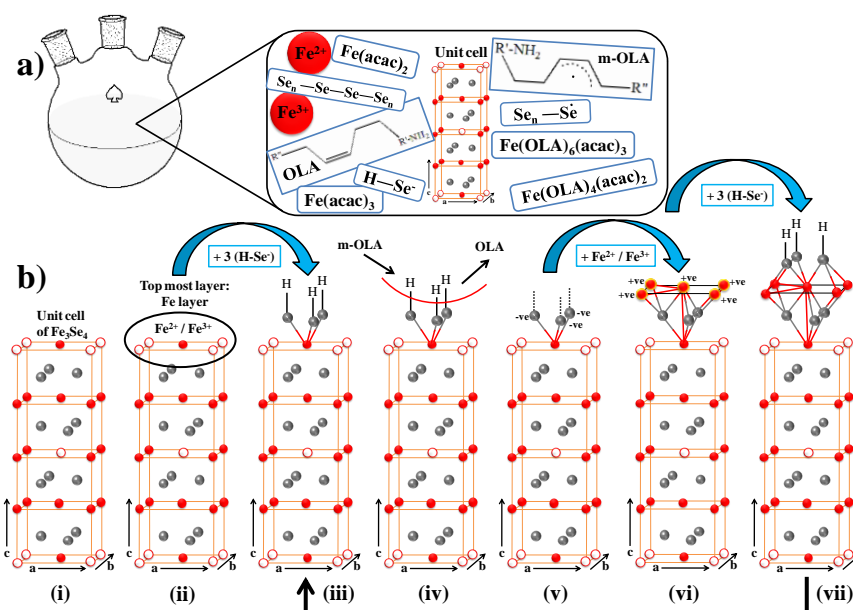
The birth of solids, starting from a few atoms, and their further growth into the larger collection of ordered or disordered atomic assemblies, is quite an intriguing process for experimentalists



due to the extreme time and length scales involved. According to the classical theory of nucleation, it requires the monomer concentration to reach well above the saturation limit in order for the solid-state matter to start forming in the solution phase. Initially, nucleation takes place with persistent monomer concentration. After a while, clusters begin to develop on the surface, reducing the monomer supply. Furthermore, because these monomer concentrations are below the threshold limit for nucleation, nucleation is terminated<sup>50</sup>. The surface-to-volume ratio of tiny particles is large. Results in the huge surface area, surface excess energy is more important in tiny particles, accounting for a major portion of the total energy. As a result, in a solution, a process that determines the production of bigger particles at the expense of smaller particles depletes the surface energy and thus plays an important function in nanocrystal development. Monomer migration towards the surface is followed by monomer reaction at the nanocrystal's surface, resulting in colloidal particles.

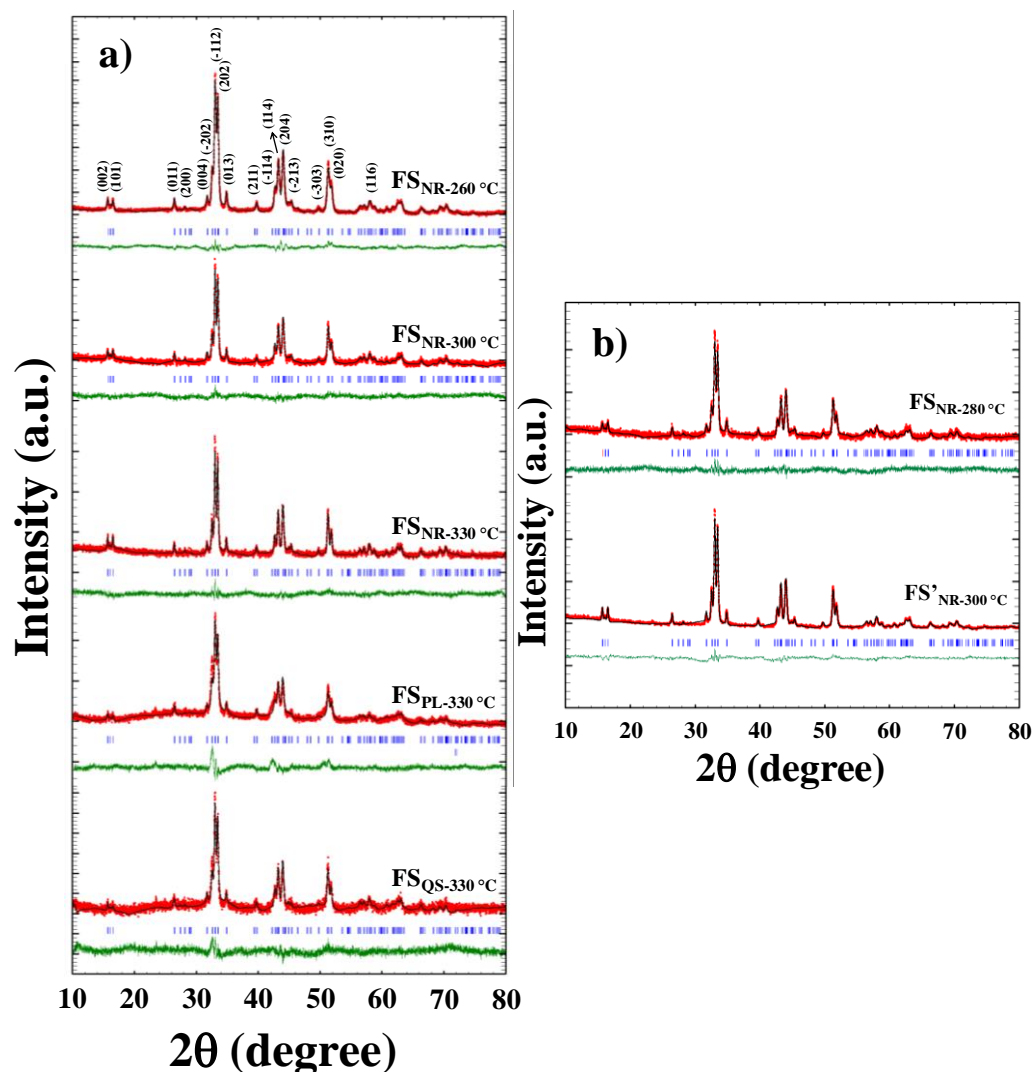
There are three basic stages in the creation of colloidal NPs in a solution phase: (i) nucleation: formation of small clusters, (ii) seed formation: evolution of nuclei into seeds with well-defined crystalline structures (or amorphous seeds), and (iii) growth: growth of seeds into nanocrystals of specific shape and size<sup>50</sup>. The results are examined by a set of thermodynamic and kinetic parameters that are not mutually exclusive and remain virtually and intricately entangled with each other in experimental conditions. During the third step, the reaction can follow various pathways. Either the smaller seeds can dissolve back into the solution contributing to the growth of relatively larger and more stable clusters (Ostwald ripening), or smaller seeds can agglomerate to generate larger clusters (made of smaller seeds) where the seed-boundaries are still well-defined with formation of single crystallite by annealing process (non-classical nucleation theory). In addition, the pre-formed seeds can continue to grow to utilize the monomers present in the solution. In this work, the latter pathway occurs (seeds are growing further after continuous addition of monomers), as discussed in Chapter 3<sup>30</sup> supported by XRD data. The addition of monomers and further growth of seeds is known to be contributed by the following two pathways — (i) diffusion-limited growth process: diffusion of the monomers or ions/atoms, (ii) reaction-limited growth process: controlled by the reaction of the monomers at the surface of solid<sup>50</sup>. We already discussed the second process based on the surface free energy of various facets, which is a major contributing factor to monomers' addition to the seed surfaces. However, the proper understanding of growth kinetics under the

actual synthetic conditions is very complicated due to several species' presence and their interaction with each other<sup>51,52</sup>.



**Scheme 2:** a) The schematic shows the molecular environment around the unit cell of  $\text{Fe}_3\text{Se}_4$  surrounded by available species that may influence the crystal growth. (1) Fe precursors—  $\text{Fe}(\text{acac})_3$ , (2) Se precursors—  $(\text{Se}_n\text{-Se-Se-Se}_n)$ , (3)  $\text{Fe}(\text{acac})_2$  (formed due to reduction of  $\text{Fe}(\text{acac})_3$  with the release of acetone and  $\text{CO}_2$ ), (4) Fe-OLA complexes ( $\text{Fe}(\text{OLA})_6(\text{acac})_3$ , and  $\text{Fe}(\text{OLA})_4(\text{acac})_2$ ), (5)  $\text{Se}_n\text{-Se}^*$  (Se reacts with OLA by homolytic cleavage of Se—Se bond that results in forming Se radicals), (6)  $\text{H-Se}^-$  anion (formed when the Se radicals attack the allylic proton of OLA), and (7) oleylamine molecules which are present in two states— stable and metastable (after giving hydrogen to the Se radicals, OLA becomes in a metastable state). b) The schematic illustrates the addition of atoms on the unit cell of  $\text{Fe}_3\text{Se}_4$  surrounded by all possible intermediate species in a typical synthesis. The proposed growth mechanism of  $\text{Fe}_3\text{Se}_4$  NPs (along the c-axis) explains the reaction-limited process (kinetic-control). (i) Unit cell of  $\text{Fe}_3\text{Se}_4$ . (ii) Consider the Fe-layer as the outermost layer. (iii) The available  $\text{H-Se}^-$ -ions present in the solution will be captured by the Fe ions due to Columbian attraction, and Se will make the covalent bond with Fe-ions. (iv) The metastable oleylamine (m-OLA) takes the hydrogen back to reconfigure itself into the stable OLA (migration of double bond). (v) This results in the formation of a fresh anionic layer. (vi) The Se-anions will capture the available Fe-cations (Columbian interaction) and form the bond. Further, the cation layer (Fe-ions) will capture the  $\text{H-Se}^-$  ions, and so on. (vii) Repeat from step (iii). Solid red circles represent the Fe-cations, while open red circles represent cations vacancies. Solid grey circles represent Se-anions.

Forming a single formula unit of  $\text{Fe}_3\text{Se}_4$  involves the dissociation of iron acetylacetonate and Se powder into various intermediate species, which finally provide Fe ions and Se ions for the nucleation process to trigger. The schematic 2a explains the addition of these atoms on the unit cell of  $\text{Fe}_3\text{Se}_4$  surrounded by all possible intermediate species in a typical synthesis; for example, (1) Fe precursors—  $\text{Fe}(\text{acac})_3$ , (2) Se precursors—  $(\text{Se}_n\text{-Se-Se-Se}_n)$ , (3)  $\text{Fe}(\text{acac})_2$  (formed due to reduction of  $\text{Fe}(\text{acac})_3$  with the release of acetone and  $\text{CO}_2$ )<sup>30,53</sup>, (4) Fe-OLA complexes  $(\text{Fe}(\text{OLA})_6(\text{acac})_3)$ , and  $(\text{Fe}(\text{OLA})_4(\text{acac})_2)$ <sup>30</sup>, (5)  $\text{Se}_n\text{-Se}^\bullet$  (Se reacts with OLA by homolytic cleavage of Se—Se bond that results in forming Se radicals)<sup>30,54</sup>, (6)  $\text{H-Se}^-$  anion (formed when the Se radicals attack the allylic proton of OLA), and (7) oleylamine molecules which are present in two states— stable and metastable (after giving hydrogen to the Se radicals, OLA becomes in a metastable state). The concentration of these intermediates, temperature, viscosity, etc. contribute strongly to the diffusion-limited growth processes along with the reaction-limited growth process where the final cation and anionic states available to react with the unit cell of  $\text{Fe}_3\text{Se}_4$  are:  $\text{Fe}^{2+}$ ,  $\text{Fe}^{3+}$ , and  $\text{H-Se}^-$ , respectively and their availability is influenced by the seven intermediates listed earlier. Schematic 2b represents the proposed qualitative growth mechanism of  $\text{Fe}_3\text{Se}_4$  NPs (along the c-axis). For clarity, omitted the schematic along the b-axis; however, the growth process (addition of atoms phenomena) will be the same. Step (i) illustrates the unit cell of  $\text{Fe}_3\text{Se}_4$ , where the outermost atomic layer is considered to be terminated by the iron ions. According to Coulombic attraction, the negatively charged  $\text{H-Se}^-$  ions will diffuse towards highly active surface Fe ions and form new bonds (reaction process). However, the seed-surface is also surrounded by the OLA molecules in the metastable state which are readily formed due to the attack of Se radicals on OLA's allylic proton which takes away the hydrogen to form  $\text{H-Se}^-$  ions. These metastable OLA (m-OLA) molecules will scavenge back the hydrogen ions from the terminating  $\text{H-Se}^-$  ions as discussed in Chapter 3<sup>30</sup>. This result in formation of a fresh atomic layer along the c-direction terminated by highly-active surface Se-ions. The negatively charged top layer captures the Fe ions from the solution over the surface of the crystal by the diffusion process and to form a fresh Fe-layer. This process continues (limited by the surface-energy minimization principal). The growth process of other facets can also be understood by the similar chemistry.

5.4.2 Structural and morphological investigations of  $\text{Fe}_3\text{Se}_4$  NPs using XRD and TEM

**Figure 1.** a) A comparison between the observed XRD patterns of  $\text{Fe}_3\text{Se}_4$  NPs (red line), calculated XRD curve after crystal structure refinement by Rietveld method (black line), the difference ( $I_{\text{obs}} - I_{\text{cal}}$ ) between observed intensity ( $I_{\text{obs}}$ ) and calculated intensity ( $I_{\text{cal}}$ ) (green line), and Bragg positions (blue vertical line) for various samples labeled as  $\text{FS}_{\text{NR-260 }^\circ\text{C}}$ ,  $\text{FS}_{\text{NR-300 }^\circ\text{C}}$ ,  $\text{FS}_{\text{NR-330 }^\circ\text{C}}$ ,  $\text{FS}_{\text{PL-330 }^\circ\text{C}}$ , and  $\text{FS}_{\text{QS-330 }^\circ\text{C}}$ . The samples  $\text{FS}_{\text{NR-260 }^\circ\text{C}}$ ,  $\text{FS}_{\text{NR-300 }^\circ\text{C}}$ , and  $\text{FS}_{\text{NR-330 }^\circ\text{C}}$  were synthesized in the presence of OLA in varying crystallite sizes. The sample  $\text{FS}_{\text{PL-330 }^\circ\text{C}}$  was synthesized in the presence of 1-ODE + OCD. The sample  $\text{FS}_{\text{QS-330 }^\circ\text{C}}$  was synthesized in the presence of OCD. b) XRD patterns of  $\text{Fe}_3\text{Se}_4$  NPs (for intermediate samples) —  $\text{FS}_{\text{NR-280 }^\circ\text{C}}$  and  $\text{FS}'_{\text{NR-300 }^\circ\text{C}}$ . The crystallite size of  $\text{FS}_{\text{NR-280 }^\circ\text{C}}$  and  $\text{FS}'_{\text{NR-300 }^\circ\text{C}}$  samples are  $35 \pm 2$  nm and  $40 \pm 2$  nm along the (-112) plane, respectively.

The Fe<sub>3</sub>Se<sub>4</sub> samples were intensively investigated for their crystallinity and phase purity using powder- XRD, followed by the Reitveld refinement using FullProf software (Figure 1). The absence of any unidentified peak in the diffraction patterns indicates that no secondary phase is present in all samples under the limit of laboratory XRD. All of the XRD patterns matched the XRD card number 73–2021<sup>55</sup> created by the Joint Committee on Powder Diffraction Standards (JCPDS) for Fe<sub>3</sub>Se<sub>4</sub> without ambiguous reflections.

**Table 2.** Comparison of the parameters obtained after Rietveld refinement of XRD data of as-synthesized Fe<sub>3</sub>Se<sub>4</sub> NPs. The values  $\chi^2$  and wR<sub>P</sub> (%) represent the chi-square and weighted profile R-value, respectively. Unit cell parameters are denoted by a, b, c,  $\alpha$ ,  $\beta$ , and  $\gamma$ .

Sample Parameters	FS <sub>NR-260 °C</sub>	FS <sub>NR-300 °C</sub>	FS <sub>NR-330 °C</sub>	FS <sub>PL-330 °C</sub>	FS <sub>QS-330 °C</sub>
$\chi^2$	3.6	1.6	1.7	2.3	1.7
wR <sub>P</sub> (%)	12.1	19.3	18.6	17.9	28.5
Space group	I2/m	I2/m	I2/m	I2/m	I2/m
Volume	245.5	245.6	246.2	246.1	246.2
a (Å)	6.185	6.186	6.190	6.190	6.190
b (Å)	3.525	3.524	3.527	3.524	3.528
c (Å)	11.264	11.270	11.279	11.287	11.276
$\alpha$	90.0°	90.0°	90.0°	90.0°	90.0°
$\beta$	91.784°	91.822°	91.801°	91.824°	91.751°
$\gamma$	90.0°	90.0°	90.0°	90.0°	90.0°

All the samples are formed in the monoclinic crystal structure with the calculated lattice parameters tabulated in Table 2, having the I2/m space group. The refinement details are also mentioned in Table 2. The order of broadening of diffraction pattern indicates that the Fe<sub>3</sub>Se<sub>4</sub> are of nano dimension.

The crystallite sizes for all the samples were calculated using the method given by Paul Scherrer<sup>47–49</sup> along three different planes corresponding to the three most intense diffraction peaks (Table 3). Scherrer's formula is in good agreement to compare the size of particles<sup>49</sup>. It is observed that the calculated crystallite sizes are directly proportional to the reaction temperature— the size increases with an increase in reaction temperature.

**Table 3.** An evolution of crystallite size for as-synthesized  $\text{Fe}_3\text{Se}_4$  NPs is compared with different crystalline planes calculated from powder XRD. The influence of temperature and solvent on the crystallite size and shape of the products has been observed, respectively.

<b>Samples</b> <b>Parameters</b>	<b>FS<sub>NR-260</sub> °C</b>	<b>FS<sub>NR-300</sub> °C</b>	<b>FS<sub>NR-330</sub> °C</b>	<b>FS<sub>PL-330</sub> °C</b>	<b>FS<sub>QS-330</sub> °C</b>
<b>Crystallite size d (<math>\pm 2</math> nm) along following planes</b>					
<b>(-112)</b>	33	37	42	34	36
<b>(202)</b>	25	31	35	28	32
<b>(204)</b>	22	24	26	21	27

It is worth mentioning that the current synthetic technique not only allows the selective synthesis of different crystallite sizes by controlling the temperature but also produces novel morphologies by adjusting the growth conditions (reaction temperature and solvents together).

The morphological properties of all the specimens were examined by TEM. As shown in Figure 2, samples FS<sub>NR-260</sub> °C, FS<sub>NR-300</sub> °C, and FS<sub>NR-330</sub> °C synthesized with OLA are quasispherical particles consisting of agglomerated rod-shaped nanostructures with multitudinous spikes grown on the surfaces pointing thoroughly outward. Moreover, as shown in Figure 2, sample FS<sub>PL-330</sub> °C represents the formation of nanoplatelets (in the presence of 1-ODE and OCD), and sample FS<sub>QS-330</sub> °C reveals the shape of nanosized quasi-spheres (in the presence of OCD).

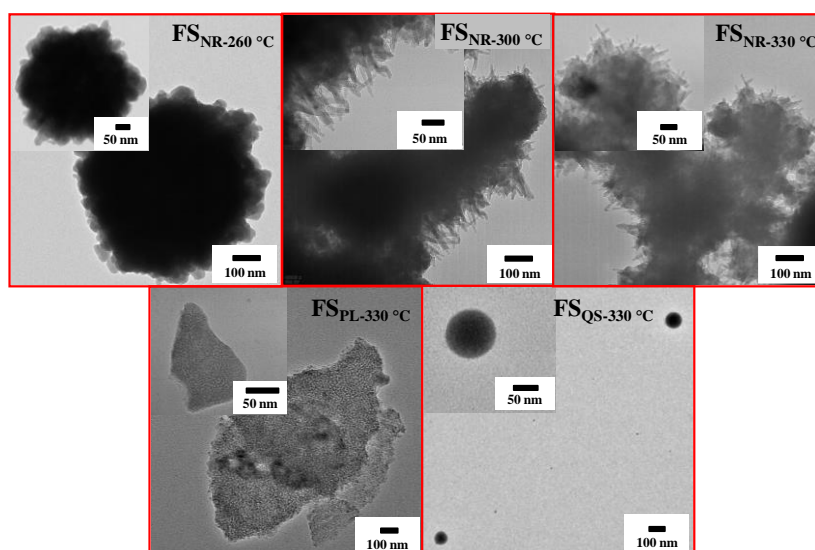
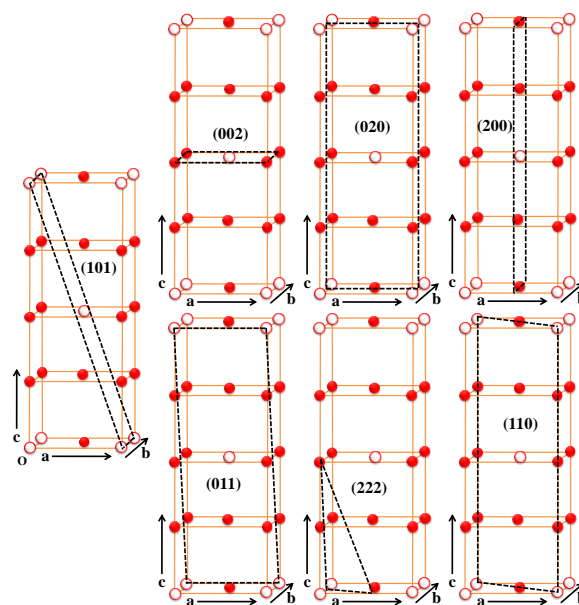


**Figure 2.** Representative TEM images of as-synthesized  $\text{Fe}_3\text{Se}_4$  NPs. The TEM images corresponding to the samples FS<sub>NR-260</sub> °C, FS<sub>NR-300</sub> °C, and FS<sub>NR-330</sub> °C (synthesized in the

presence of OLA) show that particles are analogous with rod-like features growing on the surface. The images corresponding to the sample FS<sub>PL-330 °C</sub> (in the presence of 1-ODE + OCD) and FS<sub>QS-330 °C</sub> (in OCD) reveal nanoplatelets and quasispherical morphologies. The insets show zoomed-in views with a scale bar of 50 nm. Due to intense magnetic polarization, the particles show aggregation in the TEM images.



**Scheme 3.** The unit cell of Fe<sub>3</sub>Se<sub>4</sub> with different planes drawn by black dotted lines. Solid red circles represent Fe-cations, while open red circles represent cations vacancies.

Further, the directional growth analysis examined the relationship between the relative intensities (RI) of XRD peaks and morphologies. It was observed that for all the samples, (-112) peak shows the maximum intensity, and its intensity was normalized to 100 with respect to other peaks. The RIs of all the as-synthesized Fe<sub>3</sub>Se<sub>4</sub> NPs are compared in Table 4.

It can be noticed that with respect to the most intense peak, many of the peaks show a sample to sample variation in the RI, which indicates varying growth kinetics of different facets when the reaction conditions are altered<sup>56</sup>. These results can be related to the 'morphological importance' (MI) of respective lattice planes, which, for a particular crystal, is inversely proportional to the growth rate, i.e., the faster the growth rate of a plane, the lesser will be the MI value of that plane and vice versa. Thus, the slow-growing facet will dominate the morphology in the resultant particle with a large surface area and are more exposed to the environment<sup>57</sup>. These more exposed planes will contribute toward higher RI in the XRD pattern. So, RIs of crystalline peaks can be directly related to the MIs of respective lattice

planes, which immediately makes the growth direction in a distinct environment accessible to us. Using the simple exercise, this critical information directly links the crystal formation and tunable reaction-limited growth conditions that were carefully selected in this work.

**Table 4.** List of calculated RI of powder XRD peaks along different lattice planes of all the as-synthesized Fe<sub>3</sub>Se<sub>4</sub> NPs and bulk Fe<sub>3</sub>Se<sub>4</sub> (JCPDS card no. 73-2021).

<b>Samples Parameters</b>	<b>Bulk (%) (73- 2021)</b>	<b>FS<sub>NR-260</sub> °C (%)</b>	<b>FS<sub>NR-300</sub> °C (%)</b>	<b>FS<sub>NR-330</sub> °C (%)</b>	<b>FS<sub>PL-330 °C</sub> (%)</b>	<b>FS<sub>QS-330</sub> °C (%)</b>
<b>RI (a.u.) along (-112)</b>	100	100	100	100	100	100
<b>RI (a.u.) along (101)</b>	30.4	10	14	17	10	15
<b>RI (a.u.) along (202)</b>	94.3	85	86	87	80	81
<b>RI (a.u.) along (-202)</b>	46.8	31	34	35	59	46
<b>RI (a.u.) along (002)</b>	25.3	10	14	17	11	16
<b>RI (a.u.) along (020)</b>	32.3	25	26	25	24	28
<b>RI (a.u.) along (200)</b>	7.4	4	7	7	8	12
<b>RI (a.u.) along (011)</b>	11.6	9	13	13	12	15
<b>RI (a.u.) along (222)</b>	15.5	10	13	13	12	17
<b>RI (a.u.) along (-222)</b>	10.7	10	12	12	13	16
<b>RI (a.u.) along (110)</b>	1.8	2	5	5	8	10

From TEM images, shape variation is clearly visible in Fe<sub>3</sub>Se<sub>4</sub> NPs however, the agglomeration size effect is not clearly observed. Figure 3 shows the zoomed view of Fe<sub>3</sub>Se<sub>4</sub> nanorods in the presence of OLA.



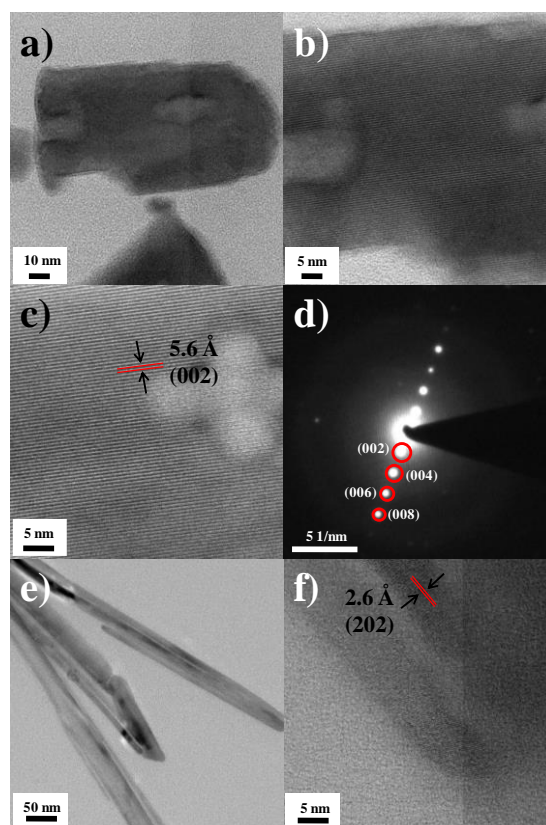


**Figure 3.** Representative TEM images of as-synthesized  $\text{Fe}_3\text{Se}_4$  (synthesized in OLA presence). a) Image shows the rod-like features of NPs. b) Zoomed-in views with a scale bar of 5 nm. c) The lattice fringes spaced at  $5.6 \text{ \AA}$  represents the (002) plane. d) The SAED pattern reveals the presence of (002) plane. e) TEM image from different areas again reveals the rod-like morphology. f) The lattice fringes spaced at  $2.6 \text{ \AA}$  represents the (202) plane. Thus, the (002) and (202) faces are parallel to longitude in a rod-like shape that results in making the longitudinal growth along the b-axis.

To better understand the size variation in these agglomerated rods, it is appropriate to take help from the theoretical aspect.

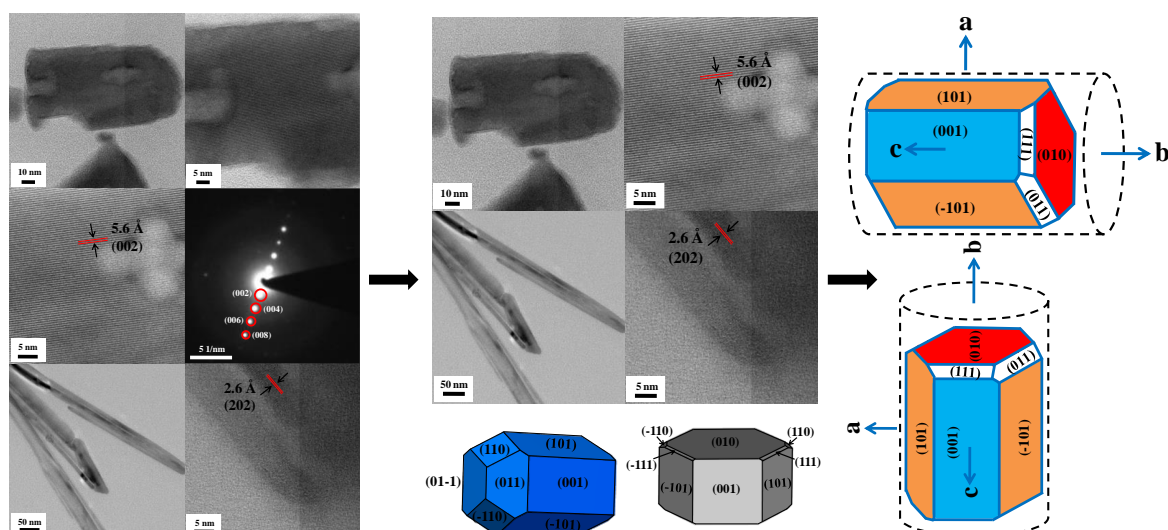
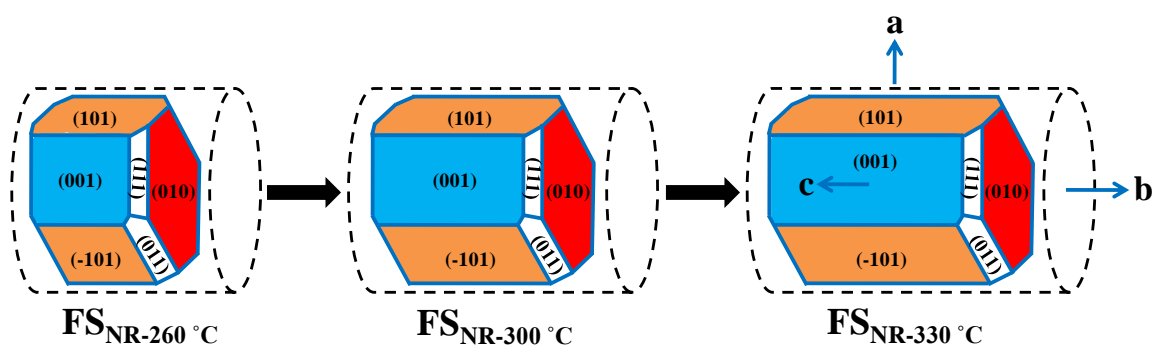


**Figure 4.** Starting from typical TEM images to the correlation between experimental and theoretical morphologies to the schematic diagram of experimental  $\text{Fe}_3\text{Se}_4$  nanorod with the help of theoretically predicted crystal morphologies.

As discussed in chapters 2 and 3, the crystal habit of  $\text{Fe}_3\text{Se}_4$  has been predicted by theoretical models and found to be a complete match of experimental morphologies. In the presence of OLA, the  $\text{Fe}_3\text{Se}_4$  will follow the crystal habit path. If all the facets are combined and tried to make a schematic, the resultant shape will be as schematically shown in Figure 4.



**Scheme 4.** Schematic diagram of  $\text{Fe}_3\text{Se}_4$  nanorods defined as  $\text{FS}_{\text{NR-260 } ^\circ\text{C}}$ ,  $\text{FS}_{\text{NR-300 } ^\circ\text{C}}$ , and  $\text{FS}_{\text{NR-330 } ^\circ\text{C}}$  samples, exhibiting size effect as confirmed by RI.

As the temperature increases, the size of the nanorods is also increasing, as shown with the help of schematic in scheme 4. This is well supported by RI of distinct planes of XRD, as shown in Figure 5.

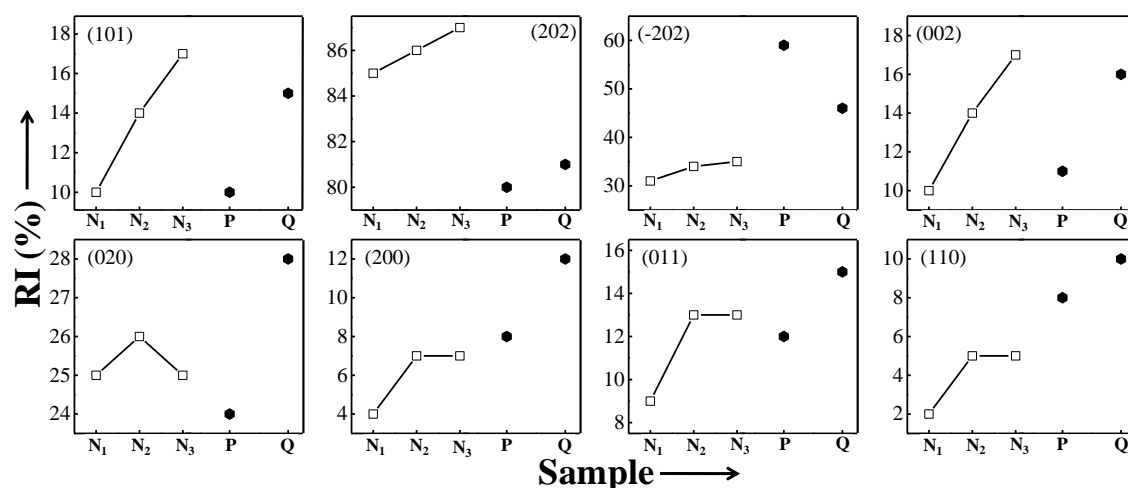


**Figure 5.** The variation in the relative intensities (RI) of diffraction pattern along different lattice planes of all the as-synthesized  $\text{Fe}_3\text{Se}_4$  NPs. The  $N_1$ ,  $N_2$ , and  $N_3$  define  $\text{FS}_{\text{NR}-260}^\circ\text{C}$ ,  $\text{FS}_{\text{NR}-300}^\circ\text{C}$ , and  $\text{FS}_{\text{NR}-330}^\circ\text{C}$  samples, exhibiting the effect of size on RI. The symbols P and Q denote the  $\text{FS}_{\text{PL}-330}^\circ\text{C}$  and  $\text{FS}_{\text{QS}-330}^\circ\text{C}$  samples, respectively— showing the variation in RI with shape.

The analysis of RIs of (101), (202), and (-202) planes suggested that for these planes, as the reaction temperature increases, the RIs increase by 7%, 2%, and 4%, respectively for the sample  $\text{FS}_{\text{NR}-330}^\circ\text{C}$  ( $330^\circ\text{C}$ ) in comparison with the sample  $\text{FS}_{\text{NR}-260}^\circ\text{C}$  ( $260^\circ\text{C}$ ). This implies that the relative growth rate of these planes decelerates with rising temperature, making these planes more significant in the resultant morphology as temperature increases (larger MI values). The (101) plane was also predicted to be morphologically dominant among all low-index planes from theoretical crystal habit. Similarly, the (002) peak also shows an increment of up to 7%, which is consistent with the theoretical calculations. These results suggest that (101), (202), (-202), and (002) faces are parallel to longitude in a rod-like shape. TEM images well support this statement, as shown in Figure 3.

As shown in Figure 3, the (002) and (202) planes are along with the rod's longitudinal directions, having lattice fringes space at  $5.6 \text{ \AA}$  and  $2.6 \text{ \AA}$ , respectively. In contrast, it was observed that RIs of the (020) plane was hardly affected for samples synthesized at higher temperatures (Figure 5); in other words, this facet does not show any significant change in its relative growth rate with an increase in the reaction-temperature. This implies that the (020) face is vertical to longitudinal planes ((101), (202), (-202), and (002)). Although the (200) peak becomes more intense (up to 5%) with an increase in reaction temperature, the RI value is very low, indicating that this plane will contribute to faster growth in this direction. Thus, this plane is less visible in resultant morphology than the other planes. Moreover, the other planes (222),

(-222), and (011) show the increment (from sample FS<sub>NR-260 °C</sub> to FS<sub>NR-300 °C</sub>) followed by no variation in RI with rising temperature. This implies that these planes were initially slowly growing; however, the growth is dormant along with these directions at high temperatures. This suggests that these planes are at the edges of the nanorods. The (110) plane is nearly invisible in the resultant morphology as it has the least RI value. In conclusion, the variation in the RI of the above planes exhibits that for nanorods, the longitudinal growth is along the b-axis and the vertical growth is along the c and a-axis in the presence of OLA.

To validate the influence of an amine group and a double bond on the resultant morphology, the controlled experiments are carried out by changing the solvents and comparing the RI of the resulting samples (Figure 5 and Table 4). The observed variations in RI clearly demonstrate the distinct direction of growth in the varied reaction environment. For sample FS<sub>PL-330 °C</sub> (nanoplatelets), the direction of growth is swift along with the c- and a-axes, making (101) the top surface of nanoplates having a lattice fringe spaced at 5.4 Å (Figure 6). The MI of (002) reduces, and of (020) is nearly constant. Consequently, the shape deviated from rods to plates in the presence of 1-ODE and OCD.

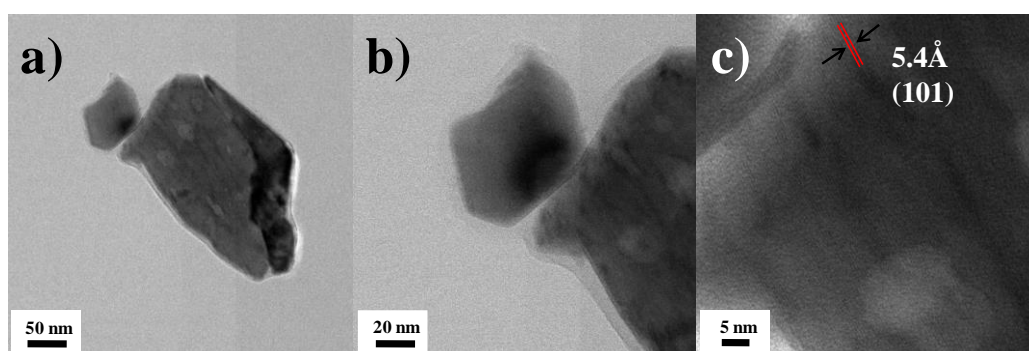


**Figure 6.** Representative TEM images of as-synthesized Fe<sub>3</sub>Se<sub>4</sub> (synthesized in the presence of 1-ODE & OCD). a) The image shows the nanoplatform morphology. b) Zoomed-in view with a scale bar of 20 nm. c) The lattice fringes spaced at 5.4 Å represents the (101) plane.

Further, the RI of sample FS<sub>QS-330 °C</sub> (quasispherical) demonstrates that the direction of growth is nearly the same along all three axes—as only an amine group is present to influence the morphology, which will behave almost identical in all the directions (a-, b- and c-axes). However, (202) is a more exposed plane having lattice fringes spaced at 2.6 Å (Figure 7)—signifies that the growth is slightly faster towards the a- and c-axes. All other planes show nearly the same MIs in the OCD environment, which fabricates the quasispherical NPs.

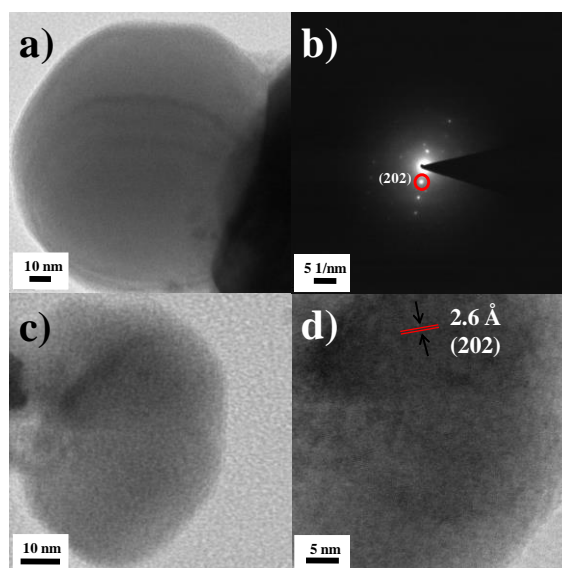


**Figure 7.** Representative TEM images of as-synthesized  $\text{Fe}_3\text{Se}_4$  (synthesized in the presence of OCD). a) The image shows the quasispherical morphology. b) The SAED pattern reveals the presence of the (202) plane. c) TEM image from different area again reveals the quasispherical morphology. d) The lattice fringes spaced at  $2.6 \text{ \AA}$  represent the (202) plane.

Therefore, after analyzing the RIs of all the planes, it is appropriate to conclude that in a distinct environment, the direction of growth varies, which leads to forming NPs with individual shapes. Additionally, as the reaction temperature rises, the growth is also increasing in a certain direction, enhancing the size of the NPs.

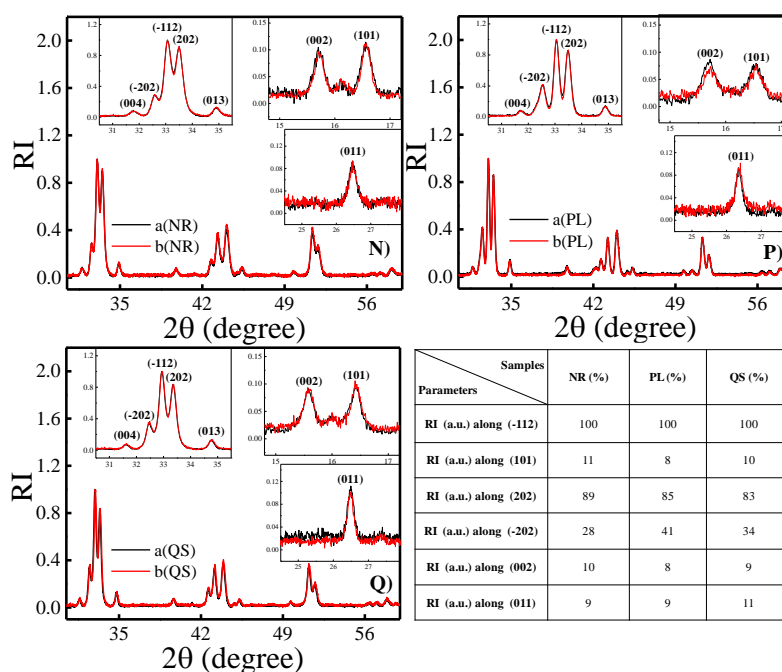


**Figure 8.** Comparing the calculated relative intensities (RI) of powder XRD peaks along different lattice planes of freshly synthesized  $\text{Fe}_3\text{Se}_4$  NPs.

To check the reproducibility of RI of XRD, the XRD of all three samples is done twice with different orientations (a and b curves for each shape), revealing that the RI changes are caused by the difference in shape, not by particle orientation. These are the re-synthesized samples, and therefore, the RI does not precisely coincide with the earlier data. However, the order of RI in different shapes is the same as mentioned earlier in the chapter (mentioned in the table). NR, PL, and QS define the  $\text{Fe}_3\text{Se}_4$  nanorods, nanoplatelets, and quasispherical, respectively, as shown in Figure 8.

### 5.4.3 Effect of $\text{Fe}_3\text{Se}_4$ crystallite size on the M-H curves at 300 K

For permanent-magnet applications, the coercivity must be high. The coercivity of NPs below the single domain size limit is known to be strongly influenced by their particle size, crystallinity, lattice defects, vacancies and their ordering, external magnetic field, anisotropic growth of crystalline facets, and overall morphology, surface spin environment, temperature, interparticle interactions, etc. Even the sample preparation method (packing of particles) can affect the coercivity values for fine particles. As the particle size is enhanced, it is generally observed that the coercivity increases and goes through a maximum up to a single domain limit size and then tends toward zero<sup>58-59</sup>.

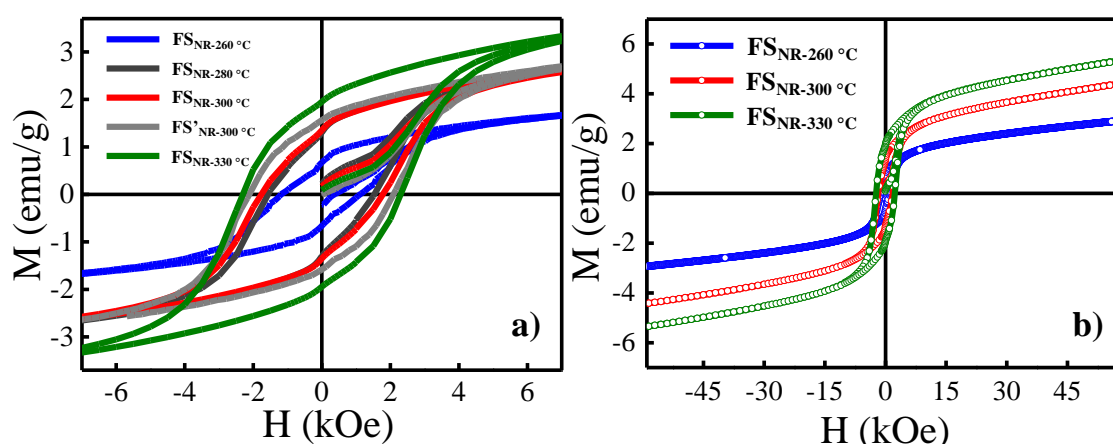


**Figure 9.** a) Magnetization vs. external magnetic field hysteresis loops at 300 K of  $\text{Fe}_3\text{Se}_4$  NPs. The blue, dark grey, red, light grey, and green loops correspond to the samples—  $\text{FS}_{\text{NR-260 °C}}$  (33 nm),  $\text{FS}_{\text{NR-280 °C}}$  (35 nm),  $\text{FS}_{\text{NR-300 °C}}$  (37 nm),  $\text{FS}'_{\text{NR-300 °C}}$  (40 nm), and  $\text{FS}_{\text{NR-330 °C}}$  (42 nm) synthesized at increasingly higher temperatures, respectively. The numbers in parentheses show the crystalline size along (-112) plane. The hysteresis curves clearly illustrate all the coercivity and remanence values of all the NPs and are rising as the crystal growth is

intensified. b) External magnetic field vs. magnetization hysteresis loops for rod-like  $\text{Fe}_3\text{Se}_4$  NPs—  $\text{FS}_{\text{NR-260 } ^\circ\text{C}}$  (33 nm),  $\text{FS}_{\text{NR-300 } ^\circ\text{C}}$  (37 nm), and  $\text{FS}_{\text{NR-330 } ^\circ\text{C}}$  (42 nm) measured at 300 K.

The magnetic properties obtained for  $\text{Fe}_3\text{Se}_4$  NPs using a SQUID-VSM show an interesting trend. Figure 9 shows a comparative study of M-H curves taken at 300 K for the specimens  $\text{FS}_{\text{NR-260 } ^\circ\text{C}}$  (33 nm),  $\text{FS}_{\text{NR-280 } ^\circ\text{C}}$  (35 nm),  $\text{FS}_{\text{NR-300 } ^\circ\text{C}}$  (37 nm),  $\text{FS}'_{\text{NR-300 } ^\circ\text{C}}$  (40 nm), and  $\text{FS}_{\text{NR-330 } ^\circ\text{C}}$  (42 nm). For clarity, the two intermediate samples [ $\text{FS}_{\text{NR-280 } ^\circ\text{C}}$  (35 nm) and  $\text{FS}'_{\text{NR-300 } ^\circ\text{C}}$  (40 nm)] have been omitted, and only three samples are considered from now onwards. All the samples indicate a typical ferrimagnetic behavior where the magnetization does not saturate until the highest applied field of 60 kOe. In earlier reports<sup>36,38</sup> also, even after applying the field of 90 kOe, the hysteresis loops of  $\text{Fe}_3\text{Se}_4$  do not saturate due to the very high anisotropy field or the spins are noncollinear in the system<sup>36</sup>.

Figure 10a reveals a zoomed-in view of the M-H curves that illustrate that the coercivity and remanence values of all the samples increase with crystal growth i.e., the magnetic properties of  $\text{Fe}_3\text{Se}_4$  are strongly affected by the crystallite size. All the samples in this study are in a single domain size. As mentioned above that the critical radius<sup>38</sup> for a single-domain particle of  $\text{Fe}_3\text{Se}_4$  is  $\sim 800$  nm at 10 K and  $\sim 2000$  nm at 300 K. The influence of crystal growth on  $H_C$  at 300 K is shown in Figure 10c, and it is observed that the  $H_C$  increases with increasing the crystallite size (33 nm to 42 nm). At 300 K,  $H_C$  of  $\text{Fe}_3\text{Se}_4$  is found to be varying from 1.1 kOe to 2.3 kOe. This increasing pattern between the  $H_C$  and crystallite size is observed because an increase in single domain size increases the magnetic moment, increasing the magnetization followed by  $H_C$ . Another important factor is surface spins. With a decrease in particle size, the surface-to-volume ratio increases, leading to a larger number of surface spins per unit volume. The surface spins are uncompensated and remain disordered or canted, which leads to the overall reduction in the magnetization with the decrease in the particle size<sup>3</sup>. As the crystallite size increases slowly from  $d = 33$  nm to 42 nm, the magnetization value ( $M_{60 \text{ kOe}}$ ) increases from 3.0 emu/g to 5.4 emu/g (higher magnetization is observed in  $\text{Fe}_3\text{Se}_4$  nanorods as compared to earlier reports<sup>36,37</sup>); the remanence magnetization ( $M_R$ ) also increases as tabulated in Table 5.

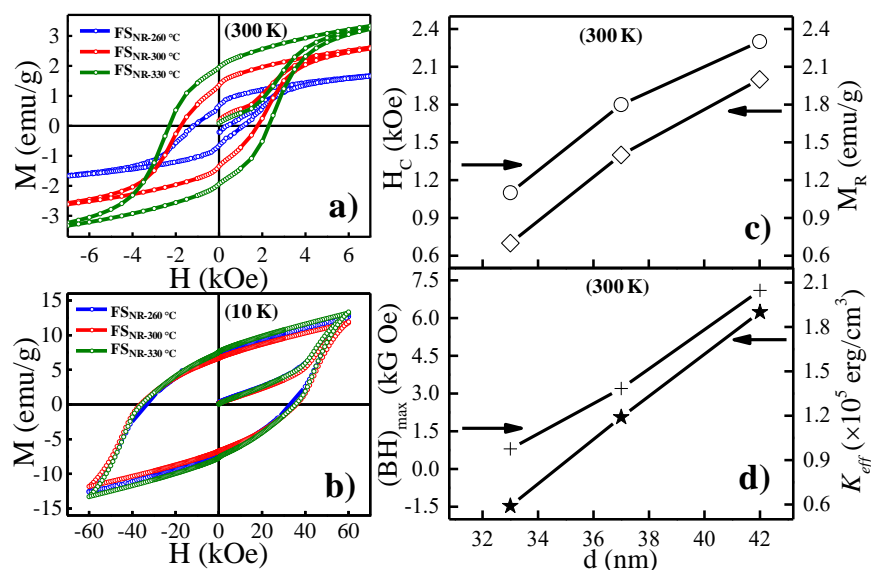
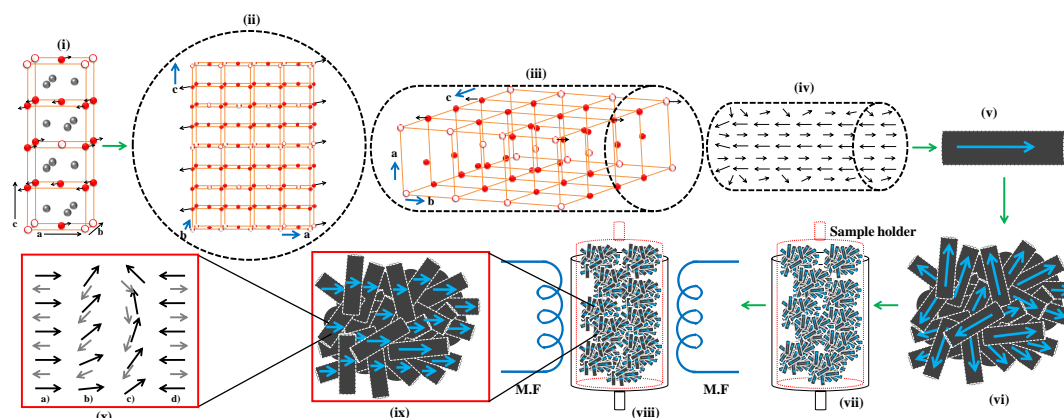


**Figure 10.** Magnetization vs. external magnetic field hysteresis loops at 300 K (Figure a) and 10 K (Figure b) of rod-like  $\text{Fe}_3\text{Se}_4$  nanoparticles. The blue, red, and green loops correspond to the samples—  $\text{FS}_{\text{NR-260 }^\circ\text{C}}$  (33 nm),  $\text{FS}_{\text{NR-300 }^\circ\text{C}}$  (37 nm), and  $\text{FS}_{\text{NR-330 }^\circ\text{C}}$  (42 nm) synthesized at increasingly higher temperatures, respectively. The numbers in parentheses show the crystalline size along the (-112) plane. Relationship between crystallite size and magnetic parameters of rod-like  $\text{Fe}_3\text{Se}_4$  NPs at 300 K. c) size dependence of coercivity ( $H_C$ ) and remanent magnetization ( $M_R$ ), and d) size dependence of energy product  $(BH)_{\max}$  and anisotropy constant ( $K_{\text{eff}}$ ).

Schematic illustration in scheme 5 shows the magnetic moments orientation of  $\text{Fe}_3\text{Se}_4$  reveals the easy axis along the b-axis<sup>37</sup>. In our samples, each building block is a single crystallite. However, the surface spins are not parallel aligned in the same direction. The resultant magnetization is in the b-axis of one single nanorod. Probably hundreds of such nanocrystallites, as building blocks, agglomerate together due to strong dipolar interactions to form a larger three-dimensional assembly (as seen in the TEM images) where the nanocrystal super-spins may remain highly disordered (or weakly ordered along the easy axis due to the interparticle interactions). In VSM, the powder sample has numerous such agglomerated particles. When the external magnetic field is applied, they try to align in one direction by incoherent spin rotation phenomena, as shown in schematic 5<sup>38</sup>.





**Scheme 5.** Schematic illustration of the actual sample situation in magnetic measurements. (i) Unit cell of  $\text{Fe}_3\text{Se}_4$  shows the magnetic moments' orientation. (ii) and (iii) Diagrammatic upper and side view of nanorod showing the orientation of magnetic moments in every layer. (iv) Nanorod shows the orientation of magnetic moments and surface spins. (v) Single nanorod reveals the resultant direction of the magnetic moment in a single particle. (vi) Agglomerated particles show the various orientation of the resulting magnetic moment in a sample. (vii) Powder sample in the sample holder of VSM in the absence of a magnetic field, the magnetic moments are randomly oriented. (viii) Powdered sample in the presence of a magnetic field. (ix) Zoomed-view reveals that all the resultant magnetic moment of particles orient in the magnetic field direction. (x) Zoomed-view reveals the phenomena followed for the spin rotation in  $\text{Fe}_3\text{Se}_4$ —the incoherent spin rotation in steps of a), b), c), and d).

It is simple to calculate the magnetic anisotropy constant ( $K$ ) in a single crystal by extrapolating the M-H curve in both easy and hard axis directions (taking the hysteresis loops in parallel and perpendicular to the easy axes). In a single crystal, the order is the same in the entire particle, making it easy to orient them in one direction. However, in a sample like us, starting from a single particle with growth in the b-axis for nanorod, many such agglomerated nanocrystallites are present (the particle shown in TEM is agglomeration single-single nanorods). Therefore, in VSM, orienting the powder sample having numerous such agglomerated particles in one easy axis and then the hard axis is not simple. There is much literature that calculated the  $K$  utilizing this method for agglomerated samples, which is not the appropriate method to calculate the actual value. However, as it is an intrinsic property of any material, calculating  $K$  by the M-H curve of such samples will give the effective  $K$  of all the particles oriented in different directions. The influence of size on the effective magnetic anisotropy constant ( $K_{eff}$ ) will be fascinating to investigate.

Generally, the anisotropy field ( $H_a$ ) of any material defines the theoretical upper limit of the coercivity. Experimentally, it is usually observed that the coercivity of any material reaches  $\sim 25\%$  of the anisotropy field<sup>37</sup>. The  $H_a$  values for all the samples were calculated by extrapolating the M-H curve in easy and hard axis directions. In view of the low magnetization of  $\text{Fe}_3\text{Se}_4$ , its shape anisotropy plays a minor contribution to the total anisotropy, while the magnetocrystalline anisotropy plays a major role<sup>36</sup>. The presence of ordered Fe vacancies in monoclinic structure gives rise to a highly anisotropic crystal field and the spin-orbit coupling, leading to a large magnetocrystalline anisotropy in the system<sup>38</sup>. The  $K_{eff}$  was calculated from  $M_S$  and  $H_a$ , according to the following equation<sup>37,38</sup>.

$$K_{eff} = \frac{1}{2} M_S H_a \text{ -----(5)}$$

The  $K_{eff}$  value was calculated for each sample and is shown in Table 5. As observed in Figure 10 d, the  $K_{eff}$  value for  $\text{Fe}_3\text{Se}_4$  increases with increasing the crystallite size due to the increase in  $M_S$  and  $H_a$ . Moreover, all the above samples' energy product ( $BH_{max}$ ) was also determined from the 2<sup>nd</sup> quadrant of the B–H loop<sup>37</sup>, as expressed in Figure 11. Figure 11 inset reveals the zoomed-in view of the 2<sup>nd</sup> quadrant of the B–H loop, and the area under the grey box represents the  $BH_{max}$  of the corresponding samples. The  $BH_{max}$  value is 0.8 kG Oe at 300 K for  $\text{FS}_{\text{NR-260}}^\circ\text{C}$  sample, which increases to 7.1 kG Oe for  $\text{FS}_{\text{NR-330}}^\circ\text{C}$ . A significant increment in the energy product values at 300 K (7.1 kG Oe) is observed compared to the earlier report<sup>37</sup> (4.377 kG Oe) for the same shape.

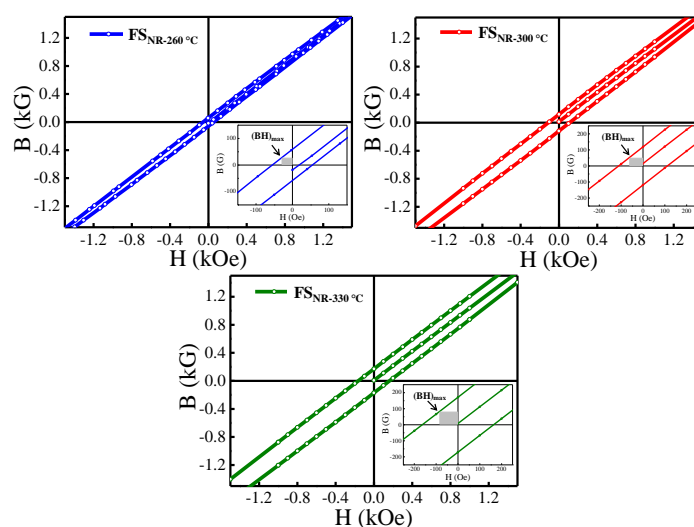


**Figure 11.** B–H plot for rod-like  $\text{Fe}_3\text{Se}_4$  NPs—  $\text{FS}_{\text{NR-260}}^\circ\text{C}$  (33 nm),  $\text{FS}_{\text{NR-300}}^\circ\text{C}$  (37 nm), and  $\text{FS}_{\text{NR-330}}^\circ\text{C}$  (42 nm) at 300 K. (Inset) Calculation of maximum energy product from the B–H hysteresis loop of  $\text{Fe}_3\text{Se}_4$  at 300 K.

Figure 10d shows the linear dependency of energy products on crystallite size. Equation 2 clearly illustrates that the energy product is directly proportional to saturation magnetization ( $M_s$ ).  $M_s$  increases with crystallization, which leads to enhancing the energy product. The practical energy product of a permanent magnet strongly influences by its processing. The development of permanent magnets necessitates the condensing of magnetic NPs with high packing densities. In order to build new rare-earth-free permanent magnets,  $\text{Fe}_3\text{Se}_4$  NPs must have a wide energy product range<sup>36,37</sup>.

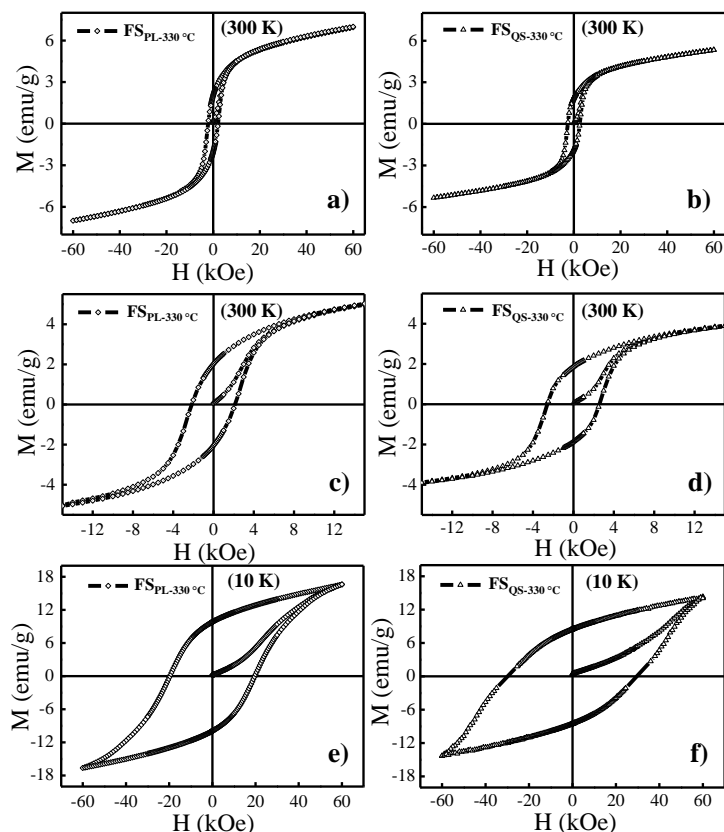
#### 5.4.4 Effect of $\text{Fe}_3\text{Se}_4$ crystallite size on the M-H curves at 10 K

Figure 10b (at 10 K), the M-H curves do not saturate for the highest applied magnetic field of 60 kOe. It is noticeable that the curves are far from saturation. Therefore, the coercive-field values (Table 5) are a gross underestimation of their true values. However, it was noted that these underestimated coercivity values of  $\text{Fe}_3\text{Se}_4$  NPs (synthesized in the presence of OLA) lie between 33 kOe to 36 kOe with crystallite size varying from 33 nm to 42 nm ( $\text{FS}_{\text{NR-260 }^\circ\text{C}}$  to  $\text{FS}_{\text{NR-330 }^\circ\text{C}}$ ), respectively. These  $H_c$  values are nearly 20 to 30-fold increase over the corresponding value at 300 K— from 2.3 kOe to 35.5 kOe ( $\text{FS}_{\text{NR-330 }^\circ\text{C}}$ ). The substantial increase in the coercivity at a lower temperature may have various contributions—the increase in the overall effective magnetic anisotropy reduction in the thermal activation energy, making more and more spins available to orient in the field direction, ferrimagnetism, etc.<sup>38</sup>. Compared to 300 K values at 10 K, the effective anisotropy rises by two orders of magnitude— from  $1.90 \times 10^5 \text{ erg/cm}^3$  (at 300 K) to  $17.2 \times 10^5 \text{ erg/cm}^3$  (at 10 K) for  $\text{FS}_{\text{NR-330 }^\circ\text{C}}$ . The  $K_{\text{eff}}$  was observed from  $16.9 \times 10^5 \text{ erg/cm}^3$  to  $17.2 \times 10^5 \text{ erg/cm}^3$  with increasing crystallite size (33 nm to 42 nm). Additionally, the energy product also shows an enhancement by nearly two orders of magnitude at 10 K— from 7.1 kG Oe (at 300 K) to 109.9 kG Oe (at 10 K), for  $\text{FS}_{\text{NR-330 }^\circ\text{C}}$ . The values of  $\text{BH}_{\text{max}}$  fluctuate from 96.6 kG Oe to 109.9 kG Oe with increasing crystallite sizes (Table 5).

#### 5.4.5 Effect of $\text{Fe}_3\text{Se}_4$ shape on the M-H curves at 300 K

The magnetic properties of  $\text{Fe}_3\text{Se}_4$  nanoplatelets ( $\text{FS}_{\text{PL-330 }^\circ\text{C}}$ ) and nanoquasispheres ( $\text{FS}_{\text{QS-330 }^\circ\text{C}}$ ) fabricated in the presence of different organic solvents (1-ODE + OCD and OCD) were also observed with SQUID magnetometer. The hysteresis loops for these shapes are compared in Figure 12, again revealing the material's ferrimagnetic and hard magnetic properties. Figures

12 c and d show a zoomed-in view of the M-H curves that clearly illustrate both samples' coercive field and remanence.



**Figure 12.** Magnetization vs. external magnetic field hysteresis loops (at 300 K and 10 K) of samples  $FS_{PL-330\text{ }^\circ\text{C}}$  and  $FS_{QS-330\text{ }^\circ\text{C}}$ —  $Fe_3Se_4$  NPs (nanoplatelets and quasispherical particles synthesized in the presence of 1-ODE + OCD and OCD, respectively).

The  $H_C$  and  $M_R$  are well affected by the shape of the NPs, Table 5. These variations in the magnetic performance arise from the distinct crystalline properties of the plate and quasisphere like NPs in comparison to the above nanorods<sup>36</sup>. At 300 K, the  $H_C$  of these compounds is distinct— 2.1 kOe for  $FS_{PL-330\text{ }^\circ\text{C}}$  and 2.6 kOe for  $FS_{QS-330\text{ }^\circ\text{C}}$ . The shape diversity also shows a variation in  $M_{60\text{ kOe}}$ ,  $H_a$ , and  $K_{eff}$  due to the small contribution from shape anisotropy also, as tabulated in Table 5. The highest magnetization to date 7.0 emu/g (at 300 K), is observed for the  $Fe_3Se_4$  compound (in the case of  $FS_{PL-330\text{ }^\circ\text{C}}$ ). The energy product of these samples was calculated at 300 K. Figure 13 reveals the zoomed-in view of the 2<sup>nd</sup> quadrant of the B–H loops, and the calculated energy product is tabulated in Table 5.

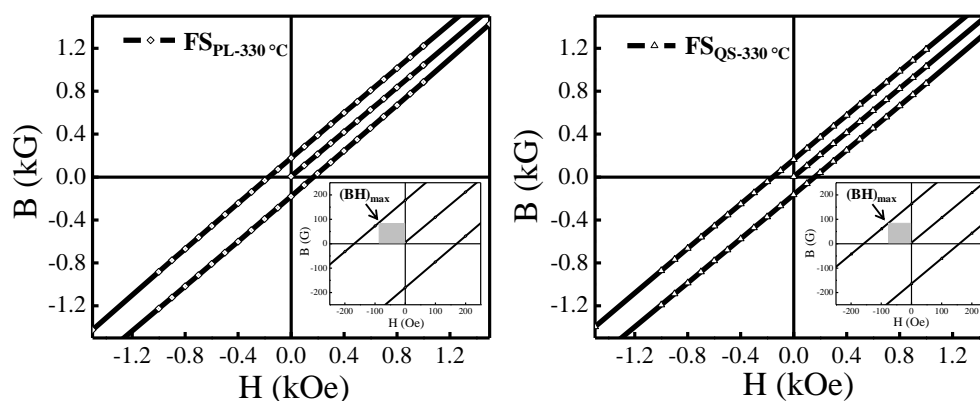


**Figure 13.** At 300 K, B–H plot for samples  $FS_{PL-330\text{ }^\circ\text{C}}$  and  $FS_{QS-330\text{ }^\circ\text{C}}$  of  $Fe_3Se_4$  NPs synthesized in 1-ODE + OCD and OCD, respectively. (Inset) Calculation of maximum energy product from the B–H hysteresis loop of  $Fe_3Se_4$  at 300 K.

#### 5.4.6 Effect of $Fe_3Se_4$ shape on the M-H curves at 10 K

Figures 12 e and f show the hysteresis loops of  $FS_{PL-330\text{ }^\circ\text{C}}$  and  $FS_{QS-330\text{ }^\circ\text{C}}$  at 10 K. The coercivity of  $FS_{PL-330\text{ }^\circ\text{C}}$  and  $FS_{QS-330\text{ }^\circ\text{C}}$  samples are 19.7 kOe and 29.6 kOe, respectively, which is again ~10-fold more significant than the value at 300 K. The substantial uniaxial magnetocrystalline anisotropy of the  $Fe_3Se_4$  with ordered Fe vacancies is responsible for the high coercivity.<sup>38</sup> Here also, the effective anisotropy is almost two orders of magnitude at 10 K compared to 300 K — from  $1.77 \times 10^5 \text{ erg/cm}^3$  (at 300 K) to  $20.3 \times 10^5 \text{ erg/cm}^3$  at (10 K) for  $FS_{PL-330\text{ }^\circ\text{C}}$ . The  $K_{eff}$  is  $20.3 \times 10^5 \text{ erg/cm}^3$  and  $14.9 \times 10^5 \text{ erg/cm}^3$  for samples  $FS_{PL-330\text{ }^\circ\text{C}}$  and  $FS_{QS-330\text{ }^\circ\text{C}}$ , respectively. The energy product of both the samples is 181.9 kG Oe and 135.7 kG Oe (Table 5).

#### 5.4.7 Magnetic property: blocking temperature

M-T curve has been examined for all the  $Fe_3Se_4$  samples in FC and ZFC modes (Figure 14). Blocking temperature depends on the particle size, its distribution, anisotropy energy, interparticle interaction, and measurement time scale. When the particle size is below the single-domain size limit; above the blocking temperature, in the absence of an external magnetic field, the particle spins are free to orient randomly as the thermal activation energy exceeds the effective anisotropy energy (superparamagnetic behavior). However, below the blocking temperature, spins freeze along their easy-axis (blocked state). The blocking temperature decreases with the decrease in the anisotropy energy and the particle volume<sup>60</sup>. Below  $T_B$ , the sample reveals the coercivity, which becomes zero above the blocking temperature.

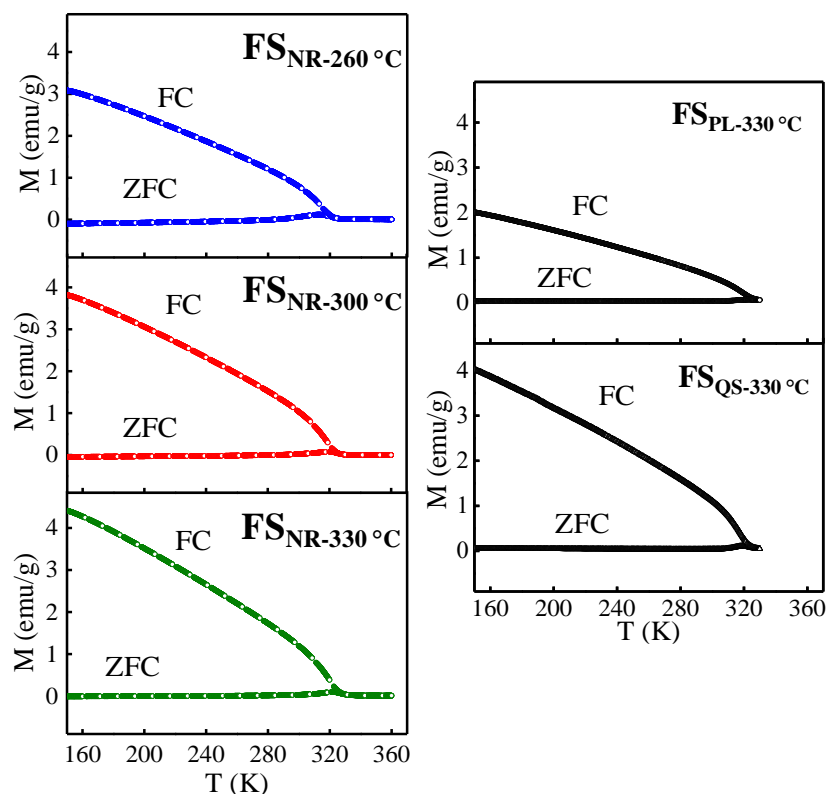


**Figure 14.** Comparison of magnetization versus temperature curves (in ZFC and FC modes) for all the as-synthesized  $\text{Fe}_3\text{Se}_4$  NPs in the applied magnetic field of 100 Oe.

As discussed earlier (schematic 5), the particles are an agglomerated mass of nanocrystalline rods that are strongly interacting with each other through dipolar interactions. Average blocking temperature ( $T_B$ ) is an indication of superparamagnetic to the blocked state transition of that material, which is taken as the peak of the ZFC curve though due to the polydispersity, the blocking events for each particle might exist on both sides of this peak and results in the separation of ZFC-FC curves well above the average  $T_B$  (the peak of the ZFC curve)<sup>60-63</sup>. Figure 15a presents the  $T_B$  for nanorod samples ( $\text{FS}_{\text{NR-260 }^\circ\text{C}}$ ,  $\text{FS}_{\text{NR-300 }^\circ\text{C}}$ , and  $\text{FS}_{\text{NR-330 }^\circ\text{C}}$ ) as 313 K, 316 K, and 322 K, respectively. Figure 15 b shows that  $T_B$  increases with increasing the crystallite size due to the increase in the anisotropy constant and the particle volume. It is noticeable that  $T_B$  also changes with shape for nanoplatelets ( $\text{FS}_{\text{PL-330 }^\circ\text{C}}$ ) and nanoquasispherical ( $\text{FS}_{\text{QS-330 }^\circ\text{C}}$ ) as 323 K and 319 K, respectively (Figures 15c and d) because of the variation in the anisotropy constant and particle volume.

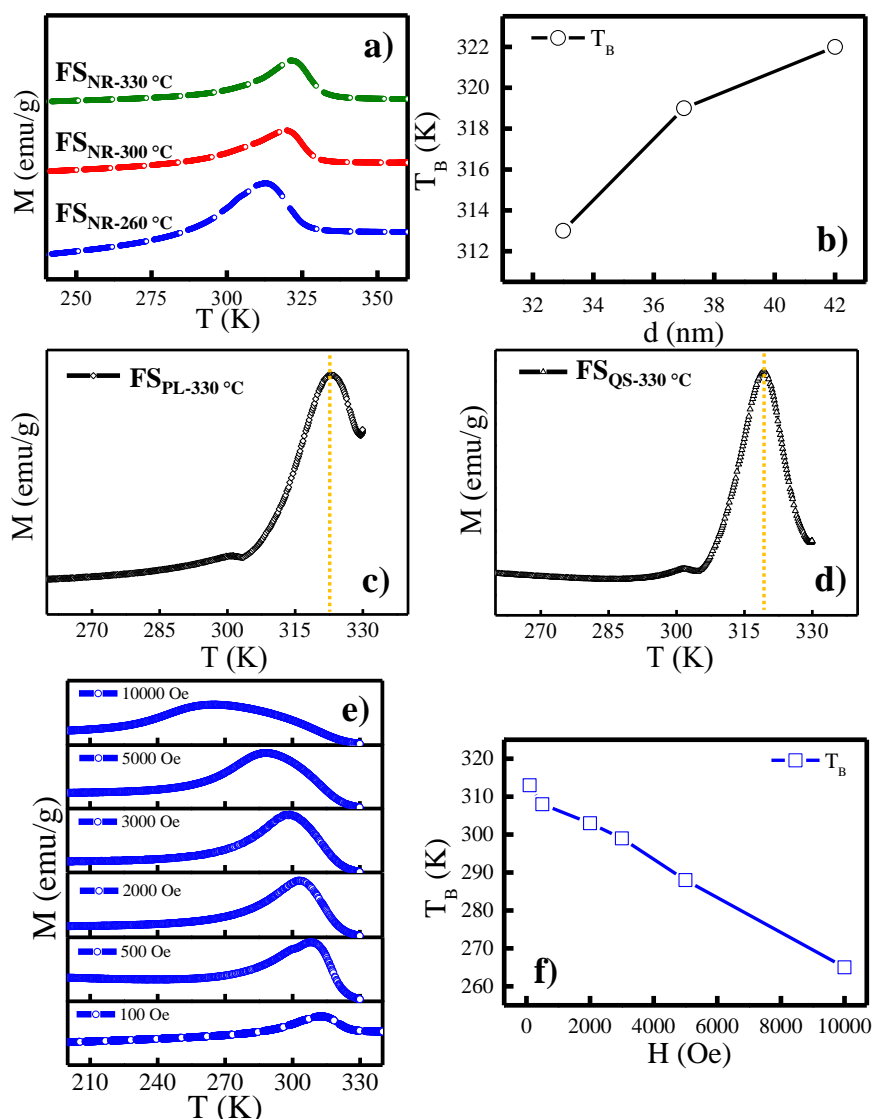


**Figure 15.** a) Zero-field-cooled (ZFC) magnetization vs. temperature (M-T) curves for rod-like Fe<sub>3</sub>Se<sub>4</sub> NPs. Blue, red, and green curves represent the sample FS<sub>NR-260 °C</sub> (33 nm), FS<sub>NR-300 °C</sub> (37 nm), and FS<sub>NR-330 °C</sub> (42 nm) synthesized at 260 °C, 300 °C, and 330 °C, respectively. b) Relationship between crystallite size and average superparamagnetic blocking temperature of rod-like Fe<sub>3</sub>Se<sub>4</sub> NPs. ZFC magnetization vs. temperature curves of the samples c) FS<sub>PL-330 °C</sub> and d) FS<sub>QS-330 °C</sub>— nanoplatforms and quasispherical Fe<sub>3</sub>Se<sub>4</sub> NPs at 100 Oe (synthesized in the presence of 1-ODE + OCD and OCD, respectively). e) M-T curves for sample FS<sub>NR-260 °C</sub> (33 nm) with varying applied magnetic fields. f) Relationship between the applied magnetic field and average superparamagnetic blocking temperature for sample FS<sub>NR-260 °C</sub>.

The thermal activation energy, magnetic anisotropy energy, and external applied magnetic field affect the blocking events of spins apart from interparticle interactions and

measurement time-scale. It is well understood that the addition of an applied magnetic field changes the energy barrier from<sup>61</sup>

$$K_u V \text{ to } K_u V [1 \pm (H/H_0)]^2 \text{ ----- (6)}$$

where  $K_u$ ,  $V$ , and  $H$  are uniaxial anisotropy constant, the particle's volume, and applied magnetic field, respectively.  $H_0$  is related to the anisotropy field by  $H_0 = 2 H_a = 2K_u/M_s$ .  $H < H_0$  and the  $\pm$  sign indicate the moment flip: + for parallel to the antiparallel direction and – for antiparallel to parallel direction. Figure 15 e presents the ZFC curves of sample FS<sub>NR-260 °C</sub> at the different external magnetic fields. It reveals that the peaks shift towards the lower temperature as the magnetic field increases. Figure 15 f shows a decrease in  $T_B$  with an increasing magnetic field, which is consistent with the quadratic dependence, as discussed by Zhang et al.<sup>61</sup>

**Table 5.** Summary of the magnetic parameters of all the samples at 300 K and 10 K. The M-H curves do not saturate for the highest applied magnetic field of 60 kOe. Therefore, these observed magnetic values are a gross underestimation of their true values.

Samples Parameters	FS <sub>NR-260 °C</sub>		FS <sub>NR-300 °C</sub>		FS <sub>NR-330 °C</sub>		FS <sub>PL-330 °C</sub>		FS <sub>QS-330 °C</sub>		
	<b>Crystallite size d (± 2 nm) along the following planes</b>										
(-112)	33		37		42		34		36		
(202)	25		31		35		28		32		
(204)	22		24		26		21		27		
<b>Magnetic parameters at different temperature</b>											
Measurement temperature (K) Magnetic parameters	300 K		10 K		300 K		10 K		300 K		10 K
	300 K	10 K	300 K	10 K	300 K	10 K	300 K	10 K	300 K	10 K	
<b>H<sub>c</sub> (kOe)</b>	1.1	32.8	1.8	35.9	2.3	35.5	2.1	19.7	2.6	29.6	
<b>M<sub>r</sub> (emu/g)</b>	0.7	7.1	1.4	6.7	2	7.6	2.1	9.8	1.9	8.5	
<b>M<sub>60 kOe</sub> (emu/g)</b>	3.0	13.0	4.5	11.9	5.4	13.3	7.0	16.6	5.3	14.3	



$M_r / M_{60 \text{ kOe}}$	0.233	0.54 9	0.311	0.56 2	0.370	0.56 9	0.30	0.59	0.356	0.594
$H_a$ (kOe)	5.7	37.3	7.6	36.2	10.1	36.8	7.2	35.0	9.0	29.9
$K_{eff}$ (erg/cm <sup>3</sup> ) x 10 <sup>5</sup>	0.59	16.9	1.19	15.1	1.90	17.2	1.77	20.3	1.68	14.9
$BH_{max}$ (kG Oe)	0.8	96.6	3.2	85.4	7.1	109. 9	7.5	181. 9	6.6	135.7

## 5.5 Conclusion

Fe<sub>3</sub>Se<sub>4</sub> NPs were intensively investigated to reveal the fundamental correlation between the size/shape and magnetic properties. The examined Fe<sub>3</sub>Se<sub>4</sub> NPs were fabricated using a one-pot thermal decomposition method under well-controlled crystal growth conditions. The grain growth of NPs estimated from the XRD pattern arise monotonically with an increase in reaction temperature. The crystallite size range is about 33 nm-42 nm depending on the reaction temperature from 260 °C to 330 °C. A discrete environment has been provided in the reactions to allow the growth of different facets, which results in the unique morphology of the NPs. All the hysteresis curves with different size/shape showed the ferrimagnetic behavior of Fe<sub>3</sub>Se<sub>4</sub>. The magnetic parameters such as  $M_s$ ,  $H_C$ ,  $K_{eff}$ ,  $BH_{max}$  and  $T_B$  exhibited a strong dependence on size and shape. The  $M_{60 \text{ kOe}}$  increases by increasing the crystallite size to a maximum value of about 5.4 emu/g at 300 K for nanorods while it becomes 7 emu/g for nanoplatelets. The  $H_C$  and  $M_R$  values also increase with increasing the crystallite size up to a maximum value of about 2.3 Oe and 2 emu/g, respectively, for nanorods. The  $BH_{max}$  increases linearly with crystallite size up to a maximum value of 7.1 kG Oe at 300 K for nanorods, and it reaches 7.5 kG Oe for nanoplatelets. These findings show that considerable attention should be given to tuning the size and shape of TMCs, which have potential industrial applications.

## 5.6 References

- (1) Jeevanandam, J.; Barhoum, A.; Chan, Y. S.; Dufresne, A.; Danquah, M. K. Review on Nanoparticles and Nanostructured Materials: History, Sources, Toxicity and Regulations. *Beilstein J. Nanotechnol.* **2018**, *9*, 1050–1074.
- (2) Khan, I.; Saeed, K.; Khan, I. Nanoparticles: Properties, Applications and Toxicities. *Arab. J. Chem.* **2019**, *12*, 908–931.

- (3) Issa, B.; Obaidat, I. M.; Albiss, B. A.; Haik, Y. Magnetic Nanoparticles: Surface Effects and Properties Related to Biomedicine Applications. *Int. J. Mol. Sci.* **2013**, *14*, 21266-21305.
- (4) Poddar, P.; Telem-Shafir, T.; Fried, T.; Markovich, G. Dipolar Interactions in Two- and Three-Dimensional Magnetic Nanoparticle Arrays. *Phys. Rev. B.* **2002**, *66*, 060403.
- (5) Poddar, P.; Fried, T.; Markovich, G. First-Order Metal- Insulator Transition and Spin-Polarized Tunneling in Fe<sub>3</sub>O<sub>4</sub> nanocrystals. *Phys. Rev. B.* **2002**, *65*, 172405.
- (6) El-sayed, M. A. Small Is Different: Shape-, Size-, and Composition-Dependent Properties of Some Colloidal Semiconductor Nanocrystals. *Acc. Chem. Res.* **2004**, *37*, 326-333.
- (7) Ray, P. C. Size and Shape Dependent Second Order Nonlinear Optical Properties of Nanomaterials and Their Application in Biological and Chemical Sensing. *Chem. Rev.* **2010**, *110*, 5332–5365.
- (8) Xia, Y.; Xia, X.; Peng, H. C. Shape-Controlled Synthesis of Colloidal Metal Nanocrystals: Thermodynamic versus Kinetic Products. *J. Am. Chem. Soc.* **2015**, *137*, 7947–7966.
- (9) Frey, N. A.; Peng, S.; Cheng, K.; Sun, S. Magnetic Nanoparticles: Synthesis, Functionalization, and Applications in Bioimaging and Magnetic Energy Storage. *Chem. Soc. Rev.* **2009**, *38*, 2532–2542.
- (10) Nistico, R.; Cesano, F. Magnetic Materials and Systems : Domain Structure Visualization and Other Characterization Techniques for the Application in the Materials Science and Biomedicine. *Inorganics* **2020**, *8*, 6.
- (11) Colombo, M.; Carregal-romero, S.; Casula, M. F.; Gutierrez, L.; Morales, M. P.; Bohm, I. B.; Heverhagen, J. T.; Prosperi, D.; Parak, W. J. Biological Applications of Magnetic Nanoparticles. *Chem. Soc. Rev.* **2012**, *41*, 4306–4334.
- (12) Zhang, H. W.; Liu, Y.; Sun, S. H. Synthesis and Assembly of Magnetic Nanoparticles For information and energy storage applications. *Front. Phys. China* **2010**, *5*, 347–356.
- (13) Sun, H. L.; Shi, H.; Zhao, F.; Qi, L.; Gao, S. Shape-Dependent Magnetic Properties of Low-Dimensional Nanoscale Prussian Blue (PB) Analogue SmFe(CN)<sub>6</sub>·4H<sub>2</sub>O *Chem. Commun.* **2005**, 4339–4341.
- (14) Oyarzún, S.; Tamion, A.; Tournus, F.; Dupuis, V.; Hillenkamp, M. Size Effects in the Magnetic Anisotropy of Embedded Cobalt Nanoparticles : From Shape to Surface. *Sci. Rep.* **2015**, *5*, 14749.
- (15) Moreno, R.; Poyser, S.; Meilak, D.; Meo, A.; Jenkins, S.; Lazarov, V. K.; Vallejo-Fernandez, G.; Majetich, S.; Evans, R. F. L. The Role of Faceting and Elongation on the Magnetic Anisotropy of Magnetite Fe<sub>3</sub>O<sub>4</sub> Nanocrystals. *Sci. Rep.* **2020**, *10*, 2722.
- (16) Liu, L.; Kou, H. Z.; Mo, W.; Liu, H.; Wang, Y. Surfactant-Assisted Synthesis of  $\alpha$ -Fe<sub>2</sub>O<sub>3</sub> Nanotubes and Nanorods with Shape-Dependent Magnetic Properties. *J. Phys. Chem. B* **2006**, *110*, 15218-15223.
- (17) Chatterjee, J.; Haik, Y.; Chen, C. J. Size Dependent Magnetic Properties of Iron Oxide Nanoparticles. *J. Magn. Magn. Mater.* **2003**, *257*, 113–118.
- (18) Park, T. J.; Papaefthymiou, G. C.; Viescas, A. J.; Moodenbaugh, A. R.; Wong, S. S. Size-Dependent Magnetic Properties of Single-Crystalline Multiferroic BiFeO<sub>3</sub> Nanoparticles. *Nano Lett.* **2007**, *7*, 3.
- (19) Ma, F.; Ma, J.; Huang, J.; Li, J. The Shape Dependence of Magnetic and Microwave Properties for Ni Nanoparticles. *J. Magn. Magn. Mater.* **2012**, *324*, 205–209.
- (20) Singh, A. K.; Srivastava, O. N.; Singh, K. Shape and Size-Dependent Magnetic Properties of Fe<sub>3</sub>O<sub>4</sub> Nanoparticles Synthesized Using Piperidine. *Nanoscale Res. Lett.* **2017**, *12*, 298.
- (21) Gabbasov, R. R.; Cherepanov, V. M.; Chuev, M. A.; Polikarpov, M. A. Size Effect of Mössbauer

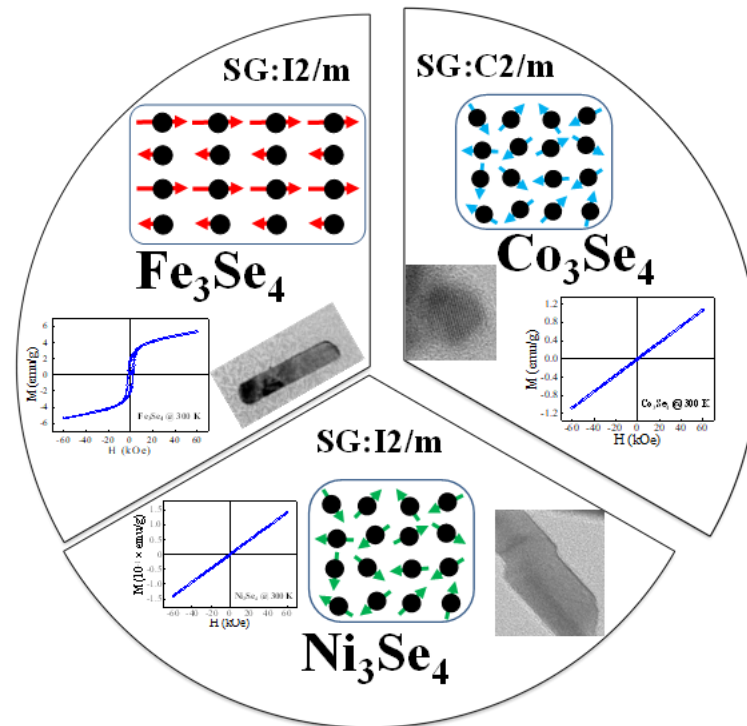
- Parameters in Iron Oxide Nanoparticles. *Hyperfine Interact.* **2014**, 226, 383–387.
- (22) Artus, M.; Tahar, L. B.; Herbst, F.; Smiri, L.; Villian, F.; Yaacoub, N.; Greneche, J.M.; Ammar, S.; Fievet, F. Size-Dependent Magnetic Properties of  $\text{CoFe}_2\text{O}_4$  Nanoparticles Prepared in Polyol. *J. Phys.: Condens. Matter.* **2011**, 23, 506001.
- (23) Song, Q.; Zhang, Z. J. Shape Control and Associated Magnetic Properties of Spinel Cobalt Ferrite Nanocrystals. *J. Am. Chem. Soc.* **2004**, 126, 6164–6168.
- (24) Tan, Y.; Zhuang, Z.; Peng, Q.; Li, Y. Room-Temperature Soft Magnetic Iron Oxide Nanocrystals: Synthesis, Characterization, and Size-Dependent Magnetic Properties. *Chem. Mater.* **2008**, 20, 5029–5034.
- (25) Vasundhara, K.; Achary, S. N.; Deshpande, S. K.; Babu, P. D.; Meena, S. S.; Tyagi, A.K. Size Dependent Magnetic and Dielectric Properties of Nano  $\text{CoFe}_2\text{O}_4$  Prepared by a Salt Assisted Gel-Combustion Method. *J. Appl. Phys.* **2013**, 113, 194101.
- (26) Rajendran, M.; Deka, S.; Joy, P. A.; Bhattacharya, A. K. Size-Dependent Magnetic Properties of Nanocrystalline Yttrium Iron Garnet Powders. *J. Magn. Magn. Mater.* **2006**, 301, 212–219.
- (27) Reddy, V. A.; Pathak, N. P.; Nath, R. Particle Size Dependent Magnetic Properties and Phase Transitions in Multiferroic  $\text{BiFeO}_3$  Nano-Particles. *J. Alloys Compd.* **2012**, 543, 206–212.
- (28) Ichiyanagi, Y.; Yamada, S. The Size-Dependent Magnetic Properties of  $\text{Co}_3\text{O}_4$  Nanoparticles. *Polyhedron.* **2005**, 24, 2813–2816.
- (29) Chen, J. P.; Sorensen, C. M.; Klabunde, K.J.; Hadjipanayis, G.C.; Devlin, E.; Kostikas, A. Size-Dependent Magnetic Properties of  $\text{MnFe}_2\text{O}_4$  Fine Particles Synthesized by Coprecipitation. *Phys. Rev. B.* **1996**, 54, 9288–9296.
- (30) Ghalawat, M.; Poddar, P. Study of the Phase-Evolution Mechanism of an Fe–Se System at the Nanoscale: Optimization of Synthesis Conditions for the Isolation of Pure Phases and Their Controlled Growth. *Langmuir* **2020** 36, 2012–2022.
- (31) Schuster, W.; Mikler, H.; Komarek, K. L. Transition Metal-Chalcogen Systems, VII.: The Iron-Selenium Phase Diagram. *Monatshefte für Chemie* **1979**, 110, 1153–1170.
- (32) Okazaki, A.; Kinshiro, H. Structural Study of Iron Selenides  $\text{FeSe}_x$ . I Ordered Arrangement of Defects of Fe Atoms. *J. Phys. Soc. Jpn.* **1956**, 11, 930–936.
- (33) Hirone, T.; Chiba, S. The Magnetic Properties of  $\text{FeSe}_x$  with the NiAs Structure. *J. Phys. Soc. Jpn.* **1956**, 11, 666–670.
- (34) Hirakawa, K. The Magnetic Properties of Iron Selenide Single Crystals. *J. Phys. Soc. Jpn.* **1957**, 12, 929–938.
- (35) Lyubutin, I. S.; Lin, C. R.; Funtov, K. O.; Dmitrieva, T. V.; Starchikov, S. S.; Siao, Y. J.; Chen, M. L. Structural, Magnetic, and Electronic Properties of Iron Selenide  $\text{Fe}_{6-7}\text{Se}_8$  Nanoparticles Obtained by Thermal Decomposition in High-Temperature Organic Solvents. *J. Chem. Phys.* **2014**, 141, 044704.
- (36) Zhang, H.; Long, G.; Li, D.; Sabirianov, R.; Zeng, H.  $\text{Fe}_3\text{Se}_4$  Nanostructures with Giant Coercivity Synthesized by Solution Chemistry. *Chem. Mater.* **2011**, 23, 3769–3774.
- (37) Sen Bishwas, M.; Das, R.; Poddar, P. Large Increase in the Energy Product of  $\text{Fe}_3\text{Se}_4$  by Fe-Site Doping. *J. Phys. Chem. C* **2014**, 118, 4016–4022.
- (38) Long, G.; Zhang, H.; Li, D.; Sabirianov, R.; Zhang, Z.; Zeng, H. Magnetic Anisotropy and Coercivity of  $\text{Fe}_3\text{Se}_4$  Nanostructures. *Appl. Phys. Lett.* **2011**, 99, 202103.

- (39) Andresen, A. F. A Neutron Diffraction Investigation of Fe<sub>3</sub>Se<sub>4</sub>. *Acta Chem. Scand.* **1968**, *22*, 827–835.
- (40) Kurmoo, M.; Kepert, C. J. Hard Magnets Based on Transition Metal Complexes with the Dicyanamide Anion, {N(CN)<sub>2</sub>}<sup>-</sup>. *New J. Chem.* **1998**, *22*, 1515–1524.
- (41) Gutfleisch, O.; Lyubina, J.; Müller, K. H.; Schultz, L. FePt Hard Magnets. *Adv. Eng. Mater.* **2005**, *7*, 208–212.
- (42) Kramer, M. J.; Mccallum, R. W.; Anderson, I. A.; Constantinides, S. Prospects for Non-Rare Earth Permanent Magnets for Traction Motors and Generators. *JOM* **2012**, *64*, 752–763.
- (43) Kharel, P.; Shah, V. R.; Li, X. Z.; Zhang, W. Y.; Skomski, R.; Shield, J. E.; Sellmyer, D. J. Structural and Magnetic Properties of Pralloyed MnBi Nanostructures. *J. Phys. D: Appl. Phys.* **2013**, *46*, 095003.
- (44) Ringe, E.; Duyne, R. P. V.; Marks, L. D. Kinetic and Thermodynamic Modified Wulff Constructions for Twinned Nanoparticles. *J. Phys. Chem. C* **2013**, *117*, 15859–15870.
- (45) Wulff, G. On the Question of Speed of Growth and Dissolution of Crystal Surfaces. *Z. Kristallogr.* **1901**, *34*, 449–530.
- (46) Srivastava, B. B.; Jana, S.; Sarma, D. D.; Pradhan, N. Surface Ligand Population Controlled Oriented Attachment: A Case of CdS Nanowires. *J. Phys. Chem. Lett.* **2010**, *1*, 1932–1935.
- (47) Holzwarth, U., Gibson, N. The Scherrer equation versus the 'Debye-Scherrer equation'. *Nature Nanotech* **2011**, *6*, 534.
- (48) Patterson, A. L. The Scherrer Formula for X-ray Particle Size Determination. *Physical review* **1939**, *56*, 978–982.
- (49) Cullity, B. D., & Stock, S. R. *Elements of X-ray Diffraction, Third Edition*. Prentice-Hall **2001**.
- (50) Viswanatha, R.; Sarma, D. D. Growth of Nanocrystals in Solution. In *Nanomaterials Chemistry: Recent Developments and New Directions*; Rao, C. N. R., Muller, A. M., Cheetham, A. K., Eds.; WileyVCH Verlag: Weinheim, Germany, 2007, 139–170.
- (51) Viswanatha, R.; Amenitsch, H.; Sarma, D. D. Growth Kinetics of ZnO Nanocrystals: A Few Surprises. *J. Am. Chem. Soc.* 2007, *129*, 4470–4475.
- (52) Viswanatha, R.; Santra, P. K.; Dasgupta, C.; Sarma, D. D. Growth Mechanism of Nanocrystals in Solution: ZnO, a Case Study. *PRL* 2007, *98*, 255501.
- (53) Hoene, J. V.; Charles, R. G.; Hickam, W. M. Thermal Decomposition of Metal Acetylacetonates: Mass Spectrometer Studies. *J. Phys. Chem.* 1958, *62*, 1098–1101.
- (54) Hou, B.; Benito-Alifonso, D.; Webster, R.; Cherns, D.; Galan, M. C.; Fermín, D. J. Rapid Phosphine-Free Synthesis of CdSe Quantum Dots: Promoting the Generation of Se Precursors Using a Radical Initiator. *J. Mater. Chem. A* 2014, *2*, 6879–6886.
- (55) Lambert-Andron, B.; Berodias, G. Etude Par Diffraction Neutronique de Fe<sub>3</sub>Se<sub>4</sub>. *Solid State Commun.* **1969**, *7*, 623–329.
- (56) Inoue, M.; Hirasawa, I. The Realationship Between Crystal Morphology and XRD Peak Intensity on CaSO<sub>4</sub>·2H<sub>2</sub>O. *J. Cryst. Growth* **2013**, *380*, 169–175.
- (57) Malik, M.; Padhye, P.; Poddar, P. Graphene Quantum Dots-Driven Multiform Morphologies of β-NaYF<sub>4</sub>:Gd<sup>3+</sup>/Tb<sup>3+</sup> Phosphors: The Underlying Mechanism and Their Optical Properties. *ACS Omega* **2018**, *3*, 1834–1849.

- (58) Cullity, B. D. Introduction to Magnetic Materials, Addison- Wesley, Reading, Mass, USA, **1974**.
- (59) Zhang, M.; Zi, Z.; Liu, Q.; Zhang, P.; Tang, X.; Yang, J.; Zhu, X.; Sun, Y.; Dai, J. Size Effects on Magnetic Properties of Prepared by Sol-Gel Method, *Adv. Mater. Sci.* **2013**, *2013*, 609819.
- (60) Coey, J. M. D. Magnetism and Magnetic Materials, 1st ed.; Cambridge University Press: Cambridge, U.K., **2010**.
- (61) Zhang, Y. D.; Budnick, J. I.; Hines, W. A.; Chien, C. L.; Xiao, J. Q. Effect of Magnetic Field on the Superparamagnetic Relaxation in Granular Co-Ag Samples *Appl. Phys. Lett.* **1998**, *72*, 16.
- (62) Mohapatra, J.; Mitra, A.; Bahadur, D.; Aslam, M. Surface Controlled Synthesis of  $MFe_2O_4$  (M = Mn, Fe, Co, Ni and Zn) Nanoparticles and Their Magnetic Characteristics *Cryst. Eng. Comm.* **2013**, *15*, 524–532.
- (63) Kolhatkar, A. G.; Jamison, A. C.; Litvinov, D.; Willson, R. C.; Lee, T. R. Tuning the Magnetic Properties of Nanoparticles; *Int. J. Mol. Sci.* **2013**, *14*, 15977-16009.

## Chapter 6

### Influence of M in Monoclinic $M_3Se_4$ (M= Fe, Co, and Ni) Compounds on the Structure, Morphology, and Magnetic Properties at Nanoscale



## Highlights

Below, we have listed some of the important 'take-away' points from this chapter:

- 1) *Herein, the conscious effort has been made in fabricating the monoclinic  $M_3Se_4$  compounds (where  $M$  can be Fe, Co or Ni) by a thermal decomposition method.*
- 2) *The deep mechanistic insight of theoretical crystal habit helped in understanding the reason behind the varied experimental morphology of  $M_3Se_4$ .*
- 3) *The influence of transition metal ( $M$ ) on the magnetic properties is investigated for monoclinic  $M_3Se_4$  NPs.*
- 4)  *$Fe_3Se_4$  is observed to be well known ferrimagnetic with Curie temperature of nearly 322 K. However, the other two compounds  $Co_3Se_4$  and  $Ni_3Se_4$  are examined to be paramagnetic over whole measurement temperature range (5 K to 300 K).*

**Keywords:** Transition metal selenides, monoclinic  $M_3Se_4$ , displacive transitions, magnetic properties.

The results of this chapter will be published as —

- ✓ Influence of M in Monoclinic  $M_3Se_4$  (M= Fe, Co, and Ni) Compounds on the Structure, Morphology, and Magnetic Properties at Nanoscale

**Monika Ghalawat**, Pankaj Poddar\* (To be communicated)

## 6.1 Introduction

TMCs are regarded as promising materials with rich phase diagrams<sup>1</sup>. However, compared to the oxides, control over chalcogenides is difficult due to complexities in phase-diagram, poor control over stoichiometry, and morphology. It is well known that the electronic (optical, magnetic, and electrical) and thermal properties of solids are extremely sensitive to the crystalline phase, stoichiometry, shape, and size<sup>2-6</sup>. Therefore, one of the critical challenges is obtaining control over the chemistry of phase formation of TMCs. Recently, among TMCs, much attention has been given to transition metal selenides (TMSes) because they potentially have interesting and unique chemical and physical properties<sup>7-9</sup>. Studying the changes in magnetic, electrical, thermal, and optical properties of these materials will be interesting, which are strongly related to the type of transition metal ions (M) and M-Se elemental ratio. The unique and novel M-dependent properties displayed by crystals have always posed curiosity, challenges, and opportunities.

In addition, the nano-dimensionality has added immense advantages in the physical and chemical property tunability through the surface to volume ratio variation. Many of the wonders seen in the nature can be understood by the nanoscale phenomena. In case of magnetic materials, their properties are extremely sensitive to their size, shape, elemental ratio, and crystallinity<sup>10-12</sup>. Moreover, their assembly needs to be precisely controlled for magnetic materials over certain other materials as subtle changes in these parameters have a relatively larger influence on the applications. Some of the well-known applications of magnetic materials include high-density magnetic memory storage, magnetic read-heads, ferrofluids, and biotechnology<sup>13-19</sup>.

In the previous chapters<sup>20</sup>, complexities in the phase diagram and control over stoichiometry have been explored in Fe-Se system, which has 4 stable phases— orthorhombic FeSe<sub>2</sub>, monoclinic Fe<sub>3</sub>Se<sub>4</sub>, hexagonal Fe<sub>7</sub>Se<sub>8</sub>, and tetragonal  $\beta$ -FeSe. The study of phase-dependent magnetic properties gave the comprehension that Fe<sub>3</sub>Se<sub>4</sub> phase possesses most interesting magnetic properties among all the 4 phases<sup>21</sup>. The ferrimagnetism of this combination is thought to be caused by ordered iron vacancies in alternate layers. The Fe<sup>2+</sup>/Fe<sup>3+</sup> cations and Se<sup>2-</sup> anions are arranged in alternating layers along the c-axis, and the deviation from (1:1) stoichiometry leads to the formation of cation vacancies in every second Fe-layer to compensate the iron deficiency, and these vacancies are distributed as far apart as possible. Each layer has a different magnetization value, as the number of vacancies and the vacancy



distribution is distinct in each layer<sup>22</sup>. In a unit cell, the cation vacancies appear in every other Fe layer with a different number in each alternating layer. These cation vacancies are lying in the (-101) plane<sup>23–24</sup>. Thus, the origin of ferrimagnetic ordering is attributed to the spins ferromagnetically aligned within each plane along the c-axis and antiferromagnetically aligned in an adjacent plane with ordered iron vacancies<sup>24</sup>.

At nano-dimensions, the  $\text{Fe}_3\text{Se}_4$  reveals semi-hard magnetic properties below its Curie temperature ( $T_C$ ) even without the noble metal or rare-earth atoms, making it a unique material. The magnetic properties of  $\text{Fe}_3\text{Se}_4$  nanoparticles (NPs) via changing cations from Fe to nearby transition metals are not completely understood so far due to the complexity of fabricating the single phase  $\text{M}_3\text{Se}_4$  ( $M = \text{Fe}, \text{Co}, \text{Ni}$ ) NPs. It has even been suggested that  $\text{Co}_3\text{Se}_4$  and  $\text{Ni}_3\text{Se}_4$  are paramagnetic in nature<sup>25</sup>; however, no experimental work has been demonstrated to critically investigate this assumption. Other than their magnetic properties, the  $\text{Co}_3\text{Se}_4$ , and  $\text{Ni}_3\text{Se}_4$  recently gained huge attention as a prominent catalysts and showed high electrocatalytic activities towards hydrogen and oxygen evolution reactions (HER and OER)<sup>26–29</sup>.

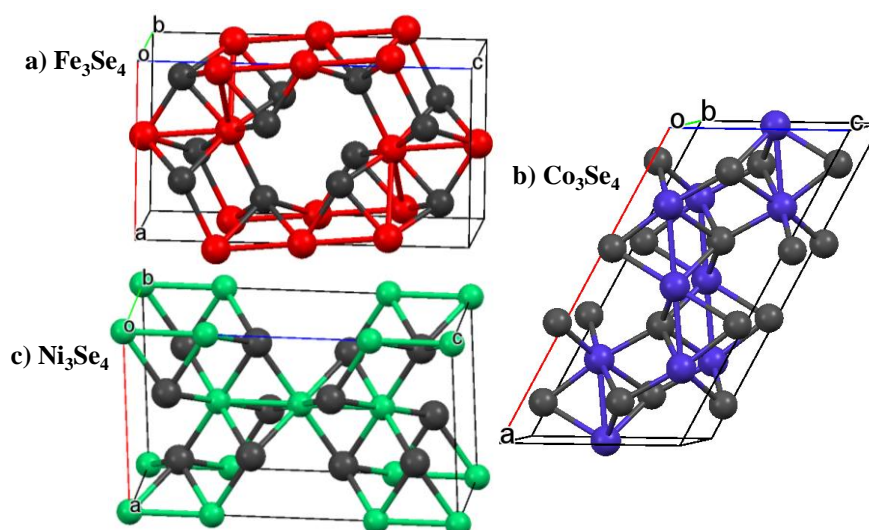


**Figure 1.** Schematic of the unit cell of a)  $\text{Fe}_3\text{Se}_4$ , b)  $\text{Co}_3\text{Se}_4$ , and c)  $\text{Ni}_3\text{Se}_4$  having monoclinic NiAs-type crystal structure. Red, blue, and green circles represent Fe, Co, and Ni cations. Grey circles represent Se anions.

The compounds  $\text{M}_3\text{Se}_4$  ( $\text{M}^{2+}$ )<sub>1</sub>( $\text{M}^{3+}$ )<sub>2</sub>( $\text{Se}^{2-}$ )<sub>4</sub> (where  $M = \text{Fe}, \text{Co},$  and  $\text{Ni}$ ) crystallizes in the monoclinic space group (SG)  $I2/m$  ( $\text{Fe}_3\text{Se}_4$  and  $\text{Ni}_3\text{Se}_4$ ) and  $C2/m$  ( $\text{Co}_3\text{Se}_4$ ) as drawn in Figure 1. For  $\text{Fe}_3\text{Se}_4$ <sup>30</sup>, the lattice parameters of unit cell are  $a=6.20 \text{ \AA}$ ,  $b=3.54 \text{ \AA}$ , and  $c=11.28 \text{ \AA}$  [ $\alpha = \gamma = 90^\circ$ ,  $\beta = 91.807^\circ$ ] and for  $\text{Ni}_3\text{Se}_4$ <sup>31</sup>  $a=6.19 \text{ \AA}$ ,  $b=3.63 \text{ \AA}$ , and  $c=10.45 \text{ \AA}$  [ $\alpha = \gamma = 90^\circ$ ,  $\beta = 90.05^\circ$ ]. Whereas, for  $\text{Co}_3\text{Se}_4$ <sup>32</sup> the parameters are  $a=12.10 \text{ \AA}$ ,  $b=3.57 \text{ \AA}$ , and  $c=6.18 \text{ \AA}$  [ $\alpha =$

$\gamma = 90^\circ$ ,  $\beta = 120.73^\circ$ ]. Two geometrically distinct cation sites are present in each crystal structure. For  $\text{Fe}_3\text{Se}_4$ —  $[\text{Fe}^{3+}]_A [\text{Fe}^{3+}\text{Fe}^{2+}]_B (\text{Se}^{2-})_4$ : Se atoms tetrahedrally coordinate A sites, which are inhabited only by  $\text{Fe}^{3+}$  cations, whereas Se atoms octahedrally coordinate B sites, which are occupied equally by  $\text{Fe}^{2+}$  and  $\text{Fe}^{3+}$  cations. For  $(\text{Co/Ni})_3\text{Se}_4$ —  $[(\text{Co/Ni})^{2+}]_A [((\text{Co/Ni})^{3+})_2]_B (\text{Se}^{2-})_4$ : A sites are tetrahedrally coordinated by Se atoms and are occupied exclusively by  $(\text{Co/Ni})^{2+}$  cations, while B sites are octahedrally coordinated by Se atoms and are occupied exclusively by  $(\text{Co/Ni})^{3+}$  cations.

In this chapter, the syntheses of single phase  $\text{M}_3\text{Se}_4$  (M= Fe, Co, and Ni) have been reported at the nanoscale. This will also open various new directions for the controlled syntheses of several other TMCs. This study also highlights the essential points— starting by observing the crystal habits of  $\text{M}_3\text{Se}_4$  compounds according to the theoretical models and discussing the underlying reason for particular experimental morphology in each of these phases. The variation of oxidation states of M ions sitting at the surface in  $\text{M}_3\text{Se}_4$  NPs is also discussed using surface-sensitive techniques compared to the sub-surface M ions. A unique distinct magnetic property is observed with changing transition metal in monoclinic  $\text{M}_3\text{Se}_4$  NPs, and the reason behind the findings is also explained.

## 6.2 Thermal decomposition-based synthesis of $\text{M}_3\text{Se}_4$ compounds at the nanoscale

A one-pot thermal decomposition method has been used to synthesize the monoclinic  $\text{M}_3\text{Se}_4$  nanocrystals. Drawing from our experiences, the synthesis method that gave us the  $\text{Fe}_3\text{Se}_4$  NPs of the largest size nanorods ( $T = 330^\circ\text{C}$  in presence of oleylamine (OLA)) was used to synthesize  $\text{Co}_3\text{Se}_4$ , and  $\text{Ni}_3\text{Se}_4$  NPs. The reaction parameters are the same in all experiments except the initial precursor of transition metal. In a typical reaction, 1.5 mmol portion of metal acetylacetonate {0.53 g for  $\text{Fe}(\text{acac})_3$  [Iron (III) acetylacetonate; 99.99%] and  $\text{Co}(\text{acac})_3$  [cobalt (III) acetylacetonate; 99.99%]; 0.38 g for  $\text{Ni}(\text{acac})_2$  [nickel (II) acetylacetonate; 95%]} were used as organometallic precursors and 2 mmol of Se powder [0.158 g] as a Se precursor. Both the precursors were added to an organic solvent of OLA (15 mL) at  $30^\circ\text{C}$  in a 100 mL three-neck round-bottom (RB) flask with constant magnetic stirring under the flow of high-purity nitrogen gas. The reaction temperature was raised from  $30^\circ\text{C}$  to  $120^\circ\text{C}$  and maintained for 30 min at  $120^\circ\text{C}$ . Further, the temperature was raised at a ramping rate of  $2^\circ\text{C min}^{-1}$  up to  $200^\circ\text{C}$ , and  $5^\circ\text{C min}^{-1}$  was used to reach  $330^\circ\text{C}$ , at which the samples were maintained for a 60 min. In all the reactions, a thermometer was placed inside the RB-flask, and the temperature

was kept stable within  $\pm 2.0$  °C. After 60 min at 330 °C, the reaction was cooled to laboratory temperature ( $\sim 30$  °C) by detaching the heating source. After cooling, the specimens were washed with 20 mL of 2-propanol, further separated from the solution by centrifugation. The obtained samples were rewashed with a mixture of 15 mL n-hexane and 10 mL 2-propanol. Finally, the resultant black precipitate was dried in the vacuum at laboratory temperature and utilized for further characterization.

### 6.3 Characterization techniques

Powder X-ray diffraction (XRD) measurements were taken on a PANalytical X'PERT PRO instrument ( $\lambda = 1.54$  Å) in  $2\theta$  range of  $10^\circ - 80^\circ$ . The size, morphology, SAED, and lattice images were characterized using a FEI Tecnai T20 transmission electron microscopy (TEM) equipped with a super twin lens (s-twin) operated at 200 keV accelerating voltage. The powders were dispersed in n-hexane and then drop-casted on a carbon-coated copper TEM grid with 200 mesh and loaded in a single tilt sample holder. The X-ray photoelectron spectroscopy (XPS) spectra were recorded on Thermo Fisher Scientific Instruments (K Alpha+) with an X-ray source ( $h\nu = 1486.6$  eV) of monochromatic Al K alpha having 6 mA beam current and 12 kV voltage operated at 150 W with the help of a Physical Electronics 04-548 dual Mg/Al anode. A UHV system has a base pressure of  $\leq 5 \times 10^{-9}$  Torr. The analysis depth was nearly 10 to 15 Å. From surface normal, both the incident and take-off angles are at  $55^\circ$ . The spot size on the sample was 400  $\mu\text{m}$ . The XPS data were resolved using XPSPEAK 4.123. Carbon was taken for reference for binding energy during the analysis. The XPS measurements were done on the exposed surface of the nanoparticles without any surface treatment. The magnetic measurements were carried out using a superconducting quantum interference device-based vibrating sample magnetometer (SQUID-VSM) manufactured by Quantum Design, Inc., San Diego, USA. The powder samples were precisely weighed and packed inside a plastic sample holder, which fits into a brass specimen holder provided by Quantum Design Inc. with a negligible contribution to the overall magnetic signal. The magnetic field dependent magnetization (M–H) loops are collected at a rate of 50 Oe  $\text{s}^{-1}$  in a field sweep from  $\pm 60$  kOe at the vibrating frequency of 40 Hz. The magnetization versus temperature (M–T) measurements was performed at a temperature sweep from 5 K to more than 300 K in a field of 100 Oe following standard field-cooled (FC) and zero-field cooled (ZFC) sequences.

Mercury 4.0.0 software was used to draw the internal crystal structures and packing diagrams of the  $M_3Se_4$  compounds ( $Fe_3Se_4$ ,  $Co_3Se_4$ , and  $Ni_3Se_4$ ) crystal using the reported crystallographic information with COD numbers 1527086<sup>30</sup>, 9012803<sup>32</sup>, and 9009245<sup>31</sup>, respectively. The indexed morphologies predicted using Bravais Friedel Donnay Harker (BFDH) and Hartman Perdok (HP) laws were drawn using the *WinXMorph* program.

## 6.4 Results and discussion

### 6.4.1 Structural and morphological investigations of $M_3Se_4$ NPs using XRD and TEM

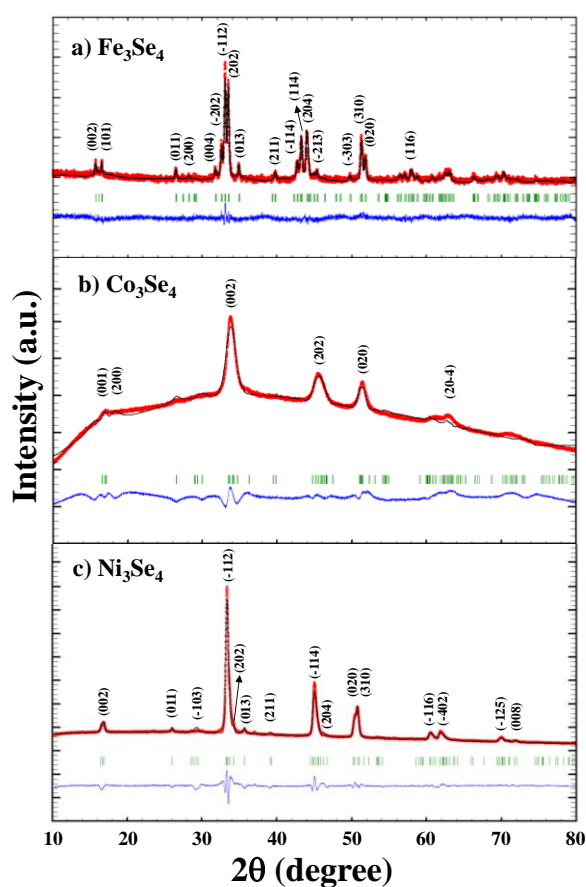


**Figure 2.** XRD pattern of a)  $Fe_3Se_4$ , b)  $Co_3Se_4$ , and c)  $Ni_3Se_4$  (red line), calculated XRD curve after crystal structure refinement by Rietveld method (black line),  $I_{obs}-I_{cal}$ , difference curve (blue line) and Bragg position (green vertical line) is displayed.

The as-synthesized  $M_3Se_4$  (where  $M= Fe, Co,$  and  $Ni$ ) compounds were intensively investigated for their crystallinity and phase purity using powder XRD, followed by the Reitveld refinement using FullProf software (Figure 2). The absence of any unidentified peak in the diffraction patterns indicates that no secondary phase is present in all samples under the limit of the laboratory XRD technique. All the diffraction patterns are according to the reported

standards diffraction patterns of corresponding samples ( $\text{Fe}_3\text{Se}_4$ ,  $\text{Co}_3\text{Se}_4$ , and  $\text{Ni}_3\text{Se}_4$ ) without ambiguous reflections. The refinement details are mentioned in Table 1.

**Table 1.** Rietveld refinement data of the as-synthesized  $\text{M}_3\text{Se}_4$  nanoparticles —  $\text{Fe}_3\text{Se}_4$ ,  $\text{Co}_3\text{Se}_4$ , and  $\text{Ni}_3\text{Se}_4$ .  $\chi^2$  and  $wR_P$  (%) represented the chi-square and weighted profile R-value, respectively. Unit cell parameters are denoted by a,b,c,  $\alpha$ ,  $\beta$ , and  $\gamma$ .

Compound Parameter	$\text{Fe}_3\text{Se}_4$	$\text{Co}_3\text{Se}_4$	$\text{Ni}_3\text{Se}_4$
$\chi^2$	1.69	15.2	24.8
$wR_P$ (%)	25.9	28.2	20.3
Space group	I2/m	C2/m	I2/m
Structure	Monoclinic	Monoclinic	Monoclinic
a (Å)	6.2	12.2	6.2
b (Å)	3.5	3.5	3.6
c (Å)	11.3	6.2	10.5
$\alpha$	90°	90°	90°
$\beta$	91.8°	121.8°	90.7°
$\gamma$	90°	90°	90°

The order of broadening of diffraction pattern indicates that all the three samples are of nano dimension. The crystallite sizes of  $\text{M}_3\text{Se}_4$  samples were calculated using the method given by Paul Scherrer<sup>33-34</sup> along different planes corresponding to the most intense diffraction peaks in individual samples. The crystallite size is nearly observed to be— for  $\text{Fe}_3\text{Se}_4 \rightarrow 42 \pm 3$  nm &  $35 \pm 3$  nm along (-112) & (202) planes, for  $\text{Co}_3\text{Se}_4 \rightarrow 8 \pm 2$  nm &  $7 \pm 2$  nm along (002) and (202) planes, and for  $\text{Ni}_3\text{Se}_4 \rightarrow 19 \pm 2$  nm &  $17 \pm 2$  nm along (-112) and (-114) plane, respectively. All the  $\text{M}_3\text{Se}_4$  compounds were formed in the monoclinic crystal structure with the calculated lattice parameters as tabulated in Table 1, having a distinct SG.

It is important to note that in the same reaction conditions with appropriate time and temperature, the atomic arrangement in monoclinic  $\text{M}_3\text{Se}_4$  compounds leads to distinct SG as the M changes from Fe to Co. In  $\text{Fe}_3\text{Se}_4$  and  $\text{Ni}_3\text{Se}_4$ , atoms are arranged in I2/m SG, while in  $\text{Co}_3\text{Se}_4$ , atoms are arranged in C2/m SG. Although both the SG belong to the same category, the atomic arrangement is different, affecting the end morphology and properties. Structural changes can explain the reason behind this observation.

In 1951, Buerger<sup>35</sup> classified phase transitions based on structural changes involving primary or higher coordination as reconstructive (sluggish) and displacive (rapid).

Reconstructive transitions necessitate the breaking and forming of bonds, which necessitates a major reorganization of the crystal structure in which many bonds must be broken and new ones established. The transformation of graphite to diamond<sup>36</sup>, for example, is a reconstruction involving a complete shift in the crystal structure. Because many bonds must break, reconstruction transitions usually require high activation energies and take place slowly. In contrast, there are only minor changes in the arrangement of coordination polyhedra during displacive transitions. It entails distorting rather than breaking the bonds, and the structural alterations are generally minor. As a result, displacive transitions occur often, with activation energies of zero or low, and cannot typically be avoided. Additionally, structural similarity is present in displacive transitions. The symmetry relationship exists between the two polymorphs— the symmetry of the low-temperature polymorph is low and belongs to a subgroup of that of the high-temperature polymorph. Thus, the displacive transitions are commonly observed in the same category of SG. For example, displacive phase transition is observed in C-centred clinopyroxenes  $\text{LiScSi}_2\text{O}_6$  and  $\text{ZnSiO}_3$ <sup>37</sup>. It is only possible to detect these transitions in *in-situ* instruments. It is believed that here also, the displacive phase transition is happening in  $\text{Fe}_3\text{Se}_4$  and  $\text{Ni}_3\text{Se}_4$ ; however, it is so fast that the *ex-situ* characterizations will not observe this phase transition. While in the case of  $\text{Co}_3\text{Se}_4$ , the reaction has just started, and the atoms have arranged in  $C2/m$  SG. They have not got enough time/energy for phase transition. The further reaction was not possible due to gel formation. From diffraction peaks broadening, it is observed that the particle size is also large in the case of  $\text{Fe}_3\text{Se}_4$  and  $\text{Ni}_3\text{Se}_4$ , while it is very small in  $\text{Co}_3\text{Se}_4$ . Later discussed, the microscopic analysis will also add essential points to this concept.

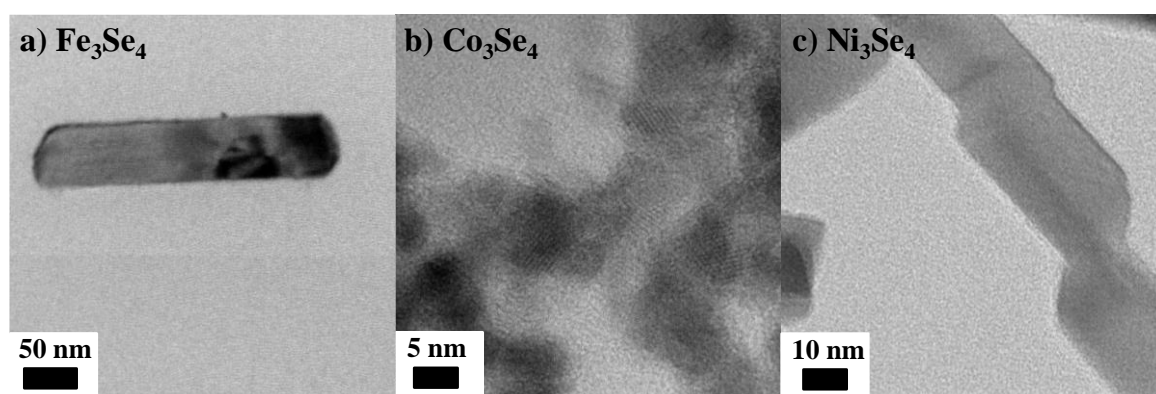


**Figure 3.** Typical TEM images of as-synthesized a)  $\text{Fe}_3\text{Se}_4$ , b)  $\text{Co}_3\text{Se}_4$ , and c)  $\text{Ni}_3\text{Se}_4$  NPs (in the presence of OLA) show the rod-like features in  $\text{Fe}_3\text{Se}_4$  and  $\text{Ni}_3\text{Se}_4$ . While small quasi-spherical-like features are observed in  $\text{Co}_3\text{Se}_4$ .

The morphology of as-synthesized  $M_3Se_4$  compounds was examined by TEM. As presented in Figure 3, the  $Fe_3Se_4$  and  $Ni_3Se_4$  are rod-like, while the  $Co_3Se_4$  is in a small quasi-spherical shape. A glance at the scale bar in all the images indicates that all the samples are in nano-dimensions. The shape of the NPs is similar in  $Fe_3Se_4$  and  $Ni_3Se_4$ , while it is entirely different in  $Co_3Se_4$ . The different scale bar of all images clearly shows the distinct size in each case. The fastest growth is achieved with  $Fe_3Se_4$ , followed by  $Ni_3Se_4$  and  $Co_3Se_4$ — nanorods of  $Fe_3Se_4$  are being made in large size, then  $Ni_3Se_4$  nanorods and the smallest of all are  $Co_3Se_4$  quasi-spheres. In the same reaction condition, all  $M_3Se_4$  are forming differently. The theoretical crystal habits have been predicted to examine the underlying reason for these observations, giving the idea about the particular morphology of individual  $M_3Se_4$  compounds with minimal energy.

#### 6.4.2 Crystal habit of $M_3Se_4$ NPs using BFDH and HP model

Usually, two successful approaches—BFDH<sup>38–40</sup> and HP<sup>41–43</sup> have been used to predict the morphology of crystals. Chapter 2 to 4 clearly shows the importance of these models. Additionally, as mentioned in the above chapters, these models have efficiently predicted the crystal morphology of numerous organic and inorganic crystals such as  $ZnO$ <sup>44</sup>,  $FeOOH$ <sup>45</sup>,  $Nd:LaVO_4$ <sup>46</sup>,  $BaSO_4$ <sup>41–43</sup>,  $GdVO_4$ <sup>47</sup>,  $GeO_2$ <sup>48</sup>,  $CaCO_3$ <sup>49</sup>, triglycine sulphate<sup>50</sup>, benzophenone<sup>51</sup>,  $Pb_{17}O_8Cl_{18}$ <sup>52</sup> etc. These models will also help in clarifying the experimental results by examining the crystal habit of  $M_3Se_4$  compounds. According to the BFDH model, Table 2 explains the relative growth rate (RGR) and morphological importance (MI) of low-index planes of  $M_3Se_4$  compounds, and the *WinXmorph*<sup>53</sup> software with these RGR and MI determine the crystal habit of corresponding compounds.

For  $Fe_3Se_4$  crystal (001) and (00-1) faces are of highest MI followed by (-101), (10-1), (101), and (-10-1) planes. The resultant crystal habit of  $Fe_3Se_4$  is a rod-like shape with longitudinal side— (001) and (00-1) faces strongly visible, followed by (-101), (10-1), (101), and (-10-1) planes. The other planes ((011), (0-11), (01-1), (0-1-1), (110), (-110), (1-10), (-1-10)) are on the edges of the rod as shown in Figure 4a.

Further, the  $Co_3Se_4$  crystallographic crystal habit is predicted. This compound is unlike  $Fe_3Se_4$  because it has a distinct unit cell parameter and SG; hence its crystallographic morphology will also be different. The predicted morphology is shown in Figure 4b. The crystal habit of  $Co_3Se_4$  is a rectangular box-like shape with longitudinal side— (100) and (-

100) faces strongly visible, followed by (-201), (20-1) (001), and (00-1) planes. The other planes (110), (-110), (-1-10), (1-10) (1-1-1), (-1-11), (11-1), and (-111) are on the edges.

$\text{Ni}_3\text{Se}_4$  shares the same crystal parameters as  $\text{Fe}_3\text{Se}_4$ ; thus, the crystallographic morphology of  $\text{Ni}_3\text{Se}_4$  is also similar to  $\text{Fe}_3\text{Se}_4$ , as shown in Figure 4c.

**Table 2.** Morphological importance of several faces of  $\text{M}_3\text{Se}_4$  crystals ( $\text{Fe}_3\text{Se}_4$ ,  $\text{Co}_3\text{Se}_4$ , and  $\text{Ni}_3\text{Se}_4$ ) based on the BFDH model. The  $d_{hkl}$  represents the interplanar spacing in Å. RGR and MI are calculated relative growth rates and morphological importance, respectively.

Phase	Faces (hkl)	$d_{hkl}$ (Å)	RGR	MI
$\text{Fe}_3\text{Se}_4$	(001), (00 $\bar{1}$ )	11.27	1	1
	( $\bar{1}$ 01), (10 $\bar{1}$ )	5.51	2.04	0.49
	(101), ( $\bar{1}$ 0 $\bar{1}$ )	5.36	2.10	0.48
	(011), (0 $\bar{1}$ 1), (0 $\bar{1}$ $\bar{1}$ ), (01 $\bar{1}$ )	3.37	3.34	0.29
	(110), ( $\bar{1}$ 10), ( $\bar{1}$ $\bar{1}$ 0), (1 $\bar{1}$ 0)	3.07	3.66	0.27
$\text{Co}_3\text{Se}_4$	(100), ( $\bar{1}$ 00)	10.40	1	1
	(001), (00 $\bar{1}$ )	5.34	1.94	0.51
	( $\bar{2}$ 01), (20 $\bar{1}$ )	5.21	1.99	0.49
	(110), ( $\bar{1}$ 10), ( $\bar{1}$ $\bar{1}$ 0), (1 $\bar{1}$ 0)	3.37	3.07	0.32
	(1 $\bar{1}$ $\bar{1}$ ), ( $\bar{1}$ $\bar{1}$ 1), (11 $\bar{1}$ ), ( $\bar{1}$ 11)	3.08	3.36	0.29
$\text{Ni}_3\text{Se}_4$	(001), (00 $\bar{1}$ )	10.25	1	1
	( $\bar{1}$ 01), (10 $\bar{1}$ ), (101), ( $\bar{1}$ 0 $\bar{1}$ )	5.32	1.96	0.50
	(011), (0 $\bar{1}$ 1), (0 $\bar{1}$ $\bar{1}$ ), (01 $\bar{1}$ )	3.43	3.04	0.32
	(110), ( $\bar{1}$ 10), ( $\bar{1}$ $\bar{1}$ 0), (1 $\bar{1}$ 0)	3.13	3.33	0.29

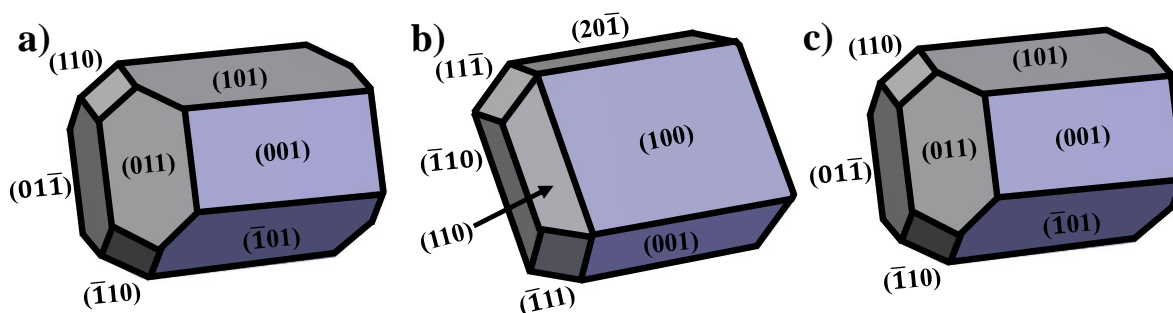


**Figure 4.** The theoretical morphology of  $\text{M}_3\text{Se}_4$  crystals is predicted using the BFDH model. a)  $\text{Fe}_3\text{Se}_4$ , b)  $\text{Co}_3\text{Se}_4$ , and c)  $\text{Ni}_3\text{Se}_4$  show the indexed morphological drawing with corresponding hkl planes.



Further, the inversion symmetry operator should be present to predict the crystal morphology using the HP model. As if the inversion operator is not present, an intrinsic dipole moment is present within the unit cell, and this model works only for crystals with non-polar unit cells. The list of symmetry operators of  $M_3Se_4$  is discussed in Figure 5.

$Fe_3Se_4$		$Co_3Se_4$		$Ni_3Se_4$	
Symm. Op.	Description	Symm. Op.	Description	Symm. Op.	Description
$x,y,z$	Identity	$x,y,z$	Identity	$x,y,z$	Identity
$-x,y,-z$	Rotation axis (2-fold)	$1/2+x,1/2+y,z$	Centring vector	$1/2+x,1/2+y,1/2+z$	Centring vector
$-x,-y,-z$	Inversion centre	$x,-y,z$	Mirror plane	$x,-y,z$	Mirror plane
$x,-y,z$	Mirror plane	$1/2+x,1/2-y,z$	Glide plane	$1/2+x,1/2-y,1/2+z$	Glide plane
$1/2+x,1/2+y,1/2+z$	Centring vector	$-x,y,-z$	Rotation axis (2-fold)	$-x,y,-z$	Rotation axis (2-fold)
$1/2-x,1/2+y,1/2-z$	Screw axis (2-fold)	$1/2-x,1/2+y,-z$	Screw axis (2-fold)	$1/2-x,1/2+y,1/2-z$	Screw axis (2-fold)
$1/2-x,1/2-y,1/2-z$	Inversion centre	$-x,-y,-z$	Inversion centre	$-x,-y,-z$	Inversion centre
$1/2+x,1/2-y,1/2+z$	Glide plane	$1/2-x,1/2-y,-z$	Inversion centre	$1/2-x,1/2-y,1/2-z$	Inversion centre

**Figure 5.** The list of symmetry operators of  $M_3Se_4$ . a)  $Fe_3Se_4$ , b)  $Co_3Se_4$ , and c)  $Ni_3Se_4$ .

The data reveals that the inversion operator is present in all  $M_3Se_4$  compounds, and hence the crystal habit of these phases could be predicted by using the HP model. Figure 6 to 8 shows the packing diagram of  $M_3Se_4$  crystal with a blue cloud shape periodic bond chain (PBC) vector.

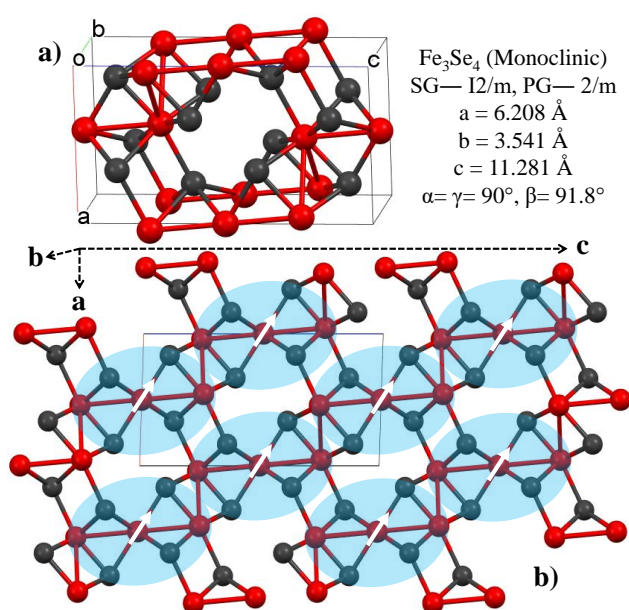


**Figure 6.** a) Unit cell of  $Fe_3Se_4$ . b) Packing diagram of  $Fe_3Se_4$  crystal along with 1 PBC vector represented by blue cloud having stoichiometry  $Fe_3Se_4$ . The three crystallographic axes are denoted by a, b, and c.

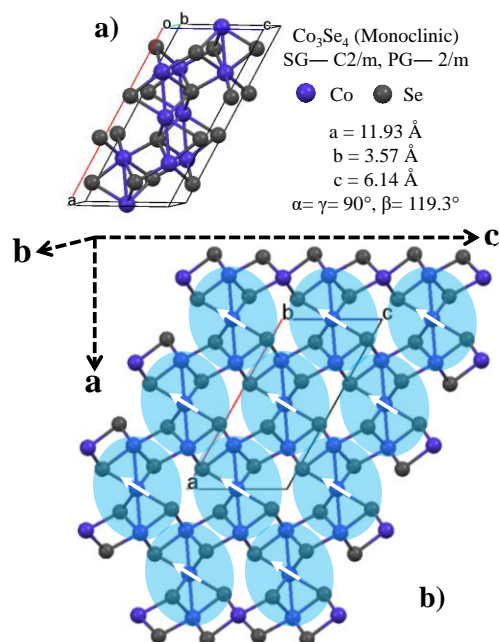


**Figure 7.** a) Unit cell of  $\text{Co}_3\text{Se}_4$ . b) Packing diagram of  $\text{Co}_3\text{Se}_4$  crystal along with 1 PBC vector represented by blue cloud having stoichiometry  $\text{Co}_3\text{Se}_4$ . The three crystallographic axes are denoted by a, b, and c.

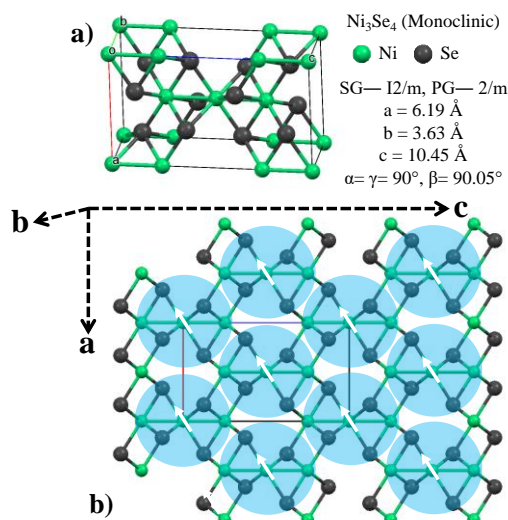


**Figure 8.** a) Unit cell of  $\text{Ni}_3\text{Se}_4$ . b) Packing diagram of  $\text{Ni}_3\text{Se}_4$  crystal along with 1 PBC vector represented by blue cloud having stoichiometry  $\text{Ni}_3\text{Se}_4$ . The three crystallographic axes are denoted by a, b, and c.

PBC vector completely lies on the (010) and (0-10) planes of the  $\text{M}_3\text{Se}_4$  structure. Accordingly, these planes are in the F (flat) category of faces and are most visible in the final crystal shape in all three compounds. In case of  $\text{Fe}_3\text{Se}_4$  and  $\text{Ni}_3\text{Se}_4$ , large component of PBC vectors lie on the (001), (00-1), (101), (-101), (10-1), (-10-1), (110), (-110), (1-10), (-1-10),

(011), (0-11), (01-1), (0-1-1), (111), (-1-1-1), (-111), (1-11), (11-1), (1-1-1), (-11-1), and (-1-11) planes. While, in  $\text{Co}_3\text{Se}_4$ , large component of PBC vectors lie on the (100), (-100), (-201), (20-1), (101), (-10-1), (10-1), (-101), (110), (-110), (1-10), (-1-10), (011), (01-1), (0-11), (0-1-1), (111), (-1-1-1), (-111), (1-11), (11-1), (1-1-1), (-11-1), (1-1-1) planes. Therefore, these planes correspond to the S faces for the corresponding samples. In the case of  $\text{Fe}_3\text{Se}_4$  and  $\text{Ni}_3\text{Se}_4$ , the (100) and (-100) planes are not parallel to any PBC vector, while, in  $\text{Co}_3\text{Se}_4$ , they are (001), (00-1) planes. Therefore, they belong to the K (kinked) category having the least visibility in the final morphology. Table 3 summarizing all  $\text{M}_3\text{Se}_4$  crystal planes of different categories based on the HP model provides the RGR and MI for distinct faces of corresponding  $\text{M}_3\text{Se}_4$  compounds.

**Table 3.** Morphological importance of several faces of  $\text{M}_3\text{Se}_4$  ( $\text{Fe}_3\text{Se}_4$ ,  $\text{Co}_3\text{Se}_4$ , and  $\text{Ni}_3\text{Se}_4$ ) crystal based on HP model. All the faces are categorized according to their alignment with PBC vectors.

S. No.	Faces (hkl)	PBC vectors lying parallel to (hkl) planes	Face category	MI
$\text{Fe}_3\text{Se}_4$ and $\text{Ni}_3\text{Se}_4$	(010), (0 $\bar{1}$ 0)	Blue	F	Largest
	(001), (00 $\bar{1}$ ), (101), ( $\bar{1}$ 0 $\bar{1}$ ), (10 $\bar{1}$ ), ( $\bar{1}$ 01), (110), ( $\bar{1}$ 10), (1 $\bar{1}$ 0), ( $\bar{1}$ 1 $\bar{0}$ ), (011), (0 $\bar{1}$ 1), (01 $\bar{1}$ ), (0 $\bar{1}$ 1 $\bar{1}$ ), (111), ( $\bar{1}$ 1 $\bar{1}$ ), ( $\bar{1}$ 11), (1 $\bar{1}$ 1), (11 $\bar{1}$ ), (1 $\bar{1}$ 1), ( $\bar{1}$ 11 $\bar{1}$ ), ( $\bar{1}$ 11 $\bar{1}$ ), ( $\bar{1}$ 11 $\bar{1}$ ), ( $\bar{1}$ 11 $\bar{1}$ )	Large component of blue	S	Large
	(100), ( $\bar{1}$ 00)	No PBC vector lie along these planes	K	Smallest
$\text{Co}_3\text{Se}_4$	(010), (0 $\bar{1}$ 0)	Blue	F	Largest
	(100), ( $\bar{1}$ 00), ( $\bar{2}$ 01), (20 $\bar{1}$ ), (101), ( $\bar{1}$ 0 $\bar{1}$ ), (10 $\bar{1}$ ), ( $\bar{1}$ 01), (110), ( $\bar{1}$ 10), (1 $\bar{1}$ 0), ( $\bar{1}$ 1 $\bar{0}$ ), (011), (0 $\bar{1}$ 1), (01 $\bar{1}$ ), (0 $\bar{1}$ 1 $\bar{1}$ ), (111), ( $\bar{1}$ 1 $\bar{1}$ ), ( $\bar{1}$ 11), (1 $\bar{1}$ 1), (11 $\bar{1}$ ), (1 $\bar{1}$ 1), ( $\bar{1}$ 11 $\bar{1}$ ), ( $\bar{1}$ 11 $\bar{1}$ ), ( $\bar{1}$ 11 $\bar{1}$ ), ( $\bar{1}$ 11 $\bar{1}$ )	Large component of blue	S	Large
	(001), (00 $\bar{1}$ )	No PBC vector lie along these planes	K	Smallest

The *WinXmorph* software with RGR and MI has been used to forecast the crystal habit of  $M_3Se_4$  compounds. It is observed that the (010) and (0-10) faces are of the highest MI for all  $M_3Se_4$  crystals. In Figure 9, the morphological drawing predicted using HP theory illustrates the resultant crystal habit as a hexagonal-cylindrical-like shape with two enormously visible upper planes (010) and (0-10). It is noted that in all the  $M_3Se_4$  compounds, the predicted crystal habit using HP model is nearly same with slight variation in  $Co_3Se_4$ .

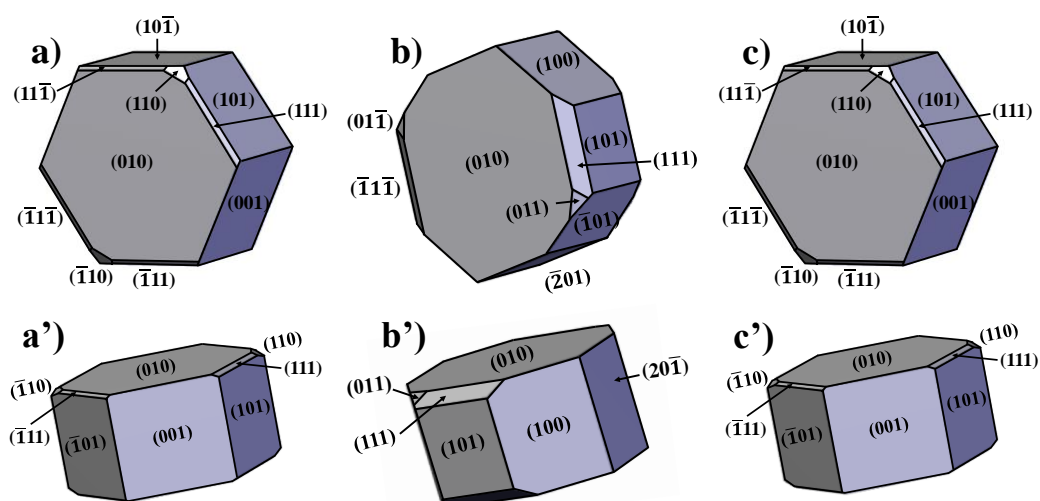


**Figure 9.** Theoretical morphology of  $M_3Se_4$  crystal predicted using Hartman-Perdok (HP) model. The figure shows the indexed morphological drawing with corresponding hkl planes. a) to c) shows the upper view of the morphologies of a)  $Fe_3Se_4$ , b)  $Co_3Se_4$ , and c)  $Ni_3Se_4$  compounds with the highest morphological importance of the (010) plane. a') to c') shows the side view of the morphologies of corresponding compounds.

In conclusion, the BFDH crystal habit of  $Co_3Se_4$  is distinct from  $Fe_3Se_4$  and  $Ni_3Se_4$ , while it slightly varies in the HP model. The underlying reason for observed dissimilarity in both models is the distinct path used for the prediction in corresponding models. In BFDH, the crystal parameters are the basis of crystal habit prediction, and  $Co_3Se_4$  has different parameters from the other two compounds (SG is distinct) that lead to different crystal habits. In contrast, the bond energies are the prime tool for the HP model, which is nearly the same in all the cases with slight variation in direction. This leads to very small changes in the final predicted morphologies of  $M_3Se_4$  compounds. It will be interesting to examine the effect of these changes in real-life experiments.

### 6.4.3 Correlation between theoretically predicted crystal habit and experimental morphological of $M_3Se_4$ NPs

The real-life reactions of materials are much more complicated than the simplified theoretical models due to the involvement of external factors in the reaction. As observed in TEM images, the  $Fe_3Se_4$  and  $Ni_3Se_4$  NPs are in a rod shape, while in the same experimental conditions, the  $Co_3Se_4$  NPs are forming in small quasi-spherical. The importance of understanding the reason behind the observed different shapes in  $M_3Se_4$  NPs cannot be overstated. Here, the theoretical observation will help in understanding these findings.

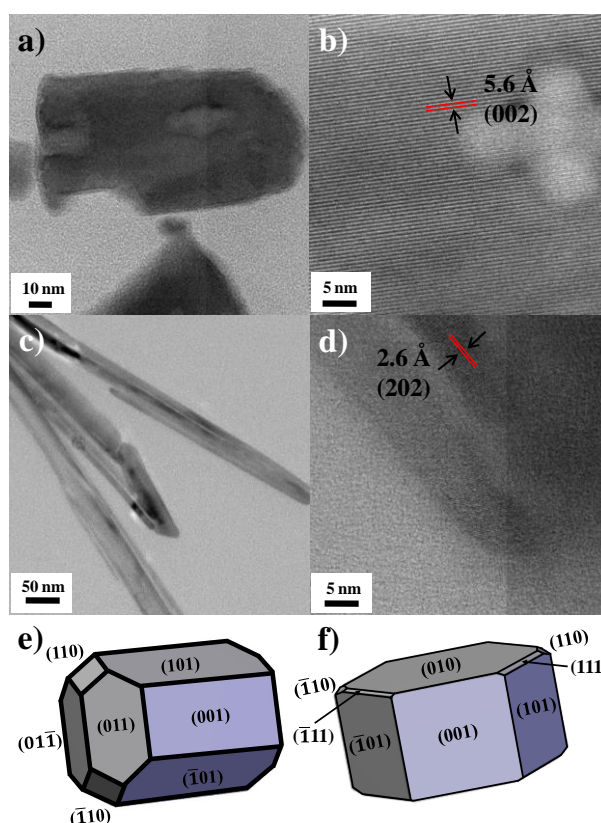


**Figure 10.** Correlation between the experimental and theoretically predicted morphologies of  $Fe_3Se_4$ . a) to d) represents the TEM images of  $Fe_3Se_4$  NPs having rod-like features. b) and d) shows the lattice fringes space at 5.6 Å, and 2.6 Å represents the (002) and (202) of  $Fe_3Se_4$ , respectively. e) and f) represent the predicted morphology of  $Fe_3Se_4$  by BFDH and HP model, respectively.

The two models were utilized to predict the morphology of  $M_3Se_4$  in this study. Figure 10 demonstrates the  $Fe_3Se_4$  morphology in both experimental and theoretical conditions. Both theoretical models predict a nearly rod-like  $Fe_3Se_4$  crystal habit, making (001), (101), and  $(-101)$  on the longitudinal sides (Figure 10e-f). Therefore, the most stable shape is rod-like based

on crystallographic and bond energies models. Taking a look at the synthesized  $\text{Fe}_3\text{Se}_4$  NPs, they also follow the theoretical growth morphology and form nanorods with (002), (202) on the longitudinal sides of rods as observed in lattice fringes space at  $5.6 \text{ \AA}$  and  $2.6 \text{ \AA}$  (Figure 10b and d). Accordingly, the  $\text{Fe}_3\text{Se}_4$  crystal shape follows the theoretical path in the above reaction conditions.

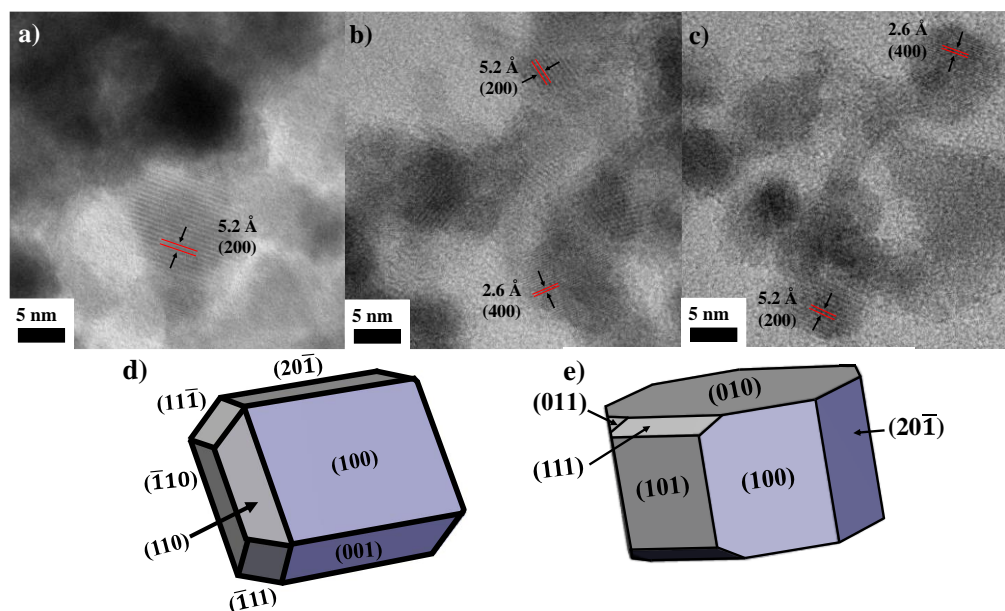


**Figure 11.** Correlation between the experimental and theoretically predicted morphologies of  $\text{Co}_3\text{Se}_4$ . a) to c) represents the TEM images of  $\text{Co}_3\text{Se}_4$  NPs having quasi-spherical-like features. a), b), and c) shows the lattice fringes space at  $5.2 \text{ \AA}$  and  $2.6 \text{ \AA}$  represents the (200) and (400) of  $\text{Co}_3\text{Se}_4$ , respectively. d) and e) represents the predicted morphology of  $\text{Co}_3\text{Se}_4$  by BFDH and HP model, respectively.

Furthermore, as discussed in the above section, the crystal habit of  $\text{Co}_3\text{Se}_4$  predicted by both models differs from each other— rectangular-box by BFDH and small cylindrical by HP model, as shown in Figure 11. Now, let's take a look at the synthesized  $\text{Co}_3\text{Se}_4$  NPs. They are small quasi-spherical in shape with (200) and (400) planes on the upper side with lattice fringes space at  $5.2 \text{ \AA}$  and  $2.6 \text{ \AA}$ . As both models predict the distinct morphology, the experimental morphology will only follow one morphological path depending on the provided conditions. Here in our reaction conditions, the  $\text{Co}_3\text{Se}_4$  has only started the fabrication, which leads to very small NPs compared to other  $\text{M}_3\text{Se}_4$ . At minimal energy, when the reaction has begun, the crystallographic model will dominate the crystal morphology, and later the bond energy theories will also participate prominently as per the reaction environment. Since the larger the area of a crystal's face, the greater the number of intermolecular interactions in that area.

Consequently, this results in the increased growth rate in that direction and subsequently decreased MI and vice versa. In  $\text{Co}_3\text{Se}_4$ , the (100) planes have a lower facial area. Therefore, the interaction and growth are slower in this face, resulting in a higher MI of (100). Thus, the crystallographic morphology dominates at the initial stage of reactions; therefore, the observed  $\text{Co}_3\text{Se}_4$  NPs are close to the BFDH model with quasi-spherical shape, having (200) and (400) planes on the upper side.

The morphology of the  $\text{Ni}_3\text{Se}_4$  compound is similar to  $\text{Fe}_3\text{Se}_4$  in both aspects— theoretically and experimentally. As mentioned above  $\text{Ni}_3\text{Se}_4$  shares the rod-like features by both theoretical models making (001), (101), and (-101) on the longitudinal sides. Additionally, the synthesized  $\text{Ni}_3\text{Se}_4$  NPs are also in rod shape, as shown in Figure 12, with (202) plane on the longitudinal side having 2.6 Å lattice fringes space, which is quite similar to the  $\text{Fe}_3\text{Se}_4$ . In conclusion, since both models are approaching the same morphology (rod-shape) in  $\text{Ni}_3\text{Se}_4$  as well, the experimental findings in these conditions will be very close to the theoretical prediction, just as they were for  $\text{Fe}_3\text{Se}_4$ .

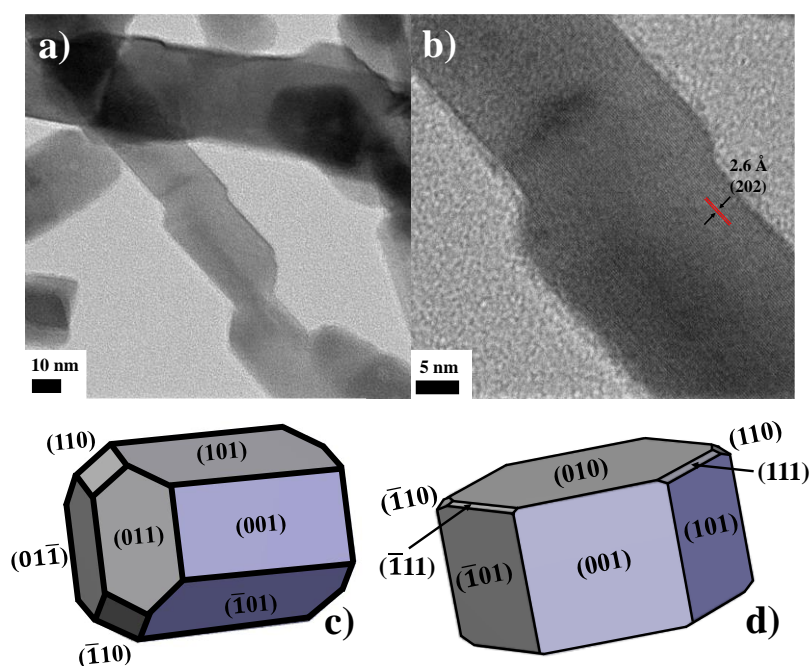


**Figure 12.** Correlation between the experimental and theoretically predicted morphologies of  $\text{Ni}_3\text{Se}_4$ . a) and b) represent the TEM images of  $\text{Ni}_3\text{Se}_4$  NPs with rod-like features. b) shows the lattice fringes space at 2.6 Å represents the (202) of  $\text{Ni}_3\text{Se}_4$ . c) and d) represent the predicted morphology of  $\text{Ni}_3\text{Se}_4$  by BFDH and HP model, respectively.

Thus, it is appropriate to conclude that if both models examine the same morphology, the experimental morphologies will most likely follow the predicted crystal habits with minimal possible energies (temperature and time). However, if both models have predicted different crystal habits, the experimental results will follow the one according to provided reaction conditions.

After studying  $M_3Se_4$  shapes, a closer look at what is responsible for the huge difference in  $M_3Se_4$  NP sizes in the same reaction conditions is crucial to understand. As outlined in the experimental section, all  $M_3Se_4$  compounds synthesized here undergo identical reactions, other than using metal acetylacetonate as a metal precursor. As mentioned in Chapters 3 and 5, when metal and selenium precursors react with OLA, they form metal-OLA complexes and selenium-OLA complexes that provide cations and anions, respectively. More availability of ions leads to the more rapid formation of compounds. Despite metal precursors, all three reactions are synthesized with the same reaction parameters in this work. Therefore, the reactivity of selenium precursors will be similar to that discussed in Chapter 3— Se-OLA complexes provide  $Se^{2-}$ . However, all three types of metal precursors are different in their reactivity. Decomposition behavior of metal precursors plays a significant role here, as it determines the formation rate of cations and compounds corresponding to those metals. Hoene et al.<sup>54</sup> investigated the thermal decomposition of multiple metal acetylacetonate. According to their report,  $Fe(acac)_3$ ,  $Co(acac)_3$ , and  $Ni(acac)_2$  begin to decompose above 184 °C, 213 °C, and ~ 200 °C. After forming complexes with OLA, this provides cations for the formation of corresponding compounds in the reaction. Thus, for the Fe-based compound, NPs growth started at the earliest stage, generating large  $Fe_3Se_4$  nanorods. However, in the case of Co-based compounds, the growth of NPs starts only after high temperatures, resulting in small size NPs. Compared with  $Fe_3Se_4$ , the  $Co_3Se_4$  has only begun the fabrication process, leading to very small NPs. Furthermore, the  $Ni(acac)_2$  decomposition occurs between these two compounds, resulting in large size NPs compared to  $Co_3Se_4$ , and small nanorods compared to  $Fe_3Se_4$ . It is reasonable to conclude that the metal precursor is critical in determining the size of  $M_3Se_4$  NPs.

#### 6.4.4 XPS analysis of $M_3Se_4$ NPs

TMCs are well known for their ease of surface oxidation after being exposed to air<sup>55</sup>. The oxidation state in  $M_3Se_4$  NPs is determined by a highly surface-sensitive technique— XPS. In the present work, the samples are exposed to the air during sample preparation. Therefore, the local electronic structure of oxygen incorporated  $M_3Se_4$  NPs is investigated by carrying out the



multi-peak fitting analysis. Figure 13 shows the metal (M) spectrum of  $M_3Se_4$  compounds corresponding to M 2p core-level spectra with the presence of various peaks at different binding energy (BE).

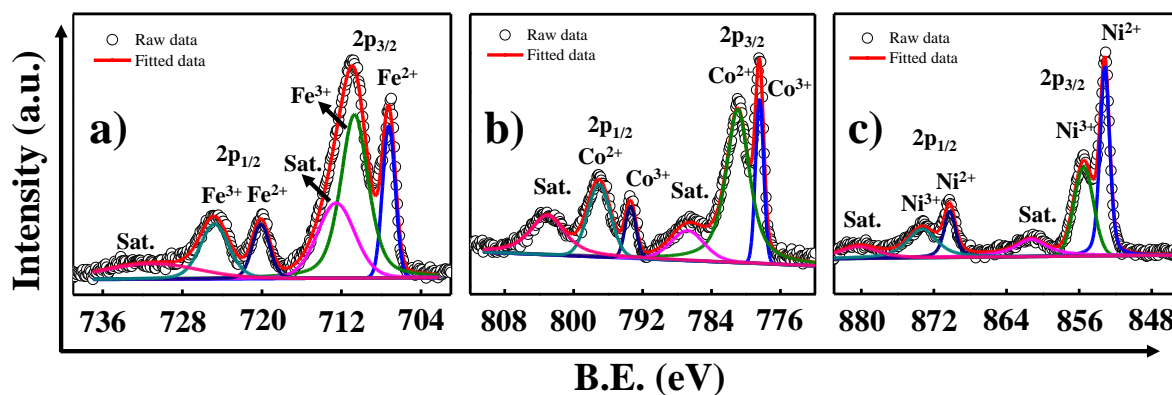


**Figure 13.** XPS spectra of as-synthesized  $M_3Se_4$  NPs. a) to c) shows the metal (Fe, Co, and Ni) spectra of  $Fe_3Se_4$ ,  $Co_3Se_4$ , and  $Ni_3Se_4$ , respectively. The red lines show a deconvoluted curve fits.

In the Fe spectrum (Figure 13a), the peaks  $\sim 707$  eV and  $720$  eV are due to spin-orbit splitting in 2p level— $2p^{3/2}$  and  $2p^{1/2}$ , corresponding to an energy gap of 13 eV, which signify the existence of  $Fe^{2+}$  state in  $Fe_3Se_4$ . The other two peaks ( $\sim 711$  eV and  $725$  eV) denote the higher oxidation state ( $Fe^{3+}$ ) of iron species in  $Fe_3Se_4$ <sup>56</sup>. In the Co spectrum (Figure 13b), the peak  $\sim 778$  eV and  $793$  eV signify the higher oxidation state ( $Co^{3+}$ ) of cobalt species in  $Co_3Se_4$ <sup>57</sup>. While the other two peaks  $\sim 781$  eV and  $797$  eV imply the existence of a  $Co^{2+}$  state in  $Co_3Se_4$ . Further, in the Ni spectrum (Figure 13c), the peaks  $\sim 853$  eV and  $870$  eV correspond to  $Ni^{2+}$  in  $Ni_3Se_4$ . While the other two peaks  $\sim 855$  eV and  $873$  eV show the presence of  $Ni^{3+}$  in  $Ni_3Se_4$ <sup>58</sup>. It is recognized that the broadness of the 2p peaks is due to a multiplet splitting caused by j-j coupling, which is too small to produce the resolved structure. The spectra of  $Co_3Se_4$ , which contains two  $Co^{3+}$  ions and one  $Co^{2+}$  ion, would then be expected to consist of a broad line from  $Co^{2+}$  (seven 3d electrons) and a narrow symmetric line from  $Co^{3+}$  (six 3d electrons). While in the other two cases,  $Fe_3Se_4$  and  $Ni_3Se_4$ , the broad line is from  $M^{3+}$  ( $Fe^{3+}$ —five 3d electrons and  $Ni^{3+}$ —seven 3d electrons) and the narrow line from  $M^{2+}$  ( $Fe^{2+}$ —six 3d electrons and  $Ni^{2+}$ —eight 3d electrons). The satellite peaks were also observed at slightly higher BE in all spectrums, as mentioned in Figure 13. The peaks observed at higher BE can be assigned to charge transfer satellites of  $M^{2+}$  and  $M^{3+}$ . This is linked to XPS shakeup excitations and is distinguished by a satellite peak at higher BE. This analysis is favorable with the expectation that monoclinic  $M_3Se_4$  compounds should have both  $M^{2+}$  and  $M^{3+}$  for electron neutrality.

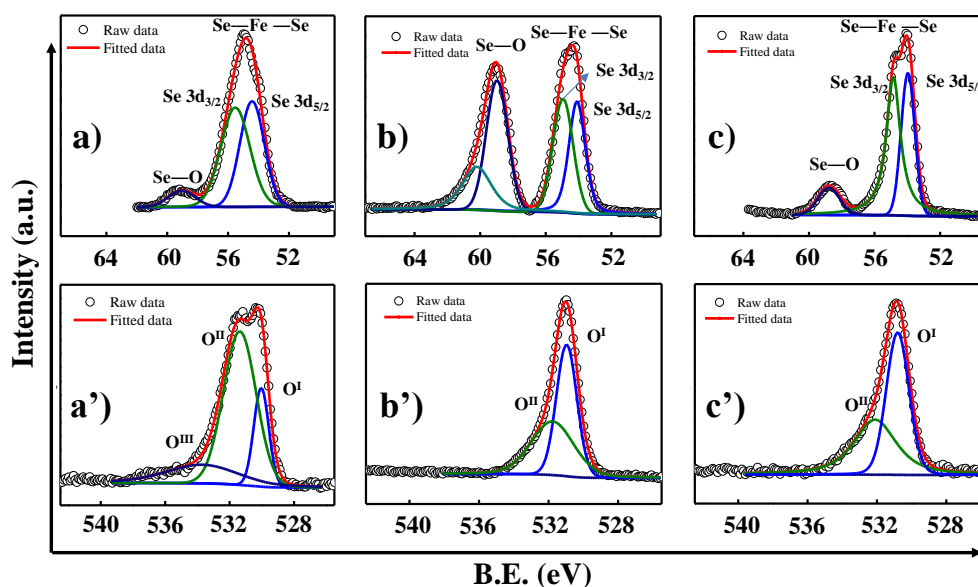


**Figure 14.** XPS spectra of as-synthesized  $M_3Se_4$  nanoparticles. a) to c) shows the chalcogenide (Se) spectra of  $Fe_3Se_4$ ,  $Co_3Se_4$ , and  $Ni_3Se_4$ , respectively. a') to c') shows the oxygen spectra of  $Fe_3Se_4$ ,  $Co_3Se_4$ , and  $Ni_3Se_4$ , respectively. The red lines show a deconvoluted curve fits.

As presented in Figure 14a - c, the peaks correspond to Se3d spectra, indicating the presence of deconvoluted peaks— Se–Fe–Se and Se–O peaks nearby 54–56 eV and 59 eV. The presence of Se–O peaks in all Se-spectrums clearly shows that the surface of these compounds became oxidized during the preparation and characterization<sup>59</sup>. Moreover, Figure 14a' - c' shows the XPS spectrum of O 1s having three deconvoluted peaks —O<sup>I</sup> (~530 eV), O<sup>II</sup> (~532 eV), and O<sup>III</sup> (~534 eV)<sup>60, 61</sup>. In  $Fe_3Se_4$ , all three peaks are present, while in  $Ni_3Se_4$  and  $Co_3Se_4$ , only the first two (O<sup>I</sup> and O<sup>II</sup>) are observed. The O<sup>I</sup> indicates partially hydroxylated NP surfaces. The O<sup>II</sup> reveals the Se species surface oxidation, which persists in the Se 3d spectrum. The O<sup>III</sup> contribution is related to the physi-/chemisorbed H<sub>2</sub>O on the surfaces due to the exposure of air, which is absent in  $Ni_3Se_4$  and  $Co_3Se_4$  NPs. Thus, it has been clearly viewed that all the materials readily undergo surface oxidation as soon as they are exposed to air (well supported by M, Se, and O spectrum).

#### 6.4.5 Remarkable effect of M in monoclinic $M_3Se_4$ compounds on magnetic properties at nano-dimensions

The influence of transition metal in  $M_3Se_4$  compounds on the magnetic properties at nano dimensions has been investigated using SQUID-VSM. Figure 15 presents the M-T curves in ZFC and FC mode of  $M_3Se_4$  NPs at 100 Oe applied magnetic field. Figure 15a presents the M-

T curve of  $\text{Fe}_3\text{Se}_4$  NPs, and the inset reveals the bifurcation below 330 K and Curie transition temperature  $\sim 322$  K, below which it goes into a ferrimagnetic phase.

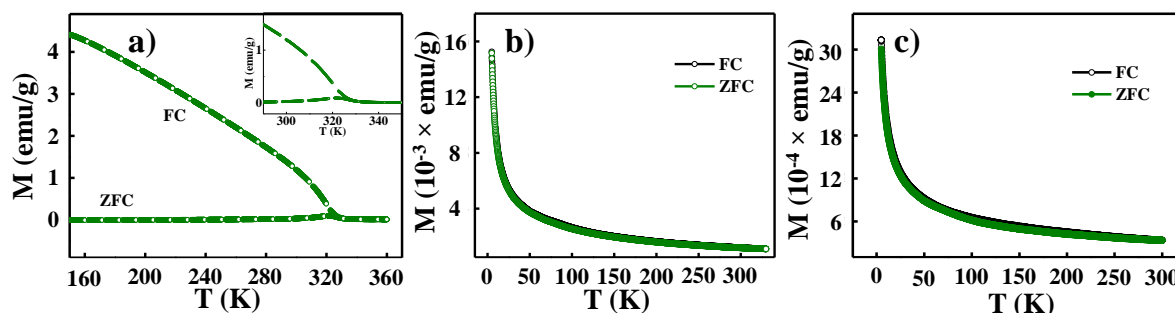


**Figure 15.** Comparison of magnetization versus temperature curves (in ZFC and FC modes) for all the as-synthesized  $\text{M}_3\text{Se}_4$  NPs. a) to c) curves correspond to the samples—  $\text{Fe}_3\text{Se}_4$ ,  $\text{Co}_3\text{Se}_4$ , and  $\text{Ni}_3\text{Se}_4$ , respectively, in the applied magnetic field of 100 Oe.

The findings align with previous reports of  $T_C \sim 320$  K for  $\text{Fe}_3\text{Se}_4$ . Figure 15b-c presents the M-T curves of  $\text{Co}_3\text{Se}_4$  and  $\text{Ni}_3\text{Se}_4$  from 5 K to more than 300 K at 100 Oe. The curves reveal the overlap of ZFC and FC curves over the whole measurement temperature range. It signifies that the  $\text{Co}_3\text{Se}_4$  and  $\text{Ni}_3\text{Se}_4$  NPs are paramagnetic in this range, and the magnetic transition temperature lies below the measurement temperature range. Figure 16 shows the magnetic susceptibility ( $\chi$ ) versus temperature curves of a)  $\text{Co}_3\text{Se}_4$  and b)  $\text{Ni}_3\text{Se}_4$ . The magnetic susceptibility of a paramagnetic material diminishes as temperature rises. The extrapolation to zero temperature does not satisfy the Curie Law, as seen by the intercepts above 0 K, both compounds follow the Curie-Weiss Law<sup>62</sup>.

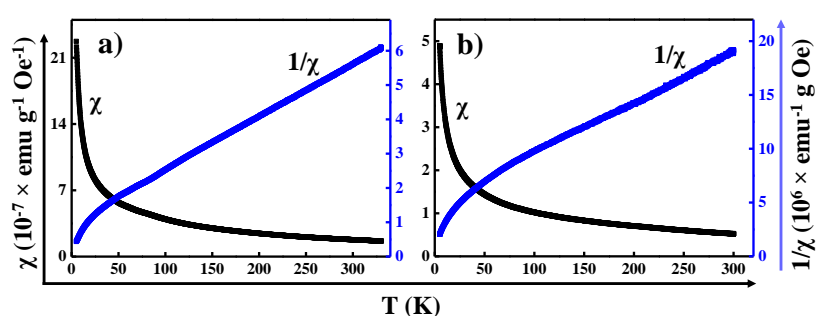


**Figure 16.** The black curve represents the magnetic susceptibility ( $\chi$ ) versus the temperature plot of a)  $\text{Co}_3\text{Se}_4$  and b)  $\text{Ni}_3\text{Se}_4$ , respectively, at 100 Oe. The blue curve denotes the inverse of the magnetic susceptibility versus temperature plot.

Further, the M-H was examined to intensively study the magnetic behavior of  $\text{M}_3\text{Se}_4$  NPs. The M-H curves of as-synthesized  $\text{M}_3\text{Se}_4$  NPs have been investigated at 300 K, and 10

K. Figure 17a shows the hysteresis loops of typical non-linear behavior common to the ferrimagnetic nature of  $\text{Fe}_3\text{Se}_4$  NPs at 300 K as reported findings. The magnetization does not saturate until the highest applied field of 60 kOe. In earlier studies, the hysteresis loops of  $\text{Fe}_3\text{Se}_4$  do not saturate even after applying 90 kOe, due to the very high anisotropy field or the spins are noncollinear in the system. Inset of Figure 17a clearly shows the coercivity ( $H_C$ ) and remanence magnetization ( $M_R$ ) values of  $\text{Fe}_3\text{Se}_4$  NPs and are determined to be 2.3 kOe and 2 emu/g at 300 K. Moreover, at 10 K, the M-H curve of  $\text{Fe}_3\text{Se}_4$  does not saturate for the highest applied magnetic field of 60 kOe (Figure 17a'). In fact, the curve is far from saturation, and the coercivity values are a gross underestimation of their true values. It is noted that these underestimated coercivity values increase nearly 30-fold over the corresponding value at 300 K— from 2.3 kOe to 35.5 kOe. The major increment in the coercivity value at a lower temperature likely has several contributions— reduction in the thermal activation energy that provides the more and more spins available to orient in the field direction, the increase in the overall effective magnetic anisotropy, ferrimagnetism, etc. The remanence magnetization increases from 2 emu/g at 300 K to 7.6 emu/g at 10 K.

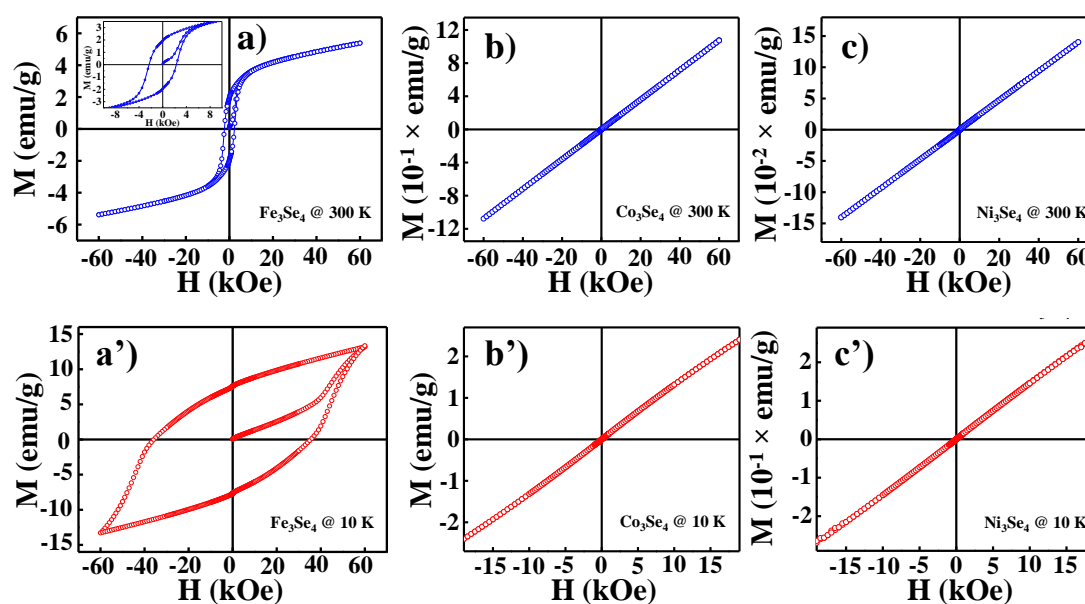


**Figure 17.** Magnetization vs. external magnetic field hysteresis loops at 300 K (blue curve) and 10 K (red curve) of  $M_3\text{Se}_4$  NPs. a) to c) blue loops correspond to the samples—  $\text{Fe}_3\text{Se}_4$ ,  $\text{Co}_3\text{Se}_4$ , and  $\text{Ni}_3\text{Se}_4$ , respectively at 300 K. a') to c') red loops correspond to the samples—  $\text{Fe}_3\text{Se}_4$ ,  $\text{Co}_3\text{Se}_4$ , and  $\text{Ni}_3\text{Se}_4$ , respectively at 10 K.

In contrast to  $\text{Fe}_3\text{Se}_4$ , the other two compounds ( $\text{Co}_3\text{Se}_4$  and  $\text{Ni}_3\text{Se}_4$ ) show the linear M-H curve at 300 K as shown in Figure 17b-c and reveals a paramagnetic nature at room

temperature. At lower temperatures (10 K) also, the M-H plot shows a linear behaviour (Figure 17 b'-c'). Thus, these compounds are paramagnetic in nature at both measured temperatures (300 K and 10 K), and the magnetic transition lies below 10 K.

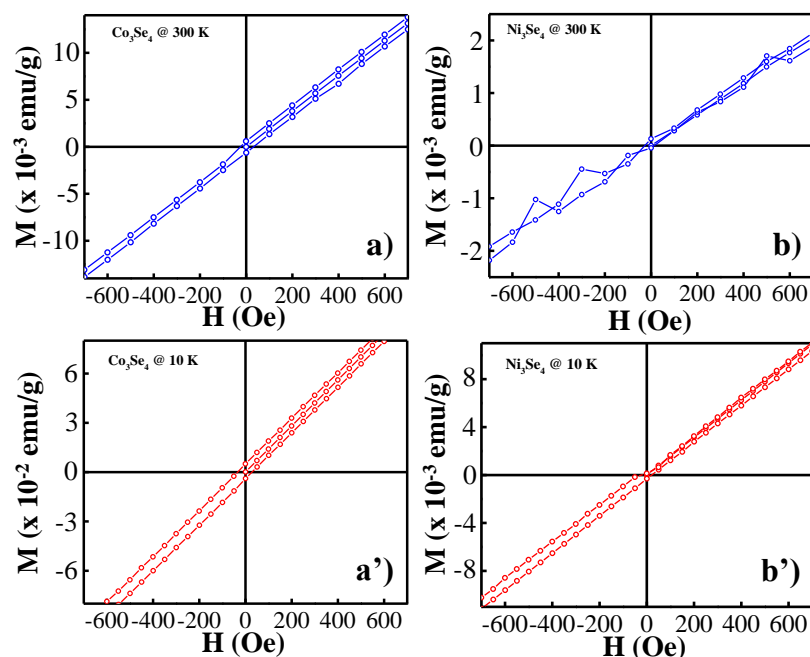


**Figure 18.** Zoomed-view of magnetization vs. external magnetic field hysteresis loops at 300 K (blue curve) and 10 K (red curve) of Co/Ni<sub>3</sub>Se<sub>4</sub> NPs. a) to b) blue loops correspond to the samples— Co<sub>3</sub>Se<sub>4</sub>, and Ni<sub>3</sub>Se<sub>4</sub>, respectively at 300 K. a') to b') red loops correspond to the samples— Co<sub>3</sub>Se<sub>4</sub>, and Ni<sub>3</sub>Se<sub>4</sub>, respectively at 10 K. Due to surface defects, a small loop is observable in the zoomed M-H measurement at both temperatures.

In M<sub>3</sub>Se<sub>4</sub> compounds having a monoclinic crystal structure, as the M varies from Fe to Co/Ni, the magnetic properties also change. At room temperature, with Fe, the monoclinic M<sub>3</sub>Se<sub>4</sub> NPs are ferrimagnetic, while in the case of Co and Ni in the same structure, the magnetic behaviour is paramagnetic. At lower temperatures (10 K), the Co<sub>3</sub>Se<sub>4</sub> and Ni<sub>3</sub>Se<sub>4</sub> compounds show paramagnetism, while Fe<sub>3</sub>Se<sub>4</sub> is ferrimagnetic. The Curie transition temperature of Fe<sub>3</sub>Se<sub>4</sub> is nearly 322 K. However, in Co<sub>3</sub>Se<sub>4</sub> and Ni<sub>3</sub>Se<sub>4</sub>, the magnetic transition temperature is below the lowest measurement temperature (5 K). Although in the same structure, the transition metal is replaced from Fe to Co/Ni, however, the magnetic properties are drastically changing: the answer to this attractive finding lies in M<sub>3</sub>X<sub>4</sub> (where M = Fe, Co or Ni, and X = O, S or Se) compounds magnetic properties.

**Table 4.** Comparison of magnetic properties of  $M_3X_4$  compounds (where M can be Fe, Co, and Ni, and X can be O, S, and Se) with their corresponding magnetic transition temperature for bulk samples.

$(M_3X_4)$			
$X \backslash M$	Fe	Co	Ni
O	Ferrimagnetic <sup>63</sup> ( $T_C \sim 858$ K)	Antiferromagnetic <sup>64</sup> ( $T_N \sim 40$ K)	Ferrimagnetic <sup>65</sup> ( $T_C \sim 808$ K)
S	Ferrimagnetic <sup>66</sup> ( $T_C \sim 606$ K)	Paramagnetic Antiferromagnetic <sup>67</sup> ( $T_N \sim 58$ K)	Ferrimagnetic <sup>68</sup> ( $T_C \sim 20$ K)
Se	Ferrimagnetic <sup>22,24</sup> ( $T_C \sim 314$ K)	Paramagnetic <sup>25</sup>	Paramagnetic <sup>25</sup>

Table 4 shows the magnetic transition temperature (Curie or Neels temperature) of  $M_3X_4$  compounds. There are two factors M (Fe, Co, or Ni) and X (O, S, or Se), and the essential question is what will happen to magnetic properties— if the M is constant and X is changing or vice versa.

1) To understand the first point,  $Fe_3X_4$  is taken as a case study. As X changes from O to S to Se, the atomic size of the anion increases resulting in increasing the lattice parameters and decreasing the exchange interaction. Additionally, the magnetic moment is also reduced due to the presence of 3d electrons delocalization and covalency effect<sup>69</sup>. Overall, the impact on magnetization is that it decreases with increasing the atomic size of X. In consequence, the required thermal energy to randomly orient the magnetic spins is reduced with increasing the atomic size of X. Thus, the magnetic transition temperature decreases from O to Se.

2) Now, coming towards the second point, keeping X constant and changing the M—  $M_3O_4$  is taken as a case study. The  $Fe_3O_4$  is in the inverse spinel structure.  $Fe^{2+}$  is diamagnetic as it is octahedral with  $t_{2g}^6$  having no unpaired electrons, while  $Fe^{3+}$  is in both tetrahedral ( $e^2 t_2^3$ ) and octahedral ( $t_{2g}^3 e_g^2$ ) having five unpaired electrons, each giving rise to high magnetic

moment; hence the arrangement of atoms leads to ferrimagnetism in  $\text{Fe}_3\text{O}_4$  compounds<sup>63</sup>. The other two compounds,  $\text{Co}_3\text{O}_4$  and  $\text{Ni}_3\text{O}_4$ , are in the normal spinel structure. In  $\text{Co}_3\text{O}_4[\text{Co}^{2+}(\text{Co}^{3+})_2\text{O}_4]$ , the  $\text{Co}^{3+}$  is in the octahedral state with no unpaired electrons (low spin:  $t_{2g}^6$ ), resulting in zero magnetic moments. In contrast, the  $\text{Co}^{2+}$  is in a tetrahedral state (high spin:  $e^4 t_2^3$ ), having  $3.26 \mu_B$  magnetic moment at 4.2 K. Thus, only  $\text{Co}^{2+}$  contributes in the magnetism of  $\text{Co}_3\text{O}_4$  compounds that result in antiferromagnetic behaviour with low Neel temperature ( $\sim 40$  K) (as the overall magnetic moment is very less and required thermal energy will be very low to randomly orient the magnetic moments). In  $\text{Ni}_3\text{O}_4$ ,  $\text{Ni}^{2+}$  is in a tetrahedral state (high spin:  $e^4 t_2^4$ ), and  $\text{Ni}^{3+}$  is in an octahedral state (low spin:  $t_{2g}^6 e_g^1$ ). Both cations have unpaired electrons and are arranged so that the overall magnetization of each layer have different magnitude, which results in ferrimagnetic nature with  $\sim 808$  K Curie temperature. Compared to  $\text{Co}_3\text{O}_4$ , the  $\text{Ni}_3\text{O}_4$  have more resultant magnetization due to the presence of a higher number of unpaired electrons in 2 types of Ni ions; therefore, the magnetic transition temperature will be very high as compared to  $\text{Co}_3\text{O}_4$ . In case of  $\text{Fe}_3\text{O}_4$  also due to the presence of five unpaired electrons in each  $\text{Fe}^{3+}$ , resultant magnetization is very high which results in high Curie temperature ( $\sim 858$  K).

These two essential points will be combined to get the answer for  $\text{M}_3\text{Se}_4$  compounds. As the compounds changes from  $(\text{Co/Ni})_3\text{O}_4$  to  $(\text{Co/Ni})_3\text{Se}_4$ , the Co and Ni ions go towards high spin states because the magnitude of octahedral crystal field stabilizing energy decreases as the size of the donor atom increases. However, the exchange interaction decreases from  $\text{O} \rightarrow \text{S} \rightarrow \text{Se}$  which decreases the overall magnetization, followed by magnetic transition temperature (as in the case of  $\text{Fe}_3\text{X}_4$ — the magnetic transition temperature decreases from O to Se). When it comes to Co-based compounds, some studies claim that  $\text{Co}_3\text{S}_4$  is a temperature-independent paramagnetic, while others claim that it has an antiferromagnetic with Neels temperature of 58 K. Therefore, we may conclude that in Co-based compounds, magnetization has decreased or has not changed much from O to S. However, further decrease in the exchange interaction (as we go from S to Se) reduces the magnetization so low in the case of  $\text{Co}_3\text{Se}_4$  that magnetic transition temperature reduces beyond the detection limits. In the case of Ni-based compounds, it drastically reduces to  $\sim 20$  K for  $\text{Ni}_3\text{S}_4$  from  $\sim 808$  K ( $\text{Ni}_3\text{O}_4$ ) and further reduces below the detection limits for  $\text{Ni}_3\text{Se}_4$ . Therefore, the magnetic transition temperature in  $\text{Co}_3\text{Se}_4$  and  $\text{Ni}_3\text{Se}_4$  is below the measurement temperature lower limit. However, these compounds are very promising in other fields of science such as recently,  $\text{Co}_3\text{Se}_4$  got huge attention for its high

OER values by electrocatalysis, photoelectrochemical water splitting, and  $\text{Ni}_3\text{Se}_4$  is also a very potential catalyst; researchers are exploring more in these areas. Therefore, it will be interesting and important to further study the other properties of these pure as-synthesized compounds in the future.

## 6.5 Conclusion

The fabrication of a transition metal selenides is not an easy task, and the compounds with higher asymmetry are harder to synthesize. In this work, the  $\text{M}_3\text{Se}_4$  compounds where M can be Fe, Co, or Ni have been synthesized via the thermal decomposition method in the monoclinic crystal structure with distinct SG, leading to varied morphologies. The SG of  $\text{Fe}_3\text{Se}_4$  and  $\text{Ni}_3\text{Se}_4$  is  $I2/m$ , while in  $\text{Co}_3\text{Se}_4$ , the atoms are arranged in  $C2/m$ . The distinct SG is most likely because of the displacive transition. The observed distinct morphologies are understood with the help of theoretical models such as BFDH and HP models. In the last section, the influence of transition metal (M) on the magnetic properties is studied for  $\text{M}_3\text{Se}_4$  NPs. The  $\text{Fe}_3\text{Se}_4$  is ferrimagnetic with a  $T_C$  of nearly 322 K. In contrast, the other two compounds ( $\text{Co}_3\text{Se}_4$  and  $\text{Ni}_3\text{Se}_4$ ) are paramagnetic in the whole measurement temperature range. The magnetic transition temperature in the last two compounds is so low that it is impossible to detect within measurement limits. In conclusion, the work provides the appropriate method for synthesizing  $\text{M}_3\text{Se}_4$  NPs with distinct M having various magnetic properties, and this route can be extended to most TMCs.

## 6.6 References

- (1) Jellinek, F. Transition Metal Chalcogenides. Relationship between Chemical Composition, Crystal Structure and Physical Properties. *React. Solids* 1988, 5, 323–339.
- (2) Lan, M.; Xiang, G.; Nie, Y.; Yang, D.; Zhang, X. The Static and Dynamic Magnetic Properties of Monolayer Iron Dioxide and Iron Dichalcogenides. *RSC Adv.* 2016, 6, 31758–31761.
- (3) Lin, C.-R.; Lu, S.-Z.; Lyubutin, I. S.; Korzhetskiy, Y. V.; Wang, S.-C.; Suzdalev, I. P. Synthesis and Magnetic Properties of Iron Sulfide Nanosheets with a NiAs-like Structure. *J. Appl. Phys.* 2010, 107, 09A335.
- (4) Liu, A.; Chen, X.; Zhang, Z.; Jiang, Y.; Shi, C. Selective Synthesis and Magnetic Properties of  $\text{FeSe}_2$  and  $\text{FeTe}_2$  Nanocrystallites Obtained through a Hydrothermal Co-Reduction Route. *Solid State Commun.* 2006, 138, 538–541.
- (5) Kamimura, T.; Sato, M.; Takahashi, H.; Mori, N.; Yoshida, H.; Kaneko, T. Pressure-Induced Phase Transition in Fe-Se and Fe-S Systems with a NiAs-Type Structure. *J. Magn. Magn. Mater.* 1992, 104–107, 255–256.



- (6) Lupu, D.; Bucur, R. V. Possible Anionic Clusters and Mixed Valence Effects in Transition Metal Chalcogenides and Oxides. *J. Phys. Chem. Solids* 1978, 39, 285–290.
- (7) Lu, T.; Dong, S.; Zhang, C.; Zhang, L.; Cui, G. Fabrication of transition metal selenides and their applications in energy storage. *Coordination Chemistry Reviews* 2017, 332, 75–99.
- (8) Xia, B.; Gao, D.; Xue, D. Ferromagnetism of two-dimensional transition metal chalcogenides: both theoretical and experimental investigations. *Nanoscale*, 2021, 13, 12772.
- (9) Zeng, C.; Dai, L.; Jin, Y.; Liu, J.; Zhang, Q.; Wang, H. Design strategies toward transition metal selenide-based catalysts for electrochemical water splitting. *Sustainable Energy Fuels*, 2021, 5, 1347.
- (10) Ray, P. C. Size and Shape Dependent Second Order Nonlinear Optical Properties of Nanomaterials and Their Application in Biological and Chemical Sensing. *Chem. Rev.* 2010, 110, 5332–5365
- (11) Jeevanandam, J.; Barhoum, A.; Chan, Y. S.; Dufresne, A.; Danquah, M. K. Review on Nanoparticles and Nanostructured Materials: History, Sources, Toxicity and Regulations. *Beilstein J. Nanotechnol.* 2018, 9, 1050–1074
- (12) Khan, I.; Saeed, K.; Khan, I. Nanoparticles: Properties, Applications and Toxicities. *Arabian J. Chem.* 2019, 12, 908–931.
- (13) Frey, N. A.; Peng, S.; Cheng, K.; Sun, S. Magnetic Nanoparticles: Synthesis, Functionalization, and Applications in Bioimaging and Magnetic Energy Storage. *Chem. Soc. Rev.* 2009, 38, 2532–2542
- (14) Nistico, R.; Cesano, F.; Garello, F. Magnetic Materials and Systems : Domain Structure Visualization and Other Characterization Techniques for the Application in the Materials Science and Biomedicine. *Inorganics* 2020, 8, 6.
- (15) Colombo, M.; Carregal-romero, S.; Casula, M. F.; Gutierrez, L.; Morales, M. P.; Bohm, I. B.; Heverhagen, J. T.; Prospero, D.; Parak, W. J. Biological Applications of Magnetic Nanoparticles. *Chem. Soc. Rev.* 2012, 41, 4306–4334.
- (16) Zhang, H. W.; Liu, Y.; Sun, S. H. Synthesis and Assembly of Magnetic Nanoparticles For information and energy storage applications. *Front. Phys. China* 2010, 5, 347–356. Lin, C.;
- (17) Sun, H. L.; Shi, H.; Zhao, F.; Qi, L.; Gao, S. Shape-Dependent Magnetic Properties of Low-Dimensional Nanoscale Prussian Blue (PB) Analogue  $\text{SmFe}(\text{CN})_6 \cdot 4\text{H}_2\text{O}$ . *Chem. Commun.* 2005, 4339–4341.
- (18) Oyarzun, S.; Tamion, A.; Tournus, F.; Dupuis, V.; Hillenkamp, M. Size Effects in the Magnetic Anisotropy of Embedded Cobalt Nanoparticles : From Shape to Surface. *Sci. Rep.* 2015, 5, 14749.
- (19) Moreno, R.; Poyser, S.; Meilak, D.; Meo, A.; Jenkins, S.; Lazarov, V. K.; Vallejo-Fernandez, G.; Majetich, S.; Evans, R. F. L. The Role of Faceting and Elongation on the Magnetic Anisotropy of Magnetite  $\text{Fe}_3\text{O}_4$  Nanocrystals. *Sci. Rep.* 2020, 10, 2722.
- (20) Ghalawat, M.; Poddar, P. Study of the Phase-Evolution Mechanism of an Fe–Se System at the Nanoscale: Optimization of Synthesis Conditions for the Isolation of Pure Phases and Their Controlled Growth. *Langmuir* 2020, 36, 2012–2022.
- (21) Ghalawat, M.; Poddar, P. Remarkable Effect of Fe and Se Composition on Magnetic Properties-Comparative Study of the Fe–Se System at the Nanoscale. *J. Phys. Chem. C* 2022, 126, 4655–4663.

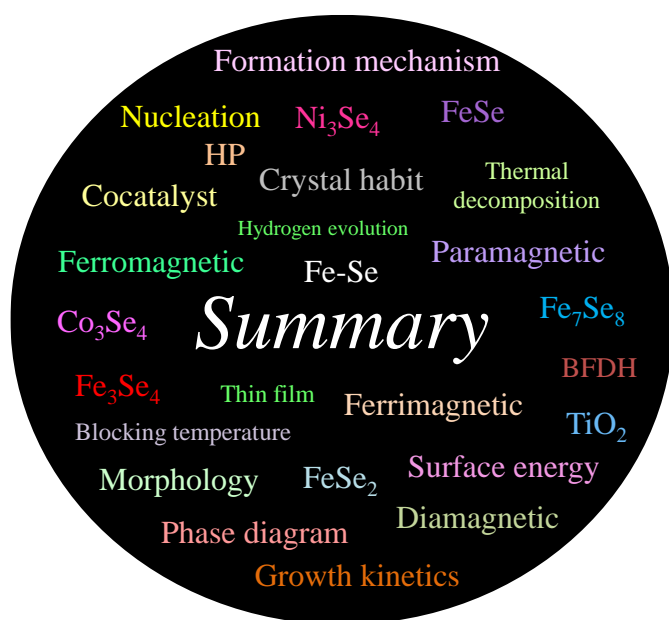
- (22) Andresen, A. F.; Vestersjø, E.; Haaland, A.; Gronowitz, S.; Christiansen, H.; Rosen, U. A Neutron Diffraction Investigation of Fe<sub>3</sub>Se<sub>4</sub>. *Acta Chem. Scand.* 1968, 22, 827–835.
- (23) Okazaki, A.; Hirakawa, K. Structural Study of Iron Selenides FeSex. I Ordered Arrangement of Defects of Fe Atoms. *J. Phys. Soc. Jpn.* 1956, 11, 930–936.
- (24) Zhang, H.; Long, G.; Li, D.; Sabirianov, R.; Zeng, H. Fe<sub>3</sub>Se<sub>4</sub> Nanostructures with Giant Coercivity Synthesized by Solution Chemistry. *Chem. Mater.* 2011, 23, 3769–3774.
- (25) Hayashi, A.; Imada, K.; Inoue, K.; Ueda, Y.; Kosuge, K. Phase Diagram of (M'<sub>X</sub>M<sub>1-X</sub>)<sub>3</sub>Se<sub>4</sub> (0 ≤ X ≤ 1) (M, M' = 3d-transition metal). *Bull. Inst. Chem. Res., Kyoto Univ.*, 1986, 64, 4.
- (26) Sim, Y.; John, J.; Surendran, S.; Moon, B.; Sim, U. Efficient Photoelectrochemical Water Splitting Reaction using Electrodeposited Co<sub>3</sub>Se<sub>4</sub> Catalyst. *Appl. Sci.* 2018, 9, 16.
- (27) Li, W.; Gao, X.; Xiong, D.; Wei, F.; Song, W.; Xu, J.; Liu, L. Hydrothermal Synthesis of Monolithic Co<sub>3</sub>Se<sub>4</sub> Nanowire Electrodes for Oxygen Evolution and Overall Water Splitting with High Efficiency and Extraordinary Catalytic Stability. *Adv. Energy Mater.* 2017, 7, 1602579
- (28) Du, J.; Zou, Z.; Liu, C.; Xu, C. Hierarchical Fe-doped Ni<sub>3</sub>Se<sub>4</sub> ultrathin nanosheets as an efficient electrocatalyst for oxygen evolution reaction. *Nanoscale*, 2018, 10, 5163.
- (29) Wu, P.; Sun, G.; Chen, Y.; Xu, W.; Zheng, H.; Xu, J.; Wang, L.; Peng, D. MoSe<sub>2</sub>-Ni<sub>3</sub>Se<sub>4</sub> Hybrid Nanoelectrocatalysts and Their Enhanced Electrocatalytic Activity for Hydrogen Evolution Reaction. *Nanoscale Research Letters*, 2020, 15, 132.
- (30) Andresen, A.F., van Laar, R., *Acta Chemica Scandinavica (1-27,1973-42,1988)* (1970), **24**, 2435
- (31) Hiller, J. E., Wegener, W., *Neues Jahrbuch fur Mineralogie, Abhandlungen* (1960), **94**, 1147
- (32) Garcia-Garcia F J, Larsson, A. K., Noren, L., Withers, R. L., *Solid State Sciences* (2004), **6**, 725
- (33) Cullity, B. D.; Stock, S. R. *Elements of X-ray Diffraction*, 3rd ed.; Prentice-Hall, 2001.
- (34) Patterson, A. L. The Scherrer Formula for X-ray Particle Size Determination. *Phys. Rev.* 1939, 56, 978–982.
- (35) Buerger, M. J. *Phase Transformations in Solids* (eds Smoluchowski, R., Mayer, J. E. & Weyl, W. A.) John Wiley, New York, 1951.
- (36) Xie, H., Yin, F., Yu, T.; Wang, J.; Liang, C. Mechanism for direct graphite-to-diamond phase transition. *Sci Rep* 2014, **4**, 5930.
- (37) Arlt, T.; Angel, R. J. Displacive phase transitions in C-centered clinopyroxenes: spodumene, LiScSi<sub>2</sub>O<sub>6</sub> and ZnSiO<sub>3</sub>. *Phys Chem Minerals*, 2000, 27, 719-731.
- (38) A. Bravais. *Etudes Crystallographiques* . Paris: Gauthier-Villars, 1866.
- (39) M. G. Friedel. *Etudes sur la loi de Bravais*. Bull. Soc. Franc. Miner., 9:326, 1907.
- (40) J. D. H. Donnay and D. Harker. A new law of crystal morphology extending the law of bravais. *Amer. Min.*, 22:446, 1937.

- (41) P. Hartman and W. G. Perdok. On the relations between structure and morphology of crystals. I. *Acta Crystallogr.*, 8:49–52, 1955.
- (42) P. Hartman and W. G. Perdok. On the relations between structure and morphology of crystals. II. *Acta Crystallogr.*, 8:521–524, 1955.
- (43) P. Hartman and P. Bennema. The attachment energy as a habit controlling factor : I. Theoretical considerations. *J. Cryst. Growth*, 49:145–156, 1980.
- (44) S. Goel, N. Sinha, H. Yadav, B. Kumar, On the prediction of external shape of ZnO nanocrystals. *Physica E: Low-dimensional Systems and Nanostructures*, 2018.
- (45) Song Li, Gaowu W. Qin\*, Yudong Zhang, Wenli Pei, Liang Zuo and Claude Esling. Anisotropic Growth of Iron Oxyhydroxide Nanorods and their Photocatalytic Activity. *Advanced engineering materials*, 2010, 12, 10.
- (46) Cong, H.; Zhang, H.; Sun, S.; Yu, Y.; Yu, W.; Yu, H.; Zhang, J.; Wang, J.; Boughton, R. Morphological Study of Czochralski-Grown Lanthanide Orthovanadate Single Crystals and Implications on the Mechanism of Bulk Spiral Formation. *J. Appl. Cryst.* (2010). **43**, 308-319.
- (47) Eftimie, E.; Avram, N.; Jelsch, C.; Nicolov, M. Morphology of the GdVO<sub>4</sub> crystal: first-principles studies. *Acta Cryst.* 2020, B76.
- (48) H. P. Wu, J. F. Liu, M. Y. Ge, L. Niu, Y. W. Zeng, Y. W. Wang, G. L. Lv, L. N. Wang, G. Q. Zhang, and J. Z. Jiang. Preparation of Monodisperse GeO<sub>2</sub> Nanocubes in a Reverse Micelle System. *Chem. Mater.* 2006, 18, 1817-1820.
- (49) W. M. M. Heijnen. The morphology of gel grown calcite. *N. Jb. Miner. Mh.*, 8:357– 371, 1985.
- (50) Goel, S.; Sinha, N.; Hussain, A.; Joseph, A.; Yadav, H.; Kumar, B. Sunset yellow dyed triglycine sulfate single crystals: enhanced thermal, mechanical, optical and di-/piezo-/ferro-/pyro-electric properties. *Journal of Materials Science: Materials in Electronics*, 2018.
- (51) K J Robertst, R Dochertyt, P Bennemas and L A M J Jetten. The importance of considering growth-induced conformational change in predicting the morphology of benzophenone. *J. Phys. D. AM, Phys.* 1993, 26, 87-821.
- (52) Zhang, H.; Zhang, M.; Pan, S.; Dong, X.; Yang, Z.; Hou, X.; Wang, Z.; Chang, K.; Poeppelmeier, K. Pb<sub>17</sub>O<sub>8</sub>Cl<sub>18</sub>: A Promising IR Nonlinear Optical Material with Large Laser Damage Threshold Synthesized in an Open System. *J. Am. Chem. Soc.* 2015, 137, 26, 8360–8363
- (53) Kaminsky, W. From CIF to virtual morphology using the WinXMorph program. *J. Appl. Cryst.* (2007). 40, 382–385.
- (54) Hoene, J. V.; Charles, R. G.; Hickam, W. M. Thermal Decomposition of Metal Acetylacetonates: Mass Spectrometer Studies. *J. Phys. Chem.* 1958, 62, 1098–1101.
- (55) Telesca, D.; Nie, Y.; Budnick, J. I.; Wells, B. O.; Sinkovic, B. Impact of Valence States on the Superconductivity of Iron Telluride and Iron Selenide Films with Incorporated Oxygen. *Phys. Rev. B: Condens. Matter Mater. Phys.* 2012, 85, 214517.
- (56) Yamashita, T.; Hayes, P. Erratum to "Analysis of XPS spectra of Fe<sup>2+</sup> and Fe<sup>3+</sup> ions in oxide materials" [*Appl. Surf. Sci.* 254 (2008) 2441-2449]. *Appl. Surf. Sci.* 2009, 255, 8194.

- (57) T.J. Chuang, C.R. Bridle and D.W. Rice. Interpretation of the X-ray photoemission spectra of cobalt oxides and cobalt oxide surfaces. *Surface Science* 59 (1976) 413-429
- (58) Mandale, A. B.; Badrinarayanan, S.; Date, S. K.; Sinha, A. P. B. Photoelectron-spectroscopic study of nickel, manganese and cobalt selenides. *Journal of Electron Spectroscopy and Related Phenomena*, 33 1984, 61-72
- (59) Zheng, Q.; Cheng, X.; Li, H. Microwave Synthesis of High Activity FeSe<sub>2</sub>/C Catalyst toward Oxygen Reduction Reaction. *Catalysts* 2015, 5, 1079–1091.
- (60) Zhang, J.-Y.; Lv, L.; Tian, Y.; Li, Z.; Ao, X.; Lan, Y.; Jiang, J.; Wang, C. Rational Design of Cobalt-Iron Selenides for Highly Efficient Electrochemical Water Oxidation. *ACS Appl. Mater. Interfaces* 2017, 9, 33833–33840.
- (61) Xia, C.; Jiang, Q.; Zhao, C.; Hedhili, M. N.; Alshareef, H. N. Selenide-Based Electrocatalysts and Scaffolds for Water Oxidation Applications. *Adv. Mater.* 2016, 28, 77–85.
- (62) Arrott, A. S. Generalized Curie-Weiss law. *Phys. Rev. B* 1985, 31, 2851
- (63) Neel, L. (1948) Propriétés magnétiques des ferrites. Ferrimagnétisme et antiferromagnétisme. *Annales des Physique* 3:137
- (64) Roth, W. L. The magnetic structure of Co<sub>3</sub>O<sub>4</sub>. *J. Phys. Chem. Solids Pergamon Press* 1964, 25, 1-10.
- (65) Buckett, M. I.; Marks, L. D. Formation of a Ni<sub>3</sub>O<sub>4</sub> spinel phase on the surface of nio during electron irradiation. *Mat. Res. Soc. Symp. Proc.* 1989, 129.
- (66) Spender, M. R.; Coey, J. M. D.; Morris, A. H. The Magnetic Properties and Mossbauer Spectra of Synthetic Samples of Fe<sub>3</sub>S<sub>4</sub>. *Canadian Journal of Physics.* 1972, 2313.
- (67) R. F. Heidelberg. A. H. Luxehz, S. Talhouk, and J. J. Baxewic. The Magnetic Susceptibilities of the Cobalt-Sulfur System. *Inorg. Chem.* 1966, 5, 2, 194–197.
- (68) Liu, Q.; Díaz, A.; Prosvirin, A.; Luo, Z.; Batteas, J D. Shape-Controlled Synthesis of Nanopyramids and Nanoprisms of Nickel Sulfide (Ni<sub>3</sub>S<sub>4</sub>). *Nanoscale*, 2014,6, 8935-8942
- (69) Chang, L.; Roberts, A. P.; Tang, Y.; Rainford, B. D.; Muxworthy, A. R.; Chen, Q. Fundamental magnetic parameters from pure synthetic greigite (Fe<sub>3</sub>S<sub>4</sub>). *Journal of geophysical research*, 2008, 113, B06104.

## Chapter 7

### Summary and Future Scope



### Highlights

*This chapter summarized the work presented in the thesis and highlights the potential direction for future work.*

**Keywords:** Summary, future scope

## 7.1 Summary of the thesis

The crystallinity of solid materials is the prime factor that decides the properties. The nucleation and growth dynamics defined the final crystallinity of the materials. The crystal formation processes have been studied for decades for several materials, including metals and metal oxides; however, their crystallization physics is not explored much due to the complexity of TMCs. In this thesis, we have made efforts in this direction.

TMCs represent an important class of materials with rich phase-diagram and diverse industrial applications. The electronic and phononic properties are extremely sensitive to the crystalline phase, stoichiometry, particle shape, and size. Therefore, it is essential to reach reasonable control over the chemistry of phase formation. TMSe have good chemical and physical properties due to the benefits of transition metal cations, selenium anions, and enhanced morphological/structural qualities. Among the TMSes,  $\text{Fe}_x\text{Se}_y$  compounds (with  $x/y$  varying from 1:2 to 1:1) are of great importance because of their exciting and unique optical, thermal, electrical, and magnetic properties that are firmly related to the Fe–Se elemental ratio as well as their crystalline structure.

The family of iron selenides has four stable phases:  $\text{FeSe}_2$  (orthorhombic marcasite),  $\text{Fe}_3\text{Se}_4$  (monoclinic NiAs-type),  $\text{Fe}_7\text{Se}_8$  (hexagonal NiAs-type), and  $\text{FeSe}$  (tetragonal PbO-type). Depending upon the composition of Fe:Se, these compounds could be metal, semiconductors, or superconductors, and their magnetic properties also vary a lot from ferro- to ferrimagnetic.

Researchers have explored different aspects (such as cation site doping, variation of Fe:Se ratio etc.) of this system to study its magnetic properties. However, the control over pure compounds of the Fe-Se system is not reported so far. This thesis describes the efforts made to understand the formation process followed by controlling the crystallinity by growth kinetics and consequently the influence on magnetic properties.

It starts by predicting the crystal morphology of the Fe-Se system via BFDH (pure crystallographic approach) and HP (periodic bond chain vector approach) models. The variation is observed in these four compounds due to the difference in the crystal structure that will add uniqueness to the magnetic behavior.

The Fe-Se system has been fabricated using the wet-chemical method. An easy-to-control synthetic procedure was developed by heating the  $\text{Fe}(\text{acac})_3$  and Se mixture in a coordinating organic solvent to synthesize the Fe-Se phases. The process provided an

appropriate nucleation and growth environment in a reaction system. We demonstrated that synthetic circumstances have a significant impact on governing the phases of the Fe-Se system. The OLA was used as a reducing agent to decompose the precursors, and 1-ODE was used as an accelerating agent to accelerate all the reaction steps, resulting in the highest temperature phase formation. It was proposed that the reactivity of Fe and Se precursors primarily governed the nucleation of Fe-Se NPs, and growth was governed primarily by the reaction temperature apart from other factors. Instead of directly forming the FeSe phase from Fe and Se precursors, intermediate products of FeSe<sub>2</sub>, Fe<sub>3</sub>Se<sub>4</sub>, and Fe<sub>7</sub>Se<sub>8</sub> phases are formed. They follow the sequence as FeSe<sub>2</sub> → Fe<sub>3</sub>Se<sub>4</sub> → Fe<sub>7</sub>Se<sub>8</sub> → FeSe, in the temperature range of 110 °C - 300 °C. This emphasizes the essential role played by temperature and time with solvents in phase transformation. The optimized reaction conditions to synthesize the pure phases were reported. Additionally, the morphology of particles formed in each Fe-Se phase is also correlated with the theoretical crystal habits. This method also provides control over shapes and sizes by tuning the solvents and reaction temperature-time, which tunes the properties of Fe-Se NPs.

Further, the magnetic properties of these as-synthesized NPs were studied. The correlation between the Fe-Se phases and the magnetic properties has been presented. The distinct arrangement of Fe and Se atoms results in drastically varying magnetic properties due to the change in Fe<sup>2+</sup>/Fe<sup>3+</sup> ratio, crystal field environment around Fe-ions, magnetocrystalline anisotropy, Fe-vacancies, and so forth. The two NiAs-based phases –Fe<sub>3</sub>Se<sub>4</sub> and Fe<sub>7</sub>Se<sub>8</sub>, are ferrimagnetic below ~ 300 K and show semi-hard magnetic properties. The other two phases – FeSe<sub>2</sub> and FeSe, exhibit weaker magnetism. The surface oxidation remarkably affects the magnetic properties, especially in the phases with weak magnetization, such as FeSe<sub>2</sub> and FeSe. The surface-oxidized FeSe<sub>2</sub> and FeSe show magnetic ordering at the nanoscale. The Fe<sub>3</sub>Se<sub>4</sub> NPs show ferrimagnetism at 300 K with a large magnetic coercivity which multiplies at low temperatures. The Fe<sub>7</sub>Se<sub>8</sub> NPs show ferrimagnetism at all temperatures with a transition temperature higher than 360 K. The FeSe NPs indicate magnetic ordering at both the temperatures with a magnetic anomaly at around 80 - 100 K due to phase transition. The Fe<sub>3</sub>Se<sub>4</sub> shows the most unique and interesting magnetic properties.

Further, the Fe<sub>3</sub>Se<sub>4</sub> NPs were prepared under well-controlled crystal growth conditions to examine the influence of morphology on magnetic properties. The grain growth of NPs estimated from the XRD patterns, rises monotonically with an increase in reaction temperature. The crystallite size range is about 33 nm-42 nm depending on the reaction temperature from

260 °C to 330 °C. A discrete environment has been provided in the reactions to allow the growth of different facets, which results in the unique morphology of the NPs. The magnetic parameters such as  $M_S$ ,  $H_C$ ,  $K_{\text{eff}}$ ,  $BH_{\text{max}}$ , and  $T_B$  exhibited a strong dependence on size and shape. The  $M_{60 \text{ kOe}}$  increases by increasing the crystallite size to a maximum observed value of about 5.4 emu/g at 300 K for nanorods, while it becomes 7 emu/g for nanoplatelets at the same temperature. The  $H_C$  and  $M_R$  values increase with the crystallite size up to a maximum observed values of about 2.3 Oe and 2 emu/g, respectively, for nanorods. The  $BH_{\text{max}}$  increases linearly with crystallite size up to a maximum value of 7.1 kG Oe at 300 K for nanorods, and it reaches 7.5 kG Oe for nanoplatelets.

To study the essential role of transition metal ions in  $M_3\text{Se}_4$  magnetic behavior, we compared the structural and magnetic properties of  $\text{Fe}_3\text{Se}_4$ ,  $\text{Co}_3\text{Se}_4$ , and  $\text{Ni}_3\text{Se}_4$  synthesized following the thermal decomposition method. The ability to manipulate solution chemistry has been established via extensive investigation of the individual role of various reaction pathways, leading to the monoclinic  $M_3\text{Se}_4$  NPs with distinct morphologies in the same reaction environment. The deep mechanistic insight helped identify the underlying reason behind the varied morphology with the help of the theoretical aspect. The  $\text{Fe}_3\text{Se}_4$  is ferrimagnetic, with a Curie temperature of nearly 322 K. In contrast, the other compounds,  $\text{Co}_3\text{Se}_4$  and  $\text{Ni}_3\text{Se}_4$ , are paramagnetic in the whole measurement temperature range. The magnetic transition temperature in the last two compounds is so low that it is impossible to detect within measurement limits.

In conclusion, after diving deeper into formation processes, the work provides the appropriate method for synthesizing controlled Fe-Se NPs with distinct stoichiometry, transition metal, size, and shape. The helpful advice about synthesizing experimental conditions for the synthesis of Fe-Se NPs has been discussed for the first time that can be extended to most TMSes.

## 7.2 Directions for future work

We believe that this thesis provides a deep understanding of formation processes and controlled fabrication of  $\text{TMSe}$ , which can be used to understand and develop most of the TMCs in the future.

The simple thermal decomposition route has been proven to be a brilliant method to synthesize any of the four phases in the Fe-Se system at the nanoscale with unique magnetic



properties. This is an excellent approach to meet the specific needs of storage devices, biomedicine, and catalyst applications.

The influence of morphology and size on the magnetic properties of  $\text{Fe}_3\text{Se}_4$  NPs has been examined for the first time. These findings show that considerable attention should be given to tuning the size and shape of TMCs, which have potential industrial applications.

Future studies on this topic will look at the effects of stoichiometry, size, morphology, and transition metal on the ferroelectric characteristics of  $\text{Fe}_3\text{Se}_4$ . The ferroelectric characteristics may be significantly improved to make the material acceptable for practical applications. Furthermore, because  $\text{Fe}_7\text{Se}_8$  is also a NiAs-based compound, future research in this sector will focus on its ferroelectric properties. It will be interesting to explore a new area of the Fe-Se system other than these compounds' magnetic and electric properties.

Other than magnetic properties, it will be interesting to explore various other properties of synthesized TMSes.  $\text{Co}_3\text{Se}_4$  and  $\text{Ni}_3\text{Se}_4$  are promising candidates for catalytic activities; in the future, it will be an excellent scope to study the single phase  $\text{Co}_3\text{Se}_4$  and  $\text{Ni}_3\text{Se}_4$  NP's catalytic activities. It is strongly believed that the catalytic properties will be unique for these synthesized compounds. Especially for  $\text{Co}_3\text{Se}_4$ , as the size of the NPs are nearly 5 nm which will increase the activity.

Thus, the thesis opens a new path for synthesizing TMCs special TMSes. It is appropriate to conclude that the thermal decomposition method used in the thesis can be used with appropriate modifications to synthesize any TMSes. In the future, it will be interesting to synthesize novel materials at the nanoscale using this synthesis route.

**ABSTRACT**

---

**Name of the Student:** Monika**Registration No.:** 10PP17A26045**Faculty of Study:** Physical Sciences**Year of Submission:** 2022**CSIR Lab:** NCL, Pune**Name of the Supervisor:** Dr. Pankaj Poddar**Title of the Thesis:** *Physics of transition metal chalcogenides based on deeper investigation of their phase-diagram and crystal growth mechanism*

---

This thesis aims to create a chemical approach for fabricating controlled Fe-Se system nanoparticles and comprehending the formation process. **Chapter 1** of this thesis gives an overview of the history and progress of essential formation processes for better understanding and controlling the Fe-Se system properties. **Chapter 2** investigates the theoretical crystal habit of all the phases of the Fe-Se system using BFDH (pure crystallographic approach) and HP (periodic bond chain vector approach) models. **Chapter 3** deals with the Fe-Se system's complete phase transformation sequence using a wet-chemical method, from plotting the phase diagram to optimizing the appropriate conditions required to synthesize individual phases. Finally, the cause for the similarities and dissimilarities in theoretical crystal habits and real-life experimental morphologies is examined. **Chapter 4** explains the correlation between the phases and the magnetic properties of the Fe-Se system. The magnetic properties vary enormously with change in Fe:Se ratio due to the change in  $\text{Fe}^{2+}/\text{Fe}^{3+}$  ratio, crystal field environment around Fe-ions, magnetocrystalline anisotropy, Fe-vacancies, and so forth. It is observed that  $\text{Fe}_3\text{Se}_4$  has the most unique and interesting magnetic properties. **Chapter 5** deals with the growth directions of  $\text{Fe}_3\text{Se}_4$  in different reaction conditions. The entire roadmap is laid-out—starting from the formation of the unit cell to the diffusion and attachment of monomers and the fate of various facet growth. Finally, we have shown how the distinct growth in various facets influences the magnetic properties. In **chapter 6**, a conscious effort has been made to fabricate the monoclinic  $\text{M}_3\text{Se}_4$  compounds (where M can be Fe, Co, or Ni). The influence of transition metal (M) on the magnetic properties is investigated for monoclinic  $\text{M}_3\text{Se}_4$  NPs. The  $\text{Fe}_3\text{Se}_4$  is observed to be well-known ferrimagnetic with a Curie temperature of nearly 322 K. However, the other two compounds,  $\text{Co}_3\text{Se}_4$  and  $\text{Ni}_3\text{Se}_4$ , are examined to be paramagnetic over the whole measurement temperature range (5 K to 300 K). **Chapter 7** summarizes the work done in this thesis and makes recommendations for future study in many domains.

## **List of Publication(s) in SCI Journal(s) Emanating from the Thesis Work**

1. **Monika Ghalawat**, Pankaj Poddar. Study of the Phase-Evolution Mechanism of an Fe-Se system at the Nanoscale: Optimization of Synthesis Conditions for the Isolation of Pure Phases and their Controlled Growth. *Langmuir* 2020, 36, 8, 2012–2022. DOI: 10.1021/acs.langmuir.9b03643
2. **Monika Ghalawat**, Pankaj Poddar. Study of Growth Kinetics of Fe<sub>3</sub>Se<sub>4</sub> Nanocrystallites and the Influence of Size and Shape Tunability on their Magnetic Properties. *J. Phys. Chem. C* 2021, 125, 14, 7932–7943. DOI: 10.1021/acs.jpcc.1c00389
3. **Monika Ghalawat**, Pankaj Poddar. Remarkable Effect of Fe and Se Composition on Magnetic Properties— Comparative Study of Fe-Se System at Nanoscale. *J. Phys. Chem. C* 2022, 126, 9, 4655–4663. DOI: 10.1021/acs.jpcc.1c10286
4. **Monika Ghalawat**, Pankaj Poddar. A Process for the Synthesis of Nanoparticles of Transition Metal Chalcogenides. 2020, World Patent Published (WO2020222249).

## **List of Papers with Abstract Presented (Oral or Poster) at National or International Conferences /Seminars**

1. Workshop on Materials Characterizations: Structure, Spectroscopy, and Microscopy at the Institute of Infrastructure, Technology, Research and Management (IITRAM), Ahmedabad, India, **2019** (Presented poster titled "*The Phase Evolution Mechanism of Fe-Se System at Nanoscale: Interplay of Reaction Temperature, Time, and Solvent in Nanocrystal Growth*")
2. National Conference on Chemistry of Chalcogenides (NC<sub>3</sub> -2021) Organized by Department of Applied Chemistry Defence Institute of Advanced Technology (Deemed to be University), Pune, India **2021** (Presented oral talk titled "*Study of Phase-Evolution Mechanism and Growth Kinetics of iron selenide at Nanoscale: Control over Structure, Size and Shape*")
3. 4<sup>th</sup> International conference on emerging technologies: Micro to Nano at the Savitribai Phule Pune university (SPPU), Pune, India 2019 (Presented poster titled "*The phase evolution mechanism of Fe-Se system at nanoscale: Interplay of reaction temperature, time, and solvent in nanocrystal growth*")
4. Science Day Celebration  
CSIR-NCL, **2019** (Presented poster titled "*The phase evolution mechanism of Fe-Se system at nanoscale: Interplay of reaction temperature, time, and solvent in nanocrystal growth*")  
CSIR-NCL, **2020** (Presented poster titled "*Is the shape and size control of nanomaterials an art or science?*")

# Study of Growth Kinetics of Fe<sub>3</sub>Se<sub>4</sub> Nanocrystallites and the Influence of Size and Shape Tunability on their Magnetic Properties

Published as part of *The Journal of Physical Chemistry virtual special issue "D. D. Sarma Festschrift"*.

Monika Ghalawat and Pankaj Poddar\*

Cite This: *J. Phys. Chem. C* 2021, 125, 7932–7943

Read Online

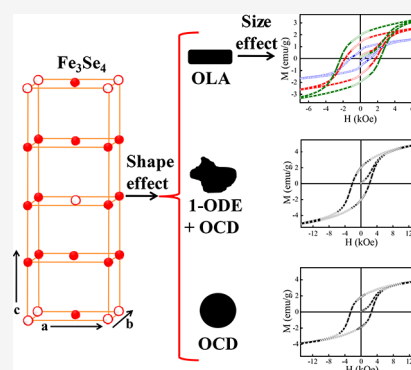
ACCESS |

Metrics & More

Article Recommendations

Supporting Information

**ABSTRACT:** Crystalline iron selenide (Fe<sub>3</sub>Se<sub>4</sub>) nanoparticles (NPs) present a useful model system for a fundamental understanding of magnetism apart from having potential applications in permanent-magnet-related technologies. Despite significant advancements in understanding of the nucleation and growth processes, control over size and shape tunability is nontrivial, especially for the transition metal chalcogenides (TMC). The Wulff theorem states that if a crystal can grow purely under thermodynamic control of parameters then it will adopt the shape determined by the surface-energy minimization, i.e., the surface energy minimization will drive the growth of each crystalline facet. However, the known or unknown, controllable or uncontrollable parameters of a typical reaction which makes kinetic growth more art than science, depending upon whether we understand them or not. There is hardly any study based on existing models and theories to explain the TMC morphology evolution. In this work, there is a conscious effort to know, understand, and control the individual role of various reaction pathways on the shape and size of the Fe<sub>3</sub>Se<sub>4</sub> nanocrystals. A qualitative growth mechanism is proposed based on the diffusion and reaction processes. Furthermore, the influence of shape/size on the magnetic parameters such as coercivity ( $H_C$ ), magnetization ( $M_{60kOe}$ ), effective magnetic anisotropy constant ( $K_{eff}$ ), energy product ( $BH_{max}$ ), and average blocking temperature ( $T_B$ ) is investigated for Fe<sub>3</sub>Se<sub>4</sub> NPs. After diving deeper into the science of crystal growth, our insight provides valuable guidance on experimental conditions for the synthesis of Fe<sub>3</sub>Se<sub>4</sub> NPs with tunable sizes/shapes which for the first time can be extended to most TMCs.



## INTRODUCTION

Nanodimensionality has added immense advantages in the physical and chemical property tunability through the surface to volume ratio variation.<sup>1–5</sup> The unique and novel size- and shape-dependent properties displayed by nanocrystals have always posed curiosity, challenges, and opportunities.<sup>6,7</sup> Many of the wonders seen in the nature can be understood by the nanoscale phenomena. Recently, considerable interest has developed in understanding the correlation between physical properties and morphology.<sup>8</sup> Besides, most electronic devices use the nanoscale components with control over the assembly of nanoscale building blocks, which in turn, is dictated by the size and shape of the nanoparticles (NPs).<sup>1</sup> The size, shape, and crystallinity of NPs and their assembly need to be precisely controlled for magnetic materials over certain other materials as subtle changes in these parameters have a relatively larger influence on the applications such as high-density memory storage using magnetic media, magnetic read-heads, ferrofluids, or the rising importance of magnetic NPs in biomagnetic applications.<sup>9–15</sup> The important role of surface and bulk arrangement of atoms in a single NP as well as the effect of three-dimensional arrangements of NPs on magnetic properties have been known for more than half a century in magnetic metals and

transition metal oxides.<sup>16–29</sup> However, these effects are poorly understood for their chalcogenide counterparts ( $M-X$  ( $M$  = transition elements,  $X$  = S, Se, and Te)) due to complexities in the phase diagram, poor control over stoichiometry, and morphology. In our previous report, the complexities in the phase diagram and control over stoichiometry were studied.<sup>30</sup> In this article, an intensive investigation on the control over the morphology of Fe<sub>3</sub>Se<sub>4</sub> NPs is presented, followed by the influence of morphology on the magnetic properties.

Among the transition metal chalcogenides (TMC), iron selenides are known, since the early 1950s and 1960s, to stabilize in four phases: FeSe<sub>2</sub>, Fe<sub>3</sub>Se<sub>4</sub>, Fe<sub>7</sub>Se<sub>8</sub>, and FeSe.<sup>31,32</sup> Two phases, Fe<sub>3</sub>Se<sub>4</sub> and Fe<sub>7</sub>Se<sub>8</sub>, are noteworthy for their unique magnetic behavior. Phases Fe<sub>7</sub>Se<sub>8</sub> and Fe<sub>3</sub>Se<sub>4</sub> show ferrimagnetic ordering at room temperature with the Curie temperatures  $\sim$ 453 and

Received: January 15, 2021

Revised: March 15, 2021

Published: March 30, 2021



~315 K, respectively.<sup>33–35</sup> Among these two, lately, Fe<sub>3</sub>Se<sub>4</sub> has been a center of attraction for researchers due to its relatively large magnetic anisotropy and coercivity at ~300 K.<sup>36–38</sup> However, to date, there is little effort on systematic studies to develop controlled nucleation and growth pathways for Fe<sub>3</sub>Se<sub>4</sub> as well as size-dependent magnetic properties to develop a fundamental understanding of size/shape-property correlations.<sup>36</sup>

In 1956, Okazaki and Hirakawa<sup>32</sup> did the structural studies on a single crystal specimen of Fe<sub>3</sub>Se<sub>4</sub>. The unit-cell lattice parameters of Fe<sub>3</sub>Se<sub>4</sub> (Fe<sup>2+</sup>Fe<sub>2</sub><sup>3+</sup>Se<sub>4</sub><sup>2-</sup>) were calculated as  $a = 6.167 \text{ \AA}$ ,  $b = 3.537 \text{ \AA}$ , and  $c = 11.17 \text{ \AA}$  with the  $I2/m$  space group.<sup>32</sup> Each Fe<sup>2+</sup>/Fe<sup>3+</sup> cation is octahedrally coordinated by six Se<sup>2-</sup> anions (FeSe<sub>6</sub> octahedra), and the coordination polyhedron of Se is the trigonal prism created by six Fe<sup>2+</sup>/Fe<sup>3+</sup> cations (SeFe<sub>6</sub> prisms).<sup>35</sup> In 1968, Andresen<sup>39</sup> performed neutron-scattering measurements and stated that the ferrimagnetism in this compound is the result of ordered iron vacancies in alternate layers. The Fe<sup>2+</sup>/Fe<sup>3+</sup> cations and Se<sup>2-</sup> anions are arranged in alternating layers along the  $c$ -axis, and the deviation from (1:1) stoichiometry leads to the formation of cation vacancies in every second Fe layer to compensate for the iron deficiency, and these vacancies are distributed as far apart as possible. Each layer has a different magnetization value, as the number of vacancies and the vacancy distribution is distinct in each layer.<sup>39</sup> As shown in Scheme S1, in a unit cell, the cation vacancies appear in every other Fe layer with a different number in each alternating layer. These cation vacancies are lying in the ( $\bar{1}01$ ) plane.<sup>32,36</sup> Thus, the origin of ferrimagnetic ordering is attributed to the spins ferromagnetically aligned within each plane along the  $c$ -axis and antiferromagnetically aligned in an adjacent plane with ordered iron vacancies.<sup>36</sup>

Many efforts have been dedicated to developing rare-earth (RE)-free magnetic materials for application as a permanent magnet.<sup>40–42</sup> This is receiving wide attention in both the scientific and industrial fields due to toxicity and expense of RE materials. Among RE-free materials, MnBi<sup>43</sup> is an ambient-temperature ferromagnet with a high coercivity (~23 kOe) and anisotropy constant (~22 Merg/cm<sup>3</sup> at 490 K). However, the high vapor pressure of Mn and a low melting point of Bi inhibit its industrial applications. Another Fe-based compound, FePt,<sup>41</sup> is also an ideal compound due to its magnetic properties, but due to the presence of Pt, it is unsuitable for mass applications. In comparison, Fe<sub>3</sub>Se<sub>4</sub> is a low-cost compound with interesting magnetic properties, as stated earlier. At nanoscale, the Fe<sub>3</sub>Se<sub>4</sub> shows semihard magnetic properties below its Curie temperature even without the presence of RE or noble metal atoms, which makes it a unique material.<sup>36,37</sup> Zhang et al. reported a coercivity of ~4 kOe at 300 K, and that increases to ~40 kOe at 10 K for nanoplatelets after applying 90 kOe of maximum external field.<sup>36</sup> For nanocacti morphology, the coercivities around 3.4<sup>36</sup> and 2.74 kOe<sup>37</sup> were observed in two different studies, which increased nearly 10-fold (about 36<sup>36</sup> and 29.5 kOe)<sup>37</sup> at 10 K for a maximum applied external field of 90 kOe field. This is unique and interesting for low-temperature applications in particular. Large magnetic coercivity arises in Fe<sub>3</sub>Se<sub>4</sub> from its monoclinic structure with ordered iron vacancies, leading to a large magnetocrystalline anisotropy:  $\sim 1.0 \times 10^7 \text{ erg/cm}^3$  at 10 K.<sup>38</sup> This value was determined for powdered bulk sample by partially aligning them in a magnetic field along the easy axis ( $b$ -axis) of Fe<sub>3</sub>Se<sub>4</sub> and confirming the alignment using the presence of a predominant peak at (020) in the diffraction pattern and measuring the  $M$ - $H$  loop along the

hard and easy axes.<sup>38</sup> Long et al.<sup>38</sup> established that the Fe<sub>3</sub>Se<sub>4</sub> has a uniaxial type magnetocrystalline anisotropy, as  $K$  is proportional to  $M_S^3$ . They also estimated the critical radius<sup>38</sup> for a single-domain particle of Fe<sub>3</sub>Se<sub>4</sub>, which is about ~800 nm at 10 K and ~2000 nm at 300 K, calculated from  $r_c$ :

$$r_c \approx 9 \frac{(AK)^{\frac{1}{2}}}{\pi M_S^2} \quad (1)$$

where  $A$  is an exchange stiffness constant,  $K$  is the magnetic anisotropy constant, and  $M_S$  is saturation magnetization. Consequently, it is appropriate to conclude that the particles below this size will lie in a single domain region.

For hard magnets, the most crucial figure of merit is the maximum energy product defined by the notation  $(BH)_{\max}$ .<sup>37</sup> Theoretically, the maximum energy product is defined as

$$BH_{\max} = \frac{1}{4} \mu_0 M_S^2 \quad (2)$$

where  $\mu_0$  defines the magnetic permeability of free space, and  $M_S$  illustrates the saturation magnetization. This equation describes a crucial role played by  $M_S$  in deciding the energy product. Therefore, for applications in hard magnetic materials, it is imperative to increase the value of  $M_S$ . For Fe<sub>3</sub>Se<sub>4</sub>, the energy product ~4.38 kG Oe was observed at 300 K for nanorods,<sup>37</sup> which was enhanced up to 10.22 kG Oe by Mn-doping in an applied magnetic field of more than 85 kOe. At 10 K, a nearly 2 orders of magnitude increase of ~0.12 MG Oe<sup>37</sup> makes this compound valuable for several low-temperature applications. Therefore, it is interesting as well as important to study the enhancement of the magnetic parameters of Fe<sub>3</sub>Se<sub>4</sub> by the influence of size and shape, at a lower external magnetic field value than 90 kOe as cited in the earlier studies.

To examine the relationship between morphology and magnetic properties, especially the energy product, control over the morphology of NPs is essential, which is generally governed by the crystal structure, lattice defects at an early stage of crystal growth, symmetry-breaking, and reaction conditions. When a single-crystal seed is allowed to grow in a vacuum precisely under thermodynamic control, it should evolve toward its equilibrium shape according to the calculated surface free energy (Wulff construction).<sup>8,44,45</sup> An equilibrium shape is evaluated by the relative magnitudes of surface free energies associated with different crystallographic facets. With this basic understanding, it is feasible to change the ratios between the surface free energies to obtain nanocrystals with the shapes desired, other than the one predicted by thermodynamic control using premeditated chemistry. Among the numerous procedures, kinetic control over the addition of chemical species from a solution phase seems to be the simplest and most versatile by selective binding of capping molecules, ionic species, and so on, to various facets on a nanocrystal to change their surface free energies.<sup>8</sup> When a capping agent is added to a reaction solution, it stabilizes some particular facets. These facets will exhibit a lower surface free energy, leading to the formation of nanocrystals having a shape that maximizes the expression of that facet. The selective affinity of the capping agents over crystalline facets, they are chemisorbed differently on any crystallographic plane leading to differential addition of atoms onto planes. Due to the availability of a comprehensive variety of molecules that can act as a capping agent, solution-phase synthesis provides a powerful route to prepare various shapes of nanocrystals.<sup>46</sup> Generally, the preferential binding of a capping

**Table 1.** Summary of the Experimental Conditions, Indicating the Influence of the Temperature and Solvent Compositions on the Crystallite Size and Shape of the Products<sup>a</sup>

samples/parameters	FS <sub>NR-260°C</sub>	FS <sub>NR-300°C</sub>	FS <sub>NR-330°C</sub>	FS <sub>PL-330°C</sub>	FS <sub>QS-330°C</sub>					
solvent		OLA		1-ODE and OCD	OCD					
reaction	1	2	3	4	5					
	Step 1									
reaction temperature ( $\pm 2$ °C)			120 °C							
time (min)			30							
	Step 2									
reaction temperature ( $\pm 2$ °C)	260 °C	300 °C	330 °C	330 °C	330 °C					
time (min)	120	80	70	120	100					
	Crystallite Size $d$ ( $\pm 2$ nm) along Following Planes									
( $\bar{1}12$ )	33	37	42	34	36					
(202)	25	31	35	28	32					
(204)	22	24	26	21	27					
	Magnetic Parameters at Different Temperatures									
measurement temperature (K)	300 K	10 K	300 K	10 K	300 K	10 K	300 K	10 K	300 K	10 K
$H_c$ (kOe)	1.1	32.8	1.8	35.9	2.3	35.5	2.1	19.7	2.6	29.6
$M_r$ (emu/g)	0.7	7.1	1.4	6.7	2	7.6	2.1	9.8	1.9	8.5
$M_{60kOe}$ (emu/g)	3.0	13.0	4.5	11.9	5.4	13.3	7.0	16.6	5.3	14.3
$M_r/M_{60kOe}$	0.233	0.549	0.311	0.562	0.370	0.569	0.30	0.59	0.356	0.594
$H_a$ (kOe)	5.7	37.3	7.6	36.2	10.1	36.8	7.2	35.0	9.0	29.9
$K_{eff}$ (erg/cm <sup>3</sup> ) $\times 10^5$	0.59	16.9	1.19	15.1	1.90	17.2	1.77	20.3	1.68	14.9
$BH_{max}$ (kG Oe)	0.8	96.6	3.2	85.4	7.1	109.9	7.5	181.9	6.6	135.7

<sup>a</sup>Fe(acac)<sub>3</sub> and Se powder were used as the Fe and Se precursors, respectively. An evolution of crystallite size for as-synthesized Fe<sub>3</sub>Se<sub>4</sub> nanoparticles is compared with different crystalline planes calculated from powder X-ray diffraction, followed by comparing the magnetic parameters of all the samples at 300 and 10 K. The  $M-H$  curves do not saturate for the highest applied magnetic field of 60 kOe. Therefore, these observed magnetic values are a gross underestimation of their true values.

agent to a specific surface may depend on many factors such as crystal structure, charge density, surface-ion–ligand interactions, the electronic and surface structure of a material, or the functional group(s) of a capping agent. Therefore, the understanding of the growth process is very crucial for control over the morphology.

In this work, the tunability of abundant magnetic parameters has been reported for Fe<sub>3</sub>Se<sub>4</sub> compound by varying the size/shape of the particle at the nanoscale. This will also open various new directions for the controlled syntheses of several other TMCs. Here, the thermal decomposition method is adopted over others in order to have particles with controlled morphology. In particular, the study of systematic changes in the nucleation and growth mechanism of Fe<sub>3</sub>Se<sub>4</sub> compounds as a function of reaction parameters at the nanometric regime has been intensively investigated. This study also highlights the important points, starting from the observation of preferential growth according to the surface energy of low-index planes followed by discussing the qualitative growth mechanism by diffusion process and reaction process in the provided reaction environment. Significant increases in the coercivity ( $H_c$ ), magnetization ( $M_{60kOe}$ ), magnetic anisotropy constant ( $K_{eff}$ ), energy product ( $BH$ )<sub>max</sub>, and average blocking temperature ( $T_B$ ) of Fe<sub>3</sub>Se<sub>4</sub> are observed with an increase in the crystallite-size.

## EXPERIMENTAL SECTION

**Materials.** Iron(III) acetylacetonate [Fe(acac)<sub>3</sub>; 99.99%], selenium powder [Se; 99.99%], oleylamine [OLA; 70%], 1-octadecene [1-ODE; 90%], and octadecylamine [OCD; 97%] were purchased from Sigma-Aldrich chemicals. All chemicals were used without further purification.

**Experiments.** In this work, a one-pot thermal decomposition method has been used to synthesize the controlled

Fe<sub>3</sub>Se<sub>4</sub> nanocrystals. In a typical reaction, Fe(acac)<sub>3</sub> was used as an organometallic precursor, and selenium powder was used as a Se precursor for synthesizing Fe<sub>3</sub>Se<sub>4</sub> in an organic solvent. A 0.53 g (1.5 mmol) portion of Fe(acac)<sub>3</sub> and a 0.158 g (2 mmol) portion of Se were added to corresponding solvent at 30 °C in a 100 mL three-necked round-bottomed flask. The solution was stirred under the flow of high-purity nitrogen gas at 30 °C. After that, the temperature was raised to 120 °C and maintained for 30 min. Subsequently, the temperature was raised at a ramping rate of 2 °C min<sup>-1</sup> up to 200 °C, and a rate of 5 °C min<sup>-1</sup> was used to reach the desired temperature at which the sample was maintained for a pertinent time. A thermometer was placed inside the round-bottomed flask, and the temperature was kept stable within  $\pm 2.0$  °C. The solution was cooled to laboratory temperature by removing the heating source. After cooling, 20 mL of 2-propanol was added to the solution to wash the specimen, which was further separated from the solution by centrifugation. The obtained sample was rewashed with a mixture of 15 mL of hexane and 10 mL of 2-propanol. Finally, the resultant black precipitate was dried under vacuum and utilized for further characterization.

The study of size effect was done over the full range of temperature scan for synthesizing single-phase Fe<sub>3</sub>Se<sub>4</sub> in the presence of OLA (15 mL). Below 260 °C, there was always FeSe<sub>2</sub> phase impurity as discussed in our previous work,<sup>30</sup> while above 330 °C, no reaction was possible because the solution turns into a gel. Therefore, the growth temperature was scanned in the range of 260–330 °C to study the kinetics of crystal formation. We tried several intermediate temperature conditions to optimize the synthesis; however, here, for the sake of brevity and clarity, the data on the samples formed at three particular temperatures are discussed. The experimental details (growth conditions and magnetic measurements) of the

remaining intermediate samples are reported in the [Supporting Information](#).

The reaction parameters including solvent and temperature were modified for shape tuning of  $\text{Fe}_3\text{Se}_4$ , as shown in [Table 1](#). The study of shape effect was done over the two solvent conditions: (1) 1-ODE and OCD are added together as an organic solvent, and (2) only OCD is added as a solvent, at 330 °C. Under these solvent conditions, there is always a presence of  $\text{FeSe}_2$  phase below the optimized temperature (330 °C), and above it, the solution turns into the gel. The details of all the characterization techniques are discussed in the [Supporting Information](#).

## RESULTS AND DISCUSSION

**Thermodynamic and Kinetic Growth.** As per the Wulff theory,<sup>45</sup> the thermodynamic growth will follow the overall surface energy minimization principle, and a hybrid shape exposing a mixture of different facets in the right proportion will become the winner of thermodynamics.<sup>8</sup> The broken bond approximation provides a simple method for evaluating the surface free energies of nanocrystals surrounded by vacuum where only interactions between the nearest neighbors are considered.<sup>8</sup> The surface free energies of different planes were calculated for  $\text{Fe}_3\text{Se}_4$ . The calculation revealed that the surface free energy of different low-index planes of  $\text{Fe}_3\text{Se}_4$  lattice increases in the following order:  $\gamma(101) < \gamma(001) < \gamma(010) < \gamma(100) \sim \gamma(011) < \gamma(111) \sim \gamma(110)$ . The details are mentioned in the [Supporting Information](#). Besides, the real-life reactions of materials are much more complicated than the simplified thermodynamical model due to the kinetic control over the reaction. The true understanding of growth kinetics under real synthetic conditions is very complicated due to the presence of several species together and their interaction with each other. The growth kinetics of  $\text{Fe}_3\text{Se}_4$  under real reaction conditions is proposed using diffusion-limited growth process and reaction-limited growth process. Starting from the unit cell followed by seven intermediate species ([Scheme S2](#)), the molecular environment around the unit cell of  $\text{Fe}_3\text{Se}_4$  surrounded with available species that may influence the crystal growth is proposed ([Supporting Information](#)). Finally, the qualitative growth mechanism of  $\text{Fe}_3\text{Se}_4$  NPs (along the *c*-axis) is proposed as shown in [Schematic S3](#). The schematic illustrates the addition of atoms on the unit cell of  $\text{Fe}_3\text{Se}_4$  surrounded with all possible intermediate species in a typical synthesis. The details of the growth mechanism are discussed in [Supporting Information](#).

**Structural and Morphological Investigations of  $\text{Fe}_3\text{Se}_4$  NPs Using X-ray Diffraction Analysis and Transmission Electron Microscopy.** The  $\text{Fe}_3\text{Se}_4$  samples were intensively investigated for their crystallinity and phase purity using powder X-ray diffraction (XRD), followed by the Rietveld refinement using FullProf software ([Figure 1](#)). [Figures S1 and S2](#) present the X-ray diffraction patterns of  $\text{Fe}_3\text{Se}_4$  NPs in detail. The absence of any unidentified peak in the diffraction patterns indicates that no secondary phase is present in all samples. All the XRD patterns were in good agreement with the Joint Committee on Powder Diffraction Standards (JCPDS) Powder Diffraction File (PDF) card number 73–2021<sup>47</sup> for  $\text{Fe}_3\text{Se}_4$  without ambiguous reflections. All the samples are formed in the monoclinic crystal structure with the calculated unit cell lattice parameters tabulated in [Table S1](#), having the *I2/m* space group. The refinement details are mentioned in the text adjoining [Table S1](#). The order of broadening of diffraction pattern indicates that the  $\text{Fe}_3\text{Se}_4$  are of nanodimensions.

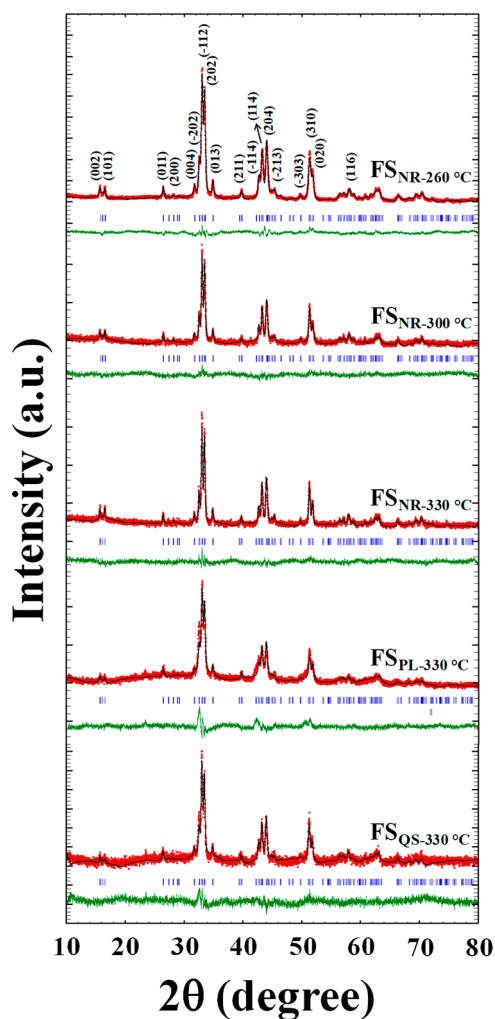


**Figure 1.** Comparison between the observed XRD patterns of  $\text{Fe}_3\text{Se}_4$  NPs (red line), calculated XRD curve after crystal structure refinement by Rietveld method (black line), the difference ( $I_{\text{obs}} - I_{\text{cal}}$ ) between observed intensity ( $I_{\text{obs}}$ ) and calculated intensity ( $I_{\text{cal}}$ ) (green line), and Bragg positions<sup>58</sup> (blue vertical line) for various samples labeled as  $\text{FS}_{\text{NR-260}^\circ\text{C}}$ ,  $\text{FS}_{\text{NR-300}^\circ\text{C}}$ ,  $\text{FS}_{\text{NR-330}^\circ\text{C}}$ ,  $\text{FS}_{\text{PL-330}^\circ\text{C}}$ , and  $\text{FS}_{\text{QS-330}^\circ\text{C}}$ . Samples  $\text{FS}_{\text{NR-260}^\circ\text{C}}$ ,  $\text{FS}_{\text{NR-300}^\circ\text{C}}$ , and  $\text{FS}_{\text{NR-330}^\circ\text{C}}$  were synthesized in the presence of OLA in varying crystallite sizes. The sample  $\text{FS}_{\text{PL-330}^\circ\text{C}}$  was synthesized in the presence of 1-ODE + OCD. The sample  $\text{FS}_{\text{QS-330}^\circ\text{C}}$  was synthesized in the presence of OCD.

The crystallite sizes for all the samples were calculated using the method given by Scherrer<sup>48–50</sup> along three different planes corresponding to the three most intense diffraction peaks ([Table 1](#)). Scherrer's formula is in good agreement to compare the size of particles.<sup>50</sup> It is observed that the calculated crystallite-sizes are directly proportional to the reaction temperature: The size increases with an increase in reaction temperature. It worth mentioning that the present synthetic route not only allows the selective synthesis of different crystallite sizes by controlling the temperature but also produces unique morphologies by conveniently adjusting the growth conditions (reaction temperature and solvents together).

The morphological properties of all the samples were characterized by TEM. As shown in [Figure 2](#), samples  $\text{FS}_{\text{NR-260}^\circ\text{C}}$ ,  $\text{FS}_{\text{NR-300}^\circ\text{C}}$ , and  $\text{FS}_{\text{NR-330}^\circ\text{C}}$  synthesized with OLA are quasi-spherical particles consist of agglomerated rod-shaped nanostructures with multitudinous spikes grown on the surfaces

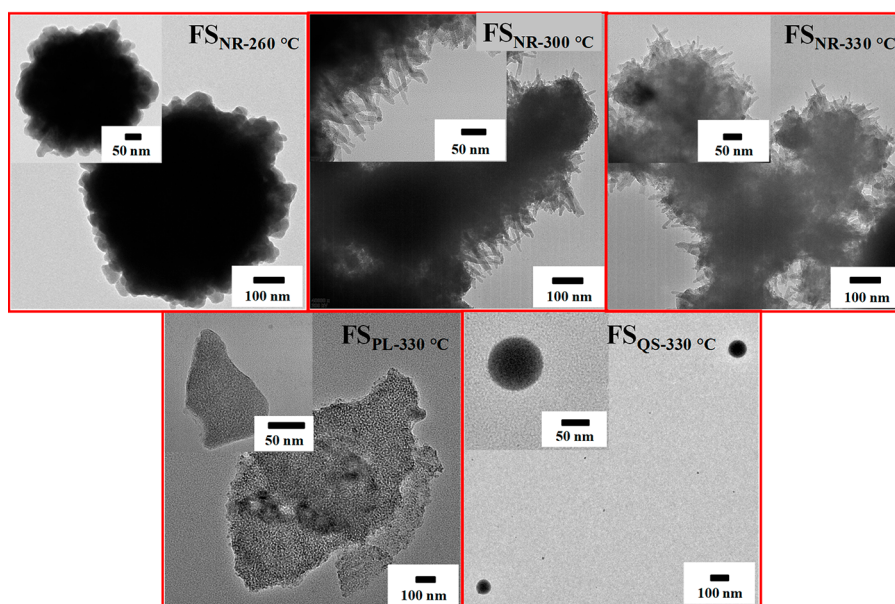
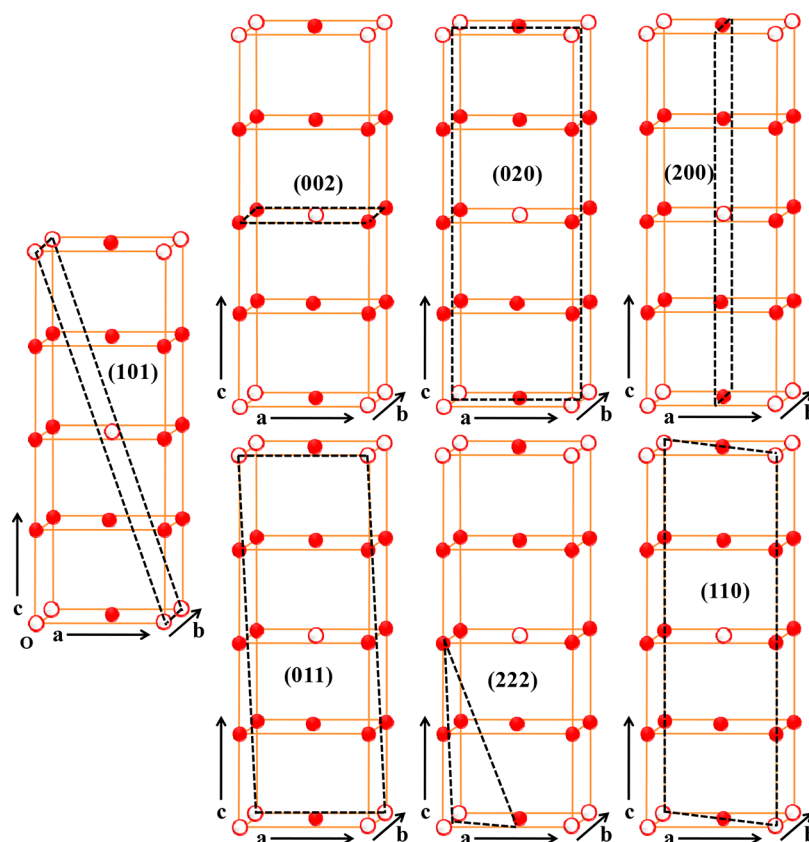


**Figure 2.** Representative TEM images of as-synthesized  $\text{Fe}_3\text{Se}_4$  NPs. The TEM images corresponding to the samples  $\text{FS}_{\text{NR-260}^\circ\text{C}}$ ,  $\text{FS}_{\text{NR-300}^\circ\text{C}}$ , and  $\text{FS}_{\text{NR-330}^\circ\text{C}}$  (synthesized in the presence of OLA) show that particles are analogous with rodlike features growing on the surface. The images corresponding to samples  $\text{FS}_{\text{PL-330}^\circ\text{C}}$  (in the presence of 1-ODE + OCD) and  $\text{FS}_{\text{QS-330}^\circ\text{C}}$  (in the presence of OCD) reveal nanosheet-like and quasi-spherical morphologies. The insets show zoomed-in views with a scale bar of 50 nm. Due to intense magnetic polarization, the particles show aggregation in the TEM images.

**Scheme 1.** Unit Cell of  $\text{Fe}_3\text{Se}_4$  with Different Planes Drawn by Black Dotted Lines<sup>a</sup>



<sup>a</sup>Solid red circles represent Fe-cations, while open red circles represent cations vacancies.

pointing thoroughly outward. Moreover, as shown in Figure 2, sample  $\text{FS}_{\text{PL-330}^\circ\text{C}}$  represents the formation of nanosheet-like (in the presence of 1-ODE and OCD), and sample  $\text{FS}_{\text{QS-330}^\circ\text{C}}$

reveals the shape of nanosized quasi-spheres (in the presence of OCD).



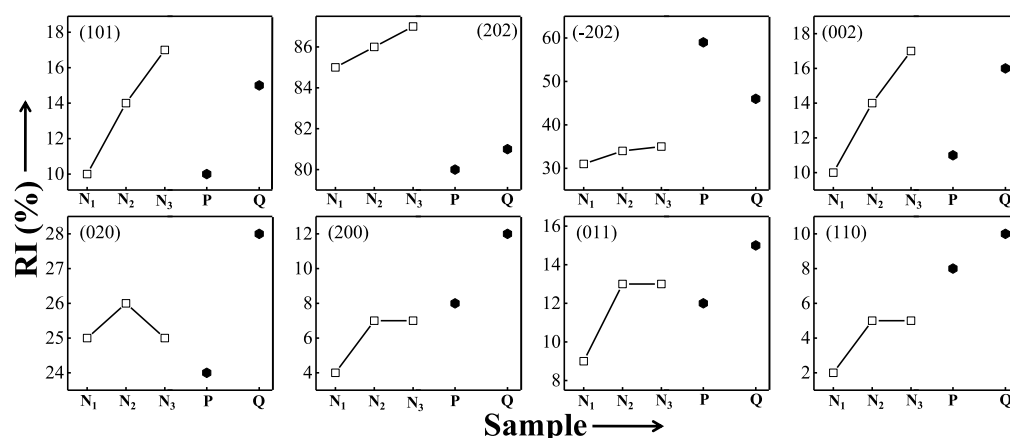


**Figure 3.** Variation in the relative intensities (RI) of diffraction pattern along different lattice planes of all the as-synthesized  $\text{Fe}_3\text{Se}_4$  NPs. The  $N_1$ ,  $N_2$ , and  $N_3$  define  $\text{FS}_{\text{NR-260}^\circ\text{C}}$ ,  $\text{FS}_{\text{NR-300}^\circ\text{C}}$ , and  $\text{FS}_{\text{NR-330}^\circ\text{C}}$  samples, exhibiting the effect of size on RI. The symbols P and Q denote the  $\text{FS}_{\text{PL-330}^\circ\text{C}}$  and  $\text{FS}_{\text{QS-330}^\circ\text{C}}$  samples, respectively, showing the variation in RI with shape.

Furthermore, the directional growth analysis was done by examining the relationship between the relative intensities (RI) of XRD peaks and morphologies. It was observed that for all the samples, the  $(\bar{1}12)$  peak shows the maximum intensity, and its intensity was normalized to 100 with respect to other peaks. Scheme 1 illustrates the various planes of  $\text{Fe}_3\text{Se}_4$  by black dotted lines. The RIs of all the as-synthesized  $\text{Fe}_3\text{Se}_4$  NPs are compared in Figure 3 and Table S2. With respect to the most intense peak, many of the peaks show a sample to sample variation in the RI, which indicates varying growth kinetics of different facets when the reaction conditions are altered.<sup>51</sup> These results can be related to the “morphological importance” (MI) of respective lattice planes, which for a particular crystal is inversely proportional to the growth rate, i.e., the faster the growth rate of a plane, the lower the MI value of that plane and vice versa. Thus, the slow-growing facet will dominate the morphology in the resultant particle with a large surface area and is more exposed to the environment.<sup>52</sup> These more exposed planes will contribute toward a higher RI in the XRD pattern, so the RIs of crystalline peaks can be directly related to the MIs of respective lattice planes, which immediately makes the growth direction in a distinct environment accessible to us. This important information by using the simple exercise actually gives us a direct link between the crystal formation and tunable reaction-limited growth conditions that were carefully selected in this report.

Further analysis of RIs of  $(101)$ ,  $(202)$ , and  $(\bar{2}02)$  planes suggested that for these planes, as the reaction temperature increases, the RIs increase by 7, 2, and 4%, respectively, for sample  $\text{FS}_{\text{NR-330}^\circ\text{C}}$  ( $330^\circ\text{C}$ ) in comparison with sample  $\text{FS}_{\text{NR-260}^\circ\text{C}}$  ( $260^\circ\text{C}$ ). This implies that the relative growth rate of these planes decelerates with rising temperature, making these planes more significant in the resultant morphology as temperature increases (larger MI values). These results are consistent with the surface free energy calculations for various low-index planes given in above section, and details are in Supporting Information. The  $(101)$  plane was predicted to be morphologically dominant among all low-index planes. Similarly, the  $(002)$  peak also shows the increment up to 7%, which is also consistent with the surface energy calculations. These results suggest that the  $(101)$ ,  $(202)$ ,  $(\bar{2}02)$ , and  $(002)$  faces are parallel to longitude in a rodlike shape. TEM images support this statement. As shown in Figure 4, the  $(002)$  and  $(202)$  planes are along the longitudinal directions of the rod

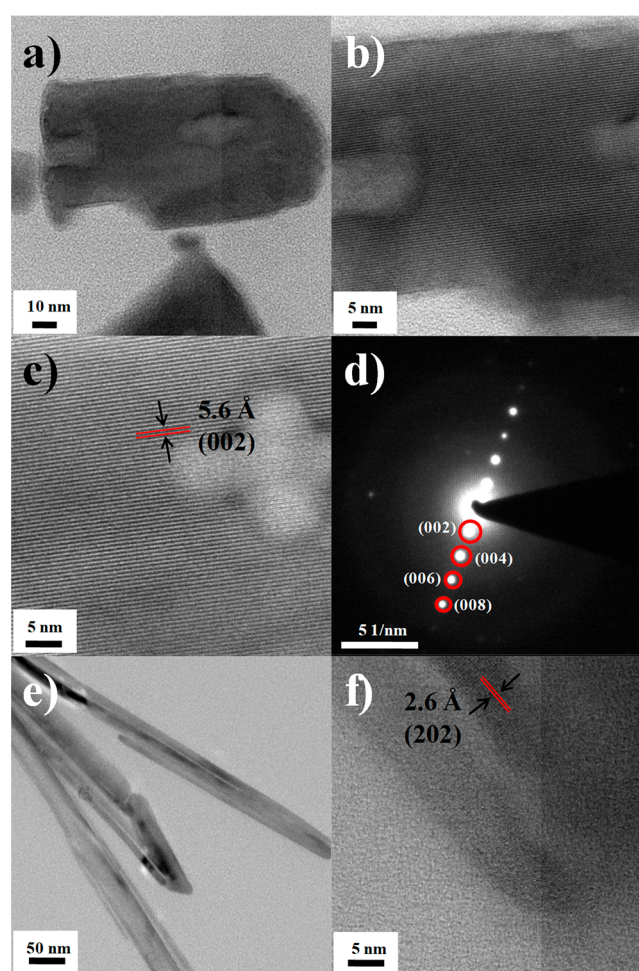


**Figure 4.** Representative TEM images of as-synthesized  $\text{Fe}_3\text{Se}_4$  (synthesized in the presence of OLA). (a) Image shows the rodlike features of nanoparticles. (b) Zoomed-in views with a scale bar of 5 nm. (c) The lattice fringes spaced at 5.6 Å represent the  $(002)$  plane. (d) The SAED pattern reveals the presence of the  $(002)$  plane. (e) TEM image from different area again reveals the rodlike morphology. (f) The lattice fringes spaced at 2.6 Å represent the  $(202)$  plane. Thus, the  $(002)$  and  $(202)$  faces are parallel to longitude in a rodlike shape that results in longitudinal growth along the  $b$ -axis.

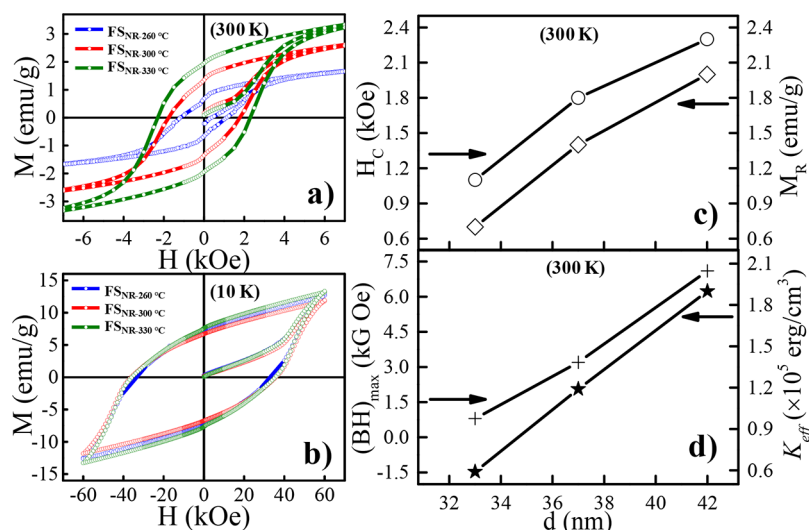


**Figure 5.** Magnetization vs external magnetic field hysteresis loops at 300 K (a) and 10 K (b) of rodlike  $\text{Fe}_3\text{Se}_4$  nanoparticles. The blue, red, and green loops correspond to the samples:  $\text{FS}_{\text{NR-260}^\circ\text{C}}$  (33 nm),  $\text{FS}_{\text{NR-300}^\circ\text{C}}$  (37 nm), and  $\text{FS}_{\text{NR-330}^\circ\text{C}}$  (42 nm) synthesized at increasingly higher temperatures, respectively. The numbers in parentheses show the crystallite size along the (112) plane. Relationship between crystallite size and magnetic parameters of rodlike  $\text{Fe}_3\text{Se}_4$  NPs at 300 K. (c) Size dependence of coercivity ( $H_c$ ) and remanent magnetization ( $M_R$ ) and (d) size dependence of energy product  $(BH)_{\text{max}}$  and anisotropy constant ( $K_{\text{eff}}$ ).

having lattice fringe spacings of 5.6 and 2.6 Å, respectively. In contrast, it was observed that the RIs of (020) plane were hardly affected for samples synthesized at higher temperatures; in other words, this facet does not show any significant change in its relative-growth-rate with an increase in the reaction temperature. This implies that the (020) face is vertical to longitudinal planes ((101), (202), ( $\bar{2}$ 02), and (002)). Although the (200) peak becomes more intense (up to 5%) with an increase in reaction temperature, the RI value is very low, which indicates that this plane will contribute to a faster growth in this direction. Thus, this plane is less visible in resultant morphology as compared to the other planes. Moreover, the other planes (222), ( $\bar{2}$ 22), and (011) show the increase (from sample  $\text{FS}_{\text{NR-260}^\circ\text{C}}$  to  $\text{FS}_{\text{NR-300}^\circ\text{C}}$ ), followed by no variation in RI with rising temperature. This implies that these planes were initially slowly growing; however, at high temperatures, the growth is dormant along with these directions. This suggests that these planes are at the edges of the nanorods. The (110) plane is nearly invisible in the resultant morphology as it has the smallest RI value. This again corresponds to the above-calculated surface free energy minimization, which shows that the (110) will have the least MI. The other planes exhibit different nature from the surface free energy minimization sequence due to the presence of kinetic control over the reaction. In conclusion, the variation in the RI of the above planes exhibits that for nanorods the longitudinal growth is along the *b*-axis and that the vertical growth is along the *c*- and *a*-axes in the presence of OLA.

To validate the influence of an amine group and a double bond on the resultant morphology, the controlled experiments are carried out by changing the solvents and comparing the RIs of the resulting samples (Figure 3 and Table S2). The observed variations in RI clearly demonstrate the distinct direction of growth in the varied reaction environment. For sample  $\text{FS}_{\text{PL-330}^\circ\text{C}}$  (nanoplatelets), the direction of growth is swift along the *c*- and *a*-axes, making (101) the top surface of nanoplates having a lattice fringe spaced at 5.4 Å (Figure S4). The MI of (002) decreases, and that of (020) is nearly constant. Consequently, the shape deviated from rods to plates in the presence of 1-ODE and OCD. Furthermore, the RI of sample

$\text{FS}_{\text{QS-330}^\circ\text{C}}$  (quasi-spherical) demonstrates that the direction of growth is nearly the same along all three axes, as only an amine group is present to influence the morphology, which will behave almost identically in all directions (*a*-, *b*-, and *c*-axes). However, (202) is a more exposed plane having lattice fringes spaced at 2.6 Å (Figure S5), which signifies that the growth is slightly faster toward *a*- and *c*-axes. All other planes show nearly the same MIs in the OCD environment, which results in fabricating the quasispherical NPs. Therefore, after analyzing the RIs of all the planes, it is appropriate to conclude that in a distinct environment, the direction of growth is varying, which leads to forming NPs with individual shapes. Additionally, as the reaction temperature rises, the growth is also increasing in a certain direction, which enhances the size of the NPs.

**Effect of  $\text{Fe}_3\text{Se}_4$  Crystallite Size on the  $M-H$  Hysteresis Curves at 300 K.** For permanent-magnet applications, the coercivity must be high. The coercivity of NPs below the single-domain size limit is known to be strongly influenced by their particle size, crystallinity, lattice defects, vacancies and their ordering, external magnetic field, anisotropic growth of crystalline facets, overall morphology, surface spin environment, temperature, interparticle interactions, and so on. Even the sample preparation method (packing of particles) can affect the coercivity values for fine particles. As the particle size is enhanced, it is generally observed that the coercivity increases and goes through a maximum up to a single-domain limit size and then tends toward zero.<sup>53,54</sup>

The magnetic properties obtained for  $\text{Fe}_3\text{Se}_4$  NPs using a SQUID-VSM show an interesting trend. Figure S6 shows a comparison of  $M-H$  hysteresis curves taken at 300 K for samples  $\text{FS}_{\text{NR-260}^\circ\text{C}}$ ,  $\text{FS}_{\text{NR-300}^\circ\text{C}}$ , and  $\text{FS}_{\text{NR-330}^\circ\text{C}}$ . All the samples indicate a typical ferrimagnetic behavior where the magnetization does not saturate until the highest applied field of 60 kOe. In earlier reports,<sup>36,38</sup> even after applying field of 90 kOe, the hysteresis loops of  $\text{Fe}_3\text{Se}_4$  do not saturate due to the very high anisotropy field or the spins are noncollinear in the system.<sup>36</sup> Figure 5 a) shows a zoomed-in view of the hysteresis curves that clearly illustrates that the coercivity and remanence values of all the samples increases with crystal growth, i.e., the

magnetic properties of  $\text{Fe}_3\text{Se}_4$  are strongly affected by the crystallite size. All the samples in this study are in a single-domain size as mentioned above that the critical radius<sup>38</sup> for a single-domain particle of  $\text{Fe}_3\text{Se}_4$  is  $\sim 800$  nm at 10 K and  $\sim 2000$  nm at 300 K. The influence of crystal growth on  $H_C$  at 300 K is shown in Figure 5c), and it is observed that the  $H_C$  increases with increasing the crystallite size (from 33 to 42 nm). At 300 K, the  $H_C$  of  $\text{Fe}_3\text{Se}_4$  is found to vary from 1.1 to 2.3 kOe. This increasing pattern between the  $H_C$  and crystallite size is observed because an increase in single domain size increases the magnetic moment, which in turn increases the magnetization followed by  $H_C$ . Another important factor is surface spins. With a decrease in particle size, the surface-to-volume ratio increases, which leads to a larger number of surface spins per unit volume. The surface spins are uncompensated and remain disordered or canted, leading to the overall reduction in the magnetization with the decrease in the particle size.<sup>3</sup> As the crystallite size  $d$  increases slowly from 33 to 42 nm, the magnetization value ( $M_{60\text{kOe}}$ ) increases from 3.0 to 5.4 emu/g (a higher magnetization is observed in  $\text{Fe}_3\text{Se}_4$  nanorods as compared to earlier reports);<sup>36,37</sup> the remanence magnetization ( $M_R$ ) also increases as tabulated in Table 1.

As illustrated in Scheme S4, the unit cell of  $\text{Fe}_3\text{Se}_4$  showing the orientation of the magnetic moments reveals the easy axis along the  $b$ -axis.<sup>37</sup> In our samples, the each building block is a single crystallite. However, the surface spins are not parallelly aligned in the same direction. The resultant magnetization is in the  $b$ -axis of one single nanorod. Probably hundreds of such nanocrystallites, as building blocks, agglomerate together due to strong dipolar interactions to form a larger three-dimensional assembly (as seen in the TEM images) where the nanocrystal superspins may remain highly disordered (or weakly ordered along the easy axis due to the interparticle interactions). In VSM, the powder sample has numerous such agglomerated particles. When the external magnetic field is applied, they try to align in one direction by incoherent spin rotation phenomena as shown in schematic S5.<sup>38</sup>

In a single crystal, it is simple to calculate magnetic anisotropy constant ( $K$ ) by extrapolating the  $M$ – $H$  curve in both easy and hard axis directions (taking the hysteresis loops as parallel and perpendicular to the easy axes). As shown in Scheme S4, in a single crystal, the order is the same in the entire particle, which facilitates orienting them in one direction. However, in a sample like ours, starting from a single particle with growth in  $b$ -axis for the nanorod, many such agglomerated nanocrystallites are present (the particle as shown in TEM is agglomeration of single–single nanorods). Therefore, in VSM, orienting the powder sample having numerous such agglomerated particles in one easy axis and then the hard axis is not simple. There is much literature that calculated the  $K$  utilizing this method for agglomerated samples, which is not the appropriate method to calculate the real value. However, as it is an intrinsic property of any material, calculating  $K$  by the  $M$ – $H$  curve of such samples will give the effective  $K$  of all the particles oriented in different directions. It will be interesting to study the effect of size on effective magnetic anisotropy constant ( $K_{\text{eff}}$ ).

Generally, the anisotropy field ( $H_a$ ) of any material defines the theoretical upper limit of the coercivity. Experimentally, it is usually observed that the coercivity of any material reaches nearly 25% of the anisotropy field.<sup>37</sup> The  $H_a$  values for all the samples were calculated by extrapolating the  $M$ – $H$  curve in both the easy and hard axis directions. In view of the low magnetization of  $\text{Fe}_3\text{Se}_4$ , its shape anisotropy plays a minor

contribution in the total anisotropy, while the magnetocrystalline anisotropy plays a major role.<sup>36</sup> The presence of ordered Fe vacancies in monoclinic structure gives rise to a highly anisotropic crystal field and the spin–orbit coupling, leading to a large magnetocrystalline anisotropy in the system.<sup>38</sup>  $K_{\text{eff}}$  was calculated from  $M_S$  and  $H_a$ , according to the following equation.<sup>37,38</sup>

$$K_{\text{eff}} = \frac{1}{2} M_S H_a \quad (3)$$

The  $K_{\text{eff}}$  value was determined for all the samples and is tabulated in Table 1. As observed in Figure 5d), the  $K_{\text{eff}}$  value for  $\text{Fe}_3\text{Se}_4$  increases with increasing crystallite size due to the increase in  $M_S$  and  $H_a$ . Moreover, all the above samples' energy product ( $BH_{\text{max}}$ ) was also determined from the second quadrant of the  $B$ – $H$  hysteresis loop,<sup>37</sup> as shown in Figure S7. The inset of Figure S7 reveals the zoomed-in view of the second quadrant of the  $B$ – $H$  loop, and the area under the gray box represents the  $BH_{\text{max}}$  of the corresponding samples. The  $BH_{\text{max}}$  value is found to be 0.8 kG Oe at 300 K for  $\text{FS}_{\text{NR-260}^\circ\text{C}}$ , which increases to 7.1 kG Oe for  $\text{FS}_{\text{NR-330}^\circ\text{C}}$ . A significant increase in the energy product values at 300 K (7.1 kG Oe) is observed compared to that in the earlier report<sup>37</sup> (4.377 kG Oe) for the same shape. Figure 5d) shows the linear dependency of energy products on crystallite size. Equation 2 clearly illustrated that the energy product is directly proportional to saturation magnetization ( $M_S$ ).  $M_S$  increases with crystallization, enhancing the energy product. The practical energy product of a permanent magnet depends strongly on its processing. Condensing the magnetic NPs with high packing densities is very vital for the development of permanent magnets. This vast varying range of the energy product in  $\text{Fe}_3\text{Se}_4$  NPs is crucial in developing the new RE-free permanent magnets.<sup>36,37</sup>

**Effect of  $\text{Fe}_3\text{Se}_4$  Crystallite-Size on the  $M$ – $H$  Hysteresis Curves at 10 K.** At 10 K, the  $M$ – $H$  curves do not saturate for the highest applied magnetic field of 60 kOe. In fact, it is noticeable that the curves are far from saturation. Therefore, the coercive-field values (Table 1) are a gross underestimation of their true values. However, it was noted that these underestimated coercivity values of  $\text{Fe}_3\text{Se}_4$  NPs (synthesized in the presence of OLA) lies between 33 and 36 kOe with crystallite size varying from 33 to 42 nm ( $\text{FS}_{\text{NR-260}^\circ\text{C}}$  to  $\text{FS}_{\text{NR-330}^\circ\text{C}}$ ), respectively. These  $H_C$  values are nearly 20- to 30-fold increase over the corresponding value at 300 K, from 2.3 to 35.5 kOe ( $\text{FS}_{\text{NR-330}^\circ\text{C}}$ ). The substantial increase in the coercivity at a lower temperature may have various contributions: the increase in the overall effective magnetic anisotropy, reduction in the thermal activation energy, which makes more and more spins available to orient in the field direction, ferrimagnetism, and so on.<sup>38</sup> In comparison to the 300 K values, at 10 K the effective anisotropy increases for  $\text{FS}_{\text{NR-330}^\circ\text{C}}$  by almost 2 orders of magnitude, from  $1.90 \times 10^5$  erg/cm<sup>3</sup> (at 300 K) to  $17.2 \times 10^5$  erg/cm<sup>3</sup> (at 10 K). The  $K_{\text{eff}}$  was observed to increase from  $16.9 \times 10^5$  to  $17.2 \times 10^5$  erg/cm<sup>3</sup> with increasing crystallite size (from 33 to 42 nm). Additionally, the energy product also shows an enhancement for  $\text{FS}_{\text{NR-330}^\circ\text{C}}$  by nearly 2 orders of magnitude at 10 K, from 7.1 kG Oe (at 300 K) to 109.9 kG Oe (at 10 K). The values of  $BH_{\text{max}}$  fluctuate from 96.6 to 109.9 kG Oe with increasing crystallite sizes (Table 1).

**Effect of  $\text{Fe}_3\text{Se}_4$  Shape on the  $M$ – $H$  Hysteresis Curves at 300 K.** The magnetic properties of  $\text{Fe}_3\text{Se}_4$  nanoplatelets ( $\text{FS}_{\text{PL-330}^\circ\text{C}}$ ) and nano-quasi-spheres ( $\text{FS}_{\text{QS-330}^\circ\text{C}}$ ) fabricated in the presence of different organic solvents (1-ODE + OCD and

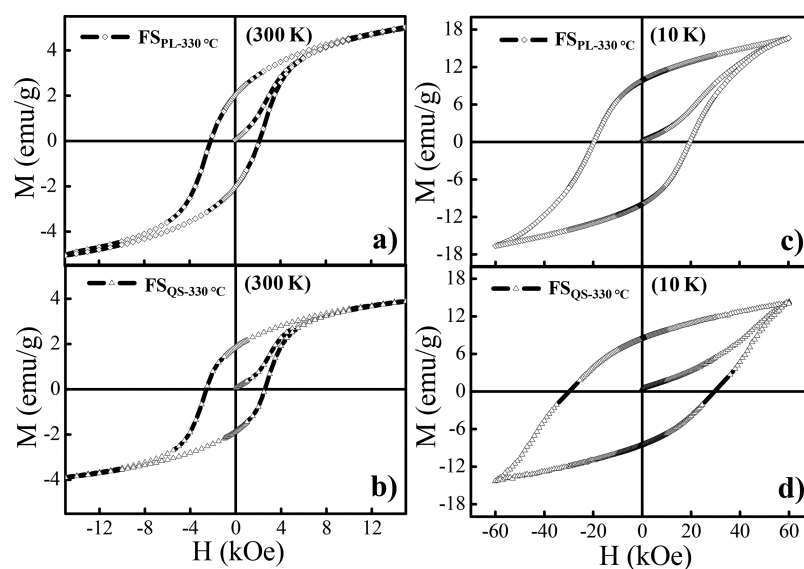


**Figure 6.** Magnetization vs external magnetic field hysteresis loops (at 300 and 10 K) of samples  $\text{FS}_{\text{PL-330}^\circ\text{C}}$  and  $\text{FS}_{\text{QS-330}^\circ\text{C}}$ .  $\text{Fe}_3\text{Se}_4$  NPs (nanoplatelets and quasi-spherical particles) synthesized in the presence of 1-ODE + OCD and OCD, respectively.

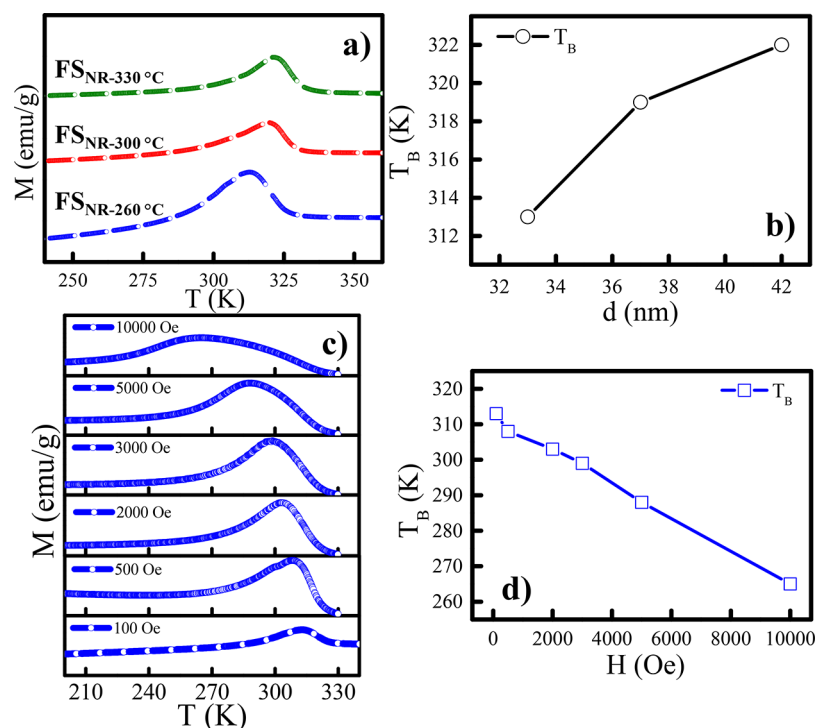


**Figure 7.** (a) Zero-field-cooled (ZFC) magnetization vs temperature ( $M-T$ ) curves for rodlike  $\text{Fe}_3\text{Se}_4$  NPs. Blue, red, and green curves represent the sample  $\text{FS}_{\text{NR-260}^\circ\text{C}}$  (33 nm),  $\text{FS}_{\text{NR-300}^\circ\text{C}}$  (37 nm), and  $\text{FS}_{\text{NR-330}^\circ\text{C}}$  (42 nm) synthesized at 260, 300, and 330 °C, respectively. (b) Relationship between crystallite size and average superparamagnetic blocking temperature of rodlike  $\text{Fe}_3\text{Se}_4$  NPs. (c)  $M-T$  curves for sample  $\text{FS}_{\text{NR-260}^\circ\text{C}}$  (33 nm) with varying applied magnetic fields. (d) Relationship between the applied magnetic field and average superparamagnetic blocking temperature for sample  $\text{FS}_{\text{NR-260}^\circ\text{C}}$ .

OCD) were also observed with SQUID magnetometer. The hysteresis loops for these shapes are compared in Figure S8, again revealing the ferrimagnetic and hard magnetic properties of the material. Figure 6a,b shows a zoomed-in view of the hysteresis curves that clearly illustrate the coercive field and remanence for both the samples.  $H_C$  and  $M_R$  are affected by the shape of the NPs (Table 1). These variations in the magnetic performance arise from the distinct crystalline properties of the plate and quasi-sphere-like NPs in comparison to the above

nanorods.<sup>36</sup> At 300 K, the  $H_C$  values of these compounds are found to be distinct: 2.1 kOe for  $\text{FS}_{\text{PL-330}^\circ\text{C}}$  and 2.6 kOe for  $\text{FS}_{\text{QS-330}^\circ\text{C}}$ . The shape diversity also shows a variation in  $M_{60\text{kOe}}$ ,  $H_A$ , and  $K_{\text{eff}}$  due to the small contribution from shape anisotropy, as tabulated in Table 1. The highest magnetization to date, 7.0 emu/g (at 300 K), is observed for  $\text{Fe}_3\text{Se}_4$  (in the case of  $\text{FS}_{\text{PL-330}^\circ\text{C}}$ ). The energy product of these samples was calculated at 300 K (from the second quadrant of the  $B-H$  hysteresis loop). Figure S9 reveals the zoomed-in view of the second

quadrant of the  $B-H$  loops, and the calculated energy product is tabulated in Table 1.

**Effect of  $\text{Fe}_3\text{Se}_4$  Shape on the  $M-H$  Hysteresis Curves at 10 K.** Figure 6c,d shows the hysteresis loops of  $\text{FS}_{\text{PL-330}^\circ\text{C}}$  and  $\text{FS}_{\text{QS-330}^\circ\text{C}}$  at 10 K. The coercivity of  $\text{FS}_{\text{PL-330}^\circ\text{C}}$  and  $\text{FS}_{\text{QS-330}^\circ\text{C}}$  samples are 19.7 and 29.6 kOe, respectively, which is again  $\sim 10$ -fold more significant than the value at 300 K. This large coercivity originates from the large uniaxial magnetocrystalline anisotropy of monoclinic structure of  $\text{Fe}_3\text{Se}_4$  with ordered Fe vacancies.<sup>38</sup> Here also the effective anisotropy for  $\text{FS}_{\text{PL-330}^\circ\text{C}}$  increases by almost 2 orders of magnitude at 10 K in comparison to that at 300 K, from  $1.77 \times 10^5 \text{ erg/cm}^3$  (at 300 K) to  $20.3 \times 10^5 \text{ erg/cm}^3$  at (10 K). The  $K_{\text{eff}}$  values are  $20.3 \times 10^5$  and  $14.9 \times 10^5 \text{ erg/cm}^3$  for  $\text{FS}_{\text{PL-330}^\circ\text{C}}$  and  $\text{FS}_{\text{QS-330}^\circ\text{C}}$ , respectively. The energy products of both the samples are 181.9 and 135.7 kG Oe (Table 1).

**Magnetic Property: Blocking Temperature.** Blocking temperature depends on the particle size, its distribution, anisotropy energy, interparticle interaction, and measurement time scale. When the particle size is below the single-domain size limit, above the blocking temperature, in the absence of an external magnetic field, the particle spins are free to orient randomly as the thermal activation energy exceeds the effective anisotropy energy (superparamagnetic behavior). However, below the blocking temperature, spins freeze along their easy axis (blocked state). The blocking temperature decreases with the decrease in the anisotropy energy and the particle volume.<sup>55</sup> Below  $T_{\text{B}}$ , the sample reveals the coercivity, which becomes zero above the blocking temperature.

Temperature-dependent magnetization ( $M-T$  curve) has been examined for all the  $\text{Fe}_3\text{Se}_4$  samples under field-cooled (FC) and zero-field cooled (ZFC) conditions. As discussed earlier (Scheme S5), the particles are an agglomerated mass of nanocrystalline rods that strongly interact with each other through dipolar interactions. Average blocking temperature ( $T_{\text{B}}$ ) is an indication of superparamagnetic to the blocked state transition of that material, which is taken as the peak of the ZFC curve though due to the polydispersity; the blocking events for each particle might exist on both sides of this peak and result in the separation of ZFC-FC curves well above the average  $T_{\text{B}}$  (the peak of the ZFC curve).<sup>55-58</sup> Figure 7a presents the  $T_{\text{B}}$  for nanorod samples ( $\text{FS}_{\text{NR-260}^\circ\text{C}}$ ,  $\text{FS}_{\text{NR-300}^\circ\text{C}}$ , and  $\text{FS}_{\text{NR-330}^\circ\text{C}}$ ) as 313, 316, and 322 K, respectively. Figure 7b shows that  $T_{\text{B}}$  increases with increasing the crystallite size due to the increase in the anisotropy constant and the particle volume. It is noticeable that  $T_{\text{B}}$  also changes with shape, e.g., for nanoplatelets ( $\text{FS}_{\text{PL-330}^\circ\text{C}}$ ) and nanoquasispherical ( $\text{FS}_{\text{QS-330}^\circ\text{C}}$ ) as 323 and 319 K, respectively (Figure S10), because of the variation in the anisotropy constant and particle volume.

The thermal activation energy, magnetic anisotropy energy, and external applied magnetic field affect the blocking events of spins apart from interparticle interactions and measurement time scale. It is understood that the addition of an applied magnetic field changes the energy barrier from<sup>56</sup>

$$K_{\text{u}}V \text{ to } K_{\text{u}}V[1 \pm (H/H_0)]^2 \quad (4)$$

where  $K_{\text{u}}$ ,  $V$ , and  $H$  are uniaxial anisotropy constant, the particle's volume, and applied magnetic field, respectively.  $H_0$  is related to the anisotropy field by  $H_0 = 2H_{\text{a}} = 2K_{\text{u}}/M_{\text{S}}$ .  $H < H_0$ , and the sign (+ or -) indicates the moment flip: (+) for parallel to the antiparallel direction and (-) for antiparallel to parallel direction. Figure 7c presents the ZFC curves of sample  $\text{FS}_{\text{NR-260}^\circ\text{C}}$  at the different external magnetic fields. This reveals

that as the magnetic field increases the peaks shift toward the lower temperature. Figure 7d shows a decrease of  $T_{\text{B}}$  with an increasing magnetic field, which is consistent with the quadratic dependence, as discussed by Zhang et al.<sup>56</sup>

## CONCLUSION

$\text{Fe}_3\text{Se}_4$  NPs were intensively investigated to reveal the fundamental correlation between the size/shape and magnetic properties. The examined  $\text{Fe}_3\text{Se}_4$  NPs were prepared under well-controlled crystal growth conditions using a one-pot thermal decomposition method. The grain growth of NPs estimated from the XRD pattern arises monotonically with an increase in reaction temperature. The crystallite size range is about 33–42 nm depending on the reaction temperature from 260 to 330 °C. A discrete environment has been provided in the reactions to allow the growth of different facets, which results in the unique morphology of the NPs. All the hysteresis curves with different size/shape showed the ferrimagnetic behavior of  $\text{Fe}_3\text{Se}_4$ . The magnetic parameters such as saturation magnetization ( $M_{\text{S}}$ ), coercivity ( $H_{\text{C}}$ ), effective anisotropy constant ( $K_{\text{eff}}$ ), energy product ( $BH_{\text{max}}$ ), and average blocking temperature ( $T_{\text{B}}$ ) exhibited a strong dependence on size and shape.  $M_{60\text{kOe}}$  increases with increasing crystallite size, up to a maximum value of about 5.4 emu/g at 300 K for nanorods, while it becomes 7 emu/g for nanoplatelets. The  $H_{\text{C}}$  and  $M_{\text{R}}$  values also increase with increasing the crystallite size up to a maximum value of about 2.3 Oe and 2 emu/g, respectively, for nanorods. The  $BH_{\text{max}}$  increases linearly with crystallite size up to a maximum value of 7.1 kG Oe at 300 K for nanorods and reaches 7.5 kG Oe for nanoplatelets. These findings show that considerable attention should be given to tuning the size and shape of transition metal chalcogenides which have potential industrial applications.

## ASSOCIATED CONTENT

### Supporting Information

The Supporting Information is available free of charge at <https://pubs.acs.org/doi/10.1021/acs.jpcc.1c00389>.

Characterization techniques, synthesize, surface free energy calculations, growth mechanism, Rietveld refinement, XRD, relative intensity, and magnetic properties (PDF)

Animations of a rotating cell of  $\text{Fe}_3\text{Se}_4$ , with different planes shown (ZIP)

## AUTHOR INFORMATION

### Corresponding Author

Pankaj Poddar – Physical & Materials Chemistry Division, CSIR-National Chemical Laboratory, Pune 411008, India; Academy of Scientific and Innovative Research (AcSIR), Ghaziabad, Uttar Pradesh 201 002, India; [orcid.org/0000-0002-2273-588X](https://orcid.org/0000-0002-2273-588X); Email: [p.poddar@ncl.res.in](mailto:p.poddar@ncl.res.in)

### Author

Monika Ghalawat – Physical & Materials Chemistry Division, CSIR-National Chemical Laboratory, Pune 411008, India; Academy of Scientific and Innovative Research (AcSIR), Ghaziabad, Uttar Pradesh 201 002, India

Complete contact information is available at: <https://pubs.acs.org/doi/10.1021/acs.jpcc.1c00389>

## Notes

The authors declare no competing financial interest.

## ACKNOWLEDGMENTS

M.G. acknowledges the support from the University Grants Commission (UGC), India, for providing the Senior Research Fellowship (SRF).

## REFERENCES

- (1) Jeevanandam, J.; Barhoum, A.; Chan, Y. S.; Dufresne, A.; Danquah, M. K. Review on Nanoparticles and Nanostructured Materials: History, Sources, Toxicity and Regulations. *Beilstein J. Nanotechnol.* **2018**, *9*, 1050–1074.
- (2) Khan, I.; Saeed, K.; Khan, I. Nanoparticles: Properties, Applications and Toxicities. *Arabian J. Chem.* **2019**, *12*, 908–931.
- (3) Issa, B.; Obaidat, I. M.; Albiss, B. A.; Haik, Y. Magnetic Nanoparticles: Surface Effects and Properties Related to Biomedicine Applications. *Int. J. Mol. Sci.* **2013**, *14*, 21266–21305.
- (4) Poddar, P.; Telem-Shafir, T.; Fried, T.; Markovich, G. Dipolar Interactions in Two- and Three-Dimensional Magnetic Nanoparticle Arrays. *Phys. Rev. B: Condens. Matter Mater. Phys.* **2002**, *66*, 060403.
- (5) Poddar, P.; Fried, T.; Markovich, G. First-Order Metal-Insulator Transition and Spin-Polarized Tunneling in Fe<sub>3</sub>O<sub>4</sub> nanocrystals. *Phys. Rev. B: Condens. Matter Mater. Phys.* **2002**, *65*, 172405.
- (6) El-sayed, M. A. Small Is Different: Shape-, Size-, and Composition-Dependent Properties of Some Colloidal Semiconductor Nanocrystals. *Acc. Chem. Res.* **2004**, *37*, 326–333.
- (7) Ray, P. C. Size and Shape Dependent Second Order Nonlinear Optical Properties of Nanomaterials and Their Application in Biological and Chemical Sensing. *Chem. Rev.* **2010**, *110*, 5332–5365.
- (8) Xia, Y.; Xia, X.; Peng, H. C. Shape-Controlled Synthesis of Colloidal Metal Nanocrystals: Thermodynamic versus Kinetic Products. *J. Am. Chem. Soc.* **2015**, *137*, 7947–7966.
- (9) Frey, N. A.; Peng, S.; Cheng, K.; Sun, S. Magnetic Nanoparticles: Synthesis, Functionalization, and Applications in Bioimaging and Magnetic Energy Storage. *Chem. Soc. Rev.* **2009**, *38*, 2532–2542.
- (10) Nistico, R.; Cesano, F.; Garello, F. Magnetic Materials and Systems: Domain Structure Visualization and Other Characterization Techniques for the Application in the Materials Science and Biomedicine. *Inorganics* **2020**, *8*, 6.
- (11) Colombo, M.; Carregal-romero, S.; Casula, M. F.; Gutierrez, L.; Morales, M. P.; Bohm, I. B.; Heverhagen, J. T.; Prosperi, D.; Parak, W. J. Biological Applications of Magnetic Nanoparticles. *Chem. Soc. Rev.* **2012**, *41*, 4306–4334.
- (12) Zhang, H. W.; Liu, Y.; Sun, S. H. Synthesis and Assembly of Magnetic Nanoparticles For information and energy storage applications. *Front. Phys. China* **2010**, *5*, 347–356.
- (13) Sun, H. L.; Shi, H.; Zhao, F.; Qi, L.; Gao, S. Shape-Dependent Magnetic Properties of Low-Dimensional Nanoscale Prussian Blue (PB) Analogue SmFe(CN)<sub>6</sub>·4H<sub>2</sub>O. *Chem. Commun.* **2005**, 4339–4341.
- (14) Oyarzún, S.; Tamion, A.; Tournus, F.; Dupuis, V.; Hillenkamp, M. Size Effects in the Magnetic Anisotropy of Embedded Cobalt Nanoparticles: From Shape to Surface. *Sci. Rep.* **2015**, *5*, 14749.
- (15) Moreno, R.; Poyser, S.; Meilak, D.; Meo, A.; Jenkins, S.; Lazarov, V. K.; Vallejo-Fernandez, G.; Majetich, S.; Evans, R. F. L. The Role of Faceting and Elongation on the Magnetic Anisotropy of Magnetite Fe<sub>3</sub>O<sub>4</sub> Nanocrystals. *Sci. Rep.* **2020**, *10*, 2722.
- (16) Liu, L.; Kou, H. Z.; Mo, W.; Liu, H.; Wang, Y. Surfactant-Assisted Synthesis of  $\alpha$ -Fe<sub>2</sub>O<sub>3</sub> Nanotubes and Nanorods with Shape-Dependent Magnetic Properties. *J. Phys. Chem. B* **2006**, *110*, 15218–15223.
- (17) Chatterjee, J.; Haik, Y.; Chen, C. J. Size Dependent Magnetic Properties of Iron Oxide Nanoparticles. *J. Magn. Magn. Mater.* **2003**, *257*, 113–118.
- (18) Park, T. J.; Papaefthymiou, G. C.; Viescas, A. J.; Moodenbaugh, A. R.; Wong, S. S. Size-Dependent Magnetic Properties of Single-Crystalline Multiferroic BiFeO<sub>3</sub> Nanoparticles. *Nano Lett.* **2007**, *7*, 766–772.
- (19) Ma, F.; Ma, J.; Huang, J.; Li, J. The Shape Dependence of Magnetic and Microwave Properties for Ni Nanoparticles. *J. Magn. Magn. Mater.* **2012**, *324*, 205–209.
- (20) Singh, A. K.; Srivastava, O. N.; Singh, K. Shape and Size-Dependent Magnetic Properties of Fe<sub>3</sub>O<sub>4</sub> Nanoparticles Synthesized Using Piperidine. *Nanoscale Res. Lett.* **2017**, *12*, 298.
- (21) Gabbasov, R. R.; Cherepanov, V. M.; Chuev, M. A.; Polikarpov, M. A.; Panchenko, V. Y. Size Effect of Mössbauer Parameters in Iron Oxide Nanoparticles. *Hyperfine Interact.* **2014**, *226*, 383–387.
- (22) Artus, M.; Ben Tahar, L.; Herbst, F.; Smiri, L.; Villain, F.; Yaacoub, N.; Greneche, J. M.; Ammar, S.; Fievet, F. Size-Dependent Magnetic Properties of CoFe<sub>2</sub>O<sub>4</sub> Nanoparticles Prepared in Polyol. *J. Phys.: Condens. Matter* **2011**, *23*, S06001.
- (23) Song, Q.; Zhang, Z. J. Shape Control and Associated Magnetic Properties of Spinel Cobalt Ferrite Nanocrystals. *J. Am. Chem. Soc.* **2004**, *126*, 6164–6168.
- (24) Tan, Y.; Zhuang, Z.; Peng, Q.; Li, Y. Room-Temperature Soft Magnetic Iron Oxide Nanocrystals: Synthesis, Characterization, and Size-Dependent Magnetic Properties. *Chem. Mater.* **2008**, *20*, S029–S034.
- (25) Vasundhara, K.; Achary, S. N.; Deshpande, S. K.; Babu, P. D.; Meena, S. S.; Tyagi, A. K. Size Dependent Magnetic and Dielectric Properties of Nano CoFe<sub>2</sub>O<sub>4</sub> Prepared by a Salt Assisted Gel-Combustion Method. *J. Appl. Phys.* **2013**, *113*, 194101.
- (26) Rajendran, M.; Deka, S.; Joy, P. A.; Bhattacharya, A. K. Size-Dependent Magnetic Properties of Nanocrystalline Yttrium Iron Garnet Powders. *J. Magn. Magn. Mater.* **2006**, *301*, 212–219.
- (27) Annapu Reddy, V.; Pathak, N. P.; Nath, R. Particle Size Dependent Magnetic Properties and Phase Transitions in Multiferroic BiFeO<sub>3</sub> Nano-Particles. *J. Alloys Compd.* **2012**, *543*, 206–212.
- (28) Ichiyanagi, Y.; Yamada, S. The Size-Dependent Magnetic Properties of Co<sub>3</sub>O<sub>4</sub> Nanoparticles. *Polyhedron* **2005**, *24*, 2813–2816.
- (29) Chen, J. P.; Sorensen, C. M.; Klabunde, K. J.; Hadjipanayis, G. C.; Devlin, E.; Kostikas, A. Size-Dependent Magnetic Properties of MnFe<sub>2</sub>O<sub>4</sub> Fine Particles Synthesized by Coprecipitation. *Phys. Rev. B: Condens. Matter Mater. Phys.* **1996**, *54*, 9288–9296.
- (30) Ghalawat, M.; Poddar, P. Study of the Phase-Evolution Mechanism of an Fe–Se System at the Nanoscale: Optimization of Synthesis Conditions for the Isolation of Pure Phases and Their Controlled Growth. *Langmuir* **2020**, *36*, 2012–2022.
- (31) Schuster, W.; Mikler, H.; Komarek, K. L. Transition Metal-Chalcogen Systems, VII.: The Iron-Selenium Phase Diagram. *Monatsh. Chem.* **1979**, *110*, 1153–1170.
- (32) Okazaki, A.; Hirakawa, K. Structural Study of Iron Selenides FeSe<sub>x</sub>. I Ordered Arrangement of Defects of Fe Atoms. *J. Phys. Soc. Jpn.* **1956**, *11*, 930–936.
- (33) Hirone, T.; Chiba, S. The Magnetic Properties of FeSe<sub>x</sub> with the NiAs Structure. *J. Phys. Soc. Jpn.* **1956**, *11*, 666–670.
- (34) Hirakawa, K. The Magnetic Properties of Iron Selenide Single Crystals. *J. Phys. Soc. Jpn.* **1957**, *12*, 929–938.
- (35) Lyubutin, I. S.; Lin, C. R.; Funtov, K. O.; Dmitrieva, T. V.; Starchikov, S. S.; Siao, Y. J.; Chen, M. L. Structural, Magnetic, and Electronic Properties of Iron Selenide Fe<sub>6–7</sub>Se<sub>8</sub> Nanoparticles Obtained by Thermal Decomposition in High-Temperature Organic Solvents. *J. Chem. Phys.* **2014**, *141*, 044704.
- (36) Zhang, H.; Long, G.; Li, D.; Sabirianov, R.; Zeng, H. Fe<sub>3</sub>Se<sub>4</sub> Nanostructures with Giant Coercivity Synthesized by Solution Chemistry. *Chem. Mater.* **2011**, *23*, 3769–3774.
- (37) Sen Bishwas, M.; Das, R.; Poddar, P. Large Increase in the Energy Product of Fe<sub>3</sub>Se<sub>4</sub> by Fe-Site Doping. *J. Phys. Chem. C* **2014**, *118*, 4016–4022.
- (38) Long, G.; Zhang, H.; Li, D.; Sabirianov, R.; Zhang, Z.; Zeng, H. Magnetic Anisotropy and Coercivity of Fe<sub>3</sub>Se<sub>4</sub> Nanostructures. *Appl. Phys. Lett.* **2011**, *99*, 202103.
- (39) Andresen, A. F.; Vestersjø, E.; Haaland, A.; Gronowitz, S.; Christiansen, H.; Rosen, U. A Neutron Diffraction Investigation of Fe<sub>3</sub>Se<sub>4</sub>. *Acta Chem. Scand.* **1968**, *22*, 827–835.

(40) Kurmoo, M.; Kepert, C. J. Hard Magnets Based on Transition Metal Complexes with the Dicyanamide Anion,  $\{N(CN)_2\}^-$ . *New J. Chem.* **1998**, *22*, 1515–1524.

(41) Gutfleisch, O.; Lyubina, J.; Müller, K. H.; Schultz, L. FePt Hard Magnets. *Adv. Eng. Mater.* **2005**, *7*, 208–212.

(42) Kramer, M. J.; Mccallum, R. W.; Anderson, I. A.; Constantinides, S. Prospects for Non-Rare Earth Permanent Magnets for Traction Motors and Generators. *JOM* **2012**, *64*, 752–763.

(43) Kharel, P.; Shah, V. R.; Li, X. Z.; Zhang, W. Y.; Skomski, R.; Shield, J. E.; Sellmyer, D. J. Structural and Magnetic Properties of Pralloyed MnBi Nanostructures. *J. Phys. D: Appl. Phys.* **2013**, *46*, 095003.

(44) Ringe, E.; Van Duyn, R. P.; Marks, L. D. Kinetic and Thermodynamic Modified Wulff Constructions for Twinned Nanoparticles. *J. Phys. Chem. C* **2013**, *117*, 15859–15870.

(45) Wulff, G. On the Question of Speed of Growth and Dissolution of Crystal Surfaces. *Z. Krystallogr.* **1901**, *34*, 449–530.

(46) Srivastava, B. B.; Jana, S.; Sarma, D. D.; Pradhan, N. Surface Ligand Population Controlled Oriented Attachment: A Case of CdS Nanowires. *J. Phys. Chem. Lett.* **2010**, *1*, 1932–1935.

(47) Lambert-Andron, B.; Berodias, G. Etude Par Diffraction Neutronique de  $Fe_3Se_4$ . *Solid State Commun.* **1969**, *7*, 623–329.

(48) Holzwarth, U.; Gibson, N. The Scherrer equation versus the 'Debye-Scherrer equation'. *Nat. Nanotechnol.* **2011**, *6*, 534.

(49) Patterson, A. L. The Scherrer Formula for X-ray Particle Size Determination. *Phys. Rev.* **1939**, *56*, 978–982.

(50) Cullity, B. D.; Stock, S. R. *Elements of X-ray Diffraction*, 3rd ed.; Prentice-Hall, 2001.

(51) Inoue, M.; Hirasawa, I. The Relationship Between Crystal Morphology and XRD Peak Intensity on  $CaSO_4 \cdot 2H_2O$ . *J. Cryst. Growth* **2013**, *380*, 169–175.

(52) Malik, M.; Padhye, P.; Poddar, P. Graphene Quantum Dots-Driven Multifunctional Morphologies of  $\beta-NaYF_4:Gd^{3+}/Tb^{3+}$  Phosphors: The Underlying Mechanism and Their Optical Properties. *ACS Omega* **2018**, *3*, 1834–1849.

(53) Cullity, B. D. *Introduction to Magnetic Materials*; Addison-Wesley: Reading, MA, 1974.

(54) Zhang, M.; Zi, Z.; Liu, Q.; Zhang, P.; Tang, X.; Yang, J.; Zhu, X.; Sun, Y.; Dai, J. Size Effects on Magnetic Properties of Prepared by Sol-Gel Method. *Adv. Mater. Sci.* **2013**, *2013*, 609819.

(55) Coey, J. M. D. *Magnetism and Magnetic Materials*; Cambridge University Press: Cambridge, U.K., 2010.

(56) Zhang, Y. D.; Budnick, J. I.; Hines, W. A.; Chien, C. L.; Xiao, J. Q. Effect of Magnetic Field on the Superparamagnetic Relaxation in Granular Co-Ag Samples. *Appl. Phys. Lett.* **1998**, *72*, 2053.

(57) Mohapatra, J.; Mitra, A.; Bahadur, D.; Aslam, M. Surface Controlled Synthesis of  $MFe_2O_4$  ( $M = Mn, Fe, Co, Ni$  and  $Zn$ ) Nanoparticles and Their Magnetic Characteristics. *CrystEngComm* **2013**, *15*, 524–532.

(58) Kolhatkar, A. G.; Jamison, A. C.; Litvinov, D.; Willson, R. C.; Lee, T. R. Tuning the Magnetic Properties of Nanoparticles. *Int. J. Mol. Sci.* **2013**, *14*, 15977–16009.

#### NOTE ADDED AFTER ASAP PUBLICATION

This paper was published on the Web on March 30, 2021, with an incomplete Supporting Information file. The corrected version was reposted on March 31, 2021.

# Remarkable Effect of Fe and Se Composition on Magnetic Properties—Comparative Study of the Fe–Se System at the Nanoscale

Monika Ghalawat and Pankaj Poddar\*

Cite This: *J. Phys. Chem. C* 2022, 126, 4655–4663

Read Online

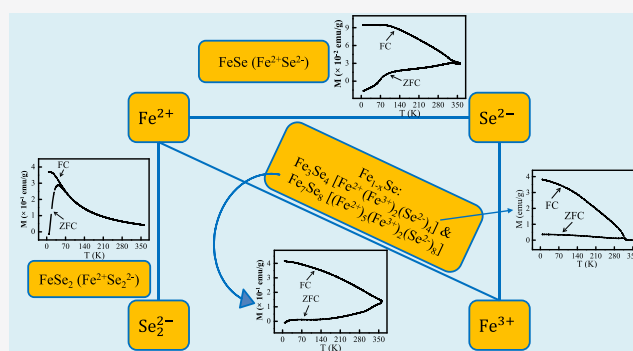
ACCESS |

Metrics & More

Article Recommendations

Supporting Information

**ABSTRACT:** Herein, for the first time, the correlation between the phase structure and the magnetic properties of the Fe–Se system has been presented for  $\text{Fe}_x\text{Se}_y$  compounds—where  $x/y$  ranges from 1:2 to 1:1. These phases—orthorhombic ( $\text{FeSe}_2$ ), monoclinic ( $\text{Fe}_3\text{Se}_4$ ), hexagonal ( $\text{Fe}_7\text{Se}_8$ ), and tetragonal ( $\beta\text{-FeSe}$ )—were synthesized using a one-pot thermal decomposition route at the nanoscale. The magnetic properties vary enormously with change in the Fe/Se ratio due to the change in the  $\text{Fe}^{2+}/\text{Fe}^{3+}$  ratio, crystal field environment around the Fe ions, magnetocrystalline anisotropy, Fe vacancies, and so forth. Among the four Fe–Se phases studied, two of them,  $\text{Fe}_3\text{Se}_4$  and  $\text{Fe}_7\text{Se}_8$ , are ferrimagnetic below  $\sim 300$  K and show semihard magnetic properties. The other two phases  $\text{FeSe}_2$  and  $\beta\text{-FeSe}$  exhibiting weaker magnetism are less known for their magnetic properties. All these phases are prone to surface oxidation despite surface passivation, and its effect on the magnetic moment will be pronounced for the phases with weak magnetization such as  $\text{FeSe}_2$  and  $\beta\text{-FeSe}$ .



## INTRODUCTION

The selenides of iron have attracted much interest in recent years because of their exciting and unique thermal, electronic, optical, and magnetic properties.<sup>1–11</sup> The richness of physical properties also comes from the richness in the stoichiometric phases these families of compounds may exhibit. The Fe–Se system shows various stable polymorphs under ambient conditions, including  $\text{FeSe}_2$ ,  $\text{Fe}_3\text{Se}_4$ ,  $\text{Fe}_7\text{Se}_8$ , and  $\text{FeSe}$ .<sup>12–14</sup> Hagg and Kindstrom's<sup>15</sup> original article referred to the iron selenides as a  $\alpha$ -phase ( $\text{FeSe}_x$  in a PbO-type structure with  $x$  up to 8/7) and  $\beta$ -phase ( $\text{FeSe}_x$  in a NiAs-type structure with  $x \sim 8/7-4/3$ ).<sup>16</sup> In the phase diagram of Okamoto,<sup>17</sup> the orthorhombic  $\text{FeSe}_2$ , monoclinic  $\text{Fe}_3\text{Se}_4$ , hexagonal  $\text{Fe}_7\text{Se}_8$ , and tetragonal  $\text{FeSe}$  are referred to as the  $\text{FeSe}_2$ ,  $\gamma$ ,  $\beta$ - $\text{Fe}_7\text{Se}_8$ , and  $\beta$  phases of the Fe–Se system, respectively.<sup>18</sup> In this work, the phases are referred to as  $\text{FeSe}_2$  (orthorhombic marcasite),  $\text{Fe}_3\text{Se}_4$  (monoclinic NiAs-type),  $\text{Fe}_7\text{Se}_8$  (hexagonal NiAs-type), and  $\beta\text{-FeSe}$  (tetragonal PbO-type). Depending upon the composition of Fe/Se, these compounds could be metals, semiconductors, or superconductors, and their magnetic properties also vary a lot from ferro- to ferrimagnetic.<sup>19–31</sup> It was recently observed that  $\text{Fe}_3\text{Se}_4$  might also show ferroelectric ordering coexisting with ferrimagnetic ordering under ambient conditions.<sup>32,33</sup> The thermal, optical (photon harvesting), energy (supercapacitors, batteries, etc.), and catalytic properties (water splitting, etc.) of these compounds have not been explored in depth so far. However, recently, the potential of

$\text{Fe}_3\text{Se}_4$  as a magnetic energy storage device was investigated, and it was found that this compound shows a colossal increase in the energy product while cooling from 300 to 10 K with the potential to replace expensive rare-earth hard magnets at lower temperatures.<sup>11,34</sup>

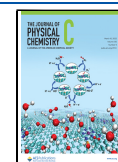
The nanoscopic forms of materials can provide additional tunability of the physical and chemical properties. Although Fe-based magnetic nanostructures, including iron, its oxides, or alloys, have all been extensively studied, however, the magnetic properties of iron chalcogenides have received relatively less attention due to the complexities associated with the synthesis of pure phases.<sup>35–48</sup>

Among the four stable phases of the Fe–Se system, two ( $\text{Fe}_3\text{Se}_4$  and  $\text{Fe}_7\text{Se}_8$ ) are well known for their rich magnetic properties, whereas the other two ( $\text{FeSe}_2$  and  $\beta\text{-FeSe}$ ) are known for their interesting optical and electronic properties.<sup>19–22</sup> Bulk and nanostructured  $\text{Fe}_3\text{Se}_4$  and  $\text{Fe}_7\text{Se}_8$  exhibit ferrimagnetic behavior at room temperature (RT) with the Curie temperatures ( $T_C$ ) of  $\sim 320$  and 453 K, respectively.<sup>23–25,34,49</sup> While it is known that  $\text{Fe}_3\text{Se}_4$  also shows

Received: December 3, 2021

Revised: February 15, 2022

Published: February 25, 2022





ferroelectric ordering at  $\sim 320$  K,<sup>32</sup> it will be interesting to study the existence of similar ordering in  $\text{Fe}_7\text{Se}_8$  in the future. Unfortunately, the magnetic ordering of  $\text{FeSe}_2$  and  $\beta\text{-FeSe}$  is still not fully understood. There are reports related to the magnetic properties of these compounds.<sup>50–59</sup> However, the clear picture is still undefined. In this article, the fundamental points of magnetic nature will be addressed, followed by properties.

The fabrication of iron selenide solids is quite challenging as slight stoichiometry variations often lead to significant changes in the structural, chemical, and physical properties. Unsurprisingly, the synthesis of iron selenides at the nanoscale is significantly more challenging as they are more reactive and less stable forms due to nanodimensions. However, the available fabrication routes are very complicated and are not flexible to achieve the desired phase. Among the various techniques for preparing iron selenide nanoparticles (NPs), thermal decomposition is a promising route for controlling the phase of the Fe–Se system, as discussed in our previous study.<sup>14</sup> The stoichiometry of Fe–Se can be influenced by many factors, such as the amount or type of precursors, reaction temperature, and time.

This article presents a comparative study of various stable phases and their magnetic properties for the Fe–Se system ( $\text{FeSe}_2$ ,  $\text{Fe}_3\text{Se}_4$ ,  $\text{Fe}_7\text{Se}_8$ , and  $\beta\text{-FeSe}$ ). The thermal decomposition-based route is used to synthesize individual phases of the Fe–Se system, and excellent tunability of their magnetic properties is observed.

## EXPERIMENTAL SECTION

**Sample Preparation.** All the phases of the Fe–Se system were developed by a one-pot thermal decomposition method in organic solvents at a minimum possible temperature with appropriate time. The chemical-synthesis details used in this study were reported by the author previously.<sup>14</sup> In addition, the details of materials and experimental methods are also mentioned in the [Supporting Information](#).

**Characterization Techniques.** The magnetic measurements were performed using the physical property measurement system manufactured by Quantum Design Inc., San Diego, California, equipped with a vibrating sample magnetometer (VSM) and superconducting magnet. The powder samples were precisely weighed and packed inside a plastic sample holder, which could fit into a brass sample holder provided by Quantum Design Inc. with a negligible contribution to an overall magnetic signal. The magnetization versus temperature ( $M$ – $T$ ) measurements were performed at a temperature sweep from 5 to 360 K in a field of 100 Oe using the VSM attachment. The magnetization versus field ( $M$ – $H$ ) loops were collected at a rate of 50 Oe  $\text{s}^{-1}$  in a field sweep from  $\pm 60$  kOe at the vibrating frequency of 40 Hz.

## RESULTS AND DISCUSSION

The crystallinity and phase purity of the as-synthesized iron selenide phases, including  $\text{FeSe}_2$ ,  $\text{Fe}_3\text{Se}_4$ ,  $\text{Fe}_7\text{Se}_8$ , and  $\beta\text{-FeSe}$ , were investigated by powder X-ray diffraction (XRD). All the diffraction patterns are in good agreement with the respective standard JCPDS cards—JCPDS#74-0247 for  $\text{FeSe}_2$ , JCPDS#73-2021 for  $\text{Fe}_3\text{Se}_4$ , JCPDS#71-0586 for  $\text{Fe}_7\text{Se}_8$ , and JCPDS#85-0735 for  $\beta\text{-FeSe}$ , as shown in [Figure S1](#). The sharp diffraction peaks in all samples indicate that all the as-synthesized phases are highly pure without the presence of any

secondary phase under the limit of laboratory XRD, as discussed in our previous work<sup>14</sup> also.

The morphology of all the phases was characterized by transmission electron microscopy (TEM). As shown in [Figure S2](#), all the as-synthesized NPs of the Fe–Se system show a quasi-spherical shape with rod-like features growing on the surface, resembling a cactus plant. [Figure S2a'–d'](#) represents the zoomed-in-view of nanocacti, which clearly reveals the rod shape of the Fe–Se system (agglomerated rods). Thus, nanorods are the building blocks in each phase of the Fe–Se system in the presence of oleylamine or oleylamine + 1-octadecene as an organic solvent.

The thermal stability study of the as-synthesized NPs was also carried out using thermogravimetric analysis (TGA) under a flowing nitrogen atmosphere to determine the decomposition behavior by heating the samples from 25 to 1000 °C at a rate of 10 °C/min.<sup>14</sup> As shown in [Figure S3](#), the first-order differentiation of weight loss with respect to the temperature displays the decomposition behavior of the Fe–Se system. The plots clearly show that all the samples exhibited different weight-loss behaviors— $\text{FeSe}_2$  underwent a four-step weight loss and the other three phases only went through a two-step weight loss. The first step ( $<460$  °C) is quite similar in each sample—related to the loss of organic fragments. Among all phases,  $\text{FeSe}_2$  is the least thermally stable as it starts the decomposition at nearly 500 °C (from  $\text{FeSe}_2$  to  $\text{Fe}_{1-x}\text{Se}$ ), followed by decomposition at  $\sim 750$  °C (from  $\text{Fe}_{1-x}\text{Se}$  to  $\text{FeSe}$ ) and finally at  $\sim 875$ –1000 °C ( $\text{FeSe}$ ). However,  $\beta\text{-FeSe}$  is highly stable; the decomposition starts after 875 °C and gradually decreases up to 1000 °C. The other two NiAs-type compounds ( $\text{Fe}_3\text{Se}_4 \sim 725$  °C and  $\text{Fe}_7\text{Se}_8 \sim 770$  °C) start decomposing between these two phases ( $\text{FeSe}_2$  and  $\beta\text{-FeSe}$ ). Please refer to Ghalawat and Poddar<sup>14</sup> for further details on the TGA of the Fe–Se system.

The oxidation state in all the phases of the Fe–Se system is determined by a highly surface-sensitive technique—X-ray photoelectron spectroscopy (XPS). The surface composition of the Fe and Se spectrum was investigated by carrying out the multiplex fitting analysis, as discussed in our previous work<sup>14</sup> also. In the Fe spectrum ([Figure S4a–d](#)), the peaks  $\sim 707$  and 720 eV imply the existence of the  $\text{Fe}^{2+}$  state in all Fe–Se compounds. The other two peaks  $\sim 711$  and 725 eV correspond to the presence of a higher oxidation state ( $\text{Fe}^{3+}$ ) of iron species in all the phases. It is well known that both  $\text{Fe}_3\text{Se}_4$  and  $\text{Fe}_7\text{Se}_8$  compounds have two oxidation states— $\text{Fe}^{2+}$  and  $\text{Fe}^{3+}$  for electron neutrality. However, the detection of a higher oxidation state ( $\text{Fe}^{3+}$ ) in the  $\text{FeSe}_2$  and  $\text{FeSe}$  Fe-spectrum clearly shows that the surface of these compounds became oxidized during the preparation and characterization. The presence of Se–O peaks (59 eV) in the Se spectra ([Figure S4a'–d'](#)) of each compound again clearly indicates the surface oxidation. Additionally, the XPS spectrum of O 1s ([Figure S4a''–d''](#)) shows three types of oxygen— $\text{O}^{\text{I}}$ ,  $\text{O}^{\text{II}}$ , and  $\text{O}^{\text{III}}$  correspond to hydroxylate, the surface oxidation of the Se species, and physi-/chemisorbed water on the surfaces due to the exposure of air, respectively. Thus, it has been clearly viewed that all the materials easily undergo surface oxidation as soon as they are exposed to air (well supported by the Fe, Se, and O spectrum, as shown in [Figure S4](#)). Please refer to Ghalawat and Poddar<sup>14</sup> for further XPS details. In this work, the magnetic properties of these samples were studied in detail.

[Scheme S1](#) presents a schematic illustration of an electronic configuration of iron. The most likely oxidation states of iron

are 2+ and 3+. The outermost shell electronic configurations of  $\text{Fe}^{2+}$  and  $\text{Fe}^{3+}$  are shown in Scheme S1. There are four unpaired electrons in  $\text{Fe}^{2+}$  and five in  $\text{Fe}^{3+}$ . The combination of these two ionic states with Se anions leads to four stable structures. The interaction between the atoms is different in all these structures, leading to distinct individual properties.

**Magnetic Properties of the  $\text{FeSe}_2$  NPs.** As mentioned above, the magnetic properties of  $\text{FeSe}_2$  are not clearly discussed. There are reports for bulk<sup>49</sup> and on the nano-scale,<sup>52,53,55–57</sup> stating that in bulk, there is no magnetic ordering; however, all the reported synthetic  $\text{FeSe}_2$  show magnetic ordering due to the several defects. In this compound, each cation is octahedrally coordinated with six anions ( $\text{FeSe}_6$  octahedra), and each anion is tetrahedrally coordinated with three cations and one anion forming the dimer pair ( $\text{Se}_2\text{Fe}_3$  tetrahedra).<sup>60</sup> A Mossbauer study of marcasite<sup>61</sup> in an external magnetic field confirmed the absence of a magnetic moment at the iron atom, suggesting that the  $\text{Fe}^{2+}$  in  $\text{FeSe}_2$  marcasite also has a low spin configuration—the completely filled  $t_{2g}$  and the completely empty  $e_g$ . Scheme S2 shows the crystal field splitting of the d-orbitals of  $\text{Fe}^{2+}$  at the octahedral site into threefold  $t_{2g}$  and twofold  $e_g$  states having the electronic configurations of  $t_{2g}^6$  and  $e_g^0$  states of 3d  $\text{Fe}^{2+}$ . Thus, iron atoms have no unpaired electron, which results in no magnetic moment in  $\text{FeSe}_2$ . In conclusion, the pure  $\text{FeSe}_2$  is diamagnetic in nature. However, there are so many literature reports that indicate magnetization.<sup>52,53,55–57</sup> The reported synthetic  $\text{FeSe}_2$  shows magnetic ordering due to the existence of either ferrimagnetic impurities or surface oxidation, spin canting, and so forth.

Figure 1 shows the schematic of the unit cell of  $\text{FeSe}_2$  and its magnetic properties. Iron diselenide ( $\text{Fe}^{2+}\text{Se}_2^{2-}$ ) has an orthorhombic marcasite structure with the unit cell lattice parameters  $a = 3.575 \text{ \AA}$ ,  $b = 4.791 \text{ \AA}$ , and  $c = 5.715 \text{ \AA}$  having the  $Pmmn$  space group (Figure 1a).<sup>14,60</sup> The temperature dependence magnetization ( $M$ – $T$ ) curves in zero-field-cooled

(ZFC) and field-cooled (FC) modes have been observed from 7 to 360 K at a 100 Oe applied magnetic field. Figure 1b shows the  $M$ – $T$  curves under the ZFC and FC conditions. The ZFC curve developed to well-defined steplike transition at 45 K; the magnetization first increased up to 45 K and then decreased with decreasing temperature, indicating that the magnetic moment configuration in the sample changes with the drop in temperature; this may be due to the spin rotation with decreasing temperature. The ZFC curve identifies an average blocking temperature of  $\sim 45 \text{ K}$ . The magnetization of the ZFC and FC process shows the bifurcation below 100 K (inset, Figure 1b).

To acquire further insights into the magnetic properties of the  $\text{FeSe}_2$  NPs, Figure 1c,d presents the magnetic field-dependent magnetization ( $M$ – $H$ ) curves for the  $\text{FeSe}_2$  nanorods measured at 300 K (red curve) and 10 K (blue curve) in an applied magnetic field up to  $\pm 60 \text{ kOe}$ . At 300 K, the  $M$ – $H$  loop indicates a two-step behavior. At a lower applied magnetic field, it reveals a nonlinear behavior. In contrast, it follows a linear  $M$ – $H$  behavior (i.e., paramagnetic) at higher field values. However, at 10 K, it reveals a nonlinear  $M$ – $H$  curve until the highest applied magnetic field. The observed prominent nonlinear hysteresis characteristics indicate the presence of magnetic ordering at both temperatures. Figure S5a,a' shows a zoomed-in view of the hysteresis curves at 300 and 10 K, clearly depicting the coercivity and remanent field of  $\text{FeSe}_2$ . By virtue of reduced thermal fluctuation of magnetic dipoles, the observed coercivity ( $H_c$ ) and remanence ( $M_R$ ) are 8 Oe and  $2.0 \times 10^{-4} \text{ emu/g}$  at 300 K that increased to 200 Oe and 0.4 emu/g at 10 K, respectively, although the pure  $\text{FeSe}_2$  exhibits diamagnetic properties, as discussed above. However, due to defects,  $\text{FeSe}_2$  generates magnetic ordering in this report.

The existence of an induced surface layer of oxides in transition-metal chalcogenides (TMCs) has been identified in many materials.<sup>62–65</sup> The TMCs are very sensitive toward oxidation. The exposure to air quickly starts the formation of an oxidation layer. As discussed above in XPS analysis (supported by the Fe, Se, and O spectra), the surface oxidized as soon as the iron selenide particles came into contact with air.<sup>14</sup> It was speculated that the surface oxidation of  $\text{FeSe}_2$  NPs generates the magnetic ordering on the surface. Thus, the surface-oxidized  $\text{FeSe}_2$  NPs are magnetically active in contrast to their fundamental magnetic behavior. It is appropriate to conclude that the as-synthesized  $\text{FeSe}_2$  NPs using organometallic chemistry are easily oxidized as soon as they come in contact with air and form a magnetic coating on the surface.

**Magnetic Properties of the  $\text{Fe}_3\text{Se}_4$  and  $\text{Fe}_7\text{Se}_8$  NPs.** In the NiAs-type crystal structures of  $\text{Fe}_3\text{Se}_4$  and  $\text{Fe}_7\text{Se}_8$ , the cations are octahedrally coordinated by six anions ( $\text{FeSe}_6$  octahedra), and the coordination polyhedron of anions is a trigonal prism created by six cations ( $\text{SeFe}_6$  prisms).<sup>19</sup> In the  $\text{Fe}_{1-x}\text{Se}$  compounds, there are two types of Fe ionic states  $\text{Fe}^{2+}$  and  $\text{Fe}^{3+}$  along with ordered Fe vacancies.<sup>66,67</sup> These arrangements give rise to the magnetic behavior of the compounds. Each layer is of the ferromagnetic order in the opposite direction from the adjacent layer, resulting in the overall ferrimagnetic nature of the compound. Scheme S3a,b shows the  $\text{Fe}_{1-x}\text{Se}$  system crystal field splitting of the d-orbitals at the octahedral site into threefold  $t_{2g}$  and twofold  $e_g$  states having the electronic configurations of  $t_{2g}^4/t_{2g}^3$  and  $e_g^2$  states of 3d Fe cations ( $\text{Fe}^{2+}/\text{Fe}^{3+}$ ). The  $\text{Fe}^{2+}$  and  $\text{Fe}^{3+}$  ions are octahedrally coordinated with four and five unpaired

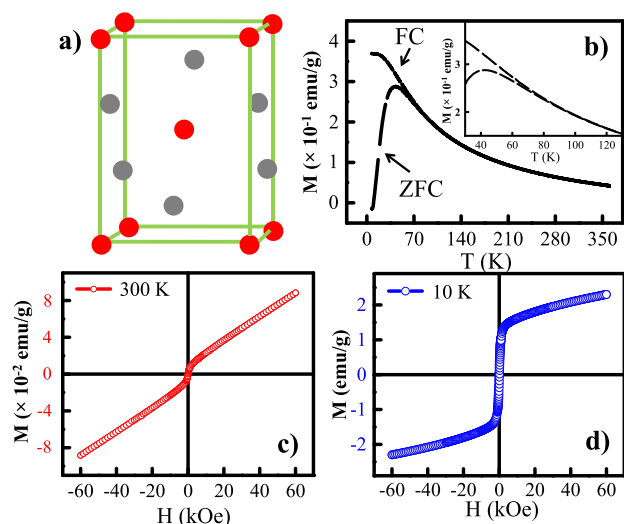


**Figure 1.** (a) Schematic of the unit cell of  $\text{FeSe}_2$ ; solid red circle represents the Fe cations, and the solid gray circle represents the Se anions. (b)  $M$ – $T$  curves for  $\text{FeSe}_2$  (black curve) measured with an applied field of 100 Oe in the FC and ZFC modes (the inset shows the zoomed-in view of the curve). Hysteresis loops of  $\text{FeSe}_2$  measured using the VSM within a field of  $\pm 60 \text{ kOe}$  at (c) 300 K (red curves) and (d) 10 K (blue curves).

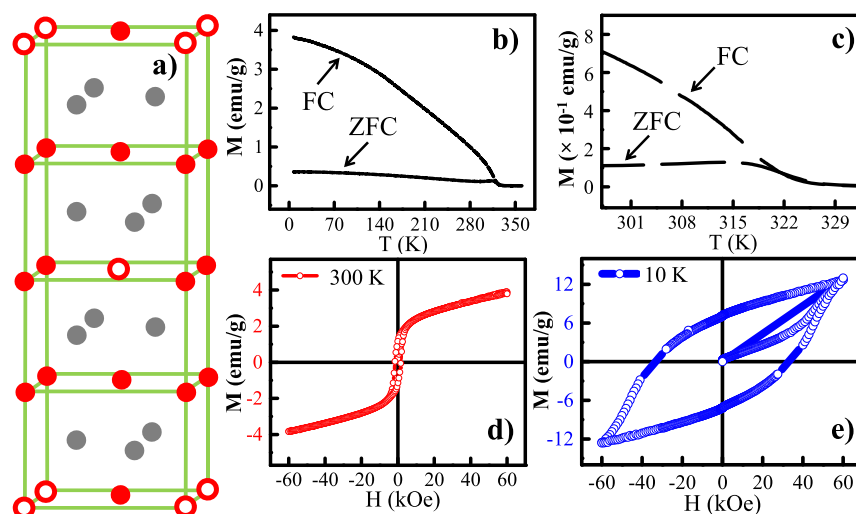


**Figure 2.** (a) Schematic of the unit cell of  $\text{Fe}_3\text{Se}_4$ ; solid red circle represents the Fe cations, open red circles represent the cation vacancies, and the solid gray circle represents the Se anions. (b)  $M$ – $T$  curves for  $\text{Fe}_3\text{Se}_4$  (black curve) measured with an applied field of 100 Oe in the FC and ZFC modes. (c) Zoomed-in view of the  $M$ – $T$  curve. The VSM-measured hysteresis loops of  $\text{Fe}_3\text{Se}_4$  with a field of  $\pm 60$  kOe at (d) 300 K (red curves) and (e) 10 K (blue curves).

electrons.<sup>66</sup> Scheme S3c shows the crystal field splitting of the d-orbitals at the tetrahedral site into twofold  $e$  and threefold  $t_2$  states having the electronic configurations of  $e^2$  and  $t_2^3$  states of  $3d \text{ Fe}^{3+}$ . Coupling is observed between the Fe ions. These compounds exhibit exchange interactions, and the overlap of the localized electronic orbital on Fe ion sites is mediated through their common Se ion. For visualization, the exchange interactions in the  $\text{Fe}_{1-x}\text{Se}$  system are shown in Scheme S3d with the superexchange interaction in  $\text{Fe}^{3+}$  octahedron–octahedron example. The exchange interaction between Fe–Fe and other Fe–Se–Fe is also present in these compounds. In bulk<sup>66,67</sup> and at nanodimensions,<sup>68</sup> both the compounds show ferrimagnetic behavior due to the presence of ordered iron vacancies in alternate layers (Figure 2a and 3a). This ferrimagnetic ordering is attributed to the ferromagnetically aligned spins within each plane toward the  $c$ -axis and antiferromagnetically aligned in an adjacent plane.<sup>66,67</sup>

$\text{Fe}_3\text{Se}_4$  ( $\text{Fe}^{2+}\text{Fe}_2^{3+}\text{Se}_4^{2-}$ ) has a monoclinic NiAs-type crystal structure with the unit cell lattice parameters  $a = 6.167 \text{ \AA}$ ,  $b = 3.537 \text{ \AA}$ , and  $c = 11.17 \text{ \AA}$  having the  $I2/m$  space group (Figure 2a).<sup>12,66</sup> In Figure 2b,c, the magnetization ZFC and FC of  $\text{Fe}_3\text{Se}_4$  show bifurcation below 330 K and the Curie transition temperature is nearly 322 K, below which it goes into a ferrimagnetic phase. These results are also consistent with the earlier reports of  $T_C \sim 320 \text{ K}$  for  $\text{Fe}_3\text{Se}_4$ .<sup>11,25,34</sup> Figure S6 shows the zoomed-in view of the  $M$ – $T$  curves in the ZFC mode, illustrating an average blocking temperature of  $\sim 313 \text{ K}$  with a peak in the ZFC curve. Consequently, ferrimagnetism exists in the  $\text{Fe}_3\text{Se}_4$  nanorods with a transition temperature of 322 K. Furthermore, this material reveals semihard magnetic properties at the nanoscale.<sup>11,25,34</sup> In earlier reports, for the  $\text{Fe}_3\text{Se}_4$  nanoplatelets, the observed coercivity was  $\sim 4 \text{ kOe}$  at 300 K, which increases to  $\sim 40 \text{ kOe}$  at 10 K for 90 kOe of the maximum external field.<sup>25</sup> The coercivity values for the  $\text{Fe}_3\text{Se}_4$  nanorods at 300 K were reported as  $\sim 3.4 \text{ kOe}$ <sup>25</sup> and  $2.74 \text{ kOe}$ .<sup>34</sup> It was also reported that at 10 K temperature, the coercivity values increased almost 10-fold, that is,  $36 \text{ kOe}$ <sup>25</sup> and  $29.5 \text{ kOe}$ <sup>34</sup> with 90 kOe of the maximum external field. The as-synthesized  $\text{Fe}_3\text{Se}_4$  nanorods reported in this article also exhibited semihard magnetic properties, and their

hysteresis loops recorded at 300 K (red curve) and 10 K (blue curve) for a field sweep up to  $\pm 60 \text{ kOe}$  are shown in Figure 2d,e, respectively. These hysteresis loops showed the nonlinear behavior typical of the ferrimagnetic nature of  $\text{Fe}_3\text{Se}_4$  NPs, as reported in the literature.<sup>11,25,34</sup> The  $H_C$  and  $M_R$  values of  $\text{Fe}_3\text{Se}_4$  were determined to be  $1.6 \text{ kOe}$  and  $1.2 \text{ emu/g}$ , respectively, which are relatively low compared to the reported data due to the reduced size of the NPs.<sup>11,25,34</sup> All the phases were synthesized at the minimal possible temperature with an appropriate time. Thus, the pure  $\text{Fe}_3\text{Se}_4$  phase reaction started from this stage and growth was terminated by stopping the reaction that resulted in small NPs. A decrease in the particle size below its single domain size is known to decrease its magnetization.<sup>11</sup> Second, as the particle size decreased, the surface-to-volume ratio increased, resulting in a more significant number of surface spins per unit volume. The surface spins were uncompensated and remained disordered or canted, leading to the overall magnetization reduction with a decreased particle size.<sup>11</sup>

At lower temperatures, a colossal increase in the coercivity was observed, and the  $H_C$  increased nearly 20-fold to about 33 kOe at 10 K, and the  $M_R$  increased to  $7.4 \text{ emu/g}$ , which is in excellent agreement with the earlier reports.<sup>11,25,34</sup> At a lower temperature, the coercivity may increase by various contributions—the reduced thermal activation energy that makes more and more spins available to orient in the field direction, the increase in the overall effective magnetic anisotropy, ferrimagnetism, and so forth.<sup>11</sup> The  $\text{Fe}_3\text{Se}_4$  NPs also induced an oxidation layer; however, their effect on the overall magnetism is negligible. This compound is highly magnetized, and any small contribution will not affect the overall magnetic behavior.

$\text{Fe}_7\text{Se}_8$  ( $\text{Fe}_5^{2+}\text{Fe}_2^{3+}\text{Se}_8^{2-}$ ) has a hexagonal NiAs-type crystal structure.<sup>67,69</sup> As shown in Figure 3a, the unit cell lattice parameters  $a = 7.21 \text{ \AA}$  and  $c = 17.67 \text{ \AA}$  have the  $P3_121$  space group.<sup>67,69</sup> The divergence of magnetization ZFC and FC curves of  $\text{Fe}_7\text{Se}_8$  over the whole range of temperature up to 360 K, as shown in Figure 3b, signifies the formation of an ordered magnetic state, which may be due to the high  $T_C$  of the sample (the Curie transition temperature lies above 360

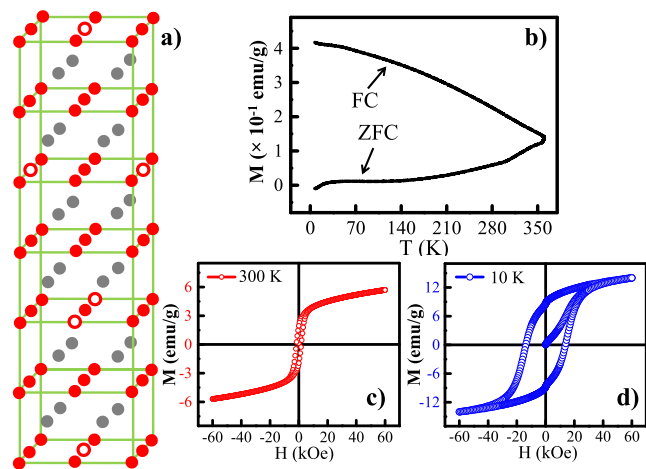


**Figure 3.** (a) Schematic of the unit cell of  $\text{Fe}_7\text{Se}_8$ ; solid red circle represents the Fe cations, open red circles represent the cation vacancies, and the solid gray circle represents the Se anions. (b)  $M$ - $T$  curves for  $\text{Fe}_7\text{Se}_8$  (black curve) measured with an applied field of 100 Oe in the FC and ZFC modes. Hysteresis loops of  $\text{Fe}_7\text{Se}_8$  were measured using the VSM with a field of  $\pm 60$  kOe at (c) 300 K (red curves) and (d) 10 K (blue curves).

K).<sup>19</sup> Thus, the  $\text{Fe}_7\text{Se}_8$  NPs are strongly coupled due to the magnetic interactions. The field-dependence magnetization curve of the as-synthesized  $\text{Fe}_7\text{Se}_8$  NPs exhibits a ferrimagnetic nature at both the temperatures (300 and 10 K), as presented in Figure 3c,d. It is observed that the  $\text{Fe}_7\text{Se}_8$  NPs exhibit hysteresis with a remanent magnetization ( $M_R$ ) of 2 emu/g at 300 K and 8.6 emu/g at 10 K. They also exhibit a coercivity field ( $H_C$ )  $\sim 1.8$  kOe at 300 K, which increases to  $\sim 13.8$  kOe at 10 K. At a lower temperature, the magnetic parameters may increase by various contributions, as discussed above for  $\text{Fe}_3\text{Se}_4$ . Here also, the oxidation layer is induced at the surface; however, as in the case of  $\text{Fe}_3\text{Se}_4$ , the effect on overall magnetism is negligible due to the high magnetization of the fundamental compound.

However, both the compounds ( $\text{Fe}_3\text{Se}_4$  and  $\text{Fe}_7\text{Se}_8$ ) exhibit a ferrimagnetic nature and their fundamental unit cell is also the same (NiAs-type).<sup>66,67</sup> However, the ratio of the Fe cations and the arrangement of atoms, including cation vacancies, are different in both the compounds, which results in a distinct magnitude of ferrimagnetism. According to the spin-only moment, the  $5 \mu_B$  value is for the  $\text{Fe}^{3+}$  ions having 5d-electrons and  $4 \mu_B$  is for the  $\text{Fe}^{2+}$  ions having 6d-electrons.<sup>66</sup> However, the electrons are lost due to the delocalization of d-electrons and/or the covalency effect.<sup>66</sup> The observed moment values in  $\text{Fe}_7\text{Se}_8$  are from covalency effects of about 25% for both kinds of ions. The moment further reduces in  $\text{Fe}_3\text{Se}_4$  that can be ascribed to an increased covalency effect due to the lattice contraction.<sup>66</sup> Additionally, in  $\text{Fe}_3\text{Se}_4$ , the delocalization of some of the d-electrons is brought about by the short metal-to-metal distance along the  $c$ -axis. These 3-d electrons are connected with the metal-to-metal distance along the  $c$ -axis, and the distance reduces from 2.94 Å to 2.79 Å upon going from  $\text{Fe}_7\text{Se}_8$  to  $\text{Fe}_3\text{Se}_4$ .<sup>66</sup> Thus, the magnetic ordering is different in both compounds because of the delocalization of the 3-d electrons and covalency effect. Besides,  $\text{Fe}_7\text{Se}_8$  requires more thermal energy to reduce the magnetic ordering than  $\text{Fe}_3\text{Se}_4$ . Thus, the magnetic transition temperature increases gradually with the increase of selenium in NiAs-type compounds.

**Magnetic Property of the  $\text{FeSe}$  NPs.** Scheme S4a shows the  $\beta$ - $\text{FeSe}$  system and crystal field splitting of the d-orbitals of  $\text{Fe}^{2+}$  at the tetrahedral site into twofold  $e$  and threefold  $t_2$  states having the electronic configurations of  $e^3$  and  $t_2^3$  states of 3d  $\text{Fe}^{2+}$ . Scheme S4b shows a schematic illustration of exchange interactions in the  $\beta$ - $\text{FeSe}$ . This compound exhibits superexchange interactions.<sup>70–72</sup>  $\beta$ - $\text{FeSe}$  ( $\text{Fe}^{2+}\text{Se}^{2-}$ ) has a tetragonal PbO-type crystal structure with the unit cell lattice parameters  $a = 3.765$  Å and  $c = 5.518$  Å having the  $P4/nmm$  space group, as shown in Figure 4a.<sup>27</sup> In this compound, each cation is

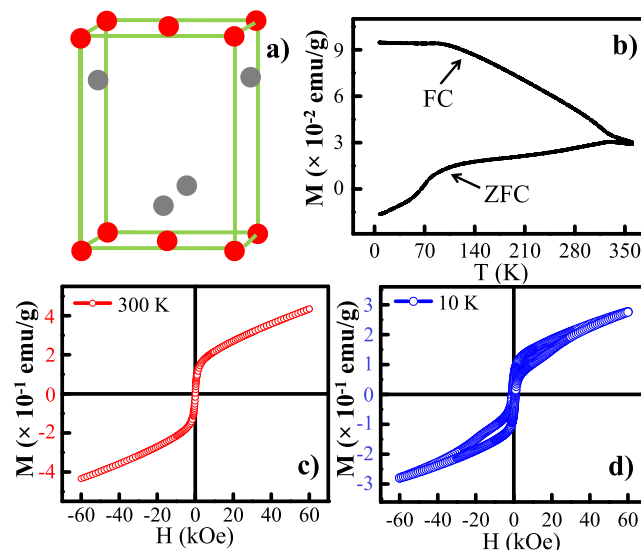


**Figure 4.** (a) Schematic of the unit cell of  $\beta$ - $\text{FeSe}$ ; solid red circle represents the Fe cations, and the solid gray circle represents the Se anions. (b)  $M$ - $T$  curves for  $\beta$ - $\text{FeSe}$  (black curve) measured with an applied field of 100 Oe in the FC and ZFC modes. Hysteresis loops of  $\beta$ - $\text{FeSe}$  were measured using the VSM with a field of  $\pm 60$  kOe at (c) 300 K (red curves) and (d) 10 K (blue curves).

tetrahedrally coordinated with four anions ( $\text{FeSe}_4$  tetrahedra), and each anion is tetrahedrally coordinated with four cations ( $\text{SeFe}_4$  tetrahedra).<sup>14,27</sup>

Figure 4b shows the ZFC and FC curve of  $\beta$ - $\text{FeSe}$ . A magnetic anomaly has developed around 80–100 K, more prominent in the FC curve. It is known that the tetragonal phase undergoes structural transitions upon cooling. These magnetic deviations are nearly at the same temperature, as observed in the resistive measurements by Hsu et al.<sup>27</sup> They reported that the  $\beta$ - $\text{FeSe}$  having a tetragonal structure with space group  $P4/nmm$  transforms into the triclinic structure with the space group  $P\bar{1}$  at  $\sim 100$  K by temperature-dependent XRD.<sup>27</sup> In another study, Margadonna et al.<sup>73</sup> observed that upon cooling, the  $\beta$ - $\text{FeSe}$  phase (tetragonal  $P4/nmm$ ) exhibits a structural transition from the tetragonal to the lower-symmetry orthorhombic  $Cmma$  phase at nearly 70 K. The transition occurs within a broad temperature range (about 70–100 K), depending on the stoichiometry of the samples,<sup>74</sup> and could be observed by temperature-dependent measurements. It is appropriate to conclude that the observed magnetic anomaly in the ZFC and FC curves is due to the phase transition of the  $\beta$ - $\text{FeSe}$  phase.

Furthermore, field dependence magnetization was examined to gain more insight into the magnetic properties of  $\beta$ - $\text{FeSe}$  at the nanoscale. In Figure 4c,d, the hysteresis loops of  $\beta$ - $\text{FeSe}$  are nonlinear and reveal the magnetic nature of NPs having a  $H_C$

and a  $M_R$  of 84 Oe and  $1.8 \times 10^{-2}$  emu/g at 300 K, respectively, which increased to about 761 Oe and 0.1 emu/g at 10 K (blue curve in Figure 4d). As in the case of  $\text{FeSe}_2$ , the  $\beta$ -FeSe NPs also induced the oxidation layer, which affects the overall magnetic behavior. Therefore, the observed properties are of surface-oxidized  $\beta$ -FeSe NPs. The nonuniform curve at 10 K may be attributed to fundamental  $\beta$ -FeSe and the surface-oxidized layer.

Moreover, here it is essential to discuss the superconductivity of the synthesized  $\beta$ -FeSe. It is known that  $\beta$ -FeSe shows a superconducting transition at  $\sim 8$  K.<sup>27</sup> Greenfield et al.<sup>29</sup> reported that exposure to oxygen will result in non-superconducting samples of  $\beta$ -FeSe. The samples exposed to air, oxygen, or ambient conditions will lose their superconductivity even in a short period of time. They proved it by preparing three types of samples—sample I (exposed to air), sample II (free from air; prepared and handled in an inert atmosphere), and sample III (free from air/ $\text{H}_2\text{O}$ ; prepared and handled in an inert atmosphere; vacuum-degassed at 100 °C and the residual water removed).<sup>29</sup> It was observed that sample I exhibited antiferromagnetic ordering, while sample III did not show any antiferromagnetic ordering; instead, it revealed the characteristic superconducting transition at 8 K. Sample II exhibited intermediate magnetic properties. Thus, the magnetic ordering and superconductivity are competitive in  $\beta$ -FeSe. The exposure of air or water appeared to completely suppress the superconductivity and allow the magnetic ordering to persist.<sup>29</sup> In this work, the as-synthesized  $\beta$ -FeSe exhibits magnetic ordering due to surface oxidation of NPs, while the superconductivity is completely suppressed.

**Magnetic Properties of the Fe–Se System.** A simple one-pot thermal decomposition route has been used to prepare the Fe–Se system with various phases, such as  $\text{FeSe}_2$  (O),  $\text{Fe}_3\text{Se}_4$  (M),  $\text{Fe}_7\text{Se}_8$  (H), and  $\beta$ -FeSe (T). In contrast with bulk,  $\text{FeSe}_2$  shows magnetic ordering at the nanoscale due to the presence of the oxide surface in NPs. The results of magnetization measurements as a function of temperature and the applied field clearly reveal the existence of magnetic ordering at the nanoscale in surface-oxidized  $\text{FeSe}_2$  NPs. As discussed in the above section (also explained in our previous study<sup>14</sup>), XPS analysis confirms that the materials readily undergo surface oxidation when exposed to air. Exposure to the atmosphere induces the magnetic behavior in the  $\text{FeSe}_2$  compound. It is most likely that the atmospheric oxygen atoms induce a vital localized magnetic moment on the neighboring Fe atoms, leading to magnetic ordering at the nanoscale. Superparamagnetism transition known as the blocking temperature occurs in the  $\text{FeSe}_2$  and  $\text{Fe}_3\text{Se}_4$  NPs at around 45 and 313 K, respectively. The ferrimagnetic nature is present in the two  $\text{Fe}_{1-x}\text{Se}$  compounds due to the number of vacancies and their ordering on every second metal layer. The shift from stoichiometry results in the formation of Fe vacancies on every second metal layer that are distributed as far apart as possible. Besides,  $\text{Fe}_3\text{Se}_4$  NPs show ferrimagnetic behavior with large magnetic coercivity at 300 K, which increases about 20 times at 10 K with a Curie transition temperature of  $T_C \sim 322$  K. The other NiAs-based structure ( $\text{Fe}_7\text{Se}_8$ ) also shows ferrimagnetic properties at both 10 and 300 K with a transition temperature higher than the measured temperature (360 K). The  $\beta$ -FeSe NPs reveal a deviation around 80–100 K due to phase transition. These NPs also show a magnetic ordering at 10 and 300 K with higher magnetization and coercivity values at 10 K.  $\beta$ -FeSe also exhibits magnetic ordering due to surface oxidation

and completely suppresses the superconductivity nature. The surface oxidation occurs in all phases of the Fe–Se system. However, in the case of  $\text{Fe}_3\text{Se}_4$  and  $\text{Fe}_7\text{Se}_8$ , the effect on magnetism is negligible due to the high magnetic nature of these compounds. While in  $\text{FeSe}_2$  and  $\beta$ -FeSe, the surface oxidation affects the magnetic behavior of the fundamental compounds.

These results confirm that the simple one-pot thermal decomposition approach can produce iron selenide NPs with any of the four different phases and substantially different physical properties, moreover vastly different magnetic properties. The magnetic parameters of the Fe–Se system at both temperatures are tabulated in Table 1. The coercivity and

**Table 1. Magnetic Parameters—Coercivity ( $H_C$ ), Remanence ( $M_R$ ), and Magnetization at 60 kOe ( $M_{60 \text{ kOe}}$ ) for Various Phases of the Fe–Se System Are Compared at 300 and 10 K**

parameters	$H_C$ (Oe)		$M_R$ (emu/g)		$M_{60 \text{ kOe}}$ (emu/g)	
	300 K	10 K	300 K	10 K	300 K	10 K
$\text{FeSe}_2$	8	200	$2.0 \times 10^{-4}$	0.4	0.09	2.30
$\text{Fe}_3\text{Se}_4$	1615	33 360	1.2	7.4	3.88	13.17
$\text{Fe}_7\text{Se}_8$	1800	13 800	2	8.6	5.70	14.01
$\beta$ -FeSe	84	761	$1.8 \times 10^{-2}$	0.1	0.43	0.28

saturation magnetization values ( $M_{60 \text{ kOe}}$ ) for all the above phases of iron selenide NPs at 300 and 10 K are compared in Figure 5. Remarkably higher magnetization and coercivity (Figure 5) are observed in both the NiAs-based compounds ( $\text{Fe}_3\text{Se}_4$  and  $\text{Fe}_7\text{Se}_8$  NPs), as compared with the other two compounds ( $\text{FeSe}_2$  and  $\beta$ -FeSe NPs) because of the presence of Fe vacancies, crystal field environment around Fe-ions, two types of Fe cations, magnetic anisotropy, and so forth. These values increase hugely at 10 K for the  $\text{Fe}_{1-x}\text{Se}$  compounds (Figure 5b). Thus, it is possible to customize the magnetic properties of iron selenides by controlling their phase structure. The well-regulated magnetism may lead to broad applications of magnetic carriers in storage devices, biomedicine, and catalysts.

## CONCLUSIONS

A simple one-pot thermal decomposition approach has been used to fabricate various phases of iron selenide NPs. The distinct arrangement of Fe and Se atoms results in drastically varying magnetic properties due to the change in the  $\text{Fe}^{2+}/\text{Fe}^{3+}$  ratio, crystal field environment around the Fe-ions, magneto-crystalline anisotropy, Fe vacancies, and so forth. The findings reported in this study explain the excellent tunability of magnetism in the Fe–Se system at the nanoscale. The two NiAs-based phases,  $\text{Fe}_3\text{Se}_4$  and  $\text{Fe}_7\text{Se}_8$ , are ferrimagnetic below  $\sim 300$  K and show semihard magnetic properties. The other two phases,  $\text{FeSe}_2$  and  $\beta$ -FeSe, exhibit weaker magnetism and are less recognized for their magnetic properties. The surface oxidation remarkably affects the magnetic properties, especially on the phases with weak magnetization, such as  $\text{FeSe}_2$  and  $\beta$ -FeSe. The surface-oxidized  $\text{FeSe}_2$  and  $\beta$ -FeSe show magnetic ordering at the nanoscale.  $\text{FeSe}_2$  and  $\text{Fe}_3\text{Se}_4$  NPs exhibit superparamagnetic transition at the blocking temperatures of  $\sim 45$  and 313 K, respectively. Also, the  $\text{Fe}_3\text{Se}_4$  NPs show ferrimagnetism at 300 K with a large magnetic coercivity, which multiplies at low temperatures. The  $\text{Fe}_7\text{Se}_8$  NPs show ferrimagnetism at all temperatures with a transition temper-

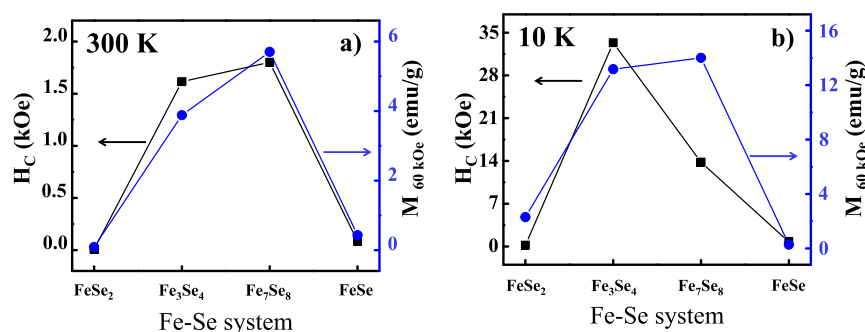


**Figure 5.** Magnetic parameters measured for the Fe–Se system at 300 and 10 K.  $H_C$  and  $M_{60 \text{ kOe}}$  denote the coercivity and saturation magnetization at 60 kOe, respectively.

ature higher than 360 K. The  $\beta$ -FeSe NPs indicate magnetic ordering at both the temperatures with a magnetic anomaly at around 80–100 K due to phase transition. The simple thermal decomposition route has been proven to be a brilliant method to synthesize any four phases in the Fe–Se system at the nanoscale with unique magnetic properties in each phase. This is an excellent approach to meet the specific needs of storage devices, biomedicine, and catalyst applications.

## ASSOCIATED CONTENT

### Supporting Information

The Supporting Information is available free of charge at <https://pubs.acs.org/doi/10.1021/acs.jpcc.1c10286>.

Experimental details, electronic configuration, XRD, TEM, TGA, XPS, and magnetic data (PDF)

## AUTHOR INFORMATION

### Corresponding Author

**Pankaj Poddar** – Physical & Materials Chemistry Division, CSIR-National Chemical Laboratory, Pune 411008, India; Academy of Scientific and Innovative Research (AcSIR), Ghaziabad 201 002 Uttar Pradesh, India; [orcid.org/0000-0002-2273-588X](https://orcid.org/0000-0002-2273-588X); Email: [p.poddar@ncl.res.in](mailto:p.poddar@ncl.res.in)

### Author

**Monika Ghalawat** – Physical & Materials Chemistry Division, CSIR-National Chemical Laboratory, Pune 411008, India; Academy of Scientific and Innovative Research (AcSIR), Ghaziabad 201 002 Uttar Pradesh, India

Complete contact information is available at: <https://pubs.acs.org/10.1021/acs.jpcc.1c10286>

### Notes

The authors declare no competing financial interest.

## ACKNOWLEDGMENTS

One of the authors—M.G.—acknowledges the support from the University Grants Commission (UGC), India, for providing the Senior Research Fellowship (SRF).

## REFERENCES

(1) Santhoshkumar, P.; Nagaraju, G.; Shaji, N.; Sim, G. S.; Nanthagopal, M.; Sekhar, S. C.; Yu, J. S.; Lee, C. W. Hierarchical Iron Selenide Nanoarchitecture as an advanced Anode Material for high-Performance Energy Storage Devices. *Electrochim. Acta* **2020**, 356, 136833.

(2) Sun, W.; Li, Y.; Liu, S.; Liu, C.; Tan, X.; Xie, K. Mechanism investigation of Iron Selenide as Polysulfide mediator for Long-Life Lithium-Sulfur Batteries. *Chem. Eng. J.* **2021**, 416, 129166.

(3) Zhao, F.; Shen, S.; Cheng, L.; Ma, L.; Zhou, J.; Ye, H.; Han, N.; Wu, T.; Li, Y.; Lu, J. Improved Sodium-Ion Storage Performance of Ultrasmall Iron Selenide Nanoparticles. *Nano Lett.* **2017**, 17, 4137–4142.

(4) Pandit, B.; Rondiya, S. R.; Shegokar, S.; Bommineedi, L. K.; Cross, R. W.; Dzade, N. Y.; Sankapal, B. R. Combined Electrochemical and DFT investigations of Iron Selenide: a Mechanically Bendable Solid-State Symmetric Supercapacitor. *Sustainable Energy Fuels* **2021**, 5, 5001–5012.

(5) Fan, H.; Yu, H.; Zhang, Y.; Guo, J.; Wang, Z.; Wang, H.; Zhao, N.; Zheng, Y.; Du, C.; Dai, Z.; Yan, Q.; Xu, J. 1D to 3D Hierarchical Iron Selenide hollow Nanocubes assembled from  $\text{FeSe}_2$ @C Core-Shell Nanorods for advanced Sodium Ion Batteries. *Energy Storage Mater.* **2018**, 10, 48–55.

(6) Thanikaikarasan, S.; Perumal, R.; Roji Marjorie, S. Influence of Potential on Structural, Compositional, Optical and Magnetic Properties of Electrochemically grown Iron Selenide Thin Films. *J. Alloys Compd.* **2020**, 848, 156348.

(7) Guterding, D.; Jeschke, H. O.; Valentí, R. Basic Electronic Properties of Iron Selenide under variation of Structural Parameters. *Phys. Rev. B* **2017**, 96, 125107.

(8) Rodriguez, J. P. Spin Resonances in Iron Selenide high- $T_c$  Superconductors by Proximity to a hidden Spin Density Wave. *Phys. Rev. B* **2020**, 102, 024521.

(9) Lu, S.; Wu, H.; Xu, S.; Wang, Y.; Zhao, J.; Li, Y.; Abdelkader, A. M.; Li, J.; Wang, W.; Xi, K.; Guo, Y.; Ding, S.; Gao, G.; Kumar, R. V. Iron Selenide Microcapsules as Universal Conversion-Typed Anodes for Alkali Metal-Ion Batteries. *Small* **2021**, 17, 2005745.

(10) Ulbrich, K. F.; Campos, C. E. M. Stability of Iron Selenide Nanophases prepared by Mechano-synthesis. *AIP Adv.* **2019**, 9, 045311.

(11) Ghalawat, M.; Poddar, P. Study of Growth Kinetics of  $\text{Fe}_3\text{Se}_4$  Nanocrystallites and the Influence of Size and Shape Tunability on their Magnetic Properties. *J. Phys. Chem. C* **2021**, 125, 7932–7943.

(12) Okazaki, A.; Hirakawa, K. Structural Study of Iron Selenides  $\text{FeSe}_x$ . I Ordered Arrangement of Defects of Fe Atoms. *J. Phys. Soc. Jpn.* **1956**, 11, 930–936.

(13) Schuster, W.; Mikler, H.; Komarek, K. L. Transition Metal-Chalcogen Systems, VII.: The Iron-Selenium Phase Diagram. *Monatsh. Chem.* **1979**, 110, 1153–1170.

(14) Ghalawat, M.; Poddar, P. Study of the Phase-Evolution Mechanism of an Fe–Se System at the Nanoscale: Optimization of Synthesis Conditions for the Isolation of Pure Phases and Their Controlled Growth. *Langmuir* **2020**, 36, 2012–2022.

(15) Hägg, G.; Kindström, A.-L. Röntgenuntersuchung am System Eisen-Selen. *Z. Phys. Chem.* **1933**, 22B, 453–464.

(16) Patel, U.; Hua, J.; Yu, S. H.; Avci, S.; Xiao, Z. L.; Claus, H.; Schlueter, J.; Vlasov, V. V.; Welp, U.; Kwok, W. K. Growth and Superconductivity of  $\text{FeSe}_x$  crystals. *Appl. Phys. Lett.* **2009**, 94, 082508.

- (17) Okamoto, H. The Fe-Se (Iron-Selenium) System. *JPE* **1991**, *12*, 383–389.
- (18) Pomjakushina, E.; Conder, K.; Pomjakushin, V.; Bendele, M.; Khasanov, R. Synthesis Crystal Structure, and Chemical Stability of the Superconductor  $\text{FeSe}_{1-x}$ . *Phys. Rev. B: Condens. Matter Mater. Phys.* **2009**, *80*, 024517.
- (19) Lyubutin, I. S.; Lin, C.-R.; Funtov, K. O.; Dmitrieva, T. V.; Starchikov, S. S.; Siao, Y.-J.; Chen, M.-L. Structural, Magnetic, and Electronic Properties of Iron Selenide  $\text{Fe}_{6-7}\text{Se}_8$  Nanoparticles Obtained by Thermal Decomposition in High-Temperature Organic Solvents. *J. Chem. Phys.* **2014**, *141*, 044704.
- (20) Mao, X.; Kim, J.-G.; Han, J.; Jung, H. S.; Lee, S. G.; Kotov, N. A.; Lee, J. Phase-Pure  $\text{FeSe}_x$  ( $x = 1, 2$ ) Nanoparticles with One- and Two-Photon Luminescence. *J. Am. Chem. Soc.* **2014**, *136*, 7189–7192.
- (21) Yuan, B.; Luan, W.; Tu, S.-t. One-Step Synthesis of Cubic  $\text{FeS}_2$  and Flower-like  $\text{FeSe}_2$  Particles by a Solvothermal Reduction Process. *Dalton Trans.* **2012**, *41*, 772–776.
- (22) Yuan, B.; Hou, X.; Han, Y.; Luan, W.; Tu, S.-t. Facile Synthesis of Flake-like  $\text{FeSe}_2$  Particles in Open-Air Conditions. *New J. Chem.* **2012**, *36*, 2101–2105.
- (23) Hirone, T.; Chiba, S. The Magnetic Properties of  $\text{FeSe}_x$  with the NiAs Structure. *J. Phys. Soc. Jpn.* **1956**, *11*, 666–670.
- (24) Gao, M.-R.; Lin, Z.-Y.; Jiang, J.; Yao, H.-B.; Lu, Y.-M.; Gao, Q.; Yao, W.-T.; Yu, S.-H. Selective Synthesis of  $\text{Fe}_7\text{Se}_8$  Polyhedra with Exposed High-Index Facets and  $\text{Fe}_7\text{Se}_8$  Nanorods by a Solvothermal Process in a Binary Solution and Their Collective Intrinsic Properties. *Chemistry* **2011**, *17*, 5068–5075.
- (25) Zhang, H.; Long, G.; Li, D.; Sabirianov, R.; Zeng, H.  $\text{Fe}_3\text{Se}_4$  Nanostructures with Giant Coercivity Synthesized by Solution Chemistry. *Chem. Mater.* **2011**, *23*, 3769–3774.
- (26) Long, G.; Zhang, H.; Li, D.; Sabirianov, R.; Zhang, Z.; Zeng, H. Magnetic Anisotropy and Coercivity of  $\text{Fe}_3\text{Se}_4$  Nanostructures. *Appl. Phys. Lett.* **2011**, *99*, 202103.
- (27) Hsu, F.-C.; Luo, J.-Y.; Yeh, K.-W.; Chen, T.-K.; Huang, T.-W.; Wu, P. M.; Lee, Y.-C.; Huang, Y.-L.; Chu, Y.-Y.; Yan, D.-C.; Wu, M.-K. Superconductivity in the PbO-Type Structure  $\alpha\text{-FeSe}$ . *Proc. Natl. Acad. Sci. U.S.A.* **2008**, *105*, 14262–14264.
- (28) Wu, X. J.; Shen, D. Z.; Zhang, Z. Z.; Zhang, J. Y.; Liu, K. W.; Li, B. H.; Lu, Y. M.; Yao, B.; Zhao, D. X.; Li, B. S.; Shan, C. X.; Fan, X. W.; Liu, H. J.; Yang, C. L. On the Nature of the Carriers in Ferromagnetic  $\text{FeSe}$ . *Appl. Phys. Lett.* **2007**, *90*, 112105.
- (29) Greenfield, J. T.; Kamali, S.; Lee, K.; Kovnir, K. A Solution for Solution-Produced  $\beta\text{-FeSe}$ : Elucidating and Overcoming Factors that Prevent Superconductivity. *Chem. Mater.* **2015**, *27*, 588–596.
- (30) Ganga, B. G.; Ganeshraj, C.; Krishna, A. G.; Santhosh, P. N. Electronic and Optical Properties of  $\text{FeSe}_2$  Polymorphs: Solar Cell Absorber, **2013**. arXiv:1303.1381v1, arXiv preprint 6 March.
- (31) Thanikaikarasan, S.; Mahalingam, T.; Sundaram, K.; Kathalingam, A.; Deak Kim, Y.; Kim, T. Growth and Characterization of Electro synthesized Iron Selenide Thin Films. *Vacuum* **2009**, *83*, 1066–1072.
- (32) Bishwas, M. S.; Poddar, P. Discovery of Room Temperature Multiferroicity and Magneto-electric Coupling in  $\text{Fe}_3\text{Se}_4$  Nanorods. **2016**, arXiv:1612.06512, arXiv preprint 20 Dec.
- (33) Singh, D.; Gupta, S. K.; He, H.; Sonvane, Y. Prediction of new multiferroic and magnetoelectric material  $\text{Fe}_3\text{Se}_4$ . **2018**, arXiv:1805.10607, arXiv preprint 27 May.
- (34) Sen Bishwas, M.; Das, R.; Poddar, P. Large Increase in the Energy Product of  $\text{Fe}_3\text{Se}_4$  by Fe-Site Doping. *J. Phys. Chem. C* **2014**, *118*, 4016–4022.
- (35) Liu, L.; Kou, H.-Z.; Mo, W.; Liu, H.; Wang, Y. Surfactant-Assisted Synthesis of  $\alpha\text{-Fe}_2\text{O}_3$  Nanotubes and Nanorods with Shape-Dependent Magnetic Properties. *J. Phys. Chem. B* **2006**, *110*, 15218–15223.
- (36) Chatterjee, J.; Haik, Y.; Chen, C.-J. Size Dependent Magnetic Properties of Iron Oxide Nanoparticles. *J. Magn. Magn. Mater.* **2003**, *257*, 113–118.
- (37) Park, T.-J.; Papaefthymiou, G. C.; Viescas, A. J.; Moodenbaugh, A. R.; Wong, S. S. Size-Dependent Magnetic Properties of Single-Crystalline Multiferroic  $\text{BiFeO}_3$  Nanoparticles. *Nano Lett.* **2007**, *7*, 766–772.
- (38) Ma, F.; Ma, J.; Huang, J.; Li, J. The Shape Dependence of Magnetic and Microwave Properties for Ni Nanoparticles. *J. Magn. Magn. Mater.* **2012**, *324*, 205–209.
- (39) Singh, A. K.; Srivastava, O. N.; Singh, K. Shape and Size-Dependent Magnetic Properties of  $\text{Fe}_3\text{O}_4$  Nanoparticles Synthesized Using Piperidine. *Nanoscale Res. Lett.* **2017**, *12*, 298.
- (40) Gabbasov, R. R.; Cherepanov, V. M.; Chuev, M. A.; Polikarpov, M. A.; Panchenko, V. Y. Size Effect of Mössbauer Parameters in Iron Oxide Nanoparticles. *Hyperfine Interact.* **2014**, *226*, 383–387.
- (41) Artus, M.; Ben Tahar, L.; Herbst, F.; Smiri, L.; Villain, F.; Yaacoub, N.; Grenèche, J.-M.; Ammar, S.; Fiévet, F. Size-Dependent Magnetic Properties of  $\text{CoFe}_2\text{O}_4$  Nanoparticles Prepared in Polyol. *J. Phys.: Condens. Matter* **2011**, *23*, 506001.
- (42) Song, Q.; Zhang, Z. J. Shape Control and Associated Magnetic Properties of Spinel Cobalt Ferrite Nanocrystals. *J. Am. Chem. Soc.* **2004**, *126*, 6164–6168.
- (43) Tan, Y.; Zhuang, Z.; Peng, Q.; Li, Y. Room-Temperature Soft Magnetic Iron Oxide Nanocrystals: Synthesis, Characterization, and Size-Dependent Magnetic Properties. *Chem. Mater.* **2008**, *20*, 5029–5034.
- (44) Vasundhara, K.; Achary, S. N.; Deshpande, S. K.; Babu, P. D.; Meena, S. S.; Tyagi, A. K. Size Dependent Magnetic and Dielectric Properties of Nano  $\text{CoFe}_2\text{O}_4$  Prepared by a Salt Assisted Gel-Combustion Method. *J. Appl. Phys.* **2013**, *113*, 194101.
- (45) Rajendran, M.; Deka, S.; Joy, P. A.; Bhattacharya, A. K. Size-Dependent Magnetic Properties of Nanocrystalline Yttrium Iron Garnet Powders. *J. Magn. Magn. Mater.* **2006**, *301*, 212–219.
- (46) Annapu Reddy, V.; Pathak, N. P.; Nath, R. Particle Size Dependent Magnetic Properties and Phase Transitions in Multiferroic  $\text{BiFeO}_3$  Nano-Particles. *J. Alloys Compd.* **2012**, *543*, 206–212.
- (47) Ichiyanagi, Y.; Yamada, S. The Size-Dependent Magnetic Properties of  $\text{Co}_3\text{O}_4$  Nanoparticles. *Polyhedron* **2005**, *24*, 2813–2816.
- (48) Chen, J. P.; Sorensen, C. M.; Klabunde, K. J.; Hadjipanayis, G. C.; Devlin, E.; Kostikas, A. Size-Dependent Magnetic Properties of  $\text{MnFe}_2\text{O}_4$  Fine Particles Synthesized by Coprecipitation. *Phys. Rev. B: Condens. Matter Mater. Phys.* **1996**, *54*, 9288–9296.
- (49) Reddy, K. V.; Chetty, S. C. Mössbauer Studies in Fe-Se System. *Phys. Status Solidi A* **1975**, *32*, 585–592.
- (50) Nouailhetas, Q.; Koblishka-Veneva, A.; Koblishka, M. R.; Naik, P. K.; Schäfer, F.; Ogino, H.; Motz, C.; Berger, K.; Douine, B.; Slimani, Y.; Hannachi, E.; Hannachi, E. Magnetic phases in Superconducting, Polycrystalline Bulk  $\text{FeSe}$  Samples. *AIP Adv.* **2021**, *11*, 015230.
- (51) Beiranvand, R.; Mehrabi, V. Structural, Electronic and Optical Properties of Bulk and Monolayer Iron Diselenide: A Density Functional Study. *Phys. Scr.* **2021**, *96*, 065803.
- (52) Lan, M.; Xiang, G.; Nie, Y.; Yang, D.; Zhang, X. The Static and Dynamic Magnetic Properties of Monolayer Iron Dioxide and Iron Dichalcogenides. *RSC Adv.* **2016**, *6*, 31758–31761.
- (53) Xu, J.; Jang, K.; Lee, J.; Kim, H. J.; Jeong, J.; Park, J.-G.; Son, S. U. Phase-Selective Growth of Assembled  $\text{FeSe}_2$  Nanorods from Organometallic Polymers and Their Surface Magnetism. *Cry. Growth Des.* **2011**, *11*, 2707–2710.
- (54) Işık, C.; Güler, N. K.; Gürsul, M.; Ekicibil, A.; Özçelik, B. The Physical and Magnetic Properties of  $\text{FeSe}$ -11 Superconductor. *J. Phys.: Conf. Ser.* **2016**, *667*, 012002.
- (55) Shi, W.; Zhang, X.; Che, G.; Fan, W.; Liu, C. Controlled Hydrothermal Synthesis and Magnetic Properties of Three-Dimensional  $\text{FeSe}_2$  Rod Clusters and Microspheres. *Chem. Eng. J.* **2013**, *215*–216, 508–516.
- (56) Sobhani, A.; Salavati-Niasari, M. Synthesis and Characterization of  $\text{FeSe}_2$  Nanoparticles and  $\text{FeSe}_2/\text{FeO}(\text{OH})$  Nanocomposites by Hydrothermal Method. *J. Alloys Compd.* **2015**, *625*, 26–33.
- (57) Liu, A.; Chen, X.; Zhang, Z.; Jiang, Y.; Shi, C. Selective Synthesis and Magnetic Properties of  $\text{FeSe}_2$  and  $\text{FeTe}_2$  Nanocrystallites Obtained Through a Hydrothermal Co-reduction Route. *Solid State Commun.* **2006**, *138*, 538–541.

- (58) Oyetunde, T.; Omorogie, M. O.; O'Brien, P. Ferromagnetic FeSe<sub>2</sub> from a Mixed Sulphur-Selenium Complex of Iron [Fe-((SePPh<sub>2</sub>NPPh<sub>2</sub>S)<sub>2</sub>N)<sub>3</sub>] Through Pyrolysis. *Heliyon* **2020**, *6*, No. e03763.
- (59) Ulbrich, K. F.; Campos, C. E. M. Nanosized Tetragonal  $\beta$ -FeSe Phase obtained by Mechanical Alloying: Structural, Microstructural, Magnetic and Electrical Characterization. *RSC Adv.* **2018**, *8*, 8190–8198.
- (60) Lavina, B.; Downs, R.; Sinogeikin, S. The Structure of Ferroselite, FeSe<sub>2</sub>, at Pressures up to 46 GPa and Temperatures down to 50 K: A Single-Crystal Micro-Diffraction Analysis. *Crystals* **2018**, *8*, 289.
- (61) Garg, R.; Garg, V. K.; Nakamura, Y. Magnetic Properties of Iron Marcasite FeS<sub>2</sub>. *Hyperfine Interact.* **1991**, *67*, 447–451.
- (62) de Kergommeaux, A.; Faure-Vincent, J.; Pron, A.; de Bettignies, R.; Malaman, B.; Reiss, P. Surface Oxidation of Tin Chalcogenide Nanocrystals Revealed by <sup>119</sup>Sn-Mössbauer Spectroscopy. *J. Am. Chem. Soc.* **2012**, *134*, 11659–11666.
- (63) Colombara, D.; Elanzeery, H.; Nicoara, N.; Sharma, D.; Claro, M.; Schwarz, T.; Koprek, A.; Wolter, M. H.; Melchiorre, M.; Sood, M.; Valle, N.; Bondarchuk, O.; Babbe, F.; Spindler, C.; Cojocar-Miredin, O.; Raabe, D.; Dale, P. J.; Sadewasser, S.; Siebentritt, S. Chemical Instability at Chalcogenide Surfaces Impacts Chalcopyrite Devices well Beyond the Surface. *Nat. Commun.* **2020**, *11*, 3634.
- (64) Guo, Y.; Zhou, S.; Zhao, J. Oxidation Behaviors of Two-dimensional Metal Chalcogenides. *ChemNanoMat* **2020**, *6*, 838–849.
- (65) Albrecht, R.; Ruck, M. Chalcogenides by Reduction of their Dioxides in Ultra-Alkaline Media. *Angew. Chem., Int. Ed.* **2021**, *60*, 22570–22577.
- (66) Andresen, A. F.; Vestersjø, E.; Haaland, A.; Gronowitz, S.; Christiansen, H.; Rosén, U. Neutron Diffraction Investigation of Fe<sub>3</sub>Se<sub>4</sub>. *Acta Chem. Scand.* **1968**, *22*, 827–835.
- (67) Andresen, A. F.; Leciejewicz, J. A Neutron Diffraction Study of Fe<sub>7</sub>Se<sub>8</sub>. *J. Phys.* **1964**, *25*, 574–578.
- (68) Chun-Rong Lin, C. R.; Yu-Jhan Siao, Y. J.; Shin-Zong Lu, S. Z.; Chie Gau, C. Magnetic Properties of Iron Selenide Nanocrystals Synthesized by the Thermal Decomposition. *IEEE Trans. Magn.* **2009**, *45*, 4275–4278.
- (69) Okazaki, A. The Superstructures of Iron Selenide Fe<sub>7</sub>Se<sub>8</sub>. *J. Phys. Soc. Jpn.* **1961**, *16*, 1162–1170.
- (70) Singh, R. Unexpected Magnetism in Nanomaterials. *J. Magn. Mater.* **2013**, *346*, 58–73.
- (71) Kramers, H. A. L'interaction Entre les Atomes Magnétogènes dans un Cristal Paramagnétique. *Physica* **1934**, *1*, 182–192.
- (72) Anderson, P. W. Antiferromagnetism. Theory of Superexchange Interaction. *Phys. Rev.* **1950**, *79*, 350–356.
- (73) Margadonna, S.; Takabayashi, Y.; McDonald, M. T.; Kasperkiewicz, K.; Mizuguchi, Y.; Takano, Y.; Fitch, A. N.; Suard, E.; Prassides, K. Crystal Structure of the new FeSe<sub>1-x</sub> Superconductor. *Chem. Commun.* **2008**, *43*, 5607–5609.
- (74) Grechnev, G. E.; Panfilov, A. S.; Desnenko, V. A.; Fedorchenko, A. V.; Gnatchenko, S. L.; Chareev, D. A.; Volkova, O. S.; Vasiliev, A. N. Magnetic Properties of Superconducting FeSe in the Normal State. *J. Phys.: Condens. Matter* **2013**, *25*, 046004.



(12) INTERNATIONAL APPLICATION PUBLISHED UNDER THE PATENT COOPERATION TREATY (PCT)

(19) World Intellectual Property

Organization

International Bureau

(43) International Publication Date

05 November 2020 (05.11.2020)



(10) International Publication Number

WO 2020/222249 A1

(51) International Patent Classification:

C01G 1/12 (2006.01)

(21) International Application Number:

PCT/IN2020/050374

(22) International Filing Date:

21 April 2020 (21.04.2020)

(25) Filing Language:

English

(26) Publication Language:

English

(30) Priority Data:

201911017480 02 May 2019 (02.05.2019) IN

(71) Applicant: COUNCIL OF SCIENTIFIC & INDUSTRIAL RESEARCH [IN/IN]; Anusandhan Bhawan, 2 Rafi Marg, New Delhi 110001 (IN).

(72) Inventors: MONIKA, Monika; National Chemical Laboratory, Dr. Homi Bhabha Road, Pune, Maharashtra 411008 (IN). PODDAR, Pankaj; National Chemical Laboratory, Dr. Homi Bhabha Road, Pune, Maharashtra 411008 (IN).

(74) Agent: SINGH, Manisha; LEXORBIS, 709/710, Tolstoy House 15-17, Tolstoy Marg, New Delhi 110 001 (IN).

(81) Designated States (unless otherwise indicated, for every kind of national protection available): AE, AG, AL, AM, AO, AT, AU, AZ, BA, BB, BG, BH, BN, BR, BW, BY, BZ, CA, CH, CL, CN, CO, CR, CU, CZ, DE, DJ, DK, DM, DO, DZ, EC, EE, EG, ES, FI, GB, GD, GE, GH, GM, GT, HN, HR, HU, ID, IL, IN, IR, IS, JO, JP, KE, KG, KH, KN, KP, KR, KW, KZ, LA, LC, LK, LR, LS, LU, LY, MA, MD, ME, MG, MK, MN, MW, MX, MY, MZ, NA, NG, NI, NO, NZ, OM, PA, PE, PG, PH, PL, PT, QA, RO, RS, RU, RW, SA, SC, SD, SE, SG, SK, SL, ST, SV, SY, TH, TJ, TM, TN, TR, TT, TZ, UA, UG, US, UZ, VC, VN, WS, ZA, ZM, ZW.

(84) Designated States (unless otherwise indicated, for every kind of regional protection available): ARIPO (BW, GH, GM, KE, LR, LS, MW, MZ, NA, RW, SD, SL, ST, SZ, TZ, UG, ZM, ZW), Eurasian (AM, AZ, BY, KG, KZ, RU, TJ, TM), European (AL, AT, BE, BG, CH, CY, CZ, DE, DK, EE, ES, FI, FR, GB, GR, HR, HU, IE, IS, IT, LT, LU, LV, MC, MK, MT, NL, NO, PL, PT, RO, RS, SE, SI, SK, SM, TR), OAPI (BF, BJ, CF, CG, CI, CM, GA, GN, GQ, GW, KM, ML, MR, NE, SN, TD, TG).

Declarations under Rule 4.17:

- as to applicant's entitlement to apply for and be granted a patent (Rule 4.17(ii))
- as to the applicant's entitlement to claim the priority of the earlier application (Rule 4.17(iii))

(54) Title: A PROCESS FOR THE SYNTHESIS OF NANOPARTICLES OF TRANSITION METAL CHALCOGENIDES

(57) Abstract: The present invention relates to a process for the synthesis of transition metal chalcogenides (TMC) having formula (I). More particularly, the present work relates to a one pot single phase process for the synthesis of Formula (I) TMC system having formula (I) by wet chemistry.

WO 2020/222249 A1

## A PROCESS FOR THE SYNTHESIS OF NANOPARTICLES OF TRANSITION METAL CHALCOGENIDES

### FIELD OF THE INVENTION:

The present invention relates to a process for the synthesis of transition metal chalcogenides (TMC) having formula (I). More particularly, the present work relates to a one-pot single phase process for the synthesis of TMC system having formula (I) by wet chemistry.

### BACKGROUND AND PRIOR ART OF THE INVENTION:

Transition-metal chalcogenides represent an important class of materials with rich phase diagram and industrial applications. The electronic (optical, magnetic, and electrical) and thermal properties are so sensitive to the crystalline phase, stoichiometry, shape, size that it is essential to reach a good control over the chemistry of phase formation. TMC consisting of metal atoms (Fe, Co, and Ni) and chalcogen atoms (S, Se, Te) have renewed interest as very attractive candidates for applications in devices including fuel-cells, solar-cells, light-emitting-diodes, sensors, memory-devices, thermoelectric devices, supercapacitors, Li- ion batteries, magnetic materials etc. Among the TMC,  $Fe_xSe_y$  compounds (with x: y varying from 1:2 to 1:1) are of great importance because of their interesting and unique magnetic, electrical, thermal, and optical properties which are strongly related on the stoichiometric ratio between Fe and Se as well as their crystalline structure. Family of iron selenides have four stable phases:  $FeSe_2$ ,  $Fe_3Se_4$ ,  $Fe_7Se_8$ , and  $FeSe$  having orthorhombic (O) marcasite, monoclinic (M) and hexagonal (H) NiAs type, and tetragonal (T) PbO type crystal structure, respectively. Existence of multiple phases with abundantly different crystal structures indicates the complexity of the system and therefore, phase-selective syntheses were quite challenging for this system. In solid state method, as reported by Grivel *et al.* (Supercond. Sci. Technol. 24 (2011) 015007) there was phase transformation of Fe-Se system with respect to temperature in a sequence of  $FeSe_2 \rightarrow Fe_3Se_4 \rightarrow Fe_7Se_8 \rightarrow \beta\text{-FeSe}$  at 300 °C, 320 °C, ~ 340 °C, 350 °C - 370 °C, respectively. In this article the phase boundaries were not sharply defined as a function of temperature. Often at a particular temperature, phases evolved out of the other phases leading to overall impurity.

Numerous solution processes have been applied to synthesize these compounds. For example,  $Fe_3Se_4$  and  $Fe_7Se_8$  nanoparticles (NPs) were obtained via the thermal decomposition method at 340 °C-350 °C,  $Fe_3Se_4$  were synthesized at 300 °C by one-pot high-temperature organic-solution-phase method, flower-like  $FeSe_2$  NPs were synthesized

via a solvothermal approach at 200 °C, FeSe<sub>x</sub> (x=1,2) NPs were synthesized via the hot-injection method at 330 °C and FeSe<sub>2</sub> NPs were synthesized via hydrothermal method at 140 °C for 13 h. The FeSe NPs were synthesized by solvothermal reaction in an autoclave at 220 °C for 24 h. These methods involved the high temperature, long reaction time, complex apparatus, expensive chemicals, or drastic conditions to synthesis the Fe-Se NPs.

Thus, adopting a simple, low-temperature, short-time, and low-cost method with well-defined shape and high crystallinity of Fe-Se NPs is much desired. To overcome the prior drawbacks the present invention provides a one pot single phase process for the synthesis of transition metal chalcogenides (TMC) system having formula I.

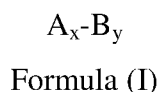
#### 10 **OBJECTIVES OF THE INVENTION:**

The objective of the present invention is to provide a one pot single phase process for the synthesis of transition metal chalcogenides (TMC) having formula (I).

#### **SUMMARY OF THE INVENTION:**

Accordingly, the present invention provides a one pot single phase process for the synthesis of transition metal chalcogenides (TMC) system having formula (I) by using wet chemistry. This method comprises mixing both precursors of transition metal and chalcogen in the presence of a reducing agent and an accelerating agent at a temperature in the range of 100 °C to 300 °C for a time period varied from 30 min to 10 h to obtain transition metal chalcogenides (TMC) having formula (I).

20 The transition metal chalcogenides (TMC) system having formula (I) is represented as



wherein,

A is selected from iron, chromium, manganese, cobalt, or nickel.

25 B is selected from selenium, sulphur, or tellurium.

The A<sub>x</sub>-B<sub>y</sub> is selected from AB<sub>2</sub>, A<sub>3</sub>B<sub>4</sub>, A<sub>7</sub>B<sub>8</sub> or AB,

wherein x and y are in ranges from 1:2 to 1:1.

#### **BRIEF DESCRIPTION OF THE DRAWINGS**

30 **Figure 1:** Powder X-ray diffraction patterns collected at various temperatures during the heating ramp a. 25 °C b. 190 °C c. 360 °C d. 394 °C and e. 486 °C for prior art.

**Figure 2:** Powder X-ray diffraction patterns collected at various temperatures during the heating ramp for present invention.

**Figure 3:** Iron - Selenium phase diagram.

**Figure 4:** XRD patterns of the as-synthesized a) FeSe<sub>2</sub> NPs, b) Fe<sub>3</sub>Se<sub>4</sub> NPs, c) Fe<sub>7</sub>Se<sub>8</sub> NPs and d) FeSe NPs.

**Figure 5:** Magnetization (M) vs. applied magnetic field (H) hysteresis loops of a) FeSe<sub>2</sub> b) Fe<sub>3</sub>Se<sub>4</sub> c) Fe<sub>7</sub>Se<sub>8</sub> and d) FeSe measured by the vibrating sample magnetometer at 300 K.

5 **Figure 6:** Magnetization (M) vs. applied magnetic field (H) hysteresis loops of a) FeSe<sub>2</sub> b) Fe<sub>3</sub>Se<sub>4</sub> c) Fe<sub>7</sub>Se<sub>8</sub> and d) FeSe measured by the vibrating sample magnetometer at 10 K.

**Figure 7:** TEM measurements of as-synthesized NPs.

**Figure 8:** Thermal Gravimetric Analysis (TGA).

**Figure 9:** Raman spectra.

10 **Figure 10:** TEM images of as-synthesized NPs with different organic solvents.

**Figure 11:** XRD patterns of the as-synthesized Co<sub>3</sub>Se<sub>4</sub> NPs.

**Figure 12:** XRD patterns of the as-synthesized Ni<sub>3</sub>Se<sub>4</sub> NPs.

**Figure 13:** XRD patterns of the as-synthesized MnSe NPs.

**Figure 14:** XRD patterns of the as-synthesized Fe<sub>3</sub>Se<sub>4</sub> NPs with different crystallite size.

15 **Figure 15:** Magnetization (M) vs. applied magnetic field (H) hysteresis loops of Fe<sub>3</sub>Se<sub>4</sub> NPs with different crystallite size measured by the vibrating sample magnetometer at 300 K.

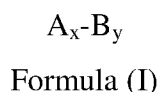
**Figure 16:** Coercive field (H<sub>c</sub>) and remanence magnetization (M<sub>r</sub>) vs. crystallite size of Fe<sub>3</sub>Se<sub>4</sub> NPs.

#### DETAILED DESCRIPTION OF THE INVENTION

20 The invention will now be described in detail in connection with certain preferred and optional embodiments, so that various aspects thereof may be more fully understood and appreciated.

The present invention provides a one-pot single phase process for the synthesis of a transition metal chalcogenide (TMC) nanoparticles (NPs) system having formula (I) by using wet chemical method, the process comprising mixing and stirring both a transition metal precursor and a chalcogen precursor in the presence of a reducing agent and an accelerating agent and stirring at a temperature in the range of 100 °C to 300 °C for a time period varied from 30 min to 10 h to obtain the TMC NPs system having formula (I).

30 The TMC NPs system having formula (I) is represented as



wherein,

A is selected from the group consisting of iron, chromium, manganese, cobalt, and nickel;

B is selected from the group consisting of selenium, sulphur, and tellurium;

$A_x-B_y$  is selected from  $AB_2$ ,  $A_3B_4$ ,  $A_7B_8$  and  $AB$ ;

5 wherein the ratio of x and y are in ranges from 1:2 to 1:1.

The system of formula (I) is selected from  $FeSe_2$ ,  $Fe_3Se_4$ ,  $Fe_7Se_8$ ,  $FeSe$ ,  $Co_3Se_4$ ,  $Ni_3Se_4$  and  $MnSe$ .

10 The size of as-synthesized TMC NPs are in the range of 5 nm to 350 nm. The shape of as-synthesized TMC NPs is selected from nano-rod, nano-sphere, nano-sheet, nano-platelet, nano-cube, and mixed shape.

Any organic solvent, which has the ability to make complex with transition metal (Fe) and chalcogen (Se) precursors, and simultaneously reduce them can be used as a reducing agent for TMC system. Moreover, any organic solvent can use as an accelerating agent which have the ability to make complex with chalcogen (Se powder). The particular  
15 temperature required for pure phase formation will strongly depends on the organic solvent. As going towards the stronger reducing and accelerating agent, the temperature and time for that particular phase changes.

The reducing agent is selected from oleylamine (OLA), oleic acid, 1-octadecene (1-ODE), octadecylamine, oleyl alcohol, pentylamine, ethylamine and n-octadecane.

20 The accelerating agent is selected from 1-octadecene, oleic acid, oleylamine, octadecylamine, oleyl alcohol, pentylamine, and ethylamine.

The transition metal precursor is selected from Tris(acetylacetonato) iron (III) ( $Fe(acac)_3$ ), Cobalt(III) acetylacetonate, Nickel(II) acetylacetonate and Manganese(III)acetylacetonate.

25 The chalcogen precursor is Se powder.

In one of the features, the present invention provides a one pot single phase process for the synthesis of transition metal chalcogenides (TMC) nanoparticles system particularly Fe-Se system comprising the steps of:

- 30 a) mixing Se powder and  $Fe(acac)_3$  at room temperature (25 °C to 30 °C) in the presence of an organic solvent under the blanket of inert gas with constant magnetic stirring;
- b) raising the temperature to 40 °C followed by stirring for 30 min and taking the first sample of only Se powder;

- c) further increasing the temperature to 50 °C followed by stirring for 30 min and taking the second sample of only Se powder and
- d) increasing the temperature up to 340 °C with the rate of 10 °C/30 min and taking the sample at every 10 °C rise in temperature, as the temperature increases, FeSe<sub>2</sub> starts forming followed by Fe<sub>3</sub>Se<sub>4</sub>, Fe<sub>7</sub>Se<sub>8</sub> and FeSe.

In each step 2 mL aliquots are withdrawn using a long needle-glass syringe. All the samples are stored in small glass vials and naturally quenched to room temperature (RT) for further investigation.

In another feature of the present invention, the organic solvent is selected from oleylamine (OLA); oleylamine & 1-octadecene (OLA & 1-ODE) and oleylamine (OLA) & pre-dissolved Se powder in 1-octadecene (1-ODE).

Three separate reactions are carried out with above procedure except the solvent conditions; in one reaction only OLA has been used as a solvent, in second reaction a combination of OLA and 1-ODE (in 3:2 ratio) has been used as a solvent; and in the last reaction Se powder was pre-dissolved in 1-ODE and used that as a Se precursor with OLA and Fe(acac)<sub>3</sub>.

Figure 1 depicts diffraction patterns collected at various temperatures during the heating ramp for prior art. The phase boundaries were not sharply defined as a function of temperature. Often at a particular temperature, phases evolved out of the other phases leading to overall impurity.

Figure 2 depicts diffraction patterns collected at various temperatures during the heating ramp for present invention. Phase boundaries were mostly sharply defined and well isolated as a function of temperatures and phase impurities were avoided. The diffraction pattern shows the phase evolution from FeSe<sub>2</sub> to Fe<sub>3</sub>Se<sub>4</sub> followed by Fe<sub>7</sub>Se<sub>8</sub> and FeSe.

Table 1. Results of diffraction patterns collected at various temperatures during the heating ramp.

Reaction	Fe Precursor	Se precursor	Solvent	Temperature-range	Phase
A	Fe(acac) <sub>3</sub>	Se powder	OLA	RT – 100 °C	Se
				110 – 130 °C	Se + FeSe <sub>2</sub>
				140 – 220 °C	FeSe <sub>2</sub>
				230 – 240 °C	FeSe <sub>2</sub> + Fe <sub>3</sub> Se <sub>4</sub>
				250 – 270 °C	Fe <sub>3</sub> Se <sub>4</sub>
				280 – 340 °C	Fe <sub>7</sub> Se <sub>8</sub>
B	Fe(acac) <sub>3</sub>	Se powder (Se was pre –	OLA + 1-ODE	RT – 100 °C	Se
				110 – 230 °C	FeSe <sub>2</sub>

		dissolved in 1-ODE at 30 °C for 6 h)		240 – 250 °C	FeSe <sub>2</sub> + Fe <sub>3</sub> Se <sub>4</sub>
				260 °C	Fe <sub>3</sub> Se <sub>4</sub> + FeSe <sub>2</sub>
				270 °C	Fe <sub>7</sub> Se <sub>8</sub>
				280 – 300 °C	FeSe

Figure 3 depicts Iron - Selenium phase diagram. Phases 1 to 5 show the results of five prolonged reactions. The experiments were done by varying the amount of Se from 37.5 to 100 at % with constant Fe precursor in presence of OLA and 1-ODE together from RT to 340 °C. The phase transformation has been confirmed by doing the WAXS (wide angle X-ray scattering) of all the samples, taken at every 10 °C rise in temperature from 30 °C - 340 °C and the data are compared with the JCPDS files to conform the phases.

Table 2: Results of phases formed at minimal possible temperature with pertinent time.

Phases	Solvent	Ramping Rate	Temp.	Time	Remarks
FeSe <sub>2</sub>	OLA	2 °C min <sup>-1</sup>	150 °C	2 h	Single phase FeSe <sub>2</sub> NPs
Fe <sub>3</sub> Se <sub>4</sub>	OLA	2 °C min <sup>-1</sup>	230 °C	8 h	Fe <sub>3</sub> Se <sub>4</sub> + FeSe <sub>2</sub> (impurity phase)
		2 °C min <sup>-1</sup>	240 °C	6 h	
		2 °C min <sup>-1</sup>	250 °C	5 h	
		120 °C - 0.5 h + 2 °C min <sup>-1</sup> up to 200 °C + 2 °C min <sup>-1</sup> up to 250 °C	250 °C	4 h	Fe <sub>3</sub> Se <sub>4</sub> + FeSe <sub>2</sub> (impurity phase)
		2 °C min <sup>-1</sup>	260 °C	5 h	
		120 °C - 0.5 h + 2 °C min <sup>-1</sup> up to 200 °C + 2 °C min <sup>-1</sup> up to 250 °C	260 °C	2 h	Single phase Fe <sub>3</sub> Se <sub>4</sub> NPs
Fe <sub>7</sub> Se <sub>8</sub>	OLA	2 °C min <sup>-1</sup>	270 °C	4 h	Fe <sub>3</sub> Se <sub>4</sub> + FeSe <sub>2</sub> (impurity phase)
		5 °C min <sup>-1</sup> up to 230 °C + 2 °C min <sup>-1</sup> up to 270 °C	270 °C	4 h	Fe <sub>7</sub> Se <sub>8</sub> + Fe <sub>3</sub> Se <sub>4</sub> (impurity phase)
		2 °C min <sup>-1</sup>	280 °C	4 h, 5 h	
		5 °C min <sup>-1</sup> up to 230 °C + 2 °C min <sup>-1</sup> up to 280 °C	280 °C	4 h	Single phase Fe <sub>7</sub> Se <sub>8</sub> NPs
	OLA	5 °C min <sup>-1</sup> up to 230 °C + 2 °C min <sup>-1</sup> up to 280 °C	280 °C	4 h	Fe <sub>7</sub> Se <sub>8</sub>

	OLA + 1-ODE	5 °C min <sup>-1</sup> up to 230 °C + 2 °C min <sup>-1</sup> up to 280 °C	280 °C	4 h	FeSe + Fe <sub>7</sub> Se <sub>8</sub> (impurity phase)
	OLA + 1-ODE	5 °C min <sup>-1</sup> up to 230 °C + 2 °C min <sup>-1</sup> up to 280 °C	280 °C	4 h	Single phase FeSe NPs (Se powder was pre-dissolved in 1- ODE)

Figure 4 depicts XRD patterns of the as-synthesized a) FeSe<sub>2</sub> NPs, b) Fe<sub>3</sub>Se<sub>4</sub> NPs, c) Fe<sub>7</sub>Se<sub>8</sub> NPs, and d) FeSe NPs. All the XRD peaks are in good agreement with the JCPDS (Joint Committee on Powder Diffraction Standards) data files— (74-0247) for FeSe<sub>2</sub>, (73-2021) for Fe<sub>3</sub>Se<sub>4</sub>, (71-0586) for Fe<sub>7</sub>Se<sub>8</sub> and (85-0735) for FeSe without ambiguous reflections. The XRD and magnetic measurements prove the high purity of as-synthesized NPs. Crystallite size of FeSe<sub>2</sub> = 23 nm, Fe<sub>3</sub>Se<sub>4</sub> = 35 nm, Fe<sub>7</sub>Se<sub>8</sub> = 29 nm, FeSe = 46 nm as estimated from the XRD pattern using Scherrer's formula.

Figure 5 depicts magnetization (M) vs. magnetic field (H) hysteresis loops of a) FeSe<sub>2</sub> b) Fe<sub>3</sub>Se<sub>4</sub> c) Fe<sub>7</sub>Se<sub>8</sub> and d) FeSe measured by the vibrating sample magnetometer at 300 K in an applied magnetic field up to ±60 kOe. The M-H curves reveal prominent M-H characteristics indicating the synthesis of pure phase. Figure a) shows the M-H curve of FeSe<sub>2</sub> NPs revealing paramagnetic behavior with coercivity (H<sub>c</sub>) 146 Oe. Figure b-c) shows the M-H curves of Fe<sub>3</sub>Se<sub>4</sub> and Fe<sub>7</sub>Se<sub>8</sub> NPs having ferrimagnetic behavior. These hysteresis loops show the coercivity 1.6 kOe and 1.8 kOe, respectively. In Figure d) the hysteresis loop of FeSe reveals ferromagnetic nature of NPs having coercivity (H<sub>c</sub>) 282 Oe.

Figure 6 depicts M-H hysteresis loops of a) FeSe<sub>2</sub> b) Fe<sub>3</sub>Se<sub>4</sub> c) Fe<sub>7</sub>Se<sub>8</sub> and d) FeSe measured by the vibrating sample magnetometer at 10 K. The coercivity (H<sub>c</sub>) of FeSe<sub>2</sub> NPs rises to 200 Oe with ferromagnetic behavior. The H<sub>c</sub> value of Fe<sub>3</sub>Se<sub>4</sub> nanorods raises nearly 20-fold to about 32 kOe. The H<sub>c</sub> value of Fe<sub>7</sub>Se<sub>8</sub> nanorods rises more than 7-fold to about 13.8 kOe. The coercivity (H<sub>c</sub>) of FeSe nanorods increases to about 4.4 kOe.

Table 3: Magnetic parameters measured at 300 K and 10 K for Fe-Se system. H<sub>c</sub> and σ<sub>R</sub> represents the coercivity and remanence respectively obtained from hysteresis loops at various temperature.



Phases	$H_c$ (Oe)		$\sigma_R$ (emu/g)	
	300 K	10 K	300 K	10 K
FeSe <sub>2</sub>	146	200	~ 0	0.4
Fe <sub>3</sub> Se <sub>4</sub>	1600	32000	1.2	7.3
Fe <sub>7</sub> Se <sub>8</sub>	1800	13800	2	8.6
FeSe	300	4400	0.1	0.4

Figure 7 shows TEM measurements of as-synthesized NPs. Typical TEM images of as-synthesized a) FeSe<sub>2</sub>, b) Fe<sub>3</sub>Se<sub>4</sub>, c) Fe<sub>7</sub>Se<sub>8</sub> and d) FeSe NPs shows the rod like features and inset shows the iron selenide nanocacti with rod like features growing on the surface [Scale bar in the insets are 100 nm]. a') to d') shows the lattice fringes space at 2.5 Å, 2.7 Å, 5.4 Å and 5.5 Å represents the (111), (-202), (101) and (001) of Fe-Se system respectively [The inset SAED pattern]. The diffraction pattern obtained for all the nanostructures were matched well with the crystal planes of Fe-Se system and have been assigned to (002), (101), (111) planes for FeSe<sub>2</sub>, (-202), (011) planes for Fe<sub>3</sub>Se<sub>4</sub>, (203), (101), (206) planes for Fe<sub>7</sub>Se<sub>8</sub> and (001), (101) planes for FeSe. Thus, d-spacing calculated in TEM are in good agreement with those given in the standard JCPDS for all the phases of Fe-Se system.

Figure 8 shows Thermal Gravimetric Analysis (TGA). All the samples were undergone with different step decomposition. The first step in all samples is related to the loss of all organic fragments capped on NPs, this step was up to 460 °C. The FeSe<sub>2</sub> NPs further go through three more step decomposition. The steps assigned to the decomposition of FeSe<sub>2</sub> NPs to Fe<sub>3</sub>Se<sub>4</sub>; Fe<sub>3</sub>Se<sub>4</sub> NPs to the Fe<sub>7</sub>Se<sub>8</sub> followed by the conversion of Fe<sub>7</sub>Se<sub>8</sub> to FeSe and final step, the decomposition of FeSe NPs started at 875 °C and remains up to 1000 °C. The Fe<sub>3</sub>Se<sub>4</sub> NPs further go through final step, assigned to the decomposition of Fe<sub>3</sub>Se<sub>4</sub> started at 725 °C and gradually decreases up to 1000 °C. The Fe<sub>7</sub>Se<sub>8</sub> NPs go through final step, assigned to the decomposition of Fe<sub>7</sub>Se<sub>8</sub> started at 770 °C and gradually decreases up to 1000 °C. The FeSe NPs go through final step assigned to the decomposition of FeSe started at 875 °C and gradually decreases up to 1000 °C.

Figure 9 shows Raman Spectra of all the samples having six characteristic peaks at 225, 244, 292, 410, 496, and 611 cm<sup>-1</sup>. The presences of Fe-Se near 225 cm<sup>-1</sup>, 292 cm<sup>-1</sup> and 610 cm<sup>-1</sup>, as well as Fe-O at 410 cm<sup>-1</sup> are identified for all the samples.

Figure 10 shows TEM images of as-synthesized NPs in the presence of different organic solvents a) n-octadecane, b) 1-octadecene, c) octadecylamine and d) oleylamine. TEM data shows the strong depends of size, shape, and stability on solvent. Figure shows the as-synthesized nanospheres in presence of n-octadecane, nanoplatelets in 1-octadecene, nano-spheres in octadecylamine and nanocacti with rod like features growing on the surface in OLA.

To control the size of transition metal chalcogenides ( $\text{Fe}_3\text{Se}_4$ ), the reaction parameters are optimized to find suitable synthesis conditions to crystallize various sizes of  $\text{Fe}_3\text{Se}_4$  compound by following the one-pot thermal decomposition method as shown in table 4 and the observed data shows that as the reaction temperature increases crystallite size also increases, table 5.

Table 4: Summary of the experimental conditions to control the size of the  $\text{Fe}_3\text{Se}_4$  NPs.

Reaction	Solvent	Fe precursor	Se precursor	Step 1		Step 2		Results
				Temp. (°C)	Time (min)	Temp. (°C)	Time (min)	
1	OLA	$\text{Fe}(\text{acac})_3$	Se powder	120	30	260	120	S1
2						300	80	S2
3						330	70	S3

Table 5 describes list of calculated crystallite size along different planes of all the as-synthesized  $\text{Fe}_3\text{Se}_4$  NPs, indicating the influence of the temperature on the crystallite size of the products evolve out of solution chemistry.

Table 5: List of calculated crystallite size along different planes of all the as-synthesized  $\text{Fe}_3\text{Se}_4$  NPs

Sample	Crystallite size along following planes: d ( $\pm 3$ nm)		
	(-112)	(202)	(204)
S1	33	25	22
S2	37	31	24
S3	42	35	26

Figure 11 depicts XRD patterns of the as-synthesized  $\text{Co}_3\text{Se}_4$  NPs. The XRD peaks are in good agreement with the 99989-ICSD (Inorganic Crystal Structure Database) data file without ambiguous reflections.

Figure 12 depicts XRD patterns of the as-synthesized  $\text{Ni}_3\text{Se}_4$  NPs. The XRD peaks are in good agreement with the JCPDS (Joint Committee on Powder Diffraction Standards) data files— (65-1220) without ambiguous reflections.

Figure 13 depicts XRD patterns of the as-synthesized  $\text{MnSe}$  NPs. The XRD peaks are in good agreement with the JCPDS (Joint Committee on Powder Diffraction Standards) data files— (65-7705) without ambiguous reflections.

Figure 14 depicts XRD patterns of the as-synthesized  $\text{Fe}_3\text{Se}_4$  NPs with different crystallite size. The XRD peaks are in good agreement with the JCPDS (Joint Committee on Powder Diffraction Standards) data files— (73-2021) without ambiguous reflections.

Figure 15 depicts M-H hysteresis loops of S1, S2 and S3 of  $\text{Fe}_3\text{Se}_4$  measured by the vibrating sample magnetometer at 300 K in an applied magnetic field up to  $\pm 60$  kOe.

Figure 16 depicts coercive field ( $H_c$ ) vs crystallite size (left) and remanence magnetization ( $M_r$ ) vs crystallite size (right) for  $\text{Fe}_3\text{Se}_4$  NPs.

**Examples:** Following examples are given by way of illustration therefore should not be construed to limit the scope of the invention.

#### **Example 1: Synthesis of the Fe–Se System to Examine the Phase Transformation**

Synthesis of the Fe–Se System in OLA and 1-ODE. To study the effect of stoichiometry on the phase-transformation five prolonged reactions were performed by varying the amount of Se from 37.5 to 100 wt %, the stoichiometry of Fe/Se ranging from 1:0.75 (0.35 g, 0.059 g) to 1:2 (0.35 g, 0.158 g). All the reactions were carried out in the presence of 10 mL of 1-ODE and 15 mL of OLA in a 100 mL three-neck round-bottom (RB) flask under the blanket of nitrogen with constant magnetic stirring. The temperature was raised from 30 to 340 °C at a ramping rate of 2 °C  $\text{min}^{-1}$ . For every 10 °C rise in the temperature, hold-time was ~30 min. In each step, 2 mL aliquots were withdrawn using a long needle glass syringe to study the phase evolution. All the samples were stored in small glass vials and naturally quenched to RT for further investigation by wide-angle X-ray scattering (WAXS). The phase diagram was plotted after assembling the WAXS results, which inferred the effect of stoichiometry along with temperature on phase transformation of the Fe–Se system.

**Example 2: Synthesis of the Fe–Se System in OLA**

To study the effect of solvents on phase transformation one synthesis was done by following the same procedure as mentioned above except that only the OLA (15 mL) was used as an organic solvent with the stoichiometry of 1:1.

**5 Example 3: Synthesis of the Fe–Se System in OLA and Predissolved Se Powder in 1-ODE**

In order to examine the effect of solvents, one more reaction was done with the same procedure as mentioned earlier except that the Se powder was predissolved in 1-ODE under a

10 nitrogen environment with constant magnetic stirring at 30 °C for 6 h.

**Example 4: Synthesis of FeSe<sub>2</sub> NPs**

In a conventional reaction, 0.353 g (1 mmol) of Fe(acac)<sub>3</sub> and 0.158 g (2 mmol) of Se powders were added to 15 ml of OLA in a 100 mL three-neck round bottom (RB) flask. The mixture was stirred under a flow of high-purity nitrogen gas at 30 °C. Then the  
15 temperature was raised to 150 °C at a ramping rate of 2 °C min<sup>-1</sup> and kept at 150 °C for 2 h. A thermometer was placed inside the RB-flask and the temperature was kept stable within ±1.0 °C during the 2 h long dwell-time at 150 °C. The solution was cooled to RT by removing the heating source. After cooling, 20 ml of 2-propanol was added to the solution to give a black precipitate, which was separated from the solution by centrifugation. The  
20 obtained NPs were rewashed with the mixture of 15 ml hexane and 10 ml 2-propanol. Finally, the product was dried in a vacuum at 28°C and utilized for further characterization.

**Example 5: Synthesis of Fe<sub>3</sub>Se<sub>4</sub> NPs**

A 0.53 g (1.5 mmol) portion of Fe(acac)<sub>3</sub> and 0.158 g (2 mmol) of Se powder were mixed in 15 mL of OLA in a 100 mL three-neck RB flask. The mixture was heated to 120  
25 °C and maintained for 30 min. Then, the temperature was raised at a heating rate of 2 °C min<sup>-1</sup> up to 200 °C and 5 °C min<sup>-1</sup> was used to reach a maximum temperature of 260 °C; at which the sample was maintained for 2 h.

**Example 6: Synthesis of Fe<sub>7</sub>Se<sub>8</sub> NPs**

A 0.618 g (1.75 mmol) of Fe(acac)<sub>3</sub> and 0.158 g (2 mmol) of Se powder were added  
30 in 15 mL of OLA in a 100 mL three-neck RB flask. The mixture was heated to the designed temperature at a ramping rate of 5 °C min<sup>-1</sup> from 30 °C to 230 °C and then after ramping rate was decreased to 2 °C min<sup>-1</sup> up to 280 °C, and kept for 4 h.

**Example 7: Synthesis of FeSe NPs**

This synthesis is similar to the synthesis of Fe<sub>7</sub>Se<sub>8</sub> NPs with stoichiometry 1:1 except that the Se powder was pre-dissolved in 11 mL of 1-ODE at 30 °C with constant magnetic stirring for 6 h.

**5 Example 8: Synthesis with different solvents**

These syntheses are similar to the above synthesis except that 1-octadecene, octadecylamine and n-octadecane was used instead of OLA.

**Example 9: Synthesis of Co<sub>3</sub>Se<sub>4</sub> NPs**

10 A 1.5 mmol portion of Cobalt(III) acetylacetonate (Co(acac)<sub>3</sub>) and 2 mmol of Se powder were mixed in 15 mL of OLA in a 100 mL three-neck RB flask. The mixture was heated to 120 °C and maintained for 30 min. Then, the temperature was raised at a heating rate of 2 °C min<sup>-1</sup> up to 200 °C and 5 °C min<sup>-1</sup> was used to reach a maximum temperature of 300 °C; at which the sample was maintained for 2 h.

**Example 10: Synthesis of Ni<sub>3</sub>Se<sub>4</sub> NPs**

15 A 1.5 mmol portion of Nickel(II) acetylacetonate (Ni(acac)<sub>2</sub>) and 2 mmol of Se powder were mixed in 15 mL of OLA in a 100 mL three-neck RB flask. The mixture was heated to 120 °C and maintained for 30 min. Then, the temperature was raised at a heating rate of 2 °C min<sup>-1</sup> up to 200 °C and 5 °C min<sup>-1</sup> was used to reach a maximum temperature of 300 °C; at which the sample was maintained for 2 h.

**20 Example 11: Synthesis of MnSe NPs**

A 2 mmol portion of Manganese(III)acetylacetonate (Mn(acac)<sub>3</sub>) and 2 mmol of Se powder were mixed in 15 mL of OLA in a 100 mL three-neck RB flask. The mixture was heated to 120 °C and maintained for 30 min. Then, the temperature was raised at a heating rate of 2 °C min<sup>-1</sup> up to 200 °C and 5 °C min<sup>-1</sup> was used to reach a maximum temperature of 25 300 °C; at which the sample was maintained for 2 h.

**Advantages of the invention:**

1. The present method is simpler and economical than solid state route and required relatively lower temperature.
2. This method is capable of giving high purity in phases and by this route it is easy to 30 control the size, shape, and crystalline structure.
3. It is possible to control the size of NPs by varying the temperature with pertinent time as well as shape by changing the solvents.
4. This route is not only applicable for these 4 phases but also for other iron chalcogenide phases.

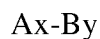
5. Various other transition metal chalcogenides consisting of metal atoms (Fe, Cr, Mn, Co, and Ni) and chalcogen atoms (S, Se, Te) can also be synthesized by this route after optimizing the reaction conditions (temperature, precursors, solvents).

**Claims:**

1. A one pot single phase process for the synthesis of a transition metal chalcogenide nanoparticle system having formula (I) by using wet chemical method, the process comprising mixing and stirring both a transition metal precursor and a chalcogen precursor in the presence of a reducing agent and an accelerating agent and stirring at a temperature in the range of 100 °C to 300 °C for a time period varied from 30 min to 10 h to obtain the transition metal chalcogenide nanoparticle system having formula (I),

wherein

the formula (I) is represented as



Formula (I)

wherein,

A is selected from the group consisting of iron, chromium, manganese, cobalt, and nickel;

B is selected from the group consisting of selenium, sulphur, and tellurium;

$A_x-B_y$  is selected from  $AB_2$ ,  $A_3B_4$ ,  $A_7B_8$  and  $AB$ ;

wherein the ratio of x and y are in ranges from 1:2 to 1:1.

2. The process as claimed in claim 1, wherein said system of formula (I) is selected from  $FeSe_2$ ,  $Fe_3Se_4$ ,  $Fe_7Se_8$ ,  $FeSe$ ,  $Co_3Se_4$ ,  $Ni_3Se_4$  and  $MnSe$ .

3. The process as claimed in claim 1, wherein the size of as-synthesized transition metal chalcogenide nanoparticle is in the range of 5 nm to 350 nm.

4. The process as claimed in claim 1, wherein the shape of as-synthesized transition metal chalcogenide nanoparticle is selected from nano-rod, nano-sphere, nano-sheet, nano-platelet, nano-cube and mixed shape.

5. The process as claimed in claim 1, wherein the reducing agent is selected from oleylamine, oleic acid, 1-octadecene, octadecylamine, oleyl alcohol, pentylamine, ethylamine and n-octadecane.

6. The process as claimed in claim 1, wherein the accelerating agent is selected from 1-octadecene, oleic acid, oleylamine, octadecylamine, oleyl alcohol, pentylamine, and ethylamine.

7. The process as claimed in claim 1, wherein the transition metal precursor is selected from Tris(acetylacetonato) iron (III), Cobalt(III) acetylacetonate, Nickel(II) acetylacetonate and Manganese(III)acetylacetonate.

8. The process as claimed in claim 1, wherein the chalcogen precursor is Se powder.

9. A one pot single phase process for the synthesis of transition metal chalcogenides nanoparticles system wherein said system is Fe-Se system comprising the steps of:
- a) mixing Se powder and  $\text{Fe}(\text{acac})_3$  at a temperature in the range of 25 °C to 30 °C in the presence of an organic solvent under the blanket of inert gas with constant magnetic stirring;
  - b) raising the temperature to 40 °C followed by stirring for 30 min and taking the first sample of only Se powder;
  - c) further increasing the temperature to 50 °C followed by stirring for 30 min and taking the second sample of only Se powder; and
  - d) increasing the temperature up to 340 °C with the rate of 10 °C/30 min and taking the sample at every 10 °C rise in temperature, as the temperature increases,  $\text{FeSe}_2$  starts forming followed by  $\text{Fe}_3\text{Se}_4$ ,  $\text{Fe}_7\text{Se}_8$  and FeSe.
10. The process as claimed in claim 9, wherein said organic solvent is selected from oleylamine; oleylamine & 1-octadecene; and oleylamine & pre-dissolved Se powder in 1-octadecene.



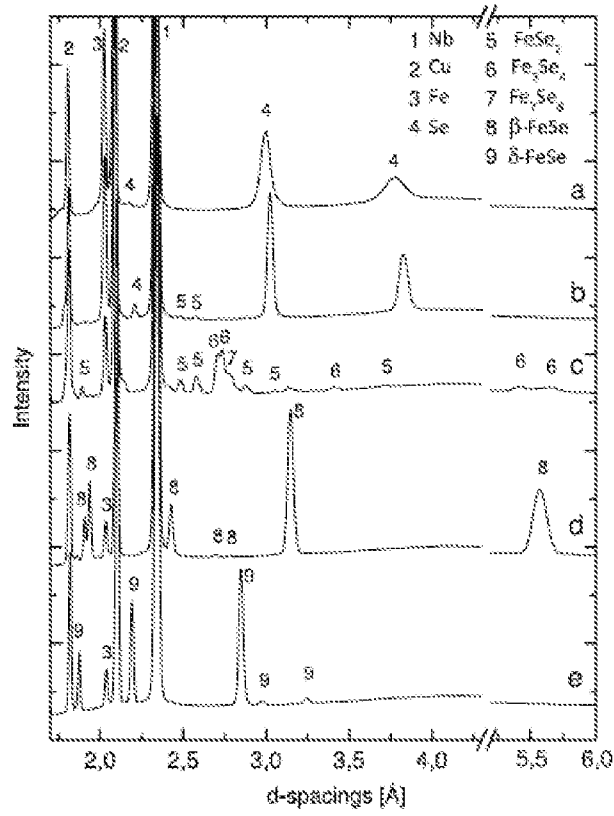


Figure 1

2/12

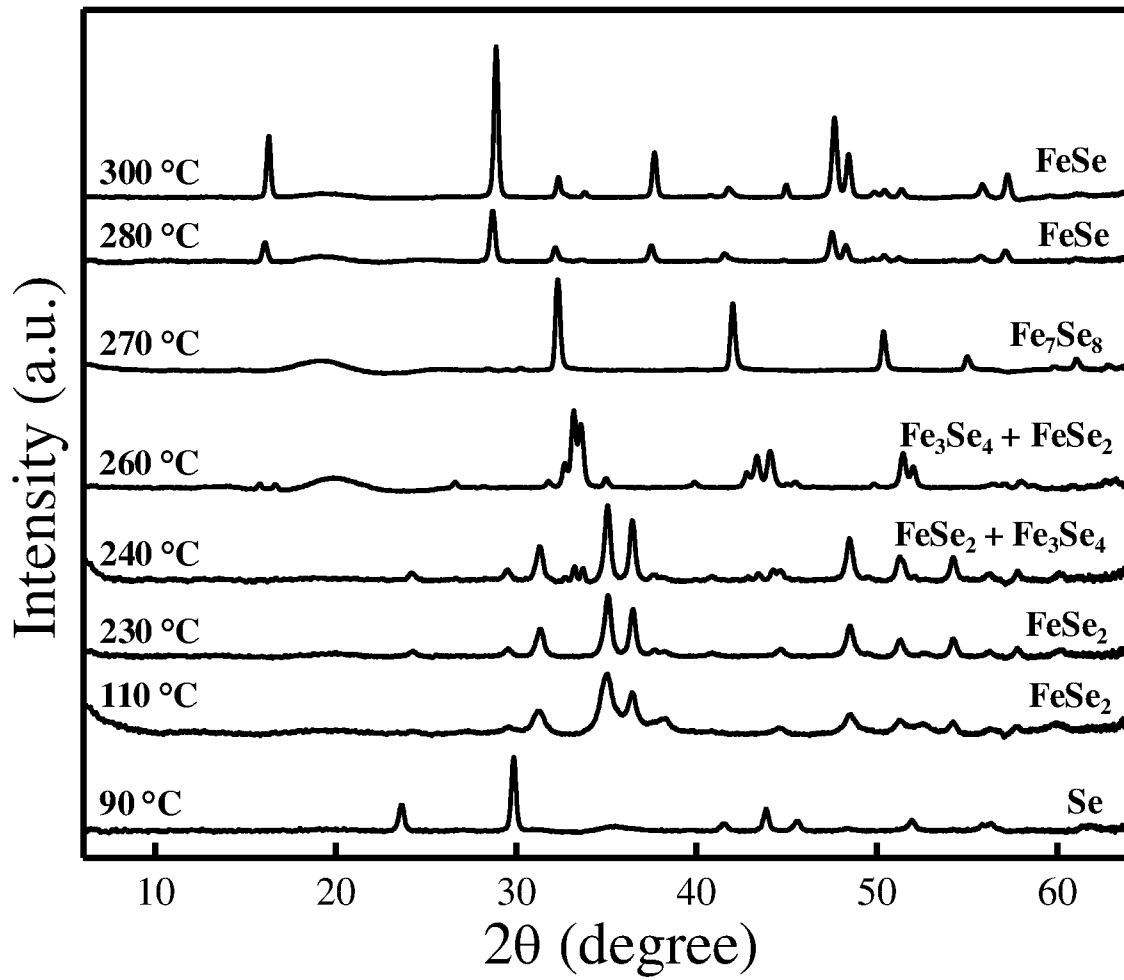


Figure 2

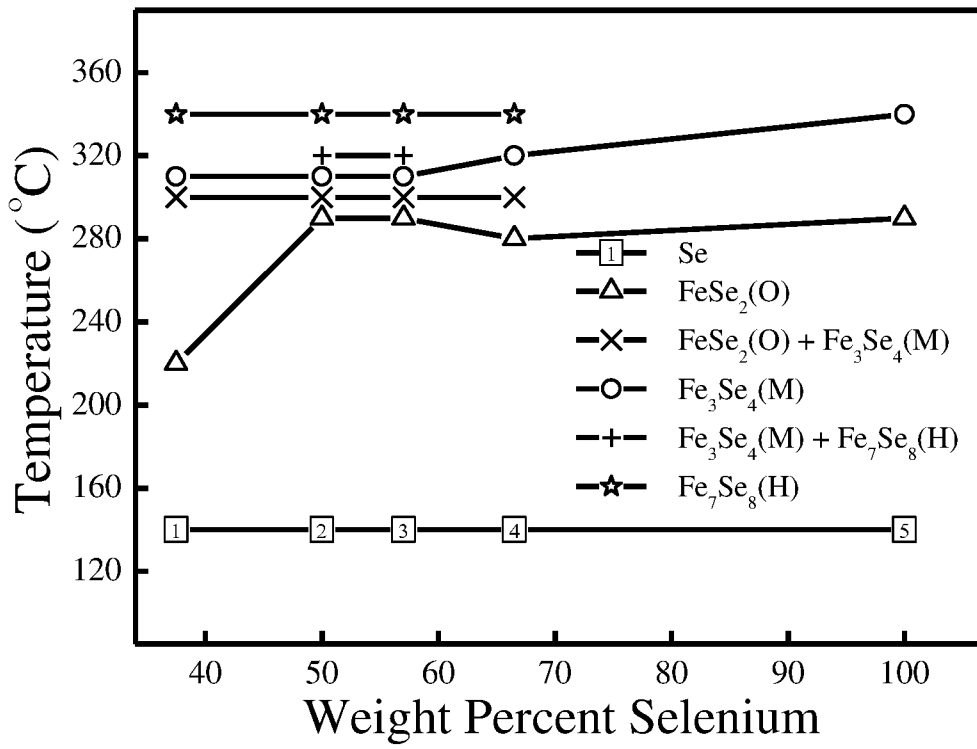


Figure 3

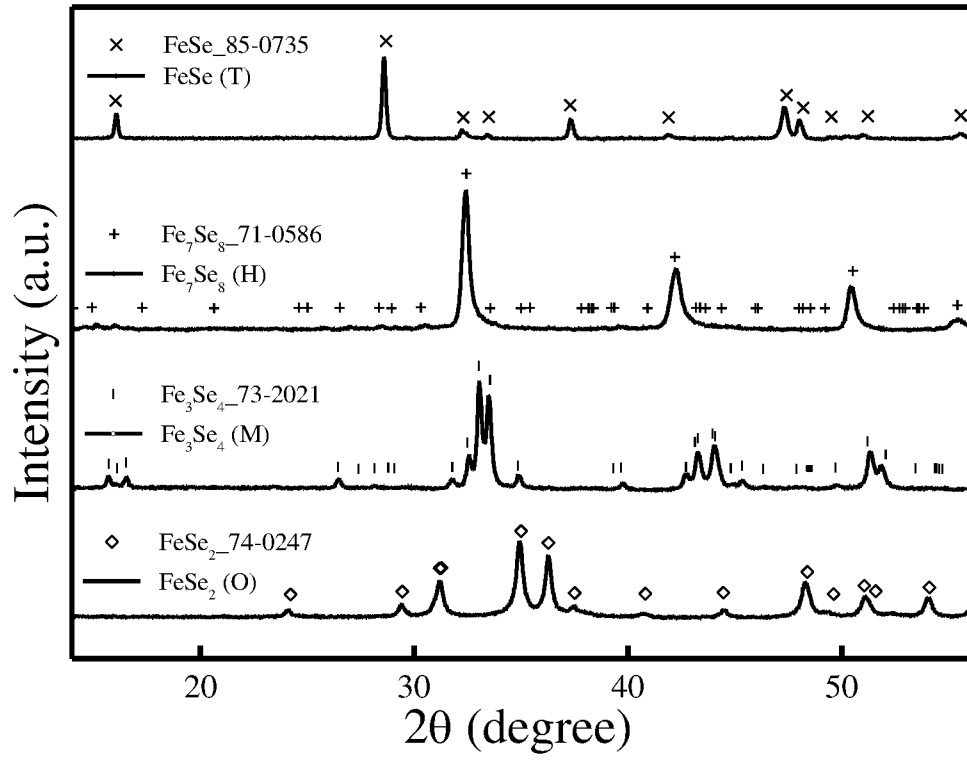


Figure 4

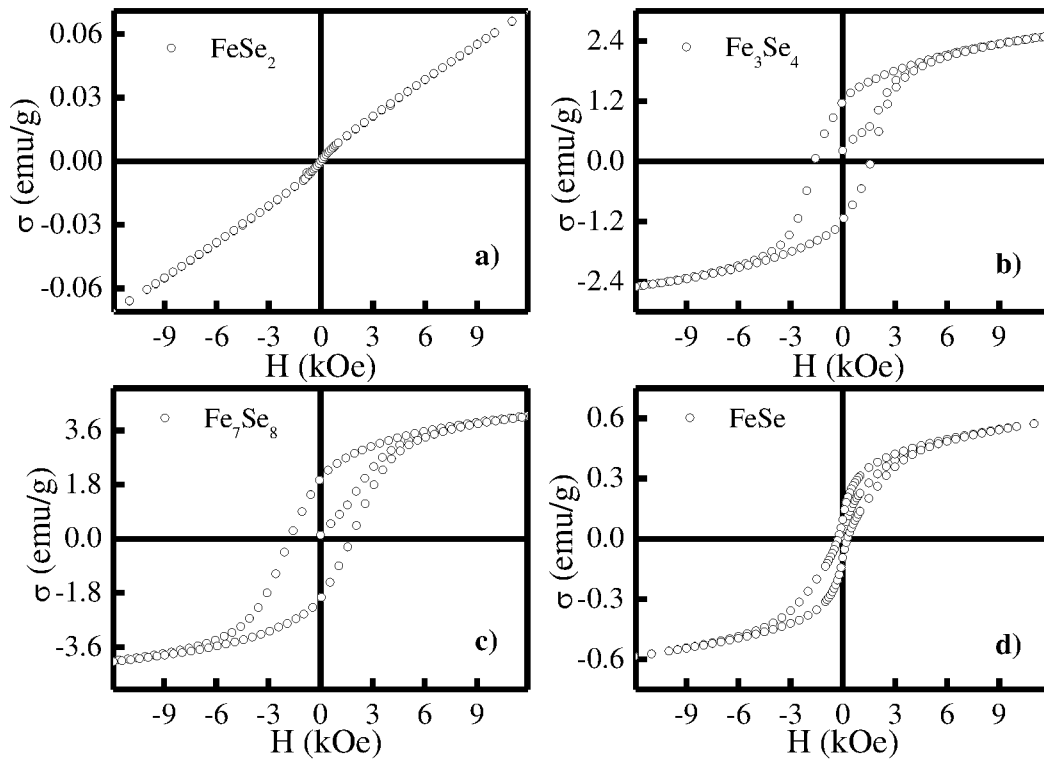


Figure 5

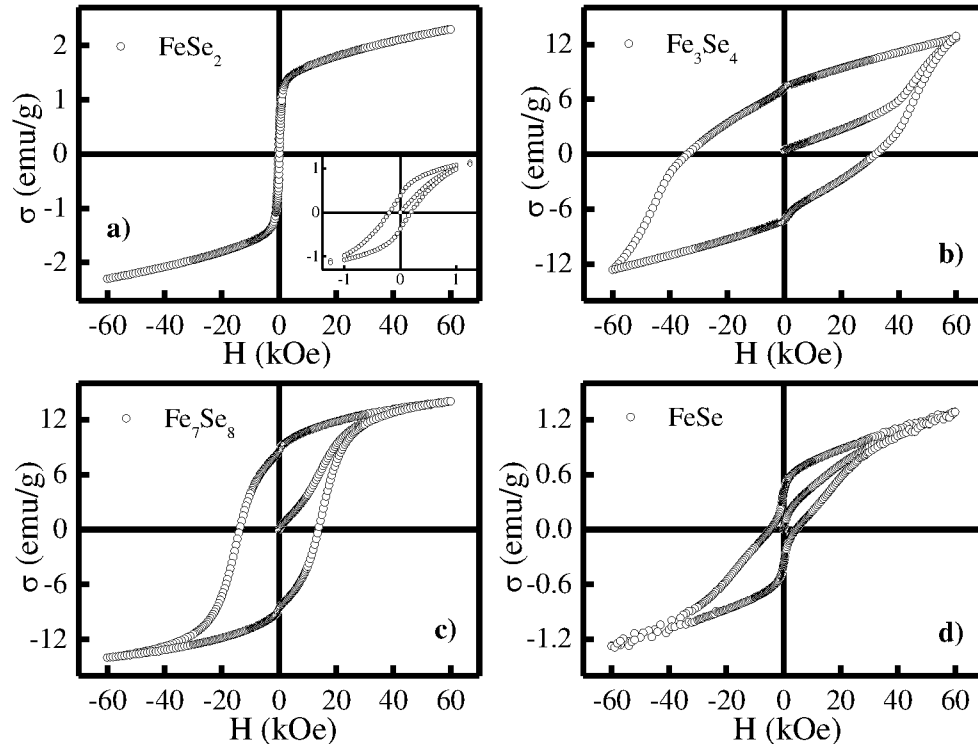


Figure 6

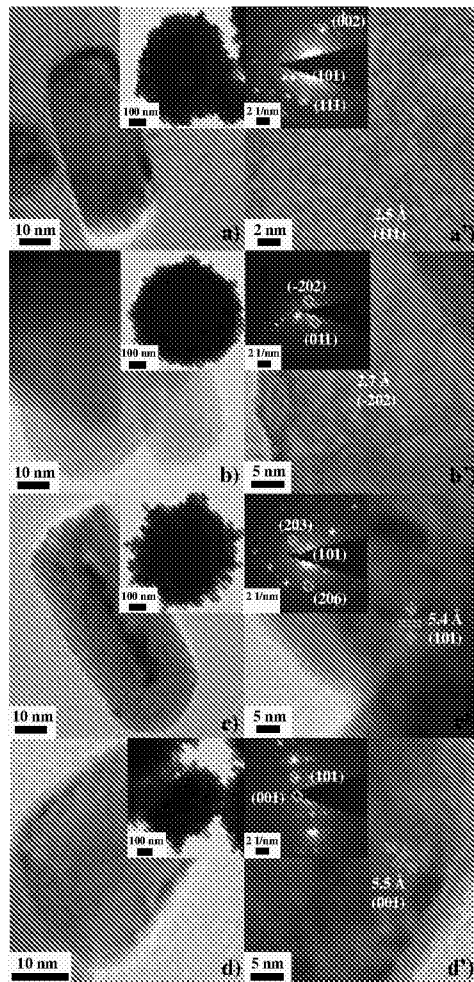


Figure 7

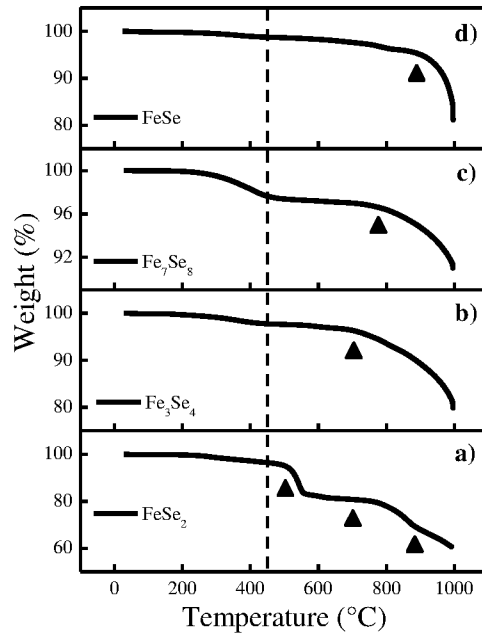


Figure 8

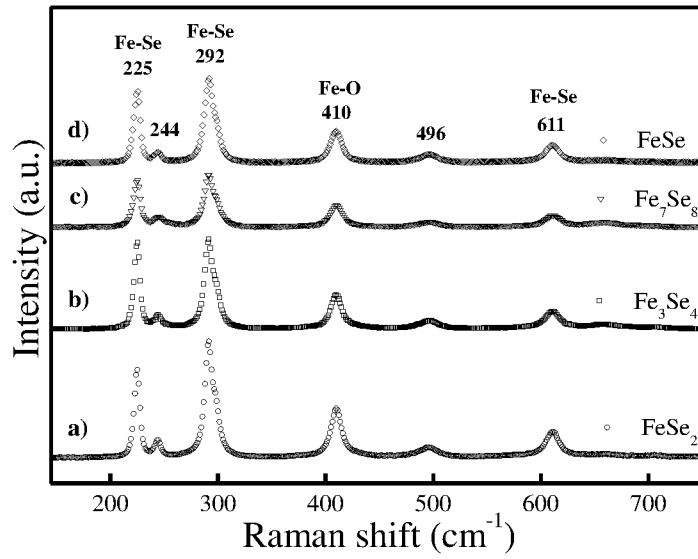


Figure 9



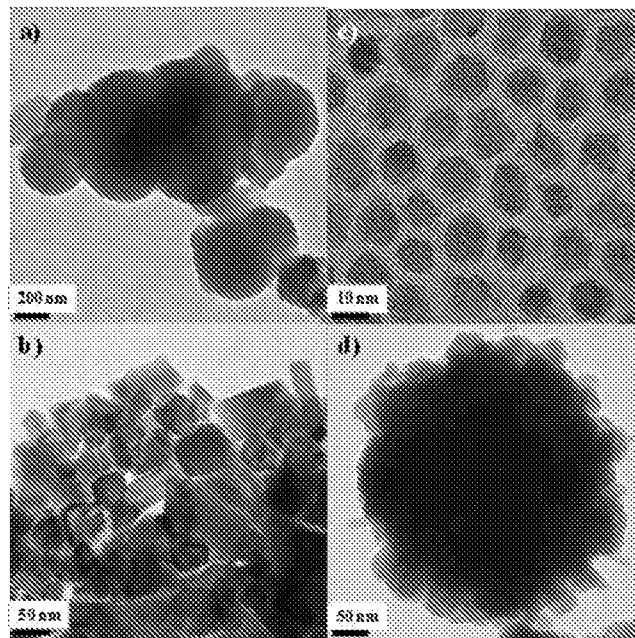


Figure 10

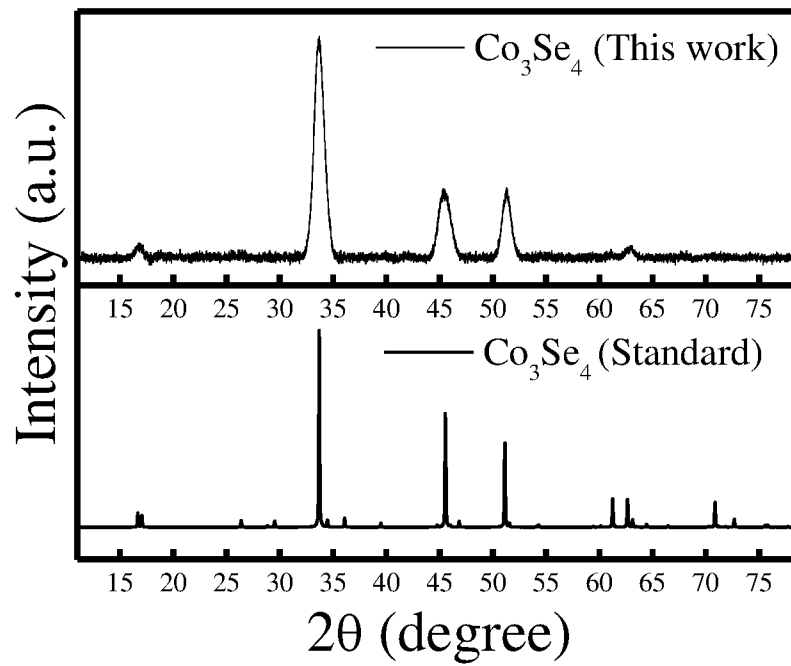


Figure 11

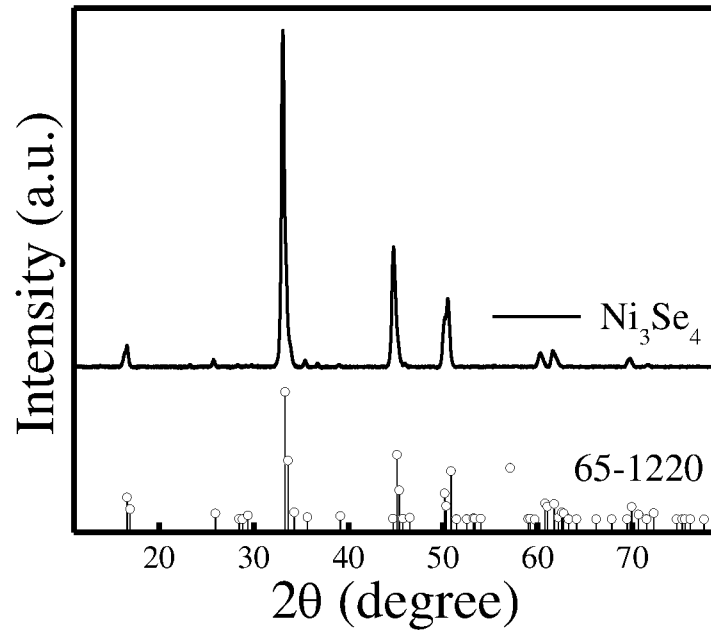


Figure 12

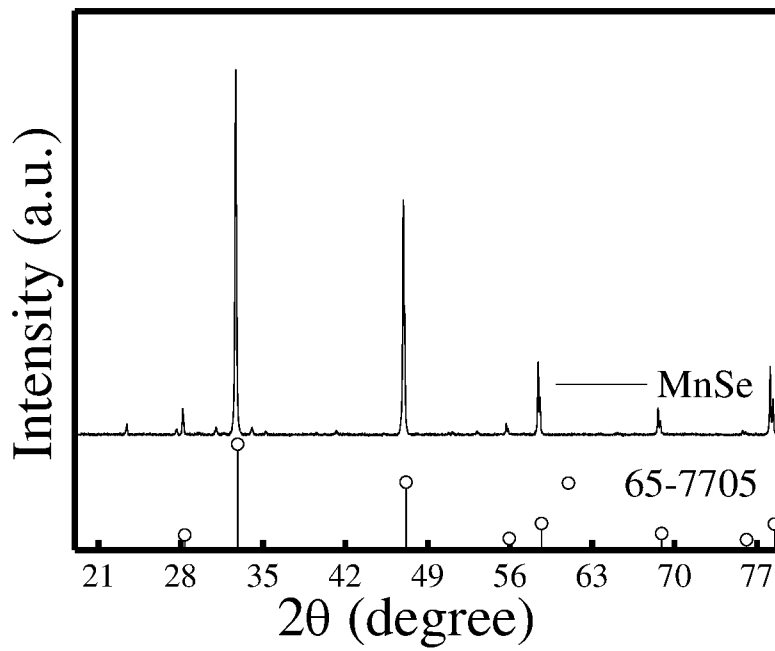


Figure 13

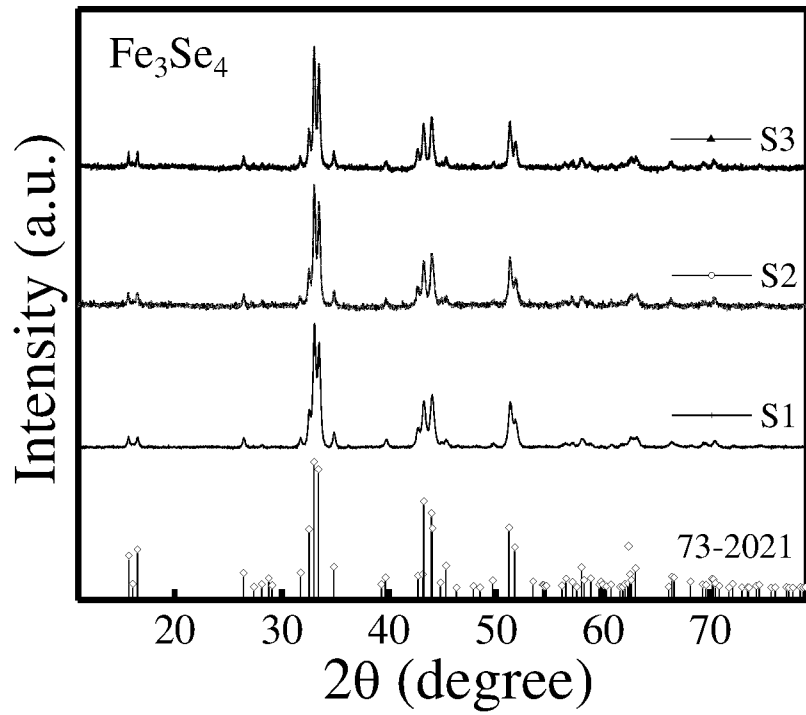


Figure 14

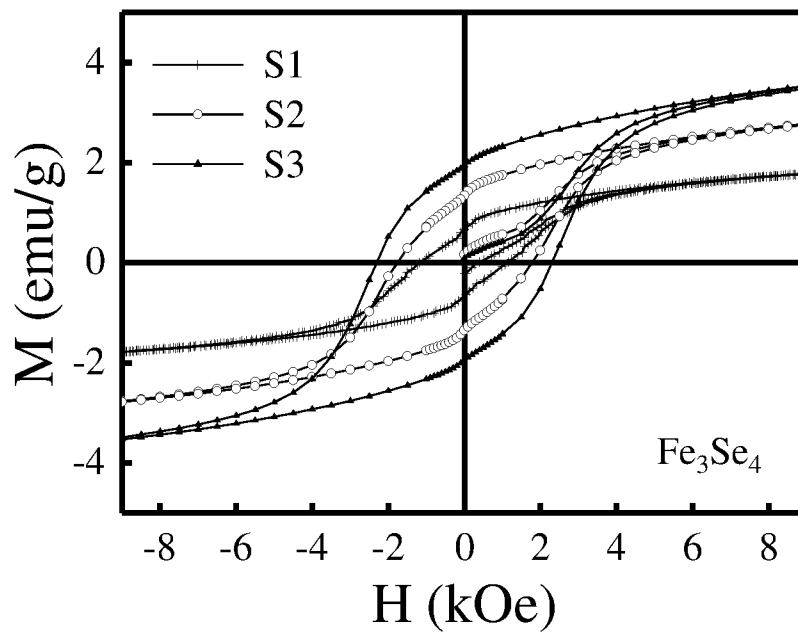


Figure 15

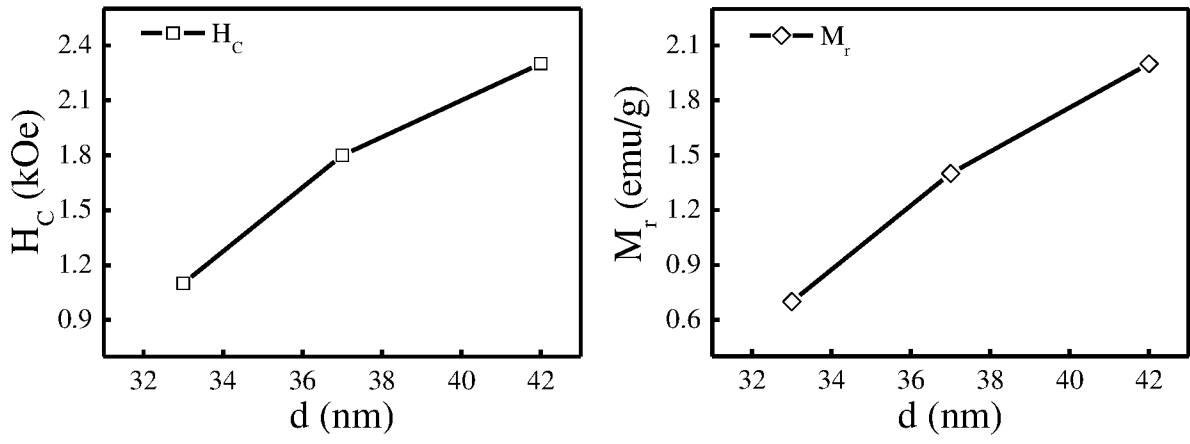


Figure 16

## INTERNATIONAL SEARCH REPORT

International application No.  
PCT/IN2020/050374

A. CLASSIFICATION OF SUBJECT MATTER C01G1/12 Version=2020.01		
According to International Patent Classification (IPC) or to both national classification and IPC		
B. FIELDS SEARCHED		
Minimum documentation searched (classification system followed by classification symbols)  C01G		
Documentation searched other than minimum documentation to the extent that such documents are included in the fields searched		
Electronic data base consulted during the international search (name of data base and, where practicable, search terms used)  TotalPatent One, IPO Internal Database		
C. DOCUMENTS CONSIDERED TO BE RELEVANT		
Category*	Citation of document, with indication, where appropriate, of the relevant passages	Relevant to claim No.
A	EP 1874686 A2 (YEDA RES & DEV) 09 January 2008 (09/01/2008) Abstract, Claims 1-30	1-10
A	US 2007111319 A1 (CENTRE NATIONAL DE LA RECHERCHE SCIENTIFIQUE) 17 May 2007 (17/05/2007) Claims 1-15	1-10
<input type="checkbox"/> Further documents are listed in the continuation of Box C. <input checked="" type="checkbox"/> See patent family annex.		
* Special categories of cited documents: "A" document defining the general state of the art which is not considered to be of particular relevance "D" document cited by the applicant in the international application "E" earlier application or patent but published on or after the international filing date "L" document which may throw doubts on priority claim(s) or which is cited to establish the publication date of another citation or other special reason (as specified) "O" document referring to an oral disclosure, use, exhibition or other means "P" document published prior to the international filing date but later than the priority date claimed "T" later document published after the international filing date or priority date and not in conflict with the application but cited to understand the principle or theory underlying the invention "X" document of particular relevance; the claimed invention cannot be considered novel or cannot be considered to involve an inventive step when the document is taken alone "Y" document of particular relevance; the claimed invention cannot be considered to involve an inventive step when the document is combined with one or more other such documents, such combination being obvious to a person skilled in the art "&" document member of the same patent family		
Date of the actual completion of the international search  21-08-2020		Date of mailing of the international search report  21-08-2020
Name and mailing address of the ISA/ Indian Patent Office Plot No.32, Sector 14, Dwarka, New Delhi-110075 Facsimile No.		Authorized officer Amar Nath Tripathi Telephone No. +91-1125300200

**INTERNATIONAL SEARCH REPORT**  
Information on patent family members

International application No.  
PCT/IN2020/050374

Citation	Pub.Date	Family	Pub.Date
EP 1874686 A2	09-01-2008	US 2008170984 A1	17-07-2008
		WO 2006106517 A2	12-10-2006
US 2007111319 A1	17-05-2007	EP 1689680 A2	16-08-2006
		WO 2005056479 A2	23-06-2005